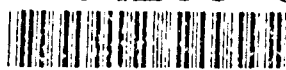


THE JOHNS HOPKINS STUDIES IN EARTH AND SPACE SCIENCES

AD-A263 094



DIRECTIONAL OCEAN WAVE SPECTRA

Edited by Robert C. Beal



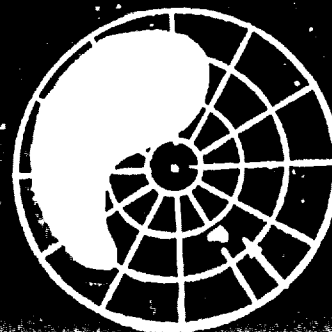
Reproduced From
Best Available Copy

THIS DOCUMENT CONTAINS
UNCLASSIFIED INFORMATION
EXCEPT WHERE SHOWN
OTHERWISE

APR 18 1993


DISTRIBUTION STATEMENT

Approved for public release
Distribution Unlimited



*DIRECTIONAL
OCEAN
WAVE
SPECTRA*

93 4 15 008

93-07859


The Johns Hopkins Studies in Earth and Space Sciences

Series Editors

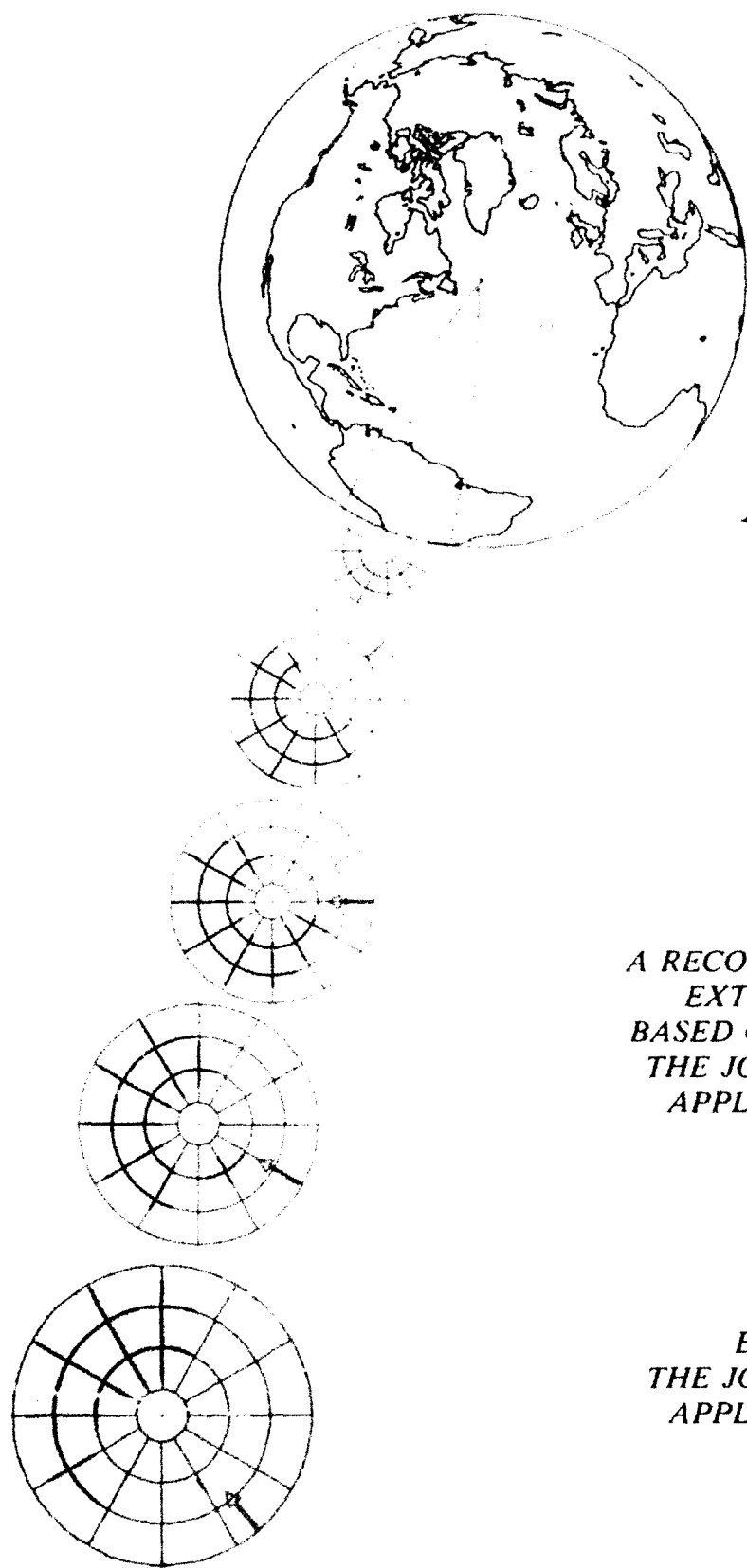
Owen M. Phillips, The Johns Hopkins University
Steven M. Stanley, Case Western Reserve University
Darrell F. Strobel, The Johns Hopkins University

The Johns Hopkins Studies in Earth and Space Sciences is a series for the publication of monographic and mutiauthored works that advance research and teaching in all disciplines of the Earth, planetary, and space sciences. Proposals and manuscripts may be submitted to either the Press or the Series Editors.

Published in the Series

Handbook of Paleozoology, Emil Kurt-Schnyder and Hans Reiber, translated by Emil Kucera

Magnetotail Physics, edited by Anthony T. Y. Lui



*MEASURING
MODELING
PREDICTING
AND APPLYING*

*DIRECTIONAL
OCEAN
WAVE
SPECTRA*

*A RECORD OF THE LABRADOR SEA
EXTREME WAVES EXPERIMENT
BASED ON A SYMPOSIUM HELD AT
THE JOHNS HOPKINS UNIVERSITY
APPLIED PHYSICS LABORATORY
APRIL 18-20, 1989*

*EDITED BY ROBERT C. BEAL
THE JOHNS HOPKINS UNIVERSITY
APPLIED PHYSICS LABORATORY*

*THE JOHNS HOPKINS UNIVERSITY PRESS
Baltimore and London*

DTIC QUALITY INSPECTED 4

Accession For	
NTIS GRA&I	<input checked="" type="checkbox"/>
DTIC TAB	<input type="checkbox"/>
Unannounced	<input type="checkbox"/>
Justification	
Available from	
By Price: HC \$65.00	
Distribution/	
Availability Codes	
Dist	Avail and/or Special
A-1	21

© 1991 The Johns Hopkins University Press
All rights reserved
Printed in the United States of America

Copyright protection does not apply to the papers by Bales, Duffy, Esteva & Chao, Foley & Bachman, Jackson, Walsh, and Wittmann & Clancy, which are works of the U.S. government; the papers by Dobson & Toulany, Keeley, Nethercote, Perrie & Toulany, Raney & Vachon, and Vachon et al., which are works of the Canadian government; the paper by Rider & Stratton, which is a work of the British government; the papers by Ezraty and Guillaume, which are works of the French government; the papers by Janssen and de Jong & Vermeij, which are works of the Dutch government, and the paper by Zambresky, which is a work of a European consortium. Each of these governments may also retain certain copyrights for its use on work performed under its sponsorship.

The Johns Hopkins University Press
701 West 40th Street
Baltimore, Maryland 21211-2190
The Johns Hopkins Press Ltd., London

The paper used in this book meets the minimum requirements of American National Standard for Information Sciences—Permanence of Paper for Printed Library Materials, ANSI Z39.48-1984.

Library of Congress Cataloging-in-Publication Data

Directional ocean wave spectra: measuring, modeling, predicting, and applying/edited by Robert C. Beal.

p. cm.—(The Johns Hopkins studies in Earth and space sciences)

“A record of the Labrador Sea Extreme Waves Experiment based on a symposium held at The Johns Hopkins University Applied Physics Laboratory April 18-20, 1989.”

Includes bibliographical references and index.

ISBN 0-8018-4261-1 (alk. paper)

- I. Ocean waves—Labrador Sea—Congresses. I. Beal, Robert C.
- II. Johns Hopkins University. Applied Physics Laboratory.
- III. Series.

GC214.L33D57 1991

551.47'02'0916343—dc20

91-16779

Contents

ix	To Blair Kinsman	<i>O. M. Phillips</i>
xi	Preface	
xiii	Acknowledgments	
xv	Editor's Notes	
INTRODUCTORY OVERVIEWS		
2	LEWEX: Motivation, Objectives, and Results	<i>R. C. Beal</i>
13	The Practical Value of Directional Ocean Wave Spectra	<i>S. P. Kjeldsen</i>
WIND-WAVE PHYSICS		
22	On the Wind-Wave Coupling Problem	<i>F. Dobson and B. Toulany</i>
30	Wind Data and the Marine Boundary Layer	<i>W. J. Pierson, Jr.</i>
34	Marine Wind Variability: Illustration and Comments	<i>R. S. Fzraty</i>
39	On the Directional Behavior of the Equilibrium Wave Number Spectrum: Implications for the Equilibrium Frequency Spectrum	<i>M. L. Banner</i>
46	On Nonlinear Wave Groups and Consequences for Spectral Evolution	<i>P. A. E. M. Janssen</i>
SEAKEEPING AND SURFACE MEASUREMENTS		
54	Some Comments on the Significance of LEWEX for Ship Design and Operations	<i>S. L. Bales</i>
55	The CFAV <i>Quest</i> 's LEWEX Experience	<i>W. C. E. Nethercote</i>
61	HNLMS <i>Tydeman</i> 's LEWEX Experience and Motion Simulation in Multimodal Seas	<i>J. H. de Jong and P. Vermeij</i>
66	Reliability and Resolution of Directional Wave Spectra from Heave, Pitch, and Roll Data Buoys	<i>H. E. Krogstad</i>
72	Directional Spectra from the Moored Datawell Wavec Buoy during LEWEX	<i>J. R. Keeley</i>
76	Directional Spectra from the Drifting Endeco Wavetrack Buoy during LEWEX	<i>E. W. Foley and R. J. Bachman</i>
80	Directional Spectra from Shipboard Navigation Radar during LEWEX	<i>F. Ziemer</i>
AIR AND SPACE MEASUREMENTS		
86	Surface Contour Radar Directional Wave Spectra Measurements during LEWEX	<i>E. J. Walsh</i>
91	Directional Spectra from the Radar Ocean Wave Spectrometer during LEWEX	<i>F. C. Jackson</i>
98	SAR Imaging of Ocean Waves: Some Observations from LIMEX/LEWEX '87	<i>R. K. Raney and P. W. Vachon</i>
104	Directional Spectra from the CCRS C-Band SAR during LEWEX	<i>P. W. Vachon, A. S. Bhogal, and N. G. Freeman</i>
110	SAR Scattering Mechanisms as Inferred from LEWEX Spectral Intercomparisons	<i>D. G. Tilley</i>
117	Interpretation and Application of SAR Wave Image Spectra in Wave Models	<i>K. Hasselmann, S. Hasselmann, C. Bruning, and A. Speidel</i>
125	Removal of 180° Ambiguity in SAR Images of Ocean Waves	<i>W. Rosenthal and F. Ziemer</i>
128	Geosat Wind and Wave Measurements during LEWEX	<i>E. B. Dobson and S. P. Chaykovsky</i>

NUMERICAL MODEL ESTIMATES

- 136 The LEWEX Wind Fields and Baseline Hindcast *V. J. Cardone*
- 147 Predictions from the GSOWM during LEWEX *P. A. Wittmann and R. M. Clancy*
- 152 Directional Spectra from the UKMO Hindcasts and the Effect of Swell from Outside the LEWEX Region *K. M. Rider and R. A. Stratton*
- 158 Results Obtained with the Wave Model VAG during LEWEX *A. Guillaume*
- 163 The NOAA Ocean Wave Model Hindcast for LEWEX *D. C. Esteva and Y. Y. Chao*
- 167 An Evaluation of Two WAM Hindcasts for LEWEX *L. F. Zambresky*
- 173 Directional Spectra from the BIO Hindcast during LEWEX: The Wave-Ice Interaction *W. Perrie and B. Toulans*
- 177 The Application of NASA's Third-Generation Wave Model to LEWEX *D. G. Duffy*
- 182 A Comparative Anatomy of the LEWEX Wave Systems *J. W. Gerling*

FUTURE DIRECTIONS

- 196 Research Needs for Better Wave Forecasting: LEWEX Panel Discussion *M. Donelan (Chair)*
- 205 Epilogue: Waves, Dreams, and Visions *K. Hasselmann*
- 209 NOTES ON CONTRIBUTORS
- 213 LEWEX PARTICIPATING ORGANIZATIONS
- 215 INDEX

TO BLAIR KINSMAN

Blair Kinsman died on 2 November 1989, and this record of the Labrador Sea Extreme Waves Experiment (LEWEX) is dedicated to his memory—most appropriately, for LEWEX was devoted to precisely those questions that occupied Blair throughout his scientific career.

He was born on 21 December 1914, graduated from the University of Chicago in 1938, and taught in secondary schools and at St. John's College in Annapolis, Maryland, for thirteen years. Both Robert Hutchins's University of Chicago and the "great books" program at Annapolis were to leave a lasting impression on him. He joined Don Pritchard at Johns Hopkins Chesapeake Bay Institute in 1951 and received his M.A. from Hopkins in 1953. I came to Hopkins five years later, and, drawn together by our mutual interest in waves, we quickly became friends. His Ph.D. thesis in 1960 described a meticulous study of wave spectra in an enclosed sub-estuary of the Chesapeake Bay and showed his great attention to detail, his concern to do things right, and his engaging literacy that flowered in his monumental book (I use the adjective with care), which was published five years later. He served on the faculty of Hopkins but left in 1966 to become a Professor of Oceanography at the University of Delaware; subsequently, he was a Visiting Professor at the State University of New York, Stony Brook, and at the University of Mexico.

Wind Waves: Their Generation and Propagation on the Ocean Surface is indeed Blair's monument, just as St. Paul's Cathedral is Christopher Wren's. Literate and eclectic, it is known to oceanographers throughout the world. Students approaching the subject have found illumination in its perspective, pleasure in its informality and style, and an example in its awareness and careful examination of complex issues. The book is, in jargon that Blair would dislike, user friendly. It gives all the

mathematical steps in a derivation, as well as the nitty-gritty of how to measure a spectrum, calculate its confidence level, and determine what it means. Discursive, perhaps even prolix to some, it stands as a delightful foil to that other book on upper ocean dynamics that appeared about the same time. The book's footnotes are a particular pleasure. On the Sverdrup-Munk model: "Be warned. What follows is entirely inadequate to account for the generation of wind waves. It represents the state of the art in 1942." The footnote on instrumental calibration digresses through physical standards, mathematical axioms, Euclid, and Gauss. Blair never really thought of

himself as an oceanographer, but as a "waves man" and primarily as a teacher; he dedicated his book to his students, and through it, he had students the world over.

We spent many Thanksgivings together at his home by the water in Riva, Maryland—my young family with him, his wife Dottie, his daughter Lisa, and their boat *Snark*. He was a delightful raconteur. He loved words—many times we browsed through Fowler's *Modern English Usage* to clarify a fine distinction in meaning or to enjoy Fowler's pedantry. He loved his students—he spent endless hours with them, and they were his pride.

He loved waves, and he would have been delighted to see the enormous strides in spectral measurement techniques,

physical understanding, and wave modeling made in LEWEX. We have come a long way since Bill Pierson's pioneering Stereo Wave Observation Project (SWOP), but LEWEX is a direct descendant. In Blair's discussion of the two-dimensional wave spectrum, SWOP was all that he had to go on. With LEWEX, we have an enormously greater base of data, wealth of detail, and range of questions; I hope that we "waves people" can do proportionately as well as Blair did. As this volume depicts vividly, we still have some way to go.

Owen M. Phillips



Blair Kinsman (1914–1989)

PREFACE

More than 30 years ago, the National Academy of Sciences and the U.S. Navy sponsored the first conference of substance on the nature of the ocean wave spectrum.* Many of the leading thinkers of the day converged to share ideas on the behavior of wind-driven ocean surface waves. Several of the fundamental questions raised then remain still unanswered. The spatial and temporal behavior of the vector wind and wave fields is perhaps not much better known today than it was then.

Progress has been more evident on other fronts. Thirty years ago, temporal wave records were yielding to one-dimensional height spectra, but full two-dimensional (directional) spectral plots were still rare. Since then, numerical wind-wave modeling techniques have progressed through three generations of development. Many institutions now routinely produce forecasts of spatially and temporally evolving directional ocean wave height spectra.

Roughly in parallel with the model development, instruments to estimate the directional spectrum have proliferated. Microwave remote sensing methods give the promise for all-weather, 24-hour global monitoring of the directional spectrum from satellites. Although it is certainly not the only technique practical from space, synthetic aperture radar (SAR) has been the one most thoroughly explored during the past decade. With the expectation of several orbiting scientific SAR missions in the 1990s (at least one each from the Soviet Union, Western Europe, Japan, Canada, and the United States), this exploration will probably accelerate.

In spite of this impressive international commitment, the specific role of spaceborne SAR in a practical wave forecasting scheme has yet to be precisely defined and demonstrated. SAR ocean wave monitoring performance will be artificially constrained by the higher platform altitudes because of excessive Doppler smearing. Of all the extended SAR missions for the 1990s, only the Soviet Almaz series, at an altitude of 300 km, appears to have the potential to overcome the fundamental Doppler smearing effect caused by the motion of the waves and exacerbated by the higher-altitude orbits.

When the platform altitude problem is resolved, there remains the question of how best to assimilate the SAR-derived spectra into global models. Moreover, these global wave models will themselves be guided by sparsely sampled satellite wind estimates. The problem is analogous to estimating global circulation with a satellite altimeter. The longer spatial and temporal scales of the fields will become clear enough, but the shorter ones, particularly those normal to the satellite tracks, will remain insufficiently sampled. The boundary between the two will be determined by the ingenuity of the assimilation scheme.

Fundamentally, however, this much seems clear: the directional wave spectrum can be estimated in the future only to the extent that it can be measured in the present. Furthermore, because the ocean is not adequately described by a single parameter such as significant wave height, global estimates of only significant wave height will not suffice. The present description of the sea surface will improve only if what is predicted globally is also measured globally.

In April 1989, APL hosted a symposium entitled "Measuring, Modeling, Predicting, and Applying Directional Ocean Wave Spectra." The symposium was based largely on results from an international waves experiment conducted in the Labrador Sea during March 1987. The Labrador Sea Extreme Waves Experiment, known as LEWEX, involved participants from eight countries (Canada, the Federal Republic of Germany, France, The Netherlands, Norway, Spain, the United Kingdom, and the United States). LEWEX produced

**Ocean Wave Spectra*, National Academy of Sciences, Prentice Hall, Englewood Cliffs, N.J. (1963).

a unique and unprecedented set of more than 2000 estimates of the directional wave spectrum, all displayed in a common format.

That symposium led to the series of papers in this volume. The papers cover four complementary themes in wind-wave physics, seakeeping and surface measurements, aircraft and spacecraft measurements, and numerical model estimates. These four major themes are framed by two introductory overview articles and two concluding articles addressing both the needs and aspirations of future research. Of the more than 2000 estimates of directional wave spectra gathered during LEWEX, over 300 are presented and compared. The result, I believe, is a broad, internationally based case for the uncompromising, continual global collection of directional ocean wave spectra.

Robert C. Beal

ACKNOWLEDGMENTS

The successful execution of LEWEX was possible only because of the splendid degree of cooperation among all of its participants. No single sponsor and no single country or organization dominated. It was, in many respects, a "grass-roots" affair, made possible by many individual efforts. Among them, Nelson Freeman of the Canada Department of Fisheries and Oceans negotiated the aircraft arrangements at Gander and coordinated the Canadian participation; Susan Bales, then of the David Taylor Research Center, coordinated and planned the NATO participation; Susan Argus, then of the Canadian Radar-sat Office, smoothed many potential resource conflicts with the Labrador Ice Margin Experiment (IIMEX); Ken Asmus of the Canada Atmospheric Environmental Service provided vital land-to-sea communications support at Gander; Chuck Livingstone of the Canada Centre for Remote Sensing labored to have the "shuttle-substitute" CV-580 aircraft SAR ready; and the crews of the two research vessels (HNLMS *Tyeman* and CFAV *Quest*) and the two research aircraft (the Canadian CV-580 and the NASA P-3) mustered all the resources to the right place at the right time, in spite of the weather.

The later transformation of spectral estimates from many diverse sources (each having its own convention on wave number or frequency bins, definition of north, wind and wave propagation direction, and spectral energy units) into a set of common formats was one of the more substantial contributions of LEWEX, and one that makes this collection of spectral comparisons unique. For this, I am grateful to Tom Gerling of the Applied Physics Laboratory, who handled the problem with great facility and even greater perseverance. The LEWEX participants have been magnanimous in sharing data and in allowing their results to be displayed and distributed in common formats, without restriction. This open philosophy did much to foster and sustain the cooperative spirit that was necessary for LEWEX to succeed.

The publication of this volume is the result of the commitment and dedication of several individuals. The editorial and graphics sections of the Applied Physics Laboratory clarified and greatly improved much of the text and graphics. They are responsible for the clean, well-balanced format and for the practical use of color that have helped make this volume a special contribution. I am especially indebted to Karen Belton for the overall editing coordination, to Jack Mothershead for the graphics and layout, and to Patrice Zurvalec for typesetting the text.

I am grateful to my institution, the Applied Physics Laboratory, for providing the professional environment and technical support that made this work possible. Financial support from the U.S. Navy Space and Naval Warfare Systems Command, the Office of the Oceanographer of the Navy, and NASA Headquarters partially underwrote the costs of publication so that this work could reach the widest possible audience.

EDITOR'S NOTES

It has not been practical to impose a universal set of symbols throughout the volume. Too much heritage is associated with each of the various disciplines represented here. As a compromise, each author has defined terms and symbols as if his paper were autonomous, thus allaying if not completely eliminating confusion.

Arriving at an acceptable convention for wave direction evoked the most discussion. Mariners describe waves in terms of their source direction. Most modelers and theoreticians think of (or at least plot) waves in terms of their propagation direction. To further complicate the matter, a propagation direction of 0° is not universally interpreted as to-the-north; sometimes it means to-the-east.

In this volume, unless otherwise stated, directional ocean wave spectra are displayed with north vertical and with the spectral energy shown in the direction of propagation. Exceptions to this rule occur in the seakeeping papers, in which a ship heading of 0° means "into head seas," and associated spectra are similarly plotted "in the direction from." Exceptions are always so noted in the caption. Unless otherwise explicitly stated, individual narratives still use the mariner's description: southerly (from the south) winds are those that produce southerly (from the south) waves.

There are many choices to be made in plotting directional ocean wave energy spectra. In this volume, the preferred format is generally linear wave number in units of rad/m plotted radially, and spectral energy density in units of m^4 plotted in equally spaced contours. This linear-linear combination permits a direct intuitive association of volume in the plot with total wave energy in units of m^2 . Unfortunately, this fully linear plot is a poor choice to display multiple wave energy modes that differ substantially in peak spectral energy density. Narrow but energetic swell can completely obscure an equally energetic wind sea in such a display. The common answer to this problem is a log-log display of both quantities, effectively relinquishing the straightforward energy association in favor of increased dynamic range. Examples of both plots exist in this volume, with appropriate description in the captions.

In a few instances, some variant of the wave energy spectrum is used. For example, the use of a slope spectrum enhances the displayed wave activity at the longer wave numbers, where much of the interesting dynamics often occurs. Spectra from the NASA airborne sensors (surface contour radar and radar ocean wave spectrometer) are often displayed in m^3/rad , a compromise that slightly enhances the activity at high wave numbers.

Insofar as knowledge of the instrument or model transfer function permits, all spectral comparisons in any given figure in this volume are displayed in equivalent formats. The range of wavelengths of interest is generally that which is believed to be assessable with a spaceborne SAR with favorable geometry, that is, from 50 or 100 m to 800 m. This range, incidentally, also well represents the energy-containing wave numbers to be found in wind-generated waves in the open ocean.

INTRODUCTORY OVERVIEWS

*IN WHICH THE VARIOUS FACETS OF LEWEX ARE
SUMMARIZED, AND A CASE IS MADE FOR
IMPROVED GLOBAL ESTIMATES OF THE
DIRECTIONAL OCEAN WAVE SPECTRUM*

LEWEX: MOTIVATION, OBJECTIVES, AND RESULTS

This overview article outlines the major events that led up to the Labrador Sea Extreme Waves Experiment, describes its international multidisciplinary scope, and summarizes the major results.

INTRODUCTION

In early March 1987, ocean researchers from eight North American and European countries converged on a pair of sites in the southern Labrador Sea to explore methods for measuring, predicting, and applying directional ocean wave spectra. The researchers were supported by ship, aircraft, and satellite estimates of wind and waves, further complemented by a number of numerical wave model estimates. From the surface, the Canadian research vessel CFAV *Quest*, and the Dutch research vessel HNLMS *Tydeman*, used wave buoys and their navigation radars. From the air, a Canadian CV-580 aircraft and a NASA P-3 aircraft employed radar remote sensors. From space, the U.S. oceanographic satellite Geosat monitored wind speed and wave height with its precision radar altimeter. The two ships used both moored and drifting directional buoys, the NASA P-3 used both a surface contour radar (SCR) and a radar ocean wave spectrometer (ROWS), and the Canadian CV-580 used a C-band synthetic aperture radar (SAR), generally at two altitudes (or two range-to-velocity ratios).

Each of six agencies used numerical models and its own (or others') estimates of the wind field to hindcast (i.e., forecast after the fact) directional spectra at the ship positions, and nine agencies (including the first six) later used a common wind field to generate a second set of hindcasts to expose even subtle differences among the various models. Over a seven-day interval (from 1200 UT on 12 March to 1200 UT on 19 March), about 2000 spectral estimates were produced, with as many as twenty-five nearly simultaneous and coincident estimates at each of the two ship locations (four from the ship, six from the aircraft, six from models using separate winds, and nine from models using common winds).

This comprehensive set of evolving directional spectra, all processed and displayed in a common format, is unique and unprecedented. Not surprisingly, no set of spectral estimates from a single source is identical to that from any other source. These disparities among the spectral comparisons have provoked valuable controversy on the source wind fields, the surface spectral estimates, the aircraft spectral estimates, and the wave model spectral estimates. The following articles in this volume present and elaborate upon many of the disparities.

The comprehensive spectral intercomparison effort was named the Labrador Sea Extreme Waves Experiment (LEWEX). There was no single impetus for LEWEX, but the

momentum that sustained it is an indication of the international interest in improving ocean wave prediction. With improved wave models, guided by anticipated satellite directional wind estimates and verified by complementary satellite directional wave estimates, wave forecasting skill should also improve, but only if the satellite information is properly assimilated. In general, there will be biases, uncertainties, and undersampling. LEWEX has revealed that many of the biases and uncertainties reside in unexpected places.

MOTIVATION FOR LEWEX

Improved ocean wave predictions are important for ship guidance in coastal areas and along the major ocean routes. They are a necessary component of any serious attempt to improve safety at sea. For example, as Kjeldsen describes in the following article, Norway has a notorious problem to ensure ship safety all along its exposed western coast. Complex, multimodal seas are transformed by variable coastal currents and bathymetry to produce some especially hazardous regions along the coast. Knowledge of the multimodal seas (or more specifically, the directional energy spectrum) can be combined with specific vessel transfer functions to predict vessel motions, and to assign safety risk factors to the vessel as a function of time and location. The accuracy of these calculations, however, can be extremely sensitive to errors in the initial (deep-water, current-free) spectral estimate. Figure 1 shows an example of an open-ocean operation in which the vessel motion clearly creates a nuisance.

On a less immediate but ultimately more profound scale, an accurate description of the sea surface can help refine our knowledge and understanding of global climate dynamics. Large-scale ocean currents (e.g., the Gulf Stream, which acts as a conduit to transfer heat from equatorial to polar regions) are driven largely by the mean surface winds over the ocean. The atmosphere is coupled to the ocean through the surface drag; higher drag allows more efficient coupling. But the drag depends intimately on the properties of the surface waves. Short, steep, wind-driven ("young") waves offer much more drag than long, gentle ("old") swell for the same wind speed. Even though this wave-dependent aspect of drag is now commonly recognized (see the panel discussion in this volume), its behavior as a function of the underlying directional wave spectrum is still poorly understood. Consequently, none of the wave models at the major forecast centers incorporates a wave-dependent drag. This omission (even as-



Figure 1. A U.S. Navy ship refueling in moderate to heavy seas (Reprinted from Ref. 10.)

suming that all other things are perfect) likely results in substantial modeling errors in the initial stages of wave growth or in rapidly evolving winds. When these and other subtle but important effects are more clearly understood, the physics can be incorporated into numerical wave models. Such models, in turn, will become an essential component of the coupled ocean-atmosphere specification, and will lead to more accurate descriptions of many of the fluxes that influence global change. In the concluding article in this volume, Hasselmann further elaborates on the important role of improved wave models in global climate modeling.

These two major problems—the first operational and immediate, and the second scientific and long-term—helped shape LEWEX and influenced the composition of its participants. But another, equally central, issue was this: the prediction of future directional wave spectra is fundamentally limited by our ability to specify it in the present. In the open ocean, especially in high seas, no absolute or even primary standard exists for determining the directional wave spectrum, either by model or by measurement, either *in situ* or remotely. Consequently, LEWEX also became a search for consensus, for systematic anomalies, and for unexpected agreements. All three issues—safety at sea, climate dynamics, and the search for consensus—become most problematic in extreme (e.g., growing, high, multimodal) seas.

THE LEWEX INTEREST GROUPS

LEWEX was born from a chance union of three separate interest groups: numerical ocean wave modelers (mainly oceanographers and physicists), radar remote sensing scientists (mainly electrical engineers and radio scientists), and ship motion experts (mainly naval architects and hydrodynamic engineers). The three groups rarely have the chance to join in a common enterprise, but in 1987, special circumstances provided an unusual opportunity.

Ocean Wave Modelers

Quantitative schemes for predicting ocean waves through estimates of the time-space history of the surface

wind have been available since the early 1950s. The first ideas were largely empirical, based on ship observations. Nevertheless, they yielded rough estimates of the wave height and period. This primitive (but useful) empiricism yielded in the 1960s to the realization that the predictive problem was better characterized by a spectral evolution based on an energy balance of generation, dissipation, and wave-wave interaction terms. Since then, as physical insight has followed careful measurement, three generations of wave models have emerged, all having the common goal of predicting directional wave spectra in the open ocean from twelve hours to three or more days in advance. All three generations use finite difference schemes to grow, propagate, disperse, and dissipate the waves. The first differs fundamentally from the second and third in assumptions about the physics that shapes the equilibrium spectrum; in particular, second- and third-generation models incorporate a wave-wave interaction mechanism that acts to enhance energy in the region of the spectral peak. Hasselmann in this volume gives a concise historical perspective of the evolution of wind-wave modeling since 1947.

Despite their empirical refinement, second-generation models are not always superior in performance to first-generation models. Most recently, third-generation models, in which approximations of the wave-wave interactions are calculated at each time step (important in rapidly turning winds), have become practical. They have tended to be computationally intensive, however, and their practical superiority to existing first- and second-generation spectral predictions is not easy to demonstrate. In early March 1987, the first and most highly refined third-generation wave model (WAM)¹ became operational at the European Centre for Medium Range Forecasts, just in time to participate in LEWEX.

Remote-Sensing Scientists

The science and technology of radar has evolved roughly in parallel with the development of wind wave models. The first crude realization of a synthetic aperture came in the late 1950s, but synthesis did not become practical until the 1960s, when large-diameter optics were intro-

duced to accomplish signal correlation.² By 1965, oceanographers were advocating "present day radar technology to give a complete description of the sea state."³ By then, potential scientific applications for military radar technology were beginning to emerge. Many of the applications were based on exploiting environmentally dependent backscatter from the ocean. In the 1970s, three quite distinct aircraft radar techniques were explored by NASA for probing the ocean surface on scales (tens to hundreds of meters) that might yield remote estimates of the directional wave spectrum: (1) the surface contour radar (SCR), a narrow-beam, nadir-centered, raster scanning altimeter;⁴ (2) the radar ocean wave spectrometer (ROWS), a fan-beam, off-nadir-centered, conically scanning altimeter;⁵ and (3) the synthetic aperture radar (SAR).⁶ All three could gather directional wave information; the raster-scanning SCR is the most direct and primary method, relying primarily on precise timing to map ocean surface elevations. Only ROWS and SAR can be practically configured for a satellite, however, and both (especially the SAR) must rely on less direct properties of radar backscatter from the ocean for their spectral estimates.

In 1978, NASA flew the first civilian SAR on Seasat, the world's first purely oceanographic radar satellite.⁷ The Seasat SAR was indeed able to monitor important aspects of the spatially evolving spectrum over hundreds of kilometers, but the moving ocean scatterers created a Doppler spread in the radar signal that acted as a severe wave filter in the along-track direction.⁸ Unfortunately, few opportunities existed under Seasat to compare the SAR-estimated directional wave spectrum with other independent estimates. This situation was partially rectified in late 1984, under the much lower-altitude (and thus less severe Doppler smearing) shuttle imaging radar (SIR-B). Off the southwest coast of Chile on four separate days, spectral estimates from the shuttle SAR and from the SCR and ROWS, both mounted on a NASA aircraft, further indicated that a lower-altitude orbiting SAR could (three times out of four) give reasonable spectral estimates.⁹ Those skeptical of remote sensors, however, could (and did) protest that no "direct" *in situ* measurements existed to verify any of the remote estimates. Indeed, previous, but far from comprehensive, separate comparisons had been made of both the SCR and ROWS against directional buoys. Since those were only two-way comparisons, they did not permit any consensus-building, and could not be construed as definitive. By the time of LEWEX, all three radar techniques, properly used, clearly could yield something closely related to the actual directional wave spectrum, but the subtleties of the SAR instrument transfer function were still very much in question.

Ship Motion Exports

Accurate prediction of ocean waves in coastal areas has been an important component of maritime planning ever since World War II. In the intervening half-century, understanding ship motion, internal stress, and fatigue (both to material and to personnel) have been central issues to hydrodynamicists and naval architects. By applying concepts of linear systems theory, the surface ocean wave spectrum (or, in the case of a moving vessel, the "en-

counter" spectrum) is transformed into vessel motion (pitch, roll, and heave) by way of the vessel transfer function.¹⁰ To the extent that the vessel response is linear and its transfer function is known, knowledge of the encounter directional spectrum is sufficient to determine the ship motions. In such cases, the problem can be scaled down by a factor of 10 to 100, permitting motion and capsize studies in model basins. By exciting synchronized orthogonal sets of paddles, the more sophisticated of these basins can simulate full directional wave spectra.

Even though ship design criteria are still specified simply in terms of wave height, or at most in terms of a one-dimensional (unimodal) spectrum, these simplifications are not normally justified. The open ocean wave spectrum is often (perhaps usually) multimodal. Accurate forecasts of directional wave spectra are therefore essential to predict vessel and offshore tower motions, internal stresses, and safety factors for various deck and tower operations. (Significantly, this point was also made nearly thirty years ago in a similar conference on ocean wave spectra.¹¹) Accurate three- to ten-day forecasts would be extremely useful for transoceanic ship guidance and for more reliable estimates of port arrivals.

In 1984, a NATO research study group on full-scale wave measurements was formed to investigate methods of measuring and specifying the multimodal (directional) behavior of the sea using ship instrumentation such as buoys and navigation radar. By 1985, "full-scale" (i.e., at-sea) trials were being planned in the North Atlantic using the *Tydemar* and the *Quest*. Also by the mid-1980s, the three-way (SCR, ROWS, and SAR) spectral comparisons from SIR-B were indicating remarkable agreement among sensors,⁹ and the WAM developers were testing global versions of their third-generation model on the Cray computer at the European Centre for Medium Range Weather Forecasts.¹²

By 1985, then, the time seemed ripe for a field experiment in high seas that would include as many methods as possible for estimating—nearly simultaneously and coincidentally—the directional wave spectrum. Those methods included first-, second-, and third-generation wave models, the three most promising radar remote sensing techniques, and various ship-based techniques, including directional buoys and marine radars.

CHOICE OF TIME AND PLACE

By early 1985, LEWEX began to take tentative form. At that time, LEWEX was envisioned as a direct successor to the NASA SIR-B Chile experiment, but to occur in the North Atlantic under the SIR-B reflight (designated SIR-B'), then scheduled for March 1987. To support the international polar ice research, SIR-B' was to have been launched from the western U.S. Test Range in California into a nearly polar (88° inclination) orbit with a slight westward drift (0.6°/day). Canadian researchers were particularly interested in exploring whether spaceborne SAR could monitor ice dynamics on the Grand Banks during March, when the ice field reaches its maximum extent. For Canada, improved ice monitoring and prediction would directly affect the economics of fisheries and oil

exploration in the eastern maritime provinces. As a precursor to their own Radarsat program, the Canadians were planning the Labrador Ice Margin Experiment (LIMEX) under the SIR-B reflight, to be supplemented by their own multifrequency aircraft SAR, which in 1985 was still under development.

Meanwhile, in the NATO research study groups, support was building to join the SIR-B ocean waves experiment. NATO scientists secured commitments for both the *Quest* and the *Tydeman* to conduct at-sea full-scale trials during March 1987. The ship commitments were an essential component of LEWEX, making it possible to extend the scope of the spectral comparisons well beyond the 1984 SIR-B experiment off Chile.

Then in January 1986, the *Challenger* accident occurred, taking with it all hope of obtaining SAR ocean imagery from orbit for several years. The next few weeks were an uncertain time for LEWEX, but by April a modified strategy had emerged, wherein the Canadian aircraft SAR came to play a central role not only for LIMEX, but also for LEWEX. A commitment from the Canada Centre for Remote Sensing for five flights of their CV-580 SAR aircraft was the final catalyst that ensured the experiment. Coordination between the two experiments became essential: LIMEX required broad near-shore coverage for generating ice mosaics, but LEWEX required multiple passes over ships well out in open water. Conversely, the merging of LIMEX and LEWEX eventually proved to have logistically important side benefits, and some of the imagery of waves traveling through floating ice provided new insight into the SAR wave-imaging mechanisms.

The final choices of time and place for LEWEX, then, emerged from the following basic constraints:

1. The *Quest* and the *Tydeman* were available only for the month of March, including two-way trans-Atlantic passage for the *Tydeman*.

2. LEWEX and LIMEX competed for a single common resource, the aircraft SAR based from a single airfield; LEWEX flights were looking for passing storms with evolving multimodal spectra, while LIMEX flights were looking for dynamic ice field conditions.

3. The NASA P-3 aircraft, containing both the SCR and ROWS, was supported for only four flight days (eighteen flight hours), including two-way transit from Wallops Island, Virginia.

Among the elements of risk and uncertainty were (1) daily constraints on the aircraft to secure acceptable alternate landing sites and to fly complicated patterns at various altitudes in one of the world's busiest air corridors; (2) constraints on the ships to deploy and recover large experimental buoys in high seas; and (3) the possibility that ice might completely close St. John's harbor just before the onset of the experiment, when both ships needed access both to enter and to exit.

Some salient features of the wave and ice climate in the winter North Atlantic are shown in Figure 2, along with the route of the *Tydeman* from southern England to St. John's, Newfoundland, during the first days of March. The figure shows a steep gradient in wave climate north and east of Newfoundland, with a broad region in which the significant wave height (SWH) exceeds 10 m

at least ten times a year. The final LEWEX sites were located well within this region, and yet close enough to the aircraft base in Gander (within 375 nmi, as it turned out) to allow overflights by the two aircraft, and sufficiently southward to allow exposure to substantial wave energy arriving from three quadrants. Figure 2 also gives a hint of a major winter storm that slowed the *Tydeman* on 8 March, and the extensive ice sheet just east of Newfoundland that nearly immobilized the ship as it approached St. John's harbor.

By March, the wave climate in the winter North Atlantic is rapidly ameliorating. Figure 3 shows that the probability of encountering a 20-ft (6.1-m) wave event in the LEWEX region in March is scarcely more than half what it is in January.¹¹ Moreover, Figure 4 (from Geosat wave height estimates)¹² shows that 1987 was one of the quieter years, with the LEWEX region experiencing only a 3-m March average, down from more than 4 m in March 1986. Ironically, the last major event of the 1986-87 winter (at least 9.5-m waves driven by 25-m/s winds) passed through the LEWEX region on 8 March and was encountered by the *Tydeman* en route to St. John's. These two obstacles (the storm and the ice pack) ultimately prevented both ships from reaching their LEWEX sites until early on 14 March. McCloskey¹³ gives a further chronology of events from 9 March to 19 March.

Figure 5 shows the extent of the ice field around St. John's harbor as the two ships traveled south on 10 and 11 March around the ice pack and then northeast into strong headwinds on 12 and 13 March. By 14 March, the two ships were positioned at adjacent numerical model grid points of the U.S. Navy Global Spectral Ocean Wave Model, GSOWM (the *Quest* at 50°N, 47.5°W; the *Tydeman* at 50°N, 45°W). From Gander,

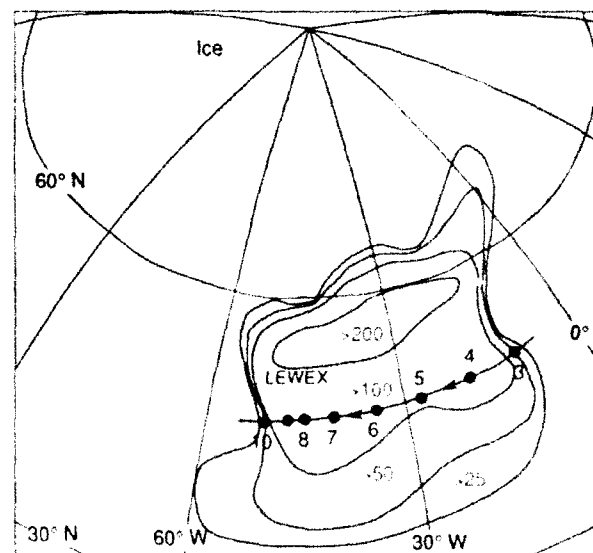


Figure 2. Wave and ice climate in the North Atlantic in winter, also showing the route of the *Tydeman* from southern England to St. John's, Newfoundland, from 3 through 10 March 1987. Contours show number of occurrences of waves exceeding 10-m significant wave height in the 10-year interval from 1959 to 1969, from U.S. Navy model hindcasts. Ice coverage is for 10 March 1987.

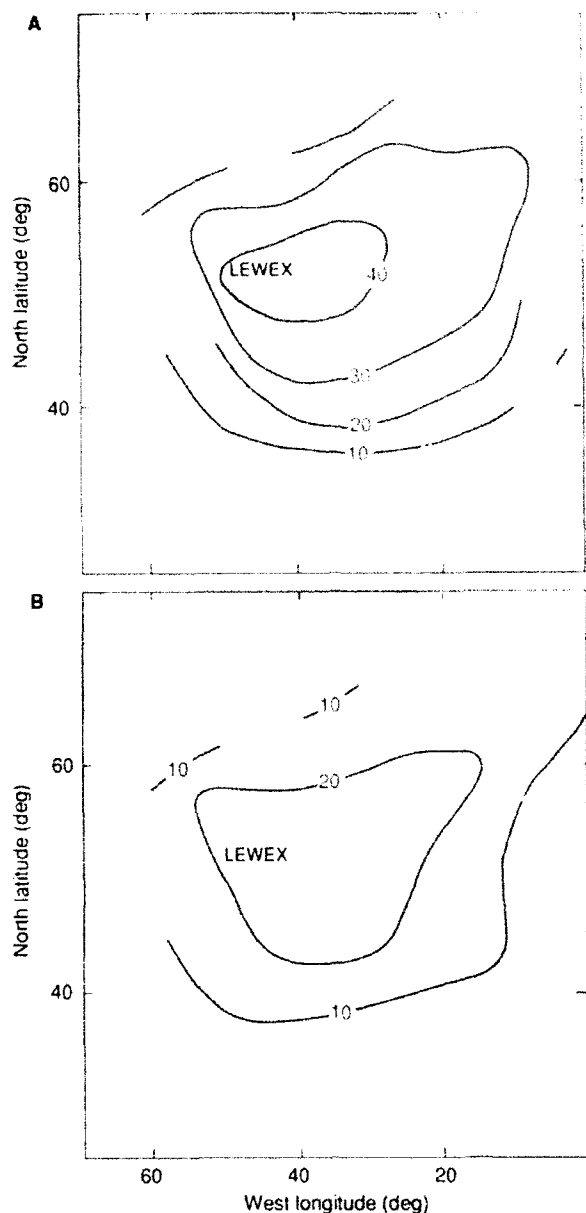


Figure 3. Probability of significant wave height exceeding 20 ft (6.1 m) in the North Atlantic. A. January. B. March.

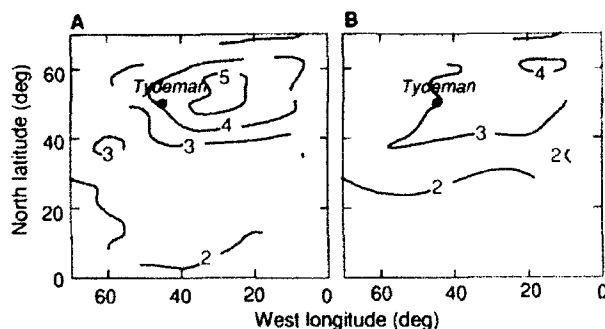


Figure 4. Monthly averages of significant wave height for the North Atlantic in March from Geosat. A. The year 1986. B. The year 1987.

the Canadian CV-580 and the NASA P-3 planned their flights to travel eastward at 50°N latitude from 50°W to 45°W, and to pass over the *Tydeman* daily at about 1200 UT (0830 local time), coincident with the various model forecasts. Aside from a single moored buoy at each ship, all buoys were deployed several hours before aircraft overpasses and were recovered several hours after the overpasses, all generally in daylight hours, but sometimes after dark and with great difficulty.

The problem of successfully deploying and recovering buoys was a major concern. Not only was personnel safety at stake, but expensive "one-of-a-kind" experimental buoys were at risk. Before the experiment, each ship had determined its own guidelines for both deployment and recovery. The larger and more versatile *Tydeman* could deploy buoys in seas up to 24 ft (7.4 m) and recover them in seas up to 15 ft (4.6 m). Comparable limits for the *Quest* were 12 ft (3.7 m) for both deployment and recovery. For this reason, the *Tydeman* was positioned at the more open (eastward) site, where sea conditions were expected to be more severe. As a graphic illustration of the potential buoy recovery problem, Figure 6 shows U.S. Navy wave forecasts in the LEWEX region for the first quarter of 1987, along with deployment and recovery limits for the two ships. Clearly, daily recovery of buoys in January or February would not have been feasible, even during the relatively quiet 1986-87 winter.

LEWEX WIND AND WAVE CONDITIONS

By the onset of the experiment, four independent sources of North Atlantic wind fields were available to

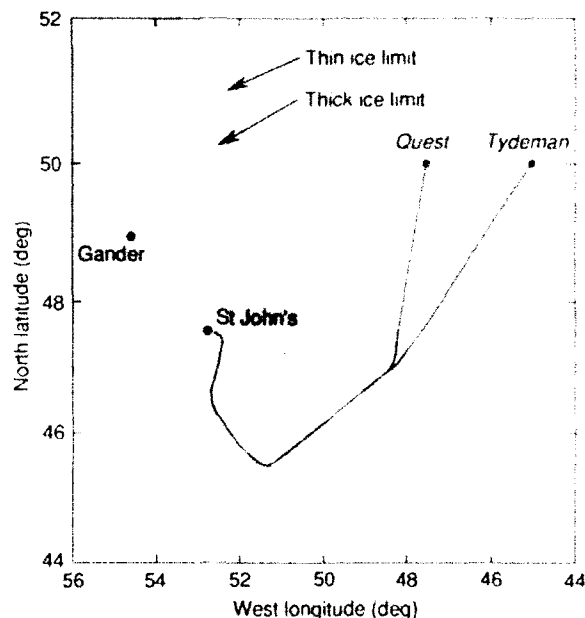


Figure 5. Ice field in the LEWEX region on 10 March 1987 (adapted from Canadian Atmospheric Environmental Service data). Also shown are the ship tracks of the *Quest* and the *Tydeman* from St. John's to their LEWEX sites. The two aircraft departed from Gander to rendezvous with the *Tydeman*, usually around 1200 UT. "Thick ice" is greater than about 1 m.

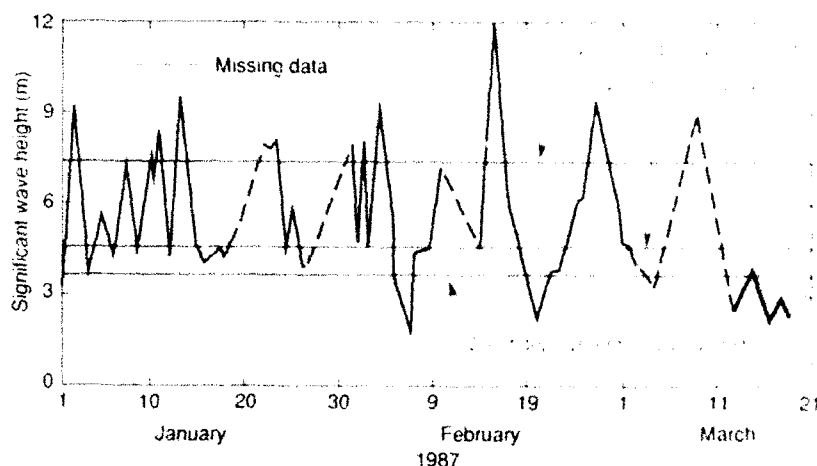


Figure 6. Twelve-hour wave height forecasts from the U.S. Navy Global Spectral Ocean Wave Model for most of the first quarter of 1987, including the LEWEX interval (the blue line) beginning around 12 March. Also shown are the buoy deployment and recovery limits for both the *Quest* and the *Tydemar*.

drive six separate wave models, three in North America and three in Europe. Even though some models were driven well after the experiment itself, the results provide a good estimate of the confidence limits of modern wave forecasting. Figure 7 shows the wide spread in 12-hour advance predictions in SWH from four models at the *Tydemar* site from 0000 UT on 12 March through 1200 UT on 19 March. Each model was driven with separate wind field estimates, but all winds were derived from essentially the same set of available ship reports. Table 1 summarizes salient features of the data sources and the pedigree of the wave models. Also included in Figure 7 for comparison are the measurements from the Norwegian Wavescan buoy, moored at the *Tydemar* site from 0430 UT on 14 March until 2200 UT on 18 March.

The disparity among estimates in even such a simple descriptor as SWH aptly illustrates the need for improved forecasts. Although each forecast correctly predicts the passage of two events separated by about three days, individual predictions of the strengths of both events vary by nearly a factor of 2, and predictions of passage time differ by up to a day. Because each model was driven by a separate wind field, individual model performance cannot be assessed from these results. Neither can the model estimates be compared with measurements for the earlier and stronger event, since the Wavescan buoy was deployed too late to capture the first peak. Differences are just as likely to be caused by the wind fields as by the model. To investigate model differences *per se*, a common LEWEX wind field was created to drive all wave models with identical winds. As some of the subsequent articles in this volume indicate, the variability seen in Figure 7 was caused at least as much by the wind fields as by the models. This conclusion was, in fact, one of the clearest results of LEWEX—that wind field errors remain one of the single largest sources of forecast errors, often masking all the potential advances made in wave model physics over the last three decades.

Although LEWEX was concerned peripherally with wave height estimates, its central interest was with the associated evolving directional wave spectrum. Figure 7 suggests that multiple wave systems were present at the *Tydemar* during LEWEX, but it reveals nothing of their

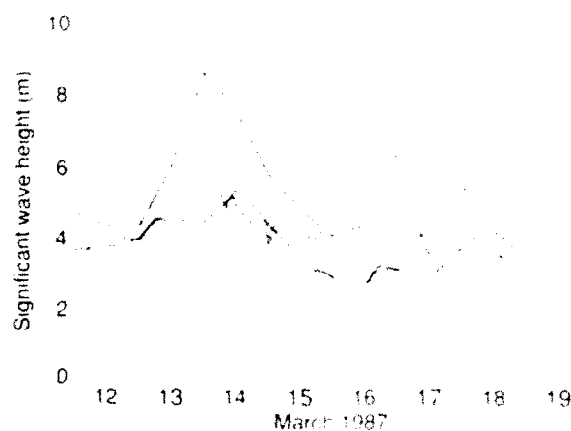


Figure 7. Twelve-hour wave height forecasts during LEWEX from four different numerical wave models, each using its own estimate of the wind field (WAM with ECMWF winds in red, ODGP with ODGP winds in blue, GSOWM with FNOC winds in green, and UKMO with UKMO winds in orange). Also shown are measurements from the Norwegian Wavescan buoy (in purple).

Table 1. Sources of wave forecasts in Figure 7 using independently generated wind fields.

Model*	Generation	Source
GSOWM	First	Fleet Numerical Oceanography Center
ODGP	First	Ocean Weather, Inc.
UKMO	Second	U.K. Meteorological Office
WAM	Third	European Centre for Medium Range Weather Forecasts

GSOWM—Global Spectral Ocean Wave Model
 ODGP—Ocean Data-Gathering Program
 UKMO—United Kingdom Meteorological Office
 WAM—Wave Model

character. In fact, at least six or seven separate, spatially and temporally evolving wave systems were passing through LEWEX during the seven-day period, each having a characteristic persistence of from one to three days.

Usually two, but occasionally even three, separate wave systems coexisted at least in some of the model estimates.

The complete time history of the evolving directional spectrum cannot be conveyed in only two dimensions. Even the evolution of the dominant wave vectors (their wave number, direction, and amplitude), however, conveys much of the information about the multiple generating sources that are totally lost in a simple time history of SWH. Figure 8 is a graphical format, further refined by Gerling in this volume, that attempts to capture the temporal wave history of LEWEX at the *Tydeman*. In this figure, the logarithm of the dominant wave number (converted to equivalent wavelength and wave period) is plotted against time. Vector sets whose base positions represent wave number, and whose direction and amplitude correspond directly to their counterparts in vector wave number, separate naturally into nearly autonomous clusters. The behavior of these clusters can reveal much about their generating sources. For example, in Figure 8, negative slopes (wave vector sets with decreasing wave number versus time) suggest developing, locally wind-driven waves, and positive slopes suggest dispersive swell arriving from a distant source. Within a cluster, negative slopes are associated with wave growth, positive slope with time and place of wave generation, and minimum wave number with time of closest approach and maximum generating winds. These associations suggest that clusters of evolving vector wave numbers contain specific information on the nature of the generating winds. If a space-

borne SAR could make reliable estimates of the vector wave number at sufficient density, it might be possible to infer errors in the generating wind fields. These inferences would be much more direct than could be accomplished with significant wave height estimates from satellite altimetry, since the SAR estimates implicitly contain the velocities of all vector wave numbers.

EXAMPLES OF LEWEX DIRECTIONAL SPECTRA

Figure 8 shows how the dominant peaks of the seven (more-or-less) separate wave systems of LEWEX evolved in time. The figure also shows sample times of the three aircraft remote sensors (daily at about 1200 UT when possible) and the intervals over which the two moored buoys were operating. The wave number evolution is only schematic, of course, since substantial scatter existed among the various estimates, and the evolution at the *Quest* was measurably different from that at the *Tydeman*. Nevertheless, the figure suggests that daily sampling by the remote sensors, if that would have been possible, would have captured the dynamics of all but the shortest (<100 m) wave systems. For various reasons alluded to above, daily sampling from all three sensors was impractical. However, at least one sensor flew on each of six days, at least two flew on four days, and all three flew on two days. On all but the first flight day, collaborating buoy estimates were available from at least one and usually both of the ships.

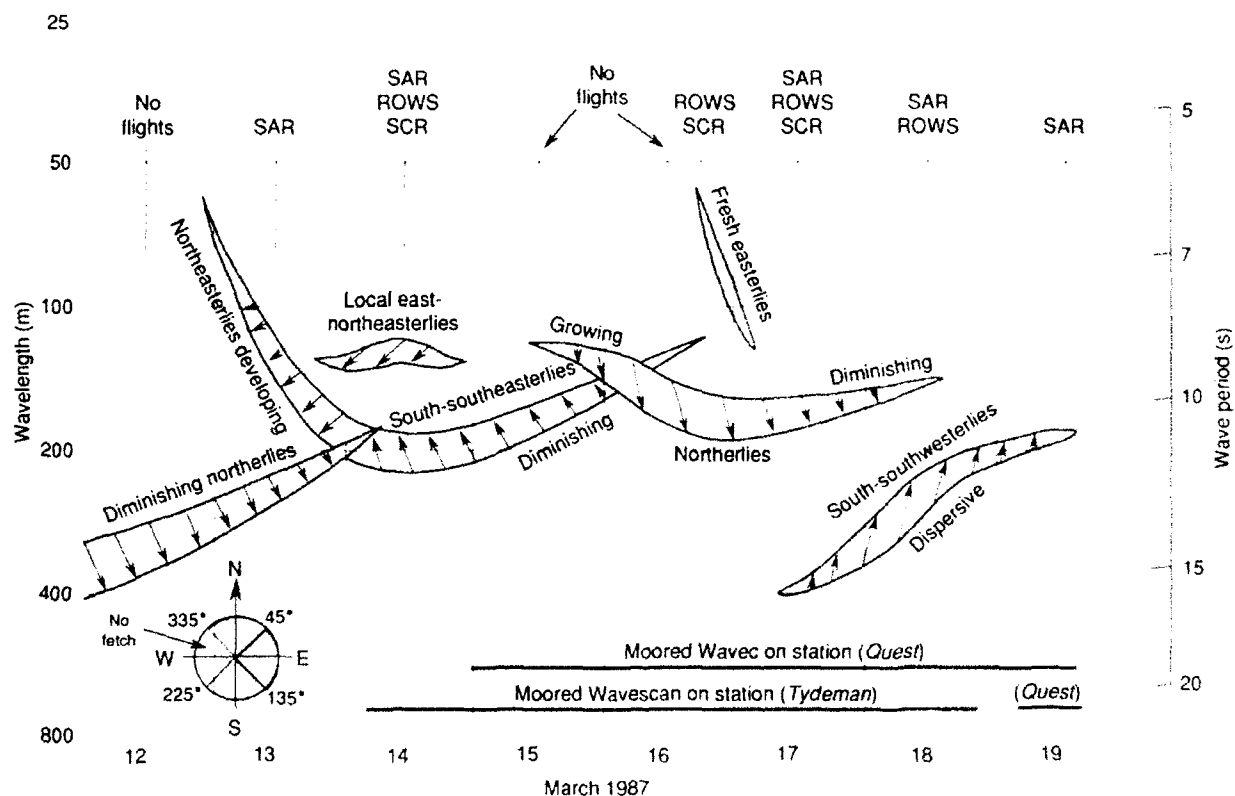


Figure 8. Temporal wave vector history of LEWEX at the *Tydeman*, showing the evolution of several distinct wave systems, along with the approximate times for both aircraft and ship measurements. The *Tydeman* moved to the *Quest* position late on 18 March.

The most dynamically interesting conditions occurred around 1800 UT on 13 March, just after the first (trial) SAR flight, and before either of the two ships were in position. At that time, diminishing dispersive northerly swell was yielding to strong northeasterlies that were in turn being overtaken rapidly by a strong south-south-easterly system. Figure 9 shows a spectral comparison from nine separate wave models at 1800 UT on 13 March, all driven by a common wind field, which at the *Tydeman* was turning from northeast to southeast at about $6^\circ/\text{h}$. In this rapidly changing wind field, large differences among models appear. Although some models retain a substantial component of old swell (e.g., both first-generation models, the NOAA second-generation model, and the NASA third-generation model), others show a nearly completed transition to the fresh wind-driven system (e.g., the second-generation U.K. Meteorological Office [UKMO] model and the third-generation Bedford Institute of Oceanography [BIO] model [WAM with ice-field modeling]).

Unfortunately, no simultaneous measurements of the spectrum were available, but even if they had been, uncertainties in the wind field would have cast doubt on any attempt to determine absolute model performance. Again, this uncertainty in the driving wind fields pervades LEWEX and would pervade any similar open-ocean experiment in which the far wind field was an important

source of wave energy. Without sufficiently dense wind-field monitoring over all the potential generation areas (typically hundreds or even thousands of kilometers from the site), no wind field can be certified as being accurate and complete. In the next few years, satellite scatterometers will alleviate, but not eliminate, this problem, since the (unknown) surface wave field influences the scatterometer wind algorithm through the surface drag relation, and fine-scale wind field variability, although extremely important (see the panel discussion in this volume), is typically unknown.

At 1200 UT on 17 March, near the time of the second peak in SWH (Fig. 7), the directional wave spectrum was simultaneously estimated at each ship by the full set of sensors and models. Figure 10 shows this full set of twenty-five spectral comparisons at the *Tydeman*. Here the format is similar to that of Figure 9, but in a linear normalized wave number plot. The figure clearly illustrates a number of inherent limitations in both sensors and models. Figure 8 (schematic only) shows two nearly opposing wave systems (one from the south, one from the north) passing through LEWEX at 1200 UT on 17 March. From Figure 10, depending on which of the twenty-five estimates is assumed to be true, one can conclude that either of the two wave systems, or various amounts of both, were present. Moreover, estimates of the direction of both systems vary by up to 45° , and estimates of the spectral width (in both wave number and angle) vary by more than a factor of 3. More specific conclusions than this are not justified, since the spectra are all individually normalized to the spectral peak, and a linear display will not expose broad-band, low-energy systems in the presence of strong narrow-band systems.

Even so, systematic, and sometimes curious, similarities occur among spectra:

1. Aside from the 15° direction anomaly, the Wavec drifting buoy and the Wavescan moored buoy give essentially identical estimates, while the Endeco drifting buoy and the ship radar agree with each other in direction, but differ radically in angular width. (Note: The Endeco buoy was the only buoy not analyzed by maximum entropy.)

2. Again, aside from a 15° to 30° direction anomaly, the (radially ambiguous) aircraft estimates, including both the low-altitude (a range-to-velocity ratio of about 30) and high-altitude (a range-to-velocity ratio of about 50) SAR, agree with one another and with the Wavec and Wavescan buoys.

3. Each of the six wave models, when driven with one of four separate wind fields, produces a dominant northward-traveling system, opposite to that measured by the buoys, and also differing from one another by up to a factor of 2 in wave number and up to 45° in angle.

4. The nine wave models, when driven with a common wind field, all produce similar (but not identical) estimates, but they too are all northerly, contrary to the results of the buoys.

One explanation for this curious set of anomalies is that insufficient strength and/or incorrect timing was assigned to the wave-generating region to the north. Alter-

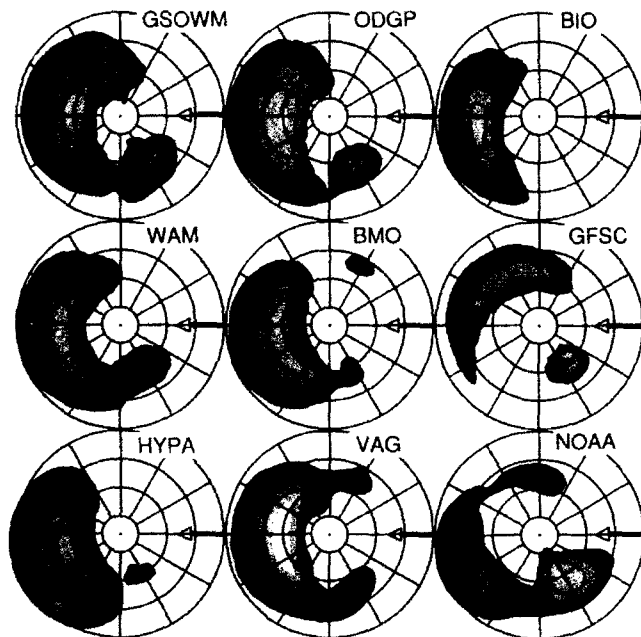


Figure 9. Directional frequency spectra at 1800 UT on 13 March from nine separate numerical wave models, all driven by a common wind field. The logarithm of spectral energy density is separated into evenly spaced contours, with each spectrum normalized to its individual peak. The radial dimension is proportional to the logarithm of frequency, with the outer circle at a frequency equivalent to a wave number of $2\pi/50$ rad/m. Circles are separated by factors of 2 in equivalent wave number; contours are separated by factors of about 2 in spectral energy density ($\text{m}^2 \cdot \text{s}^2$). Arrows indicate strong easterly wind at the time of the estimates.

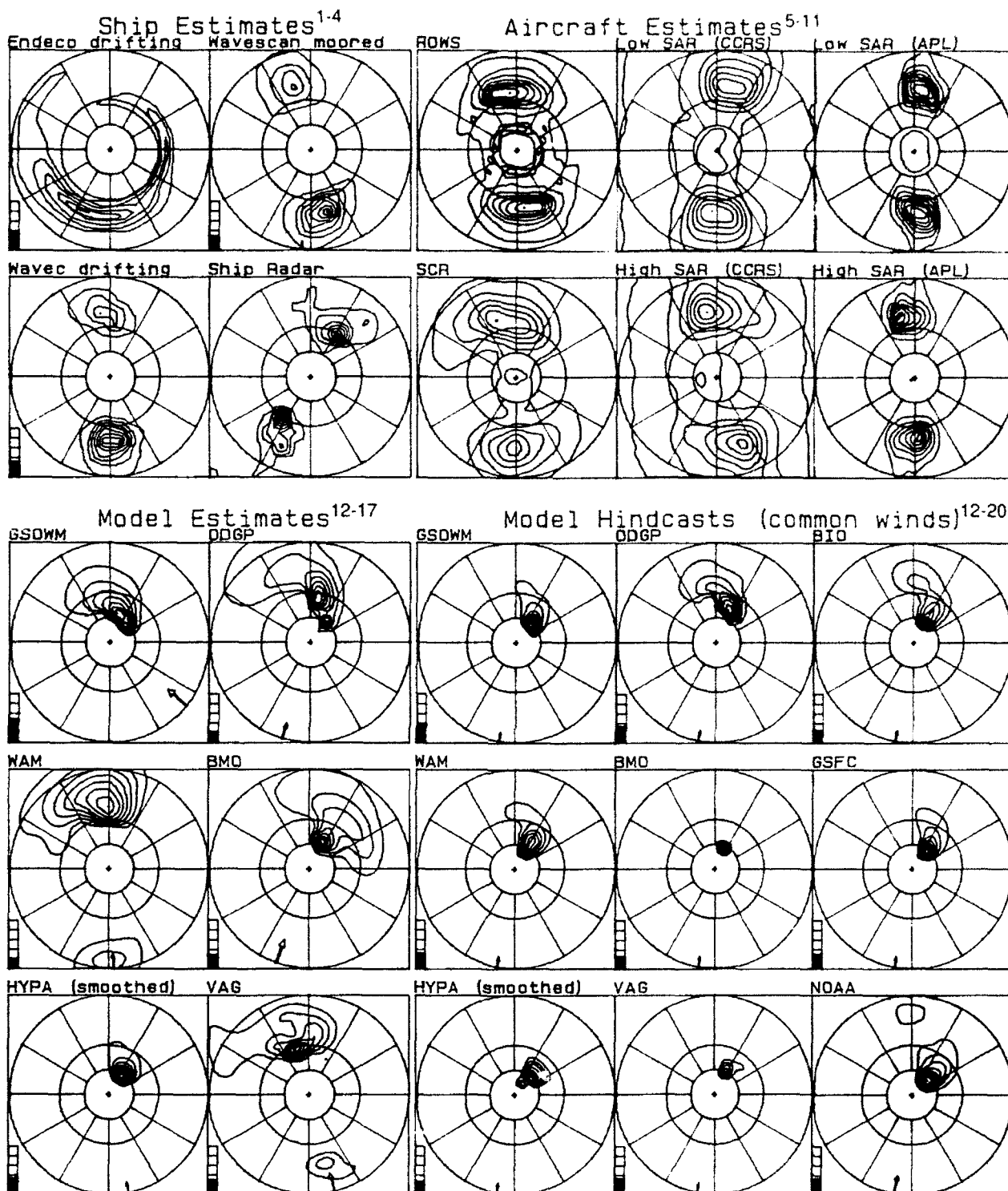


Figure 10. Twenty-five nearly simultaneous and coincident estimates of the directional wave number spectrum at 1200 UT on 17 March at the Tydemar. Ship-based estimates are at upper left, aircraft estimates are at upper right, model hindcasts with separate winds are at lower left, and model hindcasts with common winds are at lower right. Buoy frequency spectra have been converted to wave number spectra through the deep water dispersion relation. Spectra are individually normalized and are linear in wave number and spectral energy density (m^4), with the outer circle at $2\pi/100$ rad/m. Contours are linearly spaced. Model winds (3 to 10 m/s) are shown by the arrows; estimates of significant wave height are shown by the vertical bars (full scale is 10 m).

natively, all models may contain a common error in their propagation algorithm, creating excess spatial diffusion

over long distances, and causing distant swell to arrive early (see the panel discussion in this volume).

Regarding the variability within the measurements, the evidence suggests that the true wave spectrum was highly variable in both time and space, but that significant directional biases also occurred among the buoys, occasionally as high as 45° . This degree of natural variability and cross-instrument variability was somewhat unexpected. A further set of estimates two days later, however, suggests that the variability was not unusual. At 1200 UT on 19 March, after the *Tydemar* had left its original position to rendezvous with the *Quest*, both vessels encountered simple unimodal swell from the southwest with an SWH of about 2 m. Figure 11 shows spectral estimates for a six-hour interval from three separate buoys, all processed identically by the maximum entropy method. All three buoys were located within a few kilometers of one another over the six-hour interval. The evidence indicates that the Wavescan buoy was biased 15° from the other two, but also that the spectrum varied up to 15° in a three-hour interval. Thus, discrepancies of up to 30° between model and measurement are within the possible measurement error.

LESSONS FROM LEWEX

Many of the results and implications of LEWEX are expounded in considerable detail in the following articles and also in the panel discussion. However, a few common threads appear throughout many of the articles:

1. Wave model forecasts often disagree with one another because the models are not driven with identical winds. Even though the various wave model forecasts may be derived from identical sets of surface reports, the surface wind field and associated wind stress that result from a sparse set of reports apparently leave much room for interpretation. The wind field differences often overwhelm model differences. Perhaps as a direct result, there is no compelling evidence from LEWEX that forecasts from third-generation wave models are more accurate than some of their predecessors. The largest model differences, not surprisingly, arise in dynamic rapidly changing winds that produce various combinations of swell and wind sea. In such circumstances, the surface drag depends strongly on the surface directional spectrum, especially when the wind sea is in an early stage of development.

2. The directional wave spectrum in the open ocean is often multimodal. The waves in such cases are inadequately characterized by either their significant wave height or their one-dimensional (or unimodal) spectrum. Vessel motion calculations and safety risk factors derived from a reduced version of the two-dimensional (directional) wave spectrum will also be inadequate. Especially in coastal regions and in regions of strong currents, an accurate estimate of the directional spectrum is essential to calculate the stresses on marine structure.

3. With a few important caveats, the directional wave spectrum can be estimated adequately on the ocean surface with directional buoys and ship navigation radars, and remotely with radar remote sensors that include the surface contour radar, the radar ocean wave spectrometer, and the synthetic aperture radar. Each of the tech-

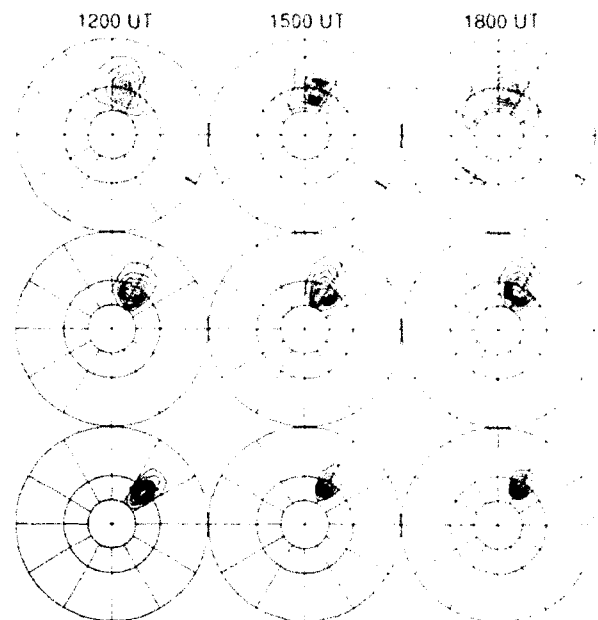


Figure 11. Three sets of three-hourly wave number spectra (converted through the deep water dispersion relation) from three directional wave buoys at the *Quest* location on 19 March 1987, all processed identically using maximum entropy. Spectra are plotted in a form identical to that of Figure 10. Top row: Wavescan buoy. Middle row: Wavec buoy No. 1. Bottom row: Wavec buoy No. 2.

niques will yield its own transformed version of the temporally and spatially varying directional spectrum. Each will have its own unique spectral and spatial or temporal resolution limits, and each will have its own unique instrument transfer function. Individual spectral estimates must be interpreted in the perspective of the appropriate (and not necessarily linear) instrument transfer function.

4. Forecasts of directional wave spectra are unlikely to improve, even with perfect wave models, until both the wind field and the wave field estimates improve. Some integrated properties of the wind field may be deduced by monitoring the wave field it produces. With satellite radar remote sensors, because wind field estimates are wave-dependent and wave field estimates are wind-dependent, any wind-wave inversion process must be iterative. The iteration process will more efficiently converge with accurate satellite estimates of the complete directional wave spectrum, rather than with simply the total significant wave height.

5. The temporal evolution of the dominant wave vector at a given position is well-behaved. In LEWEX, the wave vectors usually separated into autonomous clusters associated with individual wave systems. The analogous parameter, the spatial evolution of the dominant wave vectors at a (virtually) fixed time, can be monitored with either a spaceborne SAR or ROWS and will also separate into similar clusters associated with individual wave systems. The behavior of each autonomous cluster will contain important clues about the properties of its generating

wind field and will therefore become a vital part of any inversion strategy.

6. With the proper geometry, spaceborne SAR can give unique high-spatial-density estimates of the evolving directional ocean wave spectrum over global scales. Unfortunately, the technique will be severely constrained by sub-optimum geometry in nearly all of the space platforms planned during the next decade. For ocean wave monitoring, the SAR works best in a low-altitude (< 300 km), near-nadir ($< 30^\circ$) geometry, where its transfer function is most predictable and where its range-to-velocity ratio is low. As Figure 12 illustrates, SAR's with a low range-to-velocity ratio are rare, because the increased drag resulting from a low-altitude orbit requires active drag compensation to maintain a stable altitude, and such a requirement appreciably complicates the satellite design. Nonetheless, such a low-altitude dedicated satellite is perfectly feasible⁹ and in fact will be necessary if SAR is to realize its full potential for global ocean wave monitoring.

REFERENCES

- ¹The WAMDI Group, "The WAM Model—A Third Generation Ocean Wave Prediction Model," *J. Phys. Oceanogr.* **18**, 1775-1810 (1988).
- ²Sherwin, C. W., Ruina, J. D., and Rawcliffe, R. D., "Some Early Developments in Synthetic Aperture Radar Systems," *IRE Trans. Mil. El.* **MIL-6**, 111-115 (1962).
- ³Ewing, G. C., ed., *Oceanography from Space*, Woods Hole Oceanographic Institute, No. 65-10, p. viii (1965).
- ⁴Kenney, J. E., Uliana, E. A., and Walsh, E. J., "The Surface Contour Radar, A Unique Remote Sensing Instrument," *IEEE Trans. Microwave Theory Tech.* **MTT-27**, 1080-1092 (1979).
- ⁵Jackson, F. C., "An Analysis of Short Pulse and Dual Frequency Radar Techniques for Measuring Ocean Wave Spectra from Satellites," *Radio Sci.* **16**, 1385-1400 (1981).
- ⁶Elachi, C., Thompson, T. W., and King, D., "Ocean Wave Patterns under Hurricane Gloria: Observations with an Airborne Synthetic Aperture Radar," *Science* **198**, 609-610 (1977).
- ⁷Lame, D. B., and Born, G. H., "Seasat Measurement System Evaluation: Achievements and Limitations," *J. Geophys. Res.* **87**, 3175-3178 (1982).
- ⁸Beal, R. C., Tilley, D. G., and Monaldo, F. M., "Large- and Small-Scale Spatial Evolution of Digitally Processed Ocean Wave Spectra from Seasat Synthetic Aperture Radar," *J. Geophys. Res.* **88**, 1761-1778 (1983).

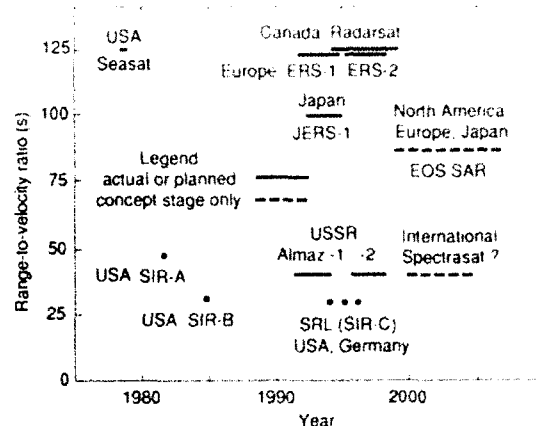


Figure 12. Minimum range-to-velocity ratios of most known past, present, and proposed scientific spaceborne SAR missions since 1978, showing associated sponsoring countries or consortia of countries. ERS: European Remote Sensing Satellite; JERS: Japanese Earth Resources Satellite; EOS: Earth Observation System; SIR: Shuttle Imaging Radar; SRL: Space Radar Laboratory.

- ⁹Beal, R. C., "Spectrasat: A Hybrid ROWS SAR Approach to Monitor Ocean Waves from Space," *Johns Hopkins APL Tech. Dig.* **8**, 107-115 (1987).
- ¹⁰Bales, S. L., "Practical Seakeeping Using Directional Wave Spectra," *Johns Hopkins APL Tech. Dig.* **8**, 42-47 (1987).
- ¹¹Munk, W., in remarks from "Sea State for Engineers," in Appendix B of *Ocean Wave Spectra*, National Academy of Sciences Conference, Prentice Hall, p. 354 (1963).
- ¹²Komen, G. J., "Recent Results with a Third-Generation Ocean Wave Model," *Johns Hopkins APL Tech. Dig.* **8**(1), 37-41 (1987).
- ¹³U.S. Navy *Hindcast Spectral Ocean Wave Model Climate Atlas, North Atlantic Ocean*, NAVAIR 50-10-538, Washington, D.C., pp. 27-29 (1983).
- ¹⁴Dobson, E. B., and Porter, D. L., "World Statistics of Wind Speed and Significant Wave Height from the Geosat Altimeter," *JHU APL SIR89U-007* (Feb 1989).
- ¹⁵McCloskey, W., "Project LEWEX: An International Reading of Ocean Waves," *Johns Hopkins APL Tech. Dig.* **10**(3), 279-287 (1989).

ACKNOWLEDGMENT: I am indebted to Tom Gerling for preparing Figures 7, 8, 10, and 11, as well as for helpful comments on the draft. This work was supported by the Office of the Oceanographer of the Navy, by NASA Headquarters, and by APL Independent Research and Development funding.

THE PRACTICAL VALUE OF DIRECTIONAL OCEAN WAVE SPECTRA

Multimodal directional seas, which often contain steep nonlinear wave groups, can create a more severe vessel design environment than simple unimodal directional seas. Using a multimodal description, a method to forecast steep wave conditions that adversely affect the operation and safety of ocean vessels is presented. Modern wave laboratories can accurately simulate multimodal directional seas to investigate the motion response of ocean vessels to realistic forcing functions.

EXAMPLES OF SENSITIVITY TO DIRECTIONAL SEA STATES

A three-dimensional sea state can be well described statistically by its directional spectrum. A multimodal directional sea state is defined as a sea state that gives two or more distinct energy peaks at different directions. Wind seas and swell systems from different directions often occur simultaneously and can be identified easily in standard polar spectral energy plots.¹

The directional spectrum has become appreciated more and more in recent years as an important engineering tool. For example, Marintek A/S began simulating directional wave spectra in its Ocean Laboratory (model basin) in 1980. Much evidence now indicates that directional seas can produce a more severe ship design environment than, for example, simple long-crested seas with identical significant wave height, H_s . Simulation experiments have shown that, for a given H_s , torsion moments on a tension leg platform are larger in directional seas than in seas approaching from only one direction. Similar results were found for an offshore loading system consisting of a double-articulated riser connected to an offshore buoy, a storage tanker, and a shuttle tanker, in which directional seas produced yaw motions that created large forces and moments. Such large forces were not present in long-crested seas. Knowledge of wave directionality is also important to assess accurately the accumulation of fatigue damage on North Sea steel jacket structures.² Directional information is essential to estimate phase lag and coherence between sea loading and the response of various members of a spatial jacket structure.

An accurate description of directional seas is also very important for calculations of sea loads on ship hulls. Fukuda³ compared results for vertical bending moments on tankers and cargo ships in both long-crested and short-crested directional seas. Clarke, Price, and Temarel⁴ performed numerical simulations of bending moments, including slamming and whipping effects, in a frigate hull driven by various directional spectra. Sea states with large directional spreading resulted in smaller bending moments.

A unimodal directional sea contains only one wave system with directional spreading. Design applications very often use a two-parameter directional spectrum with 90° spreading described by the function $\cos^2 \theta/2$, where s is the directional spread parameter. The Labrador Sea Extreme Waves Experiment (LEWEX) full-scale sea trials demonstrated the inadequacy of such sea state modeling. More complete knowledge of the various modes contained in a multimodal directional sea state can reveal strong variations in ship response with heading, and can result in a substantial improvement in ship operability.

The most severe limitations of a unimodal description for directional spectra, however, appear when designing weather-vaning systems for ocean vessels or dynamic positioning systems for semi-submersible platforms. The design requirements for such systems generally become more severe in multimodal directional seas, since mooring forces are functions of the slow drift in surge, yaw, and sway motions.

MULTIMODAL DIRECTIONAL SEAS IN COMBINATION WITH CURRENT SHEAR

In Norway, twenty-six trawlers and freighters were lost in capsizing accidents in a period of only nine years. Altogether, seventy-two lives were lost. The shipwrecks from these and other accidents are not randomly distributed along the coast of Norway, but are concentrated in the twenty-four specific areas illustrated in Figure 1. Wave refraction calculations confirm that these areas have a concentration of wave energy during certain weather conditions. Most of these areas can be classified as part of the shelf and coastal waters, where gravity waves interact with strong currents and local topography.⁵

An encounter with a steep wave condition can be disastrous, even for a large ship. In September 1979, the Norwegian ship *Austri*, loaded with a cargo of pig iron, was suddenly hit by a large wave breaking over the starboard bow in the narrow passage outside Slettringen in area 15—Sognesjøen—in Fig. 1. The ship heeled over by nearly 30° and, before it could restore itself, was hit by a new wave from another direction. The new wave

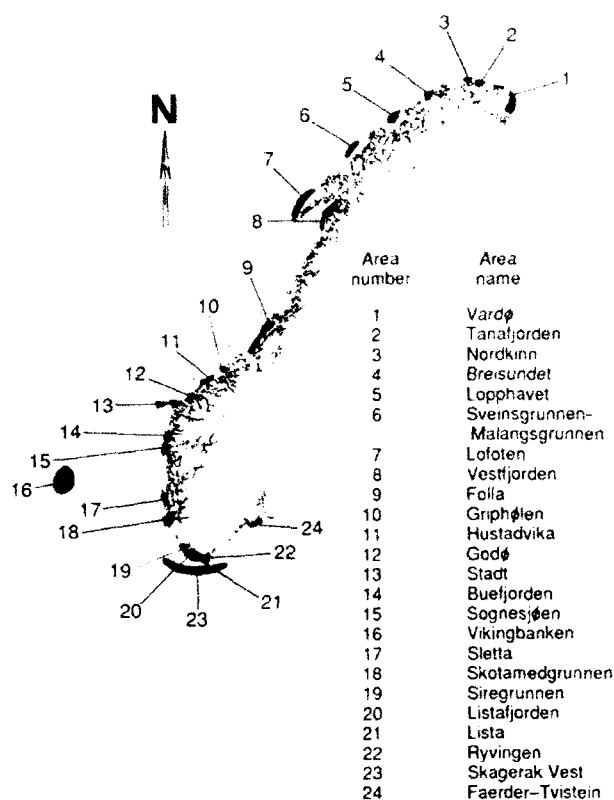


Figure 1. Twenty-four areas on the Norwegian coast that are the sites of steep and dangerous waves during certain weather conditions (depending on wave direction, wave height, and the position of coastal eddies).

increased the heel to nearly 40° , causing the cargo to shift, and the ship had to be abandoned, with no emergency calls transmitted. Shortly after, the rescue float capsized in surf near the shore and five lives were lost. The abandoned *Austri* with its shifted cargo was in fact quite stable, and maintained a list near 80° , although it drifted and turned until it struck a rock near the shore and broke in two (Fig. 2). A court of inquiry⁶ later showed that the vessel had been passing through a focal point in one of the wave refraction areas.

Storm surges and related effects may, at times, give rise to an unusually large flux of water in the Norwegian Current that travels up the west coast of Norway. The current meandering is enhanced by a sudden outflow of brackish water from the Baltic Sea, and develops to an unusually large scale. With westerly winds, a setup occurs in the Baltic Sea, and a sudden change of wind direction can then release a volume flux of up to $1.4 \times 10^6 \text{ m}^3/\text{s}$. This front travels about 30 km/day north along the Norwegian coast, producing large eddies with diameters of up to 100 km.⁷ The passage of such eddies creates very large current velocities even at great depths. Such unusual meandering is observed by satellites equipped with infrared sensors that measure the sea surface temperature. Interaction between gravity waves and the eddies can lead to the development of dangerous, plunging, and breaking waves in deep waters at predict-



Figure 2. The Norwegian ship *Austri* (499 gross register tons), which capsized from waves in area 15 of Figure 1 and subsequently broke into two pieces.

able times and locations both on the shelf and in the coastal areas.

In December 1984, the freighter *Sun Coast* was lost at Stadt in area 13 of Figure 1. The vessel encountered two large breaking waves, which caused the cargo to shift. Only four of a crew of six were rescued. A court of inquiry⁸ revealed that steep transient wave conditions can suddenly and unexpectedly occur at this location, when waves arriving from certain critical directions are influenced by the local topography. On this occasion, a large current eddy had been located in the vicinity (see Fig. 3). Similar eddies were present in seventeen of the twenty-six cases where ship accidents have occurred during a nine-year period.

In an attempt to reduce such accidents, a mathematical model to forecast steep wave conditions off the Norwegian coast has been developed. Trial forecasts have been produced that can warn mariners of severe steep and breaking waves. The mathematical model, developed as part of a research program entitled "Ships in Rough Seas," is based on extensive model-basin wave-focusing experiments. The ultimate stability of small vessels in beam seas is directly related to the crest front steepness, ϵ , of the approaching wave. The crest front steepness, as obtained from a surface elevation time series, is defined in Figure 4 (ϵ can also be defined in space⁹).

Figure 4 also shows how rms crest front slope, ϵ_{rms} , is directly correlated with the properties of the directional wave spectrum and can be calculated from m_0 and m_2 , the zeroth and second spectral moments. Using such a relationship, crest-front wave slopes can be forecast, including refraction of the directional spectrum by both current meanders and local topography. Such forecasts are based on estimates of "critical threshold values" for both wave direction and wave height for each of the twenty-four areas shown in Figure 1. Daily forecasts are checked against critical threshold values stored in a data bank. For each area, a forecast of critical wave conditions for specific types and sizes of vessels derived from model experiments⁹ can then be prepared. The general mathematical model¹⁰ that takes account of the effects

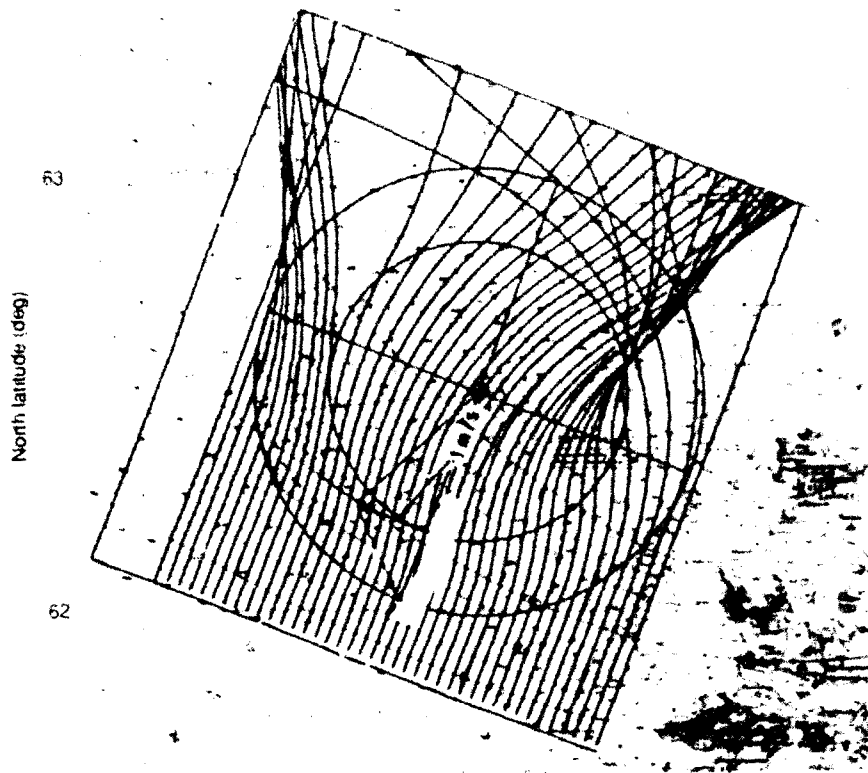


Figure 3. Reconstruction of the position for current meandering at the date and time when the *Sun Coast* capsized in area 13 of Figure 1. A current eddy of 60 km diameter rotates clockwise at a velocity of 1 m/s. Wave rays approaching from the southwest interact with the eddy, crossing on its leeward side to produce hazardous conditions (red tint) for ocean vessels.¹⁰

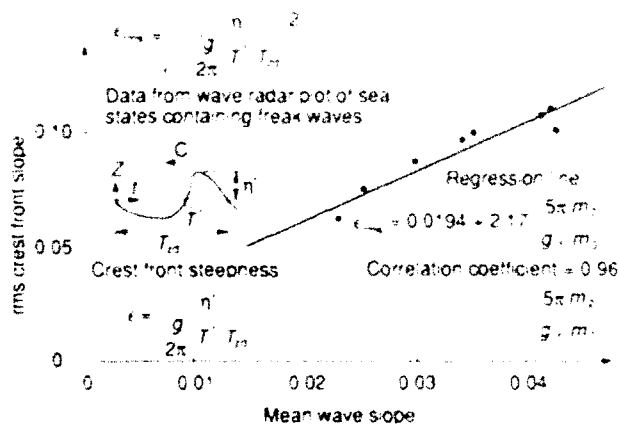


Figure 4. Root-mean-square value of crest front slope, r_{rms} , as a function of the zeroth and second spectral moments, m_0 and m_2 , respectively (g is the acceleration caused by gravity). Data were obtained with a wave radar installed on a platform on the Norwegian Continental Shelf. Results from eight time series that contained freak waves are plotted. For this work, a freak wave is defined as a wave with a height greater than twice the significant wave height, H_s . The definition of crest front steepness, r , for single waves is shown in the lower left corner, as obtained from surface elevation time series. The term z is the wave crest elevation, T_m is the zero downcross wave period, c is the wave phase velocity, and T is the time fraction between the zero upcross position and the crest position (Z is the vertical coordinate measured from mean water level and t is the time coordinate).

of multimodal directional seas and strong ocean currents is not limited, of course, to Norwegian waters. Similar areas with critical wave conditions occur off Newfoundland and Nova Scotia, Greenland, Alaska, Chile, north-west India, and southeast Africa—the last caused when swell from the Southern Ocean encounters the strong Agulhas Current.

The LEWEX experience supports the validity of the forecast model. During LEWEX, a steep critical wave was measured near 42.5°N, 55.0°W in a strong current shear where the Labrador Current from the north meets the Gulf Stream from the south.¹¹ Other examples of measurements of critical waves are given in Ref. 12. An expert committee of the International Ships and Offshore Structures Congress¹³ has recommended use of the crest-front steepness parameter in future analytical, experimental, and full-scale scientific work.

LEWEX SEA-KEEPING TRIALS

Full-scale sea-keeping trials were performed in LEWEX with the research vessels HNLMS *Tydeman* and the CEAV *Quest* at three separate locations; concurrent (side-by-side) sea-keeping trials were performed at two of the three. Ship motions in six degrees of freedom were measured independently by four teams of scientists, two on each vessel. Multimodal directional seas were measured simultaneously with many independent sensors. Subsequently, a statistical estimate of the multimodal directional seas served as an input to model basin ex-

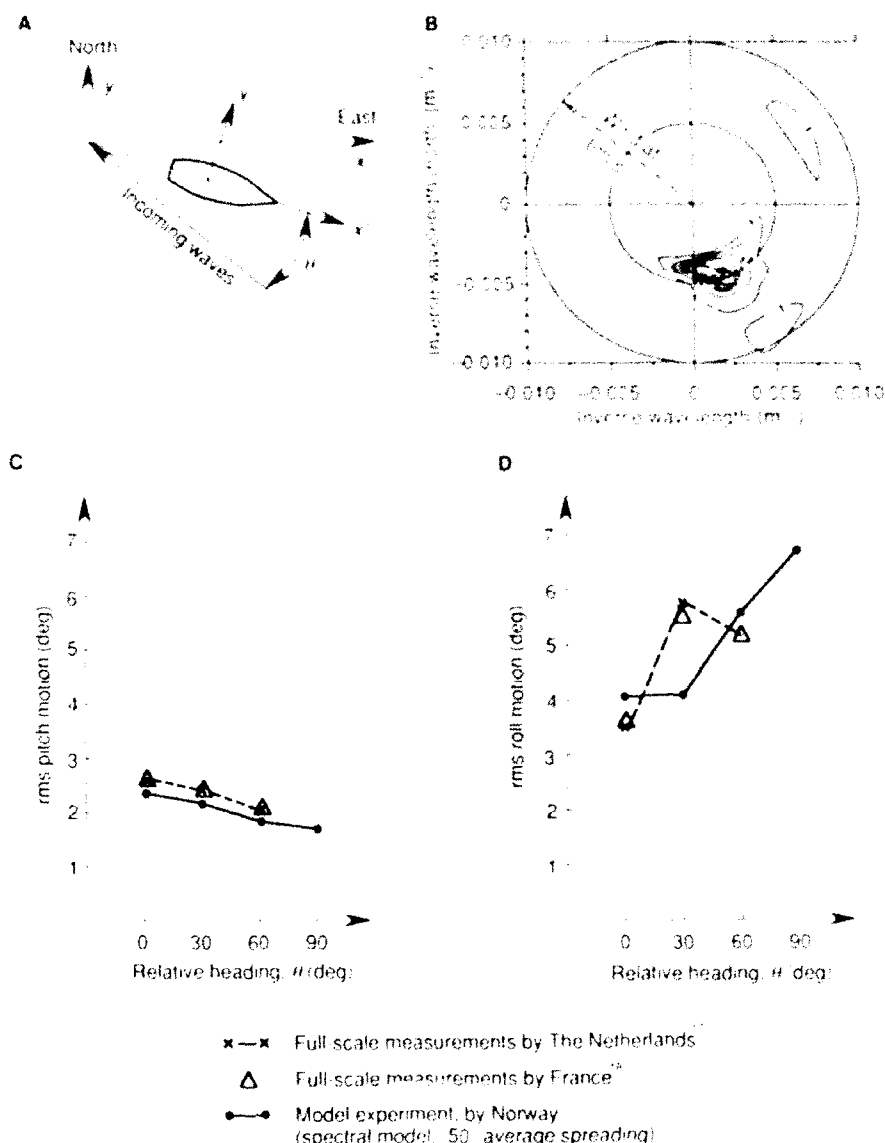
periments at Marintek.¹³ Ultimately, six legs from the full-scale sea-keeping trials, each of 20-min duration, were selected for simulation of the *Tydeman* motions at a 1/30 scale.

MODEL EXPERIMENTS IN MULTIMODAL DIRECTIONAL SEAS

The directional ocean wave model basin at Marintek is 80 m long by 50 m wide and is equipped with a hydraulically controlled movable bottom, permitting experiments at any depth between 0.3 and 10 m. The basin is equipped with two wave generator systems, which, when combined, can produce multimodal directional seas. Directional sea systems are simulated using a wave generator that drives 144 identical flaps, each individually controlled by an interactive computer system. One hundred twenty different frequencies are combined to produce a specified directional ocean wave spectrum.¹⁴ The basin is also equipped with a 50-m-wide hydraulic

double-flap wave generator. Sea-keeping tests are performed in the basin with computer-controlled free-running models. Model speed, heading, pitch, roll, heave, sway, surge, and yaw are measured accurately by an optical positioning system, using infrared light-emitting diodes and movable cameras installed at the tank walls. Computer-controlled techniques allow the testing and tuning of active antiroll fins and autopilot and dynamic positioning systems. Quantities such as vertical and lateral acceleration, propeller speed, shaft torque, rudder force and angle, quantity of water on deck, and amount of slamming can all be monitored.

Figure 5 shows model results when simulating the conditions encountered by the *Tydeman* at various headings in LEWEX on 14 March. Figure 5A shows the geometry. The associated directional wave spectrum is shown in Figure 5B, as measured by the Norwegian Wavescan buoy. A directional spectral model with an angular spread of 50° was used to simulate the Wavescan-measured spectrum. Pitch and roll motions



are shown in Figures 5C and D as functions of relative heading, using results from both model experiments and full-scale measurements. Agreement between modeled and measured motions is better than 0.5° in five out of six cases.

Figure 6 shows an example from 23 March, when both the *Tydeman* and the *Quest* were executing parallel sea trials, with motions of each monitored independently in a very complex wave situation. Figure 6A shows measured pitch motion as a function of relative heading. Each of the independent sets of measurements is in excellent agreement for each vessel. A single data point from the model basin experiment performed at Marintek also shows excellent agreement with the full-scale measurements in that very complex directional wave system, as shown in Figure 6B. For that simulation, a simplified model of the directional wave spectrum was used, with a wind sea coming from 56° having a 32° (average) directional spread superimposed on a swell coming

from 146° . For the wind sea, H_s was 2.48 m, and for the swell, H_s was 0.83 m in that simulation.

The encounter wave frequency, ω_e , (i.e., the wave frequency encountered in the reference frame of the ship) indicated that the *Tydeman* was quite close to resonance in both roll and pitch in that situation. For example, if the wind speed had increased slightly from 11 m/s to 13 m/s (26 kt), its associated equilibrium spectrum would have produced resonances for the speed and heading values illustrated in Figure 6C. With the ship at a heading directly into the primary sea at a speed of 11.6 kt, resonance occurs simultaneously in both pitch and roll. Conditions are not much improved if the ship is at b and heading instead directly into the swell at a speed of 9.9 kt; again, there are resonances in both roll and pitch. Such an assessment of potential resonances is possible, of course, only with a detailed knowledge of the multimodal directional spectrum. In this example, the swell was modeled at $H_s = 3.0$ m.

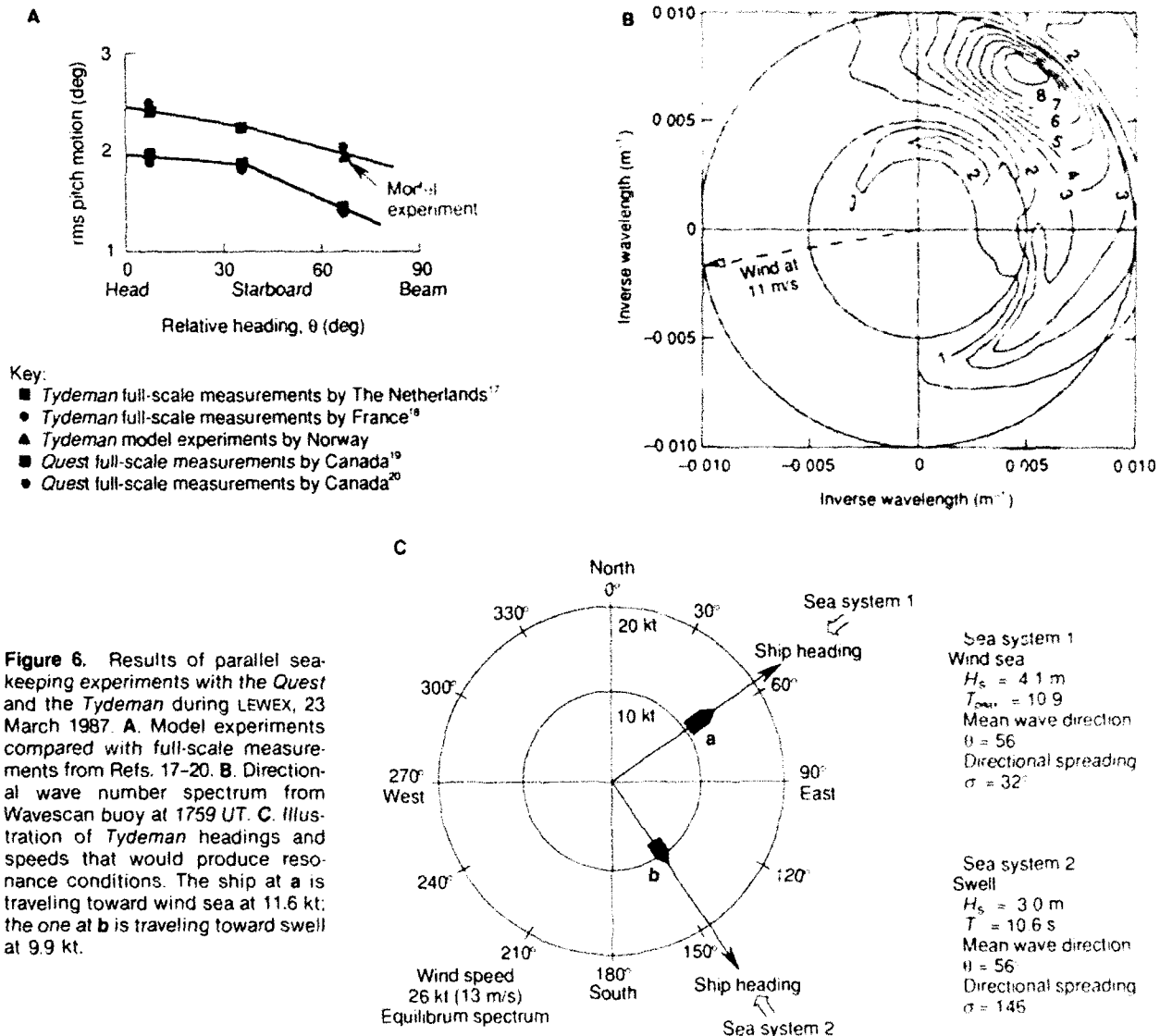


Figure 6. Results of parallel sea-keeping experiments with the *Quest* and the *Tydeman* during LEWEX, 23 March 1987. **A.** Model experiments compared with full-scale measurements from Refs. 17-20. **B.** Directional wave number spectrum from Wavescan buoy at 1759 UT. **C.** Illustration of *Tydeman* headings and speeds that would produce resonance conditions. The ship at a is traveling toward wind sea at 11.6 kt; the one at b is traveling toward swell at 9.9 kt.

Long-term wave statistics for the North Atlantic show that bimodal seas occur about 40% of the time. Navigators normally adjust both speed and heading to avoid large motion responses. As the above example from LEWEX illustrates, however, multimodal seas limit the available options and compress the range between best and worst headings. Multimodal short-crested seas may even introduce an unexpected heading-versus-response dependency, for example, as experienced by the *Quest* during LEWEX (see the article by Nethercote in this volume). Full loss of operability therefore becomes possible in much lower sea states than would be predicted for a unimodal directional sea.

NONLINEAR SHIP MOTIONS

One goal of LEWEX was to explore the limits of linear sea-keeping theory, for which rms pitch increases linearly with increasing mean wave slope if the wave frequency and the ship heading and speed are constants. Figure 7 shows full-scale measurements of rms pitch as a function of calculated mean wave slope taken on each of seven days during LEWEX. On 8 and 14 March, both the speed and the heading of the *Tydeman* were nearly identical. Further, the directional properties of the wave spectra (as indicated by the unidirectivity index, UI, which indicates the percentage of total energy contained in the primary wave system)¹⁵ were quite similar. Figure 7 also shows the results from the model experiment simulating the conditions of 14 March, confirming linearities. A dotted line is drawn between the origin and the results from 14 March extrapolating to large mean wave slopes. The 8 March data, however, are located above this line, showing that pitch motion clearly exceeds the linear extrapolation.

Since linear systems driven with Gaussian inputs have a zero-valued bi-spectrum, the energy in the bi-spectrum represents a direct measure of nonlinearity. Figure 8 shows the calculated bi-spectrum of pitch motion for 8 March, clearly indicating the nonlinear response that occurred on that day. Of all ship motions measured that day, the pitch motion contained the most significant nonlinearities.

Very long sea-keeping runs under stationary, well-controlled conditions are required to obtain good estimates of bi-spectra. Such long runs are very difficult to achieve in full-scale sea trials because sea conditions often change too rapidly. As an alternative, experimentation in a modern wave laboratory is often a more practical method for investigating nonlinear ship motions. In such a laboratory, statistics from many short runs can be efficiently combined to simulate the very long sea-keeping runs of a full-scale sea trial.

It is fairly rare to have six-degree-of-freedom model results and full-scale trials for comparisons. Data obtained from the LEWEX research program have therefore been proposed as the basis for an international development of standard sea-keeping data.¹⁶ Several numerical models based on traditional sea-keeping theory will, in the near future, attempt to simulate the ship motions that were measured in the LEWEX research program.

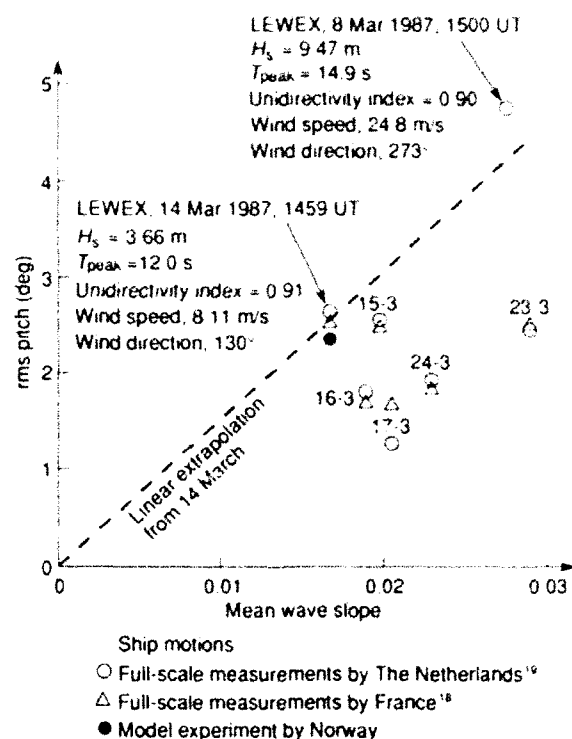


Figure 7. Measured rms pitch of the *Tydeman* shown for various calculated mean wave slopes for each of seven days during LEWEX. For ship motion measurements on 8 March 1987, the associated directional wave spectra are hindcasted from the 3G-WAM model (personal communication, J. Ooms, Laboratory for Ship Hydrodynamics, Technical University of Delft, The Netherlands, 1989). Other measurements of ship motions are from Refs. 18 and 19. Results from sea-keeping trials with nearly the same headings but with different directional spectra are shown for 15, 16, 17, 23, and 24 March.

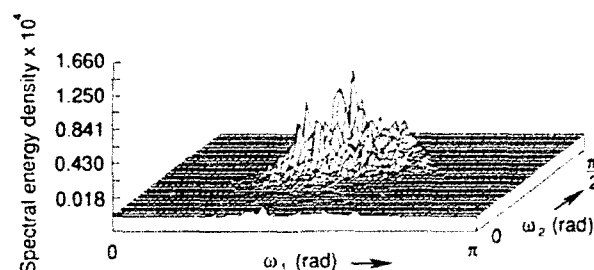


Figure 8. Nonparametric bi-spectrum estimate of pitch motion of the *Tydeman* on 8 March 1987 when $H_s \approx 9.5$ m. The maximum value reached was 0.93 (personal communication, J. Ooms, Laboratory for Ship Hydrodynamics, Technical University of Delft, The Netherlands, 1989; see also Ref. 21). The term $\omega = 2\pi/r$ is the cyclic frequency of pitch motion. For calculation of bi-spectra, see Ref. 22.

CONCLUSIONS

A unimodal short-crested sea is an inadequate description of the driving forces on an ocean vessel, and is therefore also inadequate to predict the vessel's operational performance. Long-term wave statistics show that about 40% of all sea states that occur in the North Atlantic

are multimodal. To conduct realistic operational studies in the future, this multimodal behavior of the sea must be recognized and adequately modeled.

Multimodal short-crested sea states compress the range between best and worst headings. The compressed range can cause full loss of operability in sea states lower than might be expected with a unimodal sea. Multimodal short-crested seas may even introduce an unexpected heading-versus-response dependency.

Multimodal short-crested seas increase the encounter probability for nonlinear wave groups containing steep elevated waves that can drastically affect the stability or operation of smaller vessels. Forecasts of critical wave conditions in local areas, based on calculated critical threshold values for wave direction and wave height, are possible, but wave-current interactions must be taken into account.

Critical wave conditions depend on the class of vessels under consideration. Experience gained in carefully controlled model experiments can provide detailed response data for any class of vessels.

REFERENCES

- ¹Kjeldsen, S. P., Krogstad, H. E., and Olsen, R. B., "Some Results from the Labrador Sea Extreme Waves Experiment," in *Proc. 21st International Conf. on Coastal Engineering*, Malaga, Spain, pp. 667-681 (Jun 1988).
- ²Syvertsen, K., Thuestad, T., and Remseth, S., "The Effect of Short-Crested Waves to Fatigue Damage Calculation," in *Proc. ASCE Structures Congress*, Houston, Texas (Oct 1983).
- ³Fukuda, J., "On the Families of Wave Spectra for Prediction of Wave Bending Moments," *J. Soc. Nav. Archit. Jpn.* 120 (1966).
- ⁴Clarke, J. D., Price, W. G., and Temarel, P., "The Influence of Seaway Description on Ship Responses Calculated from Computer Time Simulations," in *Proc. Symposium on Description and Modelling of Directional Seas*, Danish Hydraulic Institute and Danish Maritime Institute, Copenhagen, pp. D-5-1-D-5-17 (1984).
- ⁵Kjeldsen, S. P., Lystad, M., and Myrhaug, D., *Forecast of Breaking Waves on the Norwegian Continental Shelf*, Norwegian Meteorological Institute and Marintek, Oslo, Trondheim, Norway (Feb 1981).
- ⁶Lorentzen, P., Naeroy, A., Kjeldsen, S. P., and Mohr, J., *Report from the Court of Inquiry after the Loss of M/S Austri 19th September 1979*, Marintek, Trondheim, Norway (1980).
- ⁷"Environmental Conditions," I.S.S.C. Report of Committee I.1, *Proc. 10th International Ship and Offshore Structures Congress*, Copenhagen, Denmark, Vol. 7, pp. 19-44 (Aug 1988).
- ⁸Saeveraus, N., Kjeldsen, S. P., and Naeroy, A., *Report from the Court of Inquiry after the Loss of M/S Sun Coast at Stad 2, December 1984*, Marintek, Trondheim, Norway (1988).
- ⁹Kjeldsen, S. P., "Determination of Severe Wave Conditions for Ocean Systems in a 3 Dimensional Irregular Seaway," in *Proc. 8th Congress Pan American Institute of Naval Engineering*, Washington, Paper No. 616 (Sep 1983).
- ¹⁰Kjeldsen, S. P., *Wave Forecast - Program for Verification*, M1 51 A 88-0032, Marintek, Trondheim, Norway (1988).
- ¹¹Buchalla, H. G., and Tolstrup, E., *LEWEX, Labrador Extreme Waves Experiment*, F-522 C1433 85449, Wehrtechnische Dienststelle fuer Schiffe und Marineanlagen, Kiel, Federal Republic of Germany (1987).
- ¹²Kjeldsen, S. P., "Breaking Waves," in *Proc. NATO Advanced Research Workshop, Water Wave Kinematics*, Molde, Norway, pp. 453-473 (May 1989).
- ¹³Kjeldsen, S. P., "Current Wave Interactions Observed in the Labrador Sea Extreme Waves Experiment," in *Proc. NATO Advanced Research Workshop, Water Wave Kinematics*, Molde, Norway, pp. 613-619 (May 1989).
- ¹⁴Stansberg, C. T., and Kjeldsen, S. P., *Marintek Ocean Basic Wave Catalogue 1988*, 511031.00, Marintek, Trondheim, Norway (1988).
- ¹⁵Krogstad, H. E., *Wave Data Collected by Wavescan during the Labrador Sea Extreme Waves Experiment*, SINTEF 02 0810.00, Trondheim, Norway (Jan 1987).
- ¹⁶Johnson, B., Anderson, N., and Glinos, W., "A Progress Report on a Proposed ITC Open Architecture Standard Format from Hullform Databases," in *Proc. 22nd American Towing Tank Conf.* (1988).
- ¹⁷Ooms, J., *Wave and Ship Motion Measurements aboard HNLMS Tydeman during LEWEX, March 1987*, Report No. 760, Laboratory for Ship Hydrodynamics, Technical University of Delft, The Netherlands (1987).
- ¹⁸Davies, G. R., and Boubert, J. P., *LEWEX - French Tests - Preliminary Results*, Report No. 2401-1987, Basin d'Essais des Carènes, Paris, France (1987).
- ¹⁹Ellis, W. E., *Ship Motions, Strain, and Impact Pressures Measured on CFA Quest during LEWEX 87*, Interim Technical Memorandum, Defence Research Establishment Atlantic, Dartmouth, Canada (Jun 1988).
- ²⁰LEWEX 87 - Analysis of CFA Quest Full-Scale Sea-Keeping Data, Report No. TR-HYD-27, Institute for Marine Dynamics, National Research Council, St. Johns, Newfoundland, Canada (1988).
- ²¹de Luis, Jose E., *LEWEX-87, Hindcasting the Experiment - Part III, Study of Wave Conditions during HMS Tydeman's Trip to St. Johns*, Programa de Clima Maritimo y Banco de Datos Oceanograficos, Madrid, Spain (1988).
- ²²Chisholm, J. S. R., and Morris, R. M., *Mathematical Methods in Physics*, North-Holland, Amsterdam (1964).

ACKNOWLEDGMENTS: The LEWEX project is organized within NATO as a multilateral scientific research program. The model of the *Tydemán* in 1/30 scale was provided by the Ship Hydromechanics Laboratory at Delft University. Computations of resonant periods for roll and pitch were provided by Johan H. de Jong of the Netherlands Ministry of Defense, The Hague, The Netherlands. Polar plots of directional spectra used in Figures 5 and 6 were prepared by Harald E. Krogstad of Sima, SINTEF, Trondheim, Norway. Special thanks are given to Egil Jullumstro and Carl T. Standberg for their contributions to the LEWEX research program during the performance of model experiments in the Ocean Laboratory at Marintek, Trondheim, Norway.

WIND-WAVE PHYSICS

*IN WHICH SOME OF THE PHYSICAL CONSTRAINTS
ON DETERMINING THE DIRECTIONAL OCEAN WAVE
SPECTRUM ARE EXAMINED*

ON THE WIND-WAVE COUPLING PROBLEM

Hindcasts or forecasts of real events made with present-day wave models incorporating sophisticated physics are not much better than those made with previous generations of less sophisticated models. More complete specification of the wind input and of the wind used in calibrating the models is needed. Of crucial importance is the relation between the measured wind speed and the wind stress (the air-sea momentum transfer rate).

INTRODUCTION

The coupling between the wind and the waves, by which energy and horizontal momentum are transferred from the air to the sea, is not strong. As the wind travels over a land surface, for instance, it encounters fixed objects beneath that cause flow separation to occur on a variety of space scales. Together, these fixed objects act to produce a drag force, called the "wind stress," on the air above. A turbulent boundary layer results, which transfers wind energy and momentum downward.

The boundary layer is well characterized by a logarithmic increase of wind speed with height that starts from zero speed at a height related to the size of the fixed roughness elements, namely, the roughness height. Over the land, the roughness height is about 1/30 the size of the largest roughness elements. At sea, a logarithmic boundary layer exists, but in spite of the occurrence of large waves, its characteristic roughness is typically 2 orders of magnitude smaller. Apparently, the marine roughness is determined by the height of the rather small waves that travel at, and just above, the minimum phase speed in the dispersion (wavelength-speed) relation of gravity-capillary waves, where gravity and surface tension are equally important in determining the restoring force on the water surface. These slowest-moving waves look the most like fixed roughness elements to the air above them; they are young in the sense that they grow quickly. (The age of the waves is defined quantitatively as the ratio of the wave phase speed to the wind speed. In a fully developed oceanic wave field, the age of the shorter waves, which determine the sea surface roughness, is typically a factor of 10 less than that of the dominant waves.)

The coupling is weak because, at sea, the dominant, long-wavelength water waves propagate at speeds as high as that of the wind that generates them; in a fully developed sea, they travel about 20% faster than the wind at a height of 10 m. The wide variety of wave ages found in any wind sea suggests that several different wave-generation regimes exist at once: one for the dominant waves, one for the gravity-capillary waves, and yet another for the purely capillary ripples from which the whole process starts when the wind begins to blow. Several physical mechanisms are involved in each regime, and we will discuss the important ones.

Explanations of the primary physical mechanisms by which waves grow in the wind will be followed by a description of some of the more recent tests of the various theories that model the physics. The physical models of the wave-generation process in use today will be seen to be based on incomplete experimental evidence and an incomplete description of the physics. Recent experiments designed to measure the development of the wave field in fetch-limited winds (i.e., blowing offshore, and therefore acting over a well-defined distance, or fetch) will be described, along with the methods used for specifying the wind field. A question will be raised about the best wind to use in defining the fetch-limited growth relations, which are scaled with the wind speed and gravity.

Recent measurements of the wind stress in fetch-limited situations indicate a strong relationship between the wind stress and the state of development of the wave field. In the presence of rapidly changing wave fields, the wind stress at a given wind velocity is greater than its long-fetch, open-ocean value by a factor of 2 or more. Because the wind stress (as opposed to the wind velocity) determines the rate at which the waves develop, most of the modern, physics-related models use the wind stress in their prediction formulas, although most experimental results relate measurements of wave growth to wind velocity.

Measurements of wind stress have been made in conjunction with wave-growth measurements at sea, but experimentalists have almost always found cogent reasons for ignoring wind-stress measurements in favor of wind-velocity measurements when scaling their results. The relationship between the wind velocity and the wind stress in such measurements has invariably been poorly defined. The scatter in the relation is always large, and explanations for the scatter have been slow in coming. The consensus is that much of the scatter can be explained by making an allowance for wave age.

The relationship between wind velocity and wind stress is thus a crucial one, and our understanding of it is one of the critical factors in determining the accuracy of wave-prediction models. Some recent experimental wave-growth measurements will be scaled with various wind-velocity/wind-stress relations to illustrate the importance

of the relation. The conclusion will be that more precise definitions of the wind velocity, of its relation with the energy input to the waves and to the wind stress, and of the relation between the wind stress and the sea state will be necessary before the new generation of wave models can make use of their more sophisticated physics to improve forecasting skill. Until we get the driving force right, we cannot, without ambiguity, use better-specified physics to quantify the balance of physical processes in a growing field of ocean waves.

WAVE-GENERATION MECHANISMS

The dominant waves receive their energy from two sources: (1) nonlinear interactions, which import energy from other wavelengths; and (2) the wind, which provides the rest in several ways. The most important energy source for the growth of the dominant waves is thought to be a shear-flow instability mechanism,¹ whereby the waves, of height $\eta(t)$, modify the airstream above them, shifting the phase of the mean airflow streamlines downwind to produce wave-coherent air pressure fluctuations $p(t)$. These fluctuations do work on the waves at a mean rate per unit area

$$\left\langle p \frac{\partial \eta}{\partial t} \right\rangle = \frac{\partial E}{\partial t} , \quad (1)$$

where E is the wave energy per unit area, and the angle brackets represent ensemble averaging. The exponential growth rate per radian of wave phase is defined as

$$\zeta = \left(\frac{\partial E}{\partial t} \right) / \omega E , \quad (2)$$

where $\omega = 2\pi f$ is the radian frequency, so the wave variance grows as

$$a^2 = a_0^2 e^{\omega \zeta t} , \quad (3)$$

where a is the wave amplitude and a_0 is its initial value. The shear flow that supports the instability, maintaining its form in the presence of the mean wave-induced momentum exchange, is that of the turbulent air boundary

$$U(z) = (u_* / \kappa) \ln(z/z_0) , \quad (4)$$

where $\kappa \approx 0.4$ is von Karman's constant, z is the height above the sea surface, z_0 is the sea surface roughness height, and

$$u_* = \sqrt{\tau / \rho_a} , \quad (5)$$

where ρ_a is the air density and τ is the rate per unit area at which horizontal momentum is transferred from the air to the sea, or the wind stress. The term u_* is known as the friction velocity and is thought to be related linearly to the wind velocity U according to

$$u_*^2 = C_D U^2 , \quad (6)$$

where C_D is the drag coefficient. If C_D is constant, as is commonly assumed, the u_*-U relation is linear (but see the section entitled "Drag Coefficient")

The wave-coherent pressure can be given in the form

$$p_w(t) = \rho_w g \gamma(\mu, \lambda) \eta(t) , \quad (7)$$

where g is the acceleration due to gravity, and γ is complex. The real part of γ , $\text{Re}(\gamma)$, is the in-phase component of the wave-coherent pressure; the imaginary part,

$$\text{Im}(\gamma) = \frac{\rho_w}{\rho_a} \zeta , \quad (8)$$

is the component that does work on the waves, where ρ_w is the water density. The variable $\mu = (U \cdot k) / \omega = (U/C) \cos \theta$ is a dimensionless wind speed (inverse wave age), where θ is the wind-wave angle, and C is the wave phase speed; $\lambda = kz$ is a dimensionless height, where k is the wave number. The use of $\cos \theta$ indicates that the waves are forced by the component of the wind in the wave direction.²

The relations given are for the growth of a single wave component at a single frequency. Provided the components of the real wave spectrum are uncoupled, they can be extended to apply to the entire spectrum ($1 < \mu < 5$). If nonlinear interactions between components at different frequencies are allowed,³ or if modifications of the turbulent wind profile by the waves are permitted,^{4,5} the problem becomes less tractable. The growth mechanism is thought to explain the transfer of energy from the wind to the dominant waves quite well, although important arguments remain over the magnitude of the transfer, which we will discuss later.

A body of theory^{6,7} also exists that explains the generation of the very small capillaries that appear as soon as the wind starts up as "cat's-paws" on the sea surface during wind gusts. Another form of shear instability exists in the flow very close to the sea surface; it is found in the thin (0.1–10 mm) layers dominated by molecular viscosity near the surface in the air and the water. Strong vertical shears occur in the speed of both the air and the water, which interact with each other to form waves resonant at wavelengths of about 1.3 cm, close to the wavelength of the waves having the minimum speed for waves on water (1.73 cm).

The mechanism of flow separation, long out of fashion as a way of making waves grow, is now thought to account for some of the growth of the intermediate-scale waves, that is, the shorter-wavelength fraction of the gravity waves. When the wind speed is high relative to that of the waves, the separation of the airflow downwind of the wave crests shifts the phase of the mean airflow streamlines. This shift causes a wave-coherent pressure analogous to that of the dominant-wave shear-flow instability. No one knows, for a given wavelength or wave velocity, what fraction of the observed wave growth is due to short-wavelength shear instability⁶ and what fraction is due to flow separation. It has been shown⁸ that the actual separation of the airflow from the wave crest can occur only if the wave is breaking.

Thus, the mechanism will be most effective with the slowest-traveling fraction of the gravity wave spectrum, for which the ratio of wave speed to wind speed is the lowest.

Since the very young seas develop first, they define not only the wind stress, as mentioned earlier, but also the response of the wave field to changes in the wind. Such waves break continuously because they have reached their maximum stable amplitude, and they are in equilibrium between energy gain from the wind and energy loss due to breaking and nonlinear interactions. Although the input of energy and momentum can have little effect on the size of these equilibrium waves, their drag appears to be the dominant cause of the sea surface wind stress.

One other mechanism² has been identified by which the waves receive energy from the wind, namely, turbulent fluctuations of air pressure. The waves that grow the fastest by this mechanism are those that travel at the same speed as the highest-energy turbulent air pressure fluctuations, which are advected by the wind at a large fraction of its speed. All scales grow, but it is by a random-walk process, because the pressure fluctuations lose self-coherence with time. The growth is linear with time, and although the turbulent pressure fluctuations have since been found⁹ to retain their coherence for times at least twice as long as the original theory² supposed, the growth is too slow to be considered important in this context, except as an initiator of new waves in the absence of appreciable swell.

Although all the various mechanisms are known to be active at different parts of the wave spectrum in every field of growing waves, the implicit assumption of all modern wave models is that the energy input to the waves from the wind is by one mechanism only: shear-flow instability over the fast-moving, dominant waves, which is commonly derived from Equations 2, 3, 8, and 9. This mechanism, which is inoperative for the fastest-moving and slowest-moving waves in the spectrum ($\mu < 1$, $\mu > 5$), is inadequate to explain the physics; we will demonstrate in the next section that its use leads to serious discrepancies with the existing field data.

TESTS OF THE THEORIES

The various theories have been tested experimentally, both in the field^{9,10} and in the laboratory (wind/wave tunnels).¹¹⁻¹³ Two independent direct measurements^{9,10} of the rate of working of the wave-coherent air pressure on the waves give the same result (see Fig. 1). They indicate that, for $1 < \mu < 3$, the exponential wave-growth rate $\beta = \omega \gamma$ varies linearly with the dimensionless wind speed $\mu \approx U/C$:

$$\beta = 0.25\omega(\rho_a/\rho_w)(\mu - 1), \quad 1 < \mu < 3. \quad (9)$$

Radar measurements¹¹ in wind-wave tanks of the total growth rate of very short (1–10 cm) waves, which are responsible for the Bragg backscatter process, clearly show a stronger than linear dependence of the growth rate on μ , assuming that, at such wavelengths, the trans-

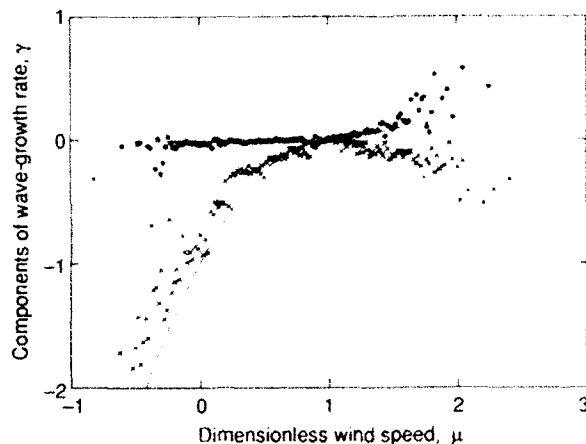


Figure 1. The measured fetch-limited exponential wave growth rate¹⁰ γ (Eqs. 7 and 8: $\text{Re}(\gamma)$ is \times , $\text{Im}(\gamma)$ is \diamond) as a function of the dimensionless wind speed $\mu = (U/C)\cos\theta$, where U is the wind velocity at a height of 5 m, θ is the wind-wave angle, and C is the wave phase velocity. The data values¹⁰ closely fit the dashed lines,⁹ which are themselves fits to data from a separate field experiment.

fer of energy by nonlinear interactions is unimportant. The relation that best fits the data has some theoretical justification⁶ and indicates a square-law dependence of the exponential growth rate on the dimensionless wind speed:

$$\beta = 0.04\omega(u_*^2/C^2)\cos\theta, \quad 0.25 < u_*/C < 2.5, \quad (10)$$

where the friction velocity u_* was obtained from the measured wind speed by using a drag coefficient wind-speed dependence¹⁴ known to contain questionable data.¹⁵ Although the coefficient of Equation 10 is doubtful, the square-law behavior is not. The radar measurements cover the range ($7.5 < \mu < 75$) of dimensionless wind speeds (μ is obtained from Eq. 6, assuming a constant $C_D = 1.5 \times 10^{-3}$), and the scatter about the fitted line contains the results of the wave-induced pressure measurements.^{9,10} Further direct-pressure measurements of wave-growth rates made¹⁶ in the North Sea at values of μ up to about 10 corroborate the square-law behavior.

The experimental evidence remains open to interpretation. The square-law behavior in the wave-induced energy gain leads to growth in wave momentum far exceeding the wind stress.⁹ Theory^{1,6} suggests that the wave-growth mechanisms in the two ranges of dimensionless wind speed ($1 < \mu < 3$, $7.5 < \mu < 75$) are different. A large uncertainty persists in the form of the parameterizations for the energy and momentum input from the wind.

FETCH-LIMITED WAVE-DEVELOPMENT MEASUREMENTS

Several field experiments have been designed to observe the development of the entire wave field under the

forcing of a steady wind. These experiments have been used to determine and define the shape of the spectrum and its time and space development, and to provide calibrated fetch-limited growth laws for the modeler. The Joint North Sea Wave Project¹⁷ led directly to the development of parametric models that included for the first time the influence of nonlinear wave-wave interactions on wave development. The most recent models compute the nonlinear interactions *ab initio* and include refraction and shallow-water effects. Most have been tested extensively in the SWAMP (Sea Wave Modeling Project)¹⁸ and SWIM (Shallow Water Intercomparison of Models)¹⁹ studies, which included not only standard tests such as steady-wind offshore growth, but also tested all the models against specific real storms, verified with at least some wave measurements. All the models were within a factor of about 2 in wave energy and about 20% in dominant wave frequency. The width of the limits of agreement is a measure of the state of the art in wave modeling.

Additional field experiments have been conducted since those tests. Two recent ones were performed in Lake Ontario²⁰ and in the open North Atlantic²¹ during the Canadian Atlantic Storms Program (CASP). The Lake Ontario measurements were performed with a wave staff array of superior directional and wavelength (high-frequency) response. (A wave staff array is a group of vertical wave-measuring wires arranged in a carefully designed horizontal pattern—an antenna of sorts.) The CASP measurements were made with directional wave buoys in the presence of large-amplitude swell. Both indicate deficiencies in the earlier field measurements and the growth laws derived from them. In addition, both clearly indicate that the growth laws for the laboratory measurements, which are of relatively young waves, differ significantly from the field growth laws. The implicit assumption in the models of a single generation mechanism that leads to the choice¹⁷ of a single regression line in fitting dimensionless wave energy to frequency and fetch, for both the laboratory and the field data, is no longer tenable.

The Lake Ontario and CASP experiments demonstrate the benefits of using the wave-age parameter C_m/U_c , where C_m is the phase speed of the dominant waves (those at the spectral maximum), and $U_c = U \cos \theta$ is the component of the wind velocity in the dominant wave direction (reliable wave-direction measurements have become available only recently). That the wave age might be estimated by spaceborne synthetic aperture radar remains a fascinating possibility.

Because an offshore wind, measured at a height of 10 m, increases by about 23% within the first 5 km off the shore²² (where the surface roughness decreases suddenly by 2 orders of magnitude), it is important for a given experiment to define the variation of the wind speed along the fetch and to specify what fetch average to use in the growth-law scaling. The discrepancy between the *in situ* wind and a fetch average is typically about 6% (Fig. 2); it is largest at a fetch of about 2 km. Although the atmospheric stability can, through its influence on the shape of the near-surface wind-speed pro-

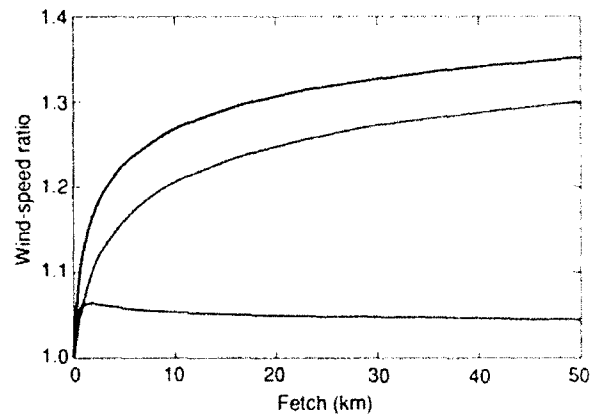


Figure 2. The CASP^{21,22} variation in the offshore wind direction of the ratio $U_{10}(X)/U_{10}(0)$ of wind speed at a height of 10 m and a fetch of X km to the shoreline wind speed (black curve), the calculated ratio $\bar{U}_{10}(X)/U_{10}(0)$ of the fetch-averaged wind speed to the shoreline wind speed (red curve), and their difference (blue curve).

file, also affect the wave-growth rate,²³ the offshore variation of air stability in the CASP aircraft study²² was small enough to be neglected.

The data from the wave staffs in Lake Ontario indicate a high-frequency spectral slope that is much closer to f^{-4} than the f^{-5} relation suggested by earlier field experiments.¹⁷ The CASP experiment indicates that the presence of swell has little, if any, effect on the growth laws and confirms the f^{-4} spectral slope of the Lake Ontario experiment.

DRAG COEFFICIENT

The transfer of horizontal momentum from the air to the sea has been the subject of many studies, largely experimental, in the wind tunnel and in the field. Over fixed topography, the scaling laws that define the characteristics of the turbulent boundary layer have been worked out in detail.²⁴ Over the sea, on the other hand, the measurements are much more difficult, and the scaling laws are not as well understood. The presence of a wave field that is withdrawing momentum from the wind at rates depending on its history has certainly led to complications in the interpretation of the data.

Micrometeorologists are not accustomed to measuring waves, and, consequently, all but the most recent publications on the marine boundary layer have ignored their effects. This circumstance has led to much controversy concerning the form of the drag coefficient over the ocean. The most recent, good determinations of the drag coefficient in the open ocean^{25,26} indicate that, when only unlimited-fetch data are considered, the drag coefficient is found to vary with wind speed:

$$C_{10} = AU_{10} + B, \quad (11)$$

where A and B are regression constants, and the subscript "10" refers to the reference height of the wind measurement. Equation 11 can be simulated²⁷ by as-

suming that the sea surface roughness is related, through the friction velocity, to the air-sea momentum transfer rate²⁸

$$z_0 = \alpha u_*^2 / g, \quad (12)$$

where the constant α is taken to be about 0.012.

The reader should note that neither Equation 11 nor Equation 12 can be justified theoretically. The former is dimensionally inconsistent, whereas the latter, although purported to apply to the small-scale waves that cause the sea surface roughness (possibly through flow separation), ignores the surface tension, which is as important as gravity in determining the restoring force for these short waves. Both are simply attempts to allow for our lack of understanding of the relationship between the wind and the sea surface drag. Thus, Equations 11 through 13 should not be taken as explanations of the physics; they only simulate the measurements.

Air-sea momentum flux measurements in Lake Ontario have been used²⁹ to produce a model of the wind speed and sea state variation of the drag coefficient on the basis of the idea that the increased drag in young seas is due to flow separation from the crests of breaking waves. The model, which can be seen in Figure 6 of Ref. 29 (not shown in this article), fits all the Lake Ontario drag coefficient data and also the open-ocean drag coefficients.^{25,26} It can be simulated with the simpler relation

$$10^3 C_D = (U_c / C_m)(AU + B), \quad (13)$$

$$0.8 < U_c / C_m < 1.25,$$

where $A \approx 0.07$ and $B \approx 0.3$.

A series of wind-stress and wave spectral measurements made in the North Sea³⁰ have been used—in conjunction with a formulation³¹ that allows the estimation of the wave age from the observed fetch-limited wave growth—to estimate the wave-age dependence of the oceanic drag coefficient. Because the drag coefficients have not been related to the wind speed, they cannot be compared directly with the predictions of Equation 13. The best that can be said is that the North Sea results indicate a doubling of the drag coefficient at low wave age, in qualitative agreement with the Lake Ontario work. Neither of these sites is influenced strongly by the presence of swell.

The latest results, from the Humidity Exchange Over the Sea (HEXOS)³² program, which was also performed in the North Sea, are subject to further correction (S. D. Smith, personal communication, 1989) because of flow distortion around the HEXOS measurement boom and for advection of the waves by currents. Direct measurements of the wind stress were made by several observers and were combined with wave measurements from directional and nondirectional wave buoys. The HEXOS measurements indicated qualitative agreement with Equation 13, except for the youngest seas ($U_c / C_m = 2.5$), where the HEXOS-measured drag coefficients were less than half those predicted by Equation 13.

Bearing the differences in mind, it remains clear that the drag coefficient is not constant with wind speed or air stability and has a strong wave-age dependence in young seas.³¹ It is common practice in most of the wave models in use today, before applying the growth laws, to convert measured wind speeds to friction velocities by using a constant drag coefficient, or one that increases slowly with wind speed. Although the growth laws themselves are scaled with friction velocities obtained from a similar (but not necessarily the same) drag coefficient, such scaling, which is u_*^4 in wave energy, will produce correct wave predictions only at intermediate wind speeds, when the wave age is similar to that at which the original measurements were made. The only remaining question is "How large will the errors in wave height be?"

SCALING THE FETCH-LIMITED GROWTH LAWS

We decided to scale the fetch-limited wave-growth data collected during CASP²¹ with values of u_* (the component of the friction velocity in the wave direction) obtained from the measured wind velocities by using three different drag coefficient formulations: (1) constant $C_D = 1.5 \times 10^{-3}$; (2) a C_D formulation²⁷ with a u_* -dependent roughness length²⁸ that simulates the wind-speed variation of the long-fetch measurements; and (3) Equation 13, which is an approximation to the wave-age-dependent drag coefficient model.²⁹

The total wave energy

$$E = \int_{\text{wind sea frequencies}} \phi(f) df, \quad (14)$$

where $\phi(f)$ is the wave-power spectrum, is regressed in the dimensionless form

$$E^* = [g^2 / (u_*^4)] E, \quad (15)$$

against the dimensionless fetch

$$X^* = [g / (u_*^3)] X \quad (16)$$

and inverse wave age

$$u_*^* / C_m = (u_* \cos \theta) / C_m, \quad (17)$$

where X is the fetch and C_m is the wave phase speed at the spectral peak. Power law relations of the form

$$E = AX^B \quad (18)$$

are assumed, and $\log_{10} E^*$ is regressed against $\log_{10} X^*$ to obtain B as the slope and A as the intercept of the log-log least-squares fit for the growth law. The least-squares-fit growth laws for the three different u_* scalings of the CASP²¹ fetch-limited data differ; scaling with wave age changes the slopes and intercepts of the growth laws substantially.

The dimensionless energy versus fetch laws for the CASP data for the constant and wave-age-dependent u_c^* scalings (Fig. 3) indicate the size of the differences. The slope of the energy versus fetch relation changes from 1.04 for a constant C_D to 1.28 for a wave-age-dependent C_D (95% confidence interval on the slope is 0.08); the corresponding correlation coefficients are 0.87 and 0.94. Large discrepancies in the dimensionless energies are seen at a given fetch; the constant C_D energy is higher by a factor of more than 3 at low fetches (10^5) and lower by a factor of more than 2 at large fetches (10^8). The dimensionless energy versus inverse wave-age relations (Fig. 4) also differ, but the differences are barely significant statistically (e.g., the slopes are just outside each other's 95% confidence intervals).

The effect of adding wave-age dependence to the drag coefficient is to reduce the scaled wave energies for low fetches and young waves. The correlation coefficient improves as the scaling goes from a constant drag coefficient to a dependence on wave parameters. Even in the fetch-limited subset of the CASP data set, and even when no wave-age dependence is allowed for in the drag coefficient, the wave age is clearly a better predictor of wave energy than is the dimensionless fetch (i.e., the scatter in E^c is less for a given wave age than for a given dimensionless fetch). The statistical significance of the larger correlation coefficients when wave age is added as a fitting parameter is the subject of a separate study.³⁴ In general, the differences in correlation between the fits for constant and wind-dependent C_D

scalings are not significant, whereas those between the constant and wave-age-scaled C_D values are.

DISCUSSION AND CONCLUSIONS

Five points have been made in this article:

1. The formulation for the energy input from the wind, which is in common use in wave models, applies over a limited range of dimensionless wind speed ($1 < U_c/C_m < 3$). Because younger waves (large U/C) are influenced by different growth mechanisms, both theoretical and experimental reasons exist for assuming that the energy input formulation in the models should be different for their dimensionless wind-speed regime, $U_c/C_m > 5$.
2. The fetch-limited growth (i.e., the sum of energy input from the wind and nonlinear transfers of energy from other wavelengths minus loss to dissipation) of young waves is observed to be substantially different from that of more fully developed waves. Attempts to include both field (old waves) and wind-wave tunnel (young waves) measurements in a general growth law cannot be reproduced in recent field measurements. Two separate growth laws are needed,²⁰ with a transition region at a wave age of $C_m/U_c \approx 0.2$. Failure to use a separate young-wave law produces wave energies too small by a factor of about 2 for young waves ($C_m/U_c < 0.1$).
3. The so-called "measured" wind in limited-fetch wave-growth experiments varies with fetch and has not been defined precisely. This variation depends in part

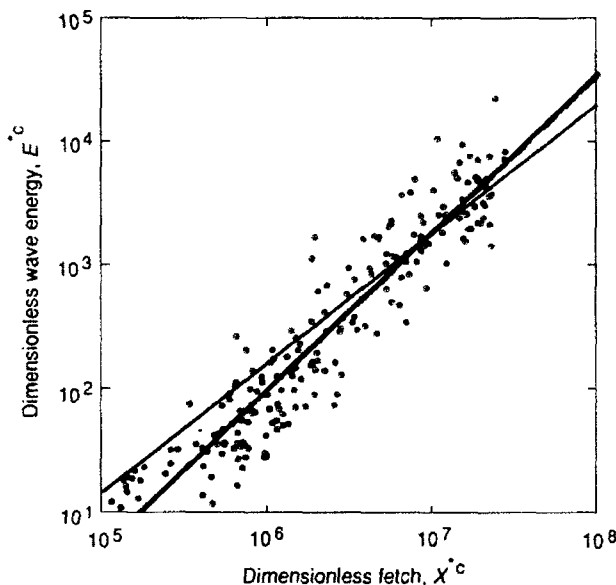


Figure 3. Log-log least-squares (Y on X) fit for the CASP dimensionless energy versus fetch relation (Eqs. 15 and 16), limited-fetch data only. The data have been scaled with friction velocity components u_c^* in the wave direction obtained from two formulations for the drag coefficient: (1) constant (red curve only), and (2) varying with wind speed and wave age according to Equation 13 (blue curve with data values). The data values for the constant drag coefficient scaling have been omitted for clarity.

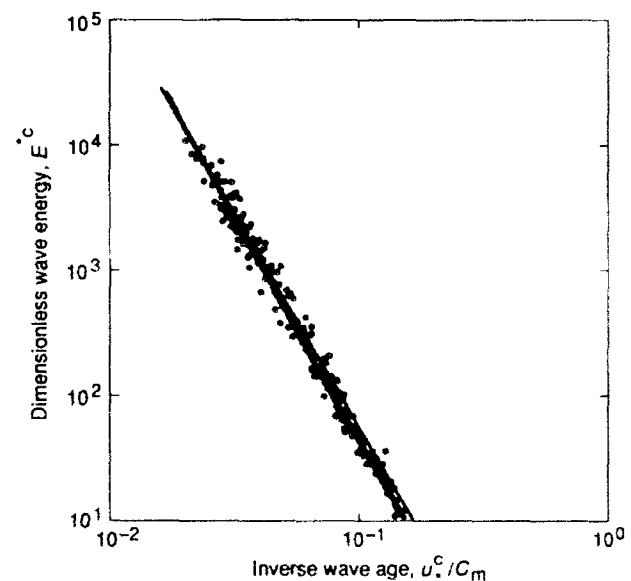


Figure 4. Log-log least-squares (Y on X) fit for the CASP dimensionless energy versus inverse wave-age parameter relation (Eqs. 15 and 17), limited-fetch data only. The data have been scaled with friction velocity components u_c^* in the wave direction obtained from two formulations for the drag coefficient: (1) constant (red curve only), and (2) varying with wind speed and wave age according to Equation 13 (blue curve with data values). The data values for the constant drag coefficient scaling have been omitted for clarity.

on the roughness of the upwind (land) surface. The variation feeds back into points 1 and 2 listed previously: If different growth laws apply at different wave ages, the wind scaling cannot be defined without accounting for it. As Figure 2 indicates, 6% errors in U (and 28% in U^4) result at intermediate fetches.

4. The relationship between the wind stress and the wind velocity at sea is not a simple square law. The most recent measurements indicate that the drag coefficient (Eq. 6) varies with both the wind speed and the wave age. The wind-speed dependence can be simulated²⁸ by allowing a dependence of the small-scale roughness of the sea surface on the wind stress, that is, on the square of the friction velocity u_* . For reasons given earlier, wave-growth measurements have been scaled invariably with the wind speed U , whereas the correct scaling for wave modeling should be with u_* . Therefore, wave predictions cannot be more accurate than our knowledge of the relation between U and u_* , that is, of the drag coefficient.

5. As Figures 3 and 4 indicate, it helps to scale the measured wave parameters with U_c/C_m . The energy versus fetch growth laws scaled with a constant drag coefficient differ from those scaled with a wave-age-dependent drag coefficient by a factor of 2 in sensitivity and 20% in the exponent of the power law. It is a simple matter to choose one drag coefficient for all wave models and obtain relative intercalibration, as was done for the SWAMP and SWIM tests. Absolute calibrations require choosing the correct drag coefficient and then looking elsewhere in the model physics for differences from calibration data (if a calibrated data set can be found).

Such difficulties suggest that all wave models must continue to revert to comparisons with the limited experimental data set when predicting wave fields from wind fields, even when the wind fields are said to be well known. The outcome of the spectral intercomparisons of the Labrador Sea Extreme Waves Experiment (LEWEX) clearly indicates this situation. The question inevitably arises, "What should we tune?" As long as the fundamental relationships between the wind velocity, the wind stress, and the sea state remain unquantified, the coefficients in those parameterizations determine the most effective tuning strategy. We cannot proceed to quantify the other physical processes in the wave field, in particular, wave dissipation.

These comments are not to say that all the physical understanding available at a given time should be left out of the models; on the contrary, without it, the problem of quantifying the physics cannot be formulated sensibly at all. Nevertheless, progress in physical understanding cannot be achieved without a well-defined strategy of theory-directed experiments that isolate the various physical mechanisms at work in the wind-wave coupling and seek to quantify them, first in isolation and then in interaction with the rest. Although LEWEX was not such an experiment, nor was it designed to be, it can nevertheless illuminate deficiencies in the process of scientific discovery, thereby leading to more focused designs in the future. Meanwhile, first- and second-generation wave models will continue to do as well in

wave forecasting as the new models do, but at a lower computational cost. The primary task at hand is to define the wind.

REFERENCES

- Miles, J. W., "On the Generation of Surface Waves by Shear Flows," *J. Fluid Mech.* **3**, 185-204 (1957).
- Phillips, O. M., "On the Generation of Waves by Turbulent Wind," *J. Fluid Mech.* **2**, 417-445 (1957).
- Miles, J. W., "On the Generation of Surface Waves by Shear Flows. Part 4," *J. Fluid Mech.* **13**, 433-448 (1962).
- Landahl, M. L., "The Effect of Short Waves on the Transfer of Wind Momentum to Long Waves," in *The Ocean Surface*, Toba, Y., and Mitsuyasu, H., eds., Reidel, Dordrecht, Holland, pp. 87-94 (1985).
- Jacobs, S. J., "An Asymptotic Theory for the Turbulent Flow over a Progressive Water Wave," *J. Fluid Mech.* **174**, 69-80 (1987).
- Valenzuela, G. R., "The Growth of Gravity-Capillary Waves in a Coupled Shear Flow," *J. Fluid Mech.* **76**, 229-250 (1976).
- Kawai, S., "Generation of Initial Wavelets by Instability of a Coupled Shear Flow and Their Evolution to Wind Waves," *J. Fluid Mech.* **93**, 661-703 (1979).
- Banner, M., and Melville, W. K., "On the Separation of Air Flow over Water Waves," *J. Fluid Mech.* **77**, 825-842 (1976).
- Snyder, R. L., Dobson, F. W., Elliott, J. A., and Long, R. B., "Array Measurements of Atmospheric Pressure Fluctuations above Surface Gravity Waves," *J. Fluid Mech.* **101**, 1-59 (1981).
- Hasselmann, D. E., Bosenburg, J., Dunkel, M., Richter, K., Grunewald, M., et al., "Measurements of Wave-Induced Pressure over Surface Gravity Waves," in *Wave Dynamics and Radio Probing of the Sea Surface*, Phillips, O. M., and Hasselmann, K., eds., Plenum Press, New York, pp. 353-368 (1986).
- Plant, W. J., "A Relationship between Wind Stress and Wave Slope," *J. Geophys. Res.* **87**, 1961-1967 (1982).
- Papadimitrakakis, Y. A., Hsu, Y.-H., and Street, R. L., "The Role of Wave-Induced Pressure Fluctuations in the Transfer Process across an Air-Water Interface," *J. Fluid Mech.* **170**, 113 (1988).
- Donelan, M. A., "The Effect of Swell on the Growth of Wind Waves," *Johns Hopkins APL Tech. Dig.* **8**, 18-23 (1987).
- Amorochio, J., and DeVries, J. J., "A New Evaluation of the Wind Stress Coefficient over Water Surfaces," *J. Geophys. Res.* **85**, 433-442 (1980).
- Smith, S. D., "Comment on 'A New Evaluation of the Drag Coefficient over Water Surfaces'," *J. Geophys. Res.* **86**, 4307 (1981).
- Hsiao, S. V., and Shemdin, O. M., "Measurements of Wind Velocity and Pressure with a Wave Follower during MARSEN," *J. Geophys. Res.* **88**, 9841-9849 (1983).
- Hasselmann, K., Barnett, T. P., Bouws, E., Carlson, H., Cartwright, D. E., et al., "Measurements of Wind-Wave Growth and Swell Decay during the Joint North Sea Wave Project (JONSWAP)," *Deut. Hydrog. Z., Reihe A* **8**, 22 (1973).
- Allender, J. H., Barnett, T. P., Bertotti, L., Bruinsma, J., Cardone, V. J., et al., "Sea Wave Modelling Project (SWAMP): An Intercomparison Study of Wind-Wave Prediction Models, Part 1—Principal Results and Conclusions," in *Proc. IUCRM Symp. on Wave Dynamics and Radio Probing of the Ocean Surface*, Plenum Press, New York (1985).
- Bouws, E., Ephraums, J. J., Ewing, J. A., Francis, P. E., Gunther, H., et al., "A Shallow Water Intercomparison of Three Numerical Wave Prediction Models (SWIM)," *Q. J. R. Meteorol. Soc.* **111**, 1087-1112 (1985).
- Donelan, M. A., Hamilton, J., and Hui, W. H., "Directional Spectra of Wind-Generated Waves," *Philos. Trans. R. Soc. London A* **315**, 509-562 (1985).
- Dobson, F. W., Perrie, W., and Toulany, B., "On the Deep-Water Fetch Laws for Wind-Generated Surface Gravity Waves," *Atmos. Ocean* **27**, 210-236 (1989).
- Smith, P. C., and MacPherson, J. J., "Cross-Shore Variations of Near-Surface Wind Velocity and Atmospheric Turbulence at the Land-Sea Boundary during CASP," *Atmos. Ocean* **25**, 279-303 (1987).
- Janssen, P. A. E. M., and Komen, G. J., "Effect of Atmospheric Stability on the Growth of Surface Gravity Waves," *Boundary-Layer Meteorol.* **32**, 85-96 (1985).
- Monin, A. S., and Yaglom, A. M., *Statistical Fluid Mechanics*, Vol. 1, MIT Press, Cambridge, Mass. (1971).
- Smith, S. D., "Wind Stress and Heat Flux over the Ocean in Gale Force Winds," *J. Geophys. Res.* **10**, 709-726 (1980).
- Large, W. G., and Pond, S., "Open Ocean Momentum Flux Measurements in Moderate to Strong Winds," *J. Phys. Oceanogr.* **11**, 324-336 (1981).
- Smith, S. D., "Coefficients for Sea Surface Wind Stress, Heat Flux, and Wind Profiles as a Function of Wind Speed and Temperature," *J. Geophys. Res.* **93**, 15,467-15,472 (1988).
- Charnock, H., "Wind Stress on a Water Surface," *Q. J. R. Meteorol. Soc.* **81**, 639-640 (1955).
- Donelan, M. A., "The Dependence of the Aerodynamic Drag Coefficient on Wave Parameters," in *Proc. First International Conf. on Meteorology and Air-Sea Interaction of the Coastal Zone*, The Hague, The Netherlands, American Meteorological Society, Boston, Mass., pp. 381-387 (1982).

- ³⁰ Geernaert, G. L., Larsen, S. P., and Hansen, E., "Measurements of the Wind Stress, Heat Flux and Turbulence Intensity during Storm Conditions over the North Sea," *J. Geophys. Res.* **92**, 13,127-13,139 (1987).
- ³¹ Mitsuyasu, H., "Wind-Wave Problems in Engineering," in *Engineering Meteorology*, Plate, E., ed., Elsevier, New York, pp. 683-729 (1982).
- ³² Anderson, R. J., and Smith, S. D., "Eddy Flux Measurements during HEN-MAX," *Eos* **69**, 1231 (1989).
- ³³ Janssen, P. A. E. M., "Wave-Induced Stress and the Drag of Air Flow over

- Sea Waves," *J. Phys. Oceanogr.* **19**, 745-754 (1989).
- ³⁴ Petric, W., and Toulary, B., "Fetch Relations for Wind-Generated Waves as a Function of Wind Stress Scaling," *J. Phys. Oceanogr.* (1990).

ACKNOWLEDGMENT: Funds for the research on which this work was based, and one of our salaries (B.T.), were provided by the Panel of Energy Research and Development, Canada Department of Energy, Mines and Resources, Marine Engineering Committee (6-2), Project No. 62131.

WIND DATA AND THE MARINE BOUNDARY LAYER

The disparities in the various estimates of wind fields from the Labrador Sea Extreme Waves Experiment can be explained by the lack of agreement on the methods used for the analysis of the marine boundary layer, the poor quality of the wind reports, and the criteria for the acceptance of the wind reports from both ships and buoys.

INTRODUCTION

The data used to define the winds in the marine boundary layer come predominantly from transient ships of opportunity and from the national data buoys. The ship data are of extremely poor quality as shown by numerous recent investigations. Ships and buoys do not adequately cover the world oceans. Even if the ship and data buoy reports were absolutely correct and represented the synoptic-scale wind, difficulties would still exist because of poor coverage and inadequate physical models. A striking result of the LEWEX (Labrador Sea Extreme Waves Experiment) analyses is that the wind speeds and directions at the two ships, the CFAV *Quest* and HNLMS *Tydeman*, as specified by the Fleet Numerical Oceanography Center (FNO), the National Meteorological Center (NMC), Ocean Weather, Incorporated, the European Centre for Medium Range Weather Forecasts, and the United Kingdom Meteorological Office, were all different. The wind fields generated by various centers also differed from one another over the entire North Atlantic (see Zambresky, this volume).

Any one of the spectral wave models, if run one at a time with each sequence of the different wind specifications, would produce different spectra. Different wave models used by the forecast centers and analyzed at The Johns Hopkins University Applied Physics Laboratory were run for a common input wind field. The wave spectra that resulted for a given model differed for the same time and place compared with the wave spectra that resulted from separately derived winds. Further, the different models still differed from one another when driven with identical winds.

All of the wind fields produced for the LEWEX spectral intercomparisons are based on the same "raw" data, that is, data from synoptic reports from land stations, ships of opportunity, and data buoys, along with both conventional and remote atmospheric soundings. Thus, differences result from variations in both the models and the methods used by the different forecast centers to analyze the synoptic data and produce the resulting gridded synoptic scale winds (see Gerling, this volume).

Wave modelers often assume that, at least for specifying the wave spectra, the input driving winds are a "given" and are correct. This assumption is not necessarily true. Wave models that are "tuned" to the wind output

of a particular model inherit the errors of that model. A major reason for these differences is that the winds reported by ships at sea are of poor quality.

Of the various wind fields, it would be difficult to show that one was more nearly correct than the others. Wave models will have inherent errors as hindcasts because of wind field errors; yet to be determined is how the errors in wave hindcasts, which are the initial value specifications for wave forecasts, affect errors in those forecasts.

ANALYSIS PROCEDURES

The various national weather forecasting centers all follow the same general procedure to produce the wind fields that would be used to drive a wave model. Their procedures differ in details, however. The objective of the analysis at a center is to produce the initial value specification as a function of latitude, longitude, and elevation of the quantities needed to time-step the finite-difference atmospheric model used by that center to forecast changes. Of particular interest are the formation, movement, and deepening or filling of low centers for wind forecasts and the advection of water vapor for the release of latent heat and the prediction of rainfall.

The details of how each center produces a marine boundary-layer wind field are difficult to find in the published literature. Moreover, in the day-to-day operation of a center changes are sometimes made. (See Ref. 1 for a description of the methods used by the NMC and Ref. 2 for those used by the FNO in 1982. Marine applications of the NMC product are described in Ref. 3.) For example, the procedures of the FNO produce a "blended" wind field, in which weights are assigned to various kinds of data and computer products on the basis of recent past data. The NMC method depends on ideas introduced by Bergman.⁴ As with the famous product from Scotland, the blends produced by other centers could have quite distinct characteristics.

The atmosphere is divided into layers, and the heights of surfaces on which the atmospheric pressure is constant are part of the initial value specification, along with the winds at each of those surfaces. The number of layers used in a model probably varies at each center, but they all may start with the height of the 1000-hectopascal (hPa)

≈ 1 mbar in the previous system of international units) surface and use a standard procedure to convert this surface to an isobaric pattern at sea level, even over land. The thicknesses of the layer nearest the Earth's surface in a model vary at each center. In addition, the velocity field in that layer must represent, by single vectors at each grid point, the behavior of a large volume of air as defined by an area around each grid point (thousands of square kilometers) and the various thicknesses of the layer (hundreds of meters) used for that particular model.

The map projections used in these models also differ, and the equations for describing the various fields are modified to account for those projections. One wonders about the effect of smoothing on different projections. A closed contour for the 1000-hPa surface on one map projection will not have the same shape on another.

Data from the land affect the analysis over the ocean by continuity. A separate research study would be necessary to find out how the various models treat the Greenland Ice Cap, the winds over the water around Greenland, the Tibetan Plateau, the various mountain ranges of the Earth, and the winds around islands. The variable winds described by Ezraty in this volume may be the effect of nearby land. Also, synoptic updates are usually available only every six hours. An interpolation for three-hour intervals may or may not be made.

The winds used for the numerical weather forecasts are not necessarily those used for the marine boundary layer, and an additional analysis step³ is required to specify the winds at either 10 or 19.5 m as the driving winds for specifying (hindcasting) or forecasting the wave spectra at each grid point of the wave model. Wave models may require a different grid than the weather forecasting model, so that an interpolation is often needed.

All analysis schemes smooth the wind fields. Sharp wind shifts at fronts are not well modeled. Smoothing tends to alter gradients in the pressure field, so that winds computed from the pressure field in areas of "true" high winds are lowered, and winds in areas of "true" low winds are made higher. (Reference 5 compares model winds from the FNOC Global Spectral Ocean-Wave Model with winds from data buoys.)

DATA ASSIMILATION

Meteorological forecasts are typically made every 12 hours for several days into the future. The forecast cycle begins with an initial value update. The forecast outputs for the previous 12-hour cycle are the startup data for the present forecasts, and these are reinitialized for the current time by assimilating the newly observed data for the present synoptic time.

These forecast 12-hour data fields are called first-guess fields for an initial value update. The measured and reported new synoptic data, such as reports from ships, are used to attempt to correct the first-guess field for changes in the meteorological fields that were not predicted by the past 12-hour forecast.

For the marine boundary layer, the available ship reports are apparently used only one at a time at some centers. The reported sea-level pressure is compared with the model value, and the accuracy of the value is judged

on the basis of how close it is to the first guess. Different centers use different methods to judge the accuracy of the report. If correct, the pressure field is changed by an area smoothing technique to agree with the new data. The reported winds are compared with the model winds. The report is then used with some sort of boundary layer model to change the wind and adjust the pressure gradient near the ship to agree with the corrected wind.

In the data assimilation procedure, the accuracy of the wind reports now becomes important. As I will discuss, very large errors in these wind reports exist. These errors are in part systematic.

Given a number of ships around a low center, some reports will agree with the first-guess winds within the required differences and will thus be used to correct the initial guess. Nevertheless, both the ship winds and the initial value update can be incorrect and contain large errors. In addition, many ships in an area of high winds may all report high winds. If the initial value update calls for lower winds, as each ship report is tested one by one, that update can be rejected. Thus, all ship reports would be rejected, and the initial value update would not show that a cyclone had deepened.

In data-sparse areas, a single report, which may or may not be accurate, may influence an area of 5° of latitude and 5° of longitude; the first-guess field may or may not be correct; and the choices as to whether to assimilate the report may or may not improve the initial value update.

A cyclone moving into an area devoid of data is carried forward by continuity as part of the first-guess field. If the field has errors (e.g., a low center at the wrong place, with a central pressure that is not low enough), it cannot be corrected.

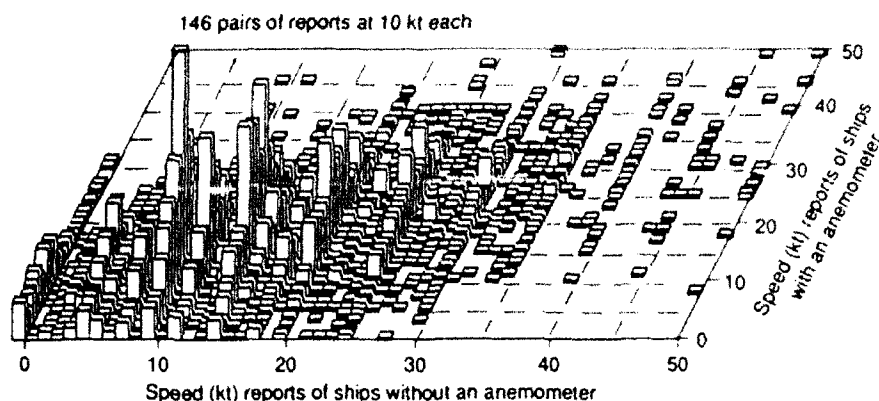
Thus, each wind field for the different meteorological centers could evolve from one synoptic time to the next, while still being different and accepting some subset of the available ship report data. Errors in the specification of the marine boundary layer, in the form of an incorrect 1000-hPa surface, propagate upward to great heights because the remotely sensed atmospheric soundings over the ocean are integrated upward to define the surfaces of constant pressure for the model.

All analysis methods must balance the field of mass and the field of motion. The winds over the ocean are an essential input to the marine boundary layer. Potentially important information is omitted if pressure data alone are used. Even if the winds were to be derived solely from the pressure field, one would still need to validate the derived winds against measurements of the winds.

THE POOR QUALITY OF SHIP REPORTS

Reference 6 contains the results of comparing wind reports that were made at the same synoptic time by pairs of ships within 100 km of each other. That article is a reevaluation and an extension of a report by Dischel and Pierson.⁷ It demonstrates the poor quality of ship reports in many different ways and recommends corrective measures. The data for Figure 1 here comprise 8265 pairs of reports from ships in the region 30°N to 40°N and 70°W to 80°W . Only one ship of the pair had an anemometer.

Figure 1. Perspective three-dimensional plot of counts (vertical axis) of the number of times ships with anemometers (into the perspective plane) and ships without anemometers (horizontal axis) within 100 km of each other reported wind speeds from 0 to 50 kt at a synoptic time for a North Atlantic location somewhere in Marsden Square 116 (30°N to 40°N; 70°W to 80°W). The largest number of counts occurred 146 times when ships both with and without an anemometer reported 10 kt. (Reprinted, with permission, from Ref. 6, p. 13,317; © 1990 by American Geophysical Union.)



The observer on the ship without an anemometer estimated the wind according to the instructions of the World Meteorological Organization. This difficult task in part depends on the assumption that there is a one-to-one relation between sea state and wind speed.

The perspective plot of Figure 1 shows a plane from which rectangular parallelepipeds project upward. The horizontal axis in the plane shows a scale from 0 to 50 kt for reports by ships without anemometers. The projection into the figure shows a scale from 0 to 50 kt for reports by ships with anemometers. The small number of omitted reports of winds over 50 kt does not affect the interpretation of this figure. The vertical height of each parallelepiped shows the total number of times pairs (one with an anemometer and one without) of ships reported the plotted speeds. For example, ships without anemometers reported 10 kt when ships with anemometers reported 10 kt 146 times. Once, a ship without an anemometer reported 50 kt while one with an anemometer reported 9 kt. Had the wind speeds reported by each pair of ships been correct for the synoptic scale, the counts would have fallen close to the 45-degree line of perfect fit.

Wind speeds for the synoptic scale separated by 100 km or less should not differ by the large amounts shown in Figure 1. For example, when ships without anemometers reported a wind of 30 kt, ships with anemometers reported speeds from 3 to 43 kt.

In Figure 7 (A through G) of Gerling (this volume), the synoptic-scale common wind fields for LEWEX have values every 1.25° of latitude (139 km or 75 nmi) and every 2.5° of longitude (at 40°, 212 km; at 50°, 178 km; at 60°, 138 km). Over these distances the wind speeds may change by 5% to 10%. They surely cannot change from one grid point to the next by the amounts shown in Figure 1. The distance between the ships is less than the distance between the winds in Gerling's figures. Moreover, the standard deviation for the wind directions (not shown) was 45°. Skeptical readers with adequate computer graphics might find it interesting to plot wind vectors from ship reports at these synoptic times to scale in some contrasting color along with the LEWEX winds.

Ships without anemometers tend to over-report speeds of 5, 10, 15, 20, or more knots in 5-kt steps along with

winds of 8, 12, 16, 18, and 22 kt. The latter represent centers of Beaufort ranges and values originally in meters per second, converted to knots. These very large differences in reported speeds result from the very poor quality of wind reports by ships. Many reasons exist for the poor quality of these reports. Even for ships with anemometers, the equipment provided to the observer makes a good synoptic-scale observation difficult.

CONCLUSIONS

The poor quality of ship reports creates difficulties in obtaining correct descriptions of the winds in the marine boundary layer. Incorrect descriptions not only make it difficult to specify and forecast wave properties, but they also make weather forecasts poor and climatological studies suspect.

Scatterometers on the European Remote Sensing Satellite (known as ERS-1) and the Japanese Advanced Earth Observing System (known as ADEOS) will help to provide better wind fields for the marine boundary for use in wave forecasts, weather forecasts, and, eventually, climatological studies. The methods used by ships at sea to measure the winds are obsolete. They could be improved using modern technology. Presently, some of the deep-sea national data buoys report six consecutive 10-min averages of the wind each hour. These data can be used to validate wave model winds and to provide conventional validation winds for remotely sensed winds.

REFERENCES

- ¹Dey, C. H., "The Evolution of Objective Analysis Methodology at the National Meteorological Center," *Weather Forecast.* **4**, 297-312 (1989).
- ²DeYoung, B., and Tang, C. L., "An Analysis of Fleet Numerical Oceanographic Center Winds on the Grand Banks," *Atmos.-Ocean* **27**, 414-427 (1989).
- ³Rao, D. B., "A Review of the Program of the Ocean Products Center," *Weather Forecast.* **4**, 427-443 (1989).
- ⁴Bergman, K., "Multivariate Analysis of Temperatures and Winds Using Optimum Interpolation," *Mon. Weather Rev.* **107**, 1423-1444 (1979).
- ⁵Zambresky, L. F., "The Operational Performance of the Fleet Numerical Oceanography Center Global Spectral Ocean-Wave Model," *Johns Hopkins APL Tech. Dig.* **8**, 33-36 (1987).
- ⁶Pierson, W. J., "Examples of, Reasons for, and Consequences of the Poor Quality of Wind Data from Ships for the Marine Boundary Layer: Implications from Remote Sensing," *J. Geophys. Res.* **95**(C8), 13,313-13,340 (1990).

⁷Dischel, R. S., and Pierson, W. J., "Comparisons of Wind Reports by Ships and Data Buoys," in *Proc. MDS'86, Marine Data Systems International Symposium*, Gulf Coast Section, Marine Technology Society, pp. 447-466 (1986).

ACKNOWLEDGMENTS: This article is sponsored by the National Aeronautics and Space Administration, Contract NAGW-690, and the Jet Propulsion Laboratory, Contract 957714-02/CH/JPL. Figure 1 was prepared by Harold Finz.

MARINE WIND VARIABILITY: ILLUSTRATION AND COMMENTS

Sea-state modelers introduce a mean wind vector at each grid point of their models that varies only once every time step. Real winds often fluctuate at much shorter space and time scales. Some examples of these fluctuating wind fields are given, along with possible implications for modeling.

INTRODUCTION

Sea-state modelers and forecasters have always expressed the need for more and "better" winds either to develop or to initialize and run their models. Usually, winds are converted into wind stress estimates by using more-or-less controversial drag relations. It is not intended here to discuss these relations, but rather to stress how wind data should be handled to improve their use in modeling and predicting sea state.

Many wind vector measurements will be available soon from the European ERS-1 remote sensing satellite scatterometer, which will provide global coverage of the ocean. As pointed out by Janssen et al.,¹ however, the increase in data quantity is useless if the data quality is not sufficient. This statement is also true for conventional *in situ* measurements.

Much effort has been spent to improve the existing measurement techniques and to plan the calibration and validation of future satellite sensors. At sea, without an absolute reference, the performance of *in situ* systems can be stated only in terms of precision. As a result, we cannot trust a single isolated wind vector value. One way to increase our faith in wind measurements is to rely on space or time continuity, provided that the meteorological condition and its associated variability permit such an assumption.

Wind buoys that are designed and calibrated carefully can achieve precisions at sea of 0.8 m/s for speed and 5° for direction. Wind reports from ships without anemometers (as shown on most weather maps) are usually rounded to the nearest 5 kt and the nearest 10°. Moreover, neither the 10-min average recommended by the World Meteorological Organization (WMO) nor a standard reference height is used systematically. This situation induces added temporal variability, which impairs the spatial variability. (See the article by Pierson, in this volume, for even more cautions.)

The next section of this article will illustrate observed spatial and temporal wind variability. The following section will focus on the spectral description of the energy of wind fluctuations and their relations for various separation distances. The final section will describe an attempt to estimate, as a function of time, a spatial mean wind vector from point measurements averaged over time.

ILLUSTRATION OF WIND VARIABILITY

Figure 1 shows simultaneous wind estimates collected in the Mediterranean between France and Corsica in January 1986.² Five ships reported quite different wind speeds, ranging from 15 to 50 kt. Such a large number of at-sea reports, all within a 250-km span, is quite unusual. Wind speeds appear to have been erratic, but at least the measurements agree that a strong westerly component existed. Automatic data validation schemes would certainly reject such widely varying simultaneous reports. An untrained analyst might comment, "How unreliable the ship reports are!"

A closer look is more revealing. Two of the ships reported high winds (45 ± 5 kt), whereas the other three reported low values (20 ± 5 kt). Moreover, the two ships located between the two high wind speed reports both indicated similar low values. Allowing for reasonable ship measurement uncertainty, it is unlikely that any of the ships was completely wrong. It is more likely that the wind was highly variable in space or in time, since individual sets of comparisons have little chance to be exactly simultaneous and coincident.

Figure 2 shows a 17-h time series of wind measurements, averaged over 1-min intervals. This record was collected in 1984 during the Promess/Toscane I experiment on board N/O *Le Suroit*, in the northeast Atlantic,

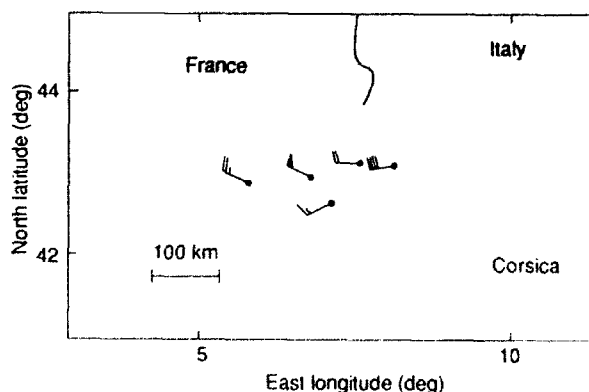


Figure 1. A sample of simultaneous ship reports in the Mediterranean on 23 January 1986 at 0000 UT, indicative of unusually high spatial variability. Each full barb indicates 10 kt, a half barb is 5 kt, and a triangle is 50 kt. (Adapted from Ref. 2.)

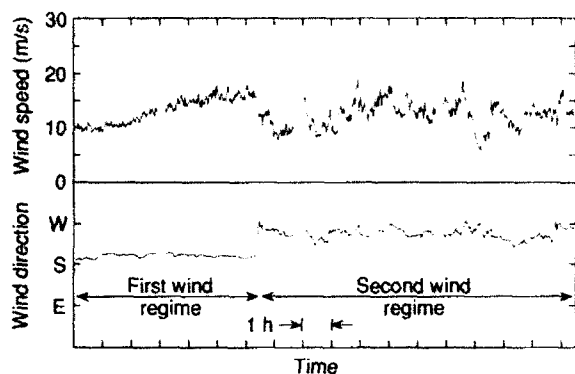


Figure 2. A time series of 1-min-averaged wind speed and direction collected at sea on board N/O *Le Suroit* (Toscane 1 data) from 1021 UT on 20 February to 0346 UT on 21 February 1984. Note the different signatures of wind fluctuations before and after the front.

southwest of Brittany. Two wind regimes separated by a cold front passage are clearly evident. The first regime corresponds to a stable atmosphere; wind direction is steady and wind speed fluctuations, at intervals of 10 to 15 min, are less than 1 m/s. The second regime corresponds to an unstable atmosphere and exhibits large wind speed variations (about 7 m/s) at intervals from 30 min up to 1 h, on top of which are the high-frequency components that are also present during the earlier stable regime. Directions also fluctuate by as much as 50° over the same intervals. These long-period oscillations persist for 12 h. Note the abrupt 12-m/s wind speed change during a time span of only 30 min that occurs about 4 h before the end of the record. For the 10-min averaging period recommended by WMO, the reported variation would have been only about 10 m/s.

In view of this time series example, the spatial wind pattern implied in Figure 1 seems likely to be real and not simply a measurement artifact. Taken together, these two examples show that representing the wind by a single mean vector, defined at a given reference level and for a given duration, may not capture its real variability over temporal scales of tens of minutes or spatial scales of a few kilometers.

THE SPECTRAL SIGNATURE OF MARINE WIND VARIABILITY

The time and space scales of concern here lie between the high frequencies, or short wavelengths, of the fine-grid meteorological models (typically 30 cycles/h and a few meters) and the lower part of the turbulent region (typically 1 cycle/h and 50 km), and thus may be influenced by both these scales. The justification for separating these two regimes is based on the well-known spectral gap of Van der Hoven³ for wind speed near the surface. This spectral energy gap, measured over land, has been used to justify a 3-h sampling interval and a 10-min averaging time for wind measurements.

At sea, evidence suggests that this spectral gap is not always present. For example, the two wind regimes of Figure 2 will each produce a different spectral shape in

the 1-h to 10-min band. The early regime will contain a spectral energy gap, but in the later regime, the spectral energy level at the gap location will be about the level of the turbulent peak, completely filling the gap.

Pierson⁴ reported overwater data from M. Donelan (personal communication), Klauss Hasselmann (personal communication), Pond et al.,⁵ and Miyake et al.⁶ He pointed out, specifically for the last two data sets (although the tendency could be detected in the others), that "the spectral estimates do not decrease toward lower values [of dimensionless frequency] as do the Kaimal et al. [see Ref. 7] overland spectra." Then he modeled this part of the spectrum as the inverse of frequency, allowing the energy level to be an increasing function of wind speed. Corrections for this model are currently in progress (C. M. Tchen, personal communication, 1986).

During the Toscane T campaign in early 1985,^{8,9} a row of seven wind-instrumented masts was installed along the shore of the Bay d'Audierne (South of Brittany, France) at a site that was well exposed and nearly perpendicular to ocean winds. The nominal altitude of the measurement locations was 12 m above mean sea level, and the separation of locations ranged from 1.5 to 10.1 km. A meteorological buoy moored off the coast provided air and water temperatures. The experimental layout permitted the investigation of spectral signatures of the along- and cross-wind fluctuations (u and v , respectively) and also of their coherence and phase as a function of separation. The following results are extracted from Champagne-Philippe.¹⁰

Twenty-seven wind records were selected on the basis of synoptic weather stationarity. The measurement duration ranged from 6 to 20 h, and the mean speed varied from 6 to 15 m/s. Each record was sliced such that representative spectral estimates of the u and v components could be computed in the 1-h to 6-s band.

As anticipated, the spectra showed variable behavior in the gap region. No global estimate of the synoptic stability of the atmospheric boundary layer was available. To sort the spectra, we used the local stability parameter, z/L (where z is the height above sea level and L is the Monin-Obukov length), computed from the buoy temperature measurements. The hypothesis was that convective situations and the corresponding instability, which are related in this region to cold air masses, will be flagged by this local and low-altitude indicator. Only 5 situations out of the 27 selected did not fit into the "gap/no gap" spectral classifications anticipated by the *a priori* sorting into stable and unstable atmospheric conditions. The unstable spectra corresponded to z/L values between 0 and -0.03 . The stable spectra were further split into two subgroups, stable and stable/neutral, whose mean z/L values were, respectively, 0.065 and 0.023.

Figure 3 presents the average of the dimensionless spectra for each of the three aforementioned categories for both the along-wind and the cross-wind components, with Pierson's 1983 model⁴ superimposed. For both components, the high-frequency parts of the spectra behave the same, regardless of the stability category, and decrease as $f^{-2/3}$, although the turbulence maximum is

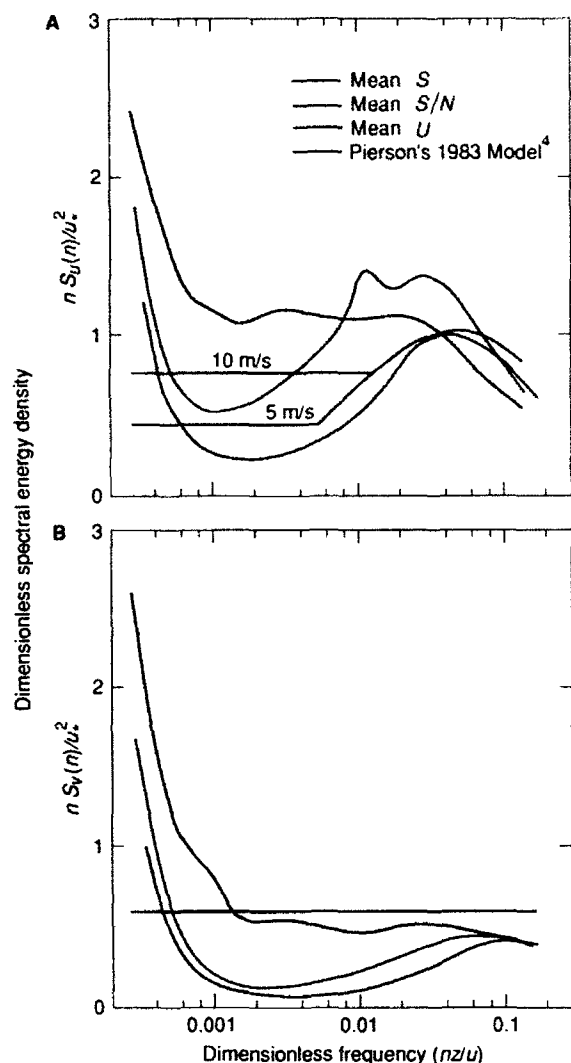


Figure 3. An averaged spectrum of wind fluctuations for the three stability regimes (S—stable, S/N—stable/neutral, U—unstable) **A.** Along-wind component. **B.** Cross-wind component. Note the energy-preserving form used to present spectral estimates; n is the natural frequency, z is the measurement altitude, u_* is friction velocity, $S_u(n)$ and $S_v(n)$ are the spectral energy densities, and u is the mean wind speed at z . (Adapted from Ref. 10.)

shifted to a lower dimensionless frequency. The striking feature is the shape change in the expected gap region. As local stability decreases, or convection increases, the gap fills up to about the energy level of the turbulent region. The plateau shape in this representation corresponds to a $1/f$ decrease, as modeled by Pierson,⁴ but does not seem to be a function of wind speed only, as he assumed. It is also related to the stability or instability of the upper layers of the atmospheric boundary layer. One might hypothesize that the spectral shape of wind fluctuations between mesoscale and turbulence is related to the profile of the Brunt-Väisälä frequency from the surface up to the first few kilometers.

Coherence and phase spectra of the u and v components were calculated for cases when winds blew either perpendicular to or along the row of masts for all separation distances.

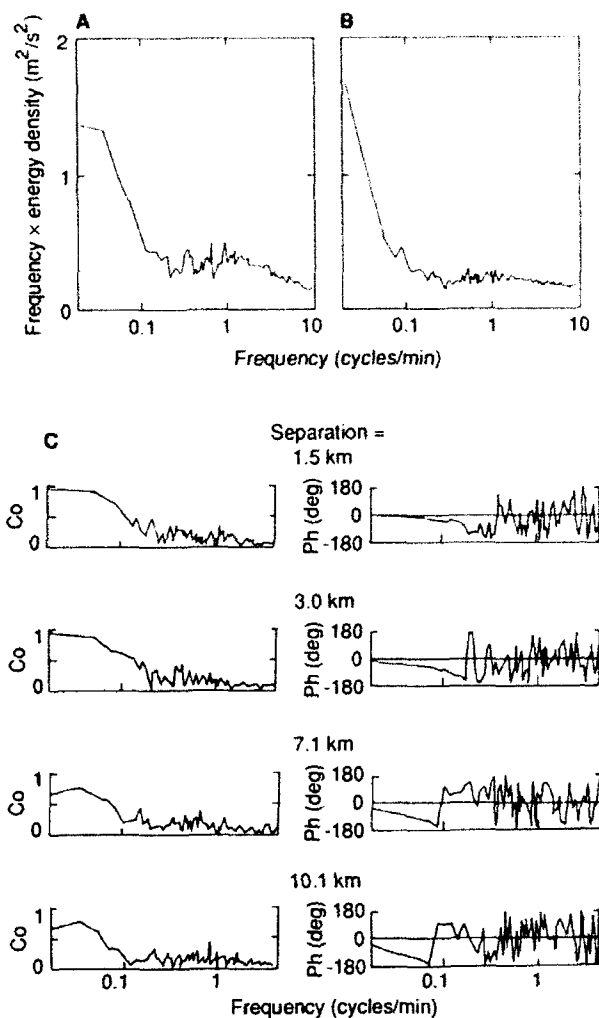


Figure 4. Spectra and cross-spectra of wind fluctuations representative of the meteorological situation: **A.** Along-wind component. **B.** Cross-wind component. **C.** Phases (Ph) and coherences (Co) of the along-wind component for separation distances of 1.5, 3.0, 7.1, and 10.1 km. (Adapted from Ref. 10.)

ration distances. For both geometric configurations and for both components, the main result is that 10-min-average small wind fluctuations are not (or are very weakly) coherent, even at the shortest separation distance of 1.5 km. Such averages are therefore noisy estimates of the mean wind speed, even in the case of neutral or stable situations. Some coherence existed beyond periods of 20 min for 8.5-km separation.

Figure 4 presents, for the case of an unstable atmosphere, the coherence and phase of u and v wind fluctuations for the wind blowing directly along the row of masts. This geometric configuration permits one to test Taylor's hypothesis, which is often used to shift between time and space without considering the respective scales. For this highly convective case, the coherence diagrams confirm that 20-min fluctuations become significantly coherent at 10.1-km spacing. The linear phase variation as a function of frequency may reveal some advection of structures. The corresponding speed was estimated

to be 24 m/s, twice the wind speed at measuring level, and is about the wind speed measured by a radiosonde for convective clouds 1 to 3 km high.

For wave modeling and prediction, these results imply that wind estimates will be improved by time averages that are at least 20 min long. One must also account for the variability at time scales of about 1 h. Analysis of the meteorology can provide the necessary information to decide which kind of wind spectrum should be used and how to model the associated variability. For scientific applications, the proper averaging time can be determined after the fact from continuous recorded data.

THE SPATIAL EQUIVALENCE OF POINT MEASUREMENTS

By definition, a discontinuity prevents a spatial average from being physically meaningful; no one expects a wind vector point measurement on one side of a front to be representative of the other side. Nevertheless, sea-state modelers and forecasters must decide what confidence limits to apply to point measurements so that the data are representative of some geographic area. This problem is especially relevant for the calibration and validation of the ERS-1 scatterometer, scheduled to be launched soon. Typical scale sizes of interest are on the order of the scatterometer elementary footprint, about 25 km on a side.

During the Toscane 2 campaign, conducted during the winter of 1987–88, a network of three wind-instrumented buoys was moored in the Atlantic in an isosceles right triangle (area 1) with two sides of 25 km. An additional measuring station was implemented on the island of Sein to extend one side of the network to 50 km, such that the larger isosceles triangle (area 2) had two sides of 35 km.¹¹

By using the wind time series from that network, a method for defining an average spatial wind vector is being developed. One promising approach is to use vector empirical orthogonal functions that describe the common relative variability observed simultaneously at the borders of the area defined by the measuring points. The assumption is that this common variability affects the whole area. The analysis is performed jointly on the components of the wind vector at each measurement location. A time series of the spatially averaged wind vector is then computed. At each measurement location, the residual time series can be defined as the difference between the spatial average and the initial time series. This method requires carefully controlled and calibrated wind speed data but allows for wind direction offsets accounted for as a relative phase shift. In the data set analyzed, the maximum wind speed difference at any of the three buoys over the entire 30-day experiment was 20 cm/s, with a standard deviation of 5 cm/s. Figures 5A and 5C show, respectively, the 20-min-averaged wind speed and the direction of the initial time series at one location; the corresponding time series of the residuals are shown in Figures 5B and 5D.

Results indicate that the estimated spatial average performed over a 625-km² area recovers most of the ki-

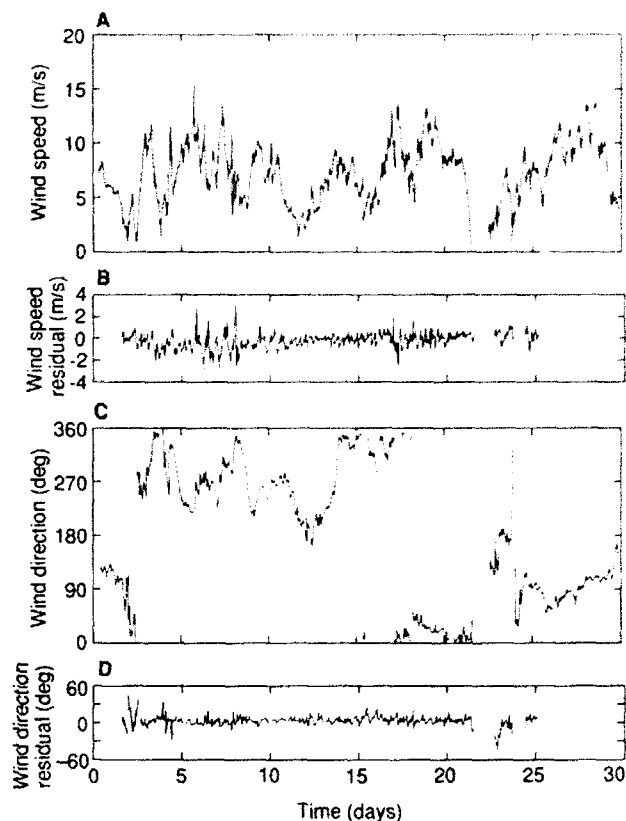


Figure 5. Twenty-minute-average time series of the wind vector at one location of the Toscane 2 network and related wind vector residuals between the spatial average and the point measurement. **A.** Wind speed. **B.** Wind speed residual. **C.** Wind direction. **D.** Wind direction residual.

netic energy from several weeks down to 50 min. Figures 6A and 6B present the standard deviations of wind speed and direction residuals at one buoy location as a function of the averaging time of the initial time series from 1 to 60 min. For the observed meteorological situations over area 1, after deleting transient events such as passing fronts and winds less than 1.5 m/s (since local thermal effects destroy the meaning of a spatial average), the standard deviation of wind speed at buoy level tends to a limit of about 0.6 m/s, and for wind direction, about 7°. The middle curve of Figure 6A is also for area 1 but is computed at a height of 10 m. The upper curve is obtained by using both the buoy array and the mast data and corresponds to area 2. To merge the two data sets at the same reference altitude, we used a logarithmic boundary layer for the mean wind profile, corrected for stability. For a given averaging time, differences in standard deviation within area 1 are the result of wind increasing with altitude, whereas the increase in standard deviation from area 1 to area 2 at the same height is simply the result of doubling the area.

For a given area, the lower limit of the residual variance can be interpreted as the minimum fluctuation energy introduced by both the measuring equipment and the geophysical wind variability (at the measuring level and for the wind conditions experienced). For a given aver-

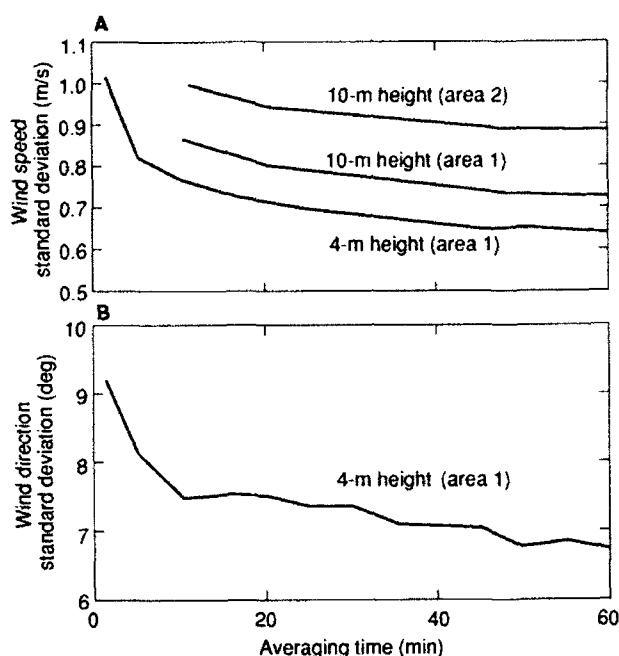


Figure 6. Standard deviation of the residual, at the same location of the Toscane 2 network, as a function of averaging time. **A.** Wind speed. **B.** Wind direction. Note the increases in the standard deviation of the wind speed residual as either the reference altitude or the averaging area increases.

aging time, assuming independence between the instrument and geophysical noise, the energy difference provides an estimate of the additional spatial variability at a given time scale.

CONCLUSIONS

We have shown that the mean wind vector fluctuates on time scales usually recommended to define the mean. The level of these fluctuations varies with meteorological conditions. Excessively short averaging times (about

10 min) will produce spurious estimates of the wind vector. For sea-state modeling and forecasting, it seems advisable to use a longer averaging time and to model the variability at shorter time scales. The estimate thus obtained still will not completely represent the wind vector over an area. Additional variability must be introduced to account for spatial effects. More research is needed to further quantify and model the real wind field variability.

REFERENCES

- Janssen, P. A., Lionello, P., Reistad, M., and Hollingsworth, T., "Hindcasts and Data Assimilation Studies with the WAM Model during the Seasat Period," *J. Geophys. Res.* **94**, 973-994 (1989).
- Wisdorff, D., "Observateurs, Aidez-Nous Pour Mieux Vous Servir," *Meteor. Mar.*, no. 133, Meteorologie Nationale (4^{eme} trimestre 1986).
- Van der Hoven, I., "Power Spectrum of Horizontal Wind Speed in the Frequency Range from 0.0007 to 900 Cycles per Hour," *J. Meteorol.* **14**, 160 (1957).
- Pierson, W. J., "The Measurement of the Synoptic Scale Wind over the Ocean," *J. Geophys. Res.* **88**, 1683-1708 (1983).
- Pond, S., Phelps, G. T., Paquin, J. E., McBean, G., and Stewart, R. W., "Measurements of the Turbulent Fluxes of Momentum Moisture and Sensible Heat over the Ocean," *J. Atmos. Sci.* **28**(6), 901-917 (1971).
- Miyake, M., Stewart, R. W., and Berling, R. W., "Spectra and Cospectra of Turbulence over Water," *Q. J. R. Meteorol. Soc.* **96**, 138-143 (1970).
- Kaimal, J. C., Wyngaard, J. C., Izumi, Y., and Cote, O. R., "Spectral Characteristics of Surface-Layer Turbulence," *Q. J. R. Meteorol. Soc.* **98**, 563-589 (1972).
- Groupe TOSCAN, "Vent et Etat de la Mer dans la Baie d'Audierne. Campagne TOSCAN T," *Campagnes Océanographiques Françaises*, IFREMER, no. 4 (1986).
- Daniault, N., Champagne-Philippe, M., Cambian, M., and Thepaut, J. N., "Comparison of Sea Surface Wind Measurements Obtained from Buoy, Aircraft and Onshore Masts during the TOSCAN T Campaign," *J. Atmos. Ocean Technol.* **5**(3), 385-404 (1988).
- Champagne-Philippe, M., "Coastal Wind in the Transition from Turbulence to Mesoscale," *J. Geophys. Res.* **94**, 8055-8074 (1989).
- Queffelecoul, P., Didailler, S., Ezraty, R., Bentamy, A., and Gouillou, J. P., "TOSCAN 2 Campaign Report," IFREMER Contribution, ESTEC Contract 7138/87/NL/BI (Jun 1988).

ACKNOWLEDGMENTS: Since the beginning of the TOSCAN project, Pierre Queffelecoul has spent a lot of energy in field activities, data handling, and scientific analysis. Jean Pierre Gouillou was in charge of the hardware, and Stéphane Didailler developed the software. During her stay, Michelle Champagne-Philippe explored some of the aspects of the wind variability. Abderahim Bentamy joined the project two years ago, and he is in charge of all the mathematical developments. I am very grateful to Willard J. Pierson for his comments and remarks.

ON THE DIRECTIONAL BEHAVIOR OF THE EQUILIBRIUM WAVE NUMBER SPECTRUM: IMPLICATIONS FOR THE EQUILIBRIUM FREQUENCY SPECTRUM

On the basis of observed wave number and frequency spectra for fetch-limited growth of wind waves, an equilibrium gravity range form is proposed for the slice through the directional wave number spectrum in the dominant wave direction. In conjunction with a model for the directional spreading, the calculated frequency and wave number spectra agree well with observations, thus offering a plausible explanation for the underlying physics governing various ranges of the frequency spectrum.

INTRODUCTION

Ocean wind waves have been traditionally described by their spatial and temporal spectra (see the boxed insert for key definitions). Wave height frequency and wave number spectra have been experimentally observed, and various equilibrium spectral subranges have been proposed for these spectra at frequencies above the spectral peak. Agreement between observations and the most recently proposed equilibrium range spectral forms for gravity wind waves is incomplete, however.

During the evolution of the ocean wave spectrum under wind forcing, wave components in statistical equilibrium are those whose net growth rate is very slow compared with the time scales associated with the internal source terms, such as wind input, nonlinear wave interactions, and dissipation. This separation of time scales underlies the concept of equilibrium spectral subranges (see Ref. 1, section 2). The quest for a physical model of a gravity equilibrium subrange for deep water waves was initiated by Phillips,² who proposed that the amplitudes of spectral components above the spectral peak were hard-limited by wave breaking, independent of the wind strength, fetch, or duration. This hypothesis led to the well-known ω^{-5} power law for the equilibrium gravity subrange of the frequency spectrum

$$F(\omega) = \alpha g^2 \omega^{-5}, \quad (1)$$

where ω is the frequency, g is the gravitational acceleration, and α is a universal constant. Shortly thereafter, Hasselmann³⁻⁵ presented the theoretical basis for weakly nonlinear wave-wave interactions in the wave spectrum. Support for the importance of this mechanism in shaping the wave spectrum has strengthened with the increasing availability of reliable data on wind wave evolution and the associated wind input source function.

Equation 1 has proven inadequate in accounting for observed frequency spectra. In particular, α has been found to decrease with fetch and the frequency depen-

dence to be closer to ω^{-4} . Also, the spectral level coefficient α shows an unexplained variability between investigators (see, e.g., Ref. 1, section 3). These discrepancies have motivated recent revisions of the Phillips equilibrium range model,² notably those proposed by Kitaigorodskii⁶ and by Phillips.¹ The latter predicted frequency spectra of the form

$$F(\omega) = \beta g u_* \omega^{-4}, \quad (2)$$

where β is a universal constant and u_* is the wind friction velocity. Also predicted were one-dimensional and two-dimensional wave number spectra of the form, respectively,

$$\phi(k_i) \approx u_* g^{-1/2} k_i^{-5/2} \quad (i = 1, 2) \quad (3a)$$

and

$$\Phi_c(k, \theta) \approx u_* g^{-1/2} k^{-7/2} G(\theta), \quad (3b)$$

where $\mathbf{k} = (k_1, k_2)$ is the wave number vector with magnitude k and polar angle θ , and $G(\theta)$ is a directional spreading function.

The envisaged spectral range of applicability was for gravity wave components with much shorter wavelengths than the spectral peak waves. Kitaigorodskii⁶ also predicted Equation 2 up to $\omega U/g \approx O(4)$ (on the order of 4), transitioning to Equation 1 for higher frequencies (U is the wind speed at a reference height, related to u_* by a drag coefficient).

A growing body of observed frequency spectra apparently supports Equation 2 (e.g., see Donelan et al.⁷), although cases of anomalous spectral behavior have been reported. For example, hurricane wave observations⁸ have shown supportive ω^{-4} behavior out to $O(3\omega_p)$, but then a transition to ω^{-5} just above that range (ω_p represents the frequency at the spectral peak). At higher

KEY SPECTRAL RELATIONSHIPS

Following Phillips* (section 4.1), the wave spectrum for a homogeneous, stationary wave field is defined as

$$X(k, \omega) = (2\pi)^{-3} \int_{-\infty}^{\infty} \int_{-\infty}^{\infty} \rho(r, t) \times \exp[-i(k \cdot r - \omega t)] dr dt,$$

where

$\rho(r, t) = \zeta(x, t_0)\zeta(x + r, t_0 + t)$ is the covariance of the surface displacement $\zeta(x, t)$,

r is the spatial separation vector,

t is the time separation,

$k = (k_1, k_2) = (k, \theta)$ is the wave number vector,

and ω is the frequency.

The term $X(k, \omega)$ has the property that $\iint X(k, \omega) dk d\omega = \bar{\zeta}^2$, the mean squared wave height, and represents the mean distribution of wave energy with wave number magnitude $k = |k|$ and frequency ω propagating in the direction θ . Various reduced spectra defined below are theoretically or observationally important in the context of this article.

1. The directional wave number spectrum

$$\Phi(k) = 2 \int_0^{\infty} X(k, \omega) d\omega$$

is the actual wave number directional distribution of wave energy propagation.

2. The wave number spectrum

$$\Phi_s(k) = \int_{-\infty}^{\infty} X(k, \omega) d\omega$$

is the folded (symmetric) wave number spectrum, and $\Phi_s(k) = 0.5 [\Phi(k) + \Phi(-k)]$. $\Phi_s(k)$ arises from frozen spatial image analysis and does not contain wave propagation information, thereby partitioning the wave energy equally into components 180° apart.

3. The one-dimensional (transverse) spectra are

$$\phi(k_1) = \int_{-\infty}^{\infty} \Phi(k_1, k_2) dk_2$$

and

$$\phi(k_2) = \int_{-\infty}^{\infty} \Phi(k_1, k_2) dk_1.$$

4. The directional frequency spectrum is

$$G(\omega, \theta) = 2 \int_0^{\infty} X(k, \omega) k dk.$$

5. The (nondirectional) frequency spectrum is

$$F(\omega) = \int_{-\pi}^{\pi} G(\omega, \theta) d\theta.$$

*Phillips, O. M., *The Dynamics of the Upper Ocean*, Cambridge University Press, N.Y. (1977).

frequencies, reliable measurements from several investigators have shown a range of frequency power law dependencies from -5 to -3.3 (see references in Banner et al.⁹). Doppler shifting effects have long been attributed to ambient and wind drift currents, as well as to orbital motions of the longer wave components. These effects can significantly influence the frequency spectrum, particularly the higher frequency components whose intrinsic phase speeds are lower.¹⁰ The extent to which these effects influence measured frequency spectra and the correspondence of each effect to the proposed equilibrium spectral form (Eq. 2) are examined in detail in this article.

The directional wave number spectrum $\Phi(k)$ is not subject to Doppler distortion effects, so it offers an alternative way to examine equilibrium spectral forms and their range of applicability. Wave number determinations typically involve greater observational complexity, resulting in a data set much more modest than that for frequency spectra. The discrepancies between observed wave number spectra and current equilibrium range predictions, however, necessitate a more careful examination of the underlying physical processes that determine the shapes of reduced spectra. That issue is addressed here via an analysis of a proposed wave spectral model in the wave number domain, developed on the basis of observed wave number and frequency spectra for fetch-limited wind wave growth situations. Calculations based

on this model reveal the underlying structure and dominant influences that appear to shape observed frequency spectra and hence provide more detailed insight into equilibrium range behavior.

FORMULATION OF A WAVE NUMBER SPECTRAL MODEL

From an analysis of published directional wave number slope spectra (Ref. 11, run 36/1), derived one-dimensional wave-height wave number spectra in the dominant wave direction (k_1) and orthogonal direction (k_2) shown in Figure 1 reveal the strong directional anisotropy of the wave energy near the spectral peak. Also seen is the subsequent tendency to merge at higher wave numbers k_i of $O(5k_p)$ (k_p = peak wave number) and to follow a k^{-n} dependence, with $n \approx 3$. One-dimensional spectra for fetch-limited growth reported by other investigators^{9,12,13} are also shown in Figure 1; they indicate good agreement with k^{-3} power law dependence over a wide range of wave numbers. The spectral level appears to depend only weakly on wind speed, but available data are inconclusive. Also, for the Jackson et al. run 36/1 data,¹¹ some attenuation may have occurred due to a wind shift several hours earlier. The corresponding equilibrium range model prediction (Eq. 3a) of $u_* k^{-5/2}$ does not appear to agree with the observed wave number dependence. And, according to the high

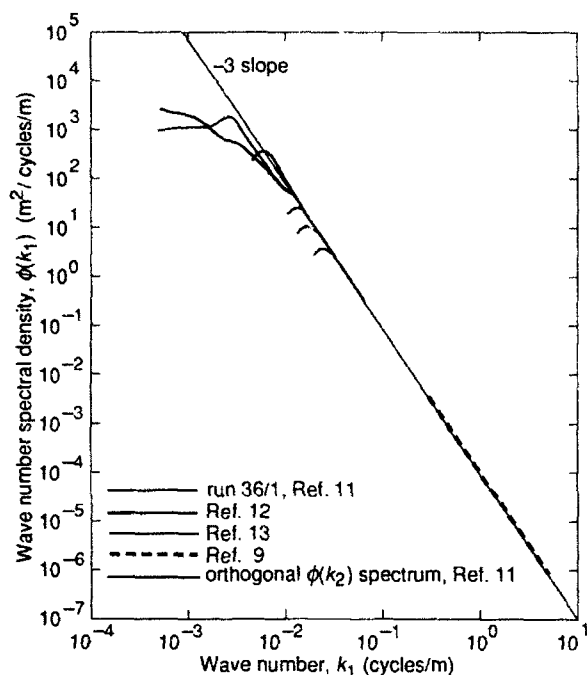


Figure 1. One-dimensional wave number spectra $\phi(k_1)$ in the wind direction for fetch-limited wind wave growth conditions. The background asymptote shown has a slope of k_1^{-3} . (This and subsequent figures in this article reprinted, with permission, from Banner, M. L., "Equilibrium Spectra of Wind Waves," *J. Phys. Oceanogr.* 20, 966-984; © 1990 by American Meteorological Society.)

wave number observations of Banner et al.,⁹ the observed dependence on the wind speed in $\phi(k_1)$ and $\phi(k_2)$ is significantly weaker than linear in the observed spectral range embracing $O(1)$ m wavelengths.

Again, the one-dimensional wave number spectra suggest the potential importance of directional effects near the spectral peak. Further insight is provided by the directional wave number spectrum $\Phi(k, \theta)$, which describes the distribution of wave energy propagation with respect to wave number magnitude k and direction θ . Observed wave number spectra, if determined from frozen spatial images (such as those found in stereophotogrammetric methods, e.g., Ref. 14), have an inherent 180° ambiguity, which can be unfolded (as discussed subsequently) using a directional spreading function $D(\theta; k)$, defined here by

$$D(\theta; k) = \Phi(k, \theta) / \Phi(k, \theta_{\max}), \quad (4)$$

where θ_{\max} is the dominant wave direction. This form of $D(\theta; k)$ does not have the customary unity polar integral, being constrained only by

$$\int_{-\pi}^{\pi} \int_0^{\infty} \Phi(k, \theta_{\max}) D(\theta; k) k dk d\theta = \zeta^2,$$

the mean squared wave height. Although this form for $D(\theta; k)$ and the customary angular spreading function (not suited to the present analysis) have different relative magnitudes, their directional dependence is the same.

Several empirical forms have been proposed for $D(\theta; k)$ based on the distribution

$$D(\theta; k) = \cos^2[(\theta - \theta_{\max})/2], \quad (5)$$

where the spreading exponent s depends on k/k_p and U/c_p (c_p is the phase speed of the spectral peak waves). In a recent, comprehensive study of fetch-limited wind wave growth, Donelan et al.⁷ proposed a variation of Equation 5 based on

$$D(\theta; k) = \text{sech}^2[\beta(\theta - \theta_{\max})], \quad (6)$$

where $\beta = \beta(k/k_p)$ controls the rate of spreading with distance from the spectral peak. The geometric differences between the two distributions in Equations 5 and 6 are small. More significantly, Donelan et al. found that using the half-power points to fit the observed angular distribution suppressed a dependence on U/c_p in the spreading function, while fitting the full angular distribution (including the noisy tail region) retained a U/c_p dependence. Those investigators advocated the former as less influenced by tail noise; on that basis, their form for $D(\theta; k)$, which depends only on k/k_p , is adopted tentatively as the "standard." The form of $\beta(\theta; k)$ they proposed was Equation 6, with $\beta = 2.28(k/k_p)^{-0.65}$ for $0.97 < k/k_p < 2.56$. For $k/k_p > 2.56$, we propose here that

$$\beta = 10^{-0.4 - 0.8393(k/k_p)^{-0.567}},$$

which extrapolates the spreading parameter to higher wave numbers. This form simply matches the ordinate and slope at the transition $k/k_p = 2.56$ and provides a proposed spreading cutoff at high wave numbers (see Banner¹⁵ for a detailed discussion). This form is also consistent with other very recent observations (M. A. Donelan, private communication, June 1989). Other $D(\theta; k)$ correlations were also considered by Banner¹⁵ to assess the relative sensitivity of the findings. The standard form for $D(\theta; k)$ adopted here is shown in Figure 2.

Extraction of a form for the slice in the dominant wave direction $\Phi(k, \theta_{\max})$ from available, observed wave number spectra for fetch-limited growth has been carried out using the form of $D(\theta; k)$ proposed by Donelan et al.⁷ On the basis of that extraction, we propose here that

$$\Phi(k, \theta_{\max}) = \alpha [U/c_p]^{1/2} k^{-4}, \quad (7)$$

where $\alpha \approx 0.45 \times 10^{-4}$. We have assumed an intrinsic wind speed dependence to be a function of the wave age c_p/U , consistent with the frequency spectral dependence on wind speed found in Ref. 7. A fuller account of the extraction of $\Phi(k, \theta)$ from the available wave number data is given in Ref. 15. Observational support for Equation 7 is shown in Figure 3, which presents data on $\Phi(k, \theta_{\max})$ weighted by k^4 and $(U/c_p)^{-1/2}$ from various studies. The tails of the individual data sets are noisy, but the quieter regions conform reasonably well

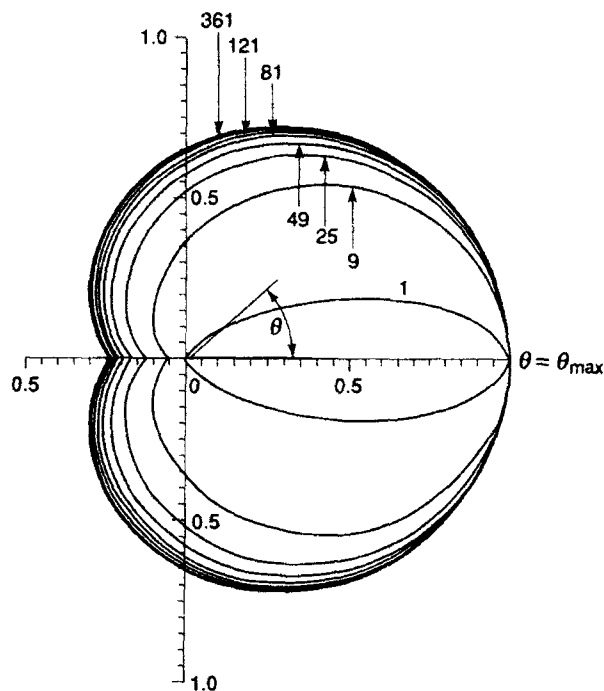


Figure 2. Polar plot of the directional spreading function⁷ $D(\theta; k)$, given by Equation 6, shown for seven values of k/k_p . Axes represent linear wave number values normalized to 1.0 in the direction of maximum response θ_{\max} .

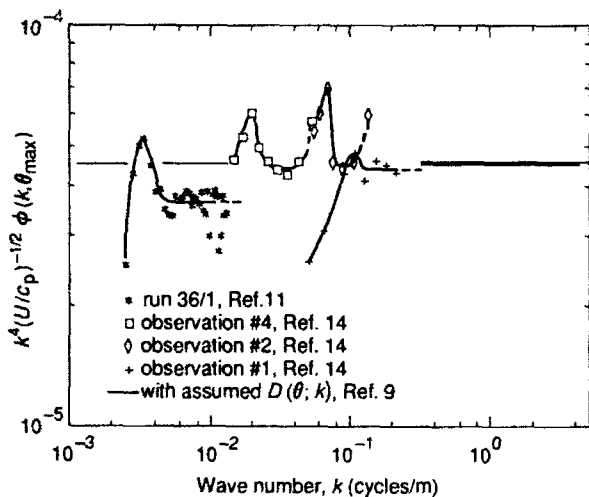


Figure 3. Slice in the dominant wave direction θ_{\max} through the directional wave number spectrum $\Phi(k, \theta_{\max})$, weighted by k^4 and $[U/c_p]^{-1/2}$ for fetch-limited wind wave growth. The horizontal asymptote shown has a spectral level of 0.45×10^{-4} .

with the proposed form of Equation 7, although further supportive data are clearly desirable.

The proposed directional wave number spectral model from Equation 4 with Equations 6 and 7 is then

$$\Phi(k, \theta) = 0.45 \times 10^{-4} [U/c_p]^{-1/2} k^{-4} D(\theta; k) \quad (8)$$

corresponding closely to the form proposed by Donelan and Pierson,¹⁶ which was in turn based on the findings of Donelan et al.⁷

MODEL CALCULATIONS

In what follows, we use Equation 8 to calculate frequency spectra, primarily to reveal the underlying influences shaping different parts of the spectra and for comparison with present equilibrium range predictions. Peak enhancement effects that influence the spectral shape near the spectral peak¹⁷ have not been included explicitly here, but their impact on the spectrum at higher frequencies is considered. Also, the linear dispersion relation for gravity water waves has been assumed throughout.

The frequency spectrum is related to $\Phi(k, \theta)$ by

$$\begin{aligned} F(\omega) &= 2g \int_{-\pi}^{\pi} [k^{3/2} \Phi(k, \theta) d\theta]_{k=\omega^2/g} \\ &= 0.9 \times 10^{-4} g^2 [U/c_p]^{-1/2} \omega^{-5} \\ &\quad \times \int_{-\pi}^{\pi} [D(\theta; k) d\theta]_{k=\omega^2/g} \end{aligned} \quad (9)$$

from which the departure from ω^{-5} behavior is predicted only where the spreading function strongly depends on k (or ω), as suggested in Ref. 7. In Figure 2, this region is largely confined to the spectral subrange below $k/k_p \approx O(25)$, or $\omega/\omega_p \approx O(5)$, which is where we expect to see the influence of $D(\theta; k)$. Results for a dominant wave number of 0.022 cycle per meter (5.4-s waves) and a wind speed of 11.2 m/s under fetch-limited growth ($U/c_p \approx 1.3$) are shown in Figure 4. Also shown are results for doubling and halving the wind speed (both at a fixed fetch), with peak wave numbers of 0.0104 cycle/m with $U/c_p \approx 1.8$ and 0.0465 cycle/m with $U/c_p \approx 1.0$, respectively. Results are based on the empirical nondimensional fetch-limited relationships proposed by Donelan et al.⁷ for the fetch dependence of the peak frequency.

The calculated $F(\omega)$ shows a dependence close to ω^{-4} below $\omega/\omega_p \approx O(3)$ and a transition to ω^{-5} dependence for higher ω/ω_p . At given frequencies below $\omega/\omega_p \approx O(3)$, the apparent wind speed dependence at a fixed fetch is nearly linear. Similar calculations have been performed using alternative formulations of $D(\theta; k)$ (e.g., Ref. 18), which incorporate a spreading function dependence on both U/c_p and k/k_p . These calculations result in slightly stronger wind speed dependences but still reproduce a frequency dependence close to ω^{-4} near the spectral peak.

Above $\omega/\omega_p \approx O(3)$, the calculated spectra become asymptotic to ω^{-5} dependence with a very low apparent wind speed dependence. As noted above, however, Doppler shifting can be important, so its effects must be considered before placing too much credence on the calculated spectra.

Banner¹⁵ undertook an analysis using the assumed model for $\Phi(k, \theta)$ to assess the typical influence on the frequency spectrum of Doppler shifting effects from (1) local advection by the orbital motions associated with

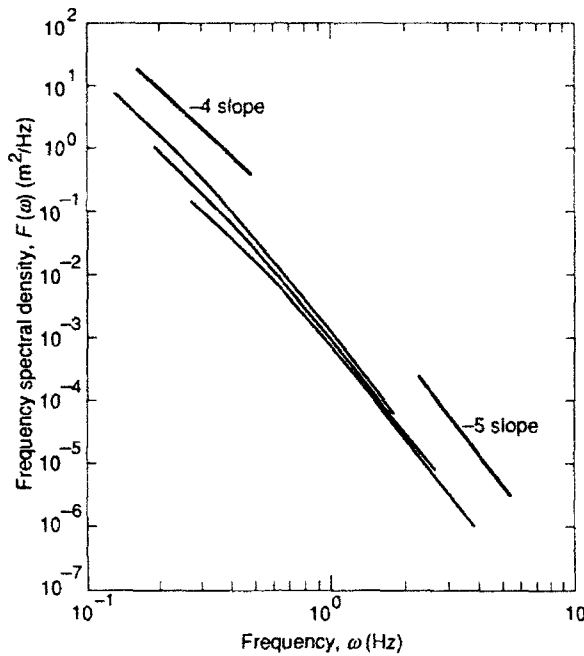


Figure 4. Calculated frequency spectra based on the proposed wave number spectral form of Equation 7 for the directional spreading function $D(\theta; k)$ shown in Figure 2. The central solid curve is for a reference spectral peak wave number of 0.022 cycle/m and a reference wind speed of 11.2 m/s. The upper and lower solid curves are for peak wave numbers of 0.014 and 0.0465 cycle/m, respectively, corresponding to doubling and halving the wind speed under fetch-limited conditions.

the dominant waves and (2) incremental wind drift current effects. Calculations were performed using a two-scale approximation model based on the modulation theory described by Phillips.¹⁹ An exact Stokes wave model for the dominant wave and a wind drift modulation model were assumed, neglecting local refraction effects (estimated to be of secondary importance). The results of the calculations for $\omega/\omega_p > 3$ and different dominant wave slopes AK (or, equivalently, peak enhancement) are shown in Figure 5. Results indicate that the effect of Doppler shifting from the specified sources is unimportant near the spectral peak, but significantly influences the frequency dependence in the tail of the frequency spectrum. The incremental effect of a very substantial wind drift level of $0.05c_p$, equivalent to a wind speed of ≈ 30 m/s for 7-s waves, appears to be secondary for typical sea states ($AK \approx 0.1$), although it becomes increasingly more important toward higher frequencies for lower dominant wave slopes.

Ambient ocean currents can also induce changes in the observed frequency spectrum. Donelan et al.⁷ showed that typical ocean current levels had minimal effect on the shape of the frequency spectrum near the spectral peak. Calculations of this influence at higher frequencies are reported elsewhere.¹⁵

The composite form shown in Figure 5 should agree closely with frequency spectra observed for fetch-limited growth conditions, given the wave number and slope AK

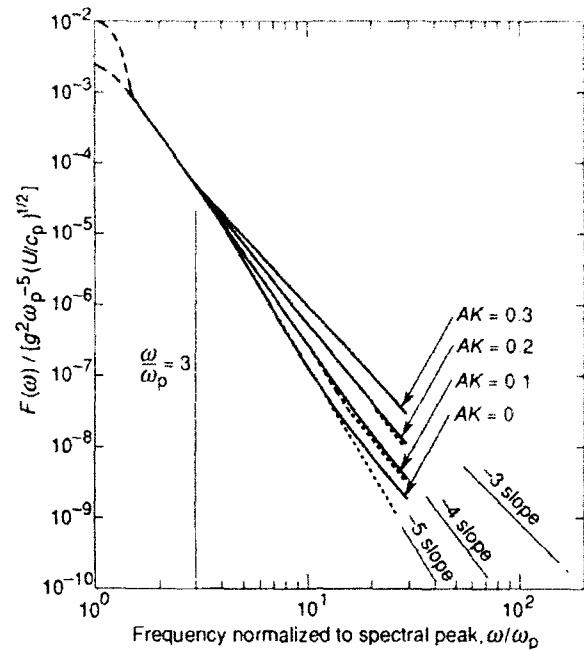


Figure 5. Effect of the slope AK of the spectral peak on the tail of the frequency spectrum over $3 < \omega/\omega_p < 30$ for the indicated slopes AK : dotted lines, spectral peak orbital motions alone; solid lines, spectral peak orbital motions and wind drift of $0.05c_p$, representing a wind speed of about 30 m/s for 7-s waves (ω is in rad/s). Also shown for $1.3 < \omega/\omega_p < 3$, in non-dimensional form, is the computed ω^{-n} dependence, with $n \approx 4$. The nonequilibrium peak enhancement region below $\omega/\omega_p \approx 1.3$ is indicated by dashes.

of the spectral peak, together with the wind speed. Indeed, this agreement has been verified for several examples, one of which is shown in Figure 6 (others are reported in detail in Ref. 15).

In addition, transitional behavior near $\omega/\omega_p \approx O(3)$ obtained from the model calculations explains the frequency dependences described previously. For example, Figure 5 shows, for the dominant wave slopes [$AK \approx 0.08$] typical of those data, an ω^{-4} dependence near the spectral peak, transitioning to ω^{-n} , with $n \approx 4.75$ for $\omega/\omega_p > O(3)$. These dependences agree well with Forristall's observations.⁸

Calculations of one-dimensional spectra for typical ocean wave and wind speed conditions are described by Banner,¹⁵ who found that both near the spectral peak and toward higher wave numbers, calculated $\phi(k_1)$ spectra agreed well with a k^{-3} behavior. The calculated wind speed dependence was found to be weaker than linear, and, toward higher wave numbers, calculated $\phi(k_2)$ and $\phi(k_1)$ had similar dependences.

DISCUSSION AND IMPLICATIONS OF RESULTS

Near the spectral peak ($1.3 < \omega/\omega_p < 3$), the directional anisotropy of the wave energy significantly influences the forms of the frequency and the one-dimensional wave number spectra. In addition, the assumed depen-

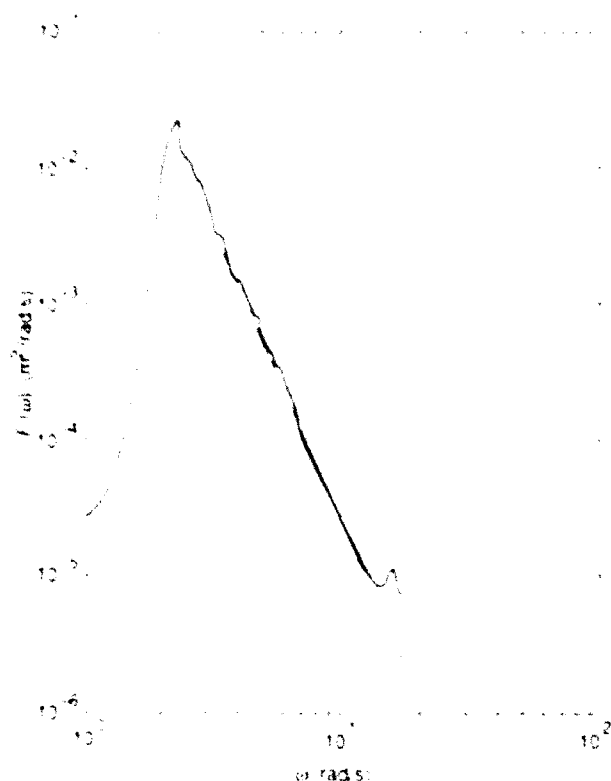


Figure 6. Comparison of calculated (black curve) and observed (colored curve) frequency spectrum. $U/c_p = 3.6$ and $z_p = 2.27$ rad/s.

dence on wave age in Equation 7 plays a role in setting the spectral levels. The one-dimensional wave number spectral results are not consistent just above the spectral peak $k/k_p < 0.9$ with the form of Equation 3a predicted by present equilibrium theories: both the observed and the calculated $\phi(k)$ spectra have very different forms from $\phi(k)$ in this subrange, and each differs from Equation 3a. At higher wave numbers, calculated one-dimensional wave number spectra in the dominant wave direction conform closely to

$$\phi(k) = 0.6 \cdot 10^{-4} [U/c_p]^{-1} k^{-2} \quad (10)$$

The model results agree with the available observational data shown in Figure 1. Thus, even at higher wave numbers, the calculated one-dimensional spectra do not appear to conform closely to Equation 3a.

In the frequency domain the model can explain several basic aspects of observed frequency spectra. Near the spectral peak, the dependence on ω^{-n} (with $n \approx 4$) and the near-linear wind speed dependence observed for $1.3 < \omega/\omega_p < 3$ arise from the strong directional anisotropy near the spectral peak through its variation with k/k_p . Also contributing to the variation in spectral level is the assumed $[U/c_p]^{-1}$ dependence, for which $U/c_p \approx (\alpha g U^2)^{-0.25}$ (α being the fetch) according to Donelan et al. At a fixed fetch, under fetch-limited growth conditions, these two effects produce in the energy-containing range an apparent near-linear dependence on the

wind speed. At a given fetch, however, a doubling of the wind speed is accompanied by an increase in c_p and an increase of only about 20% in the spectral level, most of the shift in this level arises from the rate at which $D(\theta; k)$ changes with k/k_p , as the spectral peak moves under the action of the increased wind speed. This shift is controlled largely by nonlinear wave-wave interactions, rather than from a direct response to spectrally local wind-induced wave growth. Toward higher frequencies, above $\omega/\omega_p \approx 0.3$, the effect of varying directionality becomes secondary, and Doppler shifting caused by the orbital velocity of the dominant wave significantly influences the shape of the frequency spectrum, depending on the dominant wave slope $4A$. This can appreciably distort the frequency spectrum, modifying it from the ω^{-4} dependence it would have in the absence of the Doppler shifting effects. Since these influences are not included in Equation 2, that equation is not, in general, consistent with observed frequency spectra for this spectral subrange. The wind drift also plays a role at higher frequencies and when AK is low.

Finally, the model described here allows a more detailed examination of the location and extent of the subrange of the equilibrium gravity wave spectra. Figure 2 shows that the region $0.2 < k/k_p < 0.9$ has a high directional anisotropy. As the spectral peak evolves with fetch, the energy flux $c_g \cdot \nabla \Phi$ at a fixed wave number changes; thus, this region is not strictly in equilibrium (c_g is the group velocity). A detailed analysis given elsewhere¹ indicates that these components are nearly stationary in the θ_{max} direction. For wave number components oblique to θ_{max} , however, equilibrium conditions are not well satisfied. For higher wave numbers, that is, $k/k_p > 0.20$ and within the gravity range, the rate of change of $D(\theta; k)$ with k/k_p decreases markedly, and this region conforms most closely to the requirements of an equilibrium range. The proposed wave number spectral form (Eq. 8), however, does not conform to Equation 3, an issue that is taken up elsewhere.¹

These foregoing aspects of the behavior of wave spectra above the spectral peak must be considered in the future development of equilibrium range spectral models. Also, questions remain concerning their applicability to more general wind sea situations.

CONCLUSIONS

On the basis of the equilibrium range model presented here, the following conclusions are drawn:

1. Close agreement with observations is found, both in the wave number and frequency domains.

2. The spectral form predictions of current physical models of the equilibrium gravity wave range are not in close agreement with observations or with the predictions of the model proposed here.

3. The proposed model offers a plausible basis for understanding the observed structure of frequency spectra. That is, a dominant influence of directional spreading is seen near the spectral peak, while at higher frequencies, Doppler advection by the orbital motions of the dominant waves exerts the major influence.

4. Thus, the model calculations contribute toward a refinement of existing physical models that underlie present equilibrium range models for the ocean gravity wind-wave spectrum.

REFERENCES

- ¹ Phillips, O. M., "Spectral and Statistical Properties of the Equilibrium Range in Wind-Generated Gravity Waves," *J. Fluid Mech.* **156**, 505-531 (1985).
- ² Phillips, O. M., "The Equilibrium Range in the Spectrum of Wind-Generated Waves," *J. Fluid Mech.* **4**, 426-434 (1958).
- ³ Hasselmann, K., "On the Nonlinear Energy Transfer in a Gravity Wave Spectrum. Part 1," *J. Fluid Mech.* **12**, 481-500 (1962).
- ⁴ Hasselmann, K., "On the Nonlinear Energy Transfer in a Gravity Wave Spectrum. Part 2," *J. Fluid Mech.* **15**, 273-281 (1963).
- ⁵ Hasselmann, K., "On the Nonlinear Energy Transfer in a Gravity Wave Spectrum. Part 3," *J. Fluid Mech.* **15**, 385-398 (1963).
- ⁶ Kitaigorodskii, S. A., "On the Theory of the Equilibrium Range of Wind-Generated Gravity Waves," *J. Phys. Oceanogr.* **13**, 816-827 (1983).
- ⁷ Donelan, M. A., Hamilton, J., and Hui, W. H., "Directional Spectra of Wind-Generated Waves," *Philos. Trans. R. Soc. London A* **315**, 509-562 (1985).
- ⁸ Forristall, G. Z., "Measurements of a Saturated Range in Ocean Wave Spectra," *J. Geophys. Res.* **86**, 8075-8084 (1981).
- ⁹ Banner, M. L., Jones, I. S. F., and Trinder, J. C., "Wavenumber Spectra of Short Gravity Waves," *J. Fluid Mech.* **198**, 321-344 (1989).
- ¹⁰ Kitaigorodskii, S. A., Krasitskii, V. P., and Zaslavski, M. M., "On Phillips' Theory of Equilibrium Range in the Spectra of Wind-Generated Gravity Waves," *J. Phys. Oceanogr.* **5**, 410-420 (1975).
- ¹¹ Jackson, E. J., Walton, W. F., and Baker, P. L., "Aircraft and Satellite Measurement of Ocean Wave Directional Spectra Using Scanning Beam Microwave Radars," *J. Geophys. Res.* **90**, 987-1004 (1985).
- ¹² Barnett, T. P., and Wilkerson, J. C., "On the Generation of Ocean Wind Waves as Inferred from Airborne Radar Measurements of Fetch-Limited Spectra," *J. Marine Res.* **25**, 292-321 (1967).
- ¹³ Schule, J. J., Simpson, L. S., and DeCombus, P. S., "A Study of Fetch-Limited Wave Spectra with an Airborne Laser," *J. Geophys. Res.* **76**, 4160-4171 (1971).
- ¹⁴ Holthuisen, L. J., "Observations of the Directional Distribution of Ocean Wave Energy in Fetch-Limited Conditions," *J. Phys. Oceanogr.* **13**, 191-207 (1983).
- ¹⁵ Banner, M. L., "Equilibrium Spectra of Wind Waves," *J. Phys. Oceanogr.* **20**, 966-984 (1990).
- ¹⁶ Donelan, M. A., and Pierson, W. J., "Radar Scattering and Equilibrium Ranges in Wind-Generated Waves with Applications in Scatterometry," *J. Geophys. Res.* **92**, 4971-5029 (1987).
- ¹⁷ Hasselmann, K., Barnett, T. P., Bouws, E., Carlson, H., Cartwright, D. E., et al., "Measurements of Wind Wave Growth and Swell Decay during the Joint North Sea Wave Project (JONSWAP)," *Deut. Hydrogr. Z. Suppl. A* **8** (1973).
- ¹⁸ Hasselmann, D. E., Dunckel, M., and Ewing, J. A., "Directional Wave Spectra Observed during JONSWAP 1973," *J. Phys. Oceanogr.* **10**, 1264-1280 (1980).
- ¹⁹ Phillips, O. M., "The Dispersion of Short Ocean Wave Components in the Presence of a Dominant Long Wave," *J. Fluid Mech.* **107**, 465-485 (1981).

ACKNOWLEDGMENTS: The support for the author's research on the ocean wave number spectrum from the Australian Research Council and the U.S. Office of Naval Research is gratefully acknowledged, as are useful discussions with several colleagues during this study.

ON NONLINEAR WAVE GROUPS AND CONSEQUENCES FOR SPECTRAL EVOLUTION

We review the theory of nonlinear four-wave interaction of a homogeneous, random wave field, with emphasis on the range of validity of the Hasselmann equation. For the slow time evolution of the wave field on a coarse spatial grid, the Hasselmann approach is adequate, but for the detailed evolution of the wave field on a fine mesh grid (on the order of 1–5 km), inhomogeneities in the wave field should be taken into account, resulting in a different energy balance equation.

INTRODUCTION

Since the fundamental investigations of Phillips¹ and Hasselmann,² investigators have shown considerable interest in the energy transfer due to four-wave interactions of a homogeneous, random sea.^{3–5} The effect of nonlinear interactions is twofold. First, four-wave interactions are controlling the shape of the high-frequency part of the spectrum, and second, they give rise to a considerable shift of the peak of the spectrum to lower frequencies. The discrete interaction approximation to four-wave interactions has been successfully implemented by the Wave Model Development and Implementation (WAMDI) group⁶ in the third-generation wave prediction model, called the WAM model.

In this article, we discuss the range of validity of the statistical theory of four-wave interactions of a homogeneous wave field.² The resulting nonlinear energy transfer occurs on the time scale $T_{NL} = 1/\epsilon^4\omega_0$, since the rate of change in time of the action density N is proportional to N^3 . Here, ϵ is a typical wave steepness, and ω_0 is a typical frequency of the wave field, e.g., the peak frequency. The theory is valid only for weakly nonlinear waves ($\epsilon \ll 1$) because of the assumption of (nearly) Gaussian statistics. An additional restriction of the nonlinear theory of a homogeneous wave field is that the corresponding frequency spectrum is broad enough; that is, the spectral width σ should satisfy the inequality $\sigma > \epsilon\omega_0$. This last condition can be understood only in the framework of the inhomogeneous theory of four-wave interactions.

The Hasselmann theory of four-wave interactions gives an adequate description of the slow time (and space) evolution of a random, homogeneous wave field. On a short time or spatial scale, another description of the wave field is more appropriate. And indeed, a much faster energy transfer is possible in the presence of spatial inhomogeneities. For an inhomogeneous, random sea, Alber and Saffman⁷ and Alber⁸ derived an equation describing the evolution of a narrowband wave train. Finally, Crawford et al.,⁹ following Zakharov's approach,¹⁰ obtained a unified equation for the evolution of a random field of deep water waves, which accounts

for both the effects of spatial inhomogeneities and the energy transfer associated with the homogeneous spectrum. From this analysis, it became apparent that inhomogeneities gave rise to a much faster energy transfer, $T_{NL} = 1/\epsilon^2\omega_0$, comparable with the typical time scale of the Benjamin–Feir instability.

Alber and Saffman⁷ found the important result that inhomogeneities in a homogeneous wave field were generated by an instability (which is the random version of the Benjamin–Feir instability), if the width of the frequency spectrum is sufficiently small. For a spectrum with Gaussian shape, instability was found if $\sigma \leq \epsilon\omega_0$, where ω_0 is the peak frequency. In the limit of vanishing width, the deterministic results of Benjamin and Feir¹¹ on the instability of a uniform wave train were rediscovered. Clearly, finite bandwidth is stabilizing. The stability criterion ($\sigma > \epsilon\omega_0$) tells us that the growth rate of the Benjamin–Feir instability vanishes as the correlation time of the random wave field (about $1/\sigma$) is reduced to the order of the characteristic time scale for modulational instability of the wave system (about $2\pi/\omega_{max}$, where at ω_{max} one has maximum growth for $\sigma \rightarrow 0$). Thus, decorrelation of the phases of the wave leads to stabilization of the wave train on the short time scale $T_{NL} = 1/\epsilon^2\omega_0$, and nonlinear transfer of energy is then possible only on the much longer time scale $T_{NL} = 1/\epsilon^4\omega_0$.

The result of Alber and Saffman⁷ has the following implications: (1) for sufficiently broad spectra ($\sigma > \epsilon\omega_0$), only Hasselmann's four-wave interactions are relevant; (2) spectra derived from a sufficiently long time series should have a width larger than $\epsilon\omega_0$, because for smaller spectral width the spectrum would be unstable; and (3) since the spectral width exceeds a minimum value, the average length of a wave group $\langle l \rangle$ must be smaller than some maximum. For a steepness $\epsilon = 0.1$, theory tells us that $\langle l \rangle_{max} \approx 2$.

Regarding the applicability of the statistical theory of four-wave interactions of a homogeneous wave field to wave prediction modeling, we therefore conclude the following: On the short time scale $T = 1/\epsilon^2\omega_0$, a fast

energy transfer is possible in the presence of spatial inhomogeneities (i.e., wave groups), if the spectrum is sufficiently narrow. Because of this energy transfer from the main peak of the spectrum to the side bands, however, the spectrum broadens until the random version of the Benjamin-Feir instability is quenched.¹² Nonlinear energy transfer is then possible only on the much longer time scale $T_{NL} = 1/\epsilon^4 \omega_0$, in accordance with Hasselmann's theory of four-wave interactions. This means that for (global) applications with a coarse resolution ($\Delta x > 10$ km), the Hasselmann equation gives an adequate description of the evolution of a random wave field. For fine-mesh applications ($\Delta x < 5$ km), however, the effect of inhomogeneities on nonlinear energy transfer should be taken into account.

THE ZAKHAROV EQUATION

In this section, we describe the derivation of the deterministic evolution equation for surface gravity waves in deep water from the Hamiltonian for water waves.

Consider the potential flow of an ideal fluid of infinite depth. We choose coordinates such that the undisturbed surface of the fluid coincides with the x - y plane. The z -axis is pointed upward, and the acceleration of gravity is pointed in the negative z -direction. Let η be the shape of the surface of the fluid, and let ϕ be the potential of the flow. The flow is then described by Laplace's equation,

$$\Delta \phi + \frac{\partial^2}{\partial z^2} \phi = 0, \quad \Delta = \frac{\partial^2}{\partial x^2} + \frac{\partial^2}{\partial y^2}, \quad (1)$$

with two conditions at the surface $z = \eta$,

$$\begin{aligned} \frac{\partial \eta}{\partial t} + \nabla \phi \cdot \nabla \eta &= \frac{\partial}{\partial z} \phi, \\ \frac{\partial \phi}{\partial t} + \frac{1}{2} (\nabla \phi)^2 + \frac{1}{2} \left(\frac{\partial \phi}{\partial z} \right)^2 + g\eta &= 0, \end{aligned} \quad (2)$$

where g is the acceleration due to gravity, and a condition at $z \rightarrow -\infty$

$$\frac{\partial \phi}{\partial z} = 0. \quad (3)$$

Of course, nonlinearity enters our problem through the boundary conditions at the surface $z = \eta$.

Equations 1 through 3 conserve the total energy E of the fluid, where

$$\begin{aligned} E &= \frac{1}{2} \int \int_{-\infty}^{\eta} \left[(\nabla \phi)^2 + \left(\frac{\partial \phi}{\partial z} \right)^2 \right] dz dx \\ &+ \frac{1}{2} g \int \eta^2 dx. \end{aligned} \quad (4)$$

By choosing appropriate canonical variables, Zakharov,¹⁰ Broer,¹³ and Miles¹⁴ independently found that E may be used as a Hamiltonian. The proper canonical variables are

$$\eta \text{ and } \psi(x, t) = \phi(x, z = \eta, t). \quad (5)$$

The boundary conditions at the surface are then equivalent to Hamilton's equations,

$$\frac{\partial \eta}{\partial t} = \frac{\delta E}{\delta \psi}, \quad \frac{\partial \psi}{\partial t} = - \frac{\delta E}{\delta \eta}, \quad (6)$$

where $\delta E / \delta \psi$ is the functional derivative of E with respect to ψ .

Equation 6 has certain advantages. If one is able to solve the potential problem

$$\Delta \phi + \frac{\partial^2 \phi}{\partial z^2} = 0$$

with boundary conditions

$$\phi(x, z = \eta) = \psi \quad (7)$$

$$\frac{\partial \phi(x, z)}{\partial z} = 0, \quad z \rightarrow -\infty,$$

thereby expressing ϕ in terms of the canonical variables η and ψ , then the energy E may be evaluated in terms of η and ψ , and the evolution of η and ψ follows at once from Hamilton's equations (Eq. 6). Zakharov¹⁰ obtained the deterministic evolution equations for water waves by solving the potential problem (Eq. 7) in an iterative fashion for small steepness ϵ . Substitution of this series solution into Equation 4 results in the following expansion of the total energy E :

$$E = \epsilon^2 E_2 + \epsilon^3 E_3 + \epsilon^4 E_4 + O(\epsilon^5). \quad (8)$$

Retaining only the second-order term of E corresponds to the linear theory of surface gravity waves, the third-order term corresponds to three-wave interactions, and the fourth-order term corresponds to four-wave interactions. Since three-wave interactions are absent for deep-water gravity waves, one has to go to fourth order in ϵ to obtain a meaningful description of the wave field. Also, in the absence of three-wave interactions, a separation between free and bound waves is possible. By using this distinction, the amplitude $A(k, t)$ of the free-wave part of the wave field satisfies the so-called Zakharov equation,

$$\frac{\partial}{\partial t} A_1 + i\omega_1 A_1 = -i \int T_{1234} \times \delta(k_1 + k_2 - k_3 - k_4) A_2^* A_3 A_4 dk_2 dk_3 dk_4 . \quad (9)$$

Here, an asterisk denotes the complex conjugate, δ is the Dirac delta function, and we introduced the notation $A_1 = A(k_1)$, where k_1 is the wave number vector; the dispersion relation is given by

$$\omega_1 = \sqrt{g|k_1|} . \quad (10)$$

Finally, A_1 is related to the action density, since

$$E_2 = \int \omega |A|^2 dk . \quad (11)$$

The interaction coefficient T_{1234} was obtained by Zakharov¹⁰ and Crawford et al.⁹. The properties of the Zakharov equation (Eq. 9) have been studied in great detail by, for example, Crawford et al.¹⁵ (for an overview, see Yuen and Lake¹⁶). For example, the nonlinear dispersion relation, first obtained by Stokes,¹⁷ follows from Equation 9. Also, the instability of a weakly nonlinear, uniform wave train (the so-called Benjamin-Feir instability) is well described by the Zakharov equation; the results on growth rates, for example, are qualitatively in good agreement with the exact results of Longuet-Higgins.¹⁸

The Zakharov equation is therefore a good starting point to study the properties of a random wave field.

EVOLUTION OF A HOMOGENEOUS RANDOM WAVE FIELD

The Zakharov equation (Eq. 9) predicts amplitude and phase of the waves. For a practical application such as ocean wave prediction, the detailed information regarding the phase of the waves is not really needed. One can content oneself then with knowledge about averaged quantities such as the moments,

$$\langle A_1 \rangle, \langle A_1 A_2 \rangle, \text{ etc. } , \quad (12)$$

where the angle brackets denote an ensemble average.

In this section, we sketch the derivation of the evolution equation for the second-order moment $\langle A_1 A_2 \rangle$ (assuming a zero mean value, $\langle A_1 \rangle = 0$) from the Zakharov equation (Eq. 9). It is known, however, that because of nonlinearity, the evolution of the second moment is determined by the fourth moment, and so on, resulting in an infinite hierarchy of equations. To obtain a meaningful truncation of this hierarchy, we assume that the probability distribution for A_1 is close to a

Gaussian distribution. This assumption is reasonable for weakly nonlinear waves with small steepness ϵ . In addition, we assume in this section that the ensemble of waves is spatially homogeneous. Let us discuss these assumptions in more detail first.

A wave field is considered to be homogeneous if the two-point correlation function $\langle \eta(x_1) \eta(x_2) \rangle$ depends only on the distance $x_1 - x_2$, and not on the average coordinate $x = (x_1 + x_2)/2$. Here, η is the surface elevation that is related to the action density variable A according to

$$\eta = \frac{1}{2\pi} \int \left(\frac{|k|}{2\omega} \right) [A(k)e^{i\theta} + A^*(k)e^{-i\theta}] dk ,$$

where $\theta = k \cdot x$.

It is now straightforward to verify that one deals with a homogeneous wave field if the ensemble average $\langle A_1 A_2^* \rangle$ satisfies

$$\langle A_1 A_2^* \rangle = N_1 \delta(k_1 - k_2) , \quad (13)$$

where N_1 is the spectral action density. Thus, $\omega_1 N_1$ denotes the spectral energy density. Equation 13 will have important consequences, as will be discussed at the end of this section.

To truncate the infinite hierarchy of moment equations, one has to express, in an approximate sense, the higher-order moments in terms of lower-order moments. In general, for a zero-mean stochastic variable, A_1 , the following relation between the moments can be obtained:

$$\begin{aligned} \langle A_k \rangle &= 0 ; \langle A_k A_j \rangle = B_{kj} ; \langle A_k A_j A_l \rangle = C_{kjl} ; \\ \langle A_k A_j A_l A_m \rangle &= B_{kj} B_{lm} + B_{kl} B_{jm} + B_{km} B_{jl} \\ &+ D_{kjlm} , \text{ etc. } \end{aligned} \quad (14)$$

Here, B , C , and D are called *cumulants* of the distribution function. Now, for a Gaussian probability distribution with zero mean, all the cumulants except B_{kj} vanish. The finiteness of the other cumulants is therefore a measure of the deviation from Gaussian behavior. If, however, C and D are small (because of small wave steepness), the higher-order moments may be expressed in the second-order moment so that closure of the (infinite) hierarchy of moment equations may be achieved.

In the statistical theory of the evolution of a wave field, the Gaussian distribution, therefore, plays a central role. This follows from the central limit theorem that tells us that if the A_k 's have random and independent phase, the probability distribution is Gaussian. Suppose now that initially we are dealing with a wave field with random uncorrelated phases. If the waves are noninteracting, the phases remain uncorrelated. Nonlinear inter-

actions, however, will tend to create correlations (higher cumulants), but if the waves have a small steepness, this effect may be weak. Hence, for weakly nonlinear waves, one may expect that the wave field is near-Gaussian, so that the rate of change of the wave spectrum (or second moment) is expected to be small; for large times, however, this small effect may have significant consequences regarding the evolution of the wave spectrum.

Let us now sketch the derivation of the evolution equation for the second moment $\langle A_i A_j^* \rangle$ from the deterministic evolution (Eq. 9). To that end, we multiply Equation 9 for A_i by A_j^* , add the complex conjugate with i and j interchanged, and take the ensemble average:

$$\begin{aligned} \frac{\partial}{\partial t} \langle A_i A_j^* \rangle + i(\omega_i - \omega_j) \langle A_i A_j^* \rangle = \\ -iT_0 \int \delta(2 + 3 + 4 - i) \\ \times [\langle A_2 A_3 A_4^* A_j^* \rangle - \text{C.C.}(i \rightarrow j)] \\ \times dk_2 dk_3 dk_4, \end{aligned} \quad (15)$$

where C.C. denotes complex conjugate, and $i \rightarrow j$ denotes the operation of interchanging indices i and j in the previous term. For simplicity, we took the constant value T_0 for the interaction coefficient T_{1234} .

Because of nonlinearity, the equation for the second moment involves the fourth moment. Similarly, the equation for the fourth moment involves the sixth moment. It becomes

$$\begin{aligned} \left[\frac{\partial}{\partial t} + i(\omega_i + \omega_j - \omega_k - \omega_l) \right] \langle A_i A_j A_k^* A_l^* \rangle = \\ -iT_0 \int [\delta(2 + 3 - 4 - i) \langle A_2 A_3 A_4^* A_j A_k^* A_l^* \rangle \\ + (i \rightarrow j) - \delta(2 + 3 - 4 - k) \langle A_2^* A_3^* A_4 A_i A_j A_l^* \rangle \\ + (k \rightarrow l)] dk_2 dk_3 dk_4. \end{aligned} \quad (16)$$

Perhaps surprisingly, invoking the random-phase approximation (Eq. 14) on Equation 15, combined with the assumption of a homogeneous wave field, results in constancy of the second moment $\langle A_i A_j^* \rangle$. Hence, we have to go to higher order; that is, we have to determine the fourth moment through Equation 16.

Application of the random phase approximation on the sixth moment and solving Equation 16 for the fourth moment result eventually in the Hasselmann equation for four-wave interactions,

$$\frac{\partial}{\partial t} N_1 + 4\pi \int |T_{1234}|^2$$

$$\begin{aligned} \times \delta(2 + 3 - 4 - 1) \delta(\omega_2 + \omega_3 - \omega_4 - \omega_1) \\ \times [N_2 N_3 (N_1 + N_4) \\ - N_1 N_4 (N_2 + N_3)] dk_2 dk_3 dk_4. \end{aligned} \quad (17)$$

Details of this derivation may be found in Hasselmann,² Davidson,¹⁹ and Janssen.²⁰

From Equation 17 one immediately infers a typical time scale T_{NL} for nonlinear four-wave interactions in a homogeneous wave field. With ϵ a typical wave steepness and ω_0 a typical frequency of the wave field, we find $T_{NL} = O(1/\epsilon^4 \omega_0)$.

We emphasize that Equation 17 gives an adequate description of nonlinear interactions in a homogeneous wave field if the wave steepness is sufficiently small so that the near-Gaussian assumption is satisfied. Another restriction requires that the wave spectrum be sufficiently broad so that effects of inhomogeneity of the wave field may be disregarded. We discuss this last restriction in more detail in the next section by studying nonlinear interactions of an inhomogeneous wave field.

EVOLUTION OF AN INHOMOGENEOUS RANDOM WAVE FIELD

To investigate the effect of inhomogeneities on the nonlinear energy transfer of weakly nonlinear water waves, we consider the special case of a narrowband wave train, which is described by the nonlinear Schrödinger equation. For weakly nonlinear waves, the surface elevation is given by

$$\eta = \text{Re}\{a(x, t) \exp[i(k_0 x - \omega_0 t)]\}, \quad (18)$$

where ω_0 and k_0 are the angular frequency and the wave number of the carrier wave, respectively, which obey the deep-water dispersion relation $\omega_0 = (gk_0)^{1/2}$, and $a(x, t)$ is the slowly varying envelope of the wave. The evolution of the envelope is determined by the nonlinear Schrödinger equation,

$$\begin{aligned} i \left(\frac{\partial}{\partial t} + \omega_0' \frac{\partial}{\partial x} \right) a \\ + \frac{1}{2} \omega_0'' \frac{\partial^2}{\partial x^2} a - \frac{1}{2} \omega_0 k_0^2 |a|^2 a = 0, \end{aligned} \quad (19)$$

where the prime symbols denote differentiation with respect to k_0 . Transforming to a frame moving with the group velocity ω_0' and introducing dimensionless units $\tilde{t} = 1/2 \omega_0 t$, $\tilde{x} = 2k_0 x$, and $\tilde{a} = k_0 a$, the equation for \tilde{a} (which for a uniform wave train is just the wave steepness ϵ) becomes

$$i \frac{\partial}{\partial \tilde{t}} \tilde{a} - \frac{\partial^2}{\partial \tilde{x}^2} \tilde{a} - |\tilde{a}|^2 \tilde{a} = 0, \quad (20)$$

where we have dropped the tilde. In a statistical description of waves, one is interested in the time evolution of the two-point correlation function $\rho(x_1, x_2, t)$ defined as

$$\rho(x, r, t) \equiv \langle a(x_1, t) a^*(x_2, t) \rangle, \quad (21)$$

where x is the average coordinate $(x_1 + x_2)/2$, r is the separation coordinate $x_2 - x_1$, and again the angle brackets denote an ensemble average. The inhomogeneity of the wave field is expressed by the fact that ρ is also a function of the average coordinate x . Invoking the Gaussian approximation (i.e., Eq. 14 with $D = 0$), the transport equation for ρ becomes

$$i \frac{\partial}{\partial t} \rho - 2 \frac{\partial^2}{\partial x \partial r} \rho - 2\rho \left[\rho \left(x + \frac{1}{2}r, 0 \right) - \rho \left(x - \frac{1}{2}r, 0 \right) \right] = 0. \quad (22)$$

In agreement with a remark from the previous section, the evolution of a homogeneous wave field is not interesting at this level of description, since with $\rho \neq \rho(x)$, we have $\partial \rho / \partial t = 0$ from Equation 22. Small deviations from Gaussian behavior have to be included to obtain a nontrivial evolution of a homogeneous wave field. The relevant time scale for energy transfer in a homogeneous wave field is therefore $T_{NL} O(1/\epsilon^4 \omega_0)$. In the presence of spatial inhomogeneities, a much faster energy transfer is possible. From Equation 22, one then finds $T_{NL} = O(1/\epsilon^2 \omega_0)$.

From Equation 22 one obtains for the envelope spectrum W , defined as

$$W(x, p) \equiv \frac{1}{2\pi} \int \rho(x, r) e^{ipr} dr, \quad (23)$$

the transport equation,

$$\begin{aligned} \frac{\partial}{\partial t} W + 2p \frac{\partial}{\partial x} W + 4 \sin \left(\frac{1}{2} \frac{\partial^2}{\partial p \partial x'} \right) \\ \times W(x, p) r(x', 0) |_{x'=x} = 0, \end{aligned} \quad (24)$$

where

$$\begin{aligned} \sin \left(\frac{1}{2} \frac{\partial^2}{\partial p \partial x'} \right) \\ = \frac{1}{2i} \sum_{l=0}^{\infty} \frac{\left(\frac{i}{2} \frac{\partial^2}{\partial p \partial x'} \right)^{2l+1}}{(2l+1)!}. \end{aligned}$$

Equation 24 is the basic evolution equation of the spectrum W of a random inhomogeneous wave field in the narrow band approximation. The theory for general spectral shape is given in Crawford.⁹

Alber and Saffman⁷ and Alber⁸ studied the stability of a homogeneous spectrum and found that it is unstable to long wavelength perturbations if the width of the spectrum is sufficiently small (random version of Benjamin-Feir instability). To see whether a homogeneous spectrum $W_0(p)$ is a stable solution of Equation 24, one proceeds in the usual fashion by perturbing $W_0(p)$ slightly according to

$$W = W_0(p) + W_1(p, x), \quad W_1 \ll W_0, \quad (25)$$

and one considers perturbations of the type

$$W_1 = \tilde{W}_1 \exp i(kx - \omega t). \quad (26)$$

The eventual result of the analysis is then a dispersion relation between ω and k . Instability is found for $\text{Im}(\omega) > 0$. A symmetrical spectrum is found to be marginally stable if

$$1 + \int_{-\infty}^{\infty} \frac{dp}{p} \frac{d}{dp} W_0(p) = 0, \quad (27)$$

where, for definiteness $p = (\omega - \omega_p)/\omega_p$, where ω_p is the peak frequency of the spectrum. For a Gaussian spectrum,

$$W_0(p) = \frac{\langle a_0^2 \rangle}{\sigma \sqrt{2\pi}} e^{-p^2/2\sigma^2}, \quad (28)$$

where $\langle a_0^2 \rangle$ is the mean square significant steepness and σ is the width of the spectrum, the condition for marginal stability becomes

$$\sigma = \sigma_{th} = \sqrt{\langle a_0^2 \rangle}, \quad (29)$$

where σ_{th} is the threshold spectral width.

We conjecture that in nature one should expect to find wave spectra with a width larger than σ_{th} , because for smaller widths the random version of the Benjamin-Feir instability would occur, resulting in a broadening of the spectral shape. For a random finite-band wave train, this broadening is an irreversible process because of phase mixing.¹² This conclusion contrasts with the work of Yuen and Lake,¹⁶ who claimed that the effects of inhomogeneity would give rise only to a reversible energy transfer. In Janssen,²¹ the time scale τ_{br} of broadening was estimated for a Joint North Sea Waves Project (JONSWAP) spectrum. The result for a young wind sea (JONSWAP parameters $\gamma = 3.3$, $\sigma_1 = 0.1$, $\alpha = 0.01$) is

$$\tau_{br} = 500/\omega_p . \quad (30)$$

Other effects relevant for the energy balance of wind waves have a much larger time scale. Consider, for example, the increase in wave energy by wind. Using the Bight of Abaco parameterization,²² the time scale τ_w for the increase in wave energy by wind is given by

$$\tau_w = \frac{5000}{\omega_p} \times \frac{1}{U_5/c - 1} , \quad (31)$$

where U_5 is the wind speed at a height of 5 m, and c is the phase speed of the gravity waves. Clearly, for a young wind sea, τ_{br} is much smaller than τ_w , indicating that inhomogeneous nonlinear interactions are important at the peak of a young wind sea.

To test our conjecture, Janssen and Bouws²³ decided to determine the width of measured spectra. To avoid contamination by high-frequency noise, they used, following Goda,²⁴ the quality factor,

$$Q_p = \frac{2}{m_0^2} \int \omega E^2(\omega) d\omega , \quad (32)$$

where m_0 is the zeroth-order moment of the spectrum. In terms of dimensionless quantities, Q_p becomes

$$Q_p = \frac{2}{m_0^2} \int (p+1) W_0^2(p) dp ,$$

and for the Gaussian spectrum (Eq. 28), one finds

$$Q_p = \frac{1}{\sigma \sqrt{\pi}} + \frac{1}{2\pi} . \quad (33)$$

Since the significant wave steepness $\langle a_0^2 \rangle^{1/2} = k_p m_0^{1/2}$, with k_p the peak wave number, and since according to Equation 29 a stable spectrum should have a width $\sigma \geq \langle a_0^2 \rangle^{1/2}$, we find that Q_p should obey the inequality,

$$Q_p \leq \frac{1}{k_p \sqrt{\pi m_0}} + \frac{1}{2\pi} . \quad (34)$$

Spectra with a Q_p larger than the right side of Equation 34 are unstable according to theory. Hence, if one determines Q_p from time series for which the length is larger than τ_{br} (Eq. 30), the inequality (Eq. 34) should be satisfied. In Figure 1 we have plotted the experimentally determined quality factor Q_p (from weather station Ymuiden in the North Sea) as a function of the significant steepness $k_p m_0^{1/2}$, with m_0 determined for the frequency domain immediately around the peak; Equation 34 is also shown. The agreement between experimental data and theory is good. Details regarding the selection of the data, for example, are in Ref. 23.

The theory of weakly nonlinear interactions of an inhomogeneous random wind sea predicts that the width of a wind sea spectrum is larger than a certain threshold, or that the quality factor Q_p is smaller than a certain threshold. From a selection of Ymuiden data, it may be inferred that the quality factor (taking the statistical scatter into account) is close, but always below the threshold, a result that has some immediate consequences. For instance, we can make the following remark on wave groups. Ewing²⁵ has shown that a relation exists between group length $\langle l \rangle$ and the width of a spectrum, namely,

$$\langle l \rangle = \frac{1}{k} \left[\frac{1 + (\omega_p/\sigma)^2}{2\pi} \right]^{1/2} ,$$

where $k = \rho/m_0^{1/2}$, ρ is a reference level ($k = 2$ corresponds to the significant wave height). Theory now tells us that the average length of a group has a maximum. For the Ymuiden data, $\langle l \rangle$ is typically on the order of 3.

Another consequence is a limitation to the validity of Hasselmann's evolution equation for four-wave interactions. The wave spectra should be sufficiently broad ($\sigma > \epsilon \omega_0$), because otherwise strong inhomogeneous nonlinear energy transfer would occur. Since these interactions occur on a short time scale ($T_{NL} = 1/\epsilon^2 \omega_0$), however, it may be concluded that for (global) applications with a coarse resolution ($\Delta x > 10$ km), the Hasselmann equation (Eq. 17) gives an adequate description of nonlinear interaction of a random wave field. On the other hand, for fine-mesh applications ($\Delta x < 5$ km), effects of inhomogeneous nonlinear energy transfer should be taken into account.

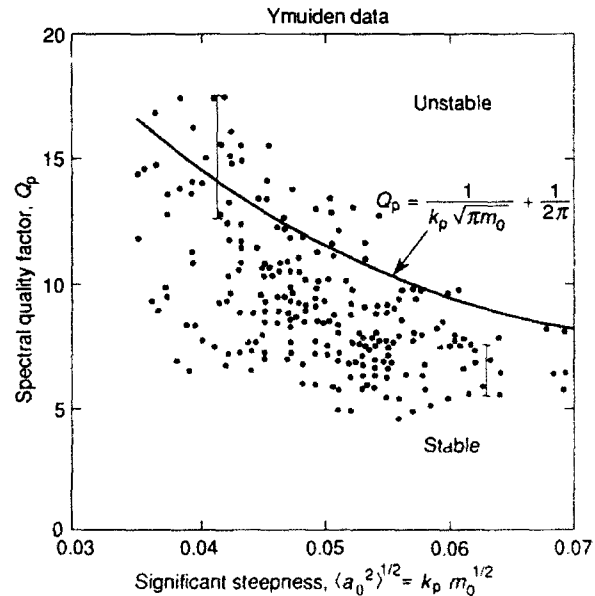


Figure 1. The quality factor Q_p versus the significant steepness for young wind waves. The solid line is the threshold for stability according to theory (Eq. 34).

CONCLUSIONS

We have reviewed the range of validity of the theory of nonlinear four-wave interactions of a random wave field. Two types of nonlinear interactions are found. On the short time scale $T_{NL} = O(1/\epsilon^2\omega_0)$, energy transfer owing to spatial inhomogeneities occurs, if the width of the spectrum is sufficiently small. This inhomogeneous energy transfer will reshape the spectrum so that the spectral width becomes larger, thereby quenching the random version of the Benjamin-Feir instability. Nonlinear energy transfer is then possible only on the much longer time scale $T_{NL} = O(1/\epsilon^4\omega_0)$, in accordance with the results of Hasselmann.² In other words, the Hasselmann equation (Eq. 17) gives an adequate description of weakly nonlinear energy transfer for coarse resolution applications ($\Delta x > 10$ km).

If one is interested in fine-mesh applications ($\Delta x < 5$ km), however, effects of inhomogeneous nonlinear energy transfer should be taken into account. These nonlinear interactions give rise to a limitation of the average length of a wave group. Other consequences of inhomogeneous energy transfer, however, still have to be explored.

REFERENCES

- ¹ Phillips, O. M., "On The Dynamics of Unsteady Gravity Waves of Finite Amplitude," *J. Fluid Mech.* **9**, 193-217 (1960).
- ² Hasselmann, K., "On the Non-Linear Energy Transfer in a Gravity-Wave Spectrum, Part I: General Theory," *J. Fluid Mech.* **12**, 481 (1962).
- ³ Hasselmann, K., Barnett, T. P., Bouws, E., Carlson, H., Cartwright, D. E., et al., "Measurements of Wind-Wave Growth and Swell Decay during the Joint North Sea Waves Project (JONSWAP)," *Deutsche Hydrog. Z., Suppl. A*(80), No. 12 (1973).
- ⁴ Watson, K. M., and West, B. J., "A Transport Equation Description of Non-linear Ocean Surface Wave Interactions," *J. Fluid Mech.* **70**, 815-826 (1975).
- ⁵ Willebrand, J., "Transport in a Nonlinear and Inhomogeneous Random Gravity Wave Field," *J. Fluid Mech.* **70**, 113-126 (1975).
- ⁶ WAMDIG (Wave Model Development and Implementation Group), "The WAM Model—A Third Generation Ocean Wave Prediction Model," *J. Phys. Oceanogr.* **18**, 1775-1810 (1988).
- ⁷ Alber, I. E., and Saffman, P. G., *Stability of Random Nonlinear Deepwater Waves with Finite Bandwidth Spectra*, 31326-6035-RU-00, TRW Defense and Space System Group (1978).
- ⁸ Alber, I. E., "The Effects of Randomness on the Stability of Two-Dimensional Surface Wave Trains," *Proc. R. Soc. London A***363**, 525-546 (1978).
- ⁹ Crawford, D. R., Saffman, P. G., and Yuen, H. C., "Evolution of a Random Inhomogeneous Field of Nonlinear Deep-Water Gravity Waves," *Wave Motion* **2**, 1-16 (1980).
- ¹⁰ Zakharov, V. E., "Stability of Periodic Waves of Finite Amplitude on the Surface of a Deep Fluid," *Zh. Prikl. Mekh. Tekh. Fiz.* **9**, 86-94 (English translation in *J. Appl. Mech. Tech. Phys.* **9**, 190-194 (1968)).
- ¹¹ Benjamin, T. B., and Feir, J. E., "The Disintegration of Wave Trains on Deep Water. Part I: Theory," *J. Fluid Mech.* **27**, 417-430 (1967).
- ¹² Janssen, P. A. E. M., "Long-Time Behaviour of a Random Inhomogeneous Field of Weakly Nonlinear Surface Gravity Waves," *J. Fluid Mech.* **133**, 113-132 (1983).
- ¹³ Broer, L. J. F., "On the Hamiltonian Theory of Surface Waves," *Appl. Sci. Res.* **29**, 430-446 (1974).
- ¹⁴ Miles, J. W., "On Hamilton's Principle for Surface Waves," *J. Fluid Mech.* **83**, 153 (1977).
- ¹⁵ Crawford, D. R., Lake, B. M., Saffman, P. G., and Yuen, H. C., "Stability of Weakly Nonlinear Deep-Water Waves in Two and Three Dimensions," *J. Fluid Mech.* **105**, 177-191 (1981).
- ¹⁶ Yuen, H. C., and Lake, B. M., "Nonlinear Dynamics of Deep-Water Gravity Waves," *Adv. Appl. Mech.* **22**, 67-229 (1982).
- ¹⁷ Stokes, G. G., "On the Theory of Oscillatory Waves," *Trans. Cambridge Philos. Soc.* **8**, 441-455, *Math. Phys. Pap.* **1**, 197-229 (1847).
- ¹⁸ Longuet-Higgins, M. S., "The Instabilities of Gravity Waves of Finite Amplitude in Deep-Water. II. Subharmonics," *Proc. R. Soc. London Ser. A***360**, 489-505 (1978).
- ¹⁹ Davidson, R. C., *Methods in Nonlinear Plasma Theory*, Academic Press, New York and London (1972).
- ²⁰ Janssen, P. A. E. M., *Nonlinear Effects in Water Waves*, ICTP course on ocean waves and tides, Trieste, Italy (1989).
- ²¹ Janssen, P. A. E. M., "Stability of a Random Inhomogeneous Field of Weakly Nonlinear Surface Gravity Waves with Application to the JONSWAP Study," in *The Ocean Surface*, Toba, Y., and Mitsuyasu, H., eds., Reidel, Dordrecht, pp. 39-49 (1985).
- ²² Snyder, R. L., Dobson, F. W., Elliot, J. A., and Long, R. B., "Array Measurements of Atmospheric Pressure Fluctuations above Surface Gravity Waves," *J. Fluid Mech.* **102**, 1 (1981).
- ²³ Janssen, P. A. E. M., and Bouws, E., *On the Minimum Width of a Gravity Wave Spectrum*, KNMI-00 Memorandum 00-86-01, KNMI, De Bilt, The Netherlands (1986).
- ²⁴ Goda, Y., "On Wave Groups," in *An International Conference on the Behaviour of Off-Shore Structures*, Vol. 1, The Norwegian Institute of Technology, Trondheim, Norway, pp. 115-128 (1976).
- ²⁵ Ewing, J. A., "Mean Length of Runs of High Waves," *J. Geophys. Res.* **78**, 1933-1936 (1973).

ACKNOWLEDGMENTS: I would like to thank Evert Bouws, Gerbrand Komen, and Philip Saffman for useful discussions.

SEAKEEPING AND SURFACE MEASUREMENTS
IN WHICH SURFACE TECHNIQUES FOR ESTIMATING
THE DIRECTIONAL OCEAN WAVE SPECTRUM ARE
DESCRIBED AND EVALUATED

SOME COMMENTS ON THE SIGNIFICANCE OF LEWEX FOR SHIP DESIGN AND OPERATIONS

Gross disagreements between measured and forecast spectra can often be explained by small errors in time or location.

During a conversation about ocean waves and linear superposition some years ago, a friend of mine noted that the sea cannot be measured by the bushel. During the Labrador Sea Extreme Waves Experiment (LEWEX), I was convinced at times that the sea could not be measured by any unit, instrument, or other means, regardless of one's intention. Then, after a few delicate days of high sea states, just as we reached our destination at the two LEWEX measurement sites, we encountered what seemed to be the lowest extreme waves ever experienced. Accordingly, the crew of HNLMS *Tydeman* renamed the experiment but kept the acronym. On the basis of climatology, most of us had predicted six- to ten-meter sea states, but only two- to five-meter seas were measured.

Other papers in this issue address scientific issues. But from the point of view of ship design and operation, I would like to discuss future requirements regarding the accuracy of ocean wave measurements. A few years ago at an ocean wave symposium at APL, I suggested that the seafaring community requires wave measurement accuracies of ± 0.3 m in significant wave height through sea states 4 to 7, ± 1 s in modal period over a range of 3 to 24 s, and $\pm 7.5^\circ$ in directional spreading in 15° increments.

Those requirements were based on the responsiveness of typical marine vehicles to the wave spectrum. I failed to address two areas not inherent in design work that make all the difference in the world at sea, namely, time and location. During LEWEX, we found that the wave forecasts available to us on board the ship did not have adequate resolution to identify important temporal and spatial variations in the ocean. Two years have passed since I examined those data, but I do not recall reasonable agreement between prediction and reality, reality in this case being the human sensor on the spot. This aspect of the forecasts is critical when one is trying to route ships, avoid damage, maximize ship system performance, or determine in real time where to drop buoys for an ocean experiment such as LEWEX. Although temporal and spatial forecast errors are not as critical for

land-based design studies, where omissions at one location or time are picked up at another, their significance at sea is an entirely different matter.

From the applications viewpoint, I think the most critical user issue in ocean waves, for the next decade at least, is that of space and time. I believe the marine vehicle design community is nearly adequately equipped with operational databases and spectral models to do its job. Although most ships, certainly those in the U.S. Navy, are not as structurally survivable as they once were, they are still adequate. We expect a certain amount of damage and can sustain it.

A reliable forecast of the weather, including wind and waves, can make a tremendous difference to a ship at sea, particularly in heavy seas. We can justify ocean wave research merely because it is good science. But can we continue to find adequate financial support without making a substantial contribution to national economic or defense goals?

Mathematicians have been experimenting with chaos theories for at least a decade. They have concluded that long-range weather forecasting is extremely sensitive to the initial conditions. Although the models may agree well with measurement initially, a slight perturbation eventually makes a huge difference.

Could small errors in initial values be our major problem in forecasting? Playing the devil's advocate for a moment, one could argue that from the viewpoint of an individual ship, global modeling is not very helpful, and that *in situ* or remote measurements in local areas are more critical. Hullborne radars, expendable buoys, and constellations of satellites with appropriate down-links to land and shore sites could provide initial values, data for climatology upgrades, and localized ocean wave data.

LEWEX can help sort out where we are, in both modeling and sensor capabilities, and can provide us with a forum to continue the multidisciplinary synergism that it has fostered. The resulting insights could shape wave research and applications for the next decade.

THE CFAV *QUEST*'S LEWEX EXPERIENCE

The seakeeping performance of the CFAV *Quest* during the Labrador Sea Extreme Waves Experiment demonstrates the inadequacy of unidirectional sea-state descriptions and, even more important, demonstrates deficiencies in the unidirectional sea-state model's accepted successor, the unimodal, two-parameter spectrum with $90^\circ \cos^2$ spreading.* A more complete, often multimodal, sea-state description can reveal strong, unexpected variations in ship response with heading, and can result in substantially improved ship operability assessments.

INTRODUCTION

A Canadian Forces Auxiliary Vessel, CFAV *Quest*, was one of two vessels participating in the Labrador Sea Extreme Waves Experiment (LEWEX). The *Quest* carried scientists and equipment from six agencies within Canada and the United States. Its work program supported the goals of two Research Study Groups (RSG1 and RSG2) of the NATO Defence Research Group Special Group of Experts on Naval Hydrodynamics and Related Problems (SGE[Hydro]), and provided open ocean data for the Labrador Ice Margin Experiment (LIMEX '87).

The *Quest* is a 2200-tonne twin-screw diesel-electric vessel that primarily supports underwater acoustics research at the Defence Research Establishment Atlantic (DREA). The ship is ice-strengthened to allow summer scientific cruises to the Canadian eastern Arctic. Figure 1 shows a view of the *Quest*; the following are its nominal particulars:

Displacement	2200 tonnes
Length between perpendiculars	71.63 m
Molded breadth	12.80 m
Midships draft	4.82 m
Installed shaft power	2000 kW
Speed	14.5 kt

The *Quest* supported the LEWEX goals relevant to the NATO SGE(Hydro) RSG1 Group on Full Scale Wave Measurement and, coincidentally, LIMEX '87 through environmental measurements with on-board instruments or wave buoys. The measurements are covered amply by other LEWEX articles in this volume and will not be discussed in detail here. The *Quest*, per se, was of more direct interest to the NATO SGE(Hydro) RSG2 Group on Sea Loads, Slamming, and Green Seas Impacts, who planned to use sea loads measured on both the *Quest* and HNLMS *Tydeman* during LEWEX.

The RSG2 group is much smaller than RSG1, with participation from Canada (DREA and the Institute for Marine Dynamics, IMD), Germany (Bundesamt für Wehrtechnik und Beschaffung), The Netherlands (Royal

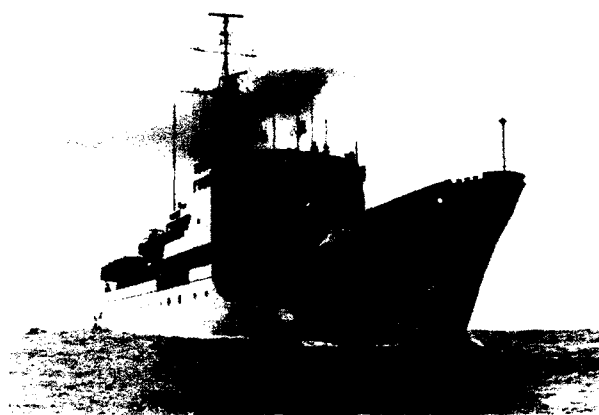


Figure 1. The CFAV *Quest*.

Netherlands Navy), Norway (Marintek), Spain (Canal de Experiencias Hidrodinámicas, El Pardo), the United Kingdom (Admiralty Research Establishment, Dunfermline), and the United States (David Taylor Research Center, DTRC). In keeping with its smaller size, RSG2's work was smaller in scope than RSG1's but, as will be seen later, proved to be more difficult to complete because of the lack of extreme seas during LEWEX.

RSG2 GOALS AND PLANS

The aim of RSG2 was to conduct research into slamming and green seas impact mechanisms, to improve surface ship operability in high sea states. Seakeeping trials with the *Quest* and *Tydeman* were to provide important full-scale data for RSG2, for comparison with model tests and for validation of theoretical methods. The RSG2 group also planned or identified a number of related studies. For example, Canada and the United Kingdom undertook a cooperative two-dimensional drop test program to assess scale effects on the girthwise bottom slam pressure distribution, and The Netherlands indicated that

*An angular spreading that varies as $\cos^2\theta$ about the dominant wave direction, that is, an effective angular spread of 90° .

the Royal Netherlands Navy full-scale green seas loading trials might become available to the group.

The RSG2 plan for the *Quest* and *Tydemar* was straightforward:

1. Perform individual and side-by-side seakeeping trials with the *Quest* and *Tydemar* during LEWEX.
2. Conduct model tests with the *Quest*, or perhaps with both ships, in scaled LEWEX directional seas in Marintek's facilities in Trondheim, Norway. (See the article by Kjeldsen in this volume.)
3. Use the trials and model test results to validate theoretical methods used or under development by the RSG2 members.

INSTRUMENTATION

During LEWEX, the *Quest* carried or deployed the systems outlined in Table 1. The moored wavebuoys were deployed in 2700 m of water. These deep-water moorings were a high-risk element in LEWEX because they were "once-only" evolutions. The moorings had to be manufactured, before sailing, for a specified water depth, and the design had only a limited margin against failure so as to reduce the cost of the lower parts of the moorings, which would not be recovered.

The "drifting" wavebuoys typically were streamed to windward of the drifting ship in series on an approximately 1000-m polypropylene tether, which produced no apparent interference with wavebuoy motions.

The navigation radar photos experiment was an offshoot of the author's interest in deriving normalized directional wave spectra using navigational radar as a means of reducing reliance on wavebuoys during seakeeping trials. All too often, when conditions are ideal for seakeeping trials, wavebuoys cannot be deployed from the ship. Given the expected LEWEX wave spectral database for

validation, it seemed appropriate to examine the navigational radar technique; Nordco Limited was contracted to develop a photographic apparatus corresponding to that used by Young et al.¹ to record radar sea-clutter information.

A number of sets of radar sea-clutter photographs were taken during LEWEX. Nordco subsequently developed analysis techniques and software^{2,3} so that the radar technique could be assessed in the LEWEX comparisons (see the article by Ziemer in this volume). In ongoing contracted research, Nordco is investigating the possibility of scaling the radar-derived spectra to allow the significant wave height to be determined.

The current meter, an InterOcean S-4 electromagnetic unit, also could measure salinity and depth. Its output, together with expendable bathythermograph records taken on station and while in transit between sites, was primarily for the benefit of LIMEX '87.

The *Quest*'s motions were measured using two ship-motion packages. The DREA's own package used strap-down pitch, roll, and yaw gyros (both angle and rate) as well as a strap-down triaxial accelerometer. Additional accelerometers were placed at other locations on the ship. The Institute for Marine Dynamics, St. John's, Newfoundland (IMD) package measured similar parameters but had a stabilized platform so that accelerations would be measured relative to Earth-fixed, rather than ship-fixed, axes.

Ten 305-mm-diameter Metrox pressure transducers, installed in the starboard bow flare (Fig. 2), were of great interest to RSG2. Large-diameter pressure transducers en-

Table 1. Instrumentation carried or deployed by the *Quest* during LEWEX.

Parameter	System	Location	Sponsor
Sea state	Wavec buoy	Moored	MEDS ^a
Sea state	Endeco buoy	Moored	DREA
		and drifting	
Sea state	Endeco buoy	Drifting	DTRC
Sea state	Delft buoy	Drifting	Delft/ DTRC
Sea state	Wavecrest buoy	Drifting	IMD
Sea state	Navigation radar photos	On board	DREA
Current	InterOcean S-4	Endeco mooring	DREA
Ship motions	"Strap-down" package	On board	DREA
Ship motions	Humphrey stable platform	On board	IMD
Sea loads	Pressure transducers	Bow flare	DREA
Sea loads	Strain gauging	Hull	DREA

^a Marine Environmental Data Service, Department of Fisheries and Oceans, Ottawa.

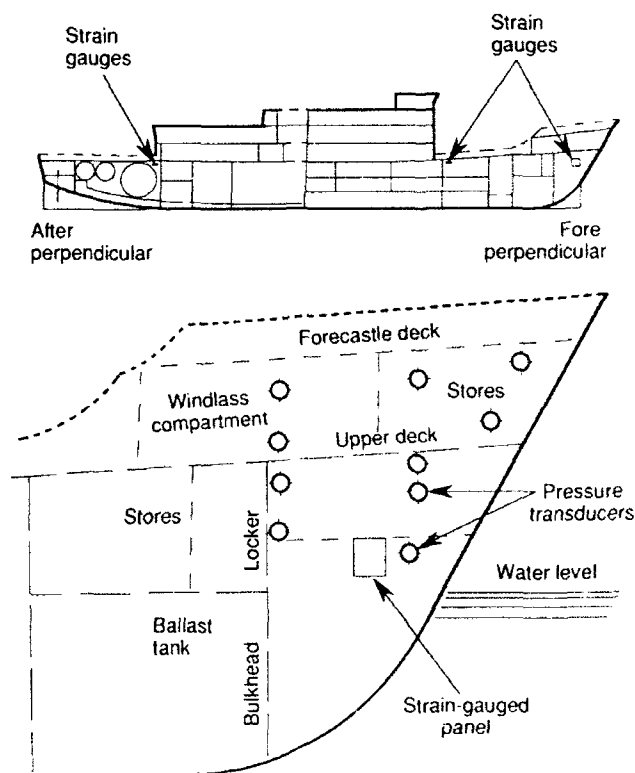


Figure 2. Starboard profile of the *Quest* and arrangement of the pressure transducers.

sured that only distributed pressures of structural significance were measured. More common small-diameter pressure transducers often detect extreme, but very localized, pressures that are of little relevance to ship structure design.

Strain gauges were also installed, both adjacent to one of the pressure transducers and on the main-deck longitudinal girders ahead of and abaft the superstructure (Fig. 2). The bow-flare gauges were arranged to complement the pressure transducers, and the deck longitudinal girder gauges assessed the bow-flare slamming-induced longitudinal bending.

SHIP PERFORMANCE AND SEA LOADS

LEWEX suffered from an excess of good weather; both the *Tydemar* and the *Quest* saw their worst weather in transit to the trials area. The *Quest* steamed from Halifax to St. John's in heavy quartering wind and sea, with freezing spray, and on the evening of 7 March 1987, while off the Laurentian Fan, an unexpectedly large wave group rolled the ship down to angles beyond the range of the bridge inclinometer (40°). Inclinometers are notably inaccurate, so it is unfortunate that neither ship-motion package was operating at the time.

The *Tydemar*'s arrival in St. John's was delayed by adverse gales and heavy pack ice, so that the *Quest* left for the LEWEX site without having made a planned pre-LEWEX rendezvous with the *Tydemar*.

On her two LEWEX sites, the *Quest* saw maximum significant wave heights, H_s , of only 4.3 m and typical significant wave heights of 2.5 to 3.5 m. Perhaps with the exception of the 4.3-m sea state of 17 March, these conditions were inadequate to provide the sea loads anticipated by RSG2 and required for full satisfaction of the RSG's goals.

The *Quest*'s seakeeping trials were planned to concentrate on the measurement of bow-flare slamming pressures, using the ten large pressure transducers described earlier. An unconventional seakeeping trial pattern was selected in recognition of that goal. Rather than measuring responses at a full range of headings to the sea, a four-heading seakeeping pattern was selected (Fig. 3). Headings ranged from head to starboard beam seas, in 30° steps (with head seas being 180° , after the standard naval architectural convention). This pattern also served to make identification of "true" head seas less critical.

Side-by-side seakeeping trials were conducted when the *Quest* and *Tydemar* were at the same site in LEWEX, with the *Tydemar* to starboard of the *Quest* so that video and cine records could be made of the relative motions at the *Quest*'s bow.

One of the most difficult on-site decisions during the LEWEX seakeeping trials was simply to determine, "In what direction are head seas?" With multimodal sea states often being the norm, leftover swell frequently was more prominent than the new wind sea; for consistency, wind direction and wind sea direction were used to select the first course to steer. On several occasions, this choice clearly proved to be wrong, as pitch angles and deck wetness were more severe on the supposed beam seas heading than the initial one in "head" seas.

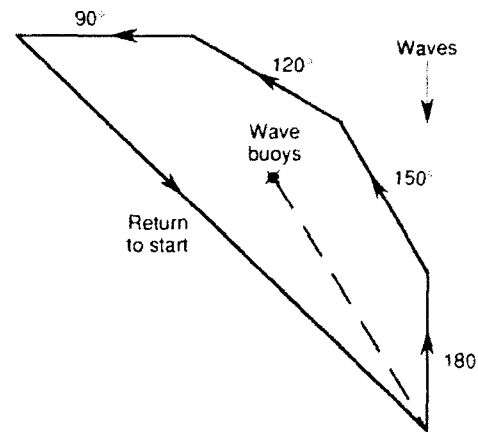


Figure 3. The *Quest*'s seakeeping pattern.

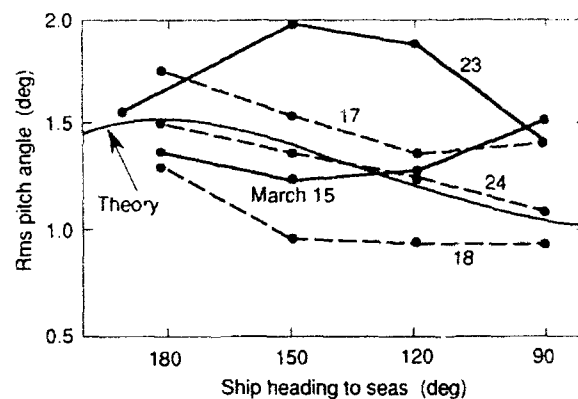


Figure 4. Variation of theoretical and trial pitch with ship heading. The theory uses a unimodal spectrum with 90° spreading.

Figure 4 illustrates this situation for the *Quest* by comparing the variation of pitch with heading with a prediction of the expected trend using SHIPMO4, a typical ship theory seakeeping computer program. The SHIPMO4 prediction was performed by using a Bretschneider two-parameter spectrum with a $90^\circ \cos^2$ spreading function. The character of the trial results for 15 and 23 March differed markedly from the strip theory trend. A similar result might be expected for roll motions, but clear trends were obscured by the *Quest*'s roll-stabilizing tank.

Pressure data show similar divergence from heading dependencies implied by an assumption of unimodal sea states. Selected pressure transducer data are shown in Figure 5, together with SHIPMO4 predictions of trends for immersions and pressures. (The theoretical pressure trend is, in fact, the square of the relative velocity, which is proportional to pressure.) Trends for other pressure transducers also diverged from unimodal expectations, although some pressure transducer data were corrupted by amplifier overloading. A repeat bow-flare slamming trial was carried out in higher sea states in March 1989 to seek further data for RSG2.

The LEWEX sea states were so low that little useful strain data were obtained, although that could also be

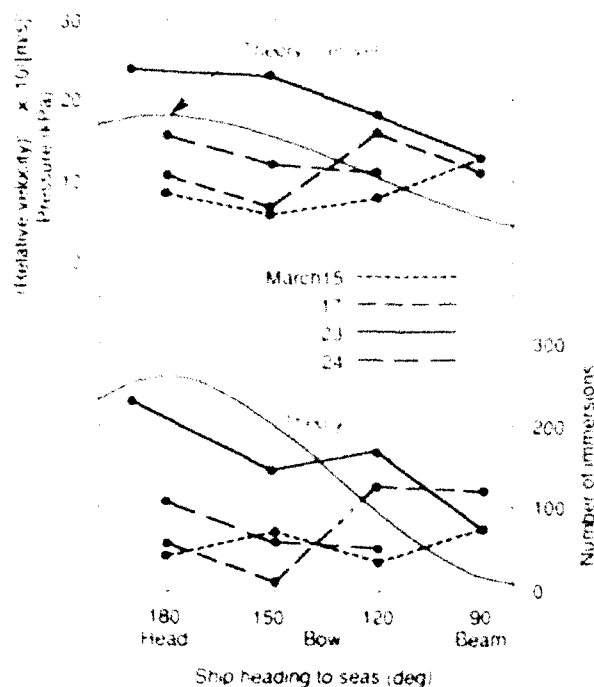


Figure 5. Immersion frequency and pressure for a selected pressure transducer, together with theoretical predictions of trends for immersion and the square of relative velocity (which is proportional to pressure) for a unimodal spectrum with 90° spreading.

attributed to the use of the *Quest* itself. A short, deep, ice-strengthened ship cannot be expected to exhibit high main-girder strains in other than exceptional conditions.

On a positive note, the bow-flare strain gauge data were used in a finite-element validating study. Pegg et al.⁷ applied measured-pressure time series to predict dynamic strains in the bow-flare region using the Vibration and Strength Analysis Program,⁸ a finite-element code developed by Martec Limited under contract from DRI V. The measured strains were used to validate the finite-element predictions for the same points. Figure 6 compares measured and finite-element-predicted strain-time histories.

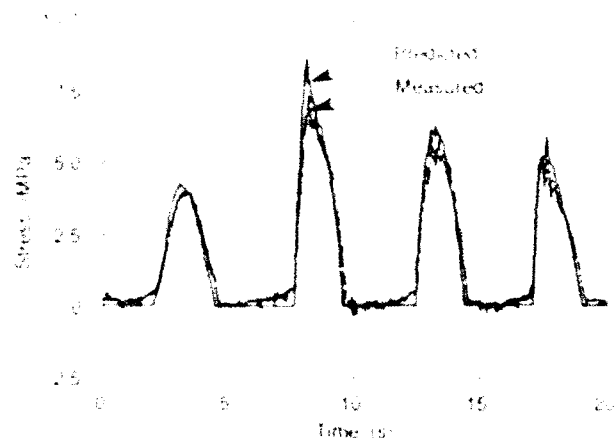


Figure 6. Experimental and finite-element strain time series for a bow flare plating strain gauge (see Fig. 2).

NAVAL ARCHITECTURAL IMPLICATIONS

Before examining the naval architectural consequences of the *Quest*'s HEWEX experience in any detail, it is worth recalling the results of an earlier *Quest* ship motions trial, when the *Quest* was operating with her roll stabilizing tank empty, so that roll performance can be included in an assessment of short-crested sea effects.

During the earlier trial, a passing low-pressure system brought 20- to 40-kt winds, which veered from south-southeast through to west-southwest in 32 hours and generated 5- to 7-m sea states. The steadily veering winds ensured that there was always a very apparent short-crested character to the sea. Table 2 summarizes some sea states and ship motions during the storm. Sea state was both measured by wavebuoys and hindcast using the Ocean Data Gathering Program (ODGP) wave model.

Large roll angles in nominal head seas (experiments D and E) are particularly noticeable in Table 2. If we combine this information with experiments B and C, which were consecutive beam and bow seas runs, it is again apparent that short-crested seas produce ship motions that do not vary with heading in the manner conventionally assumed. What are the consequences?

Table 2. Summary of *Quest* motions from an earlier trial

Experiment	Speed (kt)	Heading to sea	Rms motions				Center of gravity vertical acceleration (g)
			H_s Orb (m)	Buoys (m)	Pitch (deg)	Roll (deg)	
A	≈ 0	Beam	4.9	3.5	1.93	7.94 ^a	0.046
B	≈ 5	Beam	6.3	4.5	1.88	5.06	0.053
C	≈ 5	Bow	6.3	5.0	2.30	5.03	0.065
D	≈ 2	Head	5.5	7.0	3.06	4.80	0.066
E	≈ 2	Head	4.8	6.5	2.61	4.06	0.057

^aRoll is largest in experiment A because the sea-state modal period was near roll resonance

Many, if not most, ship seakeeping operability criteria are based on motions. For example, let us suppose that a particular shipboard operation must be curtailed when the roll angle exceeds 4° rms. Roll motions are lightly damped and thus are very sensitive to resonance. If a long-crested sea state is assumed, theory predicts that roll-curtailed operations may be restored through a simple change of heading. Even with a more realistic sea-state model using $90^\circ \cos^2$ spreading, a heading change can often restore operability, albeit over a smaller range of headings. If our sea-state model is extended to a typical LEWEX swell-corrupted directional spectrum, the heading sensitivity of motion response may be significantly modified. At times, operability may be curtailed at nearly all headings after only a small further increase in sea state. Figure 7 illustrates the effect of sea-state modeling on a 5200-tonne frigate steaming at 20 kt in sea state 7, with a 6-m significant wave height, and subject to a 4° rms roll angle limit on a shipboard operation.

An ad hoc group of five sea-state models was chosen for this example:

1. A Bretschneider spectrum, with a 12.4-s modal period and no spreading.
2. Same as (1), but with a $90^\circ \cos^2$ spreading function.
3. With (2) as the primary sea, and with (1) as the secondary, at 45° to the primary direction and with a primary-to-secondary energy ratio of 2:1, to represent conditions during the nearby passage of a low-pressure system.
4. Same as (3), but with the secondary sea 90° from the primary direction and a primary-to-secondary energy ratio of 3:1, to represent the effects of a distant weather system.
5. Same as (3), but with the secondary sea 135° from the primary direction and a primary-to-secondary energy ratio of 4:1, again to represent the effects of a distant weather system.

In reality, these models might be more representative if the total energy in models (4) and (5) were increased over that of the 6-m sea state by the amount in the secondary sea but the significant wave height were held constant to reduce the number of variables. Table 3 summarizes the results as a range of inoperable headings for both 4° and 3° roll criteria and as range of rms roll angle from best to worst heading. The 3° criterion was added because operability limits are rarely "hard" in practice. This is particularly relevant to model 4, where either a small increase in wave height or a small decrease in the acceptability criterion would significantly reduce operability. The range of roll angle between best and worst heading is so small for model 4 that degradation of operability will be very rapid with only a small sea-state increase, with little opportunity for compensatory heading change. This insensitivity of response to heading is reminiscent of much of the *Quest's* LEWEX experience.

Similar examples could be given for other criteria, using the LEWEX experience. For example, pressure transducer immersion could be correlated with relative motion records to draw conclusions about bottom slamming or deck wetness.

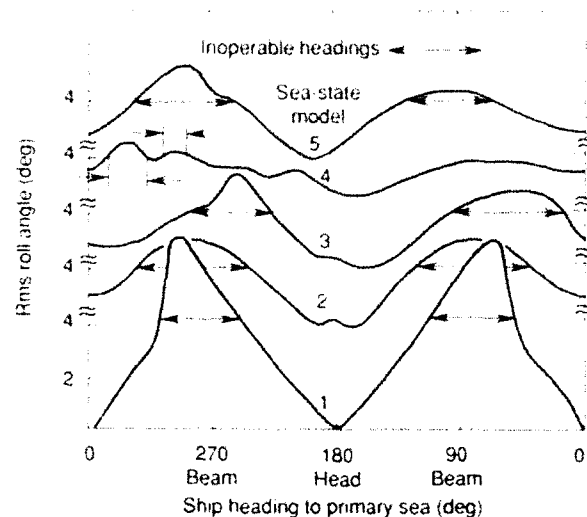


Figure 7. Operability of a 5200-tonne frigate subject to a 4° rms roll limitation on shipboard operations. See the text for the definition of a sea-state model.

Table 3. Operability of a 5200-tonne frigate in 6-m seas

Sea-state model	Inoperable heading range (deg)		Roll range (deg) Best – worst
	4° criterion	3° criterion	
1	88	168	7.0
2	164	258	3.1
3	142	231	3.5
4	43	316	2.0
5	133	254	3.4

What are the broader implications of LEWEX for naval architecture? For the most part, they are related to operability. Naval vessels are now designed with seakeeping in mind, and linear, two-dimensional theory ship-motion-prediction codes frequently are used to rank or evaluate the candidate design's lifetime or the mission's operability in locations of interest. Routinely, unimodal multidirectional seas are used, with 90° as the accepted spreading angle. The example above, together with the *Quest's* own experience, suggests that applying spreading to unimodal spectra is not enough; the common occurrence of multimodal sea states must be recognized. This is a painful conclusion.

When Bales et al.⁸ reported the results of hindcasting for NATO operational areas, they firmly established the use of short-crested sea states, in part, at least, because they reported results in a format convenient for existing frequency-domain seakeeping codes. If multimodal sea states are important to naval architecture, then the hindcasting results must be used more directly. This is considerably more onerous than simply assuming a 90° spreading angle and using a joint probability table for significant wave height and modal period.

Although feasible, simply simulating seakeeping performance and operability using an archived hindcast spectral database cannot be considered practical. To encourage the use of multimodal, multidirectional spectra, it would be better to employ a multiparameter spectrum, together with associated probability distributions for spectral parameters, to generalize an operational area hindcast for frequency-domain seakeeping calculations. Hogben and Cobb⁹ have reported a parametric directional wave spectral model that, in principle, satisfies these goals. Juszko Scientific Services, under contract to DREA, is developing this model further, to address bimodal spectral modeling in Canadian operational areas.

CONCLUSION

The good weather conditions that predominated during LEWEX prevented the achievement of goals dependent on high sea states; however, the LEWEX pressure transducer and strain data were valuable for at least two reasons. First, when compared with relative motion predictions, pressure transducer data gave further evidence of the inability of a unimodal sea-state model to describe the sensitivity of ship response to heading. Second, the bow-flare pressure and strain data provided a rare opportunity to validate the ability of a finite-element code to model stresses in a complex, three-dimensional structure under dynamic loading.

The LEWEX experience confirms that multimodal spectra must be regarded as a common occurrence at sea. As a result, the relatively recent acceptance of multidirectional unimodal spectra for routine seakeeping evaluation in the design process offers insufficient improvement over the unrealistic unidirectional, unimodal sea-state model. Results of two *Quest* seakeeping trials, one in light-to-moderate seas (LEWEX) and an earlier one in heavier seas, demonstrate that unimodal sea-state models, even with spreading, fail to model properly the relationship of ship motions and heading. A simple operability example for a destroyer gives similar results.

The use of unimodal short-crested spectra, although an advance over unidirectional spectra, is insufficient to predict ship operational capability. The multimodal nature of a significant proportion of open-ocean spectra must be recognized and modeled if operational studies are to be realistic. Hindcasts offer a way to define multimodal seas, but the practical implementation of the information depends on the reformulation of hindcasts as multiparameter spectral models, with associated joint probability tables, suitable for use in frequency-domain seakeeping codes.

REFERENCES

- ¹Young, I. R., Rosenthal, W., and Ziemer, E., "A Three Dimensional Analysis of Marine Radar Images for the Determination of Ocean Wave Directionality and Surface Currents," *J. Geophys. Res.* **90**, 1049-1059 (1985).
- ²Nickerson, W., and Clarke, C. A., *Measuring Ocean Wave Spectra from Marine Radar Sea Clutter*, Nordco Limited, Defence Research Establishment Atlantic Contractor Report CR 88-423 (1988).
- ³Clarke, C. A., and Nickerson, W., *Measuring Ocean Wave Spectra from Marine Radar Sea Clutter—Software User's Manual*, Nordco Limited, Defence Research Establishment Atlantic Contractor Report CR 88-424 (1988).
- ⁴Graham, R., and Trudelle, C., *SHIPMO: An Updated User's Manual for the SHIPMO Computer Program Incorporating an Extended Hydrostatics Capability and an Improved Viscous Roll Damping Model*, Defence Research Establishment Atlantic Technical Communication 87-304 (1987).
- ⁵Pegg, N. G., Vernon, T. A., Wegner, L., and Nethercote, W. C. E., "Finite Element Prediction of Measured Bow Flare Plate Stresses under Dynamic Wave Loading," *Trans. R. Inst. Nav. Architects* **131**, 135-143 (1989).
- ⁶Martec Limited, Defence Research Establishment Atlantic, *Vibration and Strength Analysis Program (VAST), Version 04*, Contractor Report 86-429 (1986).
- ⁷MacLaren Plansearch Limited and Oceanweather, Inc., *Development and Evaluation of a Wave Climate Data Base for the East Coast of Canada*, Contract Report for Department of Fisheries and Oceans, Ottawa (1988).
- ⁸Bales, S. I., Lee, W. T., and Voelker, J. M., *Standardized Wave and Wind Environments for NATO Operational Areas*, David Taylor Naval Ship R&D Center SPD-0919-01 (1981).
- ⁹Hogben, N., and Cobb, I. C., "Parametric Modeling of Directional Wave Spectra," in *Proc. Eighteenth Annual Offshore Technology Conf.*, Vol. 1 (1986).

ACKNOWLEDGMENTS: Ross W. Graham provided valuable discussions before and after LEWEX and most recently through his membership in the Canadian East Coast Waves Project Group. Walter Ellis analyzed the *Quest* LEWEX trials results. Bert Hartling of the Bedford Institute of Oceanography was responsible for the design and manufacture of the deep-water wavebuoy moorings. Of course, special attention must be given to the cooperation and support of Captain Bill Whyte, the officers, and crew of the *Quest*, as well as the scientific staff on board during LEWEX.

HNLMS *TYDEMAN*'S LEWEX EXPERIENCE AND MOTION SIMULATION IN MULTIMODAL SEAS

Measurements of motions of HNLMS *Tydemán* were made in a variety of multidirectional sea states during the Labrador Sea Extreme Waves Experiment. Although no extreme seas occurred, the moderate multimodal sea states illustrated that multimodality is important for time-domain predictions of ship motions and is especially useful during the design stage for assessing ultimate stability, that is, safety against capsizing.

INTRODUCTION

The Dutch vessel, Her Netherlands Majesty's Ship (HNLMS) *Tydemán* (Fig. 1), was one of two vessels participating in the Labrador Sea Extreme Waves Experiment (LEWEX). The *Tydemán* carried scientists and equipment from nine agencies within The Netherlands, United States, Federal Republic of Germany, France, United Kingdom, Norway, and Spain. The experiment was intended to support the goals of the North Atlantic Treaty Organization (NATO) Research Study Groups RSG-1 and RSG-2 of the NATO Defence Research Group, containing the Special Group of Experts on Naval Hydrodynamics and Related Problems.

HNLMS *TYDEMAN*

The *Tydemán* was the first ship in the Royal Netherlands Navy to be designed and equipped specifically for oceanographic research. The research can be for military as well as for pure scientific purposes. Civilian scientists may be assured of at least 30% of the seagoing time each year.

The *Tydemán* is well equipped for oceanographic research. Special attention was given to providing good seakeeping and maneuverability qualities, and the ability to make short, silent runs. The *Tydemán* can accommodate fifteen passengers and has ample space for laboratories, meeting areas, and various oceanographic instrumentation, including a working deck area and associated deck gear. Oceanographic and hydrographic data such as time, position, depth, temperature, salinity, wind, and pressure are all routinely and automatically collected. A summary of the *Tydemán*'s characteristics is given in Table 1.

Oceanographic research often requires overside handling of various equipment, either free-floating, towed, or anchored. The aft working deck is used mainly when traveling at normal speeds; the working deck at three-fourths of the ship's length forward is used mainly when drifting or traveling slowly. The *Tydemán* has good seakeeping properties and a passive, free surface tank to reduce roll motions to keep the working decks dry and in good operating condition up to about sea state 7.



Figure 1. The HNLMS *Tydemán*.

Table 1. The main characteristics of the *Tydemán*.

Displacement	2200 tonnes
Length	90.19 m
Molded breadth	14.43 m
Draft (excluding sonar dome)	4.75 m
Draft (including sonar dome)	7.50 m
Installed power	2100 kW
Maximum speed	15 kt

To be easily maneuverable, the *Tydemán* is equipped with a bow thruster and a rudder with its own propeller, allowing rudder angles of up to 90°.

RSG-1 OBJECTIVES

The primary objectives of RSG-1 during LEWEX were to establish reliable methods to measure the directional properties of waves, and especially to improve methods for providing both measured and predicted wave conditions for full-scale sea trials and ship operations. Meeting these objectives is fundamental to validating ship-response predictions, ocean wave models and climatologies, and seakeeping surveys.

The RSG-1 plans for the *Tydeman* and the *Quest* (see the articles by Kjeldsen and by Nethercote in this volume) were as follows:

1. To make simultaneous wave measurements with various *in situ* and remote instruments, some of which are still experimental.
2. To compare data from instruments and wave models for both validation and evaluation.
3. To conduct model tests with the *Quest* (and possibly the *Tydeman*) in scaled LEWEX directional seas in the Marintek facility in Trondheim.
4. To use sea trials and model simulations to evaluate the applicability and usefulness of directional wave data in ship design and operations planning.

INSTRUMENTATION

The instrumentation carried and deployed by the *Tydeman* during LEWEX is summarized in Table 2. For the first phase, the Wavescan buoy was moored in about 4000 m of water during the night of 13 March 1987, to be ready for the aircraft overflights on the following day. The mooring was performed from the aft working deck in 40-kt winds and 5-m seas by using an "anchor last" procedure. The deep-water mooring consisted of several separate sections, each wound on separate winches, so both the mooring and the recovery had to be performed in steps. In the first location (50°N, 45°W), the anchor and 300 m of line had to be abandoned.

Most of the drifting wave buoys were deployed from the forward working deck by using an A-frame or an L-frame. The Delft buoy could easily be dropped by

hand, however, because of its robustness and light weight. The buoys sometimes drifted several miles or more between daily recoveries.

Infrared (IR) and sonic sensors, along with navigation radar techniques (see the article by Ziemer in this volume), are being developed to attempt to reduce the need for wave buoys during sea trials. The IR sensor was mounted on a frame (or "giraffe") far forward on deck and hung over the bow to obtain a clear vertical view of the sea surface, but it was limited by spray and large pitch and roll motions during heavy weather. The IR sensor measured only wave elevation and thus could produce only nondirectional spectra. It did have one advantage over the navigation radar, however, since its data could be processed on board. Unfortunately, structural limitations prevented the sonic sensor from being placed far enough forward on the giraffe to stay clear of the bow. The navigation radar technique required special provisions to trigger a photographic camera that recorded the plan position indicator display.

Ship motions were measured in three ways. First, the Delft hydromechanics laboratory¹ employed a platform, stabilized by a pitch, roll, and yaw gyroscope (to measure both amplitude and rate), on which three accelerometers were placed. Second, an IR sensor, stabilized by a gyroscope, measured the vertical accelerations to compute the sea state; ship motions were therefore part of its measured data. Third, a French measurement system contained three accelerometers at one location, and a transducer case contained a gyroscope, three gyrometers, and three accelerometers at a second location. In addition to these three objective measures of ship motion, a small device called a "comfort meter" was also tested. The "noncomfort index" was defined as the rate at which vertical accelerations exceeded a threshold value. Such a device could be quite useful in motion sickness research.

SHIP PERFORMANCE

Heavy seas and ice during North Atlantic transit caused a delayed arrival of the *Tydeman* in St. John's, Newfoundland, preventing a pre-LEWEX rendezvous with the *Quest*. To recover some of the lost time, the *Tydeman* moored its Wavescan buoy immediately upon arriving at the first LEWEX site (50°N, 45°W). Mooring was accomplished in the middle of the night and, ironically, in the highest seas of the experiment. During the following two days, the significant wave heights were only 3.5 to 4.5 m; the remainder of LEWEX experienced even lower seas. These seas, lower than hoped for, were insufficient to investigate the nonlinear behavior of wave buoys and ship motions. On the other hand, the sea states were more often multimodal than not, and thus served the RSG-1 goals well.

The multimodal seas (composed of both swell and wind seas) made it difficult to select a principal wave direction on which to base the seakeeping experiments. The ship runs were planned to occur in 30° increments, proceeding systematically from head seas to following seas. In preparation, the anti-roll tank was emptied to assure straightforward ship-motion predictions. Com-

Table 2. Instrumentation carried and deployed by the *Tydeman* during LEWEX.

Parameter	System	Location	Country
Sea state	Wavec buoy	Drifting	The Netherlands
Sea state	Delft buoy	Drifting	The Netherlands
	(unidirectional)		
Sea state	Endevco buoy	Drifting	United States
Sea state	Wavescan buoy	Anchored	Norway
Sea state	Infrared sensor	Mounted	Federal Republic of Germany
	(unidirectional)		
Sea state	Navigation radar	On board	Federal Republic of Germany
Sea state	Wadirex buoy	Drifting	France
Sea state	Datawell wave-rider buoy	Drifting	France
Ship motions	Stabilized platform	On board	The Netherlands
Ship motions	Infrared sensor	Mounted	Federal Republic of Germany
Ship motions	Transducer case	On board	France
Ship motions	Comfort meter	On board	The Netherlands
Sea loads	Strain gauge	On board	United Kingdom
Oceanographic data	Oceanlog system	<i>Tydeman</i>	The Netherlands
Buoy location	Radio direction finder	On board	The Netherlands

puter simulations were performed for several multimodal sea conditions experienced during LEWEX, two of which will be summarized here.

As stated earlier, a three-dimensional description of the wave field is required for operational applications such as ship routing and task optimization. The Royal Netherlands Navy considers such a description useful, even during the vessel design stage. Predicted ship motions in multimodal seas can strongly influence the choice of ship design criteria. Extreme roll motion, including capsizing, is an important operational consideration.

Our plans for the future therefore include the following: (1) establishing a standard procedure to treat ship motions, including the nonlinear effects induced by multimodal high seas; (2) checking the reliability of the computed motions by comparing simulated motions with full-scale motions in multimodal high seas; (3) comparing full-scale results for unimodal and multimodal spectral representations, both having identical total energy; and (4) comparing calculated motion results for various ship designs and ship operations over a variety of sea states. These efforts will result in better ship design criteria to improve safety in high seas, and the design criteria will be extended to a set of operational rules for ships operating in extreme sea states.

Some results of a time-domain calculation are presented in the next section and are compared with the full-scale data measured during LEWEX. Ship motions, calculated with and without accounting for multimodality, are also presented.

MOTION SIMULATION

Motions of the *Tydeman* have been simulated by using computer programs developed for the Royal Netherlands Navy by the Marine Research Institute of The Netherlands.² The time-domain simulation sums all the relevant forces at each time step to solve the six equations of motion. The relevant forces include inertial effects, hull damping forces, weight and buoyancy forces, propeller and rudder forces, and wind and wave forces. In the LEWEX runs, however, only the roll, pitch, and heave motions were calculated; the wind forces were neglected, and the rudder was fixed in the zero-angle position. Pierson-Moskowitz³ spectral forms were used to model both unimodal and bimodal representations of the LEWEX wave conditions. Multimodal seas were modeled by a unimodal representation by integrating the spectral density over all wave directions and fitting the data to a Pierson-Moskowitz spectrum. A bimodal wave spectrum was modeled by identifying the two principal wave directions and by assuming that the sum of the energy from each system was equal to the total measured energy. The same assumption was also made for the energy moment, that is, the product of energy and wave direction.

RESULTS

Table 3 shows principal wave characteristics for both 14 March and 23 March; calculated bimodal values are given for significant wave height, average period, and peak period, with relative wave directions of each of the

Table 3. Summary of wave specifications at the *Tydeman* for two separate runs

Parameter	14 March Run No. 8		23 March Run No. 102	
	Unimodal model	Bimodal model	Unimodal model	Bimodal model
Significant wave height (m)	3.70	2.47	3.33	2.25
Average period (s)	9.2	9.4	7.6	8.1
Peak period (s)		8.9		6.6
Peak period (s)	11.4	11.6	9.4	10.0
Relative wave direction (deg)	0	30	0	34
		-80		-41

modes.⁴ Figure 2 compares both the unimodal and bimodal predictions for the same days with actual roll, pitch, and heave measurements at various ship headings.

On 14 March (solid curves in Fig. 2), measured roll amplitudes, most important when considering capsizing, show good agreement with the bimodal simulation, although simulated roll motions for the mean (unimodal) wave approximation are too low in head seas and too high in beam seas. Simulated pitch motions are, for some unknown reason, substantially underestimated. The simulated roll motions using a bimodal sea are more realistic than those using a unimodal, long-crested, irregular sea. The unimodal wave results are reasonably good, however, and for some types of motion are even better than the bimodal results, because those types of motion are less sensitive to changes of heading and modal characteristics.

The results of 23 March (dashed curves in Fig. 2) were collected during higher-speed runs between 11.3 and 12.6 kt in seas having a 3.3-m significant wave height. Contrary to the bimodal roll-motion simulations of 14 March, which compare rather well with the measured results, the roll comparisons of 23 March are not as favorable in either absolute values or trends. Pitch simulations again compare poorly with measurements, but bimodal heave simulations compare well at all headings. This apparent lack of success in the model simulations has several possible explanations:

1. Oversimplified multidirectional modeling: Roll is particularly sensitive to the frequency of encounter of the forcing sea state, and apparently minor changes in a simplified spectral model may have a significant effect on roll predictions. Figure 2 shows that spectral variations at nominally the same significant wave height may lead to order-of-magnitude changes in roll, whereas heave changes by 40% at most.

2. Irregularity of the seaway: Directional spectra give substantial information about a seaway. Nevertheless, although the spectra may be identical, the actual 30-min wave train experienced by a ship is not the same as that used in the motion simulation. Several simulations are required to reach a statistically significant result. Table

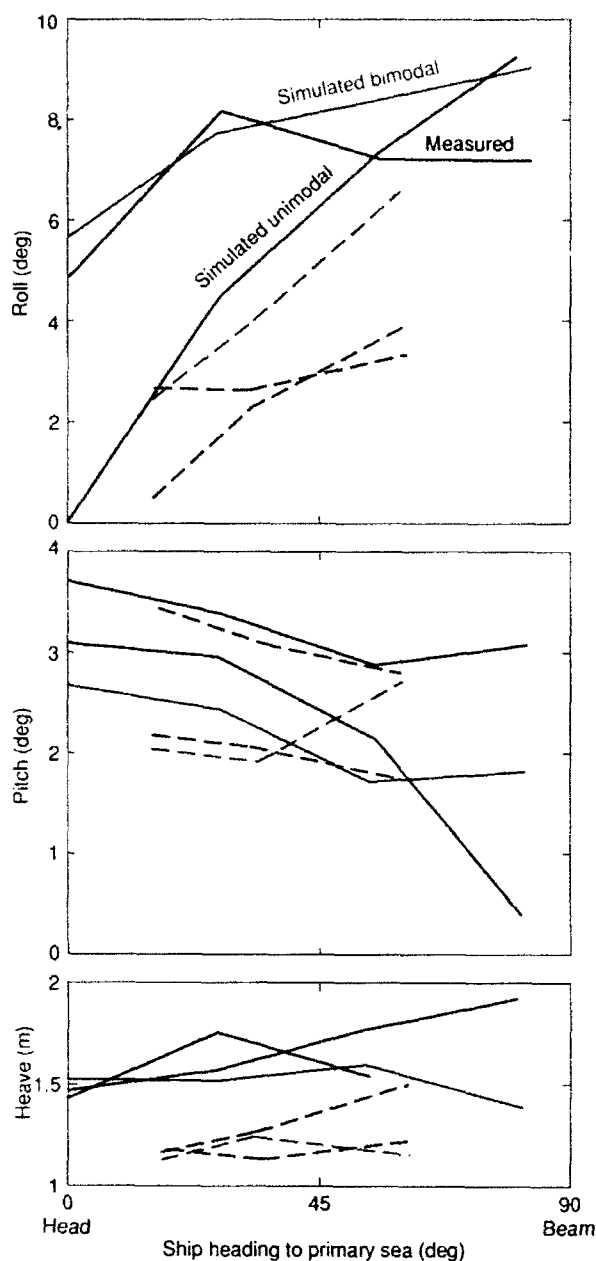


Figure 2. Comparisons of measured (black curves) and simulated significant ship motions. The red curves are the bimodal simulations, and the blue curves are the unimodal simulations. The solid curves are for 14 March, significant wave height = 3.7 m, and the dashed curves are for 23 March, significant wave height = 3.3 m.

4 shows the variation obtained from a sequence of five 30-min simulations, each driven with an identical spectrum. The results indicate the ranges of ship-motion uncertainty expected for a single simulation run.

3. Accuracy of full-scale measurements: The results of the full-scale observations are determined by the accuracy of the measuring devices and the errors in the analytical techniques. Comparisons of simultaneous measurements made with different sensors illustrate the problem. For example, simultaneous measurements of

Table 4. Variability in modeled ship motions resulting from five 30-min simulation runs.

	Run number				
	1	2	3	4	5
Wave height (m)					
Maximum	-2.94	3.05	3.00	3.20	-3.18
Heave (m)					
Maximum	-2.58	-2.45	-2.49	-2.57	-2.63
σ_H	0.76	0.76	0.75	0.75	0.76
Roll (deg)					
Maximum	12.7	13.3	13.0	12.4	13.3
σ_R	3.89	3.84	3.92	3.94	3.89
Pitch (deg)					
Maximum	-3.81	3.47	3.79	-4.02	-3.93
σ_P	1.24	1.23	1.24	1.24	1.25

Note: The ship speed was 2 kt, and the heading was 30° off the "head seas" for the LEWEX wave system of 14 March, Run No. 8, as defined in Table 3. All runs are for a significant wave height of 3.7 m; σ is the standard deviation in heave, roll, or pitch.

significant roll from two separate measurement systems sometimes disagreed by nearly a factor of 2.^{1,5}

4. Ship loading and control: Ship load condition, as well as its control, could have varied during the trial, although neither was found to influence the results when load condition and autopilot settings were varied during the simulations.

ULTIMATE STABILITY

The extreme roll behavior of a ship in complex seas is of great interest to both ship designers and operators. Methods now used to evaluate a ship's margin of safety against capsizing are based mainly on experience and do not give much physical insight into the relation between ultimate stability and ship design or operational performance. The time-domain simulation program, using multimodal sea states, revealed several concerns that involve ultimate ship stability. The differences between the bidirectional and the unidirectional simulations are too great to be neglected. Knowledge of the multimodal behavior of the sea is necessary to evaluate accurately the ultimate stability of a ship.

Additionally, to account for wave groups, freak waves, and similar inhomogeneous wave phenomena, the ship-motion simulation can and should deal with the real three-dimensional sea surface description, not simply the spectrum. The actual time history of the waves should be used as an input for motion-simulation programs and for defining the relevant parameters in ship design and operation.

In a multimodal sea, a straightforward simulation shows that a safe ship heading to prevent capsizing is not easy to find. Given the existence of extreme waves and the presence of multimodal seas, more detailed knowledge is required as to where and when these waves and seas occur so that they can be avoided. Multimodal spectra can then be used as an indication of ship safety.

CONCLUSION

The LEWEX seakeeping trials with the *Tydeman* indicate that a unimodal model of the seaway is inadequate for ship design and evaluation, whereas a multimodal description is both feasible and necessary. For ultimate stability assessment, it may even be necessary to specify wave-elevation time series.

With better sea-state models, numerical ship-motion programs offer the promise of realistic ship-performance predictions, but the predictions will need to be validated in higher sea states than those obtained in LEWEX. The simulation code used herein requires further development to reconcile pitch-prediction anomalies.

REFERENCES

- ¹Ooms, L., *Wave and Ship Motion Measurements aboard the Tydeman during LEWEX*, Delft University of Technology, Ship Hydrodynamics, Report No. 761 (1987).
- ²Hooft, J., "Computer Simulations of the Behavior of Maritime Structures," *Mar. Technol.* **23**, 139-157 (Apr. 1986).
- ³Pierson, W. J., Jr., and Moskowitz, L., "A Proposed Spectral Form for Fully Developed Windseas Based on the Similarity Theory of S. A. Kitaigorodskii," *J. Geophys. Res.* **69**, 5181-5196 (1964).
- ⁴Hooft, J., *Comparison between Simulations and Full Scale Measurements with the Tydeman*, Report No. 49642-1-RD ordered by the Royal Netherlands Navy (May 1989).
- ⁵Boubert, S., *Moyens de Mesures en Mer—Etude No. 2401, Piece No. 4, Essais LEWEX, Depouillement de la bouée BADIREA*, Report No. 8-5133, Bassin d'Essais des carènes, Paris, France.

RELIABILITY AND RESOLUTION OF DIRECTIONAL WAVE SPECTRA FROM HEAVE, PITCH, AND ROLL DATA BUOYS

Heave, pitch, and roll buoys have become common and reliable instruments for long-term unattended acquisition of directional ocean wave data. Directional wave spectra obtained from such buoys show high consistency, both among themselves and also compared with fixed-platform instrumentation. Some fundamental limitations of the spectral estimates obtained from these buoys are reviewed, emphasizing their resolution and sampling variability.

DATA ANALYSIS TECHNIQUES

The ocean surface is considered to be a homogeneous and stationary stochastic field, with a spectrum that is a function of frequency, ω , and vector wave number, k .¹ We may analyze buoy data without further assumption about the waves,² but we generally assume that the field also obeys the so-called linear wave theory, wherein a dispersion relation connects ω and k .¹ This assumption implies that the spectrum may be written in terms of ω and the direction θ of k , or $S(\omega) D(\theta, \omega)$. Here, S is the frequency spectrum and D is the directional distribution, often expanded in a Fourier series

$$D(\theta, \omega) = \frac{1}{2\pi} \left\{ 1 + 2 \sum_{n=1}^{\infty} [a_n(\omega) \cos(n\theta) + b_n(\omega) \sin(n\theta)] \right\}, \quad (1)$$

where a_n and b_n are the corresponding Fourier coefficients.

In principle, the buoy should record the surface heave and the two slopes at a fixed horizontal location. In practice, however, the buoy will make excursions from that position because of the orbital-wave-induced velocity at the surface. This condition could significantly affect the results, but on the average the first-order effects of the horizontal motion vanish. (Numerous studies have been devoted to the estimation of directional spectra from buoy data; the references given here are far from exhaustive.)

Common practice is to record a 1- to 2-Hz time series comprising 1000 to 4000 data points.² Such time series are long compared with the characteristic correlation time of the record, and the series are "well recorded," that is, the subsequent spectral analysis is simple, and no major problems exist with respect to aliasing or spectral leakage.

Estimating the cross spectra of the time series is the first step in most analytical methods. After forming the cross spectra, corrections for various filters that affect the records must be carried out. Errors may be caused

by transfer functions of buoy response, phase shifts in anti-aliasing filters, or imperfections in the integration of the accelerometer signal. Some very useful checks on the phases of the cross spectra may be applied. For any stationary and homogeneous surface, the cross spectrum between the heave and the slope in, for example, the x direction at the same location will be purely imaginary (Im), and the cross spectrum between two orthogonal slopes will be real (Re).² Any systematic deviations in the final spectra suggest transfer function errors. A related test is to compare the estimated root-mean-square wave number with the wave number obtained from the wave dispersion relation. This test is more questionable, since currents and deviations from linear wave theory also affect the estimated wave number.²

The frequency spectrum, the wave number, and the first two pairs of Fourier coefficients for the directional distribution may now be estimated from the cross spectra. When a linear wave theory with no given dispersion relation is assumed, the cross-spectral matrix between the heave and two orthogonal slopes at a certain frequency will be

$$\Phi = S \begin{bmatrix} 1 & -ika_1 & -ikb_1 \\ ika_1 & k^2(1 + a_2)/2 & k^2b_2/2 \\ ikb_1 & k^2b_2/2 & k^2(1 - a_2)/2 \end{bmatrix}. \quad (2)$$

(Here, $k = |k|$, and the dependence of ω is suppressed.)

The discrete Fourier transforms of the heave and the slope time series will asymptotically be complex, multivariate Gaussian variables with a covariance matrix given by Equation 2. By forming the joint probability density for the Fourier coefficients and solving the corresponding maximum likelihood (ML) estimation problem for the parameters in Equation 2, we see that the solution agrees with the expressions stated by Long:¹

$$S = S_{hh} \\ k = [(S_{xx} + S_{yy})/S]$$

$$\begin{aligned}
a_1 &= \text{Im} (S_{hx})/(kS) \\
b_1 &= \text{Im} (S_{hy})/(kS) \\
a_2 &= (S_{vx} - S_{vy})/(k^2S) \\
b_2 &= 2\text{Re} (S_{vy})/(k^2S) ,
\end{aligned} \quad (3)$$

where S_{hx} denotes the cross spectrum between elevation and slope in the x direction, and so on. When a dispersion relation is used in Equation 2, the ML estimation problem does not have such a simple solution.

The Fourier coefficients in Equation 3 are always meaningful, since there exist positive distributions D having exactly those Fourier coefficients. This observation follows from the ML property and may also be proved directly.

The ML estimates are relatively insensitive to errors in the buoy transfer functions as long as those functions are the same for both the roll and the pitch motion. Except for mooring effects, this will typically be true for circular buoys.

For engineering applications, the most useful directional parameters are the mean direction θ_1 and the directional spread σ_1 , which are defined from the first pair of Fourier coefficients:³

$$\begin{aligned}
\theta_1(\omega) &= \arctan 2[b_1(\omega), a_1(\omega)] , \\
\sigma_1(\omega) &= \{2[1 - r_1(\omega)]\}^{1/2}; \quad r_1^2(\omega) = a_1^2(\omega) + b_1^2(\omega) .
\end{aligned} \quad (4)$$

Kuik et al.⁴ have proposed additional parameters reflecting the skewness and kurtosis of the directional distribution, but their interpretation for general distributions is difficult.

The construction of a full directional distribution from only four Fourier coefficients represents an inverse problem. Using just the truncated Fourier series leads to non-positive distributions, which may be avoided by introducing convergence factors at the expense of directional smearing.⁵ Fitting certain model distributions, for example, $D(\theta) = N(s)\cos^{2s}(\theta/2)$, where $N(s)$ is a normalization factor, has also been popular. Goodness-of-fit tests based on the remaining Fourier coefficients are discussed in Ref. 3.

A simple construction of a directional distribution, in agreement with all four Fourier coefficients, is given in Lygre and Krogstad:⁶

$$\begin{aligned}
D(\theta) &= \frac{1}{2\pi} (1 - \phi_1 c_1^* - \phi_2 c_2^*) \\
&\quad \div |1 - \phi_1 e^{-i\theta} - \phi_2 e^{-2i\theta}|^2 \\
\phi_1 &= (c_1 - c_2 c_1^*)/(1 - |c_1|^2) \\
\phi_2 &= c_2 - c_1 \phi_1 \\
c_1 &= a_1 + ib_1 \\
c_2 &= a_2 + ib_2 ,
\end{aligned} \quad (5)$$

where $*$ denotes the complex conjugate.

This estimate, called the maximum entropy (ME) estimate, is similar to the expression for the spectrum of a complex, autoregressive, stochastic process and follows by maximizing an entropy integral while keeping the given Fourier coefficients fixed. (In contrast, the Longuet-Higgins expression for D using convergence factors⁵ corresponds to a Blackman-Tukey spectral estimate.) The ME distribution represents the "most probable" distribution consistent with the given Fourier coefficients when no further information is available.⁶ When the first pairs of Fourier coefficients of some positive function are given, the next pair must be chosen from a certain disk in the complex plane to conform with the requirement of positivity. The ME distribution corresponds to choosing the center of this disk. This choice also maximizes the diameter of the next disk in the sequence and thus poses the minimal constraints on the continuation of the process.⁶

The ME estimate does not consider any *a priori* information about the shape of the distribution. In fact, the estimate is the function closest to the uniform directional distribution that is consistent with the data in terms of a certain entropy metric. Wave directions are sometimes limited to certain directional sectors, however. Long and Hasselmann⁷ present a variational technique wherein such constraints may be considered.

When applied to certain unimodal distributions like the \cos^{2s} distribution or the boxcar distribution, the ME estimate will show two peaks, a result that is not necessarily a weakness of the estimate. If it is known that the distribution has a certain form, then additional information is available, and the estimate is no longer optimal.

A method that was first derived for general arrays of wave recorders is the maximum likelihood method of Capon.^{8,9} The method is based on a maximum likelihood estimate for the amplitude of a plane wave recorded in a background of noise. This technique has also been applied to heave, pitch, and roll data and generally produces more smeared directional estimates than the ME estimate. Contrary to the ME estimate, the Capon maximum likelihood estimate is not consistent with the Fourier coefficients. An iterative version of Capon's method improves the estimate,¹⁰ but the iteration does not converge to the ME estimate.

An ME estimate based on a different definition of entropy is discussed by Konube and Hashimoto.¹¹ Marsden and Juszko¹² discuss the use of an eigenvector expansion technique, and Hashimoto et al.¹³ have introduced a Bayesian technique into the analysis of the data. A detailed intercomparison among these recent estimation techniques does not appear to have been carried out.

RESOLUTION AND RELIABILITY

Since a buoy provides only four Fourier coefficients, one could ask how closely these coefficients define the directional distribution. The mean direction and the directional spread are, of course, defined in terms of the first pair of Fourier coefficients. Construction of positive functions conforming to a given set of Fourier

coefficients is a bit tricky. By using the extension procedure briefly mentioned in the discussion of the ME estimate, however, examples of functions with the same first four Fourier coefficients can be generated, as shown in Figure 1. The ME extension computed from Equation 5 is represented by the blue curves. From the graphs, one can see that considerable variability is still possible. Some of the distributions look doubtful, however, at least for the open ocean.

Resolution is usually defined in terms of the ability to resolve narrow double peaks in the distribution. The ME estimate will, in the absence of sampling variability, resolve two delta-function spikes, regardless of their separation, unless the peaks have finite width. The ME estimate defined from Equation 5, however, will only be able to reproduce two peaks at the same frequency.

Nevertheless, comparisons of buoy spectral estimates with those of spatial arrays show that the buoy or equivalent instrumentation can extract most of the relevant directional information.¹⁴

The sampling variability inherent in all spectral estimates is another source of uncertainty. Since the recorded time series are long, the asymptotic relations for the sampling variability of the cross spectra are reasonably valid. The basic sampling variability theory for the most common directional parameters derived from heave, pitch, and roll data has been derived by Long.³

The sampling variability for θ_1 and σ_1 for a \cos^{2s} distribution is shown in Figure 2. The variability is proportional to the square root of the inverse number of degrees of freedom (DOF) in the cross-spectral estimates. No single number quantifies how accurately the buoy can determine, for example, the mean direction. A simple rule

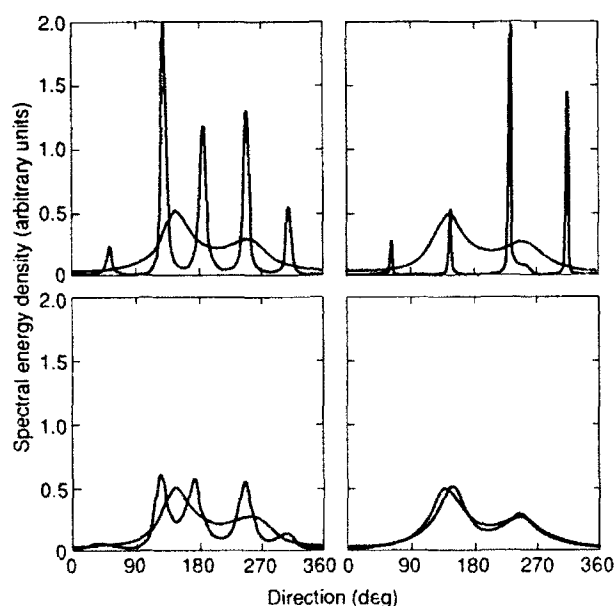


Figure 1. Examples of directional distributions having the same first four Fourier coefficients (black curves). The blue curve is the maximum entropy distribution based on the same Fourier coefficients.

is that narrow, well-defined peaks lead to narrow confidence intervals.

Examples of ME distributions computed from simulated cross spectra with 50 and 200 DOF are shown in Figure 3. The input is the ME distribution from Figure 1. A simple expression exists for the variability of $D(\theta, \omega)$ that depends linearly on the cross-spectral matrix, that is, $D(\theta, \omega) = \gamma(\theta)^H \Phi(\omega) \gamma(\theta)$, where γ is independent of Φ . Here, $\text{Var}[D(\theta, \omega)] = 2[ED(\theta, \omega)]^2/\nu$, where ν is the DOF in the estimate of Φ , H is the Hermitian transpose, and E is the expectation operator. The ME estimate is not of this form, and simple expressions for the sampling variability seem hard to obtain.¹⁵ The sampling variability for the ME estimate of a uniform distribution is 3 times the value for the linear estimate; numerical tests with general distributions typically show a variability of 3 to 10 times that value.

For comparisons with remote sensors, the directional spectra obtained from the buoys must be converted to

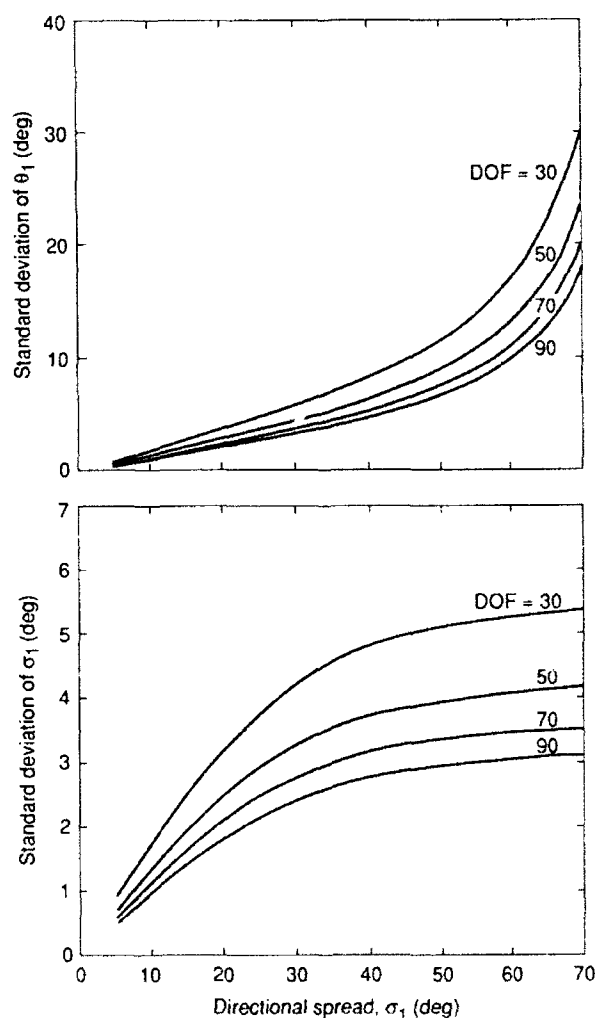


Figure 2. Sampling variability for the mean direction (θ_1) (top) and directional spread (σ_1) (bottom) for a \cos^{2s} distribution as a function of the directional spread, parameterized in terms of the degrees of freedom (DOF) in the spectral estimates.

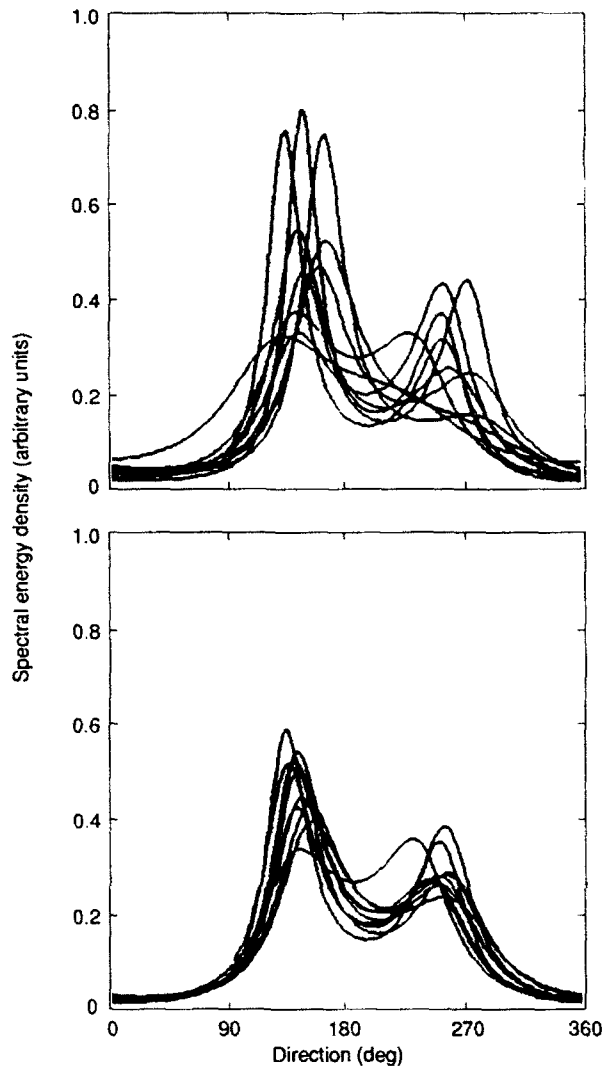


Figure 3. Maximum entropy distributions computed from simulated cross spectra with 50 (top) and 200 (bottom) degrees of freedom. The input directional distribution in Figure 3 is the maximum entropy distribution (blue curve) in Figure 1.

wave number spectra. Within linear wave theory, the transformation is

$$\Psi(k, \theta) = S[\omega(k)] D[\theta, \omega(k)] \frac{\partial \omega}{\partial k} \quad (6)$$

For simplicity, the analytical dispersion relation is used in Equation 6, although the estimated wave number would probably be more consistent. Experience shows, however, that the linear theory is good for the most energetic parts of the spectrum.

Both S and D suffer from a correlated sampling variability. Therefore, usable analytical expressions for the sampling variability of the resulting wave number spectra are difficult to find. Figure 4 shows examples of simulated wave number spectra, illustrating the typical sampling variability for a fairly complex sea state from LEWEX (Labrador Sea Extreme Waves Experiment). The LEW-

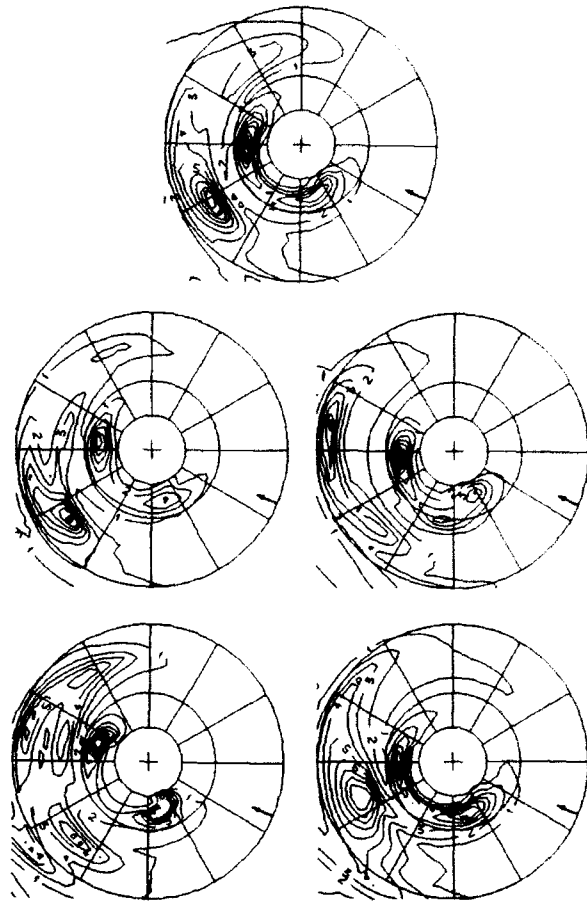


Figure 4. Four illustrations (bottom) of the sampling variability in estimates of the wave number spectrum using a "true" input wave number spectrum (top) from LEWEX. The random simulations were obtained from cross spectra of about 60 degrees of freedom. Energy density contours are proportional to m^4 , and circles correspond to 400, 200, and 100 m.

EX spectrum is assumed to be the "true" spectrum. The four simulated spectra in Figure 4 represent possible estimates using data from a heave, pitch, and roll buoy. The data were processed with about 60 DOF in the cross spectra. A simpler, more well-defined sea state would have shown much less variability (cf. Fig. 2).

COMPARISONS FROM THE WAVE DIRECTION CALIBRATION PROJECT

The objective of the Wave Direction Calibration (WADIC) Project was to evaluate operational, commercially available, directional systems of wave measurement under severe open ocean wave conditions.¹⁶ The field experiment took place over a four-month period during the winter of 1985-86 near the Edda platform on the Ekofisk field in the central North Sea. The instrumentation on the platform included eight rapid-response vector current meters, together with pressure transducers mounted on a specially built tower attached to the northwest corner of the platform. A pentagon array (diameter, 7 m) of infrared laser altimeters recorded the surface height to

the side of the instrument tower. Seven directional buoys were moored within 1 km of the platform.

All systems in the experiment were compared with a common reference data set compiled from the fixed-platform instrumentation. Low-frequency reference directional spectra were obtained from current meter/pressure-cell triplets; the laser pentagon was used for high frequencies. The reference data set comprised 920 records sampled every three hours (hourly during storms).

A series of intercomparisons between the reference data set and the heave, pitch, and roll data from the Norwegian Wavescan buoy is shown in Figure 5. The significant wave height and the peak spectral period were obtained from the frequency spectrum; the mean direction and the directional spread were obtained from the first pair of Fourier coefficients. The broken lines shown

on the graphs are crude, 90% probability intervals. The mean direction shows an average offset of about 6 degrees, which later was attributed to a faulty compass setting. The slight directionally dependent deviations were actually caused by interference from the instrument tower and represent a deficiency of the reference data set rather than of the buoy.

All instruments measuring from the surface, including the laser array, showed generally higher directional spread than the current meter/pressure-cell triplets, perhaps because of imperfect transfer functions for the buoys. The buoys showed comparable results to the laser array for directional spread. In general, the deviations between most systems in WADIC were found to be minor. (Refer to Ref. 16 for a more extensive discussion of WADIC.)

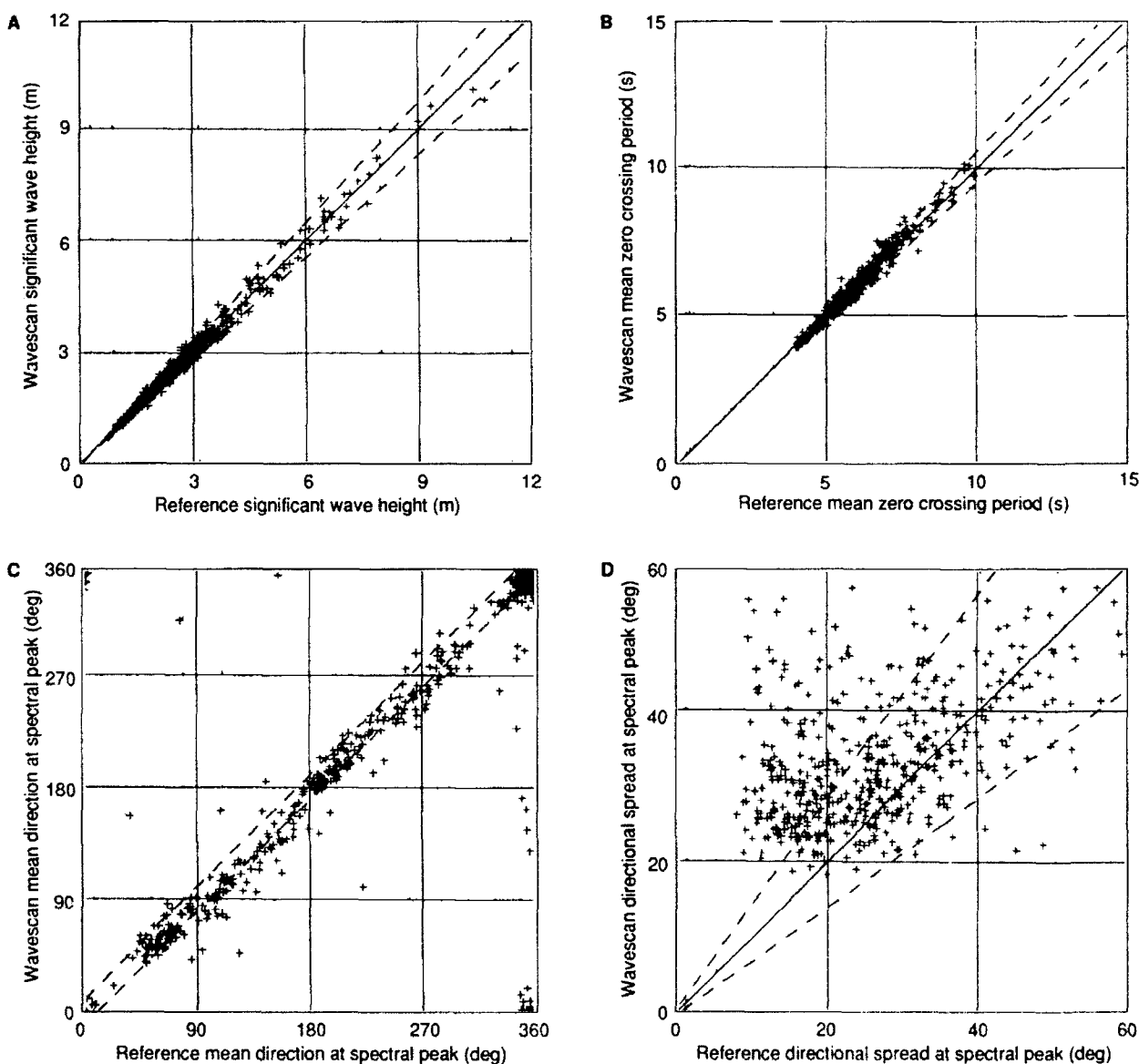


Figure 5. Intercomparison between the Wavescan heave/pitch/roll data buoy and the WADIC reference data set. **A.** Significant wave height. **B.** Mean zero crossing period. **C.** Mean direction at the spectral peak. **D.** Directional spread at the spectral peak.

CONCLUSION

An analysis of directional wave data is more complicated than a conventional, nondirectional spectral analysis. The full directional spectrum with arbitrarily high directional resolution is not available with any current technique.

The heave, pitch, and roll buoys are, however, simple and robust systems for long-term open-ocean measurements. Although limited to four Fourier coefficients, the analysis appears to extract most of the relevant directional information about the waves, since the mean direction and the directional spread are based only on the first pair of Fourier coefficients. The standard ME estimates of the Fourier coefficients and the ME directional estimate, therefore, offer simple and routine analytical methods for the heave, pitch, and roll data.

The sampling variability of computed wave number spectra is considerable. Detailed intercomparisons between spectra should therefore be based on systematic trends seen in consecutive spectra rather than on single events.

REFERENCES

- ¹ Phillips, O. M., *The Dynamics of the Upper Ocean*, 2nd Ed., Cambridge University Press, N.Y. (1977).
- ² Barstow, S. F., and Krogstad, H. E., "General Analysis of Directional Ocean Wave Data from Heave/Pitch/Roll Buoys," *Model Identif. Control* **5**, 47-70 (1984).
- ³ Long, R. B., "The Statistical Evaluation of Directional Estimates Derived from Pitch/Roll Buoy Data," *J. Phys. Oceanogr.* **9**, 373-381 (1980).
- ⁴ Kuik, A. J., van Vleet, G. Ph., and Holthuisen, J. H., "A Method for the Routine Analysis of Pitch and Roll Buoy Wave Data," *J. Phys. Oceanogr.* **18**, 1020-1034 (1988).
- ⁵ Longuet-Higgins, M. S., Cartwright, D. E., and Smith, S. D., "Observations of the Directional Spectrum of Sea Waves Using the Motion of a Floating Buoy," in *Ocean Wave Spectra*, Prentice Hall, Englewood Cliffs, N.J., pp. 111-136 (1963).
- ⁶ Lygre, A., and Krogstad, H. E., "Maximum Entropy Estimation of the Directional Distribution in Ocean Wave Spectra," *J. Phys. Oceanogr.* **16**, 2052-2060 (1986).
- ⁷ Long, R. B., and Hasselmann, K. E., "A Variational Technique for Extracting Directional Spectra from Multi-Component Wave Data," *J. Phys. Oceanogr.* **9**, 373-381 (1979).
- ⁸ Capon, J., "Maximum-Likelihood Spectral Estimation," in *Non-Linear Methods in Spectral Analysis*, Hekkin, S., ed., Springer, Berlin, pp. 155-179 (1979).
- ⁹ Isobe, M., Kondo, K., and Horikawa, K., "Extension of the MEM for Estimating Directional Wave Spectra," in *Proc. Symposium on Description and Modelling of Directional Seas*, Paper No. A6, Lyngby, Denmark (1984).
- ¹⁰ Olman Shay, J., and Guza, R. T., "A Data-Adaptive Ocean Wave Directional Spectrum for Pitch/Roll Type Measurements," *J. Phys. Oceanogr.* **14**, 1800-1810 (1984).
- ¹¹ Konube, K., and Hashimoto, N., "Estimation of Directional Spectra from the Maximum Entropy Principle," in *Proc. 5th International Offshore Mechanics and Arctic Engineering (OMAE) Symposium*, Tokyo, pp. 80-85 (1986).
- ¹² Marsden, R. E., and Jusko, B. A., "An Eigenvector Method for the Calculation of Directional Spectra from Heave, Pitch and Roll Buoy Data," *J. Phys. Oceanogr.* **17**, 2157-2167 (1987).
- ¹³ Hashimoto, N., Konube, K., and Kameyama, Y., "Estimation of Directional Spectra Using the Bayesian Approach, and Its Application to Field Data Analysis," *Rep. Port Harbour Res. Inst.* **26**, 56-100 (1987).
- ¹⁴ Krogstad, H. E., Gordon, R. L., and Miller, M. C., "High Resolution Directional Wave Spectra from Horizontally Mounted Acoustic Doppler Current Meters," *J. Atmos. Ocean. Technol.* **5**, 340-352 (1988).
- ¹⁵ Baggeer, A. B., "Confidence Intervals for Regression (MEM) Spectral Estimates," *IEEE Trans. Info. Theory* **22**, 534-545 (1976).
- ¹⁶ Allender, J., Audunson, T., Barstow, S. F., Bjerken, S., Krogstad, H. E., et al., "The WADIC Project, a Comprehensive Field Evaluation of Directional Wave Instrumentation," *Ocean Eng.* **16**, 505-536 (1989).

DIRECTIONAL SPECTRA FROM THE MOORED DATAWELL WAVEC BUOY DURING LEWEX

A Datawell Wavec directional buoy was moored near the CEAV *Quest* during the Labrador Sea Extreme Waves Experiment (LEWEX) from 14 to 20 March 1987 at 49.98°N, 47.63°W in about 2700 m of water. The buoy was one of eleven different remote and *in situ* sensors used to measure directional properties of the surface wave field. The various LEWEX wave systems were measured by the Wavec buoy and estimated by using the maximum entropy method.

THE DATA ANALYSIS PROCEDURE

The sensors of the Wavec buoy are housed inside a canister about 1 m in diameter by about 1 m high (see Fig. 1). Surrounding the canister is a flotation collar that increases the diameter to about 2.5 m; an anti-capsize hat above the canister increases its overall height, when deployed, to about 2.5 m.

The Wavec buoy uses an accelerometer to measure the vertical acceleration of the buoy as it floats at the surface. Observations are converted to vertical heaves and tilts along the magnetic north-south and east-west directions as measured by internal compasses, which are corrected to true north. Samples are taken every 0.78125 s until 2560 are collected in about 34 min. Calibration information¹ indicates that the Wavec buoys measure heave to $\pm 2\%$, pitch and roll to $\pm 1^\circ$, and direction to $\pm 2.5^\circ$.

Data recording was continuous from 2345 UT on 14 March until 1900 UT on 20 March. Except for three interruptions from on-board recorder failures (0735 UT to 1600 UT on 17 March, 1925 UT on 18 March to 0300 UT on 19 March, and 0515 UT to 1200 UT on 20 March), full directional spectra were recorded every 35 min for nearly five days.

To produce a single spectral estimate, the data are first divided into ten blocks of 256 points each. The three channel records are examined for both data gaps and noise spikes. These edited regions are filled by linear interpolation if less than eight consecutive missing or bad values are found; if more than eight are found, the entire block is rejected. A Fourier analysis is then conducted on each block. Amplitude and phase corrections are made on the basis of the known response characteristics of the instrument. Cospectral and quadrature estimates from each block are then averaged in each of 128 frequency bands over the ten (or fewer) blocks of the complete data collection record. The 256 points in each block permit a frequency resolution of 0.005 Hz in each band. Spectral estimates from adjacent bands are then averaged to produce 64 bands, each with a resolution of 0.01 Hz. Values at frequencies lower than 0.033 Hz (wave period, 30 s; wavelength, 1350 m) and greater than 0.5 Hz (wave period, 2 s; wavelength, 6 m) are discarded.

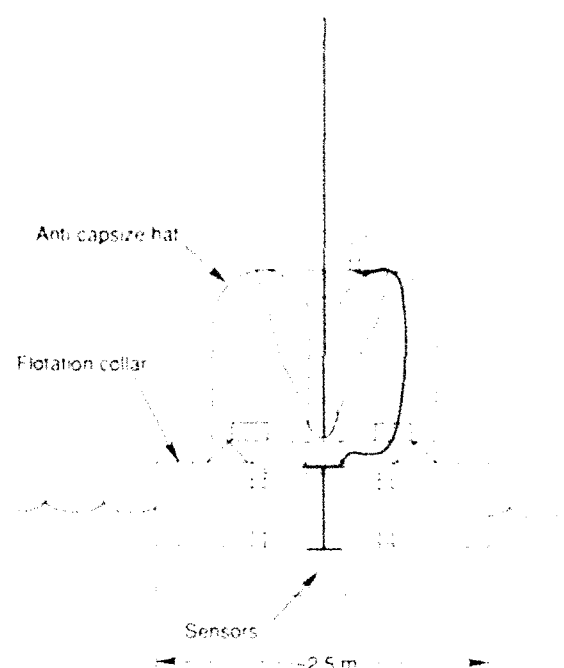


Figure 1. A vertical cross sectional diagram of the Wavec buoy, showing the instrument canister, flotation collars, and hat.

The calculation of the directional spectrum is accomplished in one of two standard ways. The first uses the technique described by Longuet-Higgins et al.² This technique can resolve only a single peak in each frequency band of the spectrum. The first five Fourier coefficients (corresponding to the mean, the fundamental mode, and its first harmonic) are derived from the cospectral and quadrature estimates as follows:

$$A_0 = C_{00} / \pi \quad A_1 = Q_{01} / \pi k \quad A_2 = (C_{02} - C_{20}) / \pi k^2$$

$$B_1 = Q_{01} / \pi k \quad B_2 = 2C_{02} / \pi k^2$$

where

C is a cospectral estimate,

Q is a quadrature estimate,

the double subscripts represent heave (1), north-south slope (2), and east-west slope (3),

k (wave number) = $\sqrt{(C_{22} + C_{33})/C_{11}}$,

A is the coefficient of the cosine portion, and

B is the coefficient of the sine portion.

All higher harmonics (not obtainable from the buoy) must be small for the partial (five-term) Fourier sum to be non-negative. Thus, a weighting function is applied that has the adverse effect of creating a spectrum heavily smoothed in direction, but that leaves it unaltered in frequency resolution.

The second standard technique used to calculate the directional spectrum is the maximum likelihood method (MLM) described by Oltman-Shay and Guza.³ The MLM has several advantages over the Longuet-Higgins technique. The primary advantage of the analysis to the Labrador Sea Extreme Waves Experiment (LEWEX) is its ability to resolve multiple spectral peaks within the same frequency band. The MLM directional resolution is therefore much improved over the Longuet-Higgins technique; the frequency resolution, however, is identical.

Several other techniques to estimate directional spectra from the motions of a buoy include the eigenvector method of Marsden and Juszko,⁴ the maximum entropy method (MEM) of Lygre and Krogstad,⁵ and iterated versions of both the MLM and MEM. (See Ref. 6 for a comparison of these techniques.) The chief advantage of the MEM is increased directional resolution compared with the Longuet-Higgins method, and improved peak resolution, even over that of the MLM. Thus, spectral estimates previously prepared by the Canadian Marine Environmental Data Service for LEWEX⁷ have been reanalyzed in this article using the MEM.

STATISTICAL PROPERTIES OF THE WAVE FIELD

Figure 2 shows, for the entire six-day measurement period during LEWEX, the significant wave height, peak period, and direction and spread calculated from the Wavec data by using the MEM. The estimates were linearly interpolated when the on-board recorder failed to operate correctly. The significant wave height is a measure of the energy in the wave field. The peak period, direction, and directional spread were all taken at the point of maximum spectral energy density. The direction was calculated from $\tan^{-1}(B_1/A_1)$. The directional spread was calculated by using the expression of Kuik et al.⁸ Figure 2 shows that the wave height during LEWEX varied between about 2 and 5 m. Until the middle of 16 March, the wave height was about 3 m, and waves approached from the southeast at a period of nearly 10 s. During the next 24 h, the wave height increased to nearly 5 m, the peak period remained nearly constant at 10 s, and the wave direction changed to waves coming from the north-northeast. During the subsequent 24-h period, the wave height fell briefly to under 4 m, then rose to nearly 5 m once more early on 18 March. At the same

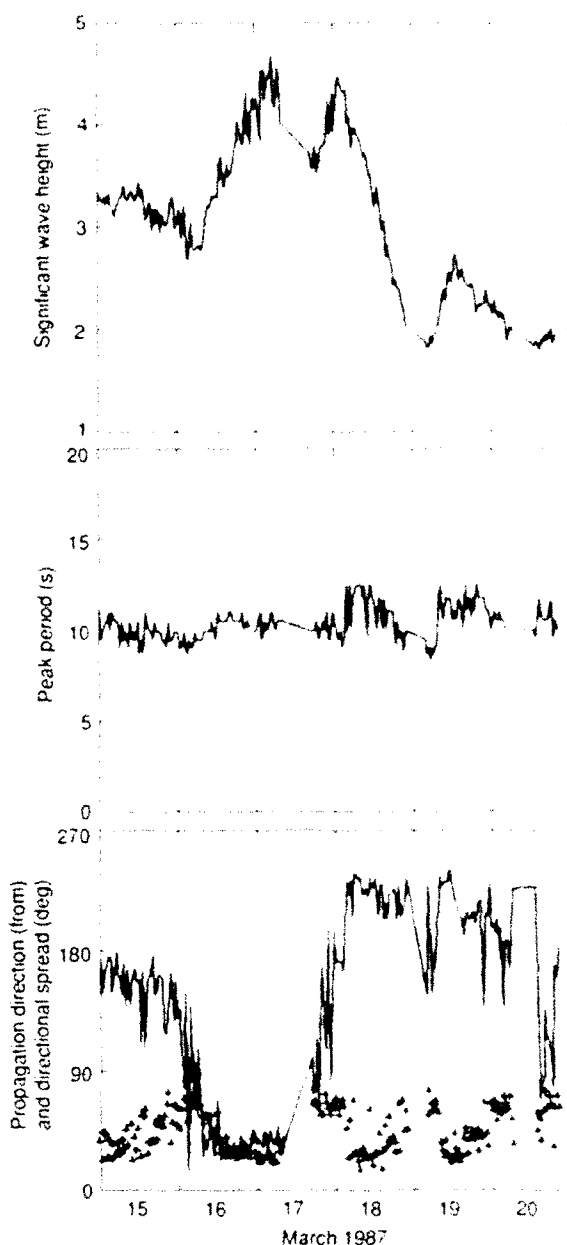


Figure 2. The significant wave height (top), peak period (middle), and direction (solid curve) and spread (---) (bottom) at the *Quest* location, calculated from the Wavec data by using the maximum entropy method.

time, the wave period increased to nearly 12 s, and the wave direction swung, so that the dominant waves were coming from the southwest. Throughout 18 March, the wave height fell rapidly to a minimum under 2 m, the wave period decreased to less than 10 s, and the waves approached generally from the southwest.

SPECTRAL ANALYSIS OF THE WAVEC DATA

The foregoing description of the evolving LEWEX wave field was derived from the set of full (two-dimensional) directional spectra from the Wavec buoy. Although the

total set (over 100) is too large to display. Figure 3 shows a sample selected from 2150 UT on 17 March. Here, up to four contour levels are presented. The spectrum indicates waves coming from the southwest and northeast simultaneously. Each spectrum was examined to determine the vector wave number of maximum energy density. The 80% confidence intervals for all spectra were then estimated to determine the significant peaks. The direction, wave number, and relative energy of each spectral peak were then calculated. Figure 4 shows these results; the time coordinates are expanded so that individual peaks can be resolved visually. The resulting sequence of spectral peaks reveals the time evolution of the wave field.

Figures 4A and 4B show the results from late on 14 March to early on 17 March. The sequence broke naturally into two distinct regimes of waves, the first beginning late on 14 March and persisting until about 0600 UT on 16 March and the second extending from 0600 UT on 16 March through much of 17 March. This latter wave regime actually persisted well into 17 March, as shown by at least one data point on Figure 4C. Waves of the first regime (Fig. 4A) approached from the south-southeast with nearly constant periods of 11 s (± 1 s), progressing from about 11 to 12 s from the beginning of this time to between 10 and 11 s near the end.

Waves of the second regime (Fig. 4B) persisted from 0600 UT on 16 March through at least 0700 UT on 17 March. A new system then appeared from the north-northeast. Early on 17 March (Fig. 4C), a relatively sharp shift in period occurred to values of typically 12 to 13 s. Throughout 18 March, the period tended to shorten as wave directions rotated slightly toward the east.

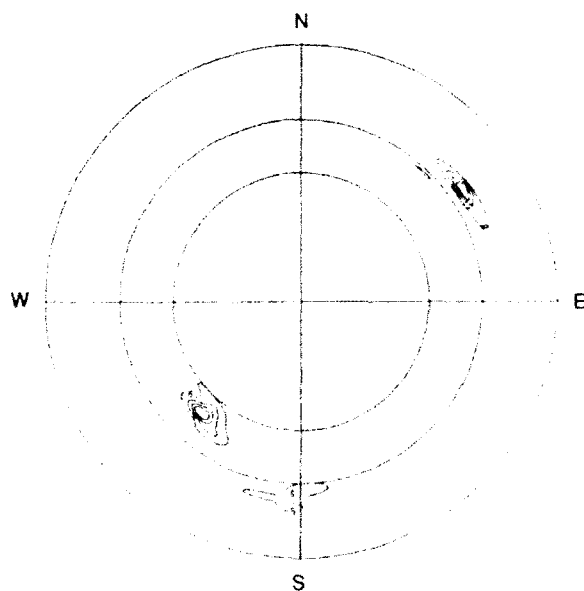


Figure 3. A sample maximum entropy method spectrum from 2150 UT on 17 March 1987. The significant wave height was 4.3 m, the peak period was 9.5 s. The direction convention is the direction from which the waves were coming. The inner circle corresponds to a wavelength of 400 m, the middle to 200 m, and the outer to 100 m.

At around 1800 UT on 17 March (Fig. 4C), two competing wave systems were apparent: waves arriving from the north with periods of about 11 s were confused and dying out (although some evidence of their presence three hours later is still apparent) as they were replaced by new waves from the south-southwest. By about 2100 UT, waves arriving from the south-southwest with periods of about 14 s dominated. This long-period swell apparently was generated in a storm centered to the south (see the article by Cardone in this volume), which just then had begun to propagate into the region. These very long-period waves generally evolve to waves of shorter period. Even until 1200 UT on 18 March, however, the major wave component had a period of about 13 s from the same south-southwesterly direction. By 1800 UT on 18 March, relatively little wave activity was measured by the Wavec.

Occasionally, we see interesting differences between the moored Wavec estimates and the model estimates. For example, at the top of Figure 5, the Ocean Data Gathering Program (ODGP) model (when driven with the 11 Wx common winds) showed an abrupt change in propagation direction at around 1200 UT on 15 March. The

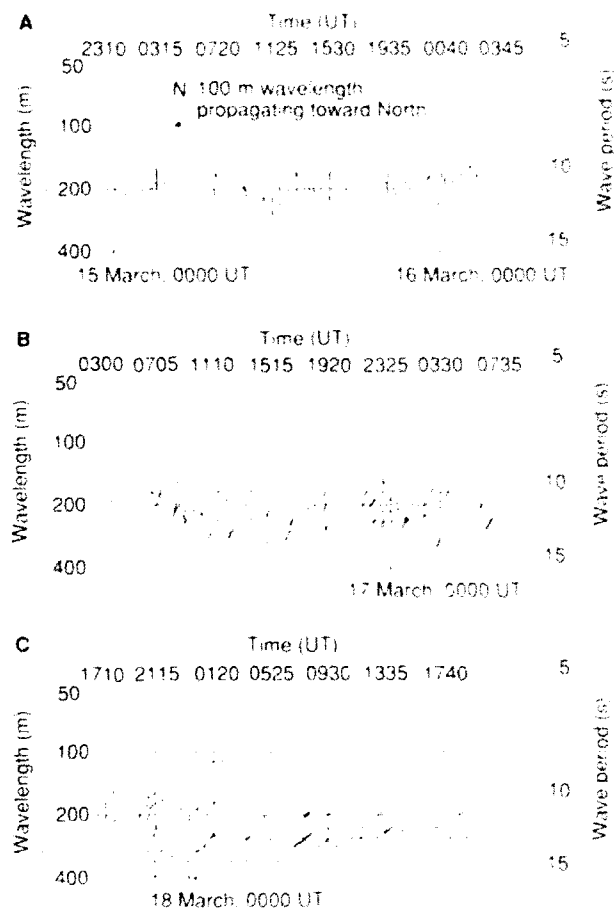


Figure 4. The directions and relative energies of the peaks identified by the maximum entropy method for 14-18 March. The direction convention is the direction to which the waves were going. **A** 14-16 March **B** 16-17 March **C** 17-18 March

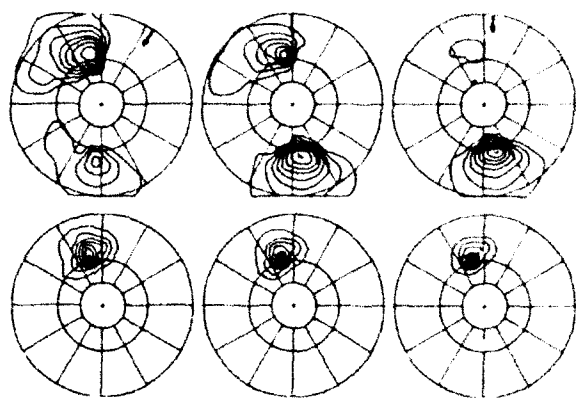


Figure 5. Comparison of Ocean Data Gathering Program hind-cast spectra (top) with Wavec buoy spectra (bottom) at (from left) 0900, 1200, and 1500 UT on 15 March. Spectra are linear in wave number with outer circle at $2\pi/100$ rad/m, and are individually normalized to the peak.

Wavec estimates, shown at the bottom of the figure, however, showed no such shift. This discrepancy between model and buoy extended well into 16 March, when wind speeds were quite low and direction was variable.

The discrepancy recurred again early on 17 March, when the ODGP model (top of Fig. 6) and Wavec (bottom of Fig. 6) showed nearly opposite directional estimates of dominant waves, again at comparable wavelengths. Some of these differences were suppressed in the smoothed Wavec estimates, possibly due to the averaging process. At that time, previously strong northeast winds were diminishing. The Wavec buoy was calibrated both before and after the experiment, and no directional biases were discovered. Overall, we may assume that a given wave model can cause changes in wave direction in response to changing winds more rapidly than the changes actually measured by *in situ* instrumentation.

CONCLUSION

The Wavec buoy estimates of directional spectra provide an excellent yardstick against which wave model outputs can be assessed. In LEWEX, the Wavec spectral estimates occasionally differed from all of the model results, independent of the input wind field. These differences were particularly evident at times of low and shifting winds. Modeled waves seem to respond much more

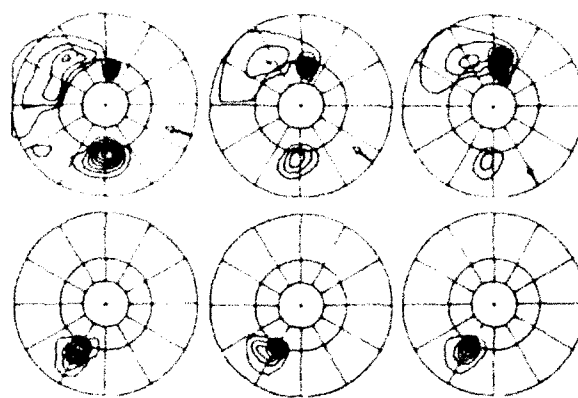


Figure 6. Comparison of Ocean Data Gathering Program hind-cast spectra (top) with Wavec buoy spectra (bottom) at (from left) 0000, 0300, and 0600 UT on 17 March. Spectra are linear in wave number with outer circle at $2\pi/100$ rad/m, and are individually normalized to the peak.

rapidly to shifts in wind direction than do actual waves measured by a buoy.

REFERENCES

- Dobson, L., Perrie, W., and Toulany, B., "On the Deep Water Fetch Laws for Wind Generated Surface Gravity Waves," *Atmos. Ocean*, **27**, 210-236 (1989).
- Longuet-Higgins, M. S., Cartwright, D. E., and Smith, S. D., "Observations of the Directional Spectrum of Sea Waves Using the Motions of a Floating Buoy," in *Ocean Wave Spectra*, Prentice Hall, Englewood Cliffs, N.J., pp. 117-136 (1964).
- Ofman-Shav, I., and Guza, R. T., "A Data Adaptive Ocean Wave Directional Estimator for Pitch and Roll Type Measurements," *J. Phys. Oceanogr.*, **14**, 1800-1810 (1984).
- Marsden, R. E., and Juszko, B. A., "An Eigenvector Method for the Calculation of Directional Spectra from Heave, Pitch and Roll Buoy Data," *J. Phys. Oceanogr.*, **17**, 2157-2167 (1987).
- Eyre, A., and Krogstad, H. E., "Maximum Entropy Estimation of the Directional Distribution in Ocean Wave Spectra," *J. Phys. Oceanogr.*, **16**, 2052-2060 (1986).
- Taylor, J., "Calculations of Directional Wave Spectra," in *Proc. Oceans '87*, p. 876, Halifax, Nova Scotia (1987).
- Marine Environmental Data Service (MEDS), *Directional Wave Data Collected during the 'Quest LEWEX' Experiment, March 14-20, 1987*, MEDS Internal Document, Ottawa, Canada (1987).
- Kirk, A. J., van Vleet, G. Ph., and Holthuisen, J. H., "A Method for the Routine Analysis of Pitch and Roll Buoy Wave Data," *J. Phys. Oceanogr.*, **18**, 1020-1034 (1988).

ACKNOWLEDGMENTS: The author thanks the staff of the Marine Environmental Data Service for the data collection and analyses. In particular, Paul A. Bolduc and John D. Taylor assisted greatly in the preparation of the article.

DIRECTIONAL SPECTRA FROM THE DRIFTING ENDECO WAVETRACK BUOY DURING LEWEX

Compared to all the other directional buoys used during the Labrador Sea Extreme Waves Experiment (LEWEX), Endeco Wavetrack buoys are relatively small and easy to handle. In general, their spectral estimates correlate well with the other buoys. The Endeco buoy, however, seems more sensitive to high frequency wind waves than the larger discus buoys, and this excessive sensitivity may bias the direction of low frequency waves.

INTRODUCTION

The U.S. Navy has placed increased importance on directional wave determination for both design and operational purposes. Improvements in ship motion programs allow a designer to evaluate candidate designs in a wider variety of directional sea conditions. Operationally, numerical tools exist to improve ship performance in waves by changing speed and heading, if the directional characteristics of the seas are known.

The state of the art of directional wave instrumentation and numerical modeling has been advanced by the Labrador Sea Extreme Waves Experiment (LEWEX). This unique experiment provided for the simultaneous evaluation of three technologies—remote sensing, *in situ* measurement, and numerical modeling—all in an identical environment.

The David Taylor Research Center (DTRC) participated in LEWEX using an Endeco type 956 directional wave buoy. The Endeco buoy, developed at the University of Rhode Island by Middleton et al.,^{1,2} is based on a design that assumes that the buoy will follow the wave orbital velocity. The Endeco buoy and its principal components are shown in Figure 1. The spherical fiberglass hull contains the principal electronics and batteries. A stainless steel shank connects to an underwater transducer package that measures pitch, roll, compass direction, and stabilized vertical acceleration. The lower strut assembly responds to the orbital particle velocity in the water column such that the buoy attains a maximum tilt angle at the crest of a wave in the direction of wave propagation. The resulting buoy motion is similar to a standard slope-following buoy (but shifted by 90°), and the data analysis is accomplished in much the same fashion. The assembled buoy weighs approximately 68 kg and is easy to launch even from platforms with minimal deck equipment.

DATA COLLECTION AND ANALYSIS

LEWEX was conducted with a broad spectrum of instruments deployed *in situ* from the CFAV *Quest* and HNLMS *Tydemar* as well as remote sensors operated from aircraft. Early in the experiment, the *Quest* deployed at 50.0°N , 47.5°W while the *Tydemar* deployed

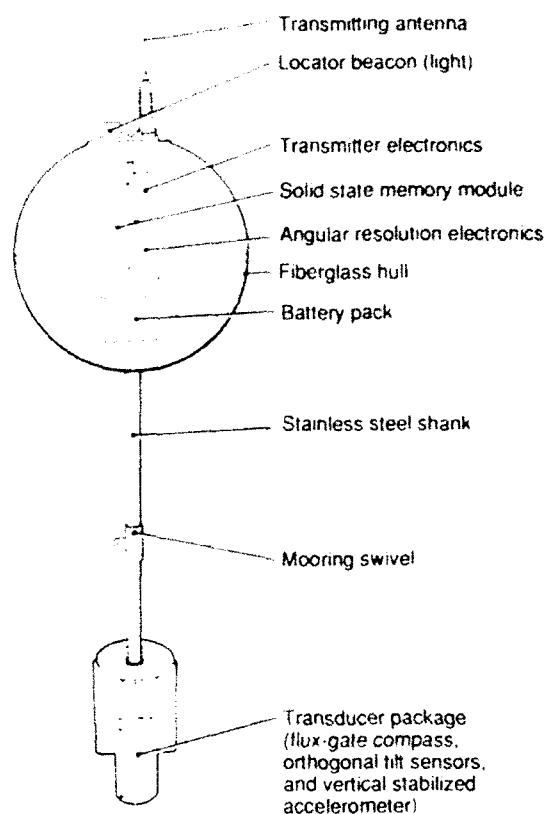


Figure 1. Schematic of the Endeco type 956 directional wave buoy showing the 0.76-m-diameter hull with bottom strut and associated electronics.

at 50.0°N , 45.0°W . The *Tydemar* later joined the *Quest* at her location, and then both vessels moved to a new location near 42.5°N , 55.0°W . A few of the wave instruments were moored, but most of the instruments, including the DTRC Endeco buoy, were deployed on a daily basis in the early morning hours. The deployments

were completed before scheduled 1200 UT aircraft overflights, and data collection continued throughout the morning. The buoys were retrieved during the afternoon, generally before dark. The *Tydemar* deployed and allowed her buoys to drift freely with the current and winds, while the *Quest* tethered the deployed buoys on a long (750-m) line such that the buoys drifted as the *Quest* responded to the wind and currents. The drift rates for the *Tydemar* and the *Quest* buoys were small, and, for the data presented here, no transformation of the measured data has been made to account for the translation of the buoys.

The Endeco buoys have FM transmitters that relay the data in real time. The buoys also have solid state memory modules that provide a backup if the FM transmissions of the data are not maintained. An Endeco receiver was used to collect and digitize the three data channels: buoy double-integrated acceleration (heave), north-south tilt, and east-west tilt. A PDP 11 23 processor was used to perform *in situ* preliminary data processing and also collect the data on floppy disks for post-experiment processing.

The Endeco buoy data were digitized at 2 samples/s for each of the three data channels. During the digitizing process, the data were passed through a 3-Hz low-pass filter. The data in the direction channels were converted from tilt angles to slopes and engineering units were applied. When necessary, the data were filtered using a two-pole high-pass digital filter to eliminate electronic drift or offsets. The stationarity of the data was checked to determine if any of the data were unusable. The lengths of the data sets were then selected. Typical run lengths varied from 1728 to 2304 s with the number of degrees of freedom for the spectral densities ranging from 51 to 68, respectively.

The DTRC analysis procedure is based on the Longuet-Higgins³ approach of calculating the first five Fourier coefficients. Initially, the auto- and cross-spectra were calculated using a fast Fourier transformation (FFT). Each data set was divided into segments of 256 samples each. A cosine window was applied to each segment, which was then overlapped with the next by 50%. The real and imaginary parts of the cross spectra of each of the three channels were calculated to yield the in-phase and the quadrature spectra. From these, the Fourier coefficients were calculated.

The Fourier coefficients were used to calculate mean angle, rms spreading, and directional spreading. The spreading was calculated using a uni-modal directional spreading formulation put forth by Longuet-Higgins et al.³ The spectral and spreading calculations used by DTRC have been detailed by Lai and Bachman.⁴

DATA RESULTS AND COMPARISONS

Forty-seven directional spectra were collected and analyzed from the Endeco buoy spectra deployed by the *Quest*. The measurements started on 15 March 1987 and ran through 25 March. During the first few days of data collection, the drifting Endeco buoy was deployed in the same general vicinity as a moored Datawell Wavec buoy. The Ma-

rine Environmental Data Service of Ottawa, Ontario, Canada, was responsible for the deployment and analysis of data for the Wavec buoy (see Keeley, in this volume). Selected samples of their data have been plotted in Figure 2 along with parameters from the DTRC data analysis. The parameters plotted include significant wave height, modal wave period, and peak wave direction. The peak wave direction is defined as the predominating direction of wave propagation at a frequency corresponding to the modal frequency of the one-dimensional spectrum.

The significant wave height comparisons are well correlated, with the possible exception of 16 March, when the Endeco buoy was indicating waves up to 0.5 m higher than was the Wavec buoy. The modal wave period comparisons are also well correlated, mainly because the spectra tended to be uni-modal with well-defined peaks. Zero-crossing-period comparisons were also made (but not shown) and found to be more closely correlated than were the modal periods, as would be expected. The most interesting comparison is the peak wave direction. On some days, such as 16, 17, 19, and 20 March, the comparison between buoys is good. On 15 March, however, a discrepancy of approximately 50° exists. That date was a transition day with a southerly wave system diminishing and winds swinging around to a northerly direction.

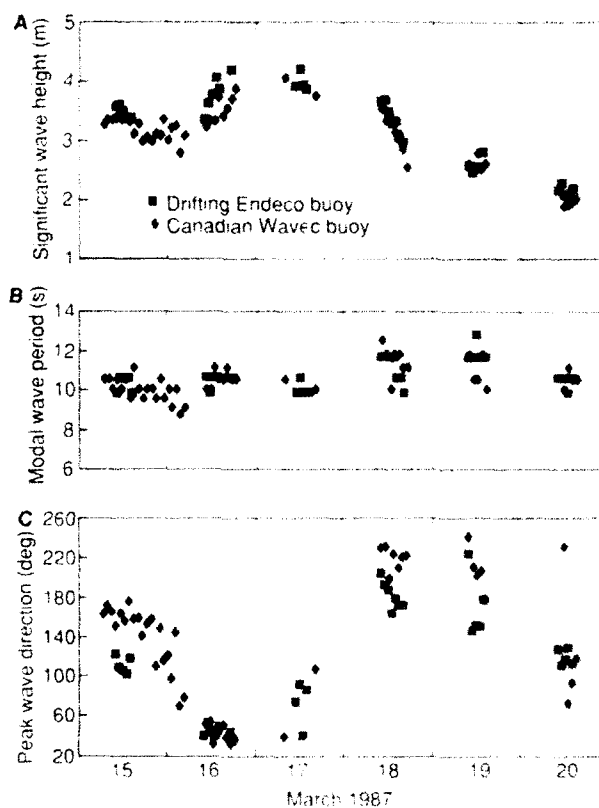


Figure 2. Comparison of Endeco Wavetrack and Datawell Wavec buoy parameters during LEWEX. (A) Significant wave height, and (B) modal wave period show general agreement. (C) Peak wave direction shows correlation; however, notable disagreement can be seen for 15 and 18 March 1987 data.

The peak directions of Figure 2 have been plotted in the direction that the waves are coming from. (This convention is standard for ship-based estimates, but is opposite to that of many wave models.) After careful study of the data, it is the authors' contention that the Endeco buoy results are biased by shorter wind waves, and the results on 15 March incorrectly indicate the predominant energy direction. About 12 hours later, the Wavec buoy results show this same shifting in energy direction toward the north. The Endeco buoy directional bias toward shorter wind waves has made it, in this instance, a correct forecaster for a shift in energy direction. The poor correlation on 18 March can also be explained by a short wave directional bias of the Endeco instrument.

An interesting day occurred on 20 March, with the Wavec buoy having the greater variability in its peak wave direction. The *Tydemar* joined the *Quest* at her location on 19 March and then deployed buoys in the vicinity. Figure 3 shows comparisons of parameters between the DTRC Endeco and Norwegian Wavescan buoys.⁵ The Wavescan buoy shows 20 March to be a day much like 15 March, with energy swinging from a southerly direction to a northerly direction. The Endeco buoy's directional results appear to be well correlated with the Wavescan buoy in this case. Indeed, the peak directions are well correlated for spectra measured later on 23, 24, and 25 March. The significant wave height

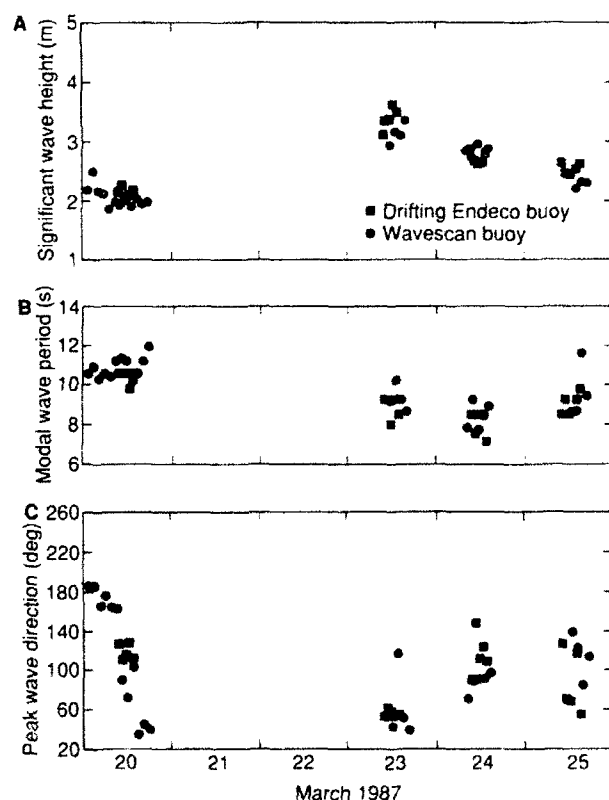


Figure 3. Comparison of Endeco Wavetrack and Seatex Wavescan buoy parameters during LEWEX. (A) Significant wave height, (B) modal wave period, and (C) peak wave direction all show good agreement.

and modal wave period parameters also compare favorably, as shown in Figure 3.

Comparison of parameters gives a good indication of the functioning of the Endeco buoy. It is, however, also interesting to look at comparisons of the entire directional spectrum. Gerling⁶ has developed a common linear wave number format for comparison of remote instruments, *in situ* instruments, and wave forecasts and hindcasts. Figures 4 and 5 have been extracted from Gerling and show comparisons of directional spectra for 15 and 16 March 1987. These figures use the wave-propagation direction convention of "toward" rather than "from," as was used on Figures 2 and 3. As discussed earlier, comparisons between the Endeco and Wavec buoys on 15 March were poor, and this difference is also seen in Figure 4. The larger angular spread of the drifting Endeco buoy data is believed to be a result of the DTRC cosine spreading method used, as opposed to the maximum entropy used to process the Wavec and Wavescan results. This tendency toward larger spreading angles from the Endeco buoy was seen throughout the entire experiment. Ignoring the differences in spreading, it is the authors' opinion that neither instrument is telling the complete story. The predominating system has been propagating toward the north, but the southerly wind has swung to an easterly direction. This wind sea change has excited and biased the Endeco buoy results. The Wavec buoy has failed to detect these higher frequency waves. The wave models have incorrectly shown a complete rotation of the wind from south to north and resulted in opposing decaying and growing wave systems. Thus, Figure 4 may be considered a classic illustration of failure to define adequately the directional spectrum either through a model or an *in situ* instrument.

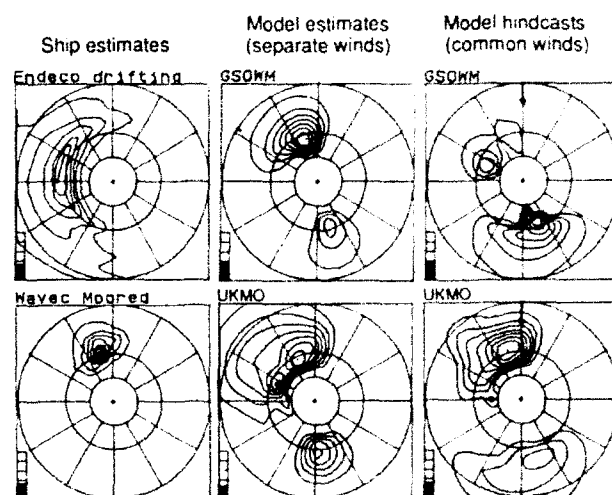


Figure 4. Directional spectra representations for 1200 UT on 15 March 1987 at the *Quest* location (50°N, 47.5°W). The "first generation" U.S. Navy Global Spectral Ocean Wave Model (GSOWM) and the "second generation" United Kingdom Meteorological Office (UKMO) model are presented using self-generated and common wind fields. The model estimates and hindcasts indicate opposing wave systems, while measurements indicate only one system in existence.

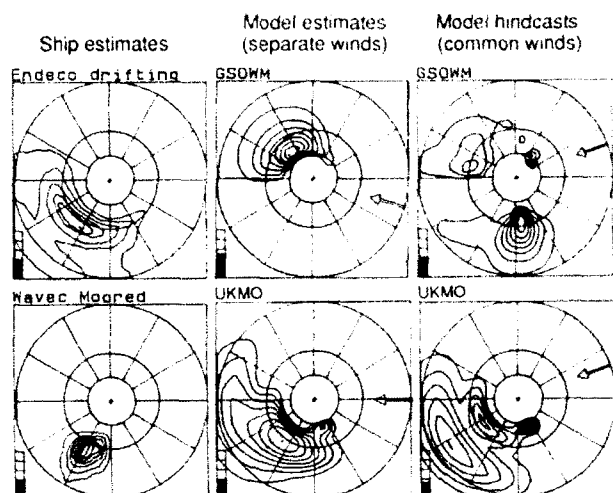


Figure 5. Directional spectra representations for 1800 UT on 16 March 1987 at the *Quest* location. The "first generation" U.S. Navy Global Spectral Ocean Wave Model (GSOWM) and the "second generation" United Kingdom Meteorological Office (UKMO) model are presented using self-generated and common wind fields. The DTRC drifting Endeco buoy shows reasonable agreement with the Wavec and the wave models.

Figure 5 shows a more stabilized situation where the northerlies are predominating. The drifting Endeco buoy results are in better agreement with the Wavec buoy and other instruments, although the Endeco buoy results may be biased a little more toward a westerly direction. The models have indicated a swing in wind direction, and the Endeco buoy may be once again biased toward the resulting short wind waves.

CONCLUSIONS

The authors' experience during LEWEX and several other deployments has proven the Endeco Wavetrack buoy to be a lightweight and easily deployable buoy. This is significant for the Navy, where deck cranes are usually not available for buoy deployments. LEWEX results showed that the drifting Endeco buoy's spectral estimates did compare favorably with other *in situ* devices. The Endeco buoy's smaller size permits better definition of higher frequency waves. The authors believe, however, that in certain cases the Endeco buoy's directional determination of lower frequency waves can be biased by shorter wind waves. The results also indicated that the DTRC analysis process (a cosine spreading function) tended to spread the energy over a broader range of headings than the maximum entropy method (described by Krogstad elsewhere in this volume) used in the analysis of the other *in situ* devices.

REFERENCES

- Middleton, F. H., LeBlond, L. R., and Cartwright, M. E., "Spectral Limits and Calibration of a Wave Follower Buoy," in *Proc. 3rd Annual Offshore Technology Conf.*, OTC 2597, Houston, Texas (1976).
- Middleton, F. H., LeBlond, L. R., and Sternberger, W. E., "Wave Direction Measurement by a Single Wave Follower Buoy," in *Proc. 4th Annual Offshore Technology Conf.*, OTC 3180, Houston, Texas (1978).
- Longuet-Higgins, M. S., Cartwright, D. E., and Smith, S. D., "Observations of the Directional Spectrum of Sea Waves Using the Motions of a Floating Buoy," *Ocean Wave Spectra*, Prentice Hall, Englewood Cliffs, N.J. (1963).
- Lai, R. L., and Bachman, R. J., *Directional Wave Measurement and Analysis*, DTRC SPD-1167-01, DTRC, Carderock, Md. (1985).
- Krogstad, H. E., *Wave Data Collected by Wavecra During the Labrador Sea Extreme Waves Experiment (LEWEX)*, Oceanographic Center Report No. 02.0810, Trondheim, Norway (1987).
- Giering, T. W., *Common Processing and Display of LEWEX Directional Ocean Wave Spectral Estimates from 12 March through 19 March 1987*, JHU/APL STR89C-011, Johns Hopkins University Applied Physics Laboratory, Laurel, Md. (1989).

DIRECTIONAL SPECTRA FROM SHIPBOARD NAVIGATION RADAR DURING LEWEX

During the Labrador Sea Extreme Waves Experiment, an experimental version of a shipboard wave-measuring radar was used to estimate directional spectra. The data analysis yields unambiguous wave spectra using a three-dimensional fast Fourier transformation operating on a time series of radar images. The technique can be employed from a rapidly moving ship and in seas with a significant wave height of up to at least 9 m.

IMAGING WAVE TIME SERIES BY SHIP RADAR

The visual inspection of wave patterns (sea clutter) displayed on the radar screen of a marine radar is routinely used to estimate the mean wave direction and the mean wavelength.¹ The technique to store such patterns and the analysis to calculate wave image spectra have been developed and improved in recent years.^{2,4} The storage of the wave pattern during the Labrador Sea Extreme Waves Experiment (LEWEX) was achieved by a photographic camera whose shutter was synchronized with the rotation of the radar scanner. The physics behind the sea clutter phenomenon has been of central interest for as long as marine radar has existed. The principles of Bragg scattering at the water surface and the imaging of the wave field of interest may be treated similarly to other microwave systems.¹

In this article, the discussion is focused on one characteristic feature of the marine radar. The low antenna height of a shipboard radar leads to a perspective in which the modulation of the radar cross section is strongly influenced. Even if a linear transfer function from the wave field to the wave image is assumed⁵ for a real aperture airborne radar, the modulation from shadowing causes a nonlinear effect when imaging waves by ship radar.⁴

Figure 1 shows the essential aspects of the technique. Measurements are taken in both space and time, so that the sample is defined in three dimensions. The Fourier presentation of this sample is defined over the two wave number components, k_x and k_y , and the frequency, ω .

The elimination of the 180° ambiguity in wave propagation (which is inherent in single radar image analysis) is an important result of the three-dimensional analysis. The article by Rosenthal and Ziemer (elsewhere in this volume) discusses how the additional frequency information is used to obtain the unique direction of wave energy propagation. As indicated in the lower part of Figure 1, the three-dimensional spectra may be used to deduce other spectral properties. To apply the three-dimensional techniques we must have sampling that is sufficiently dense in space and time to obtain an acceptable Nyquist wave number and Nyquist frequency. A sufficiently long

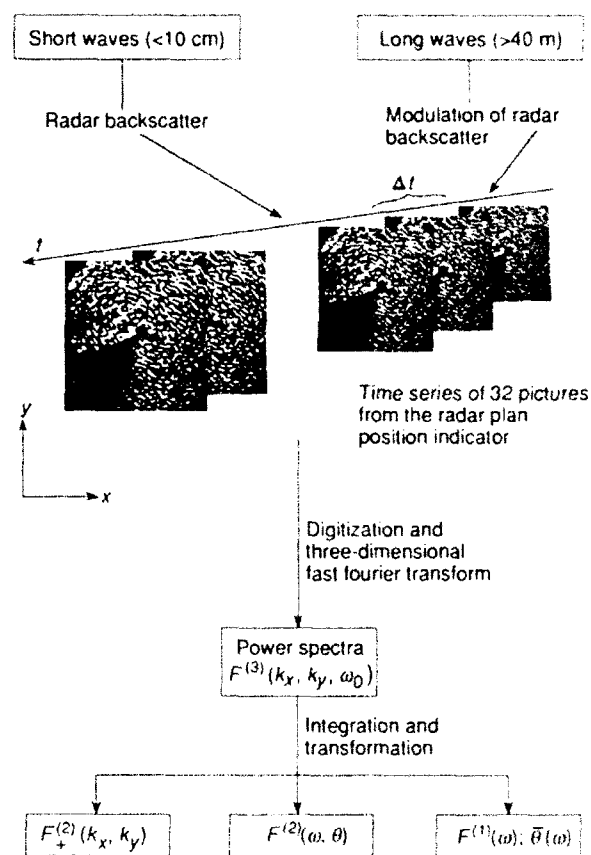


Figure 1. From time series of wave pattern to different presentations of asymmetric wave image spectra. The dimensions of the spectral arguments are given as superscripts in parentheses. Arguments are the wave numbers k_x and k_y , the frequency ω , and the direction θ . The spectrum of the mean wave direction is $\bar{\theta}(\omega)$.

time series and correspondingly large surface area are required as well, so as to include the portion of the dispersion shell containing the wave energy.

SPECTRAL PRESENTATIONS AND THEIR INTERCONNECTIONS

Wave measurements may be taken in different sample spaces, depending on the equipment used (e.g., the sample space for the image of a wave field is defined by the Cartesian coordinates x and y). The transition from the sample space to the spectral presentation is obtained through a Fourier transformation. The spectrum of an image of a wave field is defined over k_x (positive for east-traveling waves) and k_y (positive for north-traveling waves). The dimension of the Fourier space over which the spectrum is defined depends on the dimension of the sample space. The most important spectral properties and their interrelations are given in Figure 2. For clarity, the dimensions of the argument of the spectra are given as superscripts in parentheses.

On the top of Figure 2, the three-dimensional presentation is given by the output of a three-dimensional fast Fourier transformation. On the left-hand side are given the two-dimensional presentations, as they result from single-image analysis. On the right-hand side of Figure 2, the presentations are given from the analysis of time series measurements. The interrelations between the multi-dimensional and the one-dimensional spectral types are given by integrations and by transformations of coordinates, assuming linear gravity wave dispersion. For the other transfer direction (from one-dimensional to multi-dimensional presentations), a weighting function for the directional distribution of the wave energy must be assumed.

The most complete spectral presentation of the sea state is given by the three-dimensional Fourier transformation, which is discussed in more detail in the article by Rosenthal and Ziemer in this volume. Here we follow the transform from the top of Figure 2 to the left side, by considering only positive frequencies for the integration. Positive frequencies are related to the wave number vector through the unique and correct direction of propagation,

$$F^{(2)}(k) = \int_0^{\infty} F^{(3)}(\Omega) d\omega \quad (1)$$

This technique provides unambiguous results from the frequency $\omega = \Delta\omega/2$ up to the Nyquist limit. The impact of the Doppler shift, when the measurement is taken from a moving ship, is discussed later in this article. Figure 2 gives the relation to the one-dimensional presentation, necessary for the analysis discussed later. The frequency spectrum $F^{(1)}(\omega)$ and the co- and quad-frequency spectra ($C_{ij}^{(1)}(\omega)$ and $Q_{ij}^{(1)}(\omega)$), as they are known from analysis of pitch and roll buoy series, are equivalent to the directional integrals of the corresponding cross spectra. The resulting mean direction, as well as the directional spread, is independent of the absolute calibration of the measurement system.

IMAGING WAVE TIME SERIES FROM A RAPIDLY MOVING SHIP

For the improvement of data quality, the integration in Equation 1 is not performed over the full three-dimen-

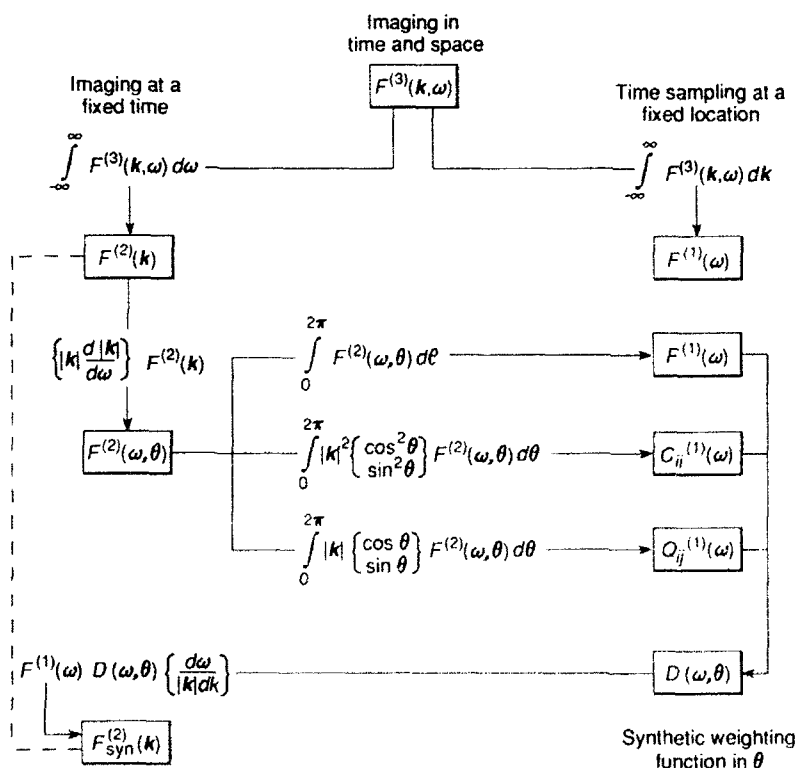


Figure 2. Different spectral presentations and their interconnections. Top: three-dimensional spectra; Left side: two-dimensional spectra; Right side: one-dimensional spectra. C_{ij} and Q_{ij} denote co- and quad-frequency spectra. $D(\omega, \theta)$ denotes a suitable synthetic weighting function.

sional space. To avoid noise signals resulting from other than the wave field of interest, only those energies that lie inside a small spectral window close to the dispersion shell (i.e. inside an interval given by the resolution cell⁴) were summed. The speed of a ship relative to the body of water carrying the wave field results in a "current of encounter" that Doppler shifts the wave frequency. Thus, for the definition of a spectral window around the dispersion shell, the distortion by this Doppler shift must be known. If no current of encounter affects the sampling of a wave with the wave number k , its frequency is given by the isotropic dispersion relationship $\omega_0^2 = gk \tanh kh$, where g is the acceleration caused by gravity and h is water depth. The same wave, observed from a ship moving with the velocity u , seen from the nonisotropic frequency of encounter has the frequency described by

$$\omega_c = \omega_0 + (\mathbf{k} \cdot \mathbf{u}) \quad (2)$$

In Figure 3 the intersection lines of the dispersion relation are plotted within the frequency-wave number plane for different speeds of the ship (in steps of 5 kt). The plane is oriented in the direction of the ship heading; that is, the ship is assumed to travel in the positive k_x direction, whereas the k_y axis lies normal to the plotted plane.

Isolines of the energy of a hypothetical wave package traveling in the direction of the ship heading are plotted in Figure 3, for various speeds. This demonstrates the impact of the resulting Doppler effect. The energy of the same wave package is shifted parallel to the frequency axis when ship speed changes. For higher ship speeds, the frequencies of encounter at higher wave numbers may become negative. To avoid ambiguous results, the separation between the energy with the unique wave direction from its mirror image must be defined by a plane described by

$$\omega_c(\mathbf{k}) - (\mathbf{k} \cdot \mathbf{u}) = 0.$$

COMPARISON OF SHIP RADAR SPECTRA WITH WAVESCAN BUOY SPECTRA

Good comparisons between the ship radar and the Wavescan buoy were made on each day from 14 through 19 March 1987. The sequence of intercomparisons is shown in Figure 4. All ship radar spectra were calculated using Equation 1. Consequently, these spectra give the unambiguous direction of wave energy propagation. The signal-to-noise ratio was increased by employing spectral window filtering (as discussed earlier).

The NNW-propagating dispersive swell at 1200 UT on 14 and 15 March 1987 was clearly detected by the ship radar as well, and are good examples of asymmetric image spectra that describe unimodal wave conditions. Similar unimodal conditions could be identified by the ship radar on 18 and 19 March as well. These situations are easy to detect by buoys as well as by imaging instruments because the ambiguous part of the spectra may simply be ignored. More important for the intercompar-

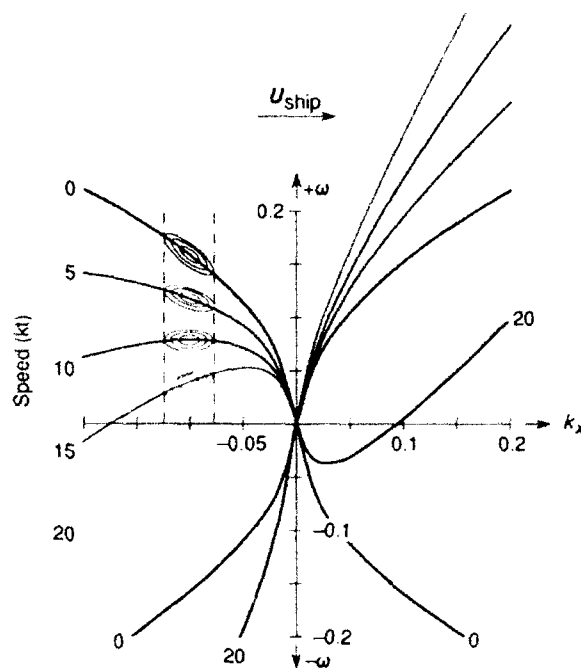


Figure 3. Intersection lines of the wave dispersion shell with the (k_x, ω) plane, for different speeds (0 to 20 kt in 5-kt increments). For the different speeds, the isolines of a wave package traveling with the ship are given. Energy propagation is given in the "coming from" direct.

ison discussion are the results from 16 March at 1800 UT and 17 March at 1200 UT, when a more complicated situation was encountered. Both events demonstrate the advantage of the dispersion technique, since two 180° opposing wave systems with similar wavelengths existed and were independently verified by the buoy on each of these days.

For other (instantaneous) imaging systems, this bimodal structure in the wave field is ambiguous. Direct separation of the two systems is not possible from single time step measurements. On 16 March at 1800 UT, a relic of the NNW-propagating swell with wavelengths close to 100 m was still detected by the ship radar. At the same time, a new swell system traveling toward SSE with a dominant wavelength of 170 m was detected, in agreement with the buoys.

On 17 March at 1316 UT, the ship radar detected rapid changes. (See Fig. 2A of Rosenthal and Ziemer in this volume.) A long swell heading to 30° had arrived. Additionally, an opposing swell heading to 210° was also detected. This spectrum is rotated clockwise compared with most other measurements. But considering the time shift of one hour (1200 UT is the comparison time) and the clockwise rotation of both wave systems as confirmed at 1800 UT by most of the other measurement systems, this result seems reasonable.

Thus, for the intercomparisons between instruments and models, the asymmetric image spectra from the ship radar can resolve many of the discrepancies between the directional features of the observed and modeled wave fields.

$$TF(f) = \text{const. } f^{b_1} \quad (3)$$

The exponent b_1 that is valid in Equation 3 for low frequencies is assumed to be a function of the particular radar. As shown in Ref. 4, the shadowing at high frequencies causes the exponent b_2 to be a function of the wave field itself. Therefore a general reference must be defined. For the LEWEX data set the actual exponent b_2 was estimated by fitting the radar spectrum to

$$E(f) = \alpha g^2 (2\pi)^{-4} f^{-5} \quad (4)$$

in the saturated portion of the wind sea spectrum ($f > 1.2 f_m$, where f_m is the frequency at maximum energy). The Phillips parameter α was assumed to be constant in this part of the spectrum, with a value of $\alpha = 0.008$.

From Ref. 4 the exponents b_2 were fitted for each measurement and applied to the spectra. The constant factor in Equation 3 was fitted from the wind sea as well, but used for the full spectrum. The significant wave heights that were evaluated from the radar measurements on board HNLMS *Tydeman* by this method were compared with the results of the other instruments.⁶ The correlation coefficients from a least squares linear regression analysis were as follows:

Wave sensor	Number of samples compared	Correlation
Delft	22	0.923
Wavescan	13	0.796
Infrared sensor	20	0.801
Wavec	17	0.840

Observation times differed considerably between measurement systems. The buoys were sampled over 30 min, whereas the radar was sampled only over 60 s. For a more detailed statistical check of this comparison it would be necessary to sample and average radar measurements during the full period of buoy measurements. Nevertheless, these results give a hint that this method of estimation holds promise for obtaining absolute value wave energy spectra from radar measurements.

As an example of a measurement of a high sea state, the data set discussed above was extended during a campaign that occurred in November 1988, in cooperation with the German Hydrographic Institute (DHI), the Norwegian Meteorological Institute, the Statoil Company, and GKSS Research Institute. During this campaign the research vessel *Gauss* of DHI operated for three weeks in the Statfjord field situated 100 nmi west of the Norwegian coast.

Figure 5 shows a time series of significant wave heights over a 48-hour period that contained an 8-hour period where the wind speed exceeded 30 m/s, surrounded by a 20-hour period where the wind speed exceeded 25 m/s. The figure gives the results of the significant wave height calculated from the measurements of four different sensors. Two instruments (the Wavec and the Wave rider) were housed in moored buoys. The other two time series are results from the navigation radars on board the

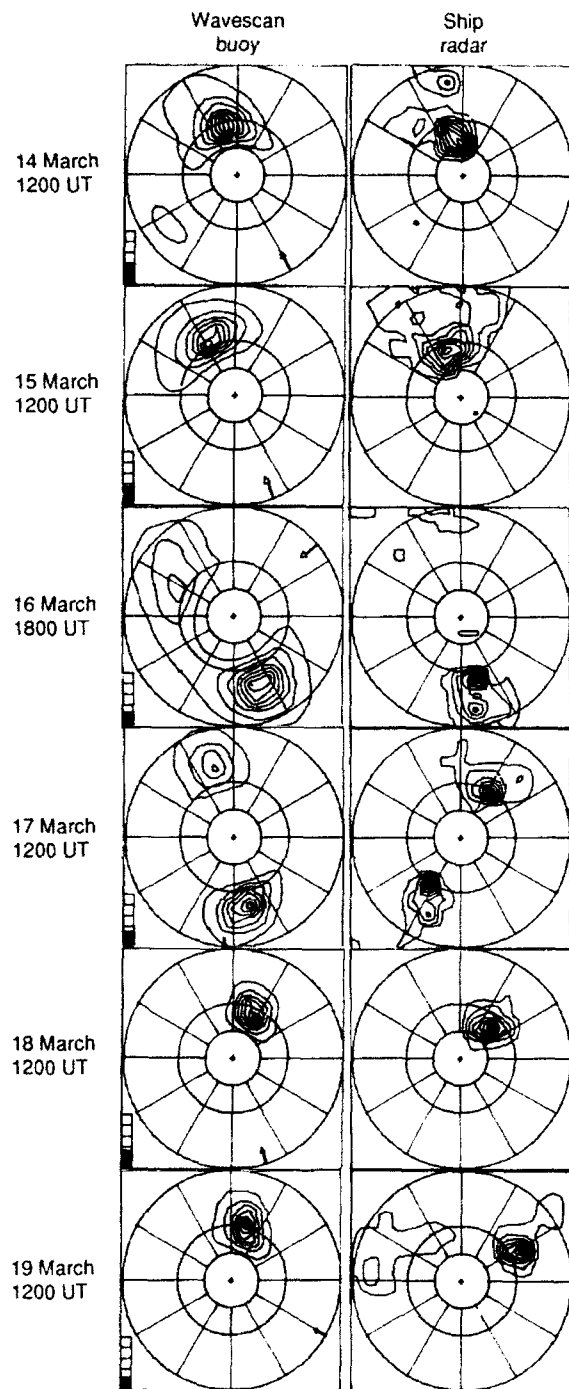


Figure 4. Wave number spectral intercomparisons of ship radar at the *Tydeman* with the Wavescan buoy for six days during LEWEX. Plots are linear in wave number with the outer circle at $2\pi/100$ rad/m.

ESTIMATE OF THE SIGNIFICANT WAVE HEIGHT

To get an independent estimate of the significant wave height from the ship radar, a one-dimensional transfer function, TF , was defined as the ratio of the radar spectrum divided by the spectrum of the wave field, parameterized for two frequency intervals by

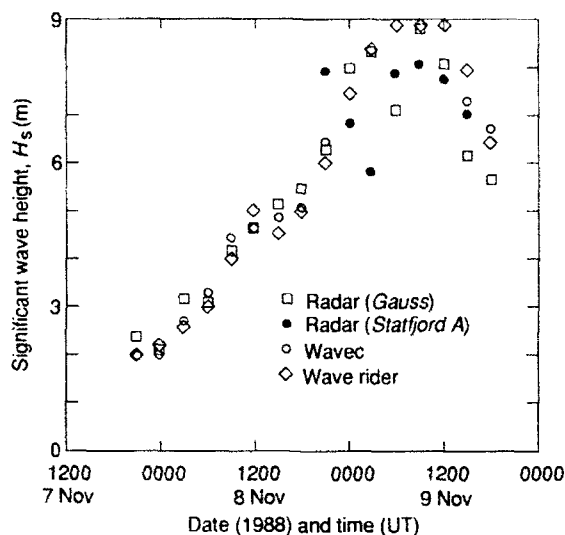


Figure 5. Time series of significant wave heights calculated from measurements of four different sensors in the *Statfjord A*'s field (November 1988).

Gauss and on board the drilling rig *MS Statfjord A*. The significant wave heights from the radar measurements were estimated as described earlier. The good agreement between the wave height time series from the different

sensors is another indication that the transfer function of the ship radar (Eq. 3) is well estimated.

CONCLUSIONS

Although only an experimental version of the ship radar technique was used during LEWEX and other similar campaigns, wave measurements have already proven to be important. This sensor, which is available on board every ship, can perform wave measurements during a ship's cruise without any added time consumption. The results provide an unambiguous direction of wave propagation. We therefore expect an increase in marine radar measurements of this type in the near future.

REFERENCES

- ¹Wright, J. W., "Detection of Ocean Waves by Microwave Radar: the Modulation of Short Gravity Capillary Waves," *Boundary Layer Meteorol.* **13**, 87-105 (1978).
- ²Mattie, M. G., and Harris, D. L., *A System for Using Radar To Record Wave Direction*, Technical Report 79-1, U.S. Army Corps of Engineers, Coast Engineering Research Center, Ft. Belvoir, Va. (1979).
- ³Young, I. R., Rosenthal, W., and Ziemer, F., "A Three-Dimensional Analysis of Marine Radar Images for the Determination of Ocean Wave Directionality and Surface Currents," *J. Geophys. Res.* **90**, 1049-1059 (1985).
- ⁴Ziemer, F., and Rosenthal, W., "On the Transfer Function of a Shipborne Radar for Imaging Ocean Waves," in *Proc. IGARSS '87 Symp.*, Ann Arbor, Mich., pp. 1559-1564 (May 1987).
- ⁵Alpers, W., Ross, D. B., and Rufenach, C. L., "On the Detectability of Ocean Surface Waves by Real and Synthetic Aperture Radar," *J. Geophys. Res.* **86**, 6481-6498 (1981).
- ⁶Maron, A., and Blanco, G., "Comparisons of In-Situ Measurements during LEWEX," Data Report Programa de Clima Martimo, Madrid (1988).

AIR AND SPACE MEASUREMENTS

*IN WHICH AIRBORNE AND SPACEBORNE RADAR
TECHNIQUES FOR ESTIMATING THE DIRECTIONAL
OCEAN WAVE SPECTRUM ARE DESCRIBED
AND EVALUATED*

SURFACE CONTOUR RADAR DIRECTIONAL WAVE SPECTRA MEASUREMENTS DURING LEWEX

Measurements of directional wave spectra made with the Surface Contour Radar in March 1987 are presented and analyzed. The spatial variation of the propagation directions on each day is used to suggest possible source regions of the wave fields. The results are also used to infer the temporal variability that might be sensed by stationary *in situ* instruments.

INSTRUMENTATION

The SCR (Surface Contour Radar) is a NASA/Goddard Space Flight Center 36-GHz computer-controlled airborne radar¹ that generates a false-color-coded elevation map of the sea surface below the aircraft in real time. With postflight data processing, it produces ocean directional wave spectra. The SCR is a straightforward remote sensing instrument. Data interpretation is easy since the SCR yields a direct range measurement. Data from the SCR have led to a new model to describe how a fetch-limited wave field evolves.²

Figure 1 shows the nominal measurement geometry of the SCR and the horizontal resolutions in terms of the aircraft altitude, h . An oscillating mirror scans a $0.96^\circ \times 1.42^\circ$ half-power-width pencil beam laterally to measure the elevations at fifty-one evenly spaced points on the surface below the aircraft. At each point across the swath, the SCR measures the slant range to the surface and corrects in real time for the off-nadir angle of the beam to produce the elevation of a given point with respect to the horizontal reference. As the aircraft advances, the SCR produces a topographic map of the surface below by generating these raster scan lines at up to 20 Hz. A two-dimensional fast Fourier transform (FFT) is used to transform this rectangular topographic map into a directional wave spectrum.¹

Whenever elevation data are transformed using a two-dimensional FFT, a 180° ambiguity exists in the wave propagation direction because the elevation data could represent waves propagating in either direction. In general, we can clearly determine which lobes in each spectrum are artifact lobes by comparing Doppler-corrected spectra for different ground tracks.

Doppler corrections to compensate for the wave translation over the data acquisition interval are applied to all wave components during data processing. The corrections shift the real lobes of the spectrum into their proper positions but double the Doppler shift for the artifact lobes. Therefore, the artifact lobes in the corrected spectra do not take positions symmetrical from the real lobes but shift along the direction of the aircraft velocity vector.³

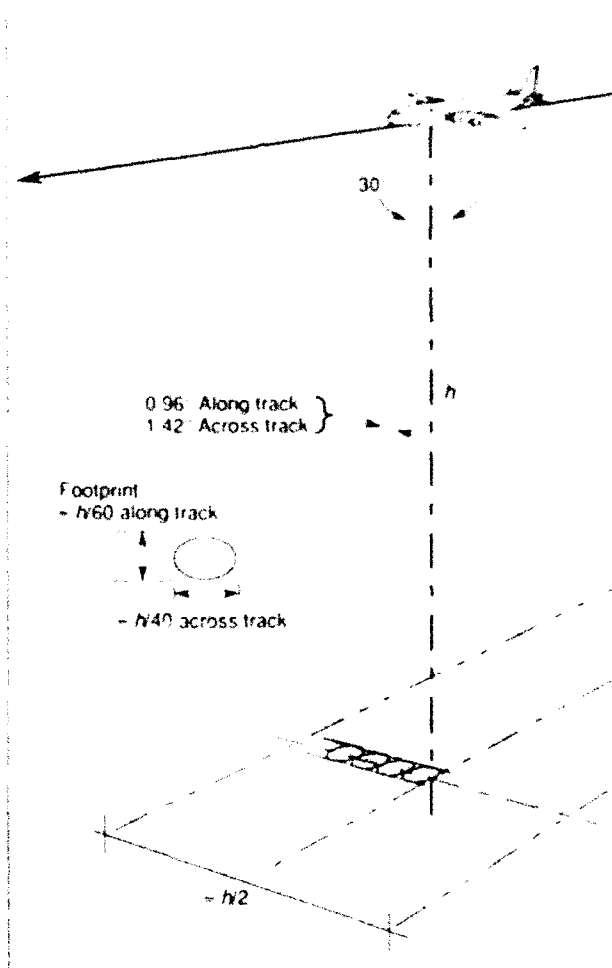


Figure 1. Measurement geometry of the SCR and the horizontal resolutions in terms of aircraft altitude (h).

DATA COLLECTION STRATEGY

During the Labrador Sea Extreme Waves Experiment, SCR data were collected on 14, 16, and 17 March 1987.

The bottom portions of Figure 2 indicate in plan view the ground track over which SCR data were acquired on those days. The positions of the research ships, the CFAV *Quest* and HNLMS *Tydeman*, are indicated by the large circles with inscribed crosses. The ground tracks on all three days proceeded from east to west. The irregular path was used to help sort out the 180° ambiguities in wave propagation.

The middle portions of Figure 2 show the variation with longitude of the direction of propagation at the peak of the various wave field components observed in the SCR spectra at the locations indicated in the bottom portions of the figure. On all three days the dominant wave field propagated generally toward either the north (14 March) or the south (16–17 March), and a trend of the propagation direction with longitude was apparent.

Figures 3, 4, and 5 show directional wave spectra for the three study days; the contour lines are at intervals

of 1 dB, the lowest contour being at the same level in absolute spectral density for all spectra. The artifact lobes in these figures are marked by a large X. Also shown for reference are the locations of peak spectra from the Radar Ocean Wave Spectrometer (ROWS) (Jackson, this volume) when the estimates were within about 50 km and 2 h of the SCR.

Figure 3 shows SCR spectra for 14 March corresponding to the locations indicated by the three solid circles on the plan view at the bottom (left) of Figure 2. The wave field has two components: one traveling slightly west of north and one traveling slightly south of west. For the spectrum at the right, which was taken near the *Tydeman*, the peak of the north-propagating wave field is 6 dB greater than that of the west-propagating system. For the middle spectrum of Figure 3, which was taken between the *Quest* and the *Tydeman*, the north-propagating wave field peak had increased by 1 dB, while the

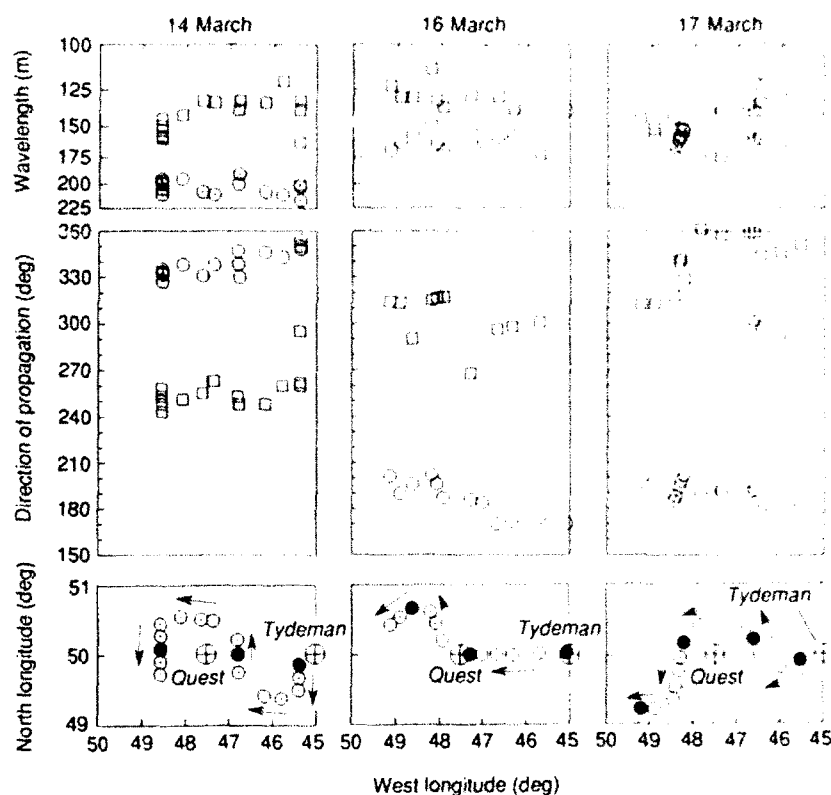


Figure 2. Variation with longitude of the wavelength (top) and direction of propagation (middle) of the various wave fields present on 14 (left), 16 (middle), and 17 March (right). Dominant wave fields are represented by circles, secondary wave fields by squares, and tertiary wave fields by triangles. Plan views of the locations of the SCR directional wave spectra for each day are shown at the bottom. The small circles show the centers of the data spans; the large circles with inscribed crosses show the locations of the ships *Quest* and *Tydeman*, and the solid circles indicate locations of spectra shown in Figures 3, 4, and 5.

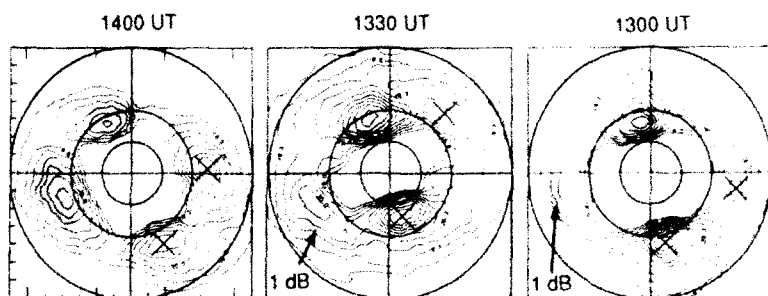


Figure 3. Directional wave number spectra for 14 March 1987 at the locations indicated by solid circles on the Figure 2 plan view (bottom). Contour lines are at 1-dB intervals in units of m^3/rad . Artifact lobes caused by 180° ambiguities are marked by an X. Note the rapidly growing easterly wave system near the *Quest*. Color overlays are estimates from nearly coincident (generally within 50 km) ROWS spectra (Jackson, this volume) at either a 3- or 1-dB level from peak.

Figure 4. Same as Figure 3 except for 16 March. Note the rapidly increasing strength of the northerly wave system shoreward of the *Quest*.

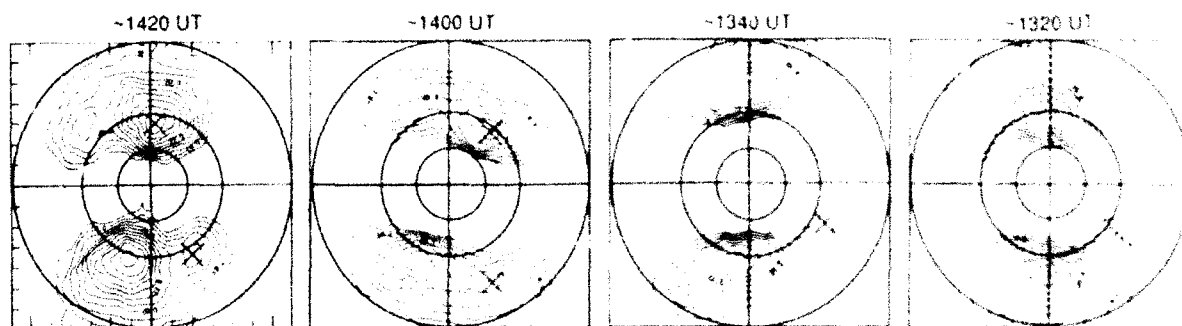
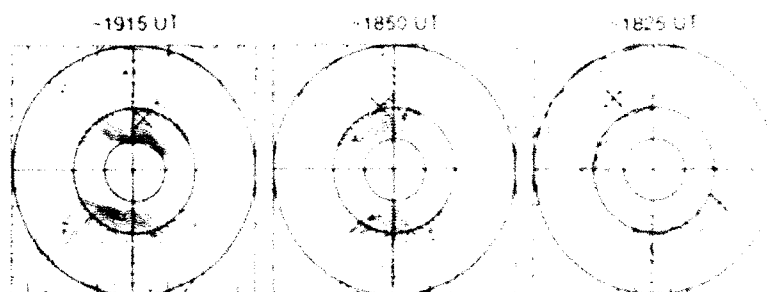


Figure 5. Same as Figure 3 except for 17 March. Note the evidence of two nearly opposing wave systems in the spatially evolving spectra.

west-propagating system increased by 2 dB. In the left spectrum, taken west of the *Quest*, the north-propagating system had diminished by 4 dB, while the west-traveling wave field had grown by another 2 dB, making it the stronger system at that position. A similar evolution is seen in the ROWS spectra.

The aircraft ground track for the middle spectrum in Figure 3 was to the north, and the ground tracks for the left and right spectra were to the south. The artifact lobes in the middle spectrum of Figure 3 were shifted significantly to the north (in the direction of the aircraft velocity vector) relative to the artifact lobes in the left and right spectra, as expected.

Figure 4 shows three spectra for the positions indicated by the solid circles in the 16 March plan view at the bottom (center) of Figure 2. The dominant wave system was propagating toward the south and was weakest near the *Tydemar* (right spectrum). Toward the west, the strength of the system increased, and the direction of propagation rotated clockwise. Two of the spectra suggest the presence of a weak secondary system propagating slightly north of west. The nearly coincident ROWS spectra show good agreement with the SCR.

Figure 5 shows four spectra from 17 March for the positions indicated by the solid circles at the bottom (right) of Figure 2. The Doppler-shift analysis suggests that the spectrum on the far right of Figure 5 (closest to the *Tydemar*) contained two wave systems of about equal wavelength propagating in opposite directions, one north, the other south. The south-propagating wave field became dominant and rotated clockwise as the aircraft progressed toward the west. The propagation direction for the north-traveling wave field rotated counterclock-

wise as the aircraft traveled toward the west. Thus, the two wave fields and their artifacts are quite clear in the two spectra on the left of the figure, but evident only in the subtle extrusions of the two spectra on the right.

Had the SCR ground track been toward the east instead of the west, each artifact in the spectrum on the right of Figure 5 would have been pushed toward the east, away from the real lobe of the other wave system instead of into it, which was seen for the westward track. For an eastward ground track, the lobes and their artifacts might have appeared distinct, even in the spectrum on the right of Figure 5.

The weak tertiary wave field that was observed briefly appears as an extrusion of the lowest contour in the second spectrum from the right in Figure 5.

IDENTIFYING PARTICULAR WAVE FIELDS

Figure 6 shows gnomonic projections in which radials from each observation point were extended in the reciprocal of the propagation direction. These extensions were used to see if source regions could be identified for the various wave fields. On 14 March, the north-propagating system appears to have been generated in the region around 44°N, 44°W. The west-propagating wave field appears to have been locally generated.

On 16 March, the south-propagating system appears to have originated near 54°N, 47°W; on 17 March, it shifted slightly eastward to 54°N, 46°W. Figure 6 suggests that the region of generation for the north-propagating system on 17 March was near 47°N, 46°W. The tertiary wave field briefly observed on 17 March, indi-

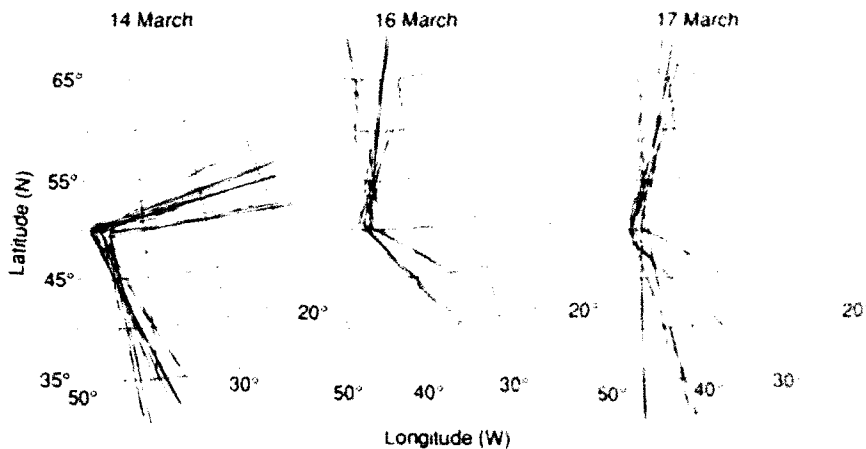


Figure 6. Gnomonic projections in which radials from each observation point are extended in the reciprocal of the propagation direction.

cated by the three radials diverging through 47.5°N , 40°W , appears to have been locally generated.

The radials in Figure 6 for the secondary wave system propagating toward the northwest on 16 March are ambiguous, probably because the secondary wave field was indistinct in the spectra (Fig. 4), thus making it difficult to determine where its peak was.

The top portions of Figure 2 show wavelength information for the primary (circles), secondary (squares), and tertiary (triangles) wave fields. The wavelength of the dominant wave system observed on 14 March was the longest during the three-day period. On both 14 and 16 March, a clear separation in wavelength between the dominant and secondary wave systems was observed, the secondary system having the shorter wavelength.

On 17 March, data from the wavelength (top) portion of Figure 2 to the west of 48°W , where the primary and secondary wave systems were distinct (see Fig. 5), suggest that the primary wave system had a slightly longer wavelength. The tertiary wave system had the shortest wavelength. To the east of 48°W on 17 March, the primary and secondary wave systems and their Doppler-shifted artifacts coalesced, and, therefore, the wavelength determination was not reliable. In that region, the dominant wave system had the longer wavelength on the north-northwest ground track, while the secondary system wavelength was longer on the two west-southwest ground tracks. This erroneous, abrupt interchange results from contamination by the Doppler-shifted artifacts.

COMPARING SPATIAL AND TEMPORAL WAVE MEASUREMENTS

Figure 7 presents an analysis of the effect of trying to compare the nearly simultaneous spatial measurements made by the airborne SCR with the *in situ* temporal measurements. The analysis, which used a log wave number versus linear time format, assumes that each wave component observed by the SCR at any location on a given day was part of a spatially homogeneous wave field that would be seen by the *in situ* sensors at both ship locations. This premise is not strictly correct, since Figure 6 indicates that the wave fields frequently diverged from nearby source regions and propagated at different

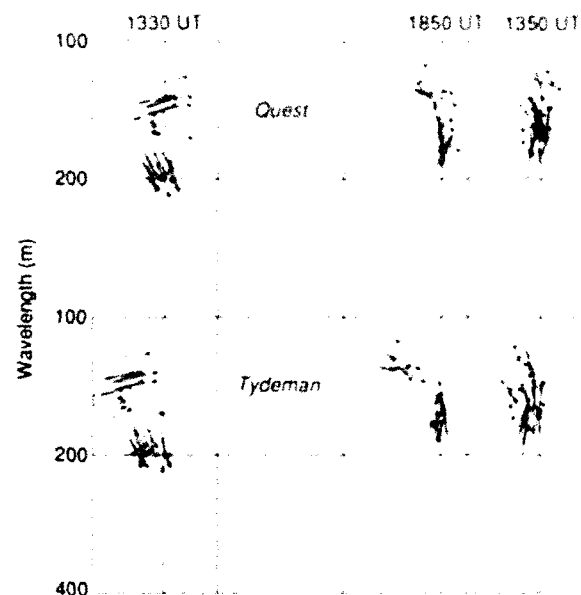


Figure 7. The times (circles) at which the *Quest* (top) and the *Tydeman* (bottom) would have observed a particular wave system measured by the SCR near the times indicated by the dashed vertical lines. Major vertical divisions are at 0000 UT on the days in March indicated. Radials extend from the circles to indicate the directions of propagation.

angles at the two ship locations. But the analysis still gives a sense of the problem involved in comparing spatial and temporal measurements.

The dashed vertical lines in Figure 7 indicate the average times of the SCR data acquisition intervals, which lasted for about one hour each day. The circles in Figure 7 show the times at which the *Quest* or the *Tydeman* would observe a particular wave system measured by the SCR. The radials extending from the circles indicate the directions of propagation, but not the strengths of the systems. The time difference between each SCR measurement and the projected ship observation was calculated using the direction of propagation and the group veloc-

ity. Figure 7 shows that the SCR observations of the west-propagating system on 14 March would have been spread out over about 13 hours in the *in situ* measurements made by the *Quest* and the *Tydemar*.

REFERENCES

- ¹ Kenney, J. E., Ulland, E. A., and Walsh, E. J., "The Surface Contour Radar: a Unique Remote Sensing Instrument," *IEEE Trans. Microwave Theory Tech.* **MTT-27**, 1080-1092 (1979).
- ² Walsh, E. J., Hancock, D. W., Hines, D. E., Swift, R. N., and Scott, J. F., "An Observation of the Directional Wave Spectrum Evolution from Shoreline to Fully Developed," *J. Phys. Oceanogr.* **19**, 670-690 (1989).
- ³ Walsh, E. J., Hancock, D. W., Hines, D. E., Swift, R. N., and Scott, J. F., "Directional Wave Spectra Measured with the Surface Contour Radar," *J. Phys. Oceanogr.* **15**, 566-592 (1985).

DIRECTIONAL SPECTRA FROM THE RADAR OCEAN WAVE SPECTROMETER DURING LEWEX

Directional wave-height spectra and mean surface roughness (wind vector) were estimated by using the airborne radar ocean wave spectrometer during the Labrador Sea Extreme Waves Experiment on 14-18 March 1987. The spectral estimates compare well with surface contour radar and buoy estimates. On all four days, the observed spectra exhibit a significant spatial evolution, which can be used to infer swell source regions.

INTRODUCTION

The NASA/Goddard Space Flight Center's radar ocean wave spectrometer (ROWS) is a 14-GHz noncoherent pulse-compression radar that has been used for several years to test the effectiveness of a potential satellite wave-measuring system.¹⁻³ Usually the ROWS is manually cycled between two modes, a spectrometer mode and an altimeter mode. The measurement geometries for the two modes are shown in Figures 1 and 2, respectively. In the spectrometer mode, surface reflectivity variations associated with surface wave tilts in the plane of incidence are sensed as a function of delay time or slant range through a low-gain, 6-rpm conically scanning antenna that has a 10° elevation by 4° azimuth beamwidth and is boresighted to 16° incidence. The slant-range resolution is about 2 m, and the nominal surface-range resolution is about 8 m around 13° incidence, the nominal angle of peak power return. At a nominal aircraft altitude of 6 to 7 km, the antenna footprint on the surface measures about 1 km in range and 500 m in azimuth. Thus at any instant the area illuminated by the (compressed) pulse is a strip measuring some 8 m in range and 500 m in azimuth. Electromagnetic wave and ocean Fourier wave component phase-front matching across the azimuthal extent of the illumination pattern provides the directional selectivity. A 3-dB angular spectral resolution varying between about 30° for a 300-m water wave and 17° for the shortest waves measured (24 m) is determined by the combination of finite footprint extent, wave-front curvature, and a 15° antenna movement during the 0.4-s pulse integration time. Corrections for wave-front curvature in the elevation plane are performed in the conversion from signal delay time to surface range, so the wave number resolution is determined solely by the finite, approximately 1200-m range extent of the antenna footprint.

During the Labrador Sea Extreme Waves Experiment (LEWEX), square-law-detected pulse-return data were recorded at 6-bit resolution, and spectra were computed off-line by one-dimensional fast Fourier transforms of normalized,* motion-corrected, rewindowed power re-

flectivity data for 15° azimuth bins.² Stable, full-resolution directional spectra with 70 to 120 degrees of freedom per elementary wave number and directional bin are produced by the following method: (1) correcting for the point target response, (2) subtracting a fading noise background, (3) averaging the turn-by-turn computed spectra for files consisting of some 18 to 30 antenna rotations (3- to 5-min files), and (4) averaging azimuth looks 180° apart to produce fully symmetrical wave number spectra. If $P_m(k, \phi)$ denotes the measured range reflectivity modulation-variance spectrum for a given 15° output azimuth bin, then the directional height-variance spectrum evaluated in that azimuth of look is determined according to the linear tilt model as

$$F(k, \phi) = [k\alpha(\phi)]^{-1} P_m(k, \phi) \quad (1)$$

where F is in units of m^3/rad , ϕ is the azimuth angle, and α is the sensitivity coefficient given by

$$\alpha(\phi) = (\sqrt{2\pi}/L_\phi)(\cot \theta - \partial(\ln \sigma^0)/\partial \theta)|_{\theta=\theta_0} \quad (2)$$

where L_ϕ is the azimuth footprint dimension (1-sigma value), σ^0 is the mean surface cross section, and $\theta = 13^\circ$ is the nominal incidence angle for peak power return, which is determined by the antenna gain pattern and the cross-section variation near nadir. In the quasi-specular backscatter regime near nadir, the surface cross section is proportional to the effective Ku-band slope probability density function (pdf), and the cross-section roll-off in the case of an isotropic, Gaussian slope pdf becomes $\partial(\ln \sigma^0)/\partial \theta = -\tan \theta/s^2$, where s^2 is the mean square slope (MSS) parameter. In the following, spectra are shown assuming a unit, isotropic $\alpha = 1 \text{ m}^{-1}$. In general, cross-

*Normalization of the pulse return data is accomplished by dividing the return by estimates of the average power profile (proportional to the product of antenna pattern and cross-section variation), which is computed for each 15° sector according to a least-squares cubic spline algorithm between 5% threshold points. Data so normalized contain virtually no low frequency (near DC) power.

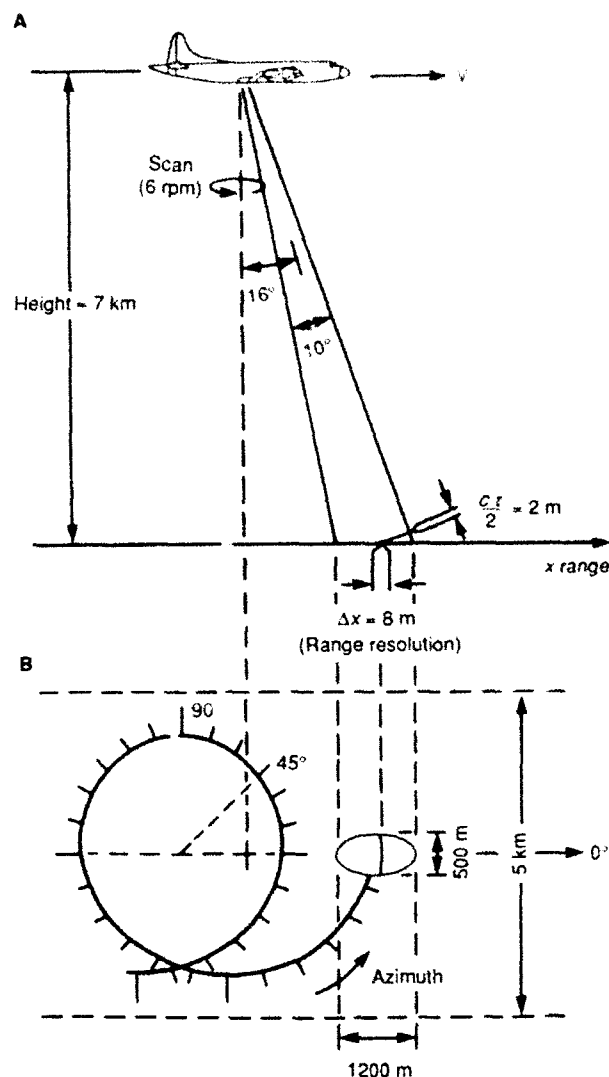


Figure 1. Measurement geometry of ROWS in the spectrometer mode. **A.** Elevation view. **B.** Plan view. V is the P-3's mean velocity and $c\tau/2$ is the slant-range resolution.

wind to along-wind MSS component ratios seldom are less than 0.8, and so the assumption of an isotropic α involves, at most, an error of 25%, or about 1 dB in the relative weighting of spectral components lying 90° to each other.

A measured MSS from the ROWS altimeter mode often is used to compute an equivalent isotropic α (see Fig. 2). Average power data from the ROWS spectrometer mode also are used to derive an MSS value; however, these data usually are used only to establish the principal component ratio and the major axis direction.

LEWEX DATA

The flight profile of the NASA P-3, which carried both the ROWS and the surface contour radar (SCR) during LEWEX, involved ascending to a nominal ROWS operating altitude of 6200 to 6400 m and flying along the 50th parallel between 50°W and 45°W . Except on the last

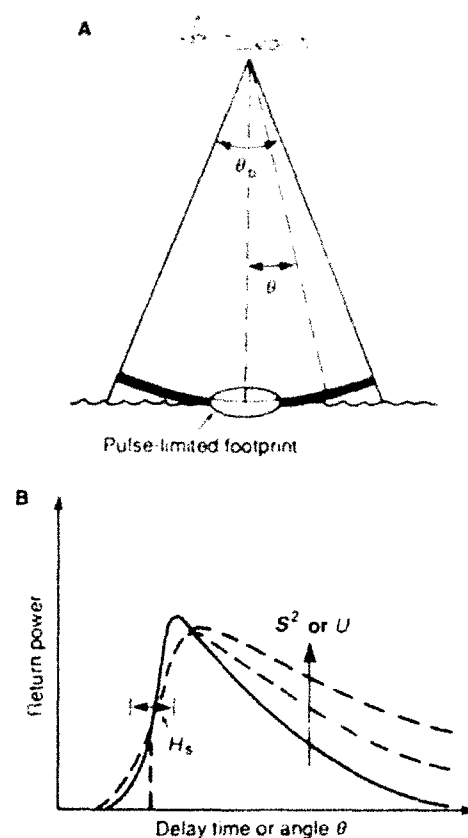


Figure 2. Measurement geometry of ROWS in the altimeter mode. **A.** Elevation view; θ is the nominal incidence angle for peak power return. **B.** Schematic of altimeter waveform; S^2 is the mean square of the slope, U is the wind speed, and H_s is the significant wave height.

flight day, when the SCR was not operated, the P-3 descended to the SCR operating altitude after flying over HNLMS *Tydemar* at 45°W . On the last day, 18 March, transit home was initiated from the *Tydemar*, precluding the collection of data from the SCR.

Table 1 summarizes the ROWS altimeter mode and rotating-antenna spectrometer mode data for LEWEX. Figure 3 shows selected ROWS directional spectra for each of the four flight days. Each spectrum is computed assuming a unit isotropic $\alpha = 1 \text{ m}^{-1}$ according to Equation 1; the contouring for all spectra except the rightmost in Figure 3A is in eight 1-dB steps down from the peak value. The data presentation is thus in identical units and directly comparable to the SCR data presented by Walsh (Figs. 3-5) elsewhere in this volume. As an indication of the excellent agreement between the ROWS and SCR spectra, colored overlays of some corresponding SCR spectral estimates are shown on Figure 3.

The quality of the ROWS data was generally good during LEWEX. An error in the ROWS software for the azimuth reckoning was discovered and corrected. The LEWEX mission data are thus more reliable directionally than data from any previous mission. The ROWS suffered from several of the usual problems associated with an old data acquisition system. Blank pulse records, which

Table 1. Summary of rows data. Shaded rows have corresponding spectra shown in Figure 3.

Flight no.	Tape/ file no.	Mode	H_s^* (m)	ALT MSS	α (m^{-1})	ROT H_s (m)	ALT H_s (m)	U_{10N} (m/s)	Noise floor ratio	Comments
1 (14 Mar)	2/2	ROT	9.17	0.0271	6.46	3.61	—	—	1.01	
	3/1	ALT	—	0.0271	—	—	5.57	5.86	—	
	3/2	ROT	8.94	0.0271	6.44	3.53	—	—	0.89	(over the Quest)
	3/3	ALT	—	0.0260	—	—	4.96	5.40	—	
	3/4	ROT	10.58	0.0260	6.87	4.04	—	—	1.03	
	3/5	ALT	—	0.0267	—	—	3.75	5.71	—	
	4/1	ROT	8.92	0.0267	6.54	3.49	—	—	1.03	(over the Tydeman)
2 (16 Mar)	1/4	ALT	—	0.0395	—	—	3.93	11.04	—	
	1/5	ROT	9.16	0.0395	3.58	4.84	—	—	1.30	
	2/1	ROT	8.66	0.0416	3.31	4.76	—	—	1.34	
	2/2	ALT	—	0.0416	—	—	3.95	11.92	—	
	2/3	ROT	9.27	0.0399	3.51	4.95	—	—	1.43	
	2/4	ALT	—	0.0399	—	—	3.00	11.22	—	
	3/1	ROT	8.01	0.0376	3.83	4.10	—	—	1.28	(over the Quest)
	3/2	ALT	—	0.0376	—	—	3.43	10.25	—	
	3/3	ROT	7.57	0.0376	3.82	3.87	—	—	1.23	
	4/1	ALT	—	0.0341	—	—	3.61	8.77	—	
	4/2	ROT	5.79	0.0341	4.42	2.75	—	—	0.81	
	4/3	ROT	6.19	0.0319	4.89	2.80	—	—	1.06	
	4/4	ALT	—	0.0319	—	—	2.44	7.88	—	
	5/2	ROT	8.70	0.0319	4.89	3.93	—	—	1.54	(over the Tydeman)
	8/1	ALT	—	0.0431	—	—	5.98	12.54	—	P-3 turning
	8/2	ROT	6.80	0.0431	3.33	3.73	—	—	0.72	
	8/3	ALT	—	0.0457	—	—	6.45	13.61	—	Going into ice
	8/4	ROT	10.36	0.0457	3.07	5.91	—	—	1.20	
3 (17 Mar)	1/2	ALT	—	0.0399	—	—	5.18	11.21	—	
	1/3	ROT	10.42	0.0399	3.64	5.47	—	—	1.12	
	1/4	ALT	—	0.0392	—	—	6.42	10.91	—	
	1/5	ROT	10.11	0.0392	3.72	5.24	—	—	1.05	
	2/1	ALT	—	0.0362	—	—	5.86	9.68	—	
	2/2	ROT	10.17	0.0362	4.13	5.00	—	—	1.25	
	2/3	ALT	—	0.0343	—	—	5.05	8.87	—	
	2/4	ROT	8.77	0.0343	4.47	4.15	—	—	1.07	(over the Quest)
	3/1	ROT	9.40	0.0266	6.60	3.66	—	—	1.17	
	3/2	ALT	—	0.0266	—	—	4.53	5.68	—	
	3/3	ROT	9.40	0.0257	6.98	3.56	—	—	1.32	
	3/4	ALT	—	0.0257	—	—	5.29	5.28	—	
	4/1	ROT	9.96	0.0305	5.28	4.33	—	—	1.47	(over the Tydeman)
	4/2	ALT	—	0.0305	—	—	5.19	7.29	—	
	7/1	ALT	—	0.0444	—	—	4.97	13.10	—	
	7/2	ROT	8.42	0.0444	2.97	4.89	—	—	0.99	
4 (18 Mar)	2/1	ROT	7.68	0.0294	5.51	3.27	—	—	1.04	(over the Quest)
	2/2	ALT	—	0.0294	—	—	3.98	6.85	—	
	2/3	ROT	8.25	0.0282	5.89	3.40	—	—	1.04	
	2/4	ALT	—	0.0282	—	—	5.51	6.34	—	
	3/1	ROT	8.75	0.0289	5.67	3.68	—	—	1.10	(over the Tydeman)
	3/2	ALT	—	0.0289	—	—	6.57	6.61	—	P-3 turning
	3/3	ROT	8.54	0.0289	5.67	3.59	—	—	1.00	
	4/2	ROT	7.72	0.0284	5.56	3.27	—	—	0.98	
	4/3	ROT	6.83	0.0284	5.58	2.89	—	—	0.98	
	4/4	ALT	—	0.0284	—	—	3.63	6.41	—	

Note: ROT = rotating-antenna spectrometer mode; ALT = altimeter mode; H_s^* = H_s for unit $\alpha = 1 m^{-1}$; α = sensitivity coefficient defined by Equation 1; and U_{10N} = 10-m height wind speeds, as defined by Equation 5.

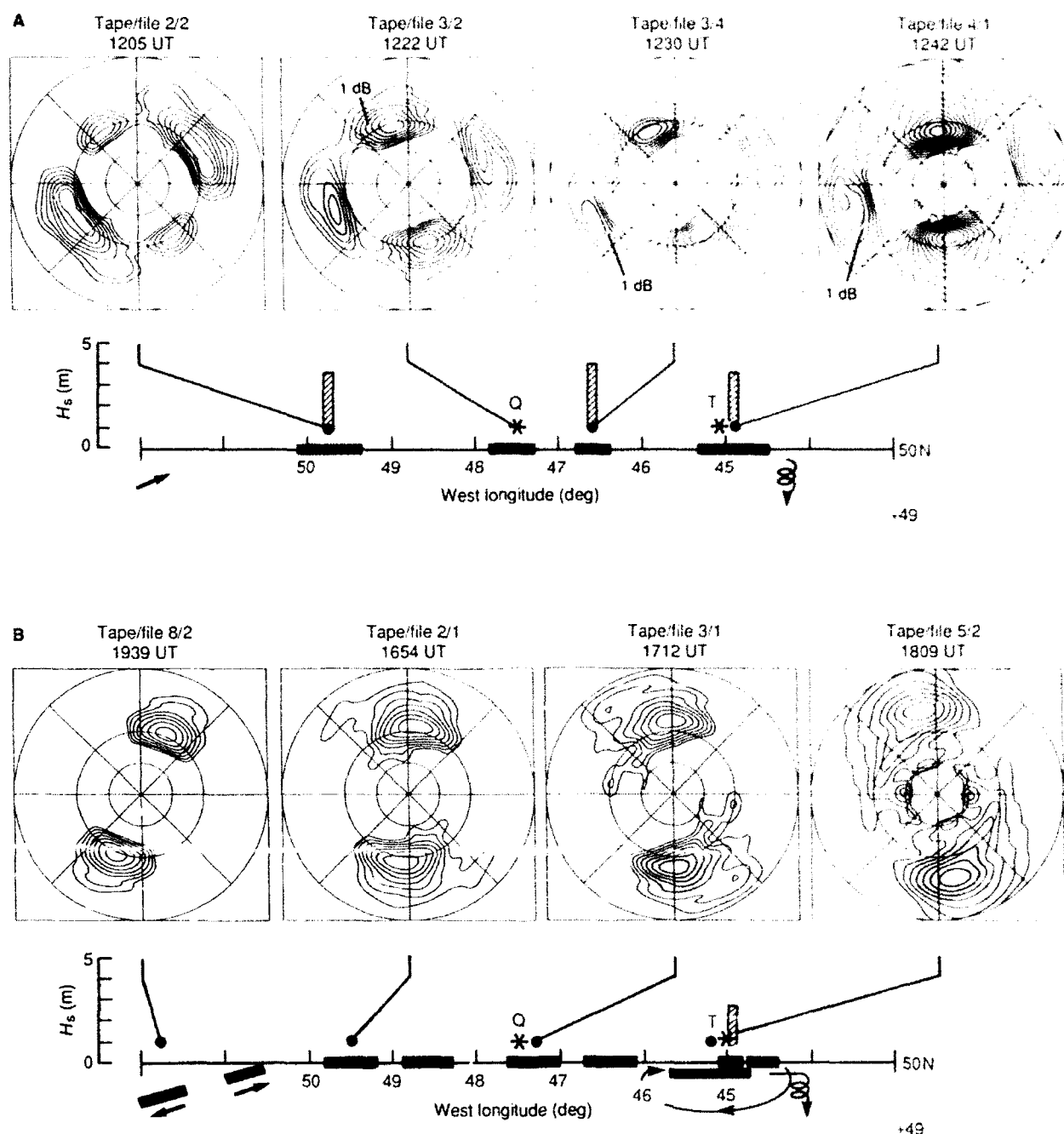


Figure 3. Selected rows directional height-variance spectra in m^3/rad , with all spectra contoured in eight 1-dB steps down from the peak value, except for the rightmost spectrum in 3A, which has thirteen 1-dB steps. Numerals such as 2/1 above the individual spectra are the original flight tape and file numbers, and the center time of each data period is as indicated. The outermost wave number ring corresponds to a 100-m wavelength, the inner rings to 200- and 400-m wavelengths. Figures A, B, C, and D show data for 14, 16, 17, and 18 March, respectively. The horizontal solid bars below the spectra indicate the appropriate file locations; the asterisks denote the positions of the *Quest* (Q) and the *Tydeman* (T); and the hatched vertical bars indicate the significant wave height computed from the individual spectra. Overlays of corresponding (≤ 60 km; ≤ 2 h) SCR spectra from Walsh (this volume) are shown at 3-dB contours (major modes) and 1-dB contours (minor modes). (Figure is continued on the next page.)

averaged about 50% of the 100-pps data frames, were accounted for in the computation of the residual background Rayleigh fading noise spectrum level. However, a departure from the predicted noise background charac-

teristics resulted from quantization noise caused by lower-than-desired levels of signal input to the digitizer. This affects particularly the data on 16 March, as can be seen from Table 1 by referring to the column labeled

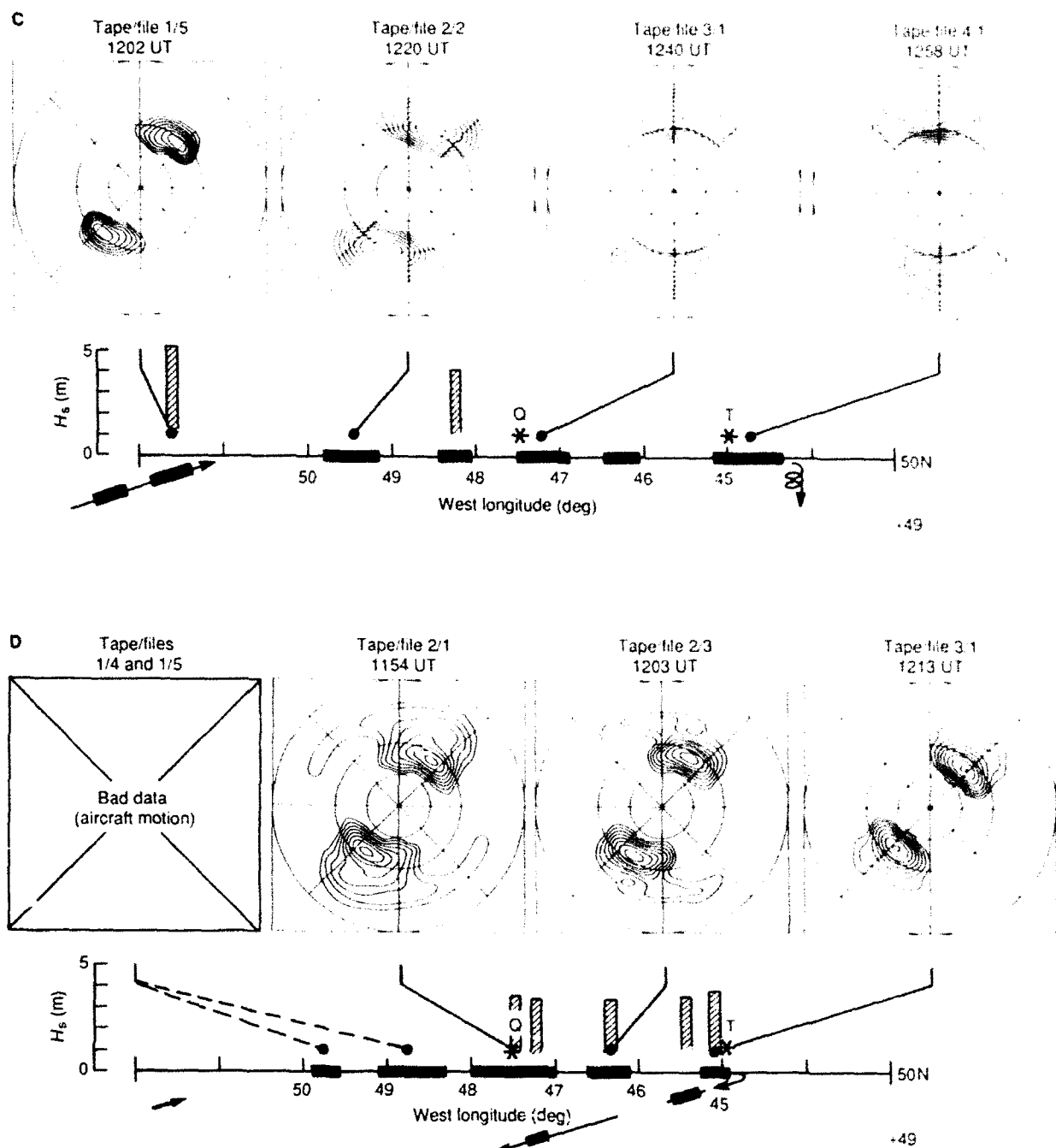


Figure 3. (continued).

noise floor ratio, which gives the ratio of the observed minimum in the directionally integrated spectral intensity to the value of the computed noise floor,¹

$$P_w = (\sqrt{2\pi} K_p N_p)^{-1}, \quad (3)$$

where the 1-sigma value of $K_p = 0.21$ rad/m corresponds to a 8.1-m surface range resolution, and N_p is the number of independent (nonblank) pulses entering into the pulse integration for any 15° azimuth bin (max $N_p = 42$). That the variation of the noise floor ratio in Table 1 is indeed related to quantization noise can

be adduced from the data of Figure 4, which show the noise floor ratio R_N plotted as a function of the observed minimum in the peak return power over all antenna rotations for each rotating-antenna file in Table 1. The distribution of R_N follows roughly a log normal distribution. Values of $R_N \approx 1.0$ result from minimum observed peak powers of 2 to 3 units out of a maximum of 63 units. Lower values of R_N approaching a possible limit around 0.6 indicate that the actual noise floor may lie below the nominal computed value; however, to compare with the original training data set,¹ we will reject for the moment any data for which R_N departs by

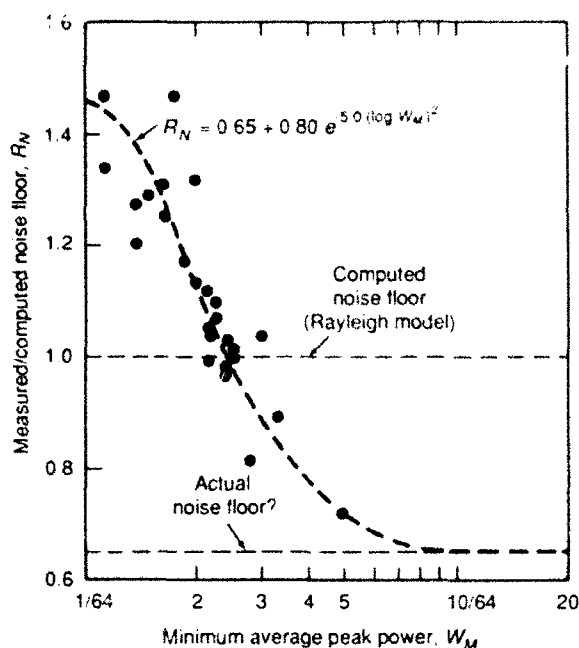


Figure 4. Ratio of measured to computed background noise levels versus the observed minimum in the peak power return over all antenna rotations for all LEWEX files.

more than $\pm 10\%$ from unity. For the several files satisfying this criterion, the significant wave height H_s computed according to

$$H_s = 4 \left[\int_0^{K_N} \int_0^{2\pi} F(k, \phi) dk d\phi \right]^{1/2}, \quad (4)$$

where the Nyquist wave number, $K_N = 2\pi/(24 \text{ m})$, agrees well with buoy-observed H_s at the *Tydemian* and the *Quest*. The wave height inferred from the leading edge of the altimeter mode return shown in Table 1 often disagrees significantly from adjacent rotating-antenna spectrometer mode files; this may be caused by an erratic triggering of the digitizer. The equivalent neutral stability, 10-m height wind speeds U_{10N} (in m/s) shown in Table 1 were derived from the altimeter-mode waveform trailing-edge MSS data, s^2 , according to the algorithm³

$$U_{10N} = 455 s^2 - 7.27. \quad (5)$$

All wind speeds except those for 14 March 1987 compare favorably with ship and buoy data; on 14 March the wind speeds appear to be too low. Because only the seas for 14 March exhibit significant bimodality, we analyzed the average power data (by a Gaussian specular point model fit) from the spectrometer mode on this day to assess the effect of slope distribution anisotropy on the measured spectra. The results are summarized in Table 2. The data are consistent with a 180° wind shift between 50°W and 45°W and isotropic total roughness conditions between the *Quest* and the *Tydemian*, where the MSS is a minimum. Not only is there a bias between the MSS values inferred from the altimeter and spectrom-

Table 2. Analysis of average power data from the spectrometer mode of ROWS for 14 March

Flight tape/file no.	Major axis direction ($^\circ\text{T}$)	Mean square slope (MSS)	Minor-major axis ratio
2-2	$3^\circ (\pm 180^\circ)$	0.044	0.78
3-2	$21^\circ (\pm 180^\circ)$	0.038	0.89
3-4	—	0.034	0.97
4-1	$0^\circ (\pm 180^\circ)$	0.042	0.82

eter modes, but we note that, curiously, the altimeter mode MSS values in Table 1 do not show the same variability as the spectrometer mode MSS values in Table 2.

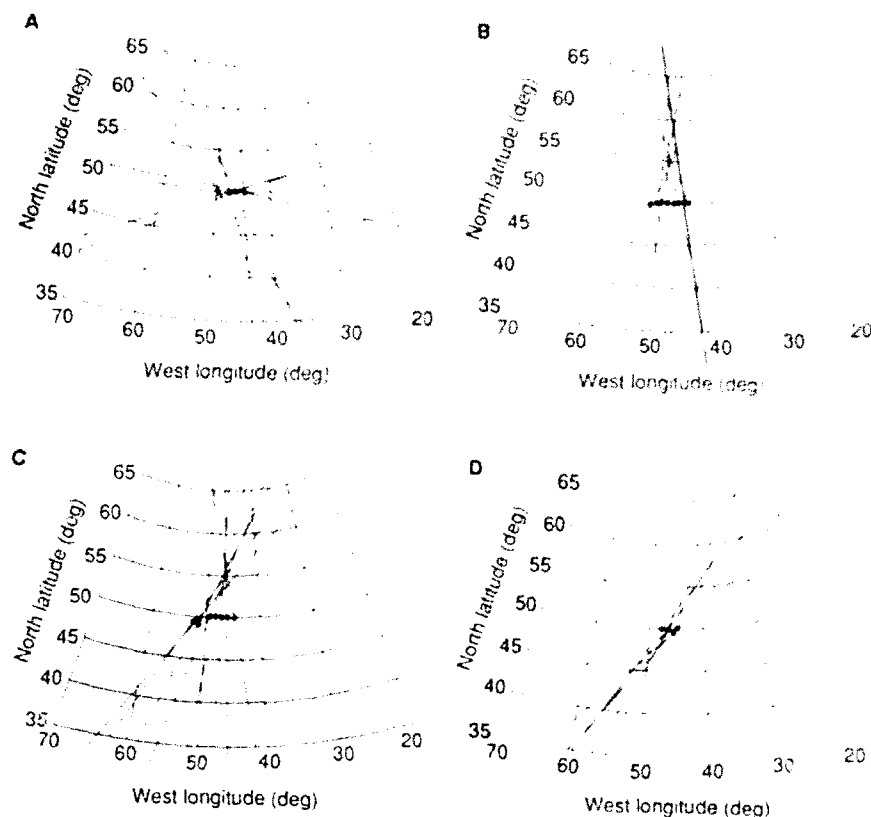
Figure 5 shows the ray characteristics on a gnomonic projection, in which great-circle routes map into straight lines, for the modes of the principal systems observed in the 28 files of rows spectrometer mode data over the four flight days. Regions of convergence of the characteristics indicative of wave generation regions are seen on all four days.

DISCUSSION

Comparison of the rows spectra in Figures 3A to 3C with SCR spectra for 14, 16, and 17 March (from the article by Walsh elsewhere in this volume) shows quite good agreement, particularly for those files near the *Tydemian* where the time difference between rows and SCR data takes was no more than 25 min. Modal directions and wave numbers as measured by the rows and SCR differ by no more than a few degrees and a few percent. Generally good agreement was seen between the rows spectra and Wavescan spectra at the *Tydemian* as well. The spatial evolution of the bimodal spectrum on 14 March is seen to be quite similar in both rows and SCR data. At the *Tydemian*, the spectral peak of the northward-traveling swell system (with the generating region to the southeast, according to Figure 5A) is about 6 dB above the peak of the more locally generated westward-traveling system, in agreement with the SCR data. By 50°W , the situation is reversed, with the peak of the westward-traveling system being some 3 to 4 dB above the northward-traveling system, as compared with a similar difference of some 2 dB in the westernmost SCR spectrum.

This spatial evolution is fairly well mirrored in the temporal evolution recorded by the Wavescan buoy (cf., Gerling, Fig. 4C, this volume). We should note that, as mentioned above, use of an anisotropic α amounts to no more than a 1-dB difference in weighting between systems running at 90° to each other. For this small difference one cannot really judge by differences in peak values, say between the rows and the SCR modes, because the different system resolution can affect the measured peak values. To really test the rows linear response model of Equations 1 and 2, one should compare the variances in the different modes rather than the

Figure 5. Great-circle ray traces of swell wave packets for the four flight days on a gnomonic projection: **A** 14 March, **B** 16 March, **C** 17 March, **D** 18 March. The small dots represent the locations of the ROWS spectra.



peak values, using the dissection method of Gerling (this volume), for example. Nevertheless, a qualitative comparison had by overlaying ROWS and SCR spectra shows remarkably good agreement between these two very different remote sensing systems. A comparison of ROWS, SCR, and SAR (synthetic aperture radar) spectra for 14 March is illustrated in Figure 4 of Tilley (this volume). Tilley shows good agreement among all three sensing systems when the SAR is employed in a low range-to-velocity geometry.

On 16 March at about 1800 UT, the spatially evolving ROWS spectra (cf. Figure 3B) indicate that the dominant swell system originates to the north somewhere between 55°N and 63°N (cf. Figure 5B). Comparison of tape/file 5/2 over the *Tydemán* with the SCR file over the *Tydemán* and with Wavescan data shows excellent agreement among all three instruments, except that the Wavescan spectrum appears to be rotated counterclockwise by about 15° with respect to the ROWS and SCR spectra (see Esteva, Fig. 3, this volume). In addition to the main southward-traveling swell, one sees the WNW-traveling component in the symmetrical ROWS spectrum as an extrusion of the main system extending toward the 200-m wave number ring and 270° azimuth.

On 17 March, the opposing wave systems at nearly the identical frequency seen in the Wavescan spectra at

Tydemán appear as a single northward- or southward-traveling system in the symmetrical ROWS spectra in Figure 3C. Overlaying the ROWS file 4/1 spectrum at the *Tydemán* with the corresponding (rightmost) SCR spectrum in Figure 5 from the article by Walsh elsewhere in this volume produces excellent agreement for the north-directed SCR lobe; however, at the *Quest* the southward-traveling SCR spectral lobe is found to match the ROWS file 3/1 spectrum. From the spatial evolution of the ROWS spectra it would appear that the dominant system is south-traveling, having originated around 55°N, 46°W (Fig. 5C).

On 18 March, the spatial evolution of the ROWS spectra in Figure 3D indicates unambiguously that the 200-m-plus wavelength swell system has its origin to the southwest (Fig. 5D). This is consistent with Wavescan data at the *Tydemán*.

REFERENCES

- Jackson, F. C., Walton, W. T., and Baker, P. L., "Aircraft and Satellite Measurement of Ocean Wave Directional Spectra Using Scanning Beam Microwave Radars," *J. Geophys. Res.* **90**, 987-1004 (1985).
- Jackson, F. C., Walton, W. T., and Peng, C. Y., "A Comparison of in Situ and Airborne Radar Measurements of Ocean Wave Directionality," *J. Geophys. Res.* **90**, 1005-1018 (1985).
- Jackson, F. C., "The Radar Ocean Wave Spectrometer," in *Measuring Ocean Waves from Space*, Johns Hopkins APL Tech. Digest **8**(1), 116-127 (1987).

SAR IMAGING OF OCEAN WAVES: SOME OBSERVATIONS FROM LIMEX/LEWEX '87

We examine synthetic aperture radar (SAR) performance for observation of ocean waves. Our results are based on analysis of airborne SAR data collected during the Labrador Sea Ice Margin Experiment and the Labrador Sea Extreme Waves Experiment, and on theoretical predictions. The data sets include both open-water waves and waves moving under a floating ice field.

INTRODUCTION

The use of synthetic aperture radar (SAR) imaging systems for quantitative observations of ocean waves depends on two principal considerations: first, the radiometric response of the instrument to the scene with an objective to estimate sea surface roughness and eventually wave height and, second, geometric fidelity in the SAR image so that wave directional spectra can be obtained. Both of these aspects of SAR imaging in the ocean context are under active investigation. Using analysis together with SAR data gathered during the Labrador Sea Ice Margin Experiment (LIMEX) and Labrador Sea Extreme Waves Experiment (LEWEX) 1987 programs, progress has been made in both areas. This paper summarizes some key aspects of the problems associated with using SAR imaging to characterize ocean waves.

A SAR is an elegant imaging system in which extensive processing of the signal received by the radar is used to achieve very fine azimuth (along track) resolution without the necessity for a correspondingly large antenna aperture. For real-aperture, side-looking radars, the azimuth resolution is determined by an antenna which produces a diffraction-limited beam. For such an antenna of length D using radar wavelength λ , the azimuth resolution is approximately $R\lambda/D$ at distance R along the radar line-of-sight, the slant range. Considering the airborne case, for azimuth resolutions on the order of meters to be achieved at ranges of several kilometers, a real aperture radar would require an antenna hundreds of meters long. Clearly, this is not practical. For a SAR, however, the best azimuth resolution is simply one-half of the aperture length itself, or $D/2$. The technique is well suited to systems carried on aircraft and also extends to spacecraft systems.

Fine azimuth resolution using a SAR depends on processing a sequence of radar observations of the scene reflectivity. For such processing, each scatterer must maintain a constant relative phase at the radar wavelength, and the relative motion between the scene and the sensor must be determined by the motion of the sensor. Under these conditions, each scattering element in the scene is coded by a known frequency shift, the Doppler effect. (Processing over the Doppler spectrum of the radar signal is analogous to the way in which a lens focuses an optical signal.)

A SAR is a range-Doppler imaging system; it works very well for terrestrial scatterers that are not themselves in motion. The dynamics of the ocean's surface, however, complicate the imaging properties of a SAR considerably. Fortunately, ocean movement is generally characterized by relative scatterer velocities that are much smaller than that of the radar platform, so the resulting image may be seen as a degraded version of what would be obtained under ideal static scene conditions. Modeling and understanding the subtleties of SAR ocean imaging is an active area of research. The objective of this research is to quantify the way in which the principal surface motions influence SAR image formation.

Two classes of ocean dynamics need to be considered: coherent and noncoherent. Coherent motions are those that impact the relative phase of the scatterer as observed by the radar, either through a change in the phase of the scattering element itself, or through a change in the Doppler modulation caused by scatterer movement. Scattering elements consist of groups of very small waves on the surface whose spatial scale is on the order of the radar illumination wavelength, typically a few centimeters. These wavelets have very small intrinsic velocities but are advected appreciably by the orbital motions of passing longer waves. Furthermore, wave-wave interactions (hydrodynamic modulation) may modify the ensemble of wavelets within the scattering element, thus changing the phase of the returned signal. The imposed orbital velocity reflects the large-scale organization of the wave field. It leads to systematic shifts of scattering elements within the image and thus an expression of the longer wave in a process termed "velocity bunching." This is in general a nonlinear process and leads to important considerations in the image modeling problem. Ensembles of orbital velocities together with scatterer phase changes lead to degradation of the time over which the signal can be coherently integrated in the processor. This constraint reduces the ability of the image to support along-track (azimuth) wave directional spectral analysis.

Noncoherent motions are those that impact image fidelity through means other than phase modulation. The most important of these is the gross movement of the wave field during the time of SAR observation. It has been shown that the wave phase velocity is significant

when compared with the velocity of most airborne radars. Resulting effects are both beneficial and detrimental. Phase velocity is helpful since it allows determination of the actual direction of wave movement in image spectral analysis, rather than the conventionally obtained result having a 180° directional ambiguity. It is not helpful in the sense that it has confused past attempts to understand the SAR wave imaging process, particularly with respect to the image focus. (These issues are discussed further in later sections of this article and in Ref. 1.)

When a SAR images open-ocean waves, all of the dynamic effects are present simultaneously, which complicates the task of comparing theory with observation. LIMEX and LEWEX, conducted in March 1987, offered the opportunity of using airborne SAR to image known surface gravity waves in both the open ocean and penetrating into floating ice.^{2,3} The presence of floating ice suppresses part of the surface dynamics, thus providing unique experimental conditions for observing and logically separating key parametric aspects of the SAR imaging process.

RADIOMETRIC RESPONSE

A correctly implemented and calibrated SAR should behave as an "imaging scatterometer." The SAR system includes the actual image processor and image spectral analysis procedures. To reduce the multiplicative noise known as speckle (which arises in any coherent imaging system), several statistically independent subimages, called looks, are normally formed and added. To preserve estimates of mean ocean reflectivity that can be calibrated, the SAR system should be implemented in an energy-conserving mode.^{4,5} In this approach, individual looks are subjected to magnitude-squared detection before summation to form the multilook image. One spectral analysis approach for such a SAR processor is the magnitude of the SAR image Fourier transform.* The mean reflectivity is then equal to the "DC digital number" in the Fourier transform domain.

The proposed processing combination preserves the mean scene reflectivity through to the spectral domain. Normalization of the spectrum by the DC digital number quantitatively expresses the relative image contrast in the directional spectral domain as a function of (vector) wave number. In this way, radar radiometric response is retained in the wave spectral measure.

It remains to relate the reflectivity variance to useful geophysical properties such as ocean wave height. Such a relationship requires understanding and modeling of the factors that govern wave reflectivity: hydrodynamic modulation, tilt modulation, velocity bunching, and coherence time limitations. Such a relationship has not yet been robustly demonstrated.

*The Fourier transform magnitude (not squared) is proposed for the image spectral analysis. Many conventional SAR processors sum the square root of the look-image powers, while some conventional spectral analyses use the square of the Fourier transform magnitude. Some combinations may not be energy conserving. The proposed detection combination, however, may have a detrimental effect on the spectral peak-to-background ratio.

IMAGE FIDELITY

We now examine the much broader topic of spatial fidelity. The key is the time dependency of a SAR's response to a dynamic ocean wave field. We include both coherent and noncoherent issues. Table 1 summarizes the key parameters introduced in this section.

Consider the case of ocean waves penetrating the marginal ice zone. The ice cover acts as a natural low-pass filter: the longer wavelengths survive, whereas waves shorter than the average ice floe size are suppressed. Our objective is to study SAR response to the longer waves. The circumstances of waves penetrating floating ice provide an ideal situation. In this case, velocity bunching is the dominant azimuth wave imaging mechanism. Understanding the importance of various imaging factors through observation of "waves in ice" is the subject of ongoing work.

Coherent Time Dependence

Velocity bunching plays a major role in the SAR image formation process for a wave with an azimuthal wave number component. Most analyses of velocity bunching are expressed in terms of the range-to-velocity ratio. Although velocity bunching arises from the coherent properties of the Doppler domain, it is a purely geometric effect in the sense that it is not proportional to the SAR coherent integration time. We prefer to express such geometric image properties in terms of the SAR dwell constant

$$T_H = \frac{h}{V} \quad (1)$$

where h is the sensor altitude above nadir, and V is the component of the platform velocity parallel to the Earth's surface.

Variations in velocity bunching occur as a function of the local incidence angle and the wave aspect angle. The first-order form for velocity-bunching mapping is given by Equation 1 in Vachon et al. (this volume). That expression shows that, when velocity bunching has a role in the image formation process, the effective scatterer density is a function of certain geometrically dependent factors only. Also, when singularities occur, the image is dominated by the sum of wave-amplitude-dependent terms. This represents a (highly) nonlinear mapping

Table 1. SAR/wave performance parameters

SAR dwell constant	$T_H = h/V$	seconds
One-look integration time	$T_I = R\lambda/2p_s V$	seconds
Integration time constant	$T_R = R/V$	seconds
Coherence time	$\tau = \lambda/2\sqrt{H}$	seconds
Exposure time	$T_A = T_R \sin(\beta)$	seconds
Relative phase velocity	$dC_0 = C_0/V \cos \theta$	
Scale perturbation	$S = (1 - dC_0)$	
Coherence factor	$V \propto 1 + (T_I/\tau)^2$	

transformation. The resulting image depends on the interplay between wave height, wave number, wave direction, SAR viewing geometry, and sensor flight direction. We were able to investigate several different combinations of these parameters using SAR data from LIMEX/LEWEX.

The single-look SAR coherent integration time is

$$T_L = \frac{R\lambda}{2\rho_1 V}, \quad (2)$$

where λ is the radar wavelength, ρ_1 is the single-look resolution, and R is the scene slant range. Note that the integration time is proportional to

$$T_R \propto \frac{R}{V}, \quad (3)$$

which denotes the radar integration time constant. In contrast with the SAR dwell time constant, this time constant is appropriate for system considerations that are time dependent in proportion to radar slant range.

For example, a scene coherence time τ that is less than T_L results in reduced azimuth wave response.⁴ This has been characterized by Monaldo and Lyzenga⁶ as an "azimuth cutoff," which is expressed in terms of the R/V ratio. If the minimum detectable ocean wavelength is taken as two azimuth resolution cells, Monaldo and Lyzenga's minimum wavelength expression may be used to find

$$\tau \approx \frac{\lambda}{2\sqrt{H_s}} \text{ (s)}, \quad (4)$$

where H_s is the significant wave height.

At this stage, the distinction between the dwell constant and the integration constant may appear to be frivolous. We wish to emphasize, however, that they play different roles in the SAR wave-imaging problem. Measurements using LIMEX waves-in-ice data³ show that wave-image contrast *increases* with increasing incidence angle, consistent with velocity-bunching predictions in the absence of coherence time limitations. When coherence time is included in the model,⁷ an additional coherence factor of

$$\frac{1}{\sqrt{1 + (T_L/\tau)^2}} \quad (5)$$

must enter the formulation. This effect has been modeled as an azimuth-oriented, low-pass-filtering operation on the image spectrum, with the cutoff wavelength defined by the coherence factor given in Equation 5. This model fails, however, in the face of a velocity-bunching imaging mechanism. Nonlinearities cause the generation of false spectral modes, often characterized by very long wavelengths.⁵ These modes would not be removed by such a low-pass-filter coherence time model.

An experiment could be designed to take advantage of certain geometric properties of velocity bunching. By gathering wave data for the aircraft velocity in both the same direction as the wave velocity, and opposed to it, the image responses could be compared, and the relative contribution of the nonlinear velocity-bunching component estimated. Image contrast resulting from other mechanisms would constitute the remainder. The approach should be qualified with waves-in-ice data, then applied to the open-water case. The first-order effects should not depend on coherence time limitations.

Noncoherent Time Dependence

The wave phase velocity is of fundamental importance in the SAR wave-imaging problem.⁷ The principal consequences of the wave phase velocity are an along-track scale (scanning) distortion and a misregistration between successive looks leading to a decrease in wave contrast. The look misregistration has benefits: it leads to "spectral-sum" processing and the opportunity to remove the directional ambiguity. We now have experimental results from LIMEX/LEWEX data that support each of these issues and are consistent with earlier predictions.

Scale Distortion. Consider a wave field moving at phase speed C_0 and in the direction ϕ relative to the along-track vector of an observing scanning sensor moving with speed V . The resulting image will have a scale error along track given by

$$S = \left[1 - \frac{C_0}{V \cos \phi} \right]. \quad (6)$$

The effect is significant for most aircraft-imaging geometries but is negligible for most satellite-imaging situations.

The scale distortion of Equation 6 may be uniquely compensated in the two-dimensional wave number domain. This compensation, in conjunction with two opposing passes of SAR imagery, may be used to resolve wave propagation direction. Such an approach is cumbersome, however, and may be used only to the extent the ocean waves being observed are uncomplicated, and if the two SAR passes exist. This technique is demonstrated in Figure 1. An alternate method is discussed in a later section ("Removal of Directional Ambiguity").

Spectral-Sum Processing. An important corollary of scale distortion is that the scene reflectivity pattern moves during SAR observation. For a SAR, the data required to form the total multilook image may be gathered over an interval T_N of several seconds from each spatial position in the scene. We introduce the total exposure time T_N as the product of the integration time constant T_R and the angular extent $\sin(\beta)$ over which the SAR beam(s) gather data for the image looks. For a moving scene, individual images of that scene taken at different times will appear in different locations. Conventional SAR processing, which combines looks as if the scene were motionless, leads to motion blur in the composite image, which subsequent processing cannot correct. For such processing, the severity of the blur is proportional to

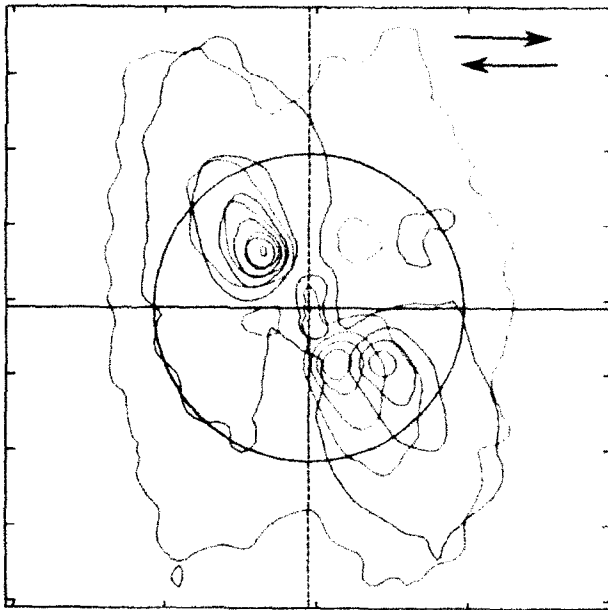


Figure 1. Demonstration of the use of scanning distortion correction to resolve wave propagation direction in SAR data. The data were from opposing LEWEX flight lines, 19 March 1987. The aircraft velocity vector is indicated by the corresponding colors. The artifact spectral lobe has diverged. The plot is linear in wave number, with the circle at $2\pi/100$ rad/m.

T_N . As a result, directional spectra derived from such an image show decreasing contrast with increasing range (all else equal). For some geometries, this blurring is an additional cause of azimuth cutoff, although in this case it results from noncoherent scene motion at the wave phase velocity.

Some improvement in spectral contrast would result for a single wave mode if the processor focus were adjusted. That adjustment, however, leads to the "focus paradox": SAR processor focus should not depend upon noncoherent scene motion. The focus paradox is resolved by noting that the relative position of look-image data is differentially shifted in the azimuth dimension at the same time that the processor focus is changed. For a simple azimuthal wave field, the result in terms of apparent wave image contrast is more satisfactory if the focus is perturbed. In general, however, this is a false solution. We call the standard approach to spectral calculations look-sum processing, since the looks are summed prior to Fourier transformation.

Better results are obtained in the following way.^{1,3} Let each look have an integration time that is much smaller than the wave period; let the processor have focus adjusted for a static scene; and let each individual look be imaged in the power domain, and then Fourier transformed. Of course, the requirement for individual-look data means a modified SAR/processor combination, or access to the unprocessed SAR signal record. The desired directional spectrum is then formed by adding the magnitudes of the resulting individual spectra, an approach we call spectral-sum processing. Figure 2 shows

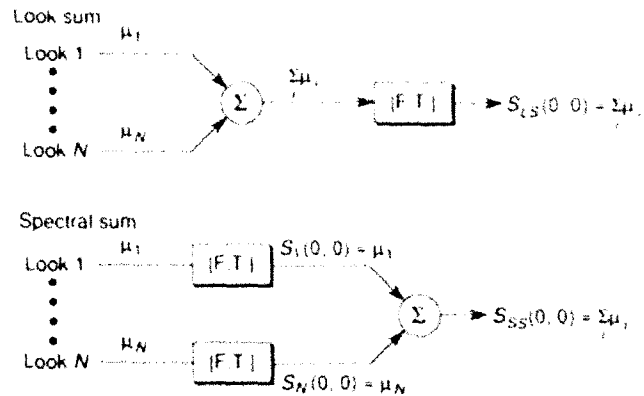


Figure 2. Flow diagrams comparing look-sum and spectral-sum processing procedures. S_{LS} represents the amplitude-mapped look-sum spectrum, S_{SS} represents the amplitude-mapped spectral-sum spectrum, S_i represents the amplitude-mapped spectra of the individual looks, μ_i is the individual look mean powers, $[F.T.]$ represents Fourier transform followed by amplitude detection, and Σ is the summation operation. Note that the DC value is equal to the image mean in each case, permitting quantitative comparison of the two approaches.

flow charts contrasting look-sum and spectral-sum processing.

Spectral-sum processing has several important advantages over conventional approaches for wave spectral analysis. First, it is an energy conservative procedure.¹ Second, by maintaining the static scene processor focus setting, our ability to observe the shorter wave scales is not compromised, as it would be if the processor focus were perturbed to "match" a longer scale wave. Third, the approach is impervious to noncoherent scene translation between looks. Look-image misregistrations become phase terms in the transform domain that are removed through the detection process. Fourth, spectral-sum processing works in the same manner when more than one wave model is present in the scene. Finally, the compensation for noncoherent wave motion applies for the vector direction of wave propagation and not simply the azimuth component of the imposed misregistration. For these reasons we recommend the spectral-sum approach.

The improvement of the spectral-sum approach over the look-sum approach is easily demonstrated. We use an example of waves-in-ice data gathered during LIMEX '87. Having formed the two different spectra from the same data set, the ratio of look-sum to spectral-sum is taken. The result is shown in Figure 3. The unity value of the central (DC) pixel value illustrates conservation of energy for both methods. The spectral-sum method, however, always shows higher spectral values and hence better wave contrasts than does the look-sum approach.

As a final note, consider a comparison between airborne-SAR-derived image spectra and spaceborne-SAR-derived image spectra. In making such comparisons, the aircraft flight lines may be designed to minimize the

¹Look-sum processing is also energy conservative if the individual looks are summed in the image power domain as indicated in Figure 2.

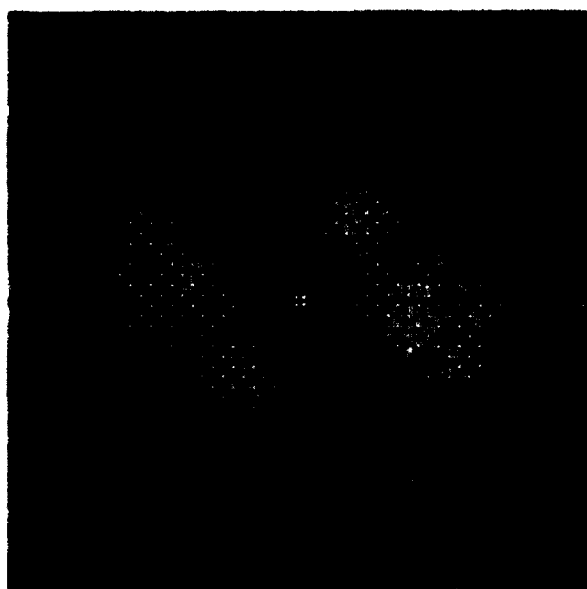


Figure 3. Ratio of look-sum to spectral-sum spectra for an example of LIMEX waves-in-ice data, 21 March 1987. The central (DC) value is unity (white); the grey levels are all (proportionately) less than unity. The scale is the same as in Figure 1.

velocity-bunching mapping nonlinearities if there is *a priori* knowledge of the wave field to be imaged. The spectral-sum approach should be used, at least for the airborne data, to minimize noncoherent motion effects. In addition, the role of the along-track wave-scaling term in the velocity-bunching mapping must be appropriately compensated in the airborne data to ensure a sensible comparison. These will be key issues considering validation requirements for upcoming spaceborne SAR missions.

Removal of Directional Ambiguity. When a periodic wave field is analyzed by Fourier transformation, both the negative and positive frequencies of the wave field lead to the well-known directional ambiguity. This ambiguity may be removed by observing the direction of motion of each wave component in the set of looks. This can be done explicitly through wave tracking or spatial correlation methods, or implicitly through Fourier analysis, either with or without the use of assumed wave dispersive properties.⁸ The individual-look processing essentially results in a time sequence of N looks, each separated by a time step

$$\Delta\tau = \frac{R\Delta\gamma}{V}, \quad (7)$$

where $\Delta\gamma$ is the angular separation between successive look images.

One technique to take advantage of this sequence and resolve the propagation direction is to perform a full three-dimensional (two spatial and one temporal) Fourier transform over the look-image data set, followed by detection and integration over the unambiguous fre-

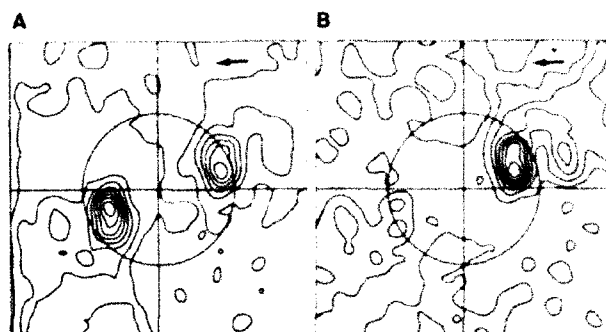


Figure 4. Ambiguous (A) and resolved (B) directional SAR image spectra for an example of waves-in-ice data, 21 March 1987. The ambiguous spectra were generated using the spectral-sum procedure. The resolved spectra were generated using the phase-weighting method. The unambiguous spectra were derived using every other pair of seven looks (total of five pairs). The data were processed such that the angular offset between successive looks was $\Delta\gamma = 0.52^\circ$. The subscenes were selected with slant ranges such that $\Delta r = 1.4$ s for each pair of looks used. The open-ocean dispersion relation was assumed. The scale is the same as in Figure 1.

quency bins. The method works well in principle but may be limited in the SAR case because of smaller practical exposure times and a small number of individual looks. (See Rosenthal and Ziemer, this volume.)

An alternative wave-number-domain technique for resolving the wave propagation direction uses a pair of successive look images, the (known) time step between the images, and the appropriate wave dispersion relation.⁹ The analysis proceeds by assuming that the look-number-dependent phase term is constant and known based on assumed knowledge of the wave dispersion relation. If the dispersion relation is known, the respective transforms from two successive look images may be combined in conjunction with a scanning distortion correction to give a correctly resolved image spectrum. This approach has the additional advantage that high-order harmonics and other spectral artifacts that do not obey the (assumed) dispersion relation are obliterated. The main drawback, of course, is the requirement for the explicit use of the wave dispersion relation. Figure 4 presents the results of applying this technique to a LIMEX SAR data set.

DISCUSSION

We can draw several conclusions from the LIMEX/LEWEX experiments and the data they generated. The general preference for a small SAR dwell constant (Ref. 11) is supported. This preference should be qualified, however, since a coherence time limitation and velocity-bunching, multimode imaging nonlinearities still exist. Such nonlinearities have been observed in airborne SAR

⁹This technique has been used successfully in marine radar applications.⁹ However, it seems to have been abandoned in that field since highly suitable sampling for the three-dimensional spectral analysis technique is easily achieved with marine radar. (See Ref. 10 and Ziemer, this volume.)

data sets, even with a small SAR dwell constant. There would seem to be a trade-off between small T_H and T_L constrained to be about the same size as, or slightly larger than, τ . Thus the coherence factor may be used to some positive degree to maintain system linearity when imaging ocean waves.

Wavelength dependence of τ could be checked by using a three-frequency airborne SAR. Care should be taken to treat each data set for optimal spectral contrast using our spectral sum approach. Otherwise, the increasing interlook translation of the waves with increasing radar wavelength (T_L and T_V) would confuse and bias the conclusions against longer radar wavelengths.

When comparing airborne data sets to those obtained or anticipated from spacecraft, the pertinent spatial and temporal scale factors (Table 1) should be considered. In particular, for typical aircraft speeds, the relative phase velocity and the associated scale perturbation require attention. For spacecraft velocities the effect is less pronounced, and for C-band orbital SARs, likely to be unimportant.

The once troublesome look misregistration may be used to advantage to resolve the wave propagation direction. This technique may potentially be applicable to spaceborne SAR systems, although it depends on suitable SAR parameters such as beamwidth. As a minimum, it should lead to a more informative comparison between

SAR-derived ocean wave spectra and on-site measured wave spectra using conventional techniques.

REFERENCES

- ¹Raney, R. K., and Vachon, P. W., "Synthetic Aperture Radar Imaging of Ocean Waves from an Airborne Platform: Focus and Tracking Issues," *J. Geophys. Res.* **93**(C10), 12,475-12,486 (1988).
- ²Vachon, P. W., Olsen, R. B., Livingstone, C. E., and Freeman, N. G., "Airborne SAR Imagery of Ocean Surface Waves Obtained During LEWEX: Some Initial Results," *IEEE Trans. Geosci. Rem. Sens.* **26**(5), 549-562 (1988).
- ³Raney, R. K., Vachon, P. W., DeAbreu, R. A., and Bhogal, A. S., "Airborne SAR Observations of Ocean Surface Waves Penetrating Floating Ice," *IEEE Trans. Geosci. Rem. Sens.* (JMEM LEWEX Special Issue) **27**(5) (September 1989).
- ⁴Raney, R. K., "Transfer Functions for Partially Coherent SAR Systems," *IEEE Trans. Aerospace Elect. Sys.* **AES-19**(5), 740-750 (1983).
- ⁵Raney, R. K., and Vachon, P. W., "SAR Seen Multi-mode Waves in Ice: Evidence of Imaging Nonlinearities," *Proc. IGARSS '88*, Edinburgh, Scotland, 141-144 (1988).
- ⁶Monaldo, F. M., and Lyzenga, D. R., "On the Estimation of Wave Slope and Height Variance Spectra from SAR Imagery," *IEEE Trans. Geosci. Rem. Sens.* **GE-24**(4), 543-551 (1986).
- ⁷Raney, R. K., "SAR Response to Partially Coherent Phenomena," *IEEE Trans. Antenn. & Propag.* **AP-28**(6), 777-787 (1980).
- ⁸Vachon, P. W., and Raney, R. K., "Resolution of Ocean Wave Propagation Direction in Single-Pass Airborne SAR Imagery," *Proc. IGARSS '89*, Vancouver, Canada (1989).
- ⁹Atanassov, W., Rosenthal, W., and Ziemer, F., "Removal of Ambiguity of Two-Dimensional Power Spectra Obtained by Processing Ship Radar Images of Ocean Waves," *J. Geophys. Res.* **90**(C1), 1061-1067 (1985).
- ¹⁰Young, I. R., Rosenthal, W., and Ziemer, F., "A Three-Dimensional Analysis of Marine Radar Images for the Determination of Ocean Wave Directionality and Surface Currents," *J. Geophys. Res.* **90**(C1), 1049-1059 (1985).
- ¹¹Beal, R. C., "Spectrasat: A Hybrid ROWS SAR Approach to Monitor Ocean Waves from Space," *Johns Hopkins APL Tech. Dig.* **8**(1), 107-115 (1987).

DIRECTIONAL SPECTRA FROM THE CCRS C-BAND SAR DURING LEWEX

The Convair 580 aircraft of the Canada Centre for Remote Sensing collected C-band synthetic aperture radar imagery on five days during the Labrador Sea Extreme Waves Experiment. There is good general qualitative agreement between the wave modes observed by the synthetic aperture radar and those observed by other wave-measurement techniques. Some clearly anomalous synthetic aperture radar spectral results are explained on the basis of velocity-bunching nonlinearities.

THE LEWEX SYNTHETIC APERTURE RADAR PROGRAM

One component of the Labrador Sea Extreme Waves Experiment (LEWEX) was the measurement of ocean waves by airborne synthetic aperture radar (SAR) to allow a detailed study of SAR ocean-wave imaging mechanisms and the subsequent extraction of useful wave information from the data. The advantages of airborne SAR are the opportunity for repeat pass coverage within a short time and the flexibility of platform geometry.

The Canada Centre for Remote Sensing (CCRS) Convair 580 aircraft was involved in LEWEX in conjunction with the concurrent Labrador Ice Margin Experiment (LIMEX).^{1,2} The LEWEX SAR flights of the aircraft, with its newly commissioned real-time processing C-band SAR system,³ occurred on 13, 14, 17, 18, and 19 March, during the principal LEWEX period in 1987, and also on 25 March. (The data from the latter flight are discussed elsewhere⁴ and will not be considered further here.) Each flight consisted of multiple passes over the key LEWEX data collection sites, and, with the exception of the flight on 13 March, at least one ship was engaged in coincidental wave-measurement activities at the principal sites that were overflown. On 14, 17, and 18 March, nearly coincidental wave measurements were also made with the surface contour radar (see Walsh, this volume) and the radar ocean-wave spectrometer (see Jackson, this volume) on the NASA P-3 aircraft.

The Convair 580 flights, the areas overflown, and the key SAR parameters are summarized in Table 1. There were two basic flight scenarios. On 13 and 19 March, the Convair 580 departed the LIMEX/LEWEX operations base in Gander, Newfoundland, and traveled to the measurement site near 50°N, 47.5°W, where five passes with different platform geometries were flown over the site. On 14, 17, and 18 March, the Convair 580 departed Gander at low altitude, overflew the measurement sites at 50°N, 47.5°W and 50°N, 45°W along an eastbound leg, climbed to a higher altitude, and overflew the same two sites along a westbound leg. A third pass was also made over the western site. The flying schedule was arranged such that the plane overflew the measurement sites at approximately 1200 UT on each date, except on

19 March, when weather forced a flight delay of about three hours.

In this article, we consider the results of an image spectral analysis of the SAR ocean wave imagery collected during LEWEX. We explicitly consider the entries in the LEWEX composite-plot spectral intercomparison plots⁴ (cf., Beal, Fig. 10, this volume) that are labeled SAR (CCRS). These SAR image spectra, corrected for scanning distortion, are the only entries in the tables that are *not* in terms of calibrated wave height. We chose not to apply a wave-height inversion algorithm (e.g., Ref. 6) to the data because the usefulness of such an inversion, in the case of airborne SAR, has yet to be demonstrated. We feel that intersensor comparisons are favorable, at least qualitatively, with respect to the SAR image spectra without the application of such algorithms. Also, existing inversion algorithms cannot account for obvious nonlinear effects in the image spectra. The results of applying one such inversion algorithm to the CCRS LEWEX SAR data are considered elsewhere (see Hasselmann et al., this volume).

The spectral processing applied to the SAR imagery at CCRS is outlined below. The contents of the composite spectral tables are reviewed on a case-by-case basis, indicating comparisons that are or are not favorable. Some clearly anomalous cases are considered from the perspective of the nonlinear effects of mapping caused by velocity-bunching mechanisms.

OVERVIEW OF SPECTRAL PROCESSING

The principal steps for the production of the SAR image spectra are summarized in Figure 1. All of the SAR data considered were processed by the real-time processor (RTP) on board the aircraft and stored on high-density digital tape. The RTP produces seven-look imagery, with the looks summed in amplitude. The image data correspond to pixel spacings of 3.89 m in azimuth and 4.00 m in slant range, with a resolution of about 6 m in each dimension.

The SAR image tapes were returned to CCRS in Ottawa, where key scenes were transferred to computer-com-

Table 1. Convair 580 SAR passes during the principal LEWEX period. Tints identify spectra in Figure 2.

Date	Time ^a (UT)	L ^b	P ^c	Loc. ^d	Track ^e (deg)	h (m)	V ^f (m/s)	Dir. ^g
3/13	1234	1	1	(Q) ^h	052	3627	108	L
	1304	2	2	(Q)	162	3688	098	R
	1322	3	3	(Q)	347	3688	115	R
	1348	4	4	(Q)	167	6126	115	R
	1406	5	5	(Q)	347	6096	129	R
3/14	1157	1	1	Q	089	3688	128	R
	1219	1	1	T	089	3688	128	R
	1259	2	2	T	270	6096	128	R
	1323	2	2	Q	269	6096	128	R
	1352	3	3	Q	227	6065	120	R
3/17	1243	1	1	Q	089	3840	111	R
	1309	1	2	T	091	3840	114	R
	1334	2	1	T	271	6096	128	R
	1358	2	2	Q	269	6096	122	R
	1422	3	1	Q	180	6096	122	R
3/18	1210	1	1	Q	089	3657	131	R
	1233	1	2	T	091	3657	127	R
	1258	2	1	T	271	6096	128	R
	1322	2	2	Q	269	6096	128	R
	1340	3	1	Q	180	6065	093	R
3/19	1516	1	1	Q(T) ^h	074	3688	126	R
	1529	1	2	Q(T)	254	3688	121	L
	1554	2	3	Q(T)	344	3688	128	R
	1613	2	4	Q(T)	164	3688	110	L
	1633	3	5	Q(T)	298	3688	122	R

Note: All data were collected in nadir mode. The 13 March data are in ground-range presentation; all others are in slant range. The 14 March data are horizontal-transmit and horizontal-receive polarization; all others are vertical-vertical polarization.

^a Approximate time of data considered in spectral intercomparisons.

^b Line number.

^c Pass number.

^d Scene location: Q = CFAV *Quest* (50°N 47.5°W); T = HNLMS *Tydemar* (50°N 45°W).

^e Aircraft track measured clockwise with respect to true north.

^f Antenna look direction: L = left; R = right.

^g The *Quest* was not yet in position.

^h The *Tydemar* had moved to the *Quest* location.

patible tape, and the image products were dumped to a computer hard disk, converted from slant range to ground range (if required), and interpolated to 3.89 m by 3.89 m image pixels. Because of a hardware fault, a bias term is present in the LEWEX RTP SAR imagery, but it is estimated and removed before subsequent spectral analysis.

Azimuth-oriented image swaths of 512 pixels (in ground range) by 4096 pixels (in azimuth) centered on a 52° incidence angle were extracted from each data set. That incidence angle ensures consistent radiometric behavior for both the high- and the low-altitude SAR passes

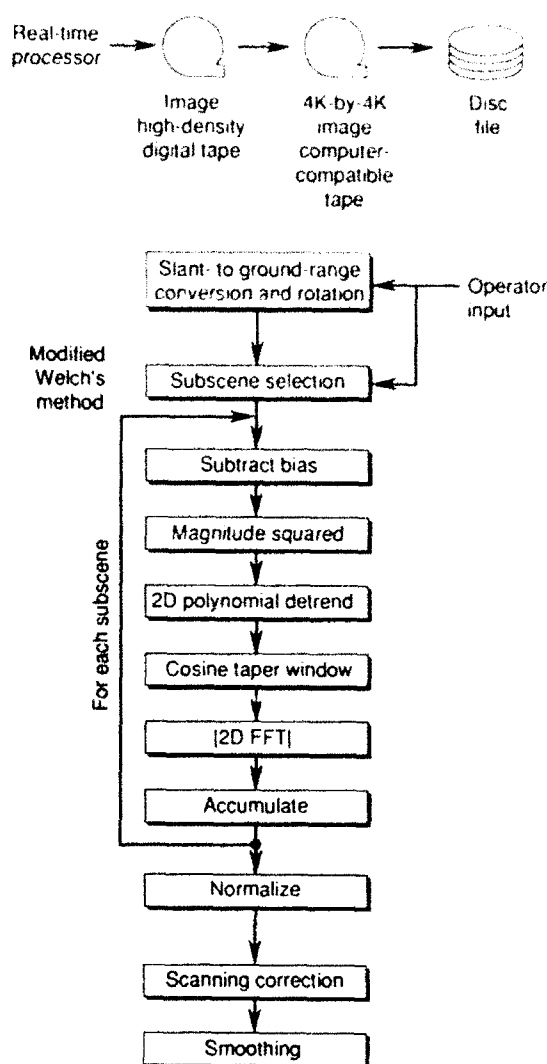


Figure 1. Flow chart showing the principal processing steps in the production of the SAR image spectra.

and avoids problems with near-nadir image data such as inaccurate slant-range to ground-range conversions and image saturation. (No sensitivity time control was available for ocean work during LEWEX.) The data were squared to move into the image power domain. (Individual look product cross terms are created from the RTP summing the looks in power. The quantitative impact of these terms has not been assessed.) This image swath was sectioned into fifteen 512 pixel by 512 pixel subscenes, each overlapping by 50%. Each subscene was subjected to a two-dimensional polynomial detrend operation, a cosine-taper window, and a fast Fourier transform. The Fourier transforms were magnitude detected and ensemble averaged using a modified Welch's method.⁷ The average spectra were then normalized by the zero wave-number value, giving a spectrum that may be interpreted in terms of wave-number-dependent spectral contrast.⁸

The symmetrical image spectra were subjected to a scanning distortion correction to account for along-track

scale changes. Interpolation in the two-dimensional wave-number domain produced asymmetrical SAR image spectra. The spectra were then smoothed using a 5 by 5 spectral bin Gaussian smoothing kernel with an equivalent rectangular width of 2.5 by 2.5 spectral bins. These spectra were submitted for inclusion in the inter-comparison plots.⁵

SPECTRAL INTERCOMPARISONS

On 14 March (Fig. 2A), data were collected in slant range, but the exact nadir location is not known. The slant-range to ground-range conversion was performed post-flight. However, some range-dependent scaling errors may be present. There is some evidence of a second wave system in the low-altitude pass. The dominant wave mode observed in all passes is consistent with the single mode measured by the Wavescan buoy.

The 17 March (Fig. 2B) data represent the first reliable data set in terms of the slant-range to ground-range conversion. For this and all subsequent nadir mode data sets, the data were collected in slant range, with the nadir explicitly appearing in the image. The slant-range to ground-range conversion was then performed accurately post-flight. The SAR directional ambiguity masks any evidence of the opposing wave systems observed by the Wavescan buoy.

The single-wave mode of 18 March (Fig. 2C) is in good agreement with the Wavescan buoy. In the high-altitude flight, however, there is a strong indication of a second wave mode. This anomalous case is discussed later.

For 19 March (Fig. 2D), the data were collected as part of multisided pattern flown only at the lower altitude. In this particular pass, there is good agreement between the principal wave mode observed by the SAR and that observed by the Wavescan buoy. In the next section, we consider this data set further because the image spectra from some of the other passes indicate a second anomalous wave mode.

SOME ANOMALOUS RESULTS

We will now attempt to explain anomalous spectral modes observed in the 18 and 19 March data sets on the basis of velocity-bunching nonlinearities. Velocity bunching is a remapping of scatterer locations in the SAR image azimuth dimension as a result of the projected radial component of the scatterers' net orbital velocity. This is an important mechanism for the imaging of azimuth traveling ocean waves by SAR systems.^{9,10}

For an airborne SAR system with the geometry shown in Figure 3, the effective radar cross section σ_{eff} due to velocity bunching is described to first order by¹¹

$$\sigma_{\text{eff}} \propto$$

$$\frac{1}{|1 + \sum_{k=1}^M W_k S_k K_p \cos \phi_k / (\theta, \phi_k) \cos(\text{ARG}_k)|} \quad (1)$$

where

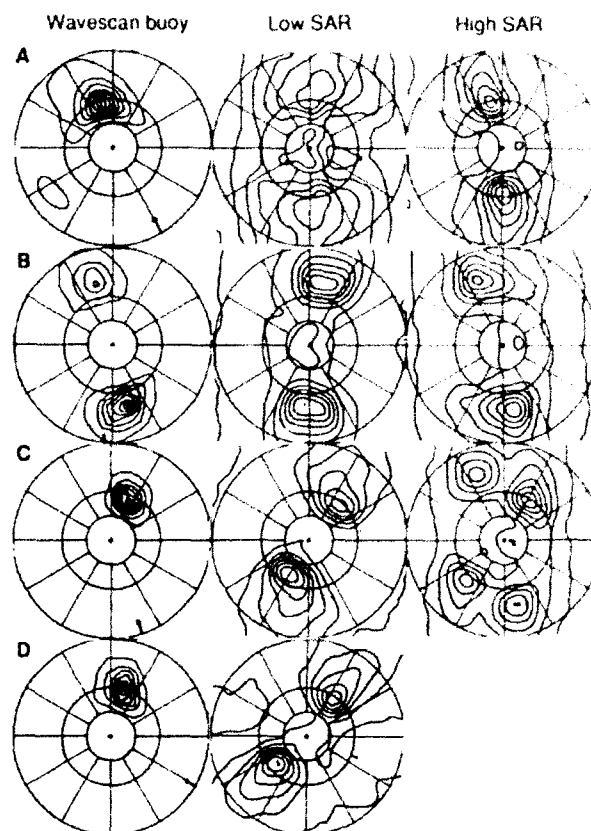


Figure 2. Uncorrected SAR wave-number spectra at low and high altitudes compared with Wavescan buoy spectra. A. 14 March 1987. B. 17 March. C. 18 March. D. 19 March. Inner and outer circles correspond to 400 m and 100 m, respectively. See tinted entries in Table 1 for headings.

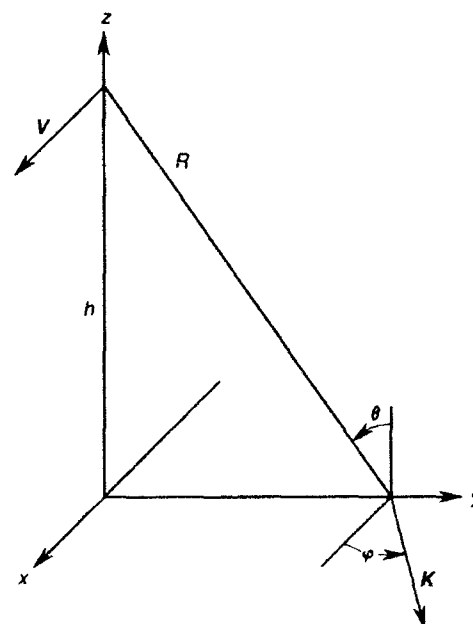


Figure 3. SAR/ocean wave geometry. x is the azimuth coordinate, y is the ground-range coordinate, V is the platform velocity vector, h is the platform height, θ is the local angle of incidence, K is the ocean-wave wave-number vector, and ϕ is the wave aspect angle.

$$W_k = A_k K_k^{3/2}, \quad (2)$$

$$S_k = \left(1 - \frac{C_{0k}}{V \cos \phi_k}\right), \quad (3)$$

$$K_p = \sqrt{g} \frac{h}{V}, \quad (4)$$

$$l(\theta, \phi_k) = \sqrt{1 + \tan^2 \theta \sin^2 \phi_k}, \quad (5)$$

$$\text{ARG}_k = (K_k S_k \cos \phi_k)x + (K_k \sin \phi_k)y, \quad (6)$$

A , K , ϕ , and C_0 are the wave-mode amplitudes (in meters), wave numbers, aspect angles, and phase velocities, respectively, V is the platform speed, h is the platform height, θ is the incidence angle, x and y are the azimuth and ground-range coordinates, and g is the acceleration of gravity. Sharp wave "crests" will be apparent in the SAR image when the denominator of Equation 1 numerically approaches zero. Such image crests are a function of parameters such as wave amplitude and are the result of the nonlinear, velocity-bunching mapping process.

It is straightforward to examine this nonlinearity. Define

$$\alpha = \sum_{k=1}^M W_k S_k K_p |\cos \phi_k| l(\theta, \phi_k), \quad (7)$$

which is the worst-case value of the coefficient in the denominator of Equation 1. The magnitude and sign of the actual coefficient vary as a function of spatial position. The velocity-bunching mapping is linear when

$$\lim_{\alpha \ll 1} \frac{1}{|1 + \alpha|} \rightarrow 1 - \alpha. \quad (8)$$

For a unimodal sea ($M = 1$),

$$H_s = 2\sqrt{2} A, \quad (9)$$

and

$$H_s = \alpha \frac{g}{2\sqrt{2}\pi^3} \frac{T^3}{(h/V)S l(\theta, \phi) \cos \phi} \quad (10)$$

describes the relation between significant wave height H_s and wave modal period T for various values of the mapping parameter α .

We now examine the role of α relative to the SAR geometries experienced during LEWEX and the expected wave climatology. Figure 4 shows plots of Equation 10 for various values of α and LEWEX SAR parameters. Wave modes occurring above the lines are in increasingly nonlinear mapping regimes. The significant wave height and peak period observed by the Wavescan buoy¹² at the HNLMS *Tydemar* location are also plotted, along with wave climatology for the month of March as measured at the Hibernia oil drilling site, approximately 300 nmi south of the principal LEWEX study region. The contour levels are in increments of 1% occurrence for the 750 historical observations included.

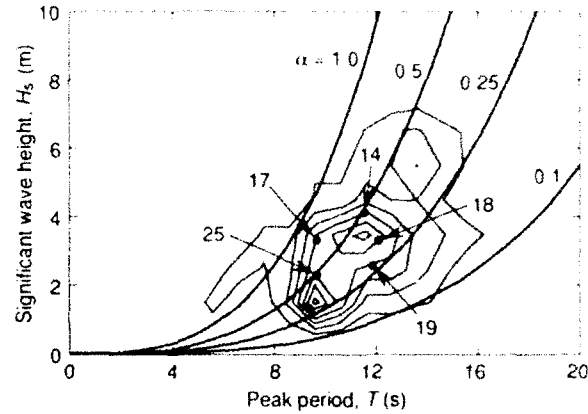


Figure 4. Representative values of the mapping parameter ($\alpha = 0.1, 0.25, 0.5$, and 1.0 for $h/V = 29$ s, $\phi = 48^\circ$, and $\theta = 52^\circ$) referenced to conditions observed during LEWEX (the day of March is indicated; the Wavescan buoy measurement was at approximately 1200 UT). The data are superimposed on the Hibernian March wave climatology with 1% observation contour increments.

The key issue in considering Figure 4 is the size of α for which velocity-bunching mapping nonlinearities become important, particularly for the very moderate set of (representative) LEWEX SAR parameters indicated in the figure. Note that the single ocean-wave mode case plotted in Figure 4 is conservative in terms of the degree of nonlinear mapping compared with the multimode case that is generally observed in nature, but the plotted curves are a reasonable guide. If $\alpha = 0.25$ represents the onset of nonlinear mapping, then nearly all wave conditions actually observed during LEWEX would be subject to imaging nonlinearity.

Spectra of 18 March

The SAR image spectra calculated from the four passes of 18 March are shown in Figure 5. As noted, the high passes show an anomalous second wave mode. We suggest that this second mode may be an expression of the velocity-bunching nonlinearity induced by changes in the SAR geometry relative to the waves being observed.

The two main differences between the high-altitude and the low-altitude SAR passes are the change by a factor of nearly 2 in the h/V ratio and the 180° change in the SAR aspect angle ϕ . The velocity-bunching mapping parameters α for these cases, based on the Wavescan buoy measurements and the SAR geometry, are shown in Table 2. The incidence angle here is 52° for both the high- and the low-altitude passes, but the slant-range-dependent coherent integration time T_L varies with h/V . Therefore, we expect that the scene coherence time τ should moderate the nonlinearity more for the high-altitude pass (larger T_L/τ) than for the low-altitude pass (smaller T_L/τ). Nevertheless, the net effect is apparently a strong (in fact, dominant) expression of the nonlinearity for the high-altitude pass only.

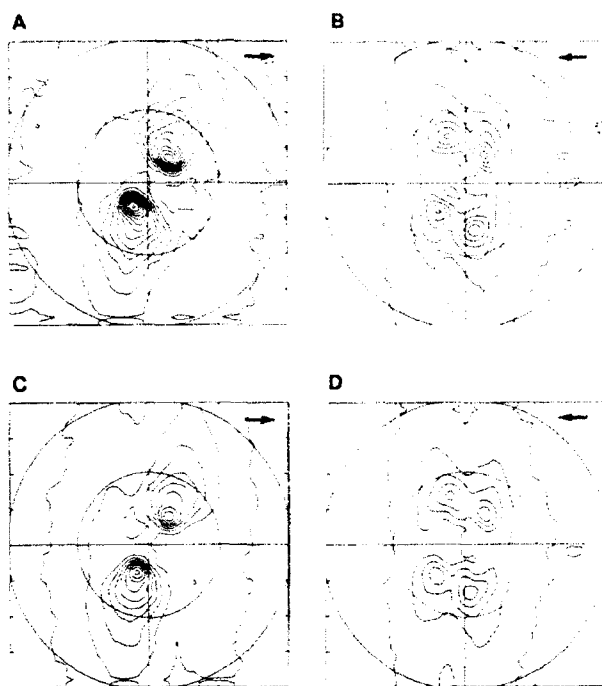


Figure 5. SAR image wave-number spectra from four passes on 18 March 1987. The platform velocity vector is indicated by the arrow. The inner circles correspond to 100-m wavelengths and the outer to 50-m wavelengths. **A.** Near the *Tydemar*, 50°N, 45°W, $\theta = 52^\circ$, 1233 UT, $h/V = 29$ s. **B.** The same as **A** but 1257 UT, $h/V = 48$ s. **C.** Near the *Quest*, 50°N, 47.5°W, $\theta = 52^\circ$, 1208 UT, $h/V = 28$ s. **D.** The same as **C** but 1321 UT, $h/V = 48$ s.

Table 2. Velocity-bunching mapping parameter α based on (nominal) Wavescan buoy measurements and the SAR/wave geometry from Table 1.

Time (UT)	L ^a	P ^b	H _s (m)	T (s)	ϕ (deg)	h/V (s)	T _L ^c (s)	α ^d
18 March								
1208	1	1	3.3	12.1	30	29	1.6	0.26
1233	1	2	3.3	12.1	30	28	1.6	0.26
1258	2	1	3.3	12.1	30	48	2.7	0.77
1322	2	2	3.3	12.1	30	48	2.7	0.77
19 March								
1516	1	1	2.6	11.9	10	29	1.6	0.18
1529	1	2	2.6	11.9	10	30	1.7	0.38
1554	2	3	2.6	11.9	10	29	1.6	0.34
1613	2	4	2.6	11.9	10	34	1.9	0.56

^aLine number.

^bPass number.

^cCoherent integration time.

^dVelocity-bunching parameter of Equation 10.

Spectra of 19 March

The 19 March data are very important with regard to the dependence of the velocity-bunching nonlinearity

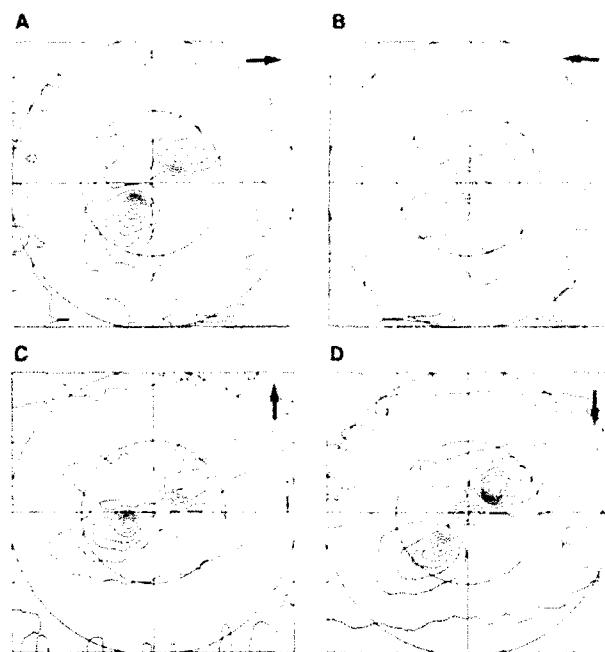


Figure 6. SAR image wave-number spectra from four passes on 19 March; near the *Quest*, 50°N, 47.5°W, $\theta = 52^\circ$. The platform velocity vector is indicated by the arrow. **A.** L1 P1, $h/V = 29$ s. **B.** L1 P2, $h/V = 30$ s. **C.** L2 P3, $h/V = 29$ s. **D.** L2 P4, $h/V = 34$ s. Horizontal scale identical to Figure 5. North (in this figure only) is 16° clockwise from vertical.

on the wave aspect angle for an airborne SAR with a small h/V ratio. There were four passes over the measurement site, each representing a different wave aspect angle. The h/V ratio was nearly identical for the four cases. The SAR image spectra are shown in Figure 6. (Corresponding sets of spectral estimates from three co-located buoys are given in Beal, this volume, Fig. 11.) Note the appearance of a second wave mode in pass 2 and, to a lesser extent, in passes 3 and 4. In Table 2, α is listed for the four passes. We see that the passes with the smallest expression of the second anomalous mode (L1 P1) correspond to the smallest value of α . All other cases have larger α and greater expression of the anomalous wave mode. The variability in α is due solely to dependence on the wave aspect angle. Although this sequence represents a seemingly controlled situation (i.e., fixed h/V and incidence angle), the variability in the results demonstrates that the SAR geometry relative to the wave being imaged is very important in governing the velocity-bunching mapping, at least for an airborne SAR system.

CONCLUSIONS

We have considered uncalibrated directional wave-number spectra derived from CCRS C-band RTP SAR imagery collected during LEWEX. We do not attempt to apply an inversion algorithm, and so we do not claim to provide a calibrated wave-height spectrum. In spite of this, we feel that the SAR generally measured wave modes that are comparable to those observed by the other wave-measuring systems deployed during LEWEX.

There is confusion in some of the spectra because of the appearance of anomalous wave modes. We claim that many of these anomalies are due to the expression of velocity-bunching mapping nonlinearities. They appear with both large and small h/V ratios and depend on the wave aspect angle.

The spectra in the current intercomparison exercise could be improved by using the spectral-sum processing procedures.⁷ Furthermore, new techniques for resolving the propagation direction in single-pass SAR image spectra, based on individual-look SAR imagery, may also help the intercomparisons (see Raney and Vachon, this volume, and Rosenthal, this volume).

REFERENCES

- ¹ McNutt, L., Argus, S., Carsey, F., Holt, B., Crawford, J., et al., "LIMEX'87: The Labrador Ice Margin Experiment, March 1987—A Pilot Experiment in Anticipation of RADARSAT and ERS 1 Data," *Eos* **69**(23), 634–643 (1988).
- ² LIMEX/LEWEX Special Issue, *IEEE Trans. Geosci. Remote Sensing* **27**(5) (1989).
- ³ Livingstone, C. E., Gray, A. L., Hawkins, R. K., Olsen, R. B., Deane, R. A., et al., "CCRS C-Band Airborne Radar—System Description and Test Results," in *Proc. 11th Canadian Symp. on Remote Sensing*, Univ. Waterloo, Waterloo, Ontario, pp. 503–517 (1987).
- ⁴ Vachon, P. W., Olsen, R. B., Livingstone, C. E., and Freeman, N. G., "Airborne SAR Imagery of Ocean Surface Waves Obtained during LIMEX: Some Initial Results," *IEEE Trans. Geosci. Remote Sensing* **26**(5), 549–562 (1988).
- ⁵ Gerling, T. W., "Common Processing and Display of LIMEX Directional Ocean Wave Spectral Estimates from 12 March through 19 March, 1987," JHU-APL Report STR89U-011, JHU-APL, Laurel, Maryland (1989).
- ⁶ Monaldi, F. M., and Lyzenga, D. R., "On the Estimation of Wave Slope and Height Variance Spectra from SAR Imagery," *IEEE Trans. Geosci. Remote Sensing* **GE-24**(4), 543–551 (1986).
- ⁷ Bhogal, A. S., and Freeman, N. G., "An Algorithm for the Computation of Intensity Spectra from Airborne Synthetic Aperture Radar Ocean Wave Imagery," in *Proc. 11th Canadian Symp. on Remote Sensing*, Univ. Waterloo, Waterloo, Ontario, pp. 727–742 (1987).
- ⁸ Raney, R. K., Vachon, P. W., DeAbreu, R. A., and Bhogal, A. S., "Airborne SAR Observations of Ocean Surface Waves Penetrating Floating Ice," *IEEE Trans. Geosci. Remote Sensing* **27**(5) (1989).
- ⁹ Alpers, W. R., and Rutenach, C. I., "The Effect of Orbital Motions on Synthetic Aperture Radar Imagery of Ocean Waves," *IEEE Trans. Antennas Propag.* **AP-27**(5), 685–690 (1979).
- ¹⁰ Swift, C. T., and Wilson, L. R., "Synthetic Aperture Radar Imaging of Moving Ocean Waves," *IEEE Trans. Antennas Propag.* **AP-27**(6), 725–729 (1979).
- ¹¹ Raney, R. K., and Vachon, P. W., "SAR Seen Multi-Mode Waves in Ice: Evidence of Imaging Non-linearities," in *Proc. IGARSS '88 Symp.*, Ref. ESA SP-284, pp. 141–144 (1988).
- ¹² Krogstad, H. E., *Wave Data Collected by Wavescan during the Labrador Sea Extreme Waves Experiment (LEWEX)*, Oceanographic Center, SINTLE report 87-111 (1987).

SAR SCATTERING MECHANISMS AS INFERRED FROM LEWEX SPECTRAL INTERCOMPARISONS

The ocean wave number response of the C-band synthetic aperture radar (SAR) system used in the Labrador Sea Extreme Waves Experiment is compared for various airborne perspectives by using a phase-coherent model of ocean wave scattering in the SAR modulation transfer function. The directional behavior of the model appears to explain a null in the SAR wave number response, close to the range axis, that is particularly evident at high range-to-velocity ratios and high off-nadir angles.

INTRODUCTION

Previous research with L-band images from both Seasat¹ and the Shuttle Imaging Radar-B (SIR-B)^{2,3} has shown that the synthetic aperture radar (SAR) azimuthal response is severely limited at the higher range-to-velocity (R/V) ratios. A simple model to explain the results was postulated by Beal et al.¹ and further extrapolated by Monaldo and Lyzenga.² To first order, the along-track component of ocean wavelength resolution or azimuthal response, λ , appears to vary according to

$$\lambda = K \left(\frac{R}{V} \right) H_s, \quad (1)$$

where H_s is the significant wave height, and K is an empirical parameter related to the sea state on spatial scales below the resolution of the SAR. A major question of interest in the Labrador Sea Extreme Waves Experiment (LEWEX) was whether this simple model could be extended to C-band ocean imagery. If so, the implications would be relevant to future planned missions such as the European Remote Sensing (ERS-1) satellite, the Canadian Radarsat, and the NASA SIR-C, all of which will use C-band synthetic aperture radars.

The LEWEX ocean images analyzed herein were collected by the Canada Centre for Remote Sensing (CCRS) C-band SAR mounted on a CV-580 aircraft.⁴ The CCRS airborne real-time processor yielded 8-bit integer data as a seven-look summation of the backscattered field intensity after azimuthal compression and amplitude detection. During the initial flight on 13 March 1987, the SAR was operated with vertical transmit and receive polarizations (VV), and the data were recorded in the ground-range perspective. On 14 March, the SAR was operated in a horizontal (HH) polarization mode, and the data were recorded in a slant-range perspective. The gain of the SAR receiver was adjusted on that day to ensure good amplitude response in a side lobe of the antenna pattern located within 30° of nadir. On 17, 18, and 19 March, the SAR was operated in the VV mode, data were recorded in the slant-range perspective, and the receiver was adjusted for optimal amplitude response in the main lobe of the antenna pattern between radar look angles of 45° and 65°. Data were acquired each day at alti-

tudes of approximately 3700 and 6100 m. Specific parameters of all SAR flights are given in Table 1 of the article by Vachon et al. in this volume.

A bimodal ocean wave field was observed on 14 March nearly simultaneously by the SAR and two other radar remote sensors located on a NASA aircraft: the surface contour radar (SCR) (see the article by Walsh in this volume) and the radar ocean wave spectrometer (ROWS) (see the article by Jackson in this volume). Between 1130 and 1400 UT, the SAR, SCR, and ROWS each estimated a surface wave spectrum consisting of a dominant swell (≈ 215 -m wavelength) arriving from the south-southeast and a weaker wind-driven sea (≈ 150 -m wavelength) arriving from the east-northeast. The estimated significant wave height was about 4 m at both the CFAV *Quest* and HNLMS *Tydeinan* according to buoys deployed in the area (e.g., see the article by Zambresky in this volume). The objectives of the SAR analyses were to determine the practical limit of the azimuthal wave number response in relatively high sea states, to apply methods of wave spectral estimation developed for L-band SAR imagery to C-band data, and to look for evidence in the wave image spectrum of substantial changes in sea surface scattering mechanisms as a function of the radar look angle.

The low-altitude flight of the SAR over the *Quest* on 14 March (designated SAR scene 14LQ11 in this article) yielded good image data in a main lobe of the down-range antenna pattern for radar look angles between 45° and 60°. This was the only day during LEWEX that the SAR was operated with horizontal polarization and calibrated to obtain good image data near nadir (e.g., 10°–30°). Hence, these data are of particular interest because they were acquired with a C-band SAR most nearly like the L-band SAR flown during the NASA Seasat and SIR-B missions. Data were converted to a ground-range format at CCRS, preserving the 4.00- and 3.89-m pixel (picture element) dimensions.

For this analysis, SAR resolution was investigated as a function of across-track R/V ratios at constant height but variable look angle. The CCRS image product was segmented into 16 strips, each approximately 0.5 km

downrange by 16.0 km along track. Each strip was Fourier analyzed, and the resulting spectra were then averaged over all range wave numbers. Figure 1 shows how the intensity, power, and azimuthal response of the SAR imagery varied as a function of R/V . Azimuthal resolution is defined as the wavelength $\lambda = 2\pi/k_a$, corresponding to the wave number k_a at which the spectral response falls to one-half of its low-frequency value. In agreement with Equation 1, these data suggest a direct proportionality between azimuthal resolution and R/V ratio. The mean return power exhibits a minimum at about 40° , corresponding to the first minimum in the antenna gain pattern.

PROPOSED SAR SPECTRAL MODULATION MODEL

Transient surface-scattering facets of spatial scale intermediate between the Bragg wavelength and the SAR cell size (e.g., between 5 and 500 cm for LEWEX) may be advected at the orbital velocity of long waves, yet fade rapidly compared with the SAR integration time. The incoherent contribution to the SAR cross section may be modeled as a Poisson random process^{5,7} with an autocorrelation function whose Fourier transform in azimuth yields a dynamic transfer function,

$$P(\kappa, k_a) = 4 \sum_{m=0}^M \frac{(2m)!}{m!m!} \frac{(\kappa/2)^{2m} \cos(2m+1)\Phi}{(\kappa^2 + k_a^2)^{(2m+1)/2}}, \quad (2)$$

where $\Phi = \arctan(k_a/\kappa)$. The wave number response parameter, κ (rad/m), describes a broadband spectrum that becomes progressively narrower along the azimuthal wave number, k_a , by the addition of M successive terms.

The LEWEX SAR spectra from 14 March over the *Quest* were examined to determine to what extent they might be described by this Poisson model. Figure 2 illustrates the resulting azimuthal wave number response of the low-altitude flight as a function of radar look angle. The white power profiles of the azimuthal data were used to estimate Poisson model parameters for computing the (black) model functions with Equation 2. The azimuthal data profiles, $D(k_a)$, were used to estimate the wave number response parameter, κ , by minimizing a squared reciprocal error function

$$R(\kappa, k_a) = \left[\frac{(\kappa^2 + k_a^2)}{\kappa} - \frac{1}{D(k_a)} \right]^2, \quad (3)$$

for the simple $M = 0$ case, such that

$$\sum_{k_a} \frac{\kappa^3}{\kappa^2 + k_a^2} \frac{\partial R}{\partial \kappa} = \sum_{k_a} \left[\frac{\kappa}{D(k_a)} - (\kappa^2 + k_a^2) \right] = 0. \quad (4)$$

The broadband response characteristics of the data profiles are well modeled with just the lowest-order term

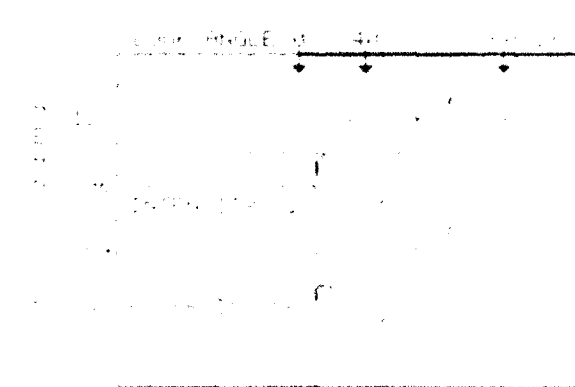


Figure 1. The mean intensity, power, and azimuthal response as a function of R/V for SAR scene 14LQ11. A minimum in the received power occurs at about 40° ($R/V \approx 36$). The system resolution is limited by sea surface motion, which influences the noncoherent aspects of SAR imaging and results in an ocean wave resolution, λ , that varies with the R/V of the radar platform.

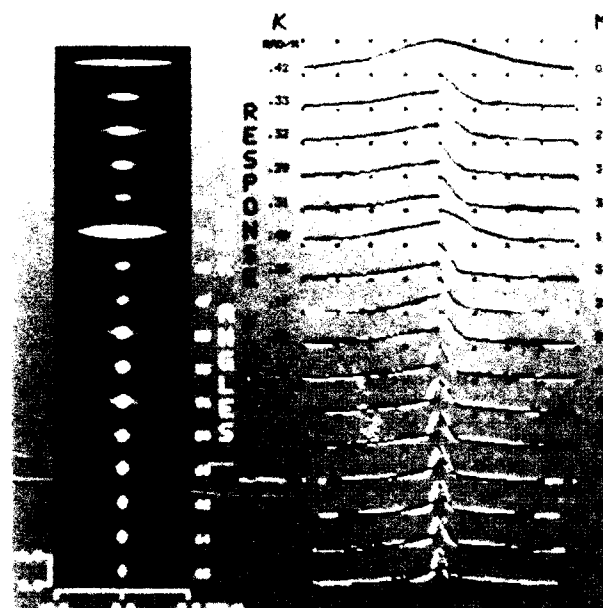


Figure 2. Fourier image power spectra over the full azimuthal extent of SAR scene 14LQ11 have been computed over 16 limited bands in the downrange coordinate. Along-track wave number profiles of these power spectra have been characterized in M terms of an incoherent scattering model described by a dynamic wave number response parameter, κ .

(i.e., $M = 0$). These model functions are displayed to the left of the origin in Figure 2. The narrowband behavior of the data profiles was approximated by adding

higher-order terms from Equation 2 to generate the model functions appearing to the right of the origin in Figure 2, stopping at $M = 0, 1, 2, 3$, or 4, when visual comparison with the data profile indicated a reasonable fit for each of the 16 values of radar look angle.

In the full-resolution version of the SAR imagery, little spectral power was evident outside $2\pi/25$ rad/m. Hence, the SAR scenes were reduced to a corresponding sample size of 12.5 m per pixel for subsequent analysis. The antenna pattern depicted in Figure 1 was first estimated by computing the mean intensity over the azimuthal coordinate to generate a smoothed estimate of the range-dependent variation. The pixel intensity at each downrange location was then normalized by dividing the mean downrange intensity during a 3×3 pixel averaging procedure. Interpolation reduced the resulting $12.00 \text{ m} \times 11.67 \text{ m}$ pixels to a $12.5 \text{ m} \times 12.5 \text{ m}$ grid. The result of applying this image processing procedure to the SAR data designated 14LQ11 (i.e., 14 March, low altitude over the *Quest* location, line 1 and pass 1) is shown in Figure 3 along with corresponding Fourier power spectra. Signal components at the higher azimuthal wave numbers clearly degrade as R/V increases, until only the range-traveling components are detected at $R/V = 89$ s, occurring at a radar look angle of 71° .

GENERALIZED DATA PROCESSING PROCEDURES

Fourier analysis was also applied to SAR imagery collected on 13, 14, 17, 18, and 19 March in the main antenna lobe after compensation for intensity variation downrange and conversion to cross-sectional power (by squaring SAR intensities). A slant-range to ground-range conversion was applied when appropriate during pixel resampling to 12.5-m pixels, approximately half the narrow swath resolution⁸ of the CCRS aircraft system. Fourier transforms were performed on sets of eight consecutive along-track image segments, each 1.6 km^2 , after subtracting the mean cross section and applying a cosine-tapered window within the square.

A Gaussian wave number response function was estimated from the average of the eight Fourier power spectra. A squared-error function, defined by the difference between the logarithm of the average power spectrum and a best-fitting two-dimensional polynomial,⁹ was minimized to generate characteristic Gaussian wave number response widths. The resulting Gaussian wave number response function was approximated by a two-dimensional surface, $G(k_r, k_a)$, where

$$G(k_r, k_a) = G_0 \exp \left[\left(\frac{-k_r^2}{2\sigma_r^2} \right) - \left(\frac{k_a^2}{2\sigma_a^2} \right) \right], \quad (5)$$

and k_r represents the radar range component of the wave number. The characteristic half-widths σ_r and σ_a , along with other significant parameters associated with image analysis, are listed in Table 1 for the complete LEWEX set of analyzed SAR data. After dividing each of the eight Fourier spectra by the Gaussian surface fitting the average power response, each spectrum was corrected for



Figure 3. Wave image spectra of SAR scene 14LQ11 have been computed in 32-km squares to relate image resolution to wave number response as each varies across the SAR swath. Left column: four contiguous 32-km SAR images. Middle column: raw spectra showing estimates of the dynamic transfer function in the azimuthal (horizontal) coordinate. Right column: smoothed spectra with the outer circle at $2\pi/50$ rad/m.

a unique dynamic transfer function, attempting to account for coherence time effects as modeled in the Fourier wave number domain according to Equation 2, with $M = 0$.

The instrument-response-corrected (i.e., level 3 of the linear process²) SAR image power spectra were subjected to several additional procedures to convert them to final estimates of ocean wave spectra. The Fourier wave number domain of the image power spectrum consisted of a 64×128 pixel database containing many zero elements. A Gaussian-weighted 3×3 pixel convolution filter was applied to eliminate these elements and obtain a reasonably continuous spectrum.

For the 14 March (near-nadir) data set only, a spatially uniform noise floor, taken at the mean power level plus one standard deviation, was subtracted from the power spectrum. In this way, the wave signal was separated from background stochastic noise by using a Gaussian statistical model¹⁰ of the spectral power distribution. This power distribution closely resembled a normal probability distribution after the Gaussian convolution and wave number response corrections.

Finally, a modulation transfer function¹¹ based on Doppler velocity bunching and large-scale surface tilting was applied to convert the SAR-response-corrected Fourier spectrum to an estimate (i.e., level 5 of the linear process²) of the surface wave height-variance spectrum. The velocity-bunching and tilt modulations of the

Table 1. LEWEX SAR data summary

File ^a	θ (deg)	R/V (s)	σ^2/μ^2	σ_t (rad/m) ^b	σ_a (rad/m) ^b	κ (rad/m) ^b
13LQ11	52	51	0.104	0.16	0.15	0.13
13LQ22	52	51	0.117	0.24	0.14	0.14
13LQ33	52	51	0.168	0.18	0.14	0.11
13HQ44	52	87	0.116	0.21	0.14	0.15
13HQ55	52	87	0.123	0.21	0.14	0.10
14LQ11	20	29	0.168	0.17	0.16	0.10
14LT11	26	31	0.185	0.18	0.16	0.11
14HT22	25	53	0.150	0.13	0.15	0.13
14HQ22	20	50	0.130	0.11	0.14	0.12
17LQ11	52	56	0.076	—	—	0.07
17LT12	52	56	0.263	0.30	0.25	0.10
17HT21	42	59	0.151	0.19	0.22	0.11
17HQ22	42	59	0.137	0.20	0.22	0.12
18LQ11	52	45	0.211	0.12	0.20	0.08
18LT12	52	47	0.265	0.12	0.20	0.07
18HT21	52	77	0.153	0.14	0.27	0.22
18HQ22	52	77	0.125	0.14	0.31	0.20
19LQ23	52	47	0.129	0.12	0.23	0.15

^aIn these file names, the first two numbers indicate the date in March by which CV-580 operations were completed; the third character indicates either low (L) or high (H) aircraft altitude; the fourth character designates the site as either the *Quest* (Q) or the *Tydemar* (T); the fifth and sixth characters indicate line number and pass number, respectively, consistent with notation accompanying Table 1 in the article by Vachon et al. in this volume.

^bThe variables σ_t , σ_a , and κ represent the wave number at which empirical response functions fall to one-half their value at the origin.

radar cross section were assumed to be additive in amplitude with coherent phase,

$$\eta(k_t, k_a) = \arctan(\tan \theta \sin \phi) - \frac{\pi}{2}, \quad (6)$$

where θ is the radar look angle, and $\phi = \arctan(k_t/k_a)$ is the direction of wave propagation¹¹ relative to the SAR azimuthal coordinate (i.e., the flight direction). Hence, a total SAR modulation transfer function was modeled by applying the sum of the velocity-bunching and tilt modulations to the SAR image power spectrum to approximate the wave height-variance spectrum (units of m^4).

The coherent phase of the velocity-bunching mechanism was included in the total modulation transfer function F^2 .^{10,11}

$$F^2(k_t, k_a) = F_t^2(k_t) + F_v^2(k_t, k_a) + 2F_t(k_t) F_v(k_t, k_a) \cos \eta(k_t, k_a), \quad (7)$$

where the subscripts t and v refer to tilt and velocity-bunching terms. The SAR image power spectrum was divided by F^2 , accounting for the estimated direction of the wave in determining the argument of Equation 6. The modulation transfer function is, in general, degenerate to the extent that the 180° ambiguity in the SAR mea-

surement of wave direction offers two interpretations of Equation 7. The tilt-modulation transfer function is

$$F_t(k_t) = \frac{4 \cot \theta}{1 + \sin^2 \theta} k_t, \quad (8)$$

where the "+" and "-" signs denote vv and hh polarizations, respectively. The velocity-bunching transfer function is

$$F_v(k_t, k_a) = \frac{R}{g} (\sin^2 \theta \sin^2 \phi + \cos^2 \theta) (k_t^2 + k_a^2) - k_a, \quad (9)$$

where g is the gravitational acceleration.

The SAR image spectra computed for LEWEX data acquired on 14 March were previously compared with SCR and ROWS ocean wave height-variance spectra, normalized in units of m^4 by subtracting an arbitrary Fourier noise power threshold between levels 3 and 5 of the linear SAR spectral correction¹² process. A similar threshold, equal to the mean Fourier power plus one standard deviation, was applied to the SCR height-variance spectra (after normalization to units of m^4) and to the ROWS spectra (after normalization to units of m^2) assumed to represent slope-variance spectra. This strategy for comparison was attractive because the same statistical threshold was applied to all three radar sensors in what was assumed to be the spectral domain corresponding to a particular instrument's measurement of cross-sectional modulation. Both SCR and ROWS spectra, however, had already been processed with instrument response functions that may well have included subtraction of noise thresholds (see the articles by Walsh and by Jackson in this volume) in formatting the Cartesian SCR and polar ROWS data products.

Figure 4 depicts the SCR spectral data in units of m^4 and the ROWS spectral data in units of m^4/rad at the *Quest* and *Tydemar* locations on 14 March. After increasing azimuthal spectral power by using a dynamic transfer function correction, the SAR level 3 spectrum most closely resembles Jackson's ROWS spectrum. Subsequent subtraction of the arbitrary noise threshold and correction for the phase-coherent modulation transfer function have the effect of diminishing SAR azimuthal spectral power to somewhat below that of the SCR spectrum, representing an estimate of spectral energy density in units of m^4 . If the SCR is taken as the primary standard, then the inverse SAR correction at level 5 appears to underestimate azimuthal wave power.

The wave spectral densities measured by an SAR will be shifted in a direction opposite the flight direction⁴ in proportion to the ratio of the phase velocity (g/k') to the platform velocity V . Here, k' represents the actual ocean wave number, as opposed to $k = (k_t^2 + k_a^2)^{1/2}$ representing the SAR estimate of wave number. The LEWEX SAR spectra were interpolated to a grid linear in the actual azimuthal ocean wave number, k'_a , from a grid linear in the SAR observed azimuthal wave number,

Figure 4. Spectra of SCR, ROWS, SAR level 3, and SAR level 5 over wave numbers increasing linearly from 0 at the center of each frame to $2\pi/100$ rad/m at the outer circle. **A.** *Quest* location. **B.** *Tydemar* location. The color bar depicts spectral power increasing to the right in units of m^4 for the SCR and m^3/rad for the ROWS. The SAR level 5 spectra have been normalized in units of m^4 for these flights at the lower altitude. The SAR level 3 spectra indicate that azimuthal wave response is adequate at an early stage of spectral data processing.

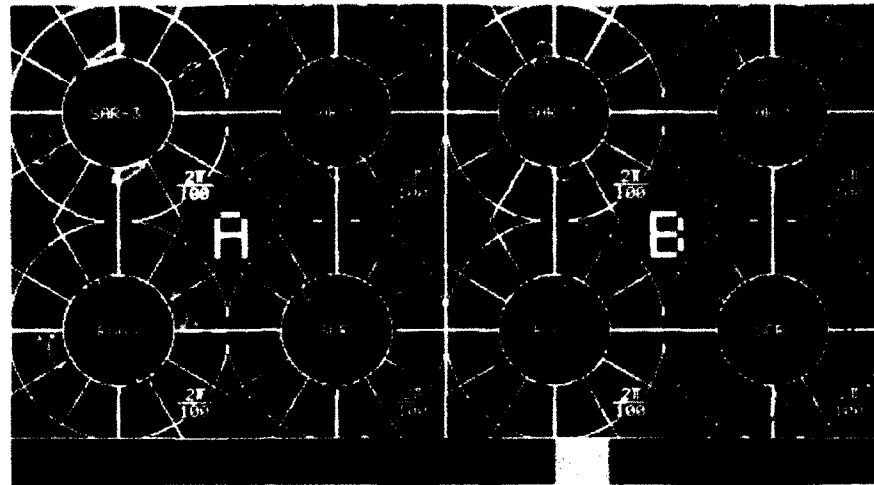
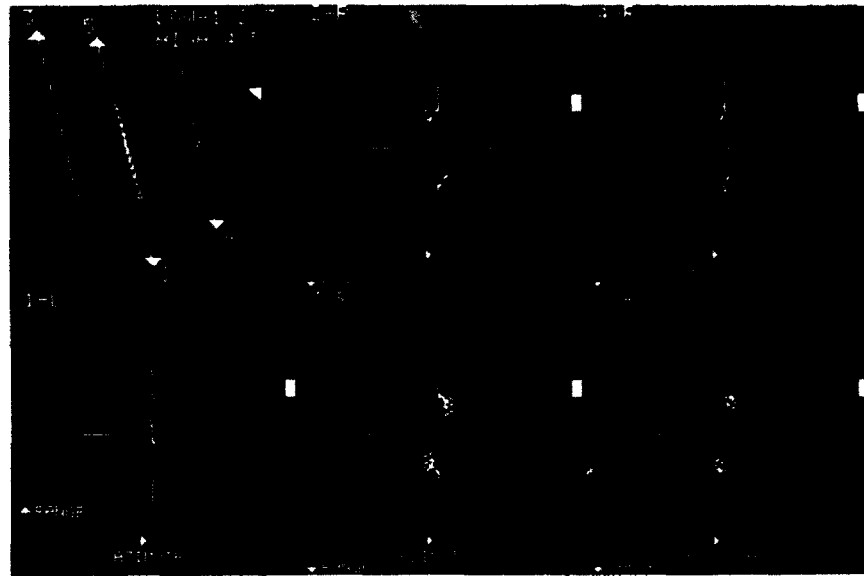


Figure 5. Average power spectra for each of the five SAR flights on 13 March 1987, showing evidence near the range axis of a characteristic null that is rotated clockwise (2 and 4) or counterclockwise (3 and 5), depending on the radar's orientation relative to the wave direction. The LEWEX common wind field estimate at the *Quest* on 13 March at 1200 UT was approximately 15 m/s from 60° , nearly opposite the heading of flight line 1. The outer circle is at $2\pi/50$ rad/m.



$$k_a = k'_a - \frac{(g/k')^{1/2}}{V} \quad (10)$$

The measured spectral estimates, $S(k'_a)$ and $S(k_a)$, at the nearest input grid points were then used to compute a revised spectral estimate,

$$S(k'_a) = S(k_a) + [S(k'_a) - S(k_a)] \frac{(k_a - k'_a)}{(k'_a - k_a)} \quad (11)$$

where the "+" and "-" signs denote the two input SAR grid nodes closest to the SAR wave number computed via Equation 10 for the desired output grid node k'_a .

The SAR imagery over the *Quest* on 13 March demonstrates the importance of accounting for the directional aspects of the velocity-bunching modulation. Figure 5 shows spectral estimates for five separate aircraft geometries, the first three at low altitude ($R/V \approx 50$ s) and the last two at high altitude ($R/V \approx 85$ s). Flights 2 and

4 are collinear, with the radar looking downwind to its right. The raw SAR power spectra for both of these flights depict a range-traveling wave that is split by a null located clockwise from the range axis. Flights 3 and 5 are also collinear, but in the opposite direction relative to flights 2 and 4; therefore, the radar is looking upwind to its right in flights 3 and 5. The raw power spectra for both of these flights also show a range-traveling wave, but the wave is split by a null located counterclockwise from the range axis. This directional behavior of the null, presumably resulting from the coherent addition of the tilt and velocity-bunching modulations, is consistent with the sign reversal implicit in Equation 6. The presence of this notch is evidence that velocity bunching is a significant modulating mechanism, even for a range-traveling wave field if it is moderately spread in the azimuthal coordinate.

Figure 6 illustrates important properties of the inverse SAR modulation transfer function as the incidence an-

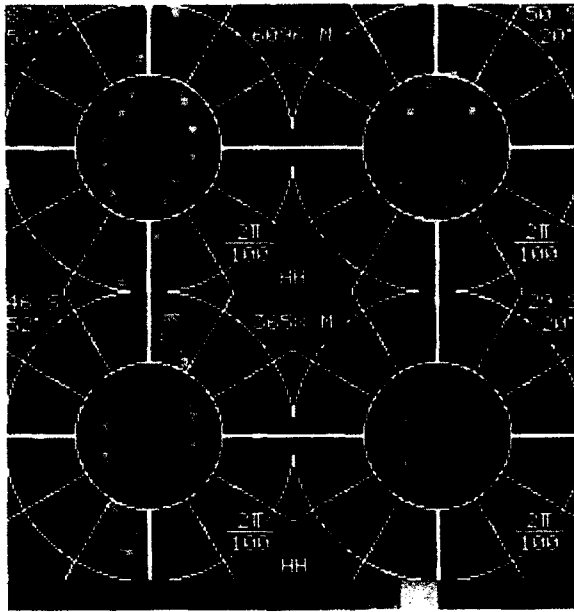


Figure 6. The SAR inverse modulation transfer function is computed as the reciprocal of Equation 7 to compare effects of platform R/V (87, 50, 46, and 29 s) and altitude (3658 and 6096 m) on its symmetry about the range axis. The outer circle is at $2\pi/100$ rad/m. A 20° look angle and an R/V of 29 s nearly balance SAR response characteristics in the range and azimuthal coordinates at the innermost circle, which is at $2\pi/200$ rad/m.

gle and the range-to-velocity ratio are varied. An SAR image spectrum will appear to be split along the maximum in the inverse $F^{-2}(k_r, k_a)$ function that was applied to estimate the ocean wave spectrum. For the LEWEX SAR data set, it was usually possible to determine whether the dominant waves were traveling toward or away from the radar by using SCR data, ship buoy data, or wave model estimates (see, e.g., the articles by Walsh, by Keeley, and by Gerling in this volume). By using these *a priori* estimates, the coherent phase relations of Equations 6 and 7 were applied to a larger LEWEX SAR data set to estimate ocean wave height-variance spectra on 13, 14, 17, 18, and 19 March. Results for the first four of these days are shown in Figure 7. By using the model described previously for the coherent modulation, the splitting of the spectra can be "healed" on 13 March, but the spectrum remains split near the range axis for the high flight of the SAR on 18 March.

CONCLUSIONS

For LEWEX, the azimuthal spectral response of the aircraft SAR is optimal in a narrow swath located between nadir and the first minimum of the antenna pattern downrange, where $R/V < 30$ s. The azimuthal wave number response degrades as the R/V ratio increases, and appears to be well described by Equation 1. This result seems to be as valid for the CCRS aircraft C-band SAR as it is for the Seasat L-band SAR.¹ For a significant wave height of 4.3 m, measured by the SCR on 14 March in the vicinity of the *Quest*, substitution of the

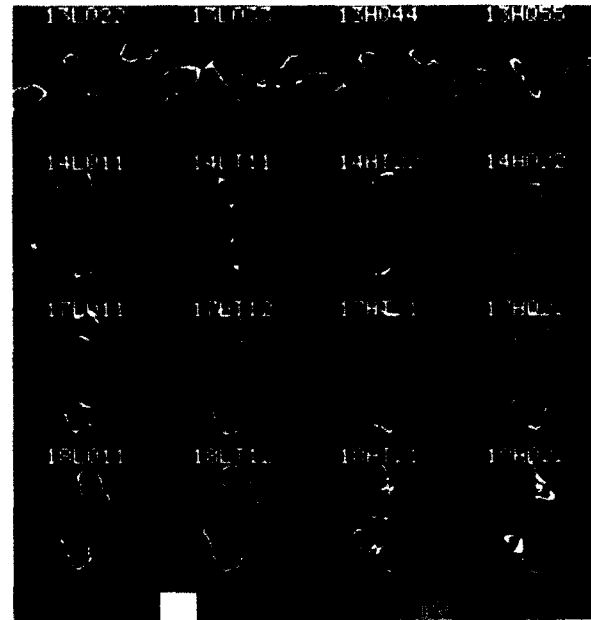


Figure 7. Ocean wave height-variance spectra computed from SAR data and rotated to a vertical north orientation are displayed with color-coded contours linearly spaced in relative units of m^4 . Low- (L) and high- (H) altitude flights of the radar over the *Quest* (Q) and *Tydemar* (T) locations on 13, 14, 17, and 18 March are depicted, yielding spectra that have been converted by using a phase-coherent model of velocity-bunching and tilt modulations. The outer circle is at $2\pi/100$ rad/m. (See Table 1 of Vachon (this volume) for a full explanation of the file names.)

measured resolution into Equation 1 yields a proportionality factor of $K = 1.1 (m/s^2)^{-1}$.

Reducing the R/V ratio, which can be achieved by lowering the altitude of the SAR platform, is beneficial in balancing the range and azimuthal components of the SAR modulation transfer function. A near-nadir look angle also increases theoretical range modulation relative to azimuthal modulation, but requires that the specular component of the surface backscatter be modeled to distinguish a wave-modulated signal from surface-glint random noise. The HH polarization is preferred over the vv polarization in increasing the surface wave tilt modulation of the model, as quantified in Equation 8.

The 14 March spectral intercomparisons⁷ show excess wave energy in the range coordinate for the SAR spectra relative to both the SCR and the ROWS spectra. This result indicates that hydrodynamic modulation of ocean surface scattering at C-band may be important. Surface roughness and radar backscatter are probably modulated by transient interactions between the wave surface and the turbulent wind field, tending to mask the coherent contributions to the cross-sectional modulation. The horizontally polarized SAR responded adequately to the azimuthally traveling wave system of 14 March (see Fig. 3) near nadir and in the main antenna lobe. The SAR imaging model² might be improved if the coherent modulation could be augmented by hydrodynamic modulation, even though such modulation is

poorly understood at present. Some combination of the dynamic transfer function (Eq. 2) and the coherent transfer function (Eq. 7) might be found to better match SAR spectra (see Fig. 4) to ROWS and SCR spectra. Better statistical models of short-scale wind and wave interactions are necessary to improve the utility of SAR transfer functions. The SAR spectra are likely to be most useful, and the SAR transfer function is likely to be most predictable and robust, at low off-nadir angles and low R/V ratios.

REFERENCES

- ¹ Beal, R. C., Tilley, D. G., and Monaldo, F. M., "Large- and Small-Scale Spatial Evolution of Digitally Processed Ocean Wave Spectra from Seasat Synthetic Aperture Radar," *J. Geophys. Res.* **88**, 1761-1778 (1983).
- ² Monaldo, F. M., and Lyzenga, D. R., "On the Estimation of Wave-Slope and Wave Height Variance Spectra from SAR Imagery," *IEEE Trans. Geosci. Remote Sens.* **GE-24**, 543-551 (1986).
- ³ Irvine, D. E., and Tilley, D. G., "Ocean Wave Directional Spectra and Wave-Current Interaction in the Agulhas from the Shuttle Imaging Radar-B Synthetic Aperture Radar," *J. Geophys. Res.* **93**, 15,389-15,401 (1988).
- ⁴ Freeman, N. G., Vachon, P. W., and Livingstone, C. W., "Airborne SAR Imaging of Azimuthally Travelling Ocean Surface Waves: The LEWEX Experimental Plan," in *Proc. IGARSS'87 Symposium*, Vol. II, Ann Arbor, Mich., pp. 1393-1398 (1987).
- ⁵ Tilley, D. G., "Use of Speckle for Determining the Response Characteristics of Doppler Imaging Radars," *Opt. Eng.* **25**, 772-779 (1986).
- ⁶ Tilley, D. G., "Approximating SIR-B Response Characteristics and Estimating Wave Height and Wavelength for Ocean Imagery," in *Proc. IGARSS'87 Symposium*, Vol. II, Ann Arbor, Mich., pp. 1581-1586 (1987).
- ⁷ Tilley, D. G., "Estimating Aircraft SAR Response Characteristics and Ocean Wave Spectra in the Labrador Sea Extreme Waves Experiment," *IEEE Trans. Geosci. Remote Sens.* **27**, 483-491 (1989).
- ⁸ Livingstone, C. E., Gray, A. I., Hawkins, R. K., Olsen, R. B., Deane, R. A., et al., "CCRS C-band Airborne Radar System Description and Test Results," in *11th Canadian Symposium on Remote Sensing*, Waterloo, Ontario, pp. 503-517 (1987).
- ⁹ Tilley, D. G., "Fourier Analysis of SAR Speckle for the Polynomial Synthesis of Spectral Corrections Applied to Seasat Oceanic Data," in *Digest IGARSS'83 Symposium*, Vol. II(a 3), San Francisco, Calif., pp. 4.1-4.6 (1983).
- ¹⁰ Monaldo, F. M., and Beal, R. C., "Limitations of the Seasat SAR in High Sea States," in *Wave Dynamics and Radio Probing of the Ocean Surface*, Phillips, O. M., and Hasselmann, K., eds., Plenum Press, New York, pp. 423-442 (1986).
- ¹¹ Bruning, C., Alpers, W., Zambresky, L. E., and Tilley, D. G., "Validation of a Synthetic Aperture Radar Ocean Wave Imaging Theory by the Shuttle Imaging Radar-B Experiment Over the North Sea," *J. Geophys. Res.* **93**, 15,403-15,425 (1988).

ACKNOWLEDGMENTS: The LEWEX image data were provided by A. S. (Pal) Bhogal of the Canada Centre for Remote Sensing (CCRS). Chuck Livingstone, Paris Vachon, and Laurence Gray of CCRS also contributed documentation of system parameters and postflight data processing operations. Funding for this work was provided primarily by the APL Independent Research and Development fund.

INTERPRETATION AND APPLICATION OF SAR WAVE IMAGE SPECTRA IN WAVE MODELS

A new closed integral transform relation describing the nonlinear mapping of a surface-wave spectrum into a synthetic aperture radar (SAR) image spectrum is presented and applied to selected Labrador Sea Extreme Waves Experiment cases. The new results agree well with observations and with computations using earlier Monte Carlo techniques. The integral transform can be expanded in a series whose terms can be computed rapidly using fast Fourier transforms. The series expansion of the integral transform expression is also useful in identifying the relative contributions of different imaging mechanisms.

INTRODUCTION

Synthetic aperture radars (SAR's) to be flown on ocean satellites and polar orbiting platforms in the 1990s will provide ocean wave modelers for the first time with global measurements of the two-dimensional ocean-wave spectrum. This should bring an unprecedented boost to ocean-wave modeling. But SAR images of the ocean-wave surface are not easily interpreted. They are often strongly nonlinear and show pronounced asymmetries with respect to range and azimuthal imaging. The development of appropriate methods for the efficient processing and assimilation of SAR wave data into ocean-wave models is not straightforward and presents a major challenge to the ocean-wave community.

The basic mechanisms of SAR ocean-wave imaging are nevertheless rather well understood today (cf. Ref. 1). In particular, the characteristic nonlinearity and range-azimuth asymmetry of SAR wave images can be explained by the large azimuthal displacements—compared with the scales of the long waves—of individual back-scattering elements in the image plane caused by the orbital motions of the long waves.

To cope with this strong nonlinearity, computations of the transformation of a surface-wave spectrum into a SAR image spectrum have been carried out in the past largely by means of "brute force" Monte Carlo simulations,²⁻⁷ in which a series of random realizations of the sea surface is generated for a given ocean-wave spectrum, and the sea surface is mapped into the SAR image plane, pixel by pixel, for each realization. The SAR images are then Fourier transformed, and the squared Fourier amplitudes are averaged over the ensemble of realizations to obtain an estimate of the image variance spectrum. Typically, 20 to 50 individual sea-surface realizations (40 to 100 degrees of freedom) need to be mapped. The method is relatively costly in computer time and suffers from the usual Monte Carlo statistical sampling uncertainty. Also, it does not offer a simple approach to the inverse problem of estimating the surface-wave spectrum from a measured SAR image spectrum.

Recently, a new closed integral relation for the mapping of a surface-wave spectrum into a SAR image spec-

trum has been derived by Hasselmann and Hasselmann.⁸ Although the transformation is strongly nonlinear, a closed relation between the input surface-wave spectrum and output SAR spectrum could nevertheless be derived by making use of the Gaussian property of the input wave field, which enables all higher order nonlinear dependencies on the input field to be reduced to the surface-wave spectrum.

The closed integral expression can be readily evaluated, after a suitable series expansion, by means of fast Fourier transforms (FFT's). The computing time (less than 1 s per spectrum on a CRAY-2 computer) is short enough for the method to be applied operationally to satellite SAR data. The integral was also evaluated directly without expansion, and although the FFT technique could not be applied, essentially identical results were obtained with comparable computation times for somewhat reduced spectral resolution.

The series expansion of the integral transform relation is also useful in clarifying the role of the various imaging mechanisms. Thus, the relative contributions from hydrodynamic and tilt modulation, from linear velocity bunching, from the interference between these processes, and from higher order nonlinear velocity-bunching interactions can be individually identified as separate spectral terms of the series expansion.

The closed transformation expression has the additional advantage of lending itself readily to inversion by means of iterative inverse modeling methods. Details are given in Ref. 8.

In this article, the results of the theory are summarized and applied to examples from the Labrador Sea Extreme Waves Experiment (LEWEX), using as input hindcast wave spectra computed with the WAM wave model.⁹ The theory is verified by comparing the new computations with the Monte Carlo simulations.

CONCEPTS AND NOTATIONS

To discuss meaningfully the new transformation relation presented in the next section and interpret its subsequent application to LEWEX SAR spectra, some basic

concepts and notation need to be introduced. See Ref. 1 for a review of the standard two-scale theory of SAR imaging of a surface-wave field on which these concepts are based. The derivation of the spectral transformation relation is given in Ref. 8.

It is convenient to regard the SAR surface-wave image as the result of two consecutive imaging mechanisms: the cross-section modulation that produces the frozen surface image, $I^R(r)$, and the additional motion effects that, together with the frozen surface contribution, yield the net SAR image, $I^S(r)$, where r is the position vector.

The Frozen Surface Contribution

The frozen surface image, $I^R(r)$, of a linear ocean-wave field corresponds to the image that would be obtained by a real aperture radar (RAR). To a good approximation, it can be linearly related to the surface-wave field.

The surface-wave elevation $\zeta(r, t)$ of a linear ocean-wave field can be decomposed into a superposition of freely propagating wave components:

$$\zeta(r, t) = \int dk \{ \zeta(k) \exp(i[k \cdot r - \omega t]) + \text{complex conjugate} \} , \quad (1)$$

where $\omega = \sqrt{gk}$ is the gravity-wave frequency, t is time, ζ is the wave height, i designates the "imaginary part of," and k is the wave number vector. To avoid a proliferation of symbols, we shall use the same symbol for a function and its Fourier transform, distinguishing the two where necessary by their arguments. If the RAR imaging mechanism is linear, the variations of the (specific) backscattering cross section, $\sigma(r, t)$, can be similarly decomposed into free wave components:

$$\sigma(r, t) = \bar{\sigma} \{ 1 + \int dk [m(k) \exp(i[k \cdot r - \omega t]) + \text{complex conjugate}] \} , \quad (2)$$

where the cross-section modulation, $m(k)$, is linearly related to $\zeta(k)$ through a modulation transfer function (MTF), $T^R(k)$,

$$m(k) = T^R(k) \zeta(k) , \quad (3)$$

and $\bar{\sigma}$ denotes the space-time averaged cross section.

The RAR MTF, $T^R(k)$, can be further decomposed into tilt and hydrodynamic contributions:

$$T^R(k) = T^t(k) + T^h(k) . \quad (4)$$

The tilt and hydrodynamic MTF's have been discussed in detail by various authors.^{5, 10-13} For the general theory, however, we require only the net frozen surface MTF, $T^R(k)$, without invoking its decomposition into tilt and hydrodynamic components. We point out also that although we present here a quantitative closed theory for the imaging mechanism as such, the details of the hydrodynamic MTF required as input (and its possible

nonlinear corrections) are still only poorly known and need further study.

The frozen surface SAR image represents a snapshot of the field $\sigma(r, t)$ at a particular time, say $t = 0$. Measuring the image modulation intensity $I^R(r)$ (after subtraction of the mean) in units of the normalized cross section, $\sigma(r, 0)/\bar{\sigma}$,

$$I^R(r) = \frac{\sigma(r, 0)}{\bar{\sigma}} - 1 , \quad (5)$$

and introducing the Fourier integral,

$$I^R(r) = \int dk I^R(k) e^{i k \cdot r} , \quad (6)$$

we have, from Equation 2,

$$I^R(k) = m(k) + m(-k)^* , \quad (7)$$

where the asterisk indicates a complex conjugate. We have ignored here the SAR system MTF. It appears simply as an additional factor in Equation 7 that we may regard as absorbed in the definition of $m(k)$.

We have also ignored, for simplicity, distortion effects because a side-looking radar does not, in fact, make a field snapshot image but builds up the image from a sequence of consecutively imaged snapshot strips. Thus, moving waves are imaged with slightly Doppler displaced "wave numbers of encounter." (This straightforward geometric effect applies equally for a RAR and a SAR and should be distinguished from the SAR motion effects summarized in the following section.)

Finally, we have not considered clutter effects. To first order, they may simply be represented as an additional clutter noise spectrum superimposed on the image spectrum discussed here.¹⁴

We note that according to Equation 7,

$$I^R(k) = I^{R*}(-k) , \quad (8)$$

in accordance with the reality condition for a frozen two-dimensional surface, whereas $\zeta(k)$, $\zeta(-k)$ and, similarly, $m(k)$, $m(-k)$ refer to different time-dependent wave components propagating in opposite directions and which, therefore, are not related.

In terms of the directional wave spectrum $F(k)$, defined by

$$\langle \zeta^*(k) \zeta(k') \rangle = \delta(k - k') \frac{F(k)}{2} \quad (9)$$

(where the angle brackets denote ensemble means) such that

$$\langle \zeta^2 \rangle = \int F(k) dk , \quad (10)$$

and the frozen surface SAR image variance spectrum $P^R(k)$ is defined by

$$\langle I^{R*}(k) I^R(k') \rangle = \delta(k - k') P^R(k) , \quad (11)$$

with

$$\langle I^R \rangle = \int P^R(k) dk, \quad (12)$$

the linear amplitude relations (Eqs. 3 and 7) translate into the linear relation

$$P^R(k) = \frac{1}{2} [|T^R(k)|^2 F(k) + |T^R(-k)|^2 F(-k)], \quad (13)$$

Motion Effects

We limit the discussion of motion effects to pure velocity bunching. Higher order acceleration smearing can be included in the general theory,⁸ but it is usually small and will be ignored here for simplicity.

Velocity bunching arises through the variable azimuthal displacements, ξ , of individual backscattering elements in the image plane caused by the spatially variable long-wave orbital velocities. According to standard SAR theory,

$$\xi = \beta v, \quad (14)$$

where v is the range component of the local long-wave orbital velocity advecting the small-scale backscattering element, and

$$\beta = \rho/U, \quad (15)$$

where ρ is the slant range and U is the platform velocity.

For displacements that are small compared with the characteristic wavelength of the long waves, the velocity-bunching mechanism can be linearized and described by a velocity bunching MTF:

$$T^{vb}(k) = -i\beta k_x T^v(k), \quad (16)$$

where the orbital velocity MTF is

$$T^v(k) = -\omega \left(\sin \theta \frac{k_l}{|k|} + i \cos \theta \right), \quad (17)$$

The SAR image spectrum is then given by the linear expression

$$P^S(k) = \frac{1}{2} [|T^S(k)|^2 F(k) + |T^S(-k)|^2 F(-k)], \quad (18)$$

where the net SAR MTF is

$$T^S(k) = T^R(k) + T^{vb}(k). \quad (19)$$

The index S refers here and in the following to the SAR image, including motion effects, while the index R refers, as before, to the frozen surface RAR image.

The linear theory has only limited applicability. As will be shown later, it breaks down in all cases, even for low sea states, for high azimuthal wave numbers. The general nonlinear transformation expression presented in the next section yields, to lowest order, a simple quasi-linear generalization of Equation 18 containing an additional nonlinear azimuthal cutoff factor. This is found to be quite widely applicable and provides a reasonable

qualitative description of the SAR spectrum, even in strongly nonlinear cases.

The above relations define all quantities needed to write the general spectral nonlinear transfer expression, with the exception of three autocovariance and covariance functions, which are formed from quadratic products of the fields v and I^R at time lag zero and finite spatial lag r :

$$\begin{aligned} f^v(r) &= \langle v(x+r)v(x) \rangle \\ &= \int F(k) |T^v(k)|^2 \exp(ik \cdot r) dk, \end{aligned} \quad (20)$$

$$\begin{aligned} f^R(r) &= \langle I^R(x+r)I^R(x) \rangle \\ &= \int \frac{1}{2} (F(k) |T^R(k)|^2 \\ &\quad + F(-k) |T^R(-k)|^2) \exp(ik \cdot r) dk, \end{aligned} \quad (21)$$

$$\begin{aligned} f^{Rv}(r) &= \langle I^R(x+r)v(x) \rangle = \int \frac{1}{2} (F(k) T^R(k) T^v(k)^* \\ &\quad + F(-k) T^R(-k)^* T^v(-k)) \exp(ik \cdot r) dk. \end{aligned} \quad (22)$$

THE CLOSED NONLINEAR SPECTRAL TRANSFORMATION RELATION

The general nonlinear spectral transformation relation derived in Ref. 8 is presented in two forms: as a closed nonlinear integral transform expression, and as a power series expansion. The general integral form does not lend itself readily to computation by fast transform techniques, whereas the terms of the power series expansion can be evaluated individually by fast Fourier transforms. Thus, the expansion form can usually be computed more rapidly. The decomposition into a series also provides a clearer picture of the interplay of the various linear and nonlinear imaging mechanisms in the formation of the final image.

The transform was computed both by direct integration (using a lower resolution representation of the spectrum) and by the fast Fourier transform expansion method. The results were essentially identical.

The closed integral expression has the form

$$\begin{aligned} P^S(k) &= (2\pi)^{-2} \exp[-k_x^2 \xi'^2] \int dr e^{-ik \cdot r} \exp[k_x^2 \beta^2 f^v(r)] \\ &\quad \times \{1 + f^R(r) + ik_x \beta [f^{Rv}(r) - f^{Rv}(-r)] \\ &\quad + (k_x \beta)^2 [f^{Rv}(r) - f^{Rv}(0)] [f^{Rv}(-r) - f^{Rv}(0)]\}, \end{aligned} \quad (23)$$

where

$$\xi' = \beta \langle v^2 \rangle^{1/2} \quad (24)$$

is the root mean square azimuthal displacement.

The power series expansion is obtained by expanding the second exponential factor in Equation 23. (It is the dependence of this factor on k_x^2 that destroys the otherwise straightforward Fourier transform structure of the integral.) One obtains a series of the form

$$P^S(k) = \exp(-k_x^2 \xi'^2) \sum_{n=1}^{\infty} \sum_{m=2n-2}^{2n} (k_x \beta)^m P_{nm}^S(k) \quad (25)$$

where the index n indicates the order in nonlinearity with respect to the input wave spectrum, and the index m the order with respect to the velocity-bunching parameter β (which is seen to occur always in combination with the azimuthal wave number k_x).

Explicitly,

$$P_{n,2n}^S = \frac{1}{n!} \Omega_n \{f^v(r)^n\} \quad (26)$$

$$P_{n,2n-1}^S = \Omega_n \left\{ \frac{i[f^{Rv}(r) - f^{Rv}(-r)]f^v(r)^{n-1}}{(n-1)!} \right\} \quad (27)$$

$$P_{n,2n-2}^S = \Omega_n \left\{ \frac{1}{(n-1)!} f^R(r) f^v(r)^{n-1} + \frac{1}{(n-2)!} [f^{Rv}(r) - f^{Rv}(0)] \times [f^{Rv}(-r) - f^{Rv}(0)] f^v(r)^{n-2} \right\} \quad (28)$$

where Ω_n denotes the Fourier transform operator

$$\Omega_n = (2\pi)^{-2} \int dr \exp(-ik \cdot r) \quad (29)$$

and n runs through all positive integers 1, 2, For nonpositive integers, the factorial function is defined as $0! = 1$ and $[(-1)!]^{-1} = 0$. We have left out a term $P_{0,0}$ in the sum representing an irrelevant δ -function contribution at $k = 0$ arising from the mean image intensity.

Summation over the velocity-bunching index m for fixed nonlinearity order n yields a stratification of the expansion with respect to the nonlinearity only:

$$P^S(k) = \exp(-k_x^2 \xi'^2) \times (P_1^S(k) + P_2^S(k) + \dots + P_n^S(k) + \dots) \quad (30)$$

The linear term, P_1^S , is found to be identical (as it must be) to the linear SAR spectrum of Equation 18.

The computation of $P^S(k)$ according to Equations 25 or 30 involves three steps:

1. Computation of the three autovariance and covariance functions $f^v(r)$, $f^R(r)$, and $f^{Rv}(r)$ using the Fourier transform relations 20, 21, and 22.
2. Computation of the various covariance product expressions in Equations 26 through 28.
3. Computation of the Fourier transforms of the covariance product expressions, yielding the series 25. (If there is no need to stratify the expansion with respect to nonlinearity order, the covariance products of different nonlinearity order n for given velocity-bunching order m can be collected together and Fourier transformed in a single operation.)

Since only Fourier transforms are involved, the computations are relatively fast. The complete transformation can be computed in less than 1 s on a CRAY 2. (The computations could also be carried out efficiently on a personal computer with hard-wired fast Fourier transform.) Good convergence is normally achieved even for strongly nonlinear spectra for $n \approx 4$ to 6. The contributions from the higher order terms are concentrated mainly in the neighborhood of the (normally not very important) azimuthal cutoff regions.

As a check, the integral (Eq. 23) was also evaluated directly. The wave-number coordinates were transformed to frequency-direction coordinates, and the integral was computed using the relatively low resolution of the wave model (30° directional resolution and a logarithmic frequency discretization with $\Delta\omega/\omega = 0.1$). The computation time was comparable with the fast Fourier transform expansion method, and the results were virtually identical.

An important feature of the expansions 25 and 30 is the occurrence of the common (nonlinear) azimuthal cutoff factor

$$C = \exp(-k_x^2 \xi'^2) \quad (31)$$

Without inclusion of this azimuthal cutoff factor, the straightforward linear approximation $F_1^S(k)$ must always break down at high azimuthal wave numbers, even for low sea states, since real wave spectra, and therefore also F_1^S , decay as a power of the wave number at high wave numbers, rather than exponentially, as required by Equation 30.

In contrast, the lowest order quasi-linear approximation

$$P^S(k) = \exp(-k_x^2 \xi'^2) P_1^S(k) \quad (32)$$

of Equation 30, with inclusion of the nonlinear azimuthal cutoff factor, remains a valid approximation for the entire spectrum. In practice, Equation 32 was found to yield a reasonable quantitative approximation for about half the SEASAT and LEWEX SAR spectra studied in Ref. 15 and by C. Brüning and L. F. Zambresky (personal communication), and was successful in capturing the qualitative features of the SAR spectrum in all cases.

If applied as a first approximation in the inverse mapping problem, the quasi-linear form can be immediately inverted analytically (for given ξ'). The solution can then be used to construct a general iterative inversion method for estimating wave spectra from observed SAR spectra.⁸ The method gave good convergence in both linear and strongly nonlinear cases.

The existence of a common azimuthal cutoff factor (Eq. 31) acting on all terms of the spectral expansion (Eq. 30) has a useful practical application. Since the cutoff scale ξ' can be readily determined for any SAR spectrum, regardless of the details of the nonlinear imaging process, it provides a robust estimate of a useful integral wave parameter: the root mean square orbital velocity component in the range direction.

It is of interest that Beal et al.,¹⁶ Lyzenga,⁶ and Monaldo and Lyzenga^{17,18} have already noted empiri-

cally that the observed azimuthal cutoff scale appeared to be proportional to the total root mean square orbital velocity integrated over the entire long-wave spectrum (or some similar integral wave parameter). Previously, this finding had been difficult to interpret theoretically. The frequently used SAR two-scale model, in which an additional scale separation is introduced at the SAR resolution scale, yields an explicit azimuthal smearing given by the so-called "velocity spread" term (cf. Refs. 1 and 19). This is determined by the subresolution scale contribution to the root mean square orbital velocity, i.e., by the integral over only the high wave-number tail of the long-wave orbital velocity spectrum. Tucker¹⁹ computed the effect of this smearing and obtained a filter function that was identical to our form C (Eq. 31), but with ξ' replaced by the root mean square azimuthal displacement (the velocity spread) arising from only the short subresolution scale waves. The present closed transformation theory indicates that the nonlinear velocity bunching from the longer waves must also contribute to the azimuthal smearing, and that the net effect of both short and long waves can be expressed very simply by the azimuthal cutoff factor C —in accordance with Beal et al.¹⁶ and Lyzenga's⁵ findings.

APPLICATION TO LEWEX

As an illustration, we apply the transform relation to two LEWEX cases. The input wave spectra for the transformation computations were taken from the observed directional wave buoy (Wavescan) data and from a wave

hindcast using the WAM third-generation wave model.⁹ Comparison of the hindcast wave fields with wave-buoy observations indicated that the hindcast was acceptable as a first guess, although some systematic deviations were found (cf. Fig. 1). The cases were selected from larger data sets that were analyzed as part of a more extensive wave hindcast study (C. Brüning and L. F. Zambresky, personal communication).

The principal SAR parameters of the two runs are listed in Table 1. The polarization was horizontal-horizontal and the look direction to the right for both runs. The damping factor and wind input modulation term in the hydrodynamic MTF were set equal to zero. The images for both runs were taken over essentially the same wave field, but the two SAR flight directions were opposite, and the aircraft altitude and thus the β parameters (ρ/U) differed by a factor of nearly two.

Figures 1 and 2 compare the observed and computed SAR spectra for the two runs. The two rows in the

Table 1. SAR parameters for two LEWEX runs on 14 March 1987 at the *Tydemar* (50°N latitude, 45°W longitude); the flight speed was 128 m/s and the incidence angle was 52°.

Run	Time (UT)	Flight direction (deg)	Altitude (m)	Slant range, ρ (m)	Range-to-velocity ratio, β
1	1219	89	3688	5990	46.8
2	1259	270	6096	9902	77.4

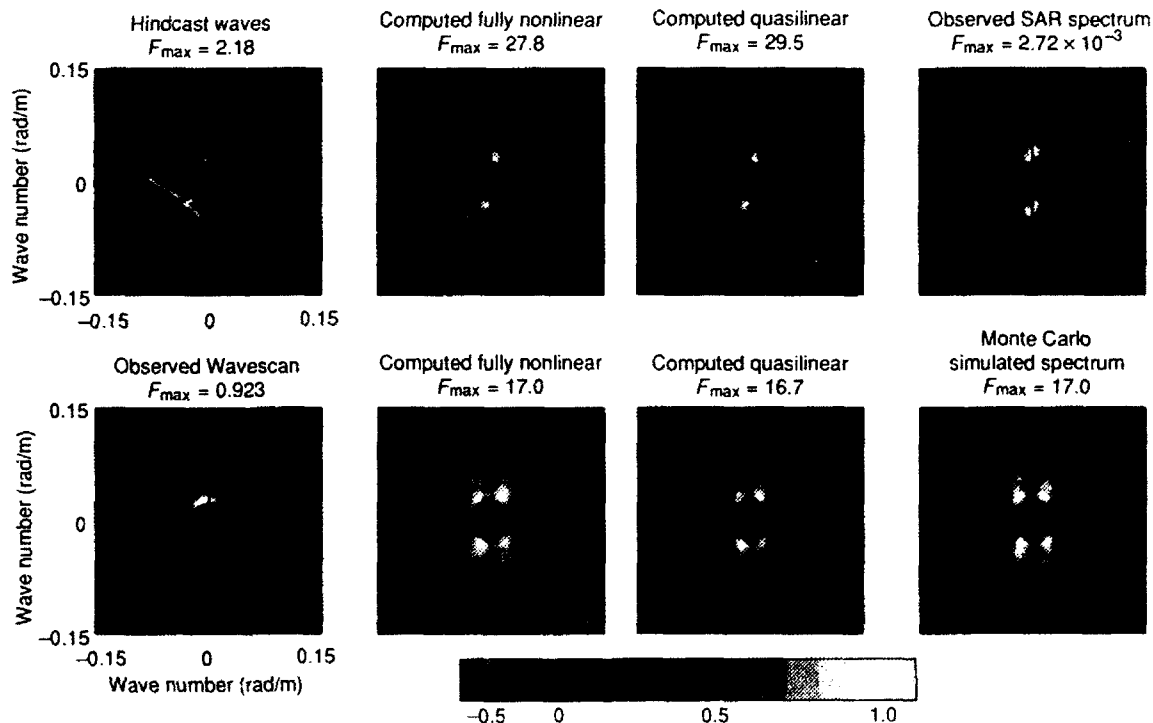


Figure 1. Hindcast (top row) and observed (Wavescan, bottom row) wave spectra together with computed SAR spectra for LEWEX run 1 over the *Tydemar*, 1219 UT on 14 March. The observed SAR spectrum is shown in the top right panel. The bottom right panel shows the Monte Carlo simulated SAR spectrum for the Wavescan wave spectrum. The aircraft flight direction is in the x -direction. Spectra are normalized with respect to the maximal spectral density F_{\max} (given in units of m^4).

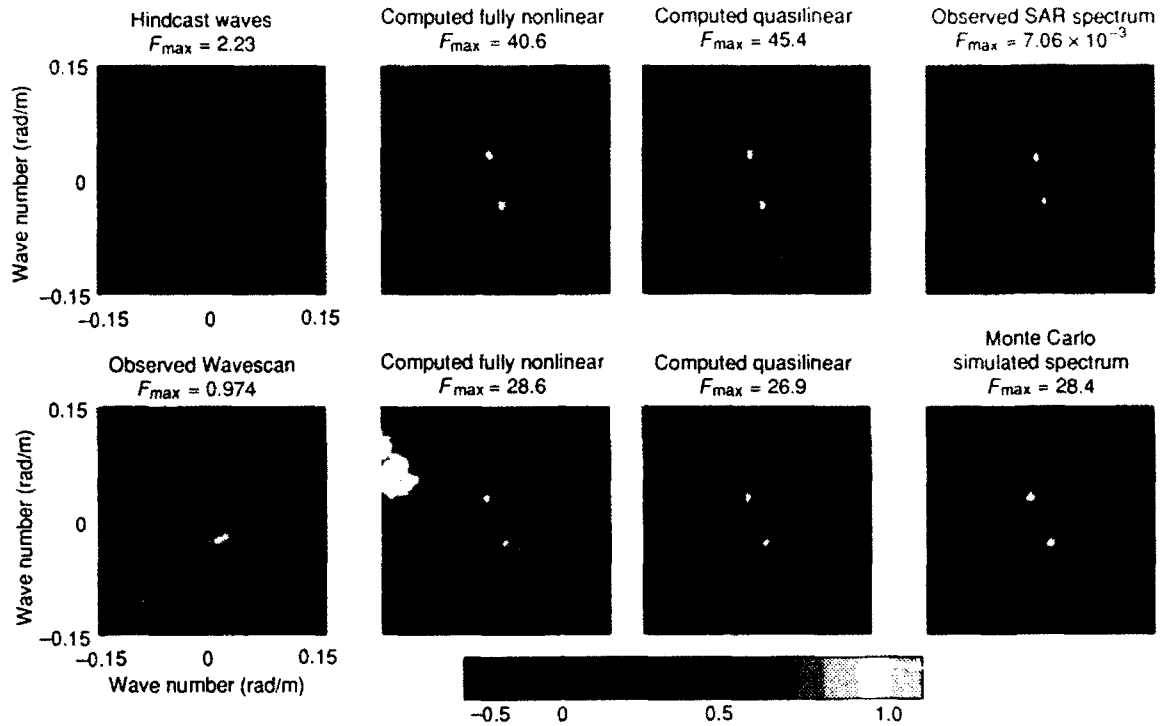


Figure 2. Same as Figure 1 but for LEWEX run 2 over the *Tydemar*, 1259 UT on 14 March. The aircraft flight direction is opposite that of run 1. Coordinates are defined as before in the aircraft frame.

figures correspond to different input wave spectra, shown in the left column. The Monte Carlo computations are shown only for the Wavescan spectra (second row).

Several features are apparent:

1. The SAR wave image spectra show little resemblance to the (symmetrized) input wave spectra. This is, of course, a well-known feature of SAR spectra. But perhaps it has not always been fully appreciated that the distortion can be pronounced not only for azimuthally traveling waves, for which the nonlinearities are large, but also for relatively linear range traveling waves, as in these examples.

2. The azimuthal cutoff is well defined and occurs at a lower wave number for the higher altitude flight, as expected.

3. The SAR spectra show evidence of some azimuthal asymmetry relative to the SAR look direction that is not apparent in the original wave spectra. The asymmetry depends on the wave propagation direction relative to the SAR look direction. In run 1 (Fig. 1), waves in the top right quadrant are enhanced relative to the waves in the top left quadrant, whereas in run 2 (Fig. 2), waves in the bottom right quadrant (corresponding to the top left quadrant in the 180° rotated spectrum of Fig. 1) are enhanced relative to the bottom left quadrant. The fact that the asymmetry depends on the SAR look direction—in both the simulations and the observations—is a clear indication that it represents an artifact of the imaging and is not a real feature of the wave spectrum.

4. The theoretical SAR spectra agree reasonably well with the measured SAR spectra in all cases. This, together with the features listed above, underlines the need for a first-guess input wave spectrum and the application of quantitative nonlinear mapping computations for the meaningful interpretation of measured SAR spectra.

5. The quasi-linear approximation (Eq. 32) yields a good first-order description, perhaps not surprising in these examples of relatively linear, predominately range-traveling waves.

6. The closed nonlinear transformation relation and the Monte Carlo computations yield essentially identical results. The small deviations between the Monte Carlo method and the closed integral computations near the azimuthal cutoff line can probably be attributed to the analytical Phillips form of the high-frequency tail of the spectrum used in the Monte Carlo computations as opposed to the modeled spectrum in the closed integral computations.

The distortions of the SAR spectra relative to the wave spectra can be explained rather simply by the structure of the SAR MTF, Equation 19. The azimuthal asymmetry is produced by interference between the frozen surface and velocity-bunching MTF's. The frozen-surface MTF is symmetrical about the look direction, whereas the velocity-bunching MTF is antisymmetrical (cf. Eqs. 5, 6, 16, and 17). Thus, while the square modulus of each MTF, taken by itself, is symmetrical about the look direction, the square modulus of the net complex SAR MTF, consisting of the sum of both MTF's is, in general, nonsymmet-

rical. It follows, moreover, that a change in sign of the look direction interchanges the enhanced and attenuated lobes of the wave spectrum, as seen in Figures 1 and 2.

The interference between the frozen surface and the velocity-bunching modulation can be identified explicitly in the expansion (Eq. 25). The relevant spectral distributions are shown in Figure 3 for run 1. The first term, $C \cdot P_{10}^S$ ($n = 1, m = 0$) (Fig. 3A), represents the frozen surface contribution (but with the inclusion of the azimuthal cutoff factor C). It is positive everywhere and reproduces the approximately symmetrical distribution of the wave spectrum about the SAR look direction. The second term, $C \cdot (k_x \beta) P_{11}^S$ ($n = 1, m = 1$) (Fig. 3B), represents the quadratic interference between the frozen surface and velocity-bunching transfer functions. It is asymmetrical, alternating in sign between quadrants. The third term, $C \cdot (k_x \beta)^2 P_{12}^S$ ($n = 1, m = 2$) (Fig. 3C), represents the pure (quasi-linear) velocity-bunching term, without the RAR contribution. It is positive and symmetrical. The sum of the first three terms yields the quasi-linear SAR spectrum, Equation 32 (Fig. 3D), which is shown also in the corresponding panel of Fig. 1. The asymmetry of the quasi-linear spectrum is seen to arise from the interference term. Asymmetries occur in general in all higher order, odd- m terms of the expansion (e.g., Figs. 3E and 3F), contributing to the asymmetry of the final nonlinear SAR spectrum (Fig. 3H). Figure 3G ($m = 10$) is an example of a higher order symmetrical spectral term. It exhibits a pronounced concentration along the azimuthal cutoff line that is characteristic of all higher

order terms and arises from the product of the factor $(k_x \beta)^m$ with the exponential azimuthal cutoff factor C .

CONCLUSIONS

A new, closed, nonlinear, integral transform relation describing the mapping of a two-dimensional surface-wave spectrum into a SAR image spectrum has been presented and discussed for two LEWEX examples. The new transform relation offers a number of advantages. It is rapid and accurate enough to be applied routinely to the processing of quasi-continuous operational satellite SAR data. It offers a simple approach to the inverse problem of inferring the optimal wave spectrum from a measured SAR spectrum for a given first-guess wave spectrum (cf. Ref. 8). By expanding the integral transform in a Fourier transform series, it provides a clearer insight into the details of the mapping mechanisms. The expansion yields separate spectral contributions for the frozen-surface (RAR) modulation term, the linear velocity-bunching mechanism, the linear interaction between the two, and the higher order nonlinear velocity-bunching interactions and distortions. The azimuthal smearing caused by nonlinear velocity-bunching effects can be expressed very simply as an exponential cutoff factor that applies to all terms of the expansion.

The LEWEX examples demonstrate that SAR ocean-wave imaging theory is in good agreement with measurements. The SAR spectra can differ strongly from the input wave spectra so that a general quantitative interpretation of SAR image spectra in all cases is possible only

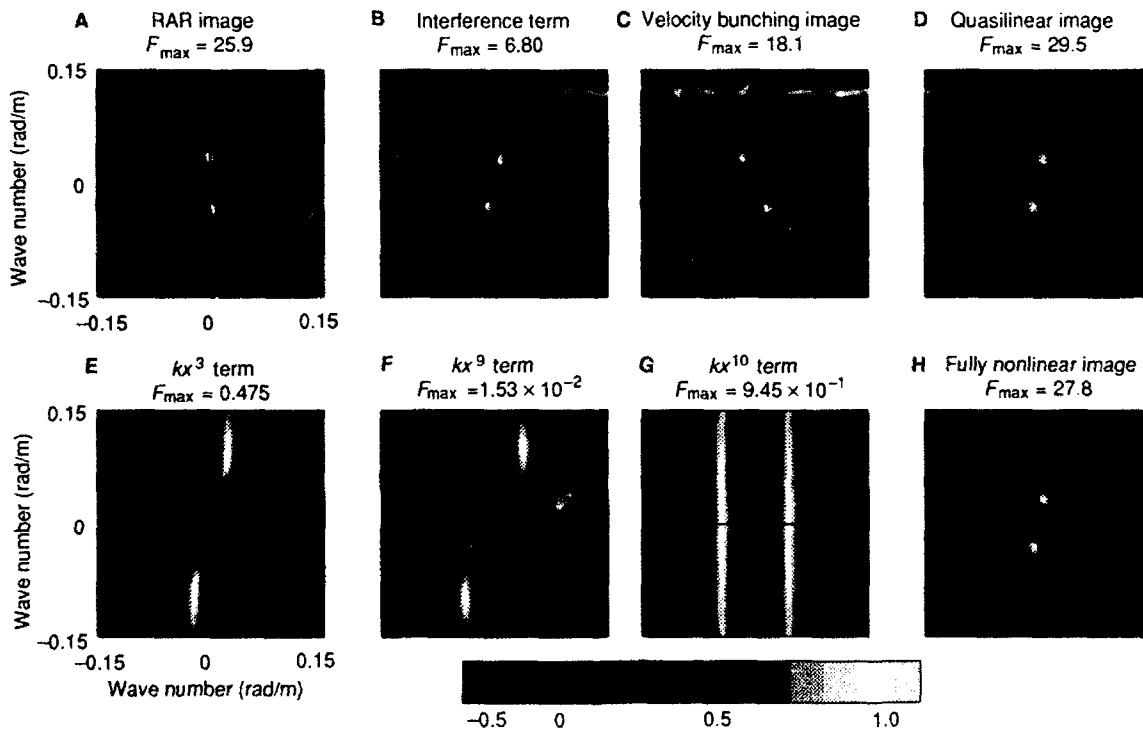


Figure 3. Contributions of various spectral expansion terms to the SAR spectral image for LEWEX run 1. Note the asymmetry about the look direction induced by the terms with odd m (k_x powers). The dominant asymmetry arises from the linear RAR velocity-bunching interference term ($m = 1, n = 1$).

with the aid of exact nonlinear transform computations and a reasonable first-guess wave spectrum derived from a model. The quasi-linear SAR image spectrum (the linear SAR spectrum augmented by the azimuthal cutoff factor) nevertheless provides a good quantitative approximation in many cases in which the nonlinearities are not too severe and also provides a useful qualitative description of the spectrum even for strongly nonlinear cases.

REFERENCES

- ¹ Hasselmann, K., Raney, R. K., Plant, W. J., Alpers, W., Shuchman, R. A., et al., "Theory of Synthetic Aperture Radar Ocean Imaging: A MARSEN View," *J. Geophys. Res.* **90**, 4659 (1985).
- ² Alpers, W., "Monte Carlo Simulations for Studying the Relationship Between Ocean Wave and Synthetic Aperture Radar Image Spectra," *Geophys. Res.* **88**, 1745 (1983).
- ³ Alpers, W., Brüning, C., and Richter, K., "Comparison of Simulated and Measured Synthetic Aperture Radar Image Spectra with Buoy-Derived Ocean Wave Spectra during the Shuttle Imaging Radar-B Mission," *IEEE Trans. Geosci. Remote Sensing* **GE-24**, 559 (1986).
- ⁴ Alpers, W., and Brüning, C., "On the Relative Importance of Motion-Related Contributions to the SAR Imaging Mechanism of Ocean Surface Waves," *IEEE Trans. Geosci. Remote Sensing* **GE-24**, 873 (1986).
- ⁵ Lyzenga, D. R., "Numerical Simulation of Synthetic Aperture Radar Image Spectra for Ocean Waves," *IEEE Trans. Geosci. Remote Sensing* **GE-24**, 863 (1986).
- ⁶ Brüning, C., Alpers, W., Zambresky, L. F., and Tilley, D. G., "Validation of a SAR Ocean Wave Imaging Theory by the Shuttle Imaging Radar-B Experiment over the North Sea," *J. Geophys. Res.* **93**, 15,403 (1988).
- ⁷ Brüning, K., Alpers, W., and Hasselmann, K., "Monte Carlo Simulation Studies of the Nonlinear Imaging of a Two-Dimensional Surface Wave Field by a Synthetic Aperture Radar," *Int. J. Remote Sensing* (1990).
- ⁸ Hasselmann, K., and Hasselmann, S., "On the Nonlinear Mapping of an Ocean Wave Spectrum into a SAR Image Spectrum and Its Inversion" (submitted to *J. Geophys. Res.*).
- ⁹ WAMDIG (Wave Model Development and Implementation Group), "The WAM Model--A Third-Generation Ocean Wave Prediction Model," *J. Phys. Oceanogr.* **18**, 1775-1810 (1988).
- ¹⁰ Keller, W. C., and Wright, J. W., "Microwave Scattering and the Straining of Wind Generated Waves," *Radio Sci.* **10**, 139-147 (1975).
- ¹¹ Plant, W. J., Keller, W. C., and Cross, A., "Parametric Dependence of the Ocean Wave Radar Modulation Transfer Function," *J. Geophys. Res.* **88**, 9747-9756 (1983).
- ¹² Schroter, J., Feindt, F., Alpers, W., and Keller, W. C., "Measurement of the Ocean-Wave Radar Modulation Transfer Function at 4.3 GHz," *J. Geophys. Res.* **91**, 932-946 (1986).
- ¹³ Feindt, F., Schroter, J., and Alpers, W., "Measurement of the Ocean Wave-Radar Modulation Transfer Function at 35 GHz from a Sea Based Platform in the North Sea," *J. Geophys. Res.* **91**, 9701-9708 (1986).
- ¹⁴ Alpers, W., and Hasselmann, K., "Spectral Signal-to-Clutter and Thermal Noise Properties of Ocean Wave Imaging Synthetic Aperture Radars," *Int. J. Remote Sensing* **3**, 423-446 (1982).
- ¹⁵ Hasselmann, K., Hasselmann, S., Bauer, E., Brüning, C., Lehner, S., et al., "Development of a Satellite SAR Image Spectra and Altimeter Wave Height Data Assimilation System for ERS-1," ESA contract report and MPI report No. 19 (1988).
- ¹⁶ Beal, R. C., Tilley, D. G., and Monaldo, F. M., "Large- and Small-Scale Spatial Evolution of Digitally Processed Ocean Wave Spectra from SEASAT Synthetic Aperture Radar," *J. Geophys. Res.* **88**, 1761-1778 (1983).
- ¹⁷ Monaldo, F. M., and Lyzenga, D. R., "On the Estimation of Slope- and Height-Variance Spectra from SAR Imagery," *IEEE Trans. Geosci. Remote Sensing* **GE-24**, 543-551 (1986).
- ¹⁸ Monaldo, F. M., and Lyzenga, D. R., "Comparison of Shuttle Imaging Radar-B Ocean Wave Spectra with Linear Model Predictions Based on Aircraft Measurements," *J. Geophys. Res.* **93**, 15,374-15,388 (1988).
- ¹⁹ Tucker, M. J., "The Imaging of Waves by Satellite Synthetic Aperture Radar: The Effects of Surface Motion," *Int. J. Remote Sensing* **6**, 1059-1074 (1985).

REMOVAL OF 180° AMBIGUITY IN SAR IMAGES OF OCEAN WAVES

Conventional methods for estimating directional wave spectra from an image of the sea lead to symmetric spectra, where the true wave directions are ambiguous by 180°. By using a time sequence of images, however, the ambiguity can be resolved. Building on previous results from shipboard navigation radars, the methodology is extended to multilook, airborne synthetic aperture radar imagery obtained during the Labrador Sea Extreme Waves Experiment.

INTRODUCTION

A conventional Fourier transformation of a real image of a wave pattern produces a radially symmetric spectrum, with the direction of the wave propagation ambiguous by 180°. The ambiguity in a single image is generally resolvable only by imposing external assumptions. A time sequence of such images, however, provides sufficient data to remove the ambiguity completely.

Before LEWEX, multidimensional methods were developed and applied to the analysis of a time series of wave images from shipboard navigation radars. Atanassov et al.,¹ using two images sampled at a time interval τ , showed that the ambiguity could be removed for wave numbers k restricted by $0 < k < \pi^2/g\tau^2$, where g is the gravitational acceleration. Young et al.² extended the method, using a three-dimensional description of the ocean wave field, where the third dimension is derived from a time series of images of the evolving wave system.

If the time series of a wave pattern comprises a sequence of single images, each covering an adequate area of the water surface, and if the images are separated by a constant and sufficiently small time step, then the multidimensional analysis can be applied. The sampling requirements can be specified with adequate knowledge of the dynamics.³ These techniques, already validated for a ship navigation radar (see the article by Ziemer in this volume), are extended here to time-sequential (multilook) airborne synthetic aperture radar (SAR) imagery. The method was successfully applied to two successive SAR images by Vachon and Raney⁴ (see also the article by Raney and Vachon in this volume). Rosenthal et al.⁵ demonstrated the application of the image-time-series analysis by using seven single looks from the signal domain of airborne SAR data.

MULTIDIMENSIONAL DESCRIPTION OF A WAVE FIELD

We may describe a time series of an image wave pattern by its measured photographic gray level (or intensity) as a function of the space-time vector: $\mathbf{\Gamma}(x, y, t)$. The Fourier presentation of this three-dimensional field $g(\mathbf{\Gamma})$ is also defined over three dimensions. Two dimensions

are defined by the two-image wave number components, and the third is defined by the frequency distribution, derived from the time sequence $\Omega(k_x, k_y, \omega)$, the corresponding vector in Fourier space. Thus, the wave-image gray-level field may be written as a discrete Fourier series:

$$g(\mathbf{\Gamma}) = \sum_{\Omega} G(\Omega) \exp(\mathbf{\Omega} \cdot \mathbf{\Gamma}) \quad (1)$$

The Fourier coefficients $G(\Omega)$ on the right side of Equation 1 are calculated by a three-dimensional fast Fourier transform

$$G(\Omega) = \frac{1}{T(L_x L_y)} \int_{\mathbf{\Gamma}} g(\mathbf{\Gamma}) \exp[-i(\mathbf{\Omega} \cdot \mathbf{\Gamma})] d\mathbf{\Gamma} \quad (2)$$

where T is the observation time, and L_x and L_y are the spatial dimensions of the image. The components of the wave number-frequency vector Ω are defined by

$$\begin{aligned} k_x &= i\Delta k_x (i = 0, 1, 2, \dots, I) \\ k_y &= j\Delta k_y (j = 0, 1, 2, \dots, J) \\ \omega_n &= n\Delta\omega (n = 0, 1, 2, \dots, N) \end{aligned} \quad (3)$$

where $\Delta k_x = 2\pi/L_x$, $\Delta k_y = 2\pi/L_y$, and $\Delta\omega_n = 2\pi/T$. The sample space is a finite grid in x , y , and t , with grid spacing Δx , Δy , and Δt , respectively. Here, the variables k_x , k_y , and ω_n have Nyquist limits given by the spacing $k_{N_x} = \pi/d$ and $\omega_{N_t} = \pi/\Delta t$, with

$$\begin{aligned} \Delta x &= L_x/I \\ \Delta y &= L_y/J \\ \Delta t &= T/N \end{aligned} \quad (4)$$

where $d = \Delta x = \Delta y$ for a square, regularly sampled footprint.

REMOVAL OF TWO-TIME-STEP AMBIGUITY

The technique described in Ref. 1 uses two images sampled at successive time steps and separated by $\tau = t_2 -$

t_1 . The phase shift of the wave field from t_1 to t_2 at each wave number is given by

$$\Phi(\mathbf{k}) = \omega(\mathbf{k})\tau, \quad (5)$$

where $\omega(\mathbf{k})$ is given by the linear surface gravity dispersion relationship for finite water depth h : $\omega(\mathbf{k}) = \omega_0(\mathbf{k}) = [gk \tanh(kh)]^{1/2}$. Equation 5 is valid for $\omega_0(\mathbf{k})$ if the current of encounter \mathbf{u} is neglected. If the Doppler shift resulting from the current of encounter has to be considered, the frequency in the equation must be replaced by $\omega(\mathbf{k}) = \omega_0(\mathbf{k}) + (\mathbf{k} \cdot \mathbf{u})$.

By splitting each Fourier coefficient in \mathbf{k} space associated with time steps t_1 and t_2 into positive and negative frequency components, respectively, a pair of simultaneous equations results that can be solved to yield the two sets of positive and negative frequency coefficients. The power spectrum defined by the set of positive frequency coefficients is the true asymmetric image power spectrum, giving the direction of energy propagation:

$$F_+(\mathbf{k}) = 2\{[1 - \cos\{\omega(\mathbf{k}) - \omega(-\mathbf{k})\}\tau] \\ \times [G(\mathbf{k}, t_1)]^2 + [G(\mathbf{k}, t_2)]^2 \\ + 2 \operatorname{Re}\{G(\mathbf{k}, t_1)G^*(-\mathbf{k}, t_2)\exp(i\omega(\mathbf{k})\tau)\}] \}, \quad (6)$$

where G^* is the complex conjugate of G . The ambiguity can be removed for all wave numbers: $0 < k < \pi^2/g\tau^2$.

REMOVAL OF TIME-SERIES AMBIGUITY

The time-series method is described by Young et al.² Its basis is a three-dimensional description of ocean waves provided by a time series of wave pattern images, given in Equation 1. From Equation 2, the normalized image power spectrum is defined by $F^{(3)}(\Omega) = |G(\Omega)|^2$. The superscript (3) gives the dimension of the implied Fourier space. The conventional (instantaneous) two-dimensional symmetric spectrum results from integration over both positive and negative frequencies:

$$F^{(2)}(\mathbf{k}) = \int_{-\infty}^{\infty} F^{(3)}(\Omega) d\omega + \int_0^{\infty} F^{(3)}(\Omega) d\omega. \quad (7)$$

In Equation 7, the frequency information allows separation of wave energy at positive frequencies from that at negative frequencies. To obtain only the energy associated with the unique direction of propagation, we omit the negative frequency contribution and rewrite the equation as

$$F^{(2)}(\mathbf{k}) = \int_0^{\infty} F^{(3)}(\Omega) d\omega. \quad (8)$$

This method provides unambiguous results from $\omega = 1/2\Delta\omega$ up to the Nyquist limit.

For navigation radars, T can be much longer than one minute. Typical values of parameters for both naviga-

tional radar and airborne SAR are given in Table 1. For the navigational radar, results are unambiguous starting at very low frequencies: $f_{\text{unamb}} = \Delta f/2$. The shorter scene observation time for typical aircraft SAR data, discussed in the following section, gives spectral ambiguity up to $f_{\text{unamb}} = 0.084$ Hz. Thus, for the SAR parameters given in Table 1, the ambiguity for wavelengths longer than 220 m cannot be resolved.

RESULTS

As part of LEWEX, spectral estimates from remote wave imaging instruments were compared with those of *in situ* buoys and numerical wave models. Such comparisons provided a firm basis for evaluating the effectiveness of the ambiguity removal technique. Two examples will be given. The first set of spectral estimates, shown in Figure 1, is an airborne SAR measurement taken off the coast of Newfoundland on 21 March 1987 over a thin ice pack that was deformed by an underlying wave train.⁴ The deformed ice yielded a simple, well-defined swell system, which was clearly detected by the SAR.

The determination of the unambiguous portion of the spectrum is shown progressively in Figures 1A through 1C. Figure 1A shows a result identical to a conventional spectral analysis, with 180° ambiguity, and was obtained by integration over both positive and negative frequencies. Figure 1B, which includes a frequency interval centered about zero, but extending into negative and positive frequencies, still shows a directional ambiguity. The zero-frequency interval contains not only the energy from stationary scatterers, but also the energy from scatterers with low frequencies. Figure 1C shows the directional spectrum obtained by omitting the er-

Table 1. Example of system parameters to produce unambiguous spectra for time series of SAR images obtained during LEWEX.

		Ship radar parameters	Aircraft SAR parameters
Time domain	N	32	7
	Δt	≈ 2	≈ 1
	T	≈ 62	≈ 6
Frequency domain	n	16	3
	f_N	≈ 0.5	≈ 1
	Δf	≈ 0.016	≈ 0.17
Unambiguous lower frequency limit	f_{unamb}	≈ 0.008	≈ 0.08

Note: In the time domain, N is the number of time steps, Δt is the length of a time step in seconds, and T is the total observation time. In the frequency domain, n is the number of positive frequency planes, f_N is the Nyquist frequency in hertz, and Δf is the frequency spacing. f_{unamb} is the lower frequency limit for unambiguous results.

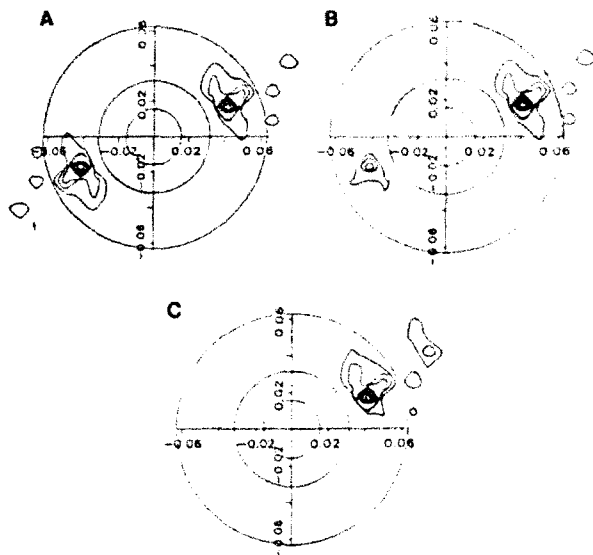


Figure 1. Spectra from the airborne synthetic aperture radar (SAR) on 21 March at 1647 UT, showing the influence of integration limits on the SAR image spectrum. **A.** Conventional, ambiguous spectrum resulting from summing over all frequencies. **B.** Intermediate spectrum, calculated from a sum over all positive frequencies, including the zero frequency. **C.** Final, unambiguous spectrum, calculated from a sum over only positive frequencies, omitting the zero-frequency plane. Outer circles are at $2\pi/100$ rad/m. Scales are linear in radians/meter.

gy in the zero-frequency plane. This spectrum contains a low-frequency cutoff at $f = \frac{1}{2}\Delta f$ (see Table 1), with the directional ambiguity resolved for higher frequencies. The cutoff frequency $f = 0.084$ Hz corresponds to a wave number $k = 0.029$ rad/m or a wavelength $\lambda = 220$ m.

The second set of spectral estimates was obtained in more complex wave field conditions. The airborne SAR measurements were made over a 30-min period on 17 March 1987 near FNLMS *Tydemar*. Estimates from both the Wavescan buoy and various wave models suggested two opposing wave systems of similar wavelength. Figure 2 compares the unambiguous spectra obtained from the shipborne radar (Fig. 2A) with two versions from the aircraft SAR (Figs. 2B and 2C) and the Wavescan buoy (Fig. 2D).

Figure 2B includes the zero-frequency interval, and is therefore ambiguous. Figure 2C is free of the 180° ambiguity, since the zero frequency is omitted from the integration. The opposing components of the spectrum here show the complex structure of the opposing wave systems, as verified by the Wavescan buoy (Fig. 2D). Thus, the SAR spectral estimate, when obtained by a sequence of images, shows a substantial rejection of the ambiguous components.

CONCLUSIONS

The results of this study demonstrate that asymmetric (true) wave image spectra may be obtained from airborne SAR measurements. The examples presented suggest that, because of a relatively short SAR observation time, the

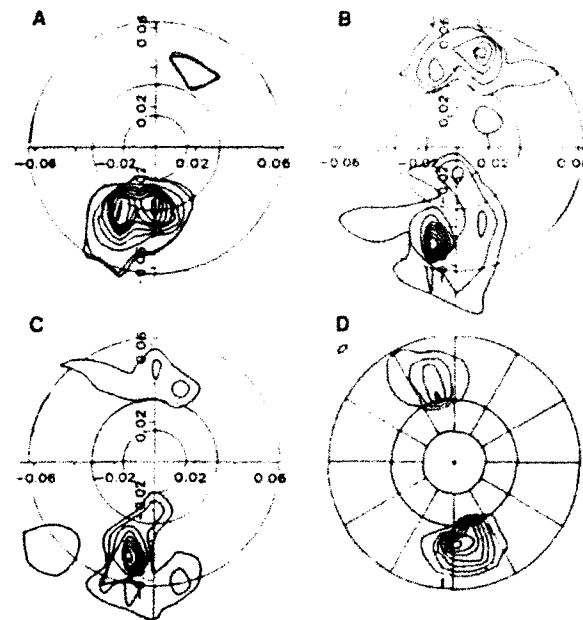


Figure 2. Spectra from three different sources near the *Tydemar* on 17 March at about 1200 UT. **A.** An asymmetric ship radar image spectrum from the *Tydemar* at 1316 UT, calculated from the sum over sixteen planes with positive frequencies. **B.** Airborne synthetic aperture radar image spectrum at 1308 UT, calculated from the sum over all positive frequencies, including the zero frequency. **C.** Same as B, but summed only over positive frequencies, excluding the zero frequency. **D.** Wavescan buoy spectrum at 1200 UT, calculated by using the maximum entropy method. Outer circles are at $2\pi/100$ rad/m. Scales are linear in radians/meter.

low-frequency portion of the spectra retains ambiguous components. Thus, for low wave numbers or long wavelengths, the two-time-step method may be preferable to the one used here. Nevertheless, the three-dimensional analysis can yield useful, unambiguous directional spectra from airborne SAR observations of the sea. The benefits will be even more enhanced with long periods of observation.

REFERENCES

- Atanassov, V., Rosenthal, W., and Ziemer, F., "Removal of Ambiguity of Two Dimensional Power Spectra Obtained by Processing Ship Radar Images of Ocean Waves," *J. Geophys. Res.* **90**, 1061-1067 (1985).
- Young, I. R., Rosenthal, W., and Ziemer, F., "A Three Dimensional Analysis of Marine Radar Images for the Determination of Ocean Wave Directionality and Surface Currents," *J. Geophys. Res.* **90**, 1049-1059 (1985).
- Ziemer, F., *Untersuchung zur quantitativen Bestimmung zweidimensionaler Seegangsspektren aus Messungen mit nautischem Radar*, GKSS Externer Bericht 87 E/10 (1986).
- Vachon, P. W., and Raney, R. K., "Resolution of Ocean Wave Propagation in Single-Pass Airborne SAR Imagery," in *Proc. IGARSS'89 Symp.*, Vancouver, B.C. (Jul 1989).
- Rosenthal, W., Ziemer, F., Raney, R. K., and Vachon, P., "Removal of 180° Ambiguity in SAR Images of Ocean Waves," in *Proc. IGARSS'89 Symp.*, Vancouver, B.C. (Jul 1989).

ACKNOWLEDGMENTS: The seven individual looks of the SAR measurements were provided to the authors by Keith Raney and Paris Vachon, both from the Canadian Centre for Remote Sensing in Ottawa.

GEOSAT WIND AND WAVE MEASUREMENTS DURING LEWEX

During the Labrador Sea Extreme Waves Experiment (LEWEX), the Geosat altimeter provided measurements of wind speed and significant wave height over a broad region. Although the Geosat wind estimates are not significantly biased from the LEWEX common winds (± 1 m/s, averaged over the entire experiment), Geosat often reveals a spatial structure in the wind field that is absent in the modeled winds.

INTRODUCTION

In the realms of remote sensing of the oceans and ocean modeling, we constantly search for absolute "ground truth" to measure the accuracy of a given instrument or model prediction. Unfortunately, no perfect yardstick exists by which any geophysical estimate can be assessed exactly. Efforts continue, however, because comparisons between various data sets can give insight into the inadequacies of each data set. Often, several different sources of data are needed to describe or predict adequately the edicts of nature.

In this context, the Labrador Sea Extreme Waves Experiment (LEWEX) was designed to include as many techniques as possible to measure both the directional and nondirectional properties of the wind and wave fields. The only spaceborne instrument yielding wind and wave estimates during LEWEX was the Geosat altimeter, built by The Johns Hopkins University Applied Physics Laboratory, which provided global estimates of wind speed and wave height from early 1985 to early 1990. This article discusses the Geosat wind speed and wave height measurements collected during LEWEX, and compares those wind speed measurements with the LEWEX common winds along the Geosat subtrack (see Cardone, this volume).

THE GEOSAT ALTIMETER

The Geosat altimeter operated in an 800-km orbit from March 1985 to January 1990, measuring (among other things) significant wave height (SWH) and wind speed on the ocean surface. The altimeter laid down a ground track pattern that repeated every seventeen days, with about 145-km spacing between ascending crossings at the equator. Between one and three ascending or descending ground tracks were laid down in the LEWEX region each day.

Wind speed is derived from the altimeter measurements of backscattered radar cross section (RCS) by applying an empirically determined algorithm. The wind speed affects the sea surface roughness, which in turn modulates the RCS. In this work, a modified Brown algorithm¹ was derived by applying a cubic spline fit at 0.2-dB intervals.² Geosat wind speed measurements are

estimated to have a 1- σ accuracy of 1.7 m/s for wind speeds up to 20 m/s (Ref. 3); above 20 m/s, the algorithm has not been adequately verified.

The SWH is determined from the slope of the altimeter-returned pulse. A smooth sea produces infinite slope; as the surface roughens, the slope decreases.⁴ Geosat wave height measurements are estimated to have a 3- σ accuracy of 0.5 m. Both wind speed and wave height are measured every 0.1 s (0.67 km) along the ground track.

GEOSAT DATA DURING THE EXPERIMENT

Originally, the Geosat contributions to LEWEX had two important aspects: to provide "near-real-time" wind and wave estimates to serve as a planning guide for the experimenters aboard the CFAV *Quest* and HNLMS *Tydeman*, and to demonstrate how quickly Geosat data could be provided to scientists in the field. Before LEWEX, no attempt had been made to provide near-real-time data to an ongoing field experiment. In practice, Geosat data were provided to the LEWEX site between twelve and twenty-four hours after the measurement. Since Geosat data are received and digitized on sensor data records (SDR) at APL, the raw data could be obtained immediately after being released from the receiving station. After processing, the data were telefaxed to the experiment site. This near-real-time transmission of Geosat data took place for five days during LEWEX.

Processing of the SDR at APL included editing according to on-board "data-quality flags," computing 1-s averages of wind and waves, and computing latitude and longitude from Keplerian elements. The near-real-time ground tracks computed from SDR Keplerian elements are accurate to a few kilometers. The results presented here, however, use an improved Naval Aeronautics Group ephemeris to achieve an accuracy of a few meters. Typical examples of the data products transmitted in near-real-time during LEWEX are shown in Figure 1. Note the strong inverse correlation between radar cross section and wind speed, and the strong direct correlation between wind speed and SWH. These data were mea-

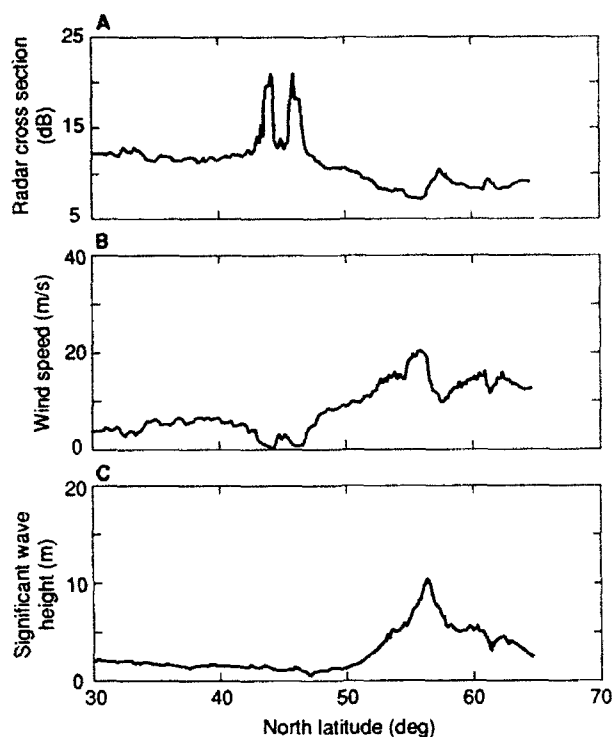


Figure 1. Example of Geosat measurements along a particular track on 18 March 1987. A. Radar cross section (dB). B. Wind speed (m/s). C. Significant wave height (m).

sured on 18 March 1987 along a track that passed to the east of both the *Quest* and the *Tydeman*.

Unfortunately, only two Geosat ground tracks were sufficiently close to the ships during LEWEX to be useful in the planning activities. Geosat proved most useful in accurately revealing the complex spatial structure of the wind and wave field. Figures 2 and 3 show composite mean wind speed estimates from 11 to 20 March, and Figures 4 and 5 present the corresponding composite SWH. Each value represents an average over 15 s along the track. Geosat passed over regions of high winds and waves around 40°N, 50°W and 53°N, 45°W. A smaller area of winds at 16 to 20 m/s also can be seen near 38°N, 38°W. The space-time sampling of Geosat was too coarse to track individual storms.

The highest wind measured by Geosat was 25 m/s, but most winds were below 16 m/s for all eleven days. The highest SWH measured was 10 m (see Fig. 1). No pass came close enough to the experiment site to allow extensive direct comparisons with the other instruments used during LEWEX.

COMPARISON: GEOSAT WIND SPEEDS AND LEWEX COMMON WIND FIELDS

The LEWEX common wind fields (referred to hereafter as the model winds) were produced by Cardone (this volume). The wind field was provided at six-hour intervals over the region from 20°N to 67.5°N and 20°W to 80°W. For comparison, Geosat data were averaged over 15 s or 100 km along track, about the same scale as Cardone's coarse model grid.

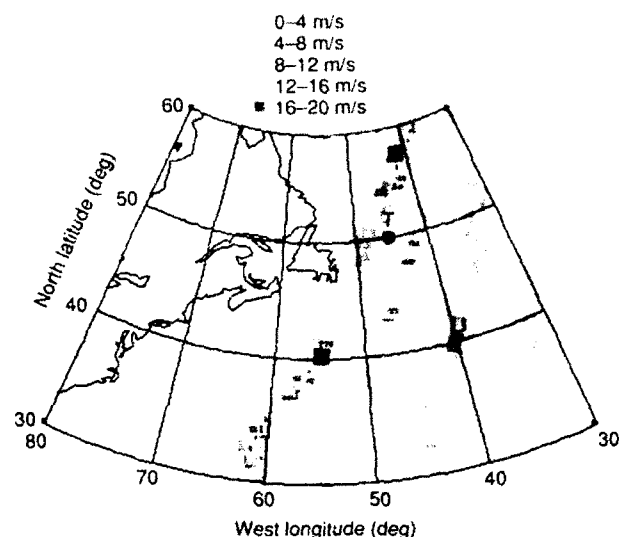


Figure 2. Composite map of descending ground tracks showing wind speed (m/s) for 11-20 March 1987. (*Tydeman* position is shown by T on this and following figures.)

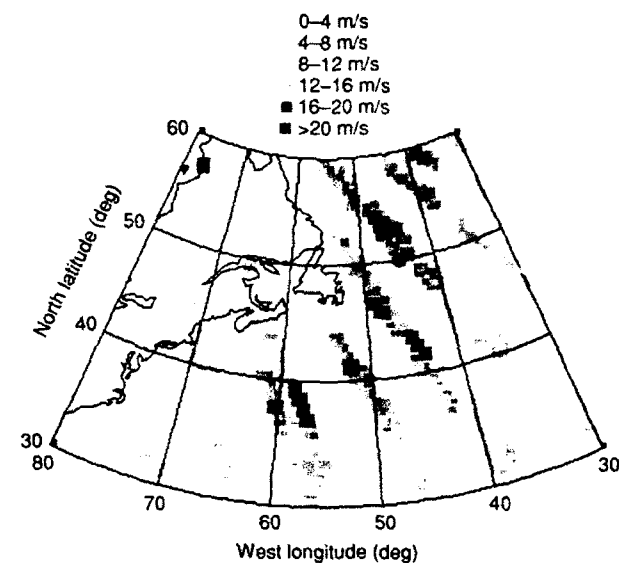


Figure 3. Composite map of ascending ground tracks showing wind speed (m/s) for 11-20 March 1987.

Geosat winds at the center of the 15-s average were compared with the LEWEX winds at the nearest grid point, resulting in a maximum spatial separation of 140 km. All comparisons were simultaneous within three hours. Over the ten-day period from 10 to 20 March, twenty-six Geosat tracks permitted 702 comparisons of Geosat wind speed with model wind speed.

Comparisons from nine of the twenty-six tracks analyzed are shown in Figures 6 through 8. Geosat track positions for the midpoint of a fifteen-point average, along with the grid points chosen from the model, are shown in the upper half of each figure. The means of some Geosat and model winds differ substantially, but others are in good agreement. For example, in Figure 6C (bottom), both estimates agree within about ± 1 m/s.

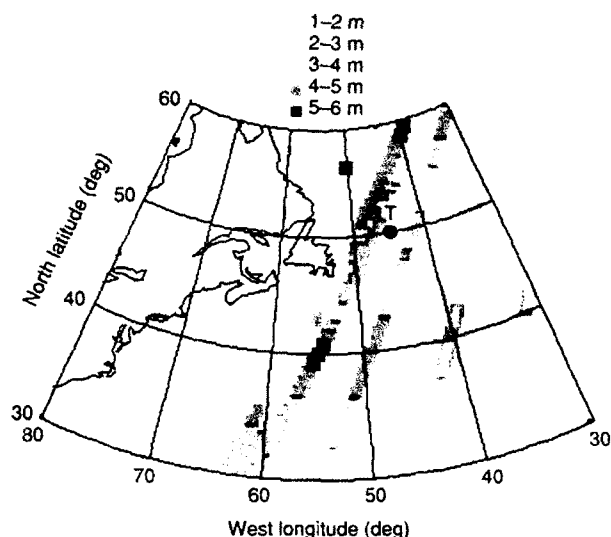


Figure 4. Composite map of descending ground tracks showing significant wave height (m) for 11-20 March 1987.

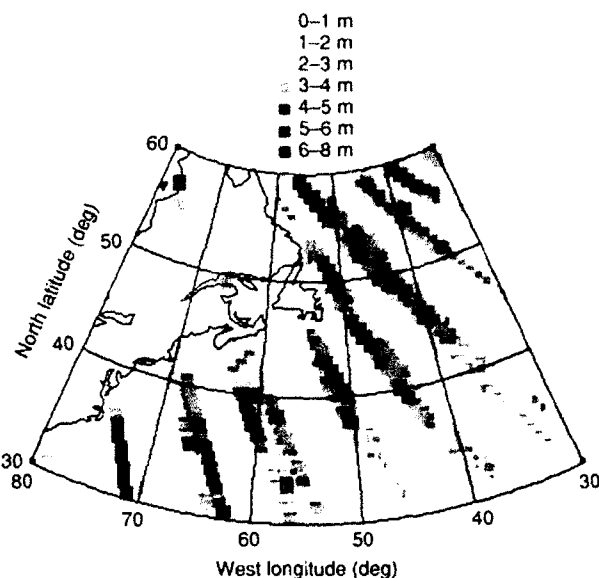


Figure 5. Composite map of ascending ground tracks showing significant wave height (m) for 11-20 March 1987.

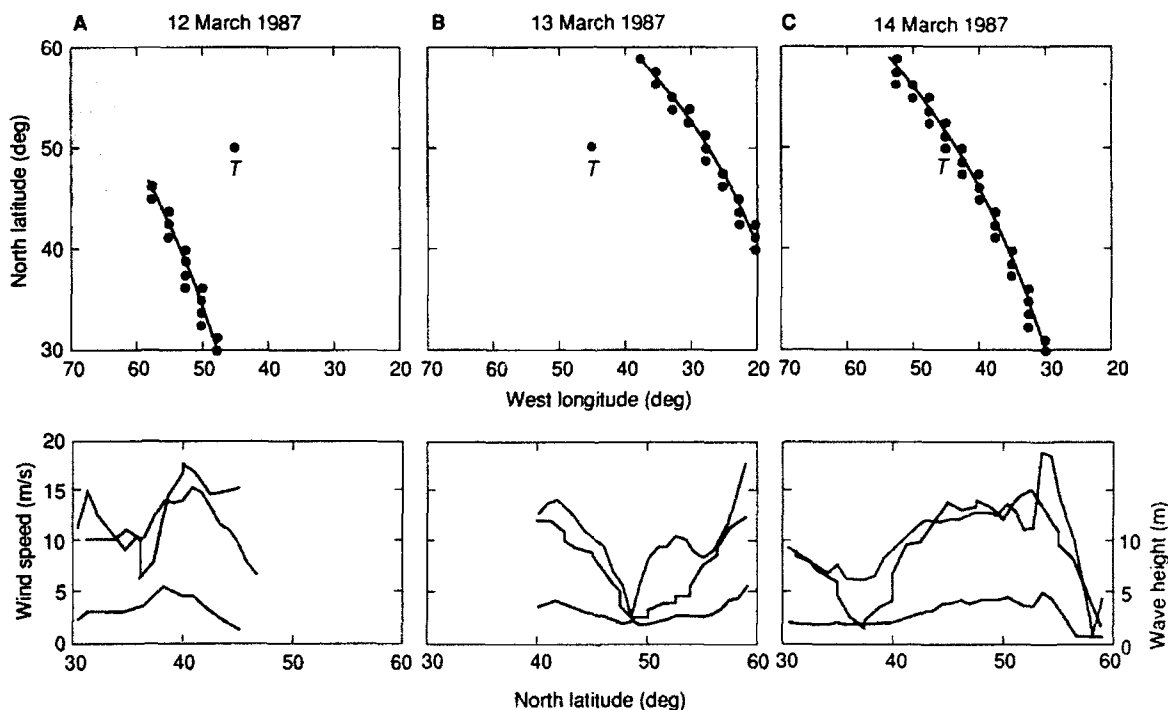


Figure 6. Plots of Geosat ascending tracks and model points closest to track points. **A.** 12 March at 1100 UT. **B.** 13 March at 0920 UT. **C.** 14 March at 1029 UT. Bottom: Corresponding plots of Geosat wind speed (blue), model wind speed (red), and significant wave height (green).

between 40°N and 50°N but differ by 3 to 5 m/s between 35°N and 40°N.

The time and spatial differences between compared estimates from Geosat and the model winds contribute to the differences between the two data sets. Thus, even if both data sets were identical, some differences would result simply from the lack of interpolation. Computations of the wind speed autocorrelation functions along

the Geosat tracks indicate that a 50% decorrelation occurs anywhere between 150 and 700 km. Monaldo⁵ found that hourly measurements of wind speed from two National Data Buoy Center buoys were essentially uncorrelated after six hours and that at least a 1.3-m/s change could be expected between wind speed measurements made two hours apart. Even so, the time and spatial differences between these LEWEX comparisons (three hours

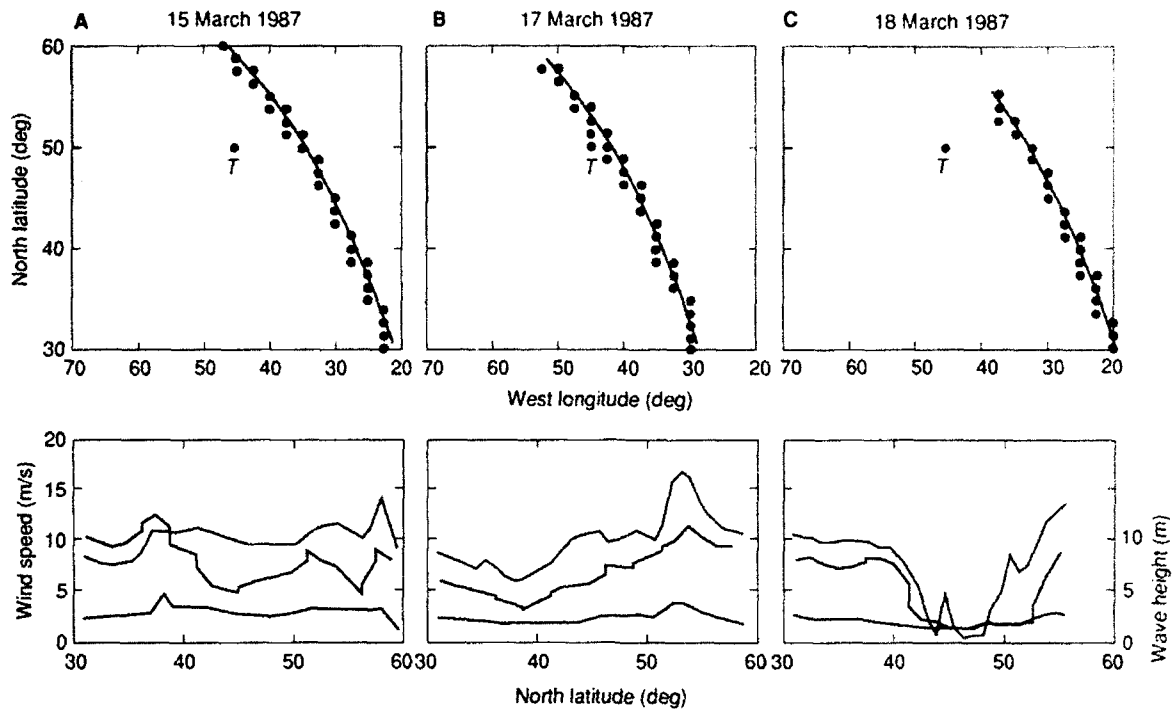


Figure 7. Same as Figure 6, except for: A. 15 March at 0958 UT. B. 17 March at 1106 UT. C. 18 March at 1036 UT.

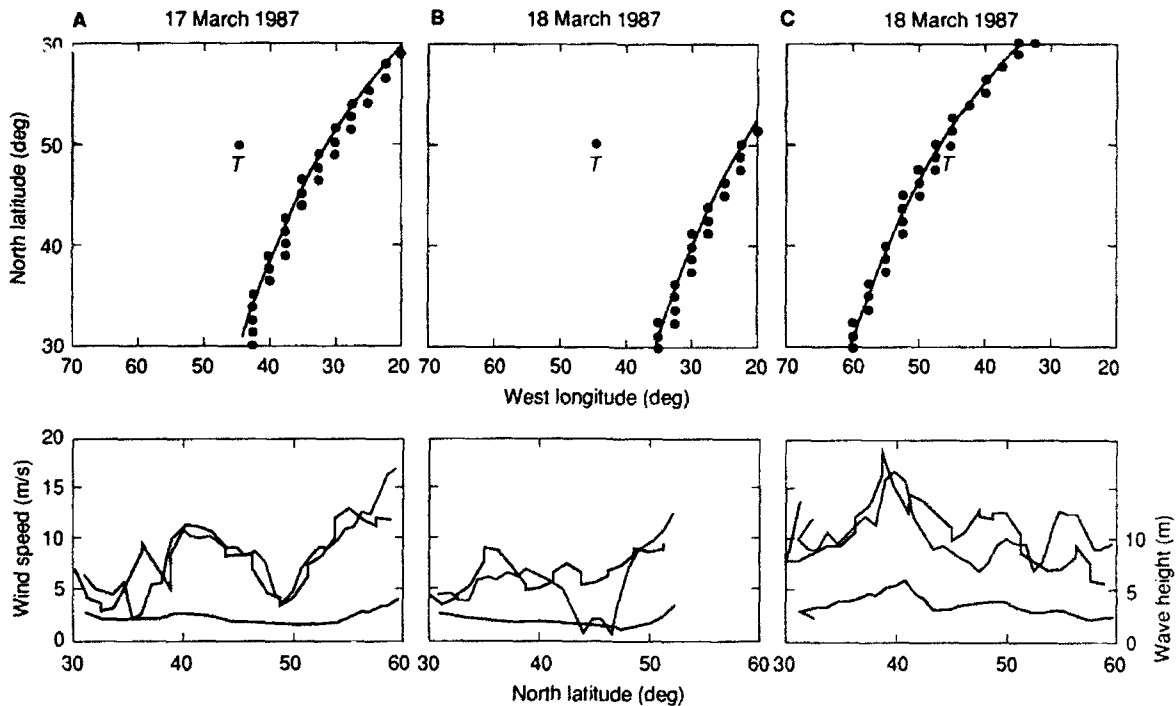


Figure 8. Same as Figure 6, except descending tracks for: A. 17 March at 0052 UT. B. 18 March at 0020 UT. C. 18 March at 0220 UT.

and 100 km) cannot account for all of the differences observed.

In Figure 6 (bottom graphs), the trends of the measurements are, in general, the same, but the differences in magnitude are quite large at certain locations. For example, in Figure 6B (bottom) between 50°N and 55°N,

both estimates are increasing with latitude, but Geosat shows a much steeper gradient than the model. This example of higher-frequency spatial structure is typical of the Geosat wind estimates and may be an indication of small-scale features not captured in the model. The Geosat SWH estimates usually correlate well with the Geosat

wind speed estimates. In Figure 7 (bottom), the Geosat winds are substantially higher (often greater than 2 or 3 m/s) than those of the model. No attempt was made to smooth the model or Geosat data along the track, thereby accounting for the jagged nature of the data. Figure 8 shows three more comparisons. In Figure 8A (bottom), both estimates track well (usually within 1 m/s), but in Figures 8B and 8C (bottom), the differences approach 5 m/s over substantial regions along the pass. Figure 8C (bottom) indicates that the model winds are biased high on this day in the northern portion of a storm to the southwest of LEWEX (45°N to 50°N).

For a statistical measure of the average disagreement between Geosat and the model wind speed estimates, Table 1 shows mean and rms differences for 692 comparisons along twenty-seven Geosat tracks. Mean differences along a single pass range from -5.1 to +3.2 m/s. The range for rms differences is from 1.0 to 6.6 m/s. The number of points in each computation is given in the last column. For all days, the mean difference was -0.6 m/s, and the rms difference was 3.4 m/s, using 692 data points. To determine whether greater bias at higher wind speed exists, we repeated the computations using

only model wind speeds greater than 10 m/s. The results are shown in Table 2. Model winds greater than 10 m/s were biased high by 1.5 m/s, whereas the rms difference for all 215 points dropped to 2.5 m/s. Again, the rms error in Geosat wind estimates is 1.7 m/s, so rms differences of 3.4 and 2.5 m/s may not be significant.

The exact error structure in the LEWEX common winds cannot be determined with a single set of Geosat estimates. Comparisons with ship measurements (see Zambresky, this volume) showed that on some days during LEWEX, the model/ship rms differences in specific regions ranged from 5 to 10 m/s, and the mean differences ranged from 0 to +2.7 m/s. We recognize, of course, that measurements obtained from ships of opportunity can have large errors (see the article by Pierson, this volume), but if even a portion of this error is due to the model winds, then the differences between Geosat and the model are probably not significant when averaged over the entire experiment. Nevertheless, a significant amount of spatial structure in the wind field clearly exists, although it is entirely missed in the model.

CONCLUSION

We have presented the wind and wave fields as estimated by Geosat during LEWEX. Geosat wind speeds

Table 1. Statistical comparison of model wind speed estimates minus Geosat wind speed estimates.

Date (March 1987)	Mean difference (m/s)	Rms difference (m/s)	Number of points
12	-1.39	4.38	32
12	1.22	4.05	20
12	-2.11	1.73	30
12	-0.09	4.86	23
13	-2.45	3.09	27
13	3.06	6.58	23
13	-1.53	1.19	3
13	-1.55	2.80	37
13	2.06	0.99	4
14	-2.43	3.06	14
14	-0.67	2.88	39
14	-5.11	3.43	17
14	-3.75	2.64	37
15	-1.58	2.84	37
15	-4.31	5.60	29
15	-0.17	2.11	29
15	1.23	4.24	27
15	1.64	2.12	17
16	0.31	3.11	37
17	-3.21	4.92	12
17	-2.37	1.92	38
17	0.09	2.58	35
18	-2.46	2.78	35
18	-0.49	2.57	14
18	1.08	2.67	27
18	0.73	3.20	37
18	3.17	4.16	12
All days	-0.60	3.44	692

Table 2. Statistical comparison of model wind speed estimates minus Geosat wind speed estimates for model winds greater than 10 m/s.

Date (March 1987)	Mean difference (m/s)	Rms difference (m/s)	Number of points
12	3.2	3.53	12
12	2.1	3.11	18
12	3.1	4.2	13
13	-2.0	3.3	11
13	6.3	5.7	15
13	-0.7	0.03	2
13	0.8	2.3	14
13	2.1	1.0	4
14	2.1	1.92	3
14	0.3	2.2	18
14	-2.3	0.4	4
15	1.8	1.4	11
15	-0.1	0.6	6
15	4.3	3.0	15
16	3.5	2.1	13
17	1.7	3.8	5
17	4.2	0.7	2
17	1.1	2.9	15
18	-3.4	0.4	2
18	1.8	3.0	5
18	-1.1	0.7	2
18	2.8	2.5	5
18	4.1	0.8	5
All days	1.5	2.5	215

were compared with slices through the LEWEX common wind fields. For the entire experiment, the rms difference was 3.4 m/s, and the mean difference (model minus Geosat) was -0.6 m/s. Geosat tracked closest to the research vessels *Quest* and *Tydemar* on 16 March, passing just to the west of the *Quest*. At closest approach, the Geosat SWH was 4.7 m, compared with 4.6 m measured by the Endeco buoy at the *Quest* and 2.9 m measured by the Wavescan buoy at the *Tydemar*. The sparse sampling of Geosat ground tracks on any given day is inadequate to initialize wind models. The Geosat estimates, however, reveal a spatial wind structure that is not well modeled.

REFERENCES

- ¹Brown, G. S., Stanley, H. R., and Roy, N. A., "The Wind Speed Measurement Capability of Spaceborne Radar Altimeters," *IEEE Oceanic Eng.* **OE-6** (2), 53-59 (1981).
- ²Dobson, E. B., *On the Computation of a Modified Brown Algorithm for Deriving Wind Speeds from Altimeter Radar Cross Section*, JHU/API S1R89U-056, The Johns Hopkins University Applied Physics Laboratory, Laurel, Md. (30 Sep 1989).
- ³Dobson, E. B., Monaldo, F. M., Goldhirsh, J., and Wilkerson, J., "Validation of Geosat Altimeter-Derived Wind Speeds and Significant Wave Heights Using Buoy Data," *J. Geophys. Res.* **10**, 719-731 (1987).
- ⁴MacArthur, J. A., Marth, P. C., Jr., Wall, J. G., Sailor, R. V., and LeSchack, A. R., "The Geosat Radar Altimeter," *Johns Hopkins APL Tech. Dig.* **8** (2), 176-181 (1987).
- ⁵Monaldo, F. M., "Expected Differences between Buoy and Radar Altimeter Estimates of Wind Speed and Significant Wave Height and Their Implications on Buoy-Altitude Comparisons," *J. Geophys. Res.* **93** (C3), 2285-2302 (1988).

NUMERICAL MODEL ESTIMATES

*IN WHICH DIRECTIONAL OCEAN WAVE SPECTRA
FROM FIRST-, SECOND-, AND THIRD-GENERATION
NUMERICAL MODELS ARE DESCRIBED AND
COMPARED BY USING VARIOUS VERSIONS OF THE
SAME WIND FIELD*

THE LEWEX WIND FIELDS AND BASELINE HINDCAST

The wave modeling component of the Labrador Sea Extreme Waves Experiment (LEWEX) involved wave hindcasts made with nine different spectral wave models, all driven by a common wind field. The LEWEX common wind field is described, including a summary of the data and methodology applied, a description of the principal wind systems responsible for the major wave systems observed in the LEWEX measurement array, and an assessment of the accuracy with which each wind system was specified.

INTRODUCTION

It is well established^{1,2} that for a given spectral ocean wave model, errors in model-generated integrated properties of the wave spectrum are highly correlated with errors in the forcing wind fields. For example, the growth of the forecast wave-height scatter index with forecast horizon tends to increase in proportion to the increase of wind-speed scatter index with forecast horizon. A basic difficulty faced by wave modelers, however, is that even with carefully reanalyzed winds, the baseline errors in the winds induce errors in wave hindcasts that are large enough to mask errors associated with model physics or numerics.

Surface marine wind fields are developed basically from conventional surface synoptic data, mainly transient ship reports. From these data, gridded surface pressure and air and sea temperature fields are derived by objective or subjective analysis; they are then used in statistical or dynamical models to derive surface winds. Some schemes also assimilate the ship reports of surface wind. Unfortunately, alternate methods used at different forecast centers typically provide significantly different surface wind fields from the same input set of observations (see Ref. 3 and Zambresky, this volume). Obviously, the comparison of hindcasts from nine different wave models in the Labrador Sea Extreme Waves Experiment (LEWEX) is greatly simplified by the use of a common wind field.

Wind fields derived from marine surface data are susceptible to both random and systematic errors. Random effects arise in the failure of the observations themselves to represent the time and space scales intended, because of short-term fluctuations (see Ezraty, this volume), large observation errors (see Pierson, this volume), and, in most schemes, failure to differentiate measured and estimated winds.³

Systematic errors are exhibited in wind speed and/or directional biases over the whole of the field or at least over spatial scales large with respect to the spacing of the grid on which the fields are specified. These effects have four major causes: First, ship reports are concentrated along major shipping lanes, often leaving vast areas devoid of observations, over which large and persistent biases are common. Second, the analytical method

introduces effects, such as differences in the boundary-layer model used. For example, in some models, the surface wind is actually derived as the wind vertically integrated over some arbitrary boundary layer depth, or as the wind at an ill-defined anemometer level. Sometimes, when surface winds are specified as part of a three-dimensional objective analysis scheme used to initialize numerical weather prediction (NWP) models, biases are introduced "from above" (e.g., Udden⁴ described the undesirable effect of a nondivergence constraint on the tropical wind analyses of the European Center for Medium-Range Weather Forecasts [ECMWF]). Finally, the effect of atmospheric stability is often not considered, either in the analytical scheme or in the interpretation of the individual observations. Since, in mid-latitudes, the stratification (air-sea temperature difference) is organized spatially by the juxtaposition of synoptic-scale air masses over large-scale water masses, failure to account for stratification introduces spatially correlated errors.

One relatively simple approach to the incorporation of stability was introduced by Cardone,⁵ who defined the "effective 20-m wind" and showed how to derive it with a marine planetary boundary layer (MPBL) model driven by pressure and air and sea temperature fields, and from measured (anemometer) or estimated (Beaufort) ship winds. Recently, Cardone et al.⁶ quantified the errors in mean monthly surface winds derived from ship reports, introduced by failure to account for stability and observation type.

Even if it were possible to specify perfectly the average effective 20-m wind speed and direction every six hours on the LEWEX grid, the wind fields might still be less than perfect for wave modeling because of several still unresolved questions. These include the issue of whether friction velocity or wind speed is the more appropriate wind variable, and whether gustiness or mesoscale variability needs to be resolved explicitly in specification of the atmospheric input source term. Ultimately, the MPBL should be coupled with the wave model,⁷ and the coupled system should be driven by the external variables of the MPBL. These issues are not addressed specifically in this article. Rather, we have attempted to develop the LEWEX common winds from the available conventional

data, as augmented by special measurements in the LEWEX array, in terms of time-averaged, synoptic-scale, effective 20-m wind speed and direction, making every effort to minimize the influence of the sources of the random and systematic errors noted earlier.

In this article, we describe the generation of the LEWEX common winds, including a summary of the data used, the methodology, the principal wind-field features that affected the wave regime sampled in the LEWEX array, and an assessment of strengths and limitations of the modeled winds.

SPECIFICATION OF COMMON WINDS

Approach

Our approach to the specification of the common winds was consistent with the experimental design of LEWEX, which was supposed to sample extreme waves generated by typical extratropical cyclones for the region and season. Extreme waves normally form near the East Coast of North America and move east-northeastward, passing near or right over the LEWEX array. (Unfortunately, this situation did not occur during LEWEX, as discussed later). Therefore, we adopted a grid system and methodology that had been successfully applied in the same area in several extensive wave hindcasting studies designed to estimate the normal and extreme wave climate.^{8,9}

The method adopted³ is a mixture of objective and subjective analyses. The objective part consists of the calculation of surface winds from grid fields of sea-level pressure using a calibrated MPBL. The subjective part consists of manually drawn kinematic analyses, applied only to selected periods and areas. The kinematic analyses are hand-gridded and then blended into the objective winds. Winds are specified on the nested grid system shown in Figure 1. The extent of the coarse grid implies exclusion of possible influences on the wave systems in the LEWEX array from generation sources in the far eastern or tropical North Atlantic and the Southern Hemisphere. The wind fields were developed before the detailed analysis of the LEWEX wave measurements and, of course, before the wave hindcasting experiments. Most wave modelers ran experiments first with so-called forecast wind fields, which in some cases extended beyond the domain of the common winds, and with results suggesting the possibility that some of the low-frequency swell energy detected in the LEWEX array may have originated outside the domain of the coarse grid. Of course, any such swell would not be modeled in the wave hindcasts driven by the common wind field.

Kinematic analysis is a tedious, labor-intensive process and therefore was applied only to the fine mesh grid (Fig. 1) and to all six-hourly map times between 1200 UT on 13 March and 1200 UT on 19 March 1987. The total period that was modeled extended from 1200 UT on 9 March to 1200 UT on 19 March, thereby allowing about a four-day period for model spin-up before the first aircraft and surface wave measurements were acquired (13 March). Therefore, the common winds consisted entirely of winds derived from pressure analyses (MPBL) for the spin-up period on both coarse and fine grids, and on the coarse grid throughout the period modeled.

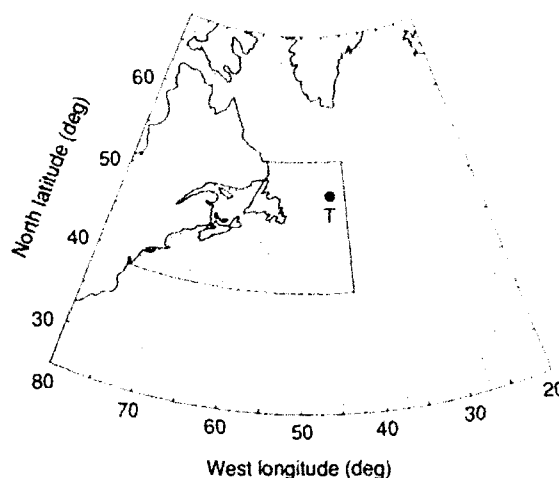


Figure 1. The coarse and fine grids used to specify LEWEX common winds. The position of the Tydemar is shown.

MPBL Winds

The MPBL model used to provide objective winds was developed by Cardone⁵ and was later updated.¹⁰ It has been used to diagnose and forecast marine surface wind fields from products of NWP models at several centers, including the National Oceanic and Atmospheric Administration (NOAA) National Meteorological Center (NMC), and the New Zealand Meteorological Service. The model links the following external factors governing the near-surface wind flow in a steady-state, horizontally homogeneous MPBL: latitude (Coriolis parameter, f), surface roughness parameter (Z_0), air-sea temperature difference ($T_a - T_s$), geostrophic wind vector (V_g), and horizontal temperature gradient (T_a).

The surface roughness is calculated implicitly in the model as a function of the friction velocity. The air-sea temperature difference is supplied at each grid point through a parametric dependence on the local geostrophic wind direction, with typically negative (unstable) values for northerly winds and positive (stable) values for southerly winds, and varying continuously in between. The horizontal air temperature gradient is specified as uniform over the entire grid and is taken from climatology for the North Atlantic in March.

The pressure fields were specified as follows. First, six-hourly isobar analyses were obtained (hard copy) from several sources, including real-time charts produced at NOAA NMC (both their preliminary and final analyses series), the Canada Atmospheric Environment Service Gander office real-time analyses, and charts produced at the MacLaren Plansearch, Ltd., weather office, Halifax. The NOAA final analysis was the main source, even though this analysis was a real-time product and was subjected to some reanalysis to impose better continuity of pressure systems, smoothing of unrealistic gradients, and addition of intermediate isobars where necessary. The final charts were each placed on an x - y digitizing table, whereon the isobars, each pressure center location, and central pressure were digitized.

The program that calculates the objective winds first converts the digitized pressures to gridded pressures. At each grid point on the coarse and fine grids, a small circle is constructed, containing seven or more points on isobars (or five or more points plus one high or low center). A paraboloid is fitted by the least-squares method to the pressures inside the circle. The pressure gradient at each point, calculated by centered differences, is then entered to the MPBL along with the other required external variables to yield the wind speed and direction at the grid point. The wind is defined as the effective neutral wind at a 20-m height.

Kinematic Winds

Where sufficient observations of the surface wind exist, kinematic analysis can provide more accurate wind fields than MPBL-derived winds, because effects not well modeled by single-point MPBL models may be captured. These effects include accelerated flow caused by large-scale spatial variations (e.g., curvature effects) or temporal variations (e.g., isallobaric effects) in pressure gradients, and the deformation in surface winds near and downstream of coasts. Also, the process of kinematic analysis implies a thorough reanalysis of the evolution of the surface wind-field pattern through time and space in a limited area (i.e., the domain of the fine grid), and the imposition of better continuity of wind-field features than afforded by a series of pressure-field "snapshots." Through this process, the influence of high-quality measured data may be propagated into nearby regions and adjacent times that may be devoid of measured data on a given map. When carried out by a synoptician experienced in kinematic analysis, the process is, in effect, a form of three-dimensional (space and time) assimilation of measured surface wind data into a background field of MPBL winds.

Kinematic analysis involves the following basic steps: (1) assembly, adjustment, and display of all available synoptic observations of marine surface winds, as overlays on displays of previously calculated six-hourly MPBL winds; (2) identification and rejection of erroneous reports, so far as possible; (3) construction of a continuity chart that defines the movement of centers of action and principal wind-field features such as wind shift lines and isotach maxima; (4) construction of streamlines and isotachs; and (5) gridding of wind speed and direction and entering of same to a disk file. Inside the boundary of the fine grid, kinematic winds override the MPBL winds.

During LEWEX, wind observations were available within the domain of the fine grid from the following sources: (1) transient ships (six-hourly), (2) three NOAA buoys moored on Georges Bank (hourly), (3) a drilling rig moored on Grand Banks (three-hourly), (4) the research vessel HNLMS *Tydeman* (recording anemometers on both the vessel and the moored Wavescan buoy), and (5) the research vessel CFAV *Quest* (hand-held anemometer, four-hourly).

The transient ship winds are probably the least accurate of this data set, but along the shipping lanes the coverage of reports usually allows some skill in the identification of grossly inaccurate reports and some reduc-

tion of error through averaging of neighboring reports. Figure 2 shows the total coverage of ship reports between 13 and 19 March in the source region. These reports were available in real time, as not enough time had elapsed between LEWEX and the production of the common winds (about four months) to use later ship report collections that included additional ship data from foreign sources and data extracted from manuscript logs. During LEWEX, swell observed in the measured data often appeared to originate outside the shipping lanes, and indeed outside the domain of the fine grid, thereby minimizing the influence of the high-quality wind data available locally (e.g., *Tydeman*).

All observed winds were reduced to effective 20-m-height neutral wind speeds following Cardone et al.³ For transient ship reports, estimated (Beaufort) and measured winds were treated differently. The efficacy of this treatment was demonstrated recently by Cardone et al.,⁶ as shown in Figure 3. Failure to account for errors in the operational Beaufort scale-wind speed equivalency table (for estimated winds) and anemometer height and stability (for measured winds) may easily induce systematic errors of up to 2 m/s for typical wind speeds and air-sea temperature differences. For the stationary platforms (buoys, ships, drilling rig), the correction of winds to a 20-m height was straightforward, given the anemometer height and air-sea temperature difference. For example, at the *Tydeman* location, the anemometer height was 3.5 m on the Wavescan buoy and 24.4 m on the vessel. Figure 4 compares the two series of adjusted winds and the kinematic winds at the grid point near the *Tydeman*. The differences between the adjusted measured series probably are at least in part due to different averaging intervals. Measured winds from the *Quest* were given less weight in the analysis because several large data gaps occurred, and often the winds were suspected to be affected by ship superstructure interference (W. Nethercote, personal communication, 1989).

WIND-FIELD EVOLUTION

In this section, we describe the principal features of the LEWEX wind field and refer both to pressure analy-

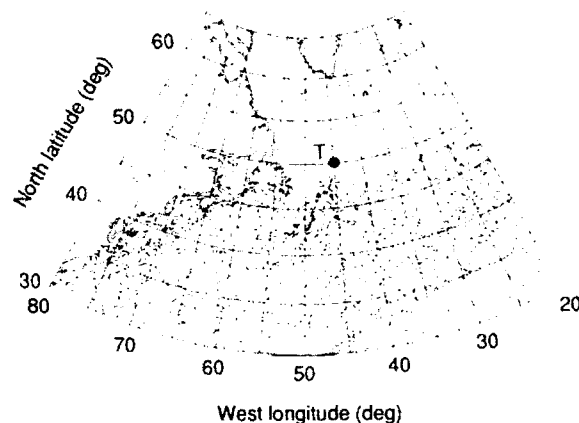


Figure 2. Ship reports available for LEWEX pressure and wind-field analysis between 1200 UT on 13 March and 1200 UT on 19 March. The position of the *Tydeman* is shown.

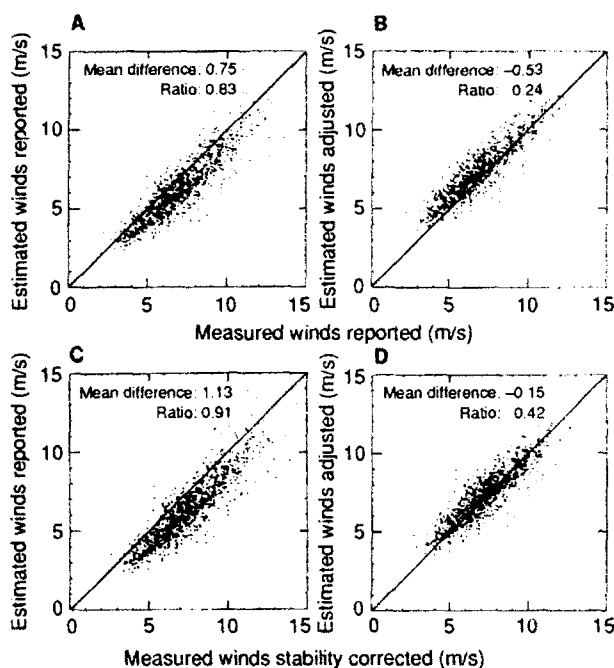


Figure 3. Comparison of monthly mean wind speeds in two-degree latitude-longitude squares of the South China Sea shipping lane (1965-84). **A.** Estimated and measured ship winds as reported. **B.** Adjusted estimated winds and reported measured winds. **C.** Reported estimated winds and adjusted measured winds. **D.** Both estimated and measured winds adjusted. The mean difference and the ratio of points below the line to the total points are given as well. (Reprinted, with permission, from Ref. 6.)

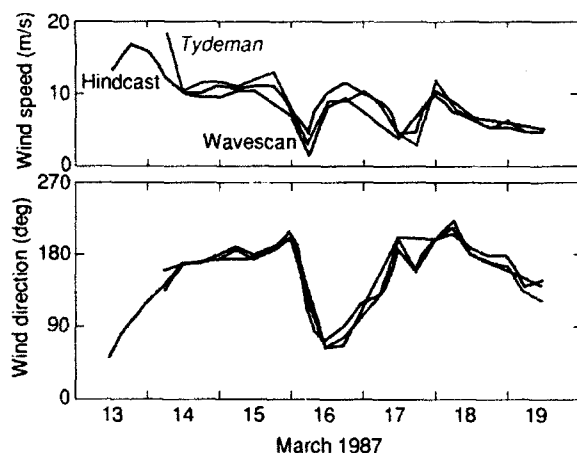


Figure 4. Comparison of Tydemán anemometer and Wavescan (at the Tydemán location) anemometer winds for storm of 13-19 March 1987, both adjusted to a 20-m height, and LEWEX common wind at a fine grid point nearest to the Tydemán.

ses and wind-barb plots. Figures 5 and 6 give the section of the NOAA NMC final analysis covering the central North Atlantic Ocean for 1200 UT each day between 9 and 19 March. Figure 7 shows the plots of the common winds (daily at 1200 UT between 13 and 19 March) displayed only at coarse grid points corresponding to the

times shown in Figure 6. The locations of the *Quest* and the *Tydemán* are very close to the coarse grid points at 50°N, 47.5°W and 50°N, 45°W, respectively. To relate the wind-field features to the wave systems observed to evolve in the LEWEX measured wave data, we will refer to the numbering system adopted by Gerling (this volume) and the nomenclature shown in Figure 8 of Beal (this volume).

Wind System 1 (Dispersive Northerly Swell)

The first weather system of interest to LEWEX was the frontal wave that formed near Cape Cod on 9 March. This cyclone moved east-northeastward and intensified, the center passing directly over the LEWEX site (before the measurements began, however) late on 10 March; it then moved north-northeastward to the southern tip of Greenland on 11 March. The strong pressure gradient between this cyclone and a strong anticyclone over the Gulf of St. Lawrence reinforced an existing area of strong north-northwesterly flow over the Davis Strait and the Labrador Sea, which had been established by the previous cyclone on 9 March. This fetch zone therefore had a duration of more than 48 hours and maximum surface winds of about 20 m/s, even though wave generation was restricted somewhat by ice cover in the Davis Strait and near the Labrador coast (see Fig. 2 of Beal, this volume). All hindcast models responded to this wind-field system and showed a system of diminishing dispersive northerly swell, which was the dominant sea state at the LEWEX site on 11 and 12 March.

Wind System 2A (Developing Northeasterly Sea)

According to most models, the northerly swell was still running through the LEWEX area early on 13 March, when a strengthening northeast wind of 10 to 15 m/s began to generate a developing northeasterly sea. These northeasterly winds were driven by a tightening pressure gradient on the north side of the cold front that trailed the previous cyclone. A new cyclone that had formed on this front on 10 March moved eastward for awhile, then turned northward and began to intensify on 12 March. The development of a blocking ridge in the central North Atlantic prevented the further development of this system and retarded its movement, however. As this cyclone slowed its northward movement on 13 March (Fig. 6), the associated front moved northward as a warm front to lie north-south between the *Quest* and the *Tydemán* from late on 13 March to early on 15 March. The local wind field in the LEWEX area during this period was adequately resolved because the measured winds from the *Quest* and the *Tydemán* were assimilated in the kinematic analyses. At the *Quest*, the surface wind was steady northeasterly between 0000 UT on 13 March and 1200 UT on 14 March at speeds of 10 to 15 m/s, whereas at the *Tydemán*, winds veered from northeasterly near 15 m/s at the beginning of this period to southerly at less than 10 m/s at the end of this period. Of course, possibly very fine structures in the wind field in the frontal zone itself between the *Quest* and the *Tydemán* would be smoothed even on the fine grid.

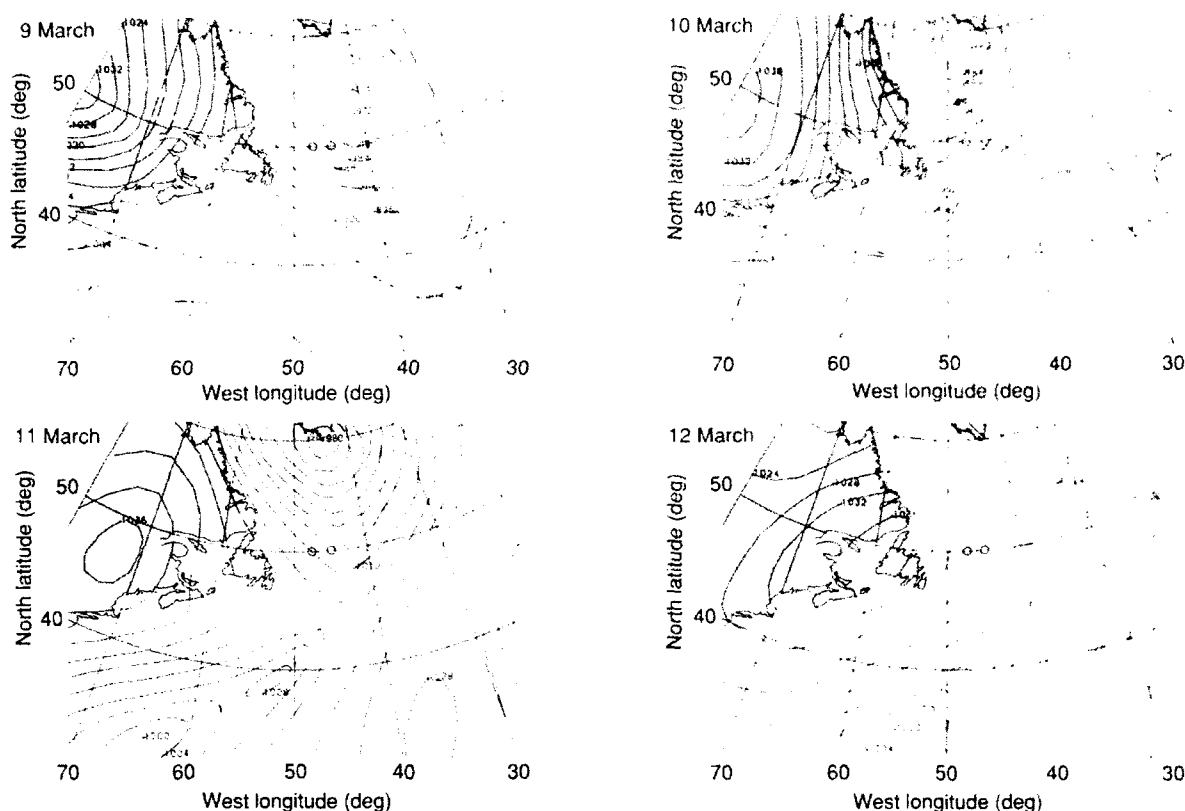


Figure 5. Isobar patterns and frontal locations taken from indicated section of NOAA Northern Hemisphere Final Analysis surface weather maps at 1200 UT on 9–12 March 1987. \circ is unoccupied ship site. The *Quest* occupied the western site from 14 to 19 March; the *Tydeman* occupied the eastern site from 14 to 18 March, then moved to the western site.

Wind System 2B (South–Southeasterly Swell)

The blocked frontal wave just described was also responsible for another wind system of interest, namely, the area of south–southeasterly winds east of the cyclone's trailing cold front on 11 March. This system was characterized by a fetch of nearly 600 nmi by 13 March (Fig. 7), which extended for a time as far north as the *Tydeman* location. Most of this system, however, was located in the domain of the coarse grid where the resolution (2.5° longitudinally) and analytical method (MPBL) somewhat limited fine details. Several transient ships in this system reported surface winds greater than 40 kt at times, but because this southerly flow was stable, the effective neutral wind was analyzed as 18 m/s at maximum intensity. The wave system generated in this wind field was observed in the LEWEX array (both the *Quest* and the *Tydeman*) by early on 14 March, and this diminishing dispersive southeast swell was seen in the directional wave data as late as early on 16 March.

Wind System 3 (Growing Northerly Sea/Swell)

The blocked frontal wave began to fill on 14 March and resumed a slow movement to the north–northeast on 15 March. As it did so, a high-pressure system over the Labrador Sea strengthened, leading to another episode of a strong pressure gradient (Fig. 6) and northerly flow (Fig. 7) in the Labrador Sea. Again, the area of wave generation lay north of the fine grid, in an area particularly void of data, so the details of the evolution

of this complex wind system are uncertain. This wind system generated a sea that propagated southward as a young swell through the LEWEX array, commencing near midday on 15 March, peaking late on 16 March, and vanishing by around midday on 18 March.

Wind System 4 (Freshening Easterlies)

As the blocked frontal wave moved away from the area and the northerly swell was building in the LEWEX array, winds at the *Quest* and the *Tydeman*, which had become light and variable by early on 16 March, shifted northeasterly and by 1200 UT increased to about 10 m/s at the *Tydeman* (see Fig. 4) and 15 m/s at the *Quest*. At the *Quest*, the hand-held anemometer provided a few wind estimates of 55 kt late on 16 March, but these readings were taken to be large overestimates of the true wind because the ship was under way in head winds, and superstructure interference tended to bias winds high at the *Quest* (W. Nethercote, personal communication, 1989). The fresh northeasterlies provided an 18-h period in which local wave generation in the presence of a swell might be studied. These local northeasterlies were associated with the approach of a strong cyclone on 16 March, which also was a significant factor in wind system 5, to be described next.

Wind System 5 (South–Southwesterly Swell)

This wind system actually was a complex response to the development and evolution of two cyclones. The first cyclone formed near Cape Hatteras (hence CH1) on 13

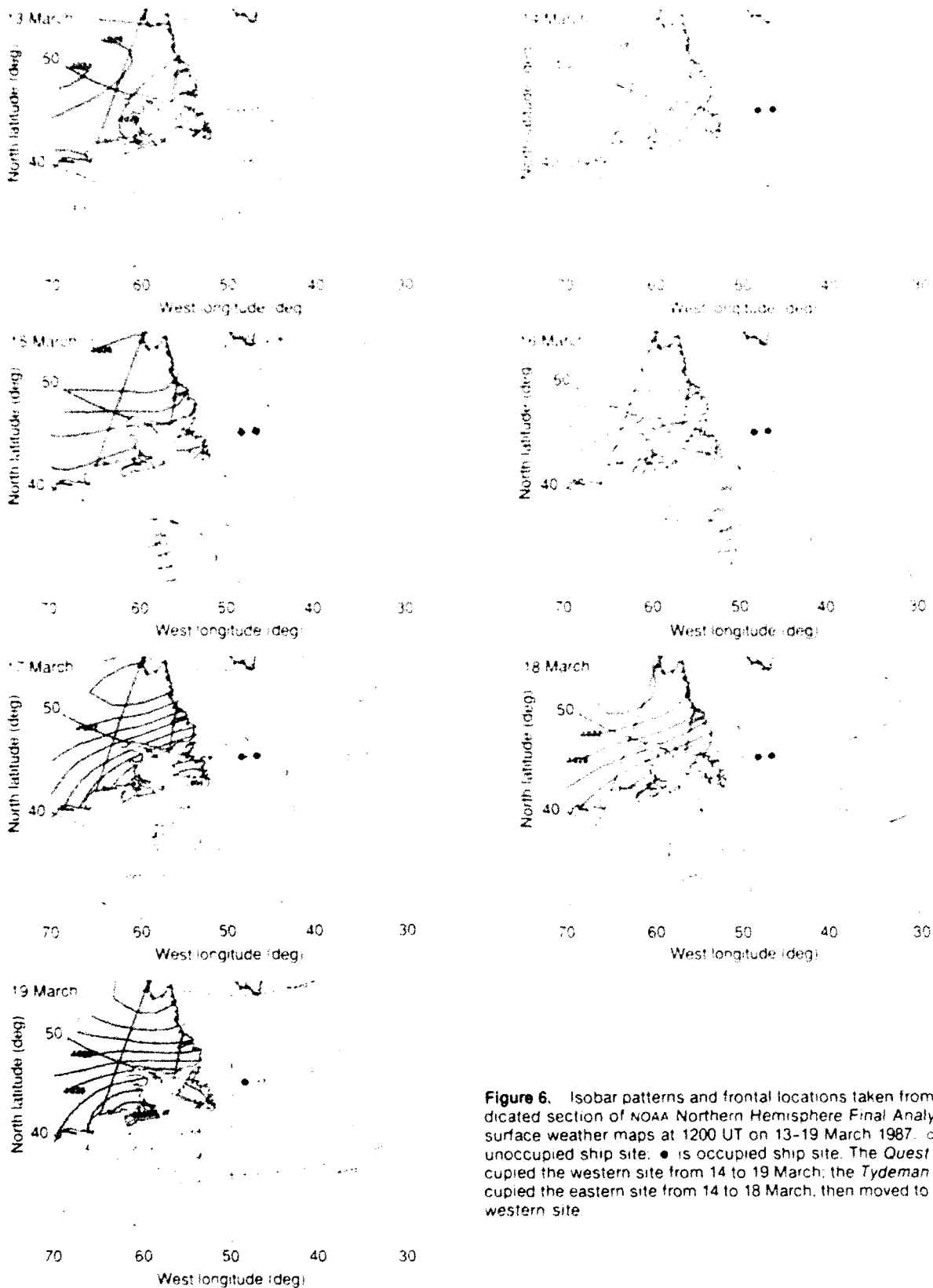


Figure 6. Isobar patterns and frontal locations taken from indicated section of NOAA Northern Hemisphere Final Analysis surface weather maps at 1200 UT on 13-19 March 1987. ○ is unoccupied ship site; ● is occupied ship site. The *Quest* occupied the western site from 14 to 19 March; the *Tydemar* occupied the eastern site from 14 to 18 March, then moved to the western site.

March, moved eastward, and deepened strongly though not explosively on 14 and 15 March. As this system encountered the blocking Atlantic ridge, however, it turned northward like its predecessors and filled rapidly on 16

March, with the center entering eastern Newfoundland on 17 March. The second cyclone (CH2) formed near Cape Hatteras on 16 March and moved eastward to become involved in the circulation of CH1 on 17 March,

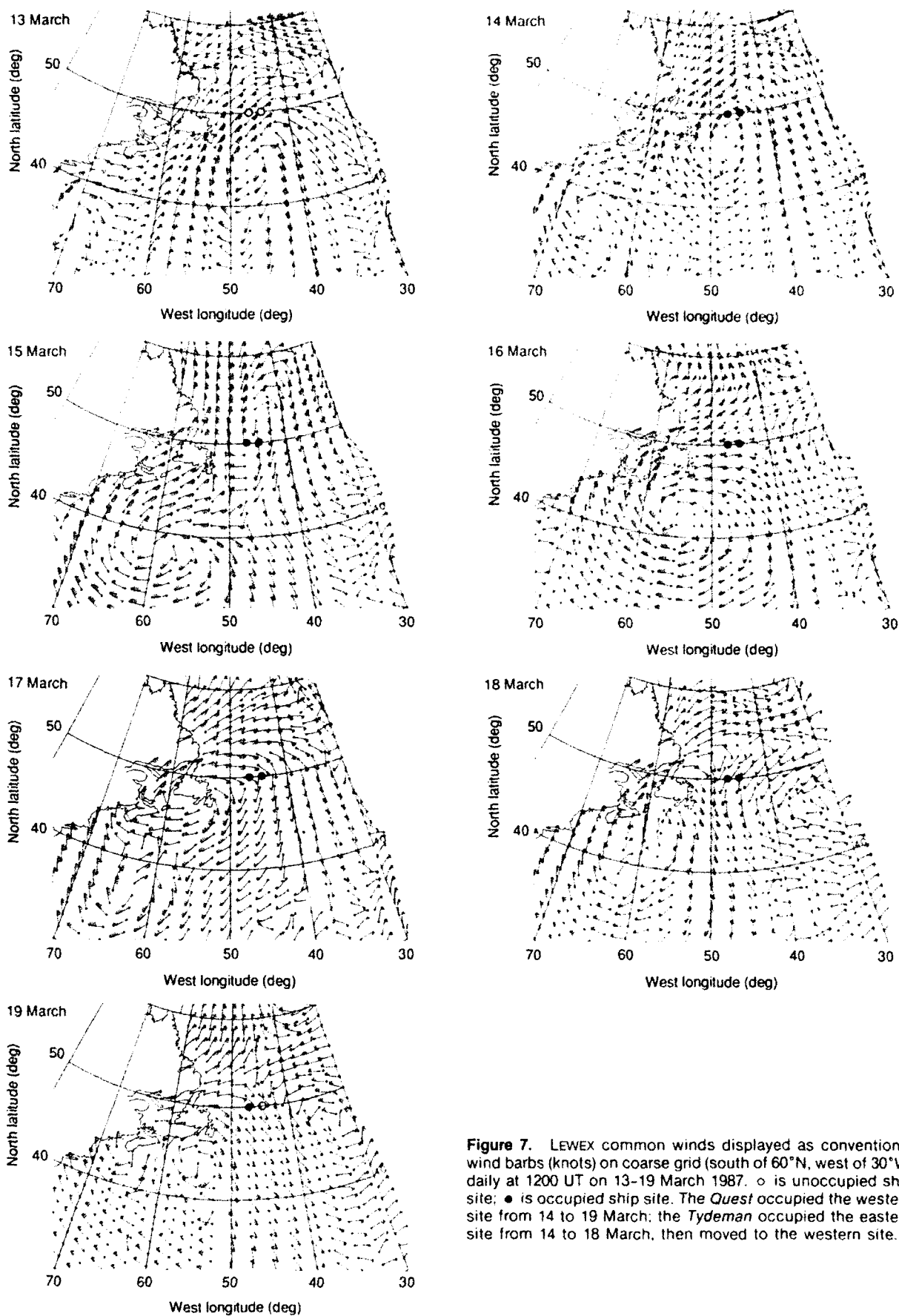


Figure 7. LEWEX common winds displayed as conventional wind barbs (knots) on coarse grid (south of 60°N, west of 30°W) daily at 1200 UT on 13–19 March 1987. ○ is unoccupied ship site; ● is occupied ship site. The *Quest* occupied the western site from 14 to 19 March; the *Tydeman* occupied the eastern site from 14 to 18 March, then moved to the western site.

resulting in a large quasi-stationary cyclonic circulation covering the North Atlantic west of about 45°N on 18 and 19 March.

Southwesterly swell first appeared in the LEWEX array late on 17 March and persisted through the end of the LEWEX measurements around 1800 UT, 19 March. This swell was generated in the south and east quadrants of CH1 and CH2, and therefore more than one fetch zone of significant generation of wave energy might have been involved as sources of swell observed in the LEWEX array. All hindcasts showed the southwest swell arriving at the LEWEX site about 18 h before it was actually observed to arrive (see Gerling, this volume), suggesting large systematic errors in the wind-field features responsible for this wave system. Those features lay south of the fine grid and south of the main shipping lane through 16 March. During 17 March, CH1 moved onto the fine grid, but as it filled, the southwesterly flow diminished steadily with maximum speeds of about 15 m/s. On 18 March, this first area of southwesterly flow passed over the LEWEX array with wind speeds of only about 10 m/s.

The second organized area of southwesterly flow, this time associated with CH2, was best developed at around 1200 UT on 17 March, with maximum wind speeds of 26 m/s, centered near 35°N, 65°W, again on the coarse grid. This surge of wind energy propagated rapidly northward onto the fine grid on 18 March, bringing

southerlies with speeds of 15 m/s to within about 300 nmi of the LEWEX array, but peak winds of only about 5 m/s at the *Quest* and the *Tydemar*. This wind system was the last one of interest in LEWEX, as by 1200 UT on 19 March, the surface winds in the North Atlantic west of 20°W had settled into a pattern of unusual summerlike tranquility!

DISCUSSION

In this section, we offer a critical assessment of the common winds and provide estimates of the accuracy achieved in the specification of each principal wind system. We also describe an attempt, only partially successful, to revise the winds in ways that might improve the poor hindcast of arrival time of swell from wind systems 3 and 5 at the LEWEX site.

To develop our error estimates, we may draw upon several previous studies of errors in marine winds, many of which used the same MPBL model used in this study. Table 1 is a summary of six such studies in which MPBL winds (all calculated with Cardone's MPBL model) are compared with observed surface winds. The comparison statistics (mean and root-mean-square [rms] wind-speed differences) group logically into four categories, depending on the type of verification data used: (1) buoys or other fixed platforms equipped with recording anemometers, (2) transient ship winds as reported, (3) transient

Table 1. Reported scalar wind-speed difference between winds derived from the indicated pressure fields, using Cardone's MPBL model, and the indicated measured data types.

Study	Comparison data	Pressure fields	Basin	Mean diff. (MPBL data) (m/s)	Scatter (rms) (m/s)
Cardone ¹⁰	NDBO buoys	NOAA LFM	USEC	-0.8	3.0
			USGC	-0.5	2.9
			USWC	-0.4	2.8
Overland & Gemmill ¹²	NDBO buoys	NOAA LFM	NY Bight	-0.5	2.4
Eid et al. ⁸	Buoys/rigs	NOAA LFM	N. Atlantic	-0.6	3.0
Gemmill et al. ¹¹	NDBO buoys	NOAA obj	N. Atlantic	-0.1	2.9
	NDBO buoys	NOAA obj	N. Pacific	+0.6	3.2
	Ships	NOAA obj	N. Atlantic	-2.9	5.1
	Ships	NOAA obj	N. Pacific	-2.0	4.7
Cardone et al. ³	Ships (adj)	NMC final	N. Pacific	-1.6	4.5
	Ships (adj)	FNOC obj	N. Pacific	-1.6	3.6
Dobson & Chaykovsky (this volume)	Geosat	LEWEX rean	N. Atlantic	-0.6	3.4
Composite	NDBO buoys			-0.3	2.9
				-0.6	3.4
	Transient ships (adjusted)			-1.6	4.0
				-2.4	4.9

Note: NDBO = NOAA National Data Buoy Office, LFM = NOAA Limited Area Fine Mesh Model, USEC = U.S. East Coast, USGC = U.S. Gulf Coast, USWC = U.S. West Coast, NMC = National Meteorological Center, FNOC = Fleet Numerical Oceanography Center, MPBL = Marine Planetary Boundary Layer model, adj = adjusted ship wind speeds, obj = objectively analyzed pressure fields, and rean = reanalyzed pressure fields.

ship winds whose wind speeds are adjusted to effective neutral 20-m wind speeds, and (4) Geosat-derived winds. Composites of difference statistics for each of these categories are also given in Table 1. In addition, the table indicates the source of pressure fields used in the study and the associated ocean basin.

The smallest differences are found for the buoy comparisons, which exhibit a scatter of about 3 m/s around a bias of less than 0.5 m/s. Unadjusted transient ship winds show the greatest differences, with statistics for adjusted transient ships and Geosat winds in between. The smaller differences for the buoy comparisons are rather consistent among the four studies involved and might be attributed to the near-shore locations (most NOAA National Data Buoy Office [NDBO] buoys are moored within 200 nmi of the U.S. coast), where the external variables of the MPBL are better defined than in the open ocean. Cardone et al.,³ however, reported a scatter of only 2.2 m/s in MPBL wind speeds in 369 comparisons against Seasat scatterometer winds measured in two passes over the eastern North Pacific Ocean, for which pressure fields were carefully reanalyzed. This finding suggests that wind-speed errors in MPBL winds derived from carefully (subjective or objective) analyzed pressure fields are about 3 m/s (rms) about a mean error (bias) of less than 1 m/s. We adopt these as the baseline wind-speed errors of the coarse-grid LEWEX common winds.

Wind-direction errors have not been as consistently reported in the cited studies, but we have extracted a consensus estimate from the statistics presented of scalar wind-direction errors in MPBL winds of 25° to 30° (rms) about a mean error of around 10°, and we adopt these as our baseline wind-direction errors for LEWEX coarse-grid common winds. Interestingly, the available studies show no particular difference between wind-direction statistics derived from ships or buoys, suggesting that transient ships estimate the wind direction about as well as buoys, although ship wind-speed estimates are subject to considerably more variability (see Pierson, this volume) than buoy-measured wind speeds.

The poorest comparisons in Table 1 are provided by the unadjusted transient ships, and no doubt the variability in the ship winds contributes significantly to the difference statistics. In several of the studies cited in Table 1, rms vector wind-difference magnitudes have also been presented, and in general these are about 50% larger than the scalar rms wind-speed errors computed from the same comparison data set for either buoys or ships.¹¹ Therefore, it should be expected that MPBL winds with baseline errors of about 3 m/s in wind speed about negligible bias, and wind direction errors of 25° to 30° about mean errors of about 10°, will exhibit apparent rms vector wind errors of about 7.5 m/s when compared with unadjusted transient ship winds. Indeed, Zambresky (this volume) reports just such differences between the LEWEX common winds and unadjusted transient ships. Somewhat lower errors were reported for the alternate ECMWF wind field also evaluated by Zambresky, but we suspect that the reduction can be attributed mainly to the comparison of the ECMWF winds

against the same ship wind reports naturally assimilated into the wind fields as part of the ECMWF analysis system.

The Geosat comparisons were made against the LEWEX common winds, and in nearly all cases were made over the coarse-grid domain from MPBL winds. The many along-orbit comparisons presented by Dobson and Chaykovsky (this volume) provide unique views of the error structure in conventional wind fields, particularly the tendency for significant spatially coherent wind-speed errors, which are no doubt more damaging to wave hindcasts (and other ocean response models) than are randomly distributed errors. Another interesting aspect of those comparisons is the systematic difference between ascending and descending passes, which (barring an instrument source) may reflect the tendency for skill in real-time synoptic marine analyses to vary systematically between day and night because of the varying numbers of transient ship reports transmitted to NWP centers.

The errors in the LEWEX winds on the fine grid cannot be estimated directly since all available measured wind data were used in the kinematic analysis, and especially in the vicinity of the LEWEX array (e.g., see Fig. 3), errors are very low. On the basis of previous experience, we estimate that the errors in the kinematic analyses on the fine grid are about 30% lower overall than the baseline errors in MPBL winds, but with somewhat greater reductions in the spatially and temporally coherent errors. Unfortunately, detailed analysis of the LEWEX measured and hindcast wave data indicates that most of the energy in the wave systems observed to evolve in the LEWEX array originated outside the fine grid, some in remote areas of the North Atlantic, where errors in the common winds locally are even greater than the baseline errors attached to the common winds overall. Thus, locally generated systems such as systems 2A and 4 should be more accurately specified than the baseline estimates, whereas wave systems developing north of LEWEX (systems 1 and 3) and far to the south of LEWEX (system 5) will be less accurately specified.

Wave hindcasts from all models indeed exhibited large errors in the simulation of systems 3 (Labrador Sea swell) and 5 (south-southwest swell). The similarity of these errors from model to model (e.g., all models predicted swell from each of these systems to arrive at the LEWEX site about 18 h before detection by the Wavescan [see Fig. 8 of Gerling, this volume]) suggests large systematic errors in the winds in the source areas of these systems. To investigate this possibility, we attempted to revise the winds in areas of the coarse-grid domain thought to contain the generation areas for systems 3 and 5. These areas were determined by backward tracing of great circles through the observed swell directions indicated by Wavescan. Because neither of these wave systems exhibited a shift of dominant wavelength with time consistent with a point source, a precise determination of source could not be made, and in fact the wind fields suggested rather dynamic fetch source zones for both systems.

The revision consisted simply of kinematic analysis of the affected parts of the coarse grid, on maps between

0000 UT on 15 March and 0000 UT on 17 March. Two new aspects of this revised kinematic analysis were as follows: (1) The wind speeds from Geosat passes over the selected reanalysis areas were used. (2) Where lack of data allowed latitude in the kinematic analysis, the revision was made in the direction of improving the specification of the wave systems of interest (a form of subjective inverse modeling). For example, the Wavescan data suggest that the source of the southwest swell is not the strong southerly flow preceding the occluded front associated with CH1 and not part of the circulation of CH2, but rather a fairly small-scale feature of CH1, namely, the area of gale force southwesterlies that develop on 16 March in advance of a secondary trough that formed in the cold-air sector of CH1 early on the 16th (see Fig. 6). Thus, wind speeds were reduced by up to 5 m/s ahead of the occlusion (as supported also by Geosat) and turned and increased in advance of the cold sector trough. Other changes included increasing the southeast flow in advance of the occlusion later on the 16th and early on the 17th, decreasing the northeasterlies around the *Tydemar* on the 16th by about 1 m/s, and shifting of the front lying north of LEWEX on the 15th to the west, making commensurate wind-field changes to the northerlies west of the front.

The effectiveness of the wind-field revisions on hindcasts of systems 3 and 5 was investigated by using the Ocean Data Gathering Program (ODGP) model (the only model that was readily available). Results of the rehindcast at the *Tydemar* are compared with the ODGP LEWEX run and with Wavescan, in Figure 8, in terms of Gerling's partitioned wave-vector representation. Of course, systems 1 and 2 are not affected by the revisions. The Labrador Sea swell that peaked on 16 March (system 3) is diminished in the revised hindcast, but its arrival is not delayed. The revised winds appear to provide a delay of about 8 h in the arrival of the southwest swell on 17 March, which is less than half of the delay needed to agree with the Wavescan arrival time. The general trend of the vectors after arrival time still does not agree with that of Wavescan on the 18th. However, the slight reduction of the wind speed at the *Tydemar* on the 16th and the increased southeasterlies in advance of the occluded front provide a better representation of the fresh easterlies (system 4).

Perhaps several iterations of the process of revision and rehindcast of the winds in the Labrador Sea could provide significantly improved specification of system 3, since little conventional data exist for that area. We are frankly surprised, however, by the insensitivity of the rehindcast to the substantial changes made to the wind field for system 5. Further changes in the wind field in the source zone of system 5 in the direction of improving the specification of the arrival time of the swell at the *Tydemar* would mostly likely require serious violation of wind observations from ships in the area and Geosat. Perhaps other wave models that participated in LEWEX would benefit more from the revised wind fields than ODGP. This sensitivity experiment suggests, however, that alternate explanations for the disagreement between model and Wavescan in system 5 should also be

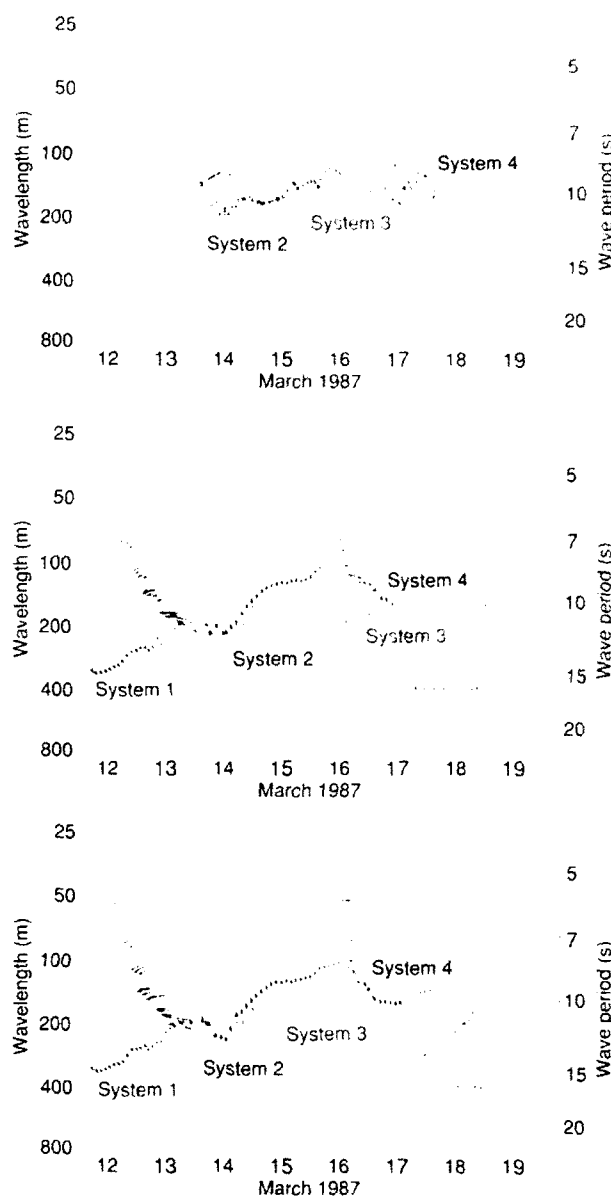


Figure 8. Comparison of Wavescan, ODGP LEWEX hindcast, and ODGP hindcast with revised winds at the *Tydemar* site.

considered. These include possible interaction of the swell with the Gulf Stream, the possibility that Wavescan is having difficulty resolving the opposing swell trains of systems 3 and 5, and the possibility that all models are lacking some physical mechanism that operates either in the source zone or on the opposing swell trains in the LEWEX area, and which is critical to an accurate specification of system 5.

REFERENCES

- Janssen, P. A. E. M., Komen, G., and de Voigt, W. J. P. "An Operational Coupled Hybrid Wave Prediction Model," *J. Geophys. Res.* **C3**, 3635-3654 (1984).
- Cardone, V. J., and Szabo, D. "Impact of Uncertainty in Specification of Offshore Wind on Accuracy of Wave Hindcasts and Forecasts," in *Proc. International Workshop on Offshore Winds and Ice*, Halifax, Nova Scotia, 7-11 October 1985 (available from Environment Canada, Downsview, Ontario).

- ³Cardone, V. J., Broccoli, A. J., Greenwood, C. V., and Greenwood, J. A., "Error Characteristics of Extratropical Storm Wind Fields Specified from Historical Data," *J. Pet. Technol.* **32**, 873-880 (1980).
- ⁴Unden, P., "Tropical Data Assimilation and Analysis of Divergence," *Mon. Weather Rev.* **117**, 2495-2517 (1989).
- ⁵Cardone, V. J., "Specification of the Wind in the Marine Boundary Layer for Wave Forecasting," Report No. TR-69-1, Geophysics Science Laboratory, New York University (1969) (available from NTIS AD#702-490).
- ⁶Cardone, V. J., Greenwood, J. G., and Cane, M. A., "Trends in Historical Marine Wind Data," *J. Clim.* **3**, 113-127 (1990).
- ⁷Janssen, P. A. E. M., "Wave Induced Stress and the Drag of Air Flow over Sea Waves," *J. Phys. Oceanogr.* **19**, 745-754 (1989).
- ⁸Eid, B. M., Cardone, V. J., Greenwood, J. A., and Saunders, J., "Real-Time Spectral Wave Forecasting Model Test during CASP," in *Proc. International Workshop on Wave Hindcasting and Forecasting*, Halifax, Nova Scotia, 23-26 September 1986, Environmental Studies Revolving Funds, Report Series No. 065, Ottawa, 370 pp. (1987).
- ⁹Cardone, V. J., Szabo, D., and Dello Stritto, E. J., "Development of Extreme Wind and Wave Criteria for Hibernia," in *Proc. 2nd International Workshop on Wave Hindcasting and Forecasting*, Vancouver, British Columbia, 25-28 April 1989 (available from Environment Canada, Downsview, Ontario).
- ¹⁰Cardone, V. J., *Specification and Prediction of the Vector Wind on the United States Continental Shelf for Application to an Oil Spill Trajectory Forecast Program*, Final Report to NOAA Techniques Development Laboratory, Silver Spring, Md., under Contract No. T-35430, City University of New York (1978).
- ¹¹Gemmell, W. H., Yu, F. W., and Feit, D. M., "A Statistical Comparison of Methods for Determining Ocean Surface Winds," *Weather and Forecasting* **3**, 153-160 (1988).
- ¹²Overland, J. E., and Gemmell, W. H., "Marine Winds in the New York Bight," *Mon. Weather Rev.* **105**, 1003-1008 (1978).

PREDICTIONS FROM THE GSOWM DURING LEWEX

Predictions from the U.S. Navy's Global Spectral Ocean Wave Model (GSOWM) are compared with observations from buoys and ship radar and with output from the WAM third-generation wave model, with both models forced in hindcast mode by identical winds. In general, the GSOWM hindcast spectra compare well with the other spectral estimates, although GSOWM tends to develop too much energy at low frequencies. Although the GSOWM predictions are generally in good agreement with the observations, on one occasion GSOWM fails to show a growing wind sea that is predicted by WAM and verified by the buoy data.

INTRODUCTION

The Global Spectral Ocean Wave Model (GSOWM) is a first-generation wave model run operationally at the U.S. Navy's Fleet Numerical Oceanography Center (FNOC). The model is forced by winds produced by the Navy Operational Global Atmospheric Prediction System numerical weather prediction model and is run on a 2.5° spherical grid twice per day.¹ GSOWM produces two-dimensional wave energy spectra, with resolution of 15 frequencies by 24 directions, out to a forecast time of 72 h. The initial conditions for these forecasts are provided by simply carrying the predicted two-dimensional energy spectra forward in time. Wave products, including significant wave height, sea height, swell height, primary wave direction, primary wave period, sea direction, swell direction, sea period, and swell period, are derived from the spectra in 12-h intervals.

BASIC MODEL FORMULATION

The basic formulation of wave growth and decay in the GSOWM is based on the work of Pierson.² The equation governing the change of the one-dimensional (i.e., direction-independent) wave energy spectrum $S(f)$ with time in the model is

$$\frac{\partial S(f)}{\partial t} = G(f) + P(f), \quad (1)$$

where f is the frequency, $G(f)$ is the wind source/dissipation function, and $P(f)$ is the change in $S(f)$ due to convergence or divergence of the energy resulting from swell propagation.

The wind source function is a modified version of the Phillips³ resonance theory and the Miles⁴ instability theory based on the work of Inoue.⁵ The Phillips resonance mechanism causes the initial wave growth from flat seas to be linear with time. As the waves grow further, the Miles instability mechanism begins to dominate and the waves exhibit exponential growth with time. The growth is slowed as the wave spectrum approaches the Pierson and Moskowitz⁶ fully developed spectrum,

which serves as the upper limit on spectral growth. An exception occurs at high frequencies, where the Kitaigorodskii⁷ spectrum becomes the limiting spectrum. Specifically, the equation for wave growth is

$$G = \left\{ A \left[1 - \left(\frac{S}{S_{\infty}} \right)^2 \right]^{\alpha} + BS \right\} \times \left[1 - \left(\frac{S}{S_{\infty}} \right)^2 \right], \quad (2)$$

where A is the resonance term, B is the instability term, and S_{∞} is the limiting spectrum. Following growth of the one-dimensional spectrum according to Equation 2, the resulting wave energy is spread over a range of azimuths that is centered on the local wind direction using an empirical function of wind speed, frequency, and angle relative to the wind.

Dissipation of energy for waves traveling against the wind is accomplished according to an empirical function of the wave energy, frequency, and angle relative to the wind. No dissipation occurs for waves running with the wind. A downstream propagation algorithm is used to advect wave energy along great circular paths at the frequency-dependent group velocity for deep-water waves. The technique simulates wave dispersion and conserves wave energy.

THE GSOWM HINDCAST FOR LEWEX

The GSOWM hindcast for the Labrador Sea Extreme Waves Experiment (LEWEX) was accomplished by forcing the full global implementation of the model from an initial state of nearly flat seas with winds obtained by embedding the common LEWEX winds into the FNOC global winds. The LEWEX winds were interpolated in time and space to match the three-hour time step and the 2.5° resolution of the GSOWM. The hindcast is for the period 9 through 18 March 1987. Directional wave energy spectra at six-hour intervals were produced for further processing and display.

COMPARISONS

Wind Speeds and Wave Heights

Time series of significant wave heights from the operational GSOWM forecast made at FNOC, the GSOWM hindcast, and the Datawell moored Wavec buoy at the CFAV *Quest* are displayed in Figure 1. The operational GSOWM wave heights are larger than both the GSOWM hindcast and the buoy-observed heights during two high-wind events on 16 and 18 March. This is explained by the wind-speed time-series plots of Figure 2, which show that the operational FNOC wind speeds are biased high compared with those of LEWEX. Part of the bias here may have been due to the coarse spatial resolution of the operational FNOC winds (2.5° latitude/longitude com-

pared with 1.25° latitude/longitude for the LEWEX winds).

Time series of wave heights and wind speeds are again displayed in Figures 3 and 4, but at the location of HNLMS *Tydeman*. As before, the operational GSOWM wave heights and FNOC winds are biased high relative to the buoy observations and the LEWEX winds. Also, in this case the GSOWM hindcast wave heights are higher than the buoy observations during the period 16 to 18 March. This is not an unusual occurrence. Routine comparisons of GSOWM spectra with buoy observations in both the Atlantic and the Pacific Oceans show a tendency for the model to develop too much energy at low frequencies, resulting in higher prediction of significant wave height.

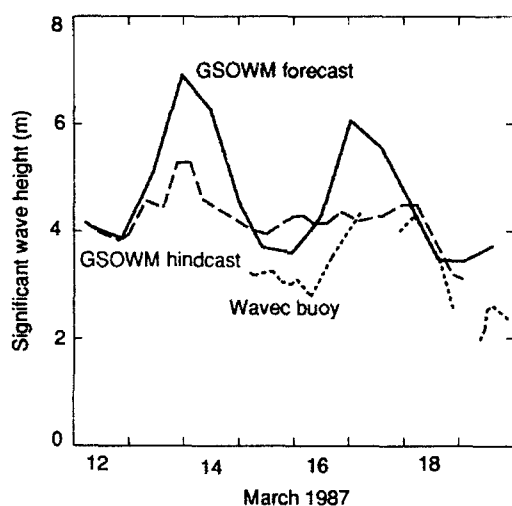


Figure 1. Time series of significant wave height at the *Quest* (50°N , 47.5°W) from the operational GSOWM (solid black), the GSOWM hindcast (dashed blue), and the Datawell moored Wavec buoy (dotted red).

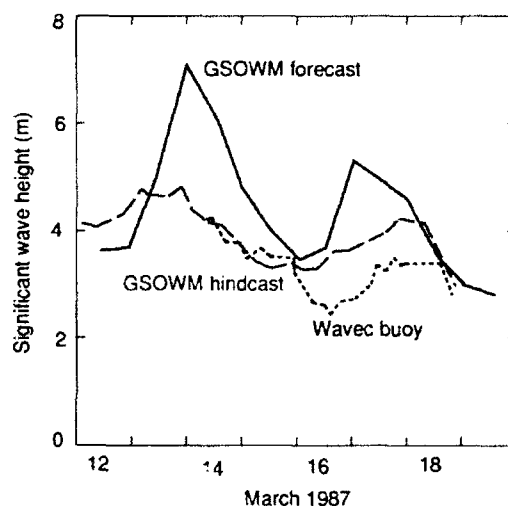


Figure 3. Time series of significant wave height at the *Tydeman* (50°N , 45°W) from the operational GSOWM (solid black), the GSOWM hindcast (dashed blue), and the Datawell moored Wavec buoy (dotted red).

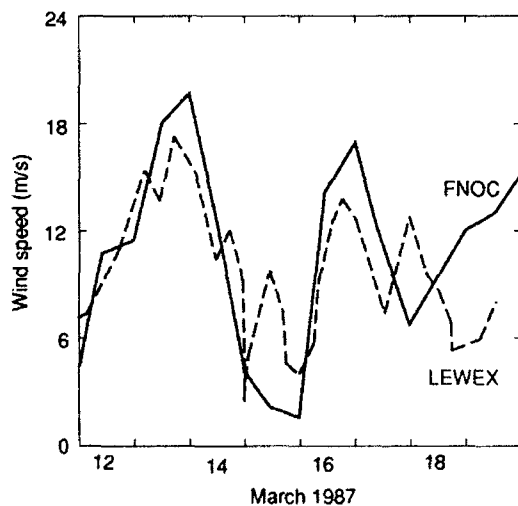


Figure 2. Time series of wind speed at the *Quest* from the operational FNOC winds (solid black) and the common LEWEX winds (dashed blue).

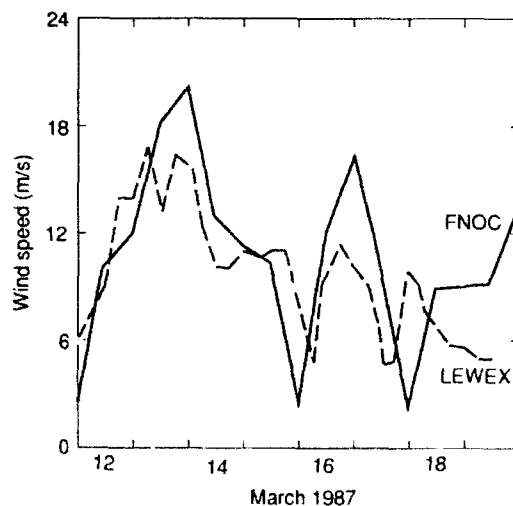


Figure 4. Time series of wind speed at the *Tydeman* from the operational FNOC winds (solid black) and the common LEWEX winds (dashed blue).

Directional Wave Energy Spectra

Comparisons are made between the GSOWM hindcast and a hindcast from the third-generation wave model (WAM⁸). Both of these hindcasts were made using the same winds within the LEWEX common grid. Available observations from the moored Wavec buoy and ship radar are then compared with the predictions of both models. Directional wave energy spectra from these sources at the location of the *Quest* for five different times are shown in Figure 5. The individually normalized directional spectra are plotted in polar coordinates with wave number increasing from the center. Compass directions in the following discussion refer to the direction toward which the waves are traveling.

At 1200 UT on 14 March, the ship radar indicates a NNW wave system with a wavelength of 200 m. This agrees more closely with the WAM hindcast (wavelength of 200 m) than with the GSOWM hindcast (wavelength of 250 m). Both models are building a wind sea in response to the local wind out of the northeast at this time. At 1200 UT on 15 March, the Wavec buoy indicates a NNW wave system with a 200-m wavelength. The GSOWM and WAM, however, both show a SSE wave system in addition to the NNW system. The SSE system dominates in GSOWM, whereas the NNW dominates in WAM. At 1200 UT on 16 March, the Wavec buoy indicates a SSW primary wave system and a NW secondary system. Both the GSOWM and the WAM show S wave systems, but the wavelength of the WAM system agrees more closely with the buoy. GSOWM predicts the NW secondary system detected by the Wavec buoy, but WAM does not. At 1800 UT on 16 March, both GSOWM and WAM show dominant S wave systems, in fair agreement with the buoy and the ship radar data. However, the GSOWM also has two secondary systems, one NW and the other NE. At 1200 UT on 18 March, GSOWM, WAM, the Wavec buoy, and the ship radar are all in good agreement and show a NNE system.

Wave Vectors

Using the format convention and display of Gerling (elsewhere in this volume), Figure 6 shows the direction and magnitude (vectors) of peak wave energy as a function of frequency/wavelength (y-axis) and time (x-axis) for the GSOWM hindcast, the WAM hindcast, and the Wavec buoy at the *Quest*. Several well-defined wave systems are evident in this plot, including the SSE system on 12 to 14 March, the SW system on 13 to 14 March, the NNW system on 14 to 15 March, the S system on 15 to 18 March, and the NNE system on 17 to 20 March. Agreement between the two wave models is generally good, although the wavelengths of the GSOWM wave systems tend to be greater than those of the WAM and the Wavec buoy. For example, the WAM and the Wavec buoy show a wavelength of 180 m for the S wave system on 16 March, while the GSOWM shows a wavelength of about 190 to 200 m for this system, which is consistent with the tendency for GSOWM to place too much energy at low frequencies.

Close scrutiny of Figure 6 points out some other interesting differences between the two models at the *Quest*.

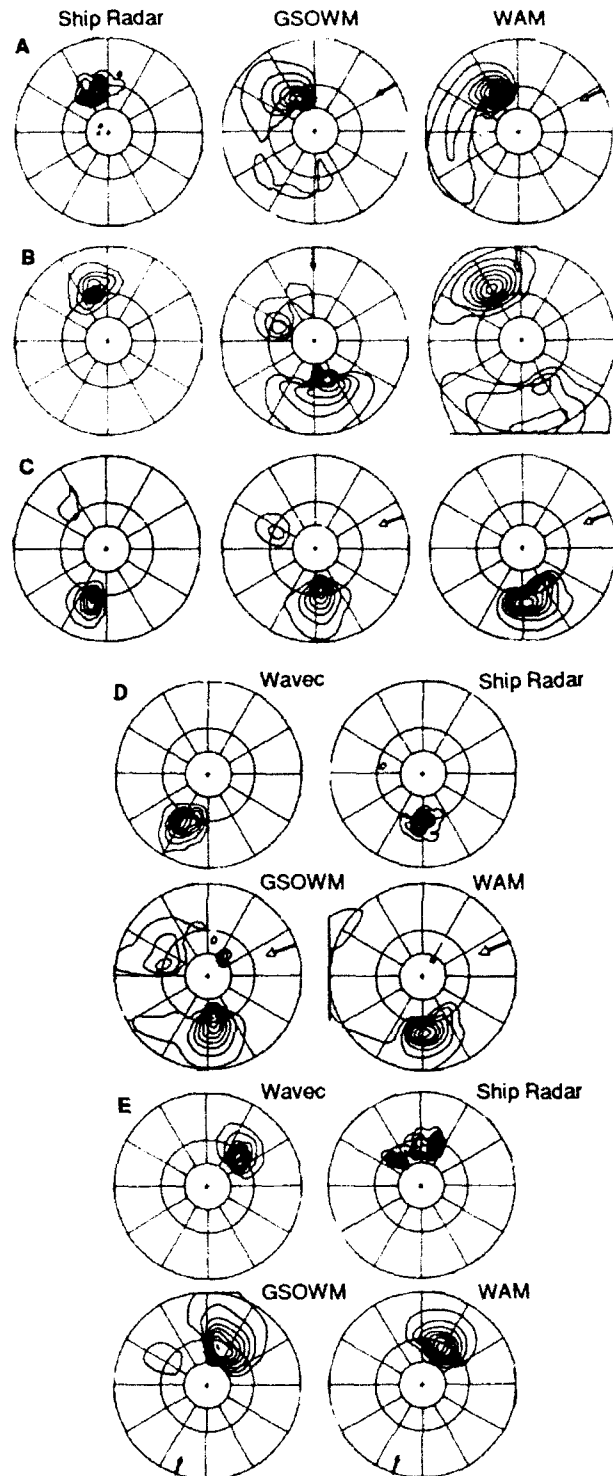


Figure 5. Directional spectra at the *Quest* from the GSOWM hindcast, the WAM hindcast, the Wavec buoy, and the ship radar at various times. **A.** 1200 UT on 14 March. **B.** 1200 UT on 15 March. **C.** 1200 UT on 16 March. **D.** 1800 UT on 16 March. **E.** 1200 UT on 18 March 1987. The outer, middle, and inner concentric circles correspond to wavelengths of 100, 200, and 400 m, respectively.

For example, on 16 March the WAM develops a WSW wind sea, which is evident in the Wavec buoy data but

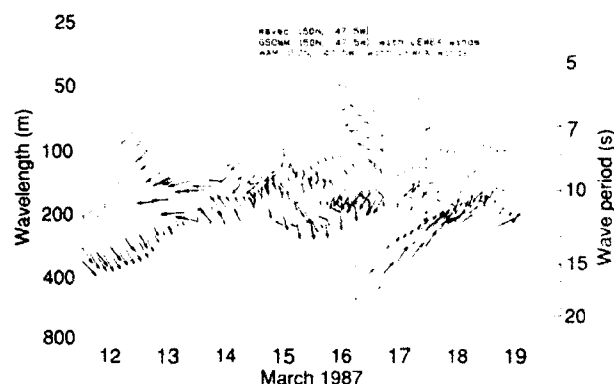


Figure 6. Wave vectors at the *Quest* from the GSOWM hindcast (black), the WAM hindcast (blue), and the Wavac buoy (red), during the period 12 to 19 March 1987. The vectors represent the magnitude and direction of the significant peaks in the directional wave energy spectra. Data are smoothed in time and frequency (courtesy of T. Gerling).

not in the GSOWM. In addition, as discussed earlier, the GSOWM exhibits a NW system at 1200 UT on 16 March that is verified by the Wavac data but not shown by the WAM.

The genesis of the 16 March NW wave system at the *Quest* is associated with a low-pressure system off the coast of North Africa several days earlier (see Fig. 7). It takes two to three days for the 10 to 11 s period wave system to propagate from the eastern Atlantic to the lo-

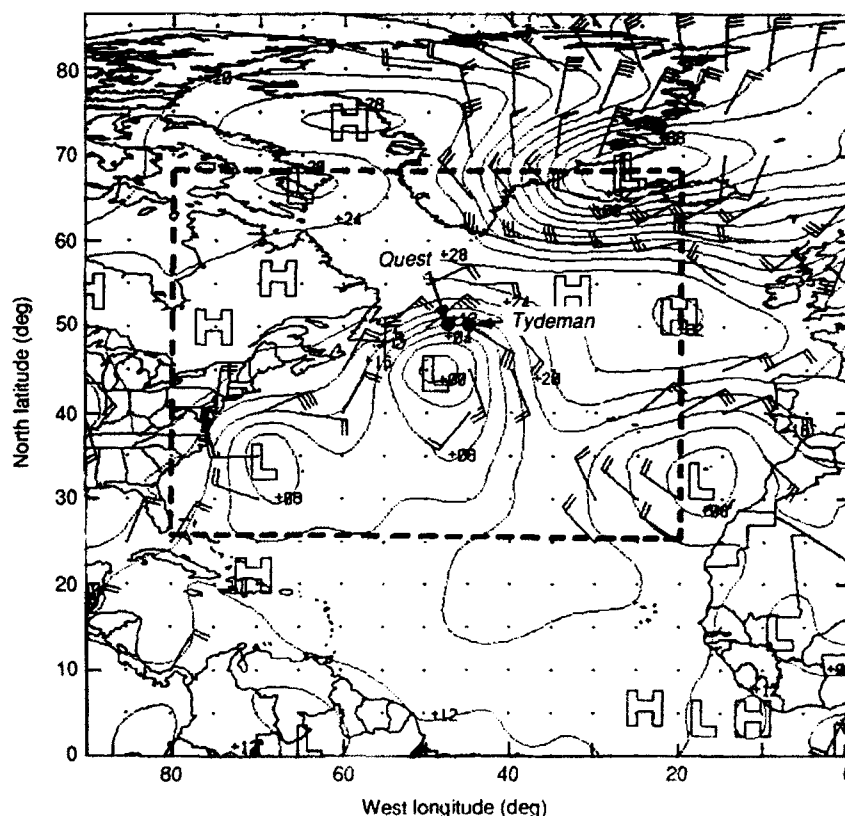
cation of the *Quest* (see Fig. 8). GSOWM correctly accounts for the system because, unlike WAM, which did not embed the LEWEX common winds into a larger field, GSOWM encompasses the entire North Atlantic and uses the FNOC winds outside of the area covered by the LEWEX winds. Note that the United Kingdom Meteorological Office model also predicts the arrival of this swell at the *Quest* on 16 March (see the article by Rider and Stratton in this volume).

SUMMARY

The GSOWM is a first-generation global wave model run operationally at FNOC. When run in hindcast mode and forced with the LEWEX winds, the GSOWM produces the major wave systems exhibited by the third-generation WAM wave model and measured by the Wavac buoy and ship radar during LEWEX. Subtle but important differences exist, however, between GSOWM and WAM predictions. The peak frequency of the GSOWM spectra tend to be lower than those of the WAM and the buoy observations, a characteristic problem with the model. In one instance GSOWM fails to produce a wind-sea system predicted by WAM and verified by the buoy data. The GSOWM correctly accounts for a wave system originating from a storm near the coast of North Africa, outside the LEWEX common wind field domain.

Although not conclusive, the LEWEX data set suggests that WAM produces more accurate predictions than GSOWM, a result that is expected on theoretical grounds. In any case, FNOC has implemented and is testing a re-

Figure 7. Synoptic weather chart at 0000 UT on 14 March 1987 for the North Atlantic. Contours show surface pressure with a 4-mbar contour interval. Wind barbs indicate surface winds (winds less than 20 kt are not displayed). The heavy dashed lines show the area covered by the LEWEX winds. Winds associated with the low-pressure system off the coast of North Africa generate a NW wave system, which is observed at the *Quest* several days later.



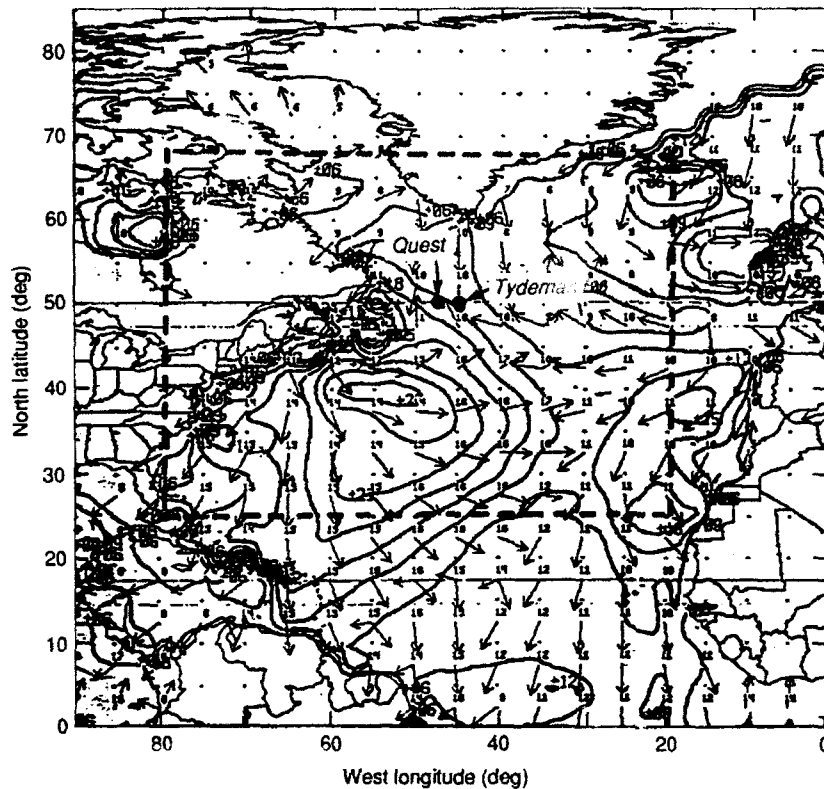


Figure 8. Output from the GSOWM hindcast for 1200 UT on 16 March 1987. The contours show significant wave height with a 3-ft contour interval. The vectors represent primary and secondary wave directions. The numbers at the base of the arrows are primary periods in seconds. The heavy dashed lines show the area covered by the LEWEX winds. Note the 10 s period NW wave system propagating toward the LEWEX area from a region of generation off the coast of North Africa.

gional version of the WAM as an eventual replacement for the operational Mediterranean Spectral Ocean Wave Model.⁹ Implementation of a global version of the WAM is planned to coincide with the installation of a Class VII supercomputer at FNOC in the near future. This model will run on a 1.25° grid with 15° angular resolution as a replacement for the GSOWM.

REFERENCES

- ¹Clancy, R. M., Kaitala, J. E., and Zambresky, L. F., "The Fleet Numerical Oceanography Center Global Spectral Ocean Wave Model," *Bull. Am. Meteorol. Soc.* **67**, 498-512 (1986).
- ²Pierson, W. J., *The Spectral Ocean Wave Model (SOWM), a Northern Hemisphere Computer Model for Specifying and Forecasting Ocean Wave Spectra*, TR DTNSRDC-82/011, David W. Taylor Naval Ship Research and Development Center, Carderock, Md. (1982).
- ³Phillips, O. M., "On the Generation of Waves by Turbulent Wind," *J. Fluid Mech.* **2**, 417-445 (1957).
- ⁴Miles, J. W., "On the Generation of Surface Waves by Shear Flow," *J. Fluid Mech.* **3**, 185-204 (1957).
- ⁵Inoue, T., *On the Growth of the Spectrum of Wind Generated Sea According to a Modified Miles-Phillips's Mechanism and Its Application to Wave Forecasting*, TR 67-5, Geophysical Sciences Laboratory, New York University, School of Engineering and Science, New York (1967).
- ⁶Pierson, W. J., and Moskowitz, L., "A Proposed Spectral Form for the Fully Developed Wind Sea Based on the Similarity Theory of S. A. Kitaigorodskii," *J. Geophys. Res.* **69**, 5181-5190 (1964).
- ⁷Kitaigorodskii, S. A., "Application of the Theory of Similarity to the Analysis of Wind Generated Wave Motion as a Stochastic Process," *Izv. Akad. Nauk. SSSR Ser. Geophys.* **1**, 105-117 (1961).
- ⁸The WAMDI Group, "The WAM Model—A Third Generation Ocean Wave Prediction Model," *J. Phys. Oceanogr.* **18**, 1775-1810 (1988).
- ⁹Lazanoff, S. M., Stevenson, N. A., and Cardone, V. J., *A Mediterranean Sea Wave Spectral Model*, TR 73-1, Fleet Numerical Oceanography Center (1973).

DIRECTIONAL SPECTRA FROM THE UKMO HINDCASTS AND THE EFFECT OF SWELL FROM OUTSIDE THE LEWEX REGION

A series of hindcasts was made using the United Kingdom Meteorological Office wave model. The effect of swell from outside the Labrador Sea Extreme Waves Experiment (LEWEX) region was shown to be negligible. The model was compared with measured wave height data and with spectra from other models. It is not obvious which are the more accurate spectral estimates, as the variation between measured spectra can be as large as that between models.

INTRODUCTION

Second-generation wave models have been run at the United Kingdom Meteorological Office (UKMO) since 1976. Early versions were on a polar stereographic grid.¹ The current global wave model is a second-generation latitude/longitude model that became operational in July 1986. Little change was made to the physics of the original models until 1987, when the physics subroutines were updated. The dissipation term given by Komen et al.² was included, and the rate of wave growth was adjusted to balance the dissipation terms at full development.³

The global wave model is run twice daily to provide five-day forecasts. The model's grid covers the entire globe, except for the extreme northern and southern latitudes, with a resolution of 1.5° of latitude and 1.875° of longitude, but the model can easily use other latitude/longitude grids with different resolutions. The model holds wave-energy information in spectral form by binning it into one of sixteen directions and thirteen frequencies at each point. The model is driven by surface wind fields extracted from the UKMO global atmospheric model and has wind and physics time steps of one hour. For the Labrador Sea Extreme Waves Experiment (LEWEX) hindcast, one-dimensional spectra were produced every six hours and the full directional spectra hourly at selected grid points.

The UKMO's contribution to LEWEX consisted of wave spectra from two hindcasts: an operational hindcast run using the independently derived UKMO wind fields and a dedicated hindcast run using the specially prepared LEWEX common winds. The common winds were defined on a small fine-mesh grid, which was contained within a coarse-mesh grid covering a larger area (see Fig. 1). The resolutions of the grids are given in Table 1.

Three additional hindcasts were run to see whether the LEWEX coarse-mesh grid, used in the dedicated hindcast, covered a large enough area. There was the possibility of some long-fetch swell propagating into the area around the two ship positions of interest (see Fig. 1), from the more eastern and southern parts of the North

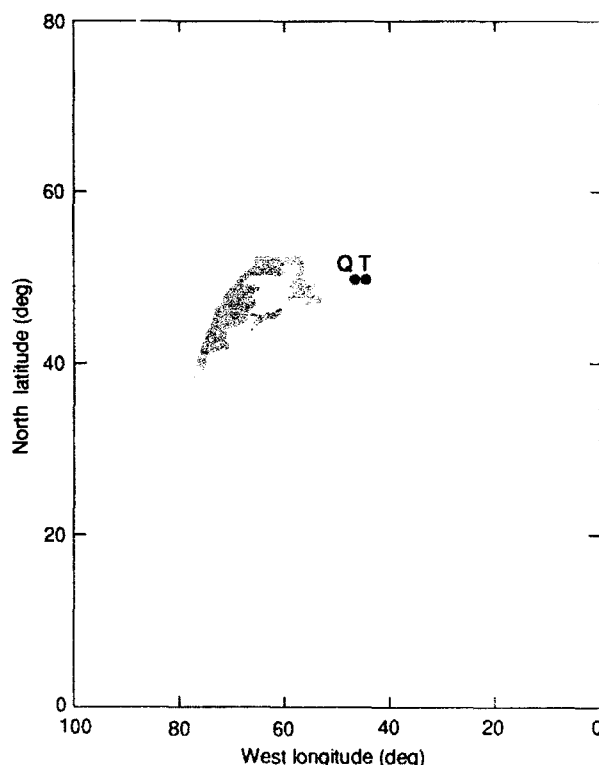


Figure 1. LEWEX grid areas. The blue area indicates coarse-mesh grid; the blue-gray area indicates fine-mesh grid. T is the location of HNLMS Tydeman at 50.0°N and 45.0°W , and Q is the location of CFAV Quest at 50.0°N and 47.5°W .

Atlantic Ocean not covered by the coarse-mesh LEWEX grid.

Additionally, the LEWEX database provided an opportunity to verify the UKMO model performance in the Labrador area against buoy measurements of wave heights and energy spectra.

Table 1. Summary of grid resolutions.

Grid	Resolution (deg)	
	Latitude	Longitude
LEWEX coarse mesh	1.250	2.500
UKMO coarse mesh	1.500	1.875
LEWEX fine mesh	0.625	1.250

HINDCASTS

The first UKMO model run for LEWEX used wind fields from the UKMO atmospheric model and will be referred to as the UKMO hindcast. The second model run used the LEWEX common winds and will be referred to as the common hindcast. Table 2 summarizes the five hindcasts, which differ according to which grid or grids were used and whether the initial energy start field was zero. In all cases, the forcing wind fields were on the same grid as the wave model, and a great-circle turning term was included in all coarse grid runs. Each hindcast started at 1200 UT on 9 March 1987.

The UKMO hindcast was run on the UKMO global grid using hourly surface winds from the UKMO global atmospheric model. The hindcast started with a nonzero energy start field, which had been archived from another hindcast not connected with LEWEX. Thus, the model was fully warmed up at the beginning of the hindcast.

The second, or common, hindcast used the LEWEX fine-mesh and coarse-mesh winds, and the energy start fields for both grids were zero. The LEWEX coarse- and fine-mesh two-hourly wind fields were interpolated to one-hourly values. The coarse grid provided hourly boundary values for the fine-mesh area.

The third, or control, hindcast was made in a similar way to the common hindcast except that the UKMO global grid and associated winds were used. The UKMO grid has a higher resolution than the LEWEX coarse-mesh grid (see Table 1). The nonzero energy start field for the UKMO hindcast was used to initialize the UKMO global grid in the control hindcast and was interpolated in space onto the LEWEX fine-mesh grid. Effectively, the control run was a global hindcast similar to the UKMO run but with a small, higher resolution grid inserted in the Labrador Sea area, driven by the common LEWEX winds.

To ensure that the LEWEX coarse-mesh grid covered an area large enough to contain all the significant advected energy systems, a fourth hindcast was run, and the resulting spectral data were compared with those from the control hindcast. The fourth hindcast was run using the UKMO winds over a subsection of the UKMO global grid equivalent to the LEWEX coarse grid starting from a nonzero energy field. The fifth hindcast was a repeat of the fourth hindcast but started from a zero energy field to assess the time required to warm up the model.

PLOTTING TWO-DIMENSIONAL WAVE SPECTRA

Before proceeding further, it is important to discuss the method used to plot the LEWEX spectral data. Be-

Table 2. Summary of hindcasts run at the UKMO.

Hindcast	LEWEX grid	UKMO grid	Start field
UKMO	—	Global	Nonzero
Common	Fine and coarse mesh	—	Zero
LEWEX	Fine mesh	Global	Nonzero
Control	Fine mesh	Limited area	Nonzero
Fourth run	Fine mesh	Limited area	Zero
Fifth run	Fine mesh	Limited area	Zero

fore being plotted, each spectrum is normalized with respect to its peak energy value in k-space. Therefore, it is possible for two spectra with similar structures in frequency-space to look different when the spectra are transformed to k-space, normalized, and then plotted.

For example, consider the two-dimensional wave number plots in Figure 2. They represent output from two different hindcasts—the UKMO and the control—at the same time and location. The original frequency spectra were quite similar. They both had two major components, namely, a component coming from the southwest and a weaker component coming from the east. The main difference between them was that the spectrum from the UKMO hindcast had a larger energy peak in the southwesterly swell component. When the UKMO spectrum is transformed to k-space and plotted in the standard way, the effect of normalizing is that the easterly swell component is not contoured because the other component is dominant. Also, this southwesterly component is plotted with a different shape compared with the plot from the control hindcast.

Conclusions about the wave model performance should not be made on the evidence of these plots alone, because the results could be misleading.

The Effect of Swell from Outside the LEWEX Region

The results of the control hindcast were compared with those of the fourth hindcast by finding the difference in wave height at the ship positions. A positive difference indicated more energy in the control run. Significant negative differences, 0.12 m for a control wave height

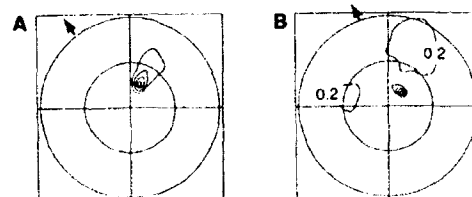


Figure 2. Two-dimensional spectra at 0300 UT on 19 March at the Tydemar. **A.** Based on the UKMO hindcast. Wind speed is 5.8 m/s, total energy is 0.30 m², and significant wave height is 2.2 m. **B.** Based on the control hindcast. Wind speed is 5.4 m/s, total energy is 0.28 m², and significant wave height is 2.1 m. The plots are linear in wave number, with the outer circle at $2\pi/100$ rad/m.

of 3.19 m, as well as positive differences were found. On calculating the total energy over the whole grid for each run, the fourth hindcast was found to have less energy than the control.

The difference in distribution of energy in the fine-mesh grid can be attributed to the dependence of energy growth and dissipation terms on the total amount of energy at each grid point at the beginning of a time step, and to a slight change in the advection calculation introduced by the difference in the northernmost latitude of the two coarse grids. Once a difference occurs, it can be amplified. Figure 3 shows the total energy on 13 and 14 March for the control, fourth, and common hindcasts. The difference in energy of the common hindcast is due to the difference between the UKMO and LEWEX wind fields.

COMPARING SPECTRA

Output from the fourth and control hindcasts was used to look for differences in wave heights that might indicate swell coming from outside the LEWEX region. The three hourly plots of two-dimensional wave spectra for both hindcasts were compared at the ship locations. Most of the normalized plots for each hindcast are similar, but some exceptions occur early on 16 March (e.g., at HNLMS *Tydeman* at 0300 UT).

Figure 4A shows the plot of the spectral data from the fourth hindcast. The plot is bimodal with a spreading, southerly wind-sea component and a northeasterly swell component. Figure 4B shows the trimodal plot of the spectral data from the control run. This plot is similar to the plot in Figure 4A, except for a component of low-energy, long-fetch swell coming from the east. The UKMO hindcast also has a trimodal spectrum on 16 March, which demonstrates that the extra swell component is not attributable to the use of the LEWEX fine-mesh winds.

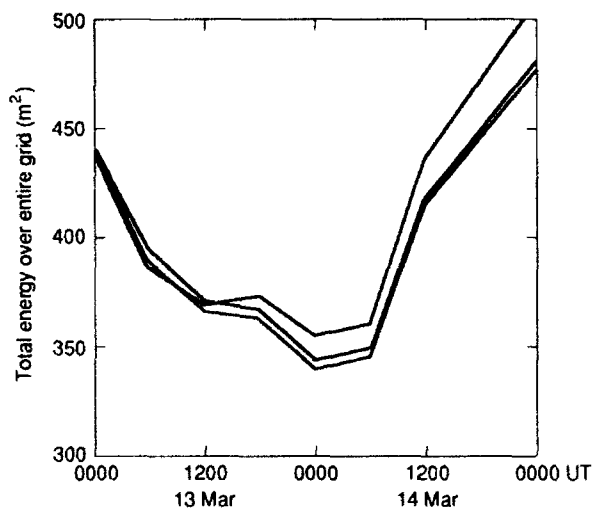


Figure 3. Total energy values for the LEWEX grid during different hindcasts. Red, common hindcast; black, control hindcast; blue, fourth hindcast.

Identifying the Source of the Swell

Figure 5 shows a North Atlantic chart with the UKMO global wind analysis for 0000 UT on 14 March. Just off the coast of North Africa was a small storm system with southeasterly winds of up to 25 kt on its northeast flank. Swell generated by such a system would take about 48 hours to reach the LEWEX ship positions. This is the most likely origin of the extra swell seen in the UKMO and the control hindcasts, since the generating area is outside the common LEWEX coarse-mesh grid.

Although it has been shown that swell may penetrate the LEWEX area, the greatest difference found in wave height was 0.24 m for a control value of 3.51 m; therefore, the effects of swell from outside the LEWEX area are not important for this study.

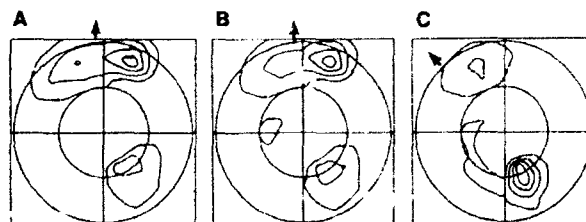


Figure 4. Two-dimensional spectra at 0300 UT on 16 March at the *Tydeman*. A. Based on the fourth hindcast. Wind speed is 6.3 m/s, total energy is 0.45 m², and significant wave height is 2.7 m. B. Based on the control hindcast. Wind speed is 6.3 m/s, total energy is 4.8 m², and significant wave height is 2.8 m. C. Based on the UKMO hindcast. Wind speed is 4.1 m/s, total energy is 0.33 m², and significant wave height is 2.3 m. The plots are the same scale as in Figure 2.

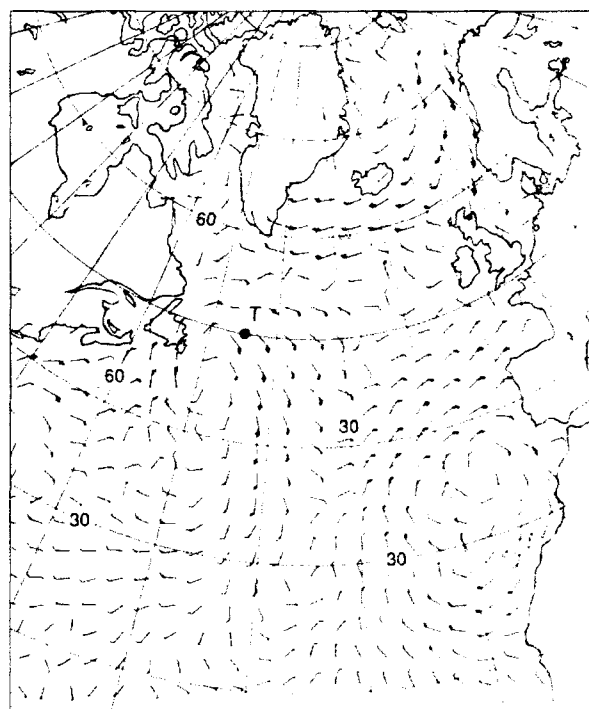


Figure 5. North Atlantic chart with UKMO global wnds at 0000 UT on 14 March. (Standard meteorological convention is used: each full barb is 10 kt, half barb is 5 kt.) The location of the *Tydeman* (T) is shown.

The Effect of a Zero Energy Start Field

By comparing the fourth and fifth hindcasts, it is possible to estimate the time needed for the UKMO wave model to overcome the effects of starting from a zero start field. Figure 6 shows that the wave heights from the two hindcasts converged with a difference of less than 0.1 m by 0900 UT on 12 March at CFAV *Quest*. From this time onward, the wave heights continued to differ but by no more than 0.1 m, except between 1200 and 1500 UT on 16 March, when the difference went up to 0.2 m. Thus the model took about 72 hours to warm up, and 0.1 m is the wave height difference expected between two hindcasts when only one of them starts with a nonzero energy start field. Such comparisons provide a useful yardstick by which to assess differences arising from other effects, for example, the distant swell effect discussed above.

Wave Heights

In this section, the integrated wave heights from the UKMO and the common LEWEX hindcasts are presented and compared with measured wave heights. No measurements were available until 13 March, at which time the models were warmed up. Many of the measurements were made at irregular time intervals not often coincident with the hourly model values, so no direct difference statistics were calculated. Time series of wave heights for the different hindcasts and the measured values are used to make the comparisons.

The Quest. Figure 7A shows how the wave heights from the UKMO hindcast compare with measured wave heights at the *Quest*. The model wave heights compare well with the available measured wave heights with errors of less than 1.0 m, except on 17 March, when the model substantially underestimates an observed peak. On the whole, the wave height estimates are lower than the measured values. One feature of the model wave height time series is a wave height of more than 6.0 m at 1800 UT on 13 March, but there are no measured values against which to verify this estimate. Also, on 18 March at about 0300 UT, the model shows a peak of just under 5.0 m, 0.5 m greater than the measured wave height.

Figure 7B shows the model wave heights from the common LEWEX hindcast compared with the measured wave heights. The model wave heights are not uniformly improved with the introduction of the common winds. The peak wave event on 13 March is reduced to 5.0 m, more than 1.0 m lower than for the UKMO hindcast. This reduction is caused by the common winds being weaker close to the ship position, although the UKMO wind speeds remain steady at about 17 m/s close to the ship. On 18 March, the LEWEX common winds around the *Quest* are again weaker than the UKMO winds, and so the wave height at the peak event is 1.0 m lower, 0.5 m less than the measured wave height. The peak occurs slightly earlier when the common winds are used.

From 1200 UT on 15 March to 1800 UT on 16 March, the wave heights are a better fit to those measured, and the drop in wave height on 17 March is not repeated. From 0000 UT on 18 March to 2100 UT on 19 March, however, the model wave heights, which were fairly ac-

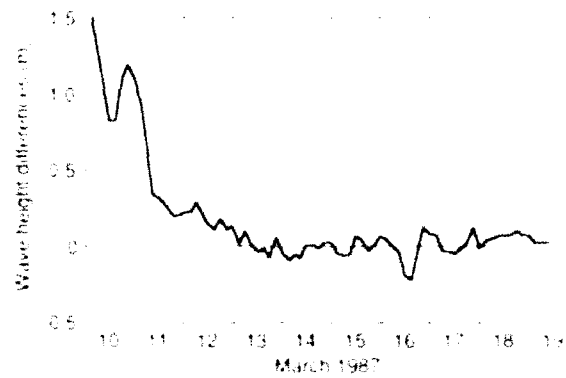


Figure 6. Differences between wave heights from the fourth and fifth hindcasts at CFAV *Quest*.

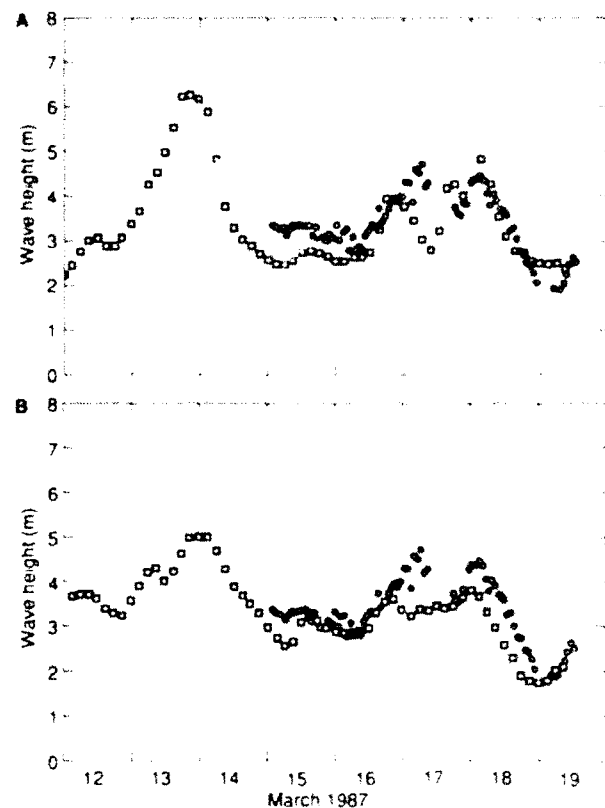


Figure 7. UKMO model wave heights and measurements from the Wavec buoy at the *Quest*. □ indicates model data; ○ indicates buoy data. **A** Based on the UKMO hindcast. **B** Based on the common LEWEX hindcast.

curate compared with the measured values in the UKMO hindcast, are underestimated by 0.5 m or more in the common hindcast.

The Tydeman. Figure 8A shows a time series of the wave heights from the UKMO hindcast that uses UKMO global winds and measured wave heights at the *Tyde-*
man. The UKMO model appears to underestimate wave heights by about 0.5 m for most of the period when measurements are available. The main exception to this is

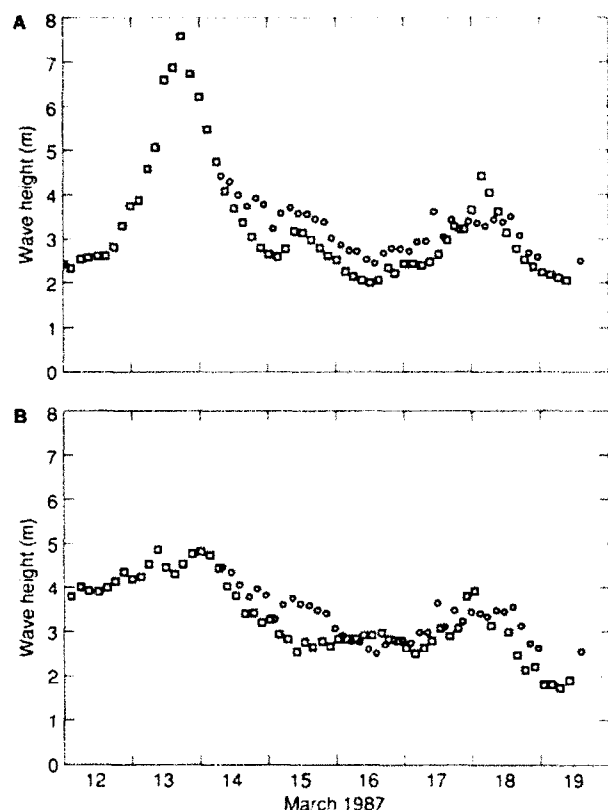


Figure 8. UKMO model wave heights and measurements from the Wavescan buoy at the *Tydemar*. \square indicates model data; \circ indicates buoy data. **A.** Based on the UKMO hindcast. **B** Based on the common LEWEX hindcast.

at 0300 UT on 18 March, when the UKMO wave height estimate is 1.0 m greater than the measured value. A wave height peak of more than 7.5 m appears at 1200 UT on 13 March, but cannot be substantiated.

Figure 8B shows the UKMO model wave heights from the control hindcast run. The introduction of the LEWEX winds has brought the model wave height estimates slightly closer to the measurements on some occasions, but gives a worse performance on others. At the peak wave height event on 18 March, the model peak occurs slightly earlier than in the UKMO hindcast and has dropped from 4.4 m to 3.8 m, due to the weaker common winds at this time. The measured wave height is even lower. At 1200 UT on 13 March, the common winds at and around the *Tydemar* are slightly weaker than the UKMO winds, and the model wave height is reduced by about 3.0 m. On 15 March, the UKMO evolution of a peak and subsequent decay matches the data better than does the evolution of wave heights in the common hindcast results.

COMPARISON WITH OTHER MODELS

The spectral estimates from the UKMO common hindcast have been compared with those from some of the other models. The agreement is good in most cases, with one or two exceptions. One example of an exception occurred on 13 March.

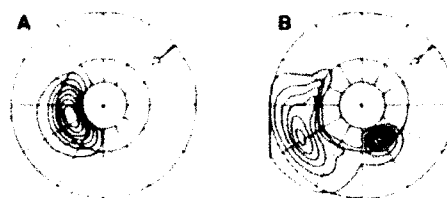


Figure 9. Two-dimensional spectra at 1200 UT on 13 March at the *Tydemar*. **A.** UKMO model using common winds. **B.** WAM model using common winds. The plots are the same scale as in Figure 2.

Figure 9A shows that at the *Tydemar* at 1200 UT on 13 March the UKMO wave model estimates a very well-developed northeasterly wind-sea component. Compared with results from other wave models, this component is more developed and centered at a lower frequency. For example, Figure 9B shows the WAM wave model results. (A logarithmic display showing the behavior of nine different models at this time is shown in Beal, this volume.) Furthermore, the northwesterly swell component seen in the WAM model spectrum does not appear in the UKMO spectrum, at least in this linear display of spectral energy density. This is not a result of individual normalizing of spectral plots. The swell component, seen in both model spectra at 1200 UT on 12 March, has been dissipated by the UKMO model by 1200 UT on 13 March but is still present at 0000 UT on 14 March in the WAM model. Unfortunately, no measurements are available at 1200 UT on 13 March, except those made by the aircraft synthetic aperture radar, which showed considerable variability (see Tilley, this volume).

The more fully developed wind-sea component in the UKMO model is probably a result of faster initial growth of a developing wind sea. This is a feature of the UKMO wave model, which has growth curves more like the World Meteorological Organization values,⁴ whereas the WAM model fits the Joint North Sea Wave Project growth curve for duration-limited growth.⁵ The UKMO model energy dissipation depends on properties of the wave spectrum, including the mean frequency. The wind-sea component in the UKMO spectrum is at a lower frequency than in the WAM spectrum, and so the UKMO model dissipates the northwesterly swell component more quickly.

SUMMARY AND CONCLUSIONS

The area covered by the coarse-mesh LEWEX grid has been shown to be enough, for the duration of the experiment, to encompass all significant swell properly. Although it was possible for long-fetch swell to reach the area of interest around the ships from across the Atlantic, the effects from storms outside the LEWEX grid area were not significant enough to invalidate the results by using the common winds.

The wave heights produced by the UKMO hindcast run with the UKMO global winds compare well with the measurements that are available for the period. Most of the differences can probably be explained by instrumental

spread in the measured wave heights or by errors in the UKMO wind fields.

Some differences exist between the spectra of the UKMO common hindcast and spectra from other model hindcasts that were run using common winds. Some are due to the model formulations and some to the ways in which the models were run (e.g., with initialized or noninitialized energy fields). It is not obvious which spectra are better estimates of the truth, even with measured spectra available, because differences between instruments are as great as differences between models.

As a result of running the extra three hindcasts, some interesting features of the UKMO wave model were discovered. First, when two different sets of boundary values are entered into two identical limited-area grids, as in the control and fourth hindcasts, the subsequent evolution of energy density at grid points is governed not only by the differences at the boundary but also by the computational processes of the model. Second, differences in the length of time used for the wave model

warm up can result in differences in wave height of 0.1 m in the final results. Both these effects are small when compared with the difference in wave height between the model¹ run using the UKMO winds and the run using the common LEWEX winds.

REFERENCES

- ¹Golding, B.W., "A Wave Prediction System for Real Time Sea State Forecasting," *Quart. J. R. Meteorol. Soc.* **109**, 393-416 (1983).
- ²Komen, G. J., Hasselmann, S., and Hasselmann, K., "On the Existence of a Fully Developed Wind Sea Spectrum," *J. Phys. Oceanogr.* **14**, 1271-1285 (1984).
- ³Ross, C. H., "The Operational Wave Models, Documentation Paper 5.1," Available from the Meteorological Office Library, London Road, Bracknell, Berkshire RG12 2SZ, England.
- ⁴World Meteorological Organization, "Guide to Wave Analysis and Forecasting," Chap. 3 in *WMO-No. 702*, Secretariat of the World Meteorological Organization, Geneva, Switzerland (1988).
- ⁵Hasselmann, K., Barnett, T. P., Bouws, E., Carlson, H., Cartwright, D. E., et al., "Measurements of Wind Wave Growth and Swell Decay During the Joint North Sea Wave Project (JONSWAP)," *Deut. Hydrogr. Z. Suppl.* **A**, 8 (1973).

RESULTS OBTAINED WITH THE WAVE MODEL VAG DURING LEWEX

The second-generation wave model VAG was used to run two hindcasts: one using the common winds from the Labrador Sea Extreme Waves Experiment and the other using 10-m analyzed winds from the European Centre for Medium-Range Weather Forecasts. The resulting significant wave heights are compared with buoy observations. From the decomposition of the evolution of the two-dimensional spectra into wave trains, the behavior of the model is analyzed and compared with the observations of the Wavescan buoy. The discrepancies between the two hindcasts are used to evaluate the impact of the wind errors.

INTRODUCTION

The Labrador Sea Extreme Waves Experiment (LEWEX), by the quantity and the quality of the measurements produced, provided an exceptional opportunity to test a new wave model such as VAG.¹ This second-generation model is now operational at the French Météorologie Nationale for the North Atlantic marine forecasts. For LEWEX, a higher than normal spectral resolution and a finer grid were used.

The VAG (from VAGUE, meaning wave in French) model was used to produce two hindcasts: one with LEWEX common winds and the other with 10-m analyzed winds extracted from the archives of the European Centre for Medium-Range Weather Forecasts (ECMWF). The significant wave heights from both hindcasts were then compared. This kind of comparison has been used for many years to evaluate the accuracy of wave models. Because significant wave heights can now be observed worldwide by satellite altimeters, the future use of this parameter in wave modeling greatly depends on the results of such comparisons. Such results also are essential to estimate the operational impact of more sophisticated sensors, such as spaceborne synthetic aperture radar. Based on comparisons with directional information collected during LEWEX, the potential of spaceborne altimeters is evaluated below.

The directional behavior of VAG also is analyzed, based on the decomposition of the evolving directional spectra into composite wave systems (see the article by Gerling elsewhere in this volume). The Gerling diagrams are further interpreted to summarize the particular results from VAG.

The VAG model is based on the energy balance equation for deep-water waves:

$$\delta E / \delta t + c_g \cdot E = S = S_{in} + S_{ds} + S_{nl}, \quad (1)$$

where $E(f, \theta, x, t)$, the directional spectrum, is a function of time (t), frequency (f), direction (θ), and position (x); c_g is the propagation velocity and, in deep wa-

ter, depends only on the frequency (f) of the wave ($c_g = g/2\pi f$, where g is the acceleration caused by gravity). The source term S takes into account the three main processes involved in the modification of the energy of the deep-water waves: the forcing wind fields, S_{in} , the dissipation due to wave breaking, S_{ds} , and the nonlinear interactions between components, S_{nl} . Following the SWAMP² terminology, a coupled discrete approach is used to solve Equation 1. For the LEWEX analysis, the spectral function E is made discrete as follows: the angular resolution is 20° ; 22 frequencies range from 0.04 to 0.3 Hz, with an increment $\delta f/f$ of 0.1; and the grid is polar stereographic with a 100-km mesh size at 60°N . A second-order Lax-Wendroff scheme, in a version modified by Gadd,³ is used for the advection, and an explicit first-order scheme is used for the integration of the source term. Following Miles' and Phillips' theories, linear and exponential growths are parameterized in the wind input term. The dissipation is parameterized by using the theoretical results of Hasselmann,⁴ as adapted by Golding.⁵

To match the operational constraints of a short running time, a method of second-generation modeling is adopted for the treatment of the nonlinear interactions. Once the growth and the dissipation are computed, the components of the spectrum, modified by the nonlinear energy transfers, are selected. The process employed is based mainly on experimental results^{6,7} and is expressly designed for the model to respond to rapidly changing wind fields. Nonlinear transfers are not computed directly but are the consequence of a modification of the shape of the spectrum resulting from these components. A Joint North Sea Wave Project (JONSWAP) spectrum is adjusted according to

$$E(f, \theta) = \alpha g^2 (2\pi)^{-4} f^{-5} \times \exp[-1.25(f/f_p)^{-4}] \gamma^{-1} G(\theta - \phi), \quad (2)$$

with

$$J = \exp[-(f - f_p)^2 / 2\sigma^2 f_p^2] \quad (3)$$

$G(\theta - \phi)$, the cosine-squared spreading function,

$$\begin{aligned} &= 2 \cos^2(\theta - \phi) / \pi \\ &\quad \text{for } -\pi/2 \leq \theta - \phi \leq \pi/2 \\ &= 0 \quad \text{otherwise.} \end{aligned} \quad (4)$$

The value of σ is set to 0.08, the mean value observed during JONSWAP; f_p and γ are derived from the value of the total energy of the selected components; and α is adjusted to keep this energy unchanged.

The VAG model was run with two separate wind fields. Both hindcasts used input winds referred to 10-m height. For the VAG-LEWEX hindcast, the 10-m wind fields were prepared by L. Zambresky at ECMWF from the 20-m wind fields produced by V. Cardone of Oceanweather using a 6% reduction in wind magnitude to account for the difference in levels, on a $1^\circ \times 1^\circ$ grid, every two hours. For the VAG-ECMWF hindcast, the 10-m analyzed wind fields were extracted from the archives of ECMWF on a $1^\circ \times 1^\circ$ grid every six hours.

COMPARISON OF THE MODELS

A detailed description of the LEWEX common winds is given by Cardone elsewhere in this volume, and a detailed comparison of the LEWEX and ECMWF wind fields is given by Zambresky elsewhere in this volume. Here, only some of the main features of the wind fields at the locations of the CFAV *Quest* and HNLMS *Tydemman* are discussed. At the *Tydemman* (Fig. 1), the directions of the ECMWF and LEWEX wind fields are comparable and are close to the observed value. The rapid variation on 16 March 1987 at 0300 UT is well reproduced, even if smoothed in amplitude. Some differences in wind speeds are appreciable: smaller-scale effects with rapid variations are smoothed, and the two models overestimate at the very beginning of the period. At the *Quest* (Fig. 2), the two models disagree, especially at the beginning of the period. Unfortunately, no reliable wind measurements from the *Quest* were available.

Significant Wave Heights

At the *Tydemman* (Fig. 3), the significant wave heights obtained with VAG-LEWEX and VAG-ECMWF are compared with the measurements of the Wavescan buoy (see the article by Krogstad elsewhere in this volume). At the *Quest* (Fig. 4), they are compared with the observations of the Wavec buoy (see the article by Keeley elsewhere in this volume). Both hindcasts show close agreement with the observations. The previously mentioned differences in the wind fields do not show up. Moreover, at the *Quest* location, where the winds most disagree, the significant wave heights are the closest.

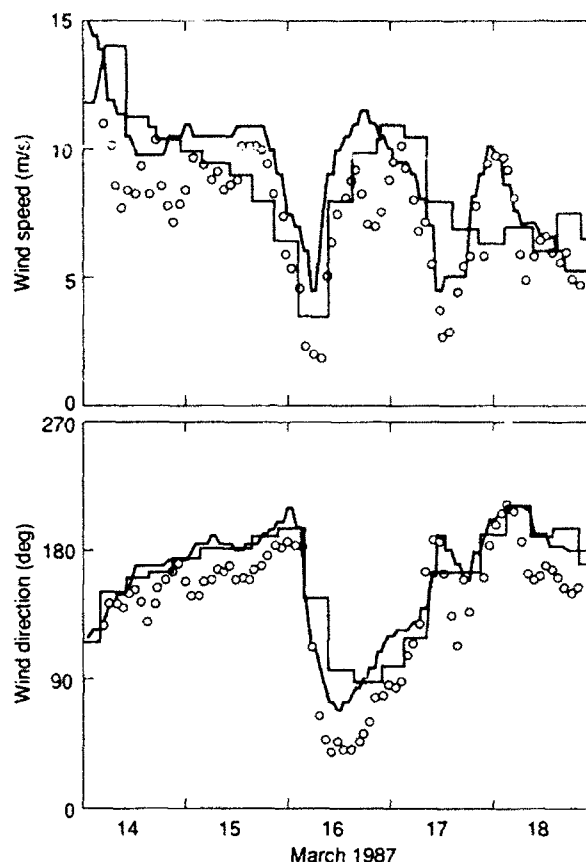


Figure 1. Wind speed and direction at the *Tydemman* location (50°N , 45°W). Buoy measurements (\circ), VAG-LEWEX (black), and VAG-ECMWF (red).

Directional Spectra

The analysis of the directional spectra presented in this section is based on the work of T. Gerling (elsewhere in this volume) but uses a decomposition of wave trains proposed by this author using the Gerling diagrams. The analysis focuses on the *Tydemman* location with particular emphasis on directional spectral estimates from the Wavescan buoy.

Wavescan Observations

From the data of the Wavescan buoy (Fig. 5), six major wave trains are apparent: (1) (blue) until 17 March at 0300 UT, a south-southeasterly wave train of wavelength ranging from 200 to 100 m; (2) (red) until 15 March at 0300 UT, a northeasterly wave train of 125-m wavelength; (3) (black) on 16 March at 0300 UT and 17 March at 0300 UT, an easterly short wind sea; (4) (green) from 16 March at 0300 UT until the end of the period, a northerly swell around 150-m wavelength; (5) (purple) on 17 March, a southerly wave train ranging from 100 to 150 m; and (6) (orange) on 18 March, a south-southwesterly swell around 200-m wavelength.

The VAG Model Results

With the VAG-LEWEX hindcast (Fig. 6), only the northeasterly wave train at the beginning (wave train 2) is not

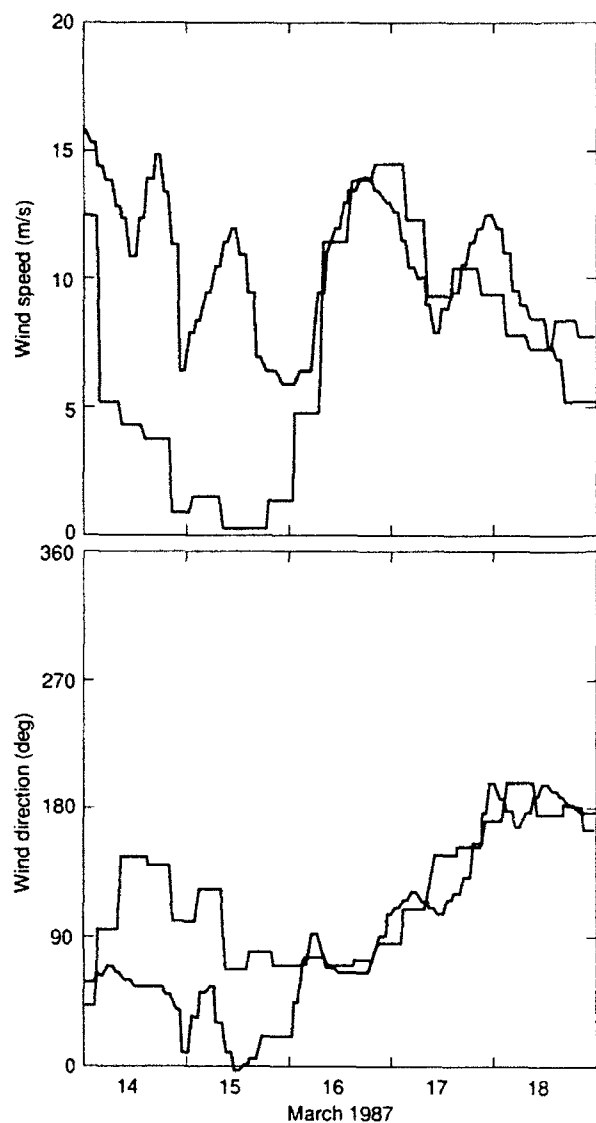


Figure 2. Wind speed and direction at the *Quest* location (50°N , 47.5°W). VAG-LEWEX (black), and VAG-ECMWF (red).

seen. However, other trains are apparent, consisting mainly of residual northwesterly waves at the beginning, and of southerly waves of various wavelengths and intensities until 17 March at 0300 UT. With VAG-ECMWF (Fig. 7), all the observed wave trains are produced, but additional ones are also seen including residual northwesterlies and southerlies, the latter at a lower intensity.

We now give a more precise description and analysis of the model results for each observed wave train, referring to the wave vector plots of Figures 5, 6, and 7.

(1) Wave train 1 (blue) finishes at the same time for both VAG-LEWEX and VAG-ECMWF but nine hours in advance of the buoy measurements. The wavelength and the wave direction evolutions are properly modeled by VAG-ECMWF: a SSE initial direction changing to the SE, with the wavelength increasing at the very beginning and decreasing afterwards. The evolution of VAG-LEWEX differs: the wave train seems to be split in two, both

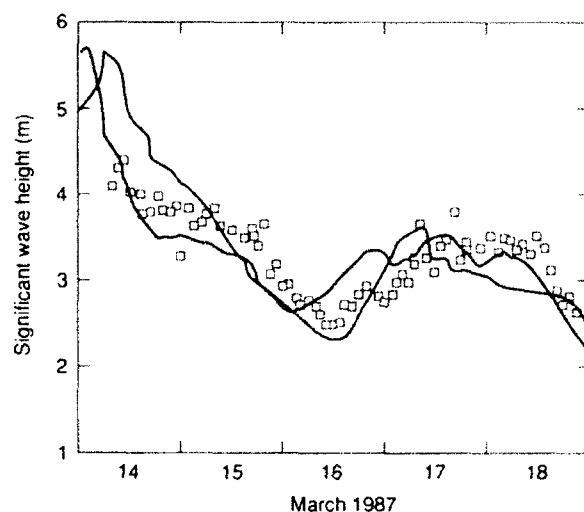


Figure 3. Significant wave heights at the *Tydemar* location (50°N , 45°W). Wavescan observations (\square), VAG-LEWEX (black), and VAG-ECMWF (red).

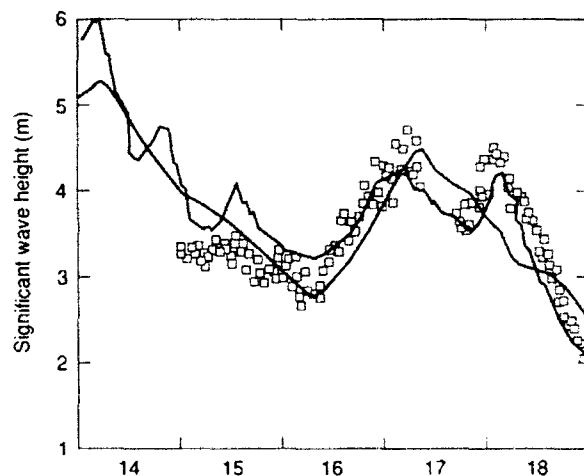


Figure 4. Significant wave heights at the *Quest* location (50°N , 47.5°W). Wavec observations (\square), VAG-LEWEX (black), and VAG-ECMWF (red).

south and southeast waves of various (and somewhat erratic) lengths are produced.

(2) Wave train 2 (red) is not produced by VAG-LEWEX. At the beginning, VAG-ECMWF agrees with the observations. Later on, short waves of low intensity persist.

(3) The short, mainly easterly, waves of wave train 3 (black) are emphasized in both hindcasts, but they are hardly observed by the Wavescan buoy.

(4) Wave train 4 (green) arrives at the same time for the two hindcasts but nine hours in advance of the buoy measurements, showing the same shift in time as for wave train 1. Both hindcasts give a direction and an evolution of direction in agreement with observations. Both show persisting short waves at the end, which are not observed. Otherwise, the wavelengths given by VAG-

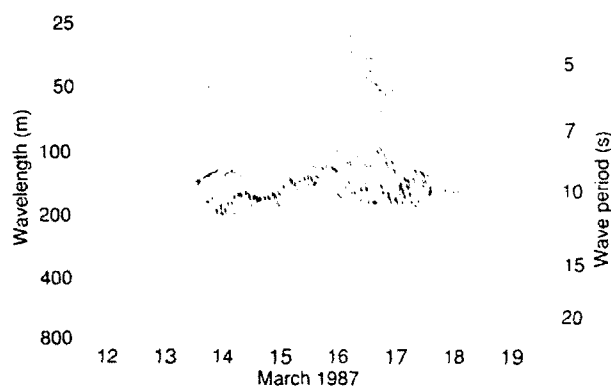


Figure 5. Wave vector evolution at the Tydeman location from the Wavescan observations. Six wave trains are identified and numbered as follows: 1 (blue), 2 (red), 3 (black), 4 (green), 5 (purple), and 6 (orange). Additional wave trains are shown in gray.

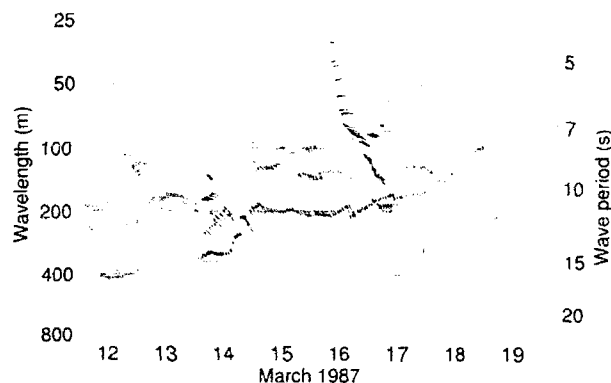


Figure 6. Wave vector evolution at the Tydeman location from the VAG hindcast with the LEWEX common winds. Five of the six observed wave trains (Fig. 5) are obtained: 1 (blue), 3 (black), 4 (green), 5 (purple), and 6 (orange). Additional wave trains are shown in gray.

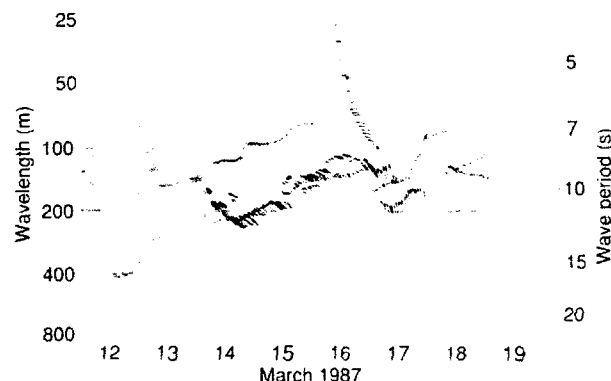


Figure 7. Wave vector evolution at the Tydeman location from the VAG hindcast with the ECMWF winds. All of the six observed wave trains (Fig. 5) are obtained: 1 (blue), 2 (red), 3 (black), 4 (green), 5 (purple), and 6 (orange). Additional wave trains are shown in gray.

ECMWF are close to the observations; for VAG-LEWEX, they are longer than the observation.

(5) Wave train 5 (purple) shows southerly waves superimposed on the existing northerly wave field (wave train 4). The arrival times are the same for the two hindcasts and agree with the observations. The measured duration, about 24 hours, agrees well with VAG-ECMWF but is longer than VAG-LEWEX. In both cases, the models tend to split the wave train into two separate wavelength regimes, in contrast to the Wavescan results.

(6) For wave train 6 (orange), the two VAG runs agree well with the buoy on both wave direction and the evolution of this direction, from SSW initially, then turning slightly to SW. However, each model suggests a completely different timing: VAG-LEWEX arrives first, 12 hours in advance, with the longest wavelengths; VAG-ECMWF arrives 6 hours later, with shorter waves, but still longer than those measured by the buoy.

DISCUSSION OF THE RESULTS

A number of possible explanations exist for the above discrepancies. Errors in wave modeling are usually attributable to errors in either the input winds or the wave model physics. It is not an easy task to decide between the two. Running the same model with the two different wind fields results in some valuable information. From the analysis of the differences between the two VAG hindcasts (which are entirely due to wind differences), it is possible to comprehend the nature of the wave discrepancies expected to be related to wind differences. In the current situation, they include differences concerning the wavelengths, as shown in wave train 4, or at the beginning of wave train 6; the wave train timing, as for example, the arrival time of wave train 6 or the duration of wave train 5; the wave intensity, as in wave trains 4 and 5 on 17 March at 0300 UT; the wave train structure, as in wave train 1; and even the wave train occurrence in the case of wave train 2, which is only obtained with VAG-ECMWF.

Most of the differences between the VAG hindcasts and the Wavescan measurements fall into one of these categories (there are even larger differences between the two hindcasts than between the VAG-ECMWF hindcast and the Wavescan observations). The only possible exception is the persistence of short waves at the end of most wave trains, suggesting too small a dissipation of these waves.

These many examples also emphasize the sensitivity of the directional spectrum obtained with the VAG model to the input wind field and to its spatial structure in regions far away from the buoy location.

With the ECMWF winds, detailed model results of the Wavescan observations are obtained with VAG: all the wave trains are modeled, even in the complex situation on 16 March at 0300 UT when the wind turns and swell is superimposed. These improved results suggest that most of the discrepancies obtained with the VAG-LEWEX winds are likely to be related to errors in the wind field.

Nearly equal model estimates of significant wave height can thus obscure significantly different model estimates of the directional spectra. For example, at 0300 UT on 16 March, both VAG hindcasts and the Wave-

scan buoy produce identical wave heights (Fig. 3), but the buoy gives SSE waves only (Fig. 5), whereas VAG-LEWEX shows SSE waves together with longer NW waves of comparable intensity (Fig. 6), and the VAG-ECMWF model yields waves in two different directions, but with similar wavelengths (Fig. 7).

CONCLUSIONS

Results of two hindcasts from the second-generation wave model VAG, using both the LEWEX common winds and the 10-m-height analyzed winds from ECMWF, have been presented. At both the *Quest* and the *Tydemar*, the two VAG hindcasts produce comparable significant wave heights, in agreement with the buoy observations.

However, an analysis of the evolution of the directional spectra, based on the decomposition of wave trains (see Gerling, this volume), demonstrates that comparable estimates of significant wave height disguise significantly different model estimates of the directional spectra.

By analyzing the differences between the two VAG hindcasts, we can better understand the nature of the wave discrepancies to be expected from wind errors. Such discrepancies include differences in the model estimates of the wavelengths, the wave intensity, and the timing and even the structure of a wave train. These various discrepancies indicate the high sensitivity of the VAG model to small changes in the input wind field.

Most of the discrepancies between the VAG model and the Wavescan buoy observations can thus be explained by wind field errors, except perhaps for the persistence of short waves at the end of most wave trains. The likely cause here is an improper dissipation of these waves, which should not have left their generation area. The discrepancies are most pronounced with the LEWEX winds. With the ECMWF winds, detailed agreement with the Wavescan observations is obtained: all the wave trains are modeled, even in the complex situation on 16 March at 0300 UT, when the wind turns and swell is superimposed.

REFERENCES

- ¹ Guillaume, A., "VAG-Model de Prevision de l'Etat de la Mer en Eau Profonde," Note de travail de l'Etablissement d'Etudes et Recherches Meteorologie, No. 178 (1987).
- ² SWAMP (Sea Wave Modelling Project) Group, "An Intercomparison of Wind Wave Prediction Models, Part 1: Principal Results and Conclusions," in *Ocean Wave Modelling*, Plenum Press, New York (1985).
- ³ Gadd, A. J., "A Numerical Advection Scheme with Small Phase Speed Error," *Q. J. R. Meteorol. Soc.* **104**, 569-592 (1978).
- ⁴ Hasselmann, K., "On the Spectral Dissipation of Ocean Waves due to White Capping," *Boundary Layer Met.* **6**, 107-127 (1974).
- ⁵ Golding, B., "A Wave Prediction System for Real Time Sea State Forecasting," *Q. J. R. Meteorol. Soc.* **109**, 393-416 (1983).
- ⁶ Pierson, W. J., and Moskowitz, L., "A Proposed Spectral Form for Fully Developed Wind Seas Based on the Similarity Theory of S. A. Kitaigorodskii," *J. Geophys. Res.* **69**, 5181-5190 (1964).
- ⁷ Hasselmann, K., Barnett, T. P., Bouws, E., Carlson, H., Cartwright, D. E., et al., "Measurements of Wind-Wave Growth and Swell Decay During the Joint North Sea Wave Project (JONSWAP)," *Disch. Hydrogr. Z., supp. A* **8**(12) (1973).

THE NOAA OCEAN WAVE MODEL HINDCAST FOR LEWEX

Directional wave spectra from the National Oceanic and Atmospheric Administration (NOAA) model hindcast during the Labrador Sea Extreme Waves Experiment are discussed in detail. The hindcast significant wave heights and spectra are found to be in reasonable agreement with the available estimates from two moored buoys. The NOAA spectra exhibit more energy at high frequencies than other models, possibly because of the lack of a proper dissipation term for whitecapping.

INTRODUCTION

The National Oceanic and Atmospheric Administration (NOAA) global ocean wave model has been operating at the National Meteorological Center since late 1985. It is a second-generation model with the source terms, directional relaxation, and propagation scheme of Cardone's SAIL II model.¹ A swell attenuation term similar to that in the Ocean Data Gathering Project (ODGP) model and the U.S. Navy Global Spectral Ocean Wave Model (GSOWM) was added in September 1988 because the operational forecasts produced by the original model showed that it was retaining an excessive amount of energy in the swell portion of the spectrum.

The NOAA model provides forecasts of the directional wave spectra up to 72 h in the future at 3-h intervals over a $2.5^\circ \times 2.5^\circ$ latitude/longitude grid. Directional spectra are computed in fifteen frequency bands of variable width, with the first band centered at 0.03889 Hz and the last at 0.30833 Hz, and twenty-four directional bands of equal width. Wave growth is limited by the Pierson-Moskowitz (PM) fully developed spectrum corresponding to the input wind speed with Mitsuyasu's directional spreading function.²

The operational NOAA model, with the swell attenuation term included and no changes in time step or grid resolution, was used for the Labrador Sea Extreme Waves Experiment (LEWEX) hindcasts. As described by Cardone elsewhere in this volume, LEWEX winds were generated using a subjective blend of all available ship and buoy reports. These winds were provided at 2-h intervals on a $2.5^\circ \times 2.5^\circ$ latitude/longitude grid over the region of interest. Hindcasts were done over this enclosed region with the winds interpolated to the model 3-h time steps.

The NOAA wave model started from a flat sea on 9 March 1987 at 1200 UT. Hindcasts starting 72 h later, from 12 March at 1200 UT, were compared with the available data from a Norwegian Wavescan buoy (see Krogstad, this volume) at the location of HNLMS *Tydeman* (50°N , 45°W), and a Canadian-deployed Wavec buoy (see Keeley, this volume) at the CFAV *Quest* lo-

cation (50°N , 47.5°W). Each ship was located at a NOAA model grid point.

SIGNIFICANT WAVE HEIGHT

Figures 1 and 2 give the time histories of analyzed wind speed and direction, and hindcast and observed significant wave height H_s at the *Tydeman* and *Quest*, respectively.

In general, the hindcast made at the *Tydeman* agrees better with the Wavescan buoy estimates than the one at the *Quest* agrees with the Wavec buoy. On 15 March, the wind speed at the *Quest* increased from approximately 2 m/s to about 10 m/s and then decreased rapidly, while the wind direction also changed rapidly. The buoy H_s decreased substantially during the second half of 15 March and into 16 March, while the model H_s decreased only during the first half of 15 March and then remained relatively constant. On 16 March, the wind speed at the *Quest* increased from about 4.5 m/s to more than 14 m/s while turning by almost 90° . Although the buoy H_s increased sharply during this time, the model H_s remained almost constant, suggesting a need for improving the directional relaxation mechanism in the model.

During 18 March, the measured wind direction was relatively constant toward the north, while the wind speed decreased. Meanwhile, the buoy H_s decreased more rapidly and to lower values than those of the model, suggesting an insufficient dissipation term in the model.

DIRECTIONAL SPECTRA AT THE TYDEMAN

Buoy data were not available at the *Tydeman* until 14 March at 0600 UT. Selected directional spectra from the model and the buoy are shown in Figure 3.

In Figure 3A, the sea toward the north in the model spectrum is still developing, with a peak period of 9.7 s, in fair agreement with the Wavescan buoy (Fig. 3B). The

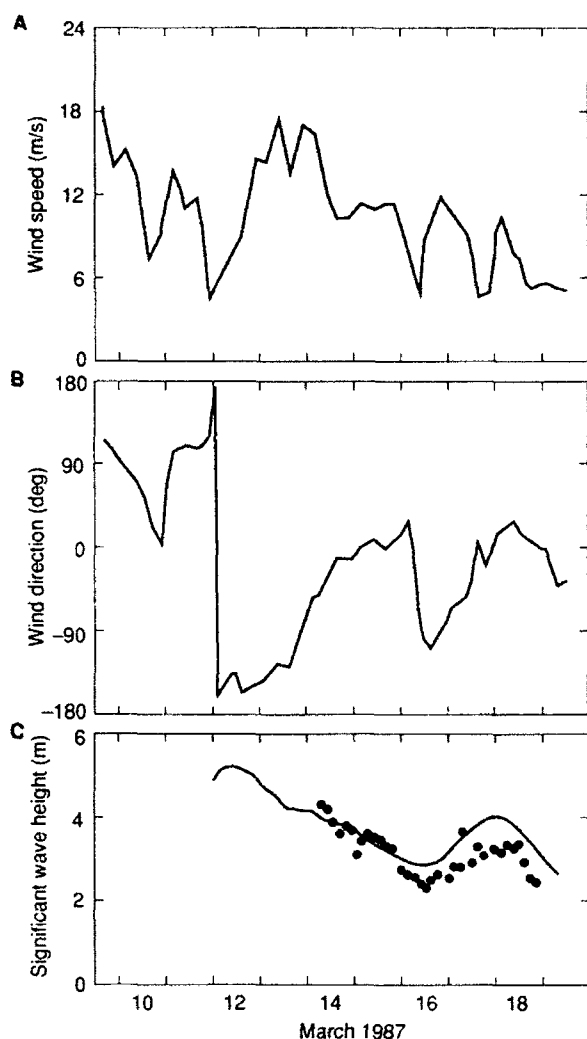


Figure 1. Time histories at the *Tydeman* from 9 March through 19 March. **A.** Wind speed. **B.** Wind direction. **C.** Significant wave height. **A** and **B** are LEWEX common winds; **C** is the NOAA model significant wave height hindcast (solid line) compared to Wave-scan buoy measurements (solid dots). Wind directions are positive clockwise from north.

buoy shows an energetic system traveling toward the west-southwest, but this system is absent in the model. In contrast, the model shows a wave system to the south-southeast. This wave system can be traced back to swell from the Labrador Sea and was present in the model spectra since 12 March at 1200 UT.

This south-southeast-traveling swell was generated by strong winds over the Labrador Sea. Although these winds had turned toward the east, a wind toward the south-southeast at the 55°N , 50°W grid point contributed to the swell at the *Tydeman*. The long swell was traveling faster than the wind, with no attenuation in the model until the waves were propagating more than 90° from the local wind direction.

The development of the sea toward the north in the model is consistent with the hindcast winds at the *Tydeman* producing a nearly fully developed PM spectrum. Figures 1A and 1B show that the wind speed at the *Tyde-*

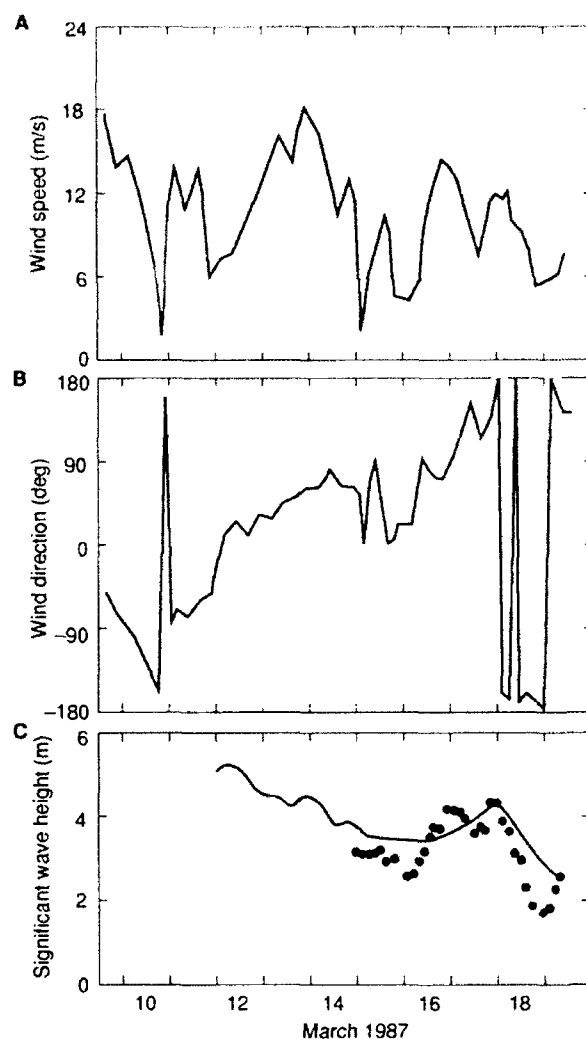


Figure 2. Same as Figure 1, but at the *Quest*. **C.** Solid dots indicate Wave-buoy measurements.

man during 12 March increased monotonically from less than 6 m/s to less than 14 m/s, with constant direction. On 13 March, the wind speed remained steady at about 15 m/s but began to turn clockwise. The peak period for a fully developed PM spectrum generated by a constant 15-m/s wind is 10.9 s, in fair agreement with the peak period of 9.7 s shown by the model at 0600 UT on 14 March, when the wind speed began to decrease. During 14 March, the local wind continued turning clockwise but decreased in speed to 10.5 m/s at 1200 UT and remained relatively constant through 15 March.

The winds in the Labrador Sea and Davis Strait ceased blowing toward the southeast at 1500 UT on 12 March, decreased, and became intermittent. From 1200 UT, however, weak winds toward the southeast existed in the northern Labrador Sea, and they increased in intensity and extent well into 15 March. On 15 March at 1200 UT, a new Labrador swell arrived at the *Tydeman* with a phase speed of 15.2 m/s, consistent with a travel distance of about 650 km in 24 h. Even 6 h later, however, when this new swell was well established in the model

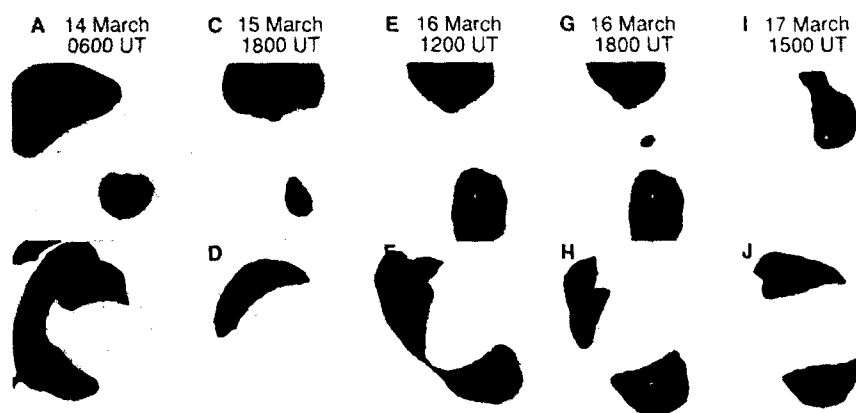


Figure 3. Normalized wave number spectral intercomparisons at the Tydeman. Top row: NOAA hindcast using LEWEX common winds. Bottom row: simultaneous estimates from Norwegian-deployed Wavescan buoy. Spectra are linear in wave number; outer circle is $2\pi/100$ rad/m. The arrows indicate wind direction and magnitude. All spectra are shown in the direction of propagation, with north toward the top.

(Fig. 3C), the buoy spectrum (Fig. 3D) showed no signs of it, although the buoy did show a system to the north-northwest with substantial angular spreading. It is not clear whether this discrepancy is from shortcomings in the model or in the LEWEX common wind field. It should be noted, however, that no measurements of surface winds were available in the Labrador Sea to guide the common wind estimates (see Cardone, this volume).

By 1200 UT on 16 March, the new swell to the south-southeast had become quite energetic in the model spectrum (Fig. 3E). The buoy spectrum (Fig. 3F), while not in good agreement, showed two strong systems. The new swell became the dominant peak in the model spectrum at 1800 UT on 16 March (Fig. 3G), with a wavelength at the peak of approximately 148 m, in good agreement with the swell toward the southeast in the buoy spectrum (Fig. 3H).

The 1800 UT model spectrum on 16 March also shows the arrival at the Tydeman of a very long (500-m wavelength) swell toward the northeast, generated by a strong wind system well to the south-southwest. The Wavescan buoy spectrum does not show this swell until 1800 UT on 17 March, fully 24 h later than the model. As Cardone (this volume) and Gerling (this volume) discuss, this timing problem may be caused at least in part by errors in the LEWEX common winds.

With the local wind decreasing and turning from nearly west toward the northeast, the swell to the northeast becomes sea, and by 1500 UT on 17 March (Fig. 3I), it is the only wave system shown in the model. The buoy (Fig. 3J) continues to show a southerly propagating system.

DIRECTIONAL SPECTRA AT THE QUEST

Wave buoy spectra were available at the Quest starting at 0000 UT on 15 March. Selected NOAA model and buoy spectra are shown in Figure 4. At 0000 UT the model (Fig. 4A) shows a sea to the southwest and a swell to the northwest. The buoy spectrum (Fig. 4B) shows swell only to the north. During the latter part of 15 March, the NOAA model turned the wind sea (wind-driven sea) counterclockwise following the wind, and the wind sea coalesced with the existing swell toward the south. Both model and buoy retained the swell to the

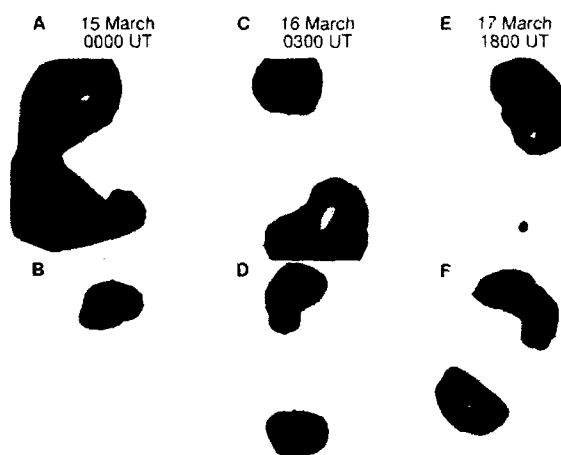


Figure 4. Normalized wave number spectral intercomparisons at the Quest. Top row: NOAA hindcast using LEWEX common winds. Bottom row: Canadian-deployed Wavec buoy. See Figure 3 caption for more details.

north during 15 March and most of 16 March. Early on 16 March, the buoy began to show a young sea toward the south. By 0300 UT, the model (Fig. 4C) and buoy (Fig. 4D) spectra showed a dominant wind sea toward the south.

By 1800 UT on 16 March, the model showed a swell to the northeast arriving at both the Quest and the Tydeman. Buoy spectra were not collected at the Quest between 0300 and 1200 UT on 17 March, but by 1800 UT the buoy (Fig. 4F) shows this swell to the northeast as a strong system. The model (Fig. 4E) has attenuated the system to the south almost completely, and the buoy, while still retaining it, shows it traveling more toward the southwest.

SUMMARY AND CONCLUSIONS

Except for 16 March and early 17 March, the model H_1 and buoy H_1 are in good agreement. Apparently the model does not respond well to rapidly turning winds increasing in speed. This problem might be attributable to inadequate directional relaxation. Further testing is needed.

In general, the NOAA spectra agree reasonably well with those estimated from the buoys and are consistent with the hindcast wind patterns. Discrepancies between the model and the buoys, as described above, may be caused by errors in the hindcast winds, by the buoy reflecting other processes such as swells propagating from outside the considered region, or by interactions with the Gulf Stream not accounted for in the model.

The NOAA model appears at times to inadequately account for dissipation of wave energy from whitecapping

and opposing winds. Improvement in these areas is being considered.

REFERENCES

- ¹ Greenwood, J. A., Cardone, V. J., and Lawson, L. M., "Intercomparison Test Version of the SAIL Wave Model," in *Ocean Wave Modeling*, Plenum, New York, pp. 221-233, The SWAMP Group (1985).
- ² Mitsuyasu, H., Tasai, F., Suhara, T., Mizuno, S., Ohkusu, M., et al., "Observations of the Directional Spectrum of Ocean Waves Using a Cloverleaf Buoy," *J. Phys. Oceanogr.* **5**, 750-760 (1975).

AN EVALUATION OF TWO WAM HINDCASTS FOR LEWEX

Two wave hindcasts were made by the WAM model during the Labrador Sea Extreme Waves Experiment (LEWEX). One used surface wind fields from the European Centre for Medium-Range Weather Forecasts, while the other used the common wind fields provided as part of LEWEX. Both sets of wind fields were evaluated against available ship observations, and the two wave hindcasts were evaluated with *in situ* wave observations. Although each set of wind fields was of reasonable operational quality, the resulting wave hindcasts were markedly different.

INTRODUCTION

Two separate wave spectra hindcasts produced by the third-generation ocean wave model WAM were executed as part of the Labrador Sea Extreme Waves Experiment (LEWEX). The first hindcast used operational-quality surface wind fields from the European Centre for Medium-Range Weather Forecasts (ECMWF); the second used specially prepared common (LEWEX) winds (see Cardone, this volume). The common winds were provided to all wave models participating in LEWEX to separate model performance differences from model input differences. The evaluation of wave hindcasts was *incomplete* without also having some knowledge of the accuracy of the wind fields; an analysis of both sets of wind fields was made with available ship observations of surface winds. A correspondence was found between features of the wind fields and components of modeled wave spectra.

THE WAM MODEL

At ECMWF, WAM is executed four times daily and computes two-dimensional ocean wave spectra, $E(f, \theta; x, t)$, over the entire globe, where f and θ are the frequency and direction of the waves at position x and time t . The foundations of this model were established at the Max-Planck-Institut für Meteorologie in Hamburg.^{1,2} At ECMWF, work has been carried out largely by an international group of wave researchers representing institutes from 10 countries.

The WAM model implicitly integrates a basic transport equation that describes the evolution of the two-dimensional wave spectrum:

$$\frac{\partial E}{\partial t} + \nabla \cdot (C_g E) = S_{in} + S_{nl} + S_{ds} \quad (1)$$

The left-hand side of the equation describes the wave energy E propagating at the group velocity C_g . The physical processes affecting the wave state are modeled by the three source terms on the right-hand side: S_{in} represents the source function describing the transfer of

energy from wind to waves, S_{nl} represents the nonlinear transfer due to resonant four-wave interactions, and S_{ds} is the dissipation resulting from whitecapping and turbulence.

For the LEWEX hindcasts, the WAM model was implemented on a $1^\circ \times 1^\circ$ spherical grid. The wave spectrum $E(f, \theta)$ (at a given position x and time t) is divided into 26 frequency bins; the center frequencies range from 0.04 to 0.42 Hz on a logarithmic scale with a relative frequency resolution of $\Delta f/f = 0.1$, and 12 directions yield 30° angular resolution. Beyond the high-frequency cutoff, an empirical parameterization is used. Wave propagation is computed by a first-order, upwind, finite-difference scheme.

The performance of the WAM model has already been evaluated through the hindcasts of six extratropical storms on the northwest European shelf,³ three hurricanes in the Gulf of Mexico,¹ several storms in the Mediterranean,⁴ and, most recently, daily verification at ECMWF of the global version in near real time using buoys of the National Oceanic and Atmospheric Administration.⁵

WIND FIELDS

Although both Oceanweather, Inc., and ECMWF wind fields are of high operational quality, the wave fields produced by the two hindcasts differed significantly. Figures 1A and 1B compare portions of the wave height fields on 16 March 1987 at 1200 UT. The LEWEX hindcast was more energetic, having a maximum significant wave height of 11 m for the large storm system to the southwest of the LEWEX area, whereas the highest waves in the ECMWF hindcast were only 7 m. The differences between the two hindcasts made at the locations of the research vessels CFAV *Quest* (50.0°N , 47.5°W) and HNLMS *Tydeman* (50.0°N , 45.0°W) were only minor, however.

Since the WAM model was unchanged for the two hindcasts, the differences between them arose from differences in the forcing wind fields. The correspond-

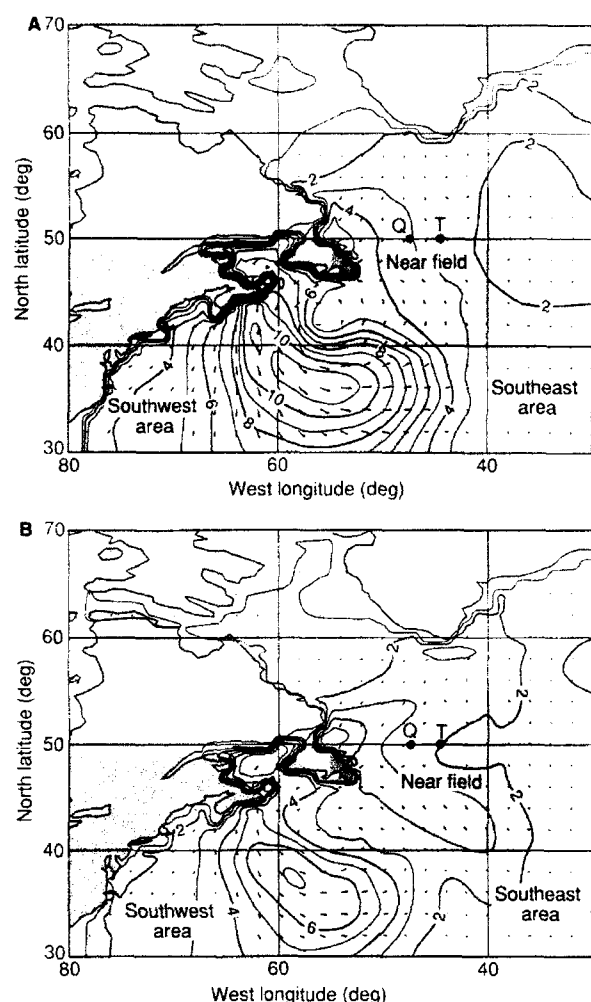


Figure 1. Wave height for 16 March at 1200 UT. The wave-height contours are in meters, and the arrows point in the mean wave direction. **A.** LEWEX waves. **B.** ECMWF waves. Q and T designate the *Quest* and *Tydeman* positions, respectively.

ing LEWEX and ECMWF wind fields for 16 March at 1200 UT may be seen in Figures 2A and 2B. Available ship observations of winds are superimposed on the wind fields as wind barbs in knots. The LEWEX winds resulted in a more highly developed storm system, with a large area of northwesterly to westerly 20-m/s winds; the ECMWF winds were lower, on the average, at 16 m/s. Just to the southwest of the *Quest* and the *Tydeman*, however, the ECMWF wind field contained higher southeasterlies (16 m/s) than did the LEWEX wind field (12 m/s).

The differences in the wind field structure directly affected the components of the modeled wave spectra in the LEWEX observing area. Since a wave model cannot be evaluated properly without considering its input wind fields, both sets of wind fields were verified by using available ship wind observations.

Because ship wind observations themselves contain significant error, their usefulness is sometimes questioned. At ECMWF, the root-mean-square (rms) ship observation

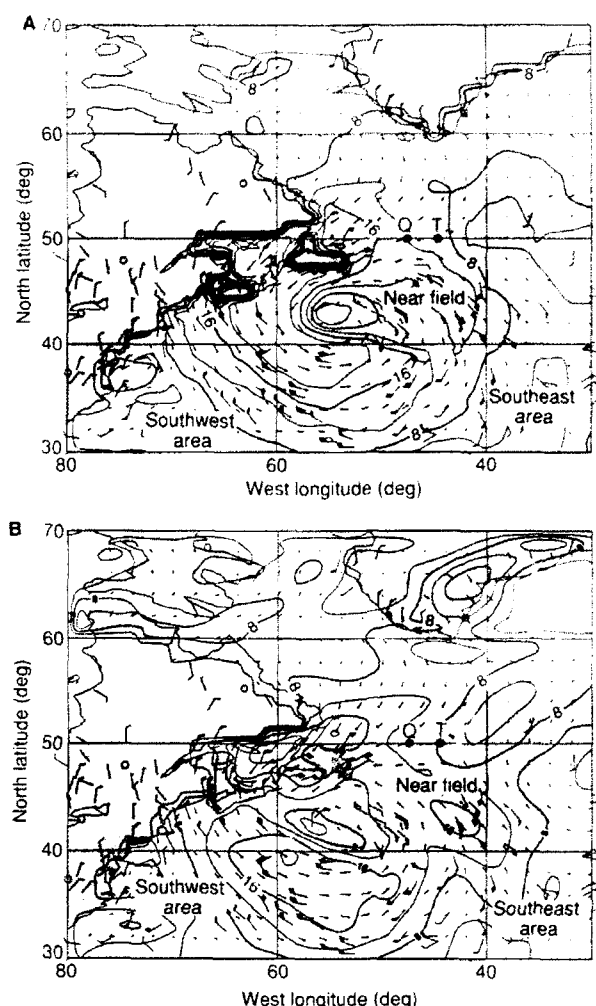


Figure 2. Wind fields for 16 March at 1200 UT. The wind-speed contours are in meters per second, and the arrows point in the wind direction. The ship observations are plotted as wind barbs in knots. **A.** LEWEX winds. **B.** ECMWF winds.

error (including instrument error, human error, and ship motion) is estimated at 3.6 m/s per component in the North Atlantic, giving a vector rms wind error of about 5 m/s. The vector rms error of the ECMWF wind fields for the LEWEX period was close to 5 m/s, so it can hardly be improved.

Using the hindsight gained by the wave hindcasts, the wind fields were compared to ship observations by dividing the LEWEX geographical grid into three regions. At the *Quest* and the *Tydeman*, the wave spectra contained components generally from the northwest, the southwest, and the southeast, as well as a component of locally generated wind sea. Unfortunately, no ship observations were made in the Labrador Basin (50°–60°W and 50°–60°N), so no analysis was possible there. Therefore, the three areas chosen were the following, defined by the lower left-hand and upper right-hand corners of each region: the southwest (30°N, 80°W and 48°N, 48°W); the southeast (35°N, 48°W and 55°N, 30°W); and for locally generated wind sea, the near field (40°N, 55°W

and 55°N, 35°W). In the southwest area, the average number of observations available during a six-hour interval was 60, but in both the southeast and the near field, the average was only 25.

Southwest Area

The genesis, growth, and decay of a moderately large storm system occurred in the southwest area. The storm system influenced wave spectra observations at the *Quest* and the *Tydemar* in the form of long-period southwesterly swell that arrived during the latter part of LEWEX. This storm was a major factor in all model hindcasts and was handled in a substantially different fashion by each of the two sets of wind fields.

The wind bias statistics for the southwest area are presented in Figures 3A and 3B. The vector rms biases for ECMWF versus ships were substantially lower than they were for the LEWEX common winds versus ships. The mean bias showed the LEWEX common winds to be higher than those of the ships, especially on 15 March, whereas the ECMWF winds were slightly lower. The scatter index (time series not presented), defined as the vector rms divided by the mean wind speed, was on the average about 75% for the common winds, whereas for ECMWF, it was about 50%. Thus, we may conclude that for the common LEWEX wind field hindcast, estimates of wave spectra at the *Quest* and *Tydemar* by an unbiased wave model should show an early and overdeveloped arrival of southwesterly swell during the latter part of LEWEX. Conversely, for the ECMWF hindcast, the arrival of southwesterly swell should be slightly underestimated.

Southeast Area

The wind bias statistics for the southeast area are presented in Figures 4A and 4B. Differences between the two wind fields were not as great as in the southwest, but the common winds generally had the higher biases, as can be seen particularly in the mean bias. On 12 and 13 March, the LEWEX common winds were biased unusually high, but on 15 March, the southeasterly flow was underpredicted. Curiously, this underprediction happened at the same time as the overprediction in the southwest. The mean bias for the ECMWF winds hovered consistently around zero. This analysis indicates that between 14 and 17 March, the southeasterly swell generated by an unbiased wave model driven by the LEWEX common winds would be too weak, whereas for the ECMWF hindcast, it should be reasonably well estimated.

Near-Field Area

Figures 5A and 5B present the wind bias statistics for the area in the immediate vicinity of the ships. This area is the source of locally generated wind sea and is referred to as the near field. The vector rms differences were only slightly higher for the common winds. The mean bias for both wind fields was close to zero, so no significant difference existed between the ship winds and those of either wind field. Between 14 March and 16 March, however, the LEWEX common winds were biased high in the southwest and low in the southeast, as shown in Figures 3B and 4B. These opposite biases tended to cancel one another in the overall bias of the near field. The large

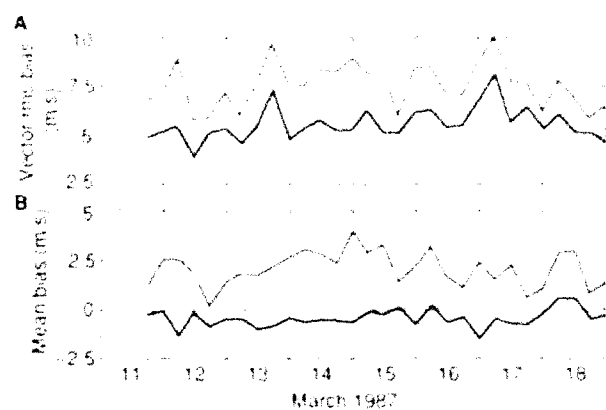


Figure 3. Wind bias statistics for the southwest area. **A** Root-mean-square bias in the wind vector. **B** Mean bias in the wind speed. The black curves represent ECMWF winds minus ship winds, and the red curves represent LEWEX common winds minus ship winds.

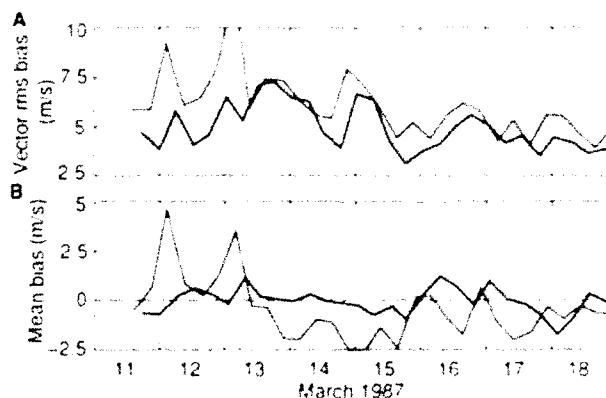


Figure 4. Wind bias statistics for the southeast area. **A** Root-mean-square bias in the wind vector. **B** Mean bias in the wind speed. The black curves represent ECMWF winds minus ship winds, and the red curves represent LEWEX common winds minus ship winds.

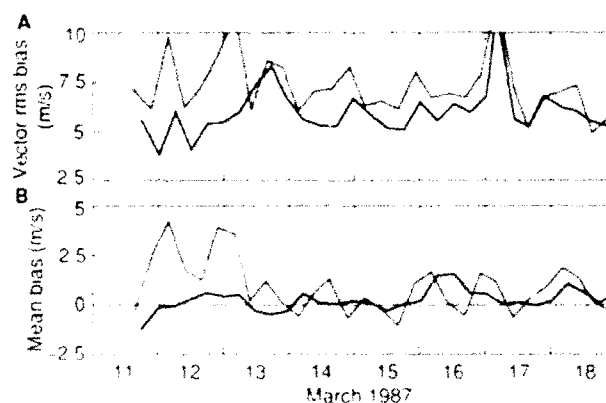


Figure 5. Wind bias statistics for the near-field area surrounding the *Quest* and the *Tydemar*. **A** Root-mean-square bias in the wind vector. **B** Mean bias in the wind speed. The black curves represent ECMWF winds minus ship winds, and the red curves represent LEWEX common winds minus ship winds.

jumps in the vector rms biases in both wind fields on 17 March were caused by outlying observations near shore and were of no consequence.

WAVE-HEIGHT FIELDS AND SPECTRA

With a better understanding of the wind fields and their effect on individual components of wave spectra, some of the features of the two WAM hindcasts can be interpreted more easily. Wave-height time series, both modeled and observed, are shown in Figure 6A at the *Tydemar* and in Figure 6B at the *Quest*. A summary of wave height bias statistics, averaged over the entire interval for which buoy observations were available, is presented in Table 1. In Figure 6, the Norwegian Wavescan buoy observations are from Krogstad,⁶ the Dutch Wavec observations are from Datawell bv,⁷ the Dutch Delft observations are from Ooms,⁸ and the Canadian Endeco observations are from a report of the David W. Taylor Naval Ship Research and Development Center.⁹

At the beginning of the experiment on 13 March, the significant wave height from the common LEWEX wind field hindcast was substantially higher than that from the ECMWF hindcast. Unfortunately, no wave height observations were made, so we do not know which hindcast is more correct. During that early period, however, the LEWEX common wind field biases were large and positive nearly everywhere (Figs. 3–5), so the wave heights from those winds were probably too high. Between 14 March and 16 March, the wave heights from the ECMWF hindcast were in better agreement with the observations, probably because the southeasterly flow was better estimated. For the remainder of the experiment, the wave heights from the common LEWEX wind hindcast were in remarkable agreement with observations.

Interesting differences between the two WAM spectral hindcasts occurred between 16 March at 0000 UT and 17 March at 1200 UT. Four sets of spectra from the two WAM model hindcasts are shown in Figure 7, along with the associated Wavescan buoy spectra. In general, the WAM model spectra were broader than those from the Wavescan buoy, reflecting the coarse 30° angular resolution of the model.

On 16 March at 0000 UT (Fig. 7A), the Wavescan spectrum showed a unimodal southeasterly component (from the southeast, toward the northwest). The ECMWF spectrum was bimodal, with a dominant southerly component in rough agreement with the Wavescan and a weak northwesterly component not observed by the Wavescan. The LEWEX spectrum was bimodal, with a weak southerly component and a dominant northwesterly component in complete disagreement with the Wavescan. For a period of 12 hours from 15 March at 2100 UT until 16 March at 0900 UT, the LEWEX hindcast spectra were nearly unimodal with northwesterly swell. During the same period, the Wavescan spectra were also nearly unimodal, but with a southeasterly component, so the LEWEX hindcast spectra differed from the observed spectra by nearly 180°. The ECMWF hindcast during this same period had a dominant southeasterly component, although a weaker level of northwesterly swell

Table 1. WAM hindcast statistics from Wavescan buoy estimates of wave height at the *Tydemar*, 14 March at 0600 UT to 19 March at 1200 UT.

Hindcast statistic	WAM hindcast with ECMWF winds	WAM hindcast with LEWEX winds
Average bias (m)	0.51	-0.18
Root-mean-square bias (m)	0.66	0.37
Scatter index	0.20	0.11
Correlation coefficient	0.87	0.75

Note: Results are given as hindcast estimates minus buoy estimates.

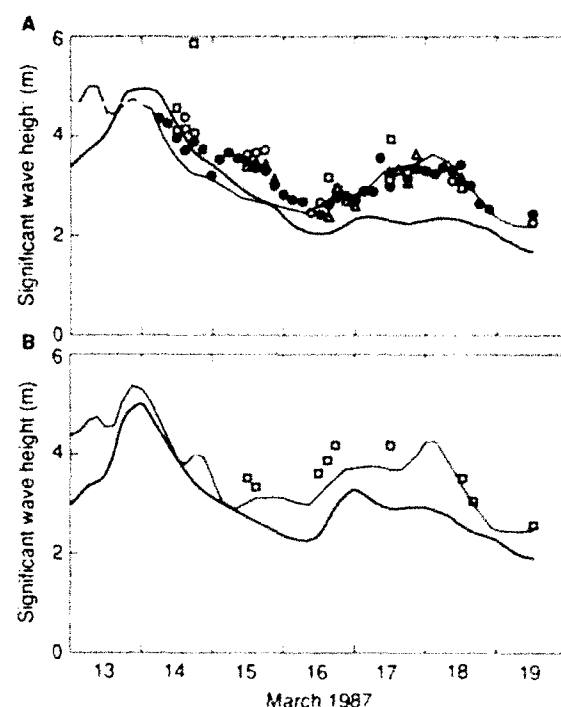


Figure 6. Modeled and observed significant wave heights **A.** *Tydemar*. **B.** *Quest*. The black curves represent the ECMWF hindcast, and the red curves represent the LEWEX hindcast. The symbols designate the following buoy observations: ●, Wavescan; △, Wavec; ○, Delft; □, Endeco.

was also present. The differences between hindcasts during this time support the earlier conclusion regarding biases in the southeasterly winds; that is, the LEWEX southeasterlies were underestimated, and the ECMWF southeasterlies were reasonably correct.

On 16 March at 1200 UT (Fig. 7B), both the Wavescan and the ECMWF spectra present opposing wave systems. The northwesterly components were in good agreement in peak wave number and direction, but the southeasterly component of the ECMWF spectrum lacked the double peaked structure evident in the Wavescan

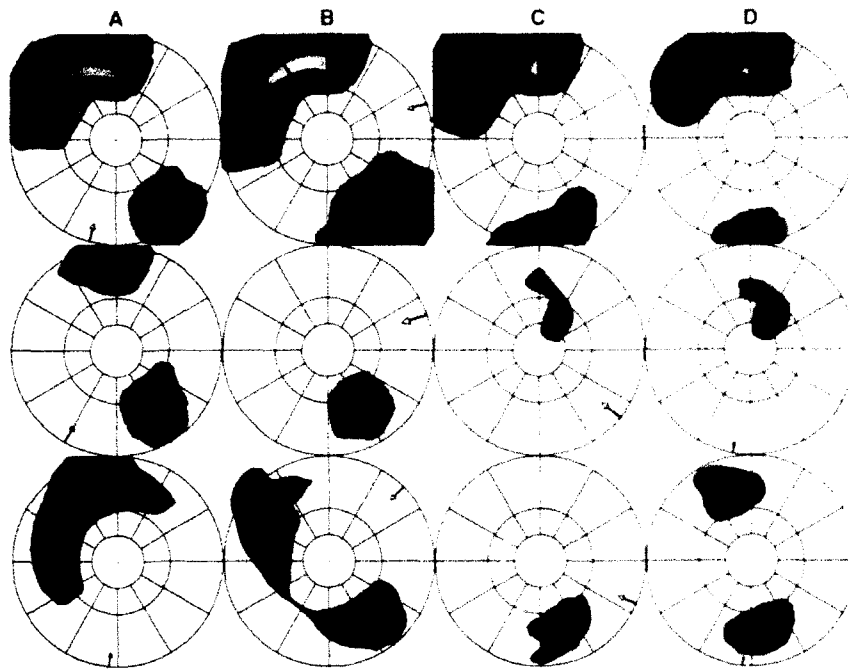


Figure 7. Comparison of normalized WAM spectra for ECMWF (top) and LEWEX (middle) wind fields with observed Wavescan buoy spectra (bottom) at the Tydemar. **A** 16 March at 0000 UT. **B** 16 March at 1200 UT. **C** 17 March at 0600 UT. **D** 17 March at 1200 UT. The spectra are shown in a linear wave number format, with calibration circles at $2\pi/400$ m, $2\pi/200$ m, and $2\pi/100$ m. Wave energy is shown in the direction of propagation.

spectrum and was more northerly by about 45° . The LEWEX spectrum was unimodal, having only the northwesterly component. The peak wave direction was in good agreement with the Wavescan, but the peak wavelength was too long.

On 17 March at 0600 UT (Fig. 7C), the ECMWF hindcast had a strong southerly wind sea and a weak northerly component, whereas the LEWEX hindcast was dominated entirely by long-period southwesterly swell, and the Wavescan had only northwesterly swell. Thus, although the wave-height estimate from the LEWEX hindcast was in remarkable agreement with observations made on 17 March at 0600 UT (see Fig. 6A), the modeled wave direction differed from the Wavescan by 135° . At the Tydemar, the LEWEX hindcast first showed the arrival of long-period southwesterly wave energy on 16 March at 2100 UT, a full 24 hours ahead of the arrival observed by the Wavescan. The ECMWF hindcast had this southwesterly energy arriving only three hours early, which was half the six-hour time step of the ECMWF winds. The hindcast spectra thus reflected the previously identified biases in the development of the storm to the southwest by each of the two wind fields.

On 17 March at 1200 UT, the Wavescan observed a bimodal spectrum with the two components nearly 180° apart, with the northerly component dominant. The ECMWF hindcast came closer to reproducing this situation, as it also showed a bimodal spectrum, but with only a weak northerly component. The LEWEX spectrum was unimodal, with all the energy in long-period southwesterly swell, completely unobserved by the Wavescan. Both model hindcasts, then, had insufficient energy coming from the north. Although the estimate of wave height for the LEWEX hindcast was excellent (Fig. 6A), the wave energy came entirely from the wrong generating area.

SUMMARY AND CONCLUSIONS

Two hindcasts were made by the WAM model in support of LEWEX, one using wind fields from ECMWF and the other using LEWEX common wind fields. The modeled wave heights and spectra were compared with *in situ* buoy observations, and the modeled wind fields were compared with ship wind observations.

Although the spectra for the LEWEX hindcast at times differed significantly from those of the Wavescan, the wave height estimates were clearly more accurate than those from the ECMWF hindcast. Significant wave height, however, does not necessarily provide a reliable measure of skill for a wave model, because it is an integrated (total energy) parameter. Different components of the wave spectrum may be simultaneously under- and overpredicted in a fashion that only coincidentally leads to the correct total wave energy. In summary, the ECMWF hindcast was more successful than the LEWEX hindcast in reproducing individual components of the observed wave spectra, even though it performed less well in estimating total significant wave height.

A clear correlation existed between biases in the wind fields estimated from ship observations and the under- and overprediction of wave components by the two hindcasts. The wind-wave model system must be considered as a whole because the wave model is highly sensitive to the wind fields driving it. The difficulty of specifying wind fields correctly for operational wave forecasting is again revealed by LEWEX.

Identifying specific problems in WAM model physics is difficult in an area of such complex geography and meteorology. One observation can be made, however, that WAM spectra were often broader in frequency and direction than Wavescan spectra.

REFERENCES

- ¹WAMDIG (Wave Model Development and Implementation Group), "The WAM Model—A Third-Generation Ocean Wave Prediction Model," *J. Phys. Oceanogr.* **18**, 1775-1810 (1988).
- ²Komen, G. J., and Zambresky, L., "A Third-Generation Ocean Wave Model," in *Proc. International Workshop on Wave Hindcasting and Forecasting*, Halifax, Nova Scotia, 23-26 Sep 1986, Environmental Studies Revolving Funds, Report Series No. 065, pp. 233-242 (1987).
- ³Bertotti, L., Guillaume, A., and Janssen, P. A. E. M., "The WAMS Project: First Test of a Shallow Water Third Generation Model Against Data," KNMI, P.O. Box 201, 3730 AE De Bilt, The Netherlands (1986).
- ⁴Cavaleri, L., Bertotti, L., and Lionello, P., "Shallow Water Application of the Third-Generation WAM Wave Model," *J. Geophys. Res.* **94**, 8111-8124 (1989).
- ⁵Zambresky, L. F., "A Verification Study of the Global WAM Model, December 1987–November 1988," ECMWF Technical Report No. 63, European Centre for Medium-Range Weather Forecasts, Shinfield Park, Reading, Berkshire RG2 9AX, England (1989).
- ⁶Krogstad, H. E., "Wave Data Collected by Wavescan During the Labrador Sea Extreme Waves Experiment (LEWEX)," Oceanographic Center, Sintel Group, N-7034 Trondheim, NTH, Norway (1987).
- ⁷Datawell bv, "LEWEX WAVEC (Hr. Ms. *Tydeman*)," Datawell bv, Laboratorium voor Instrumentatie, Haarlem, The Netherlands (1987).
- ⁸Ooms, J., "Wave Measurements with the Delft Wave Buoy Aboard HNLMS *Tydeman* During LEWEX, March 1987," Report No. 760, Delft University of Technology, Ship Hydromechanics Laboratory, Mekelweg 2, 2628 CD Delft, The Netherlands (1987).
- ⁹David W. Taylor Naval Ship Research and Development Center, "Preliminary ENDECO Directional Analysis, LEWEX—March 1987, *Quest* and *Tydeman* Deployments," David W. Taylor Naval Ship Research and Development Center, Bethesda, Md., 20084 (1987).

DIRECTIONAL SPECTRA FROM THE BIO HINDCAST DURING LEWEX: THE WAVE-ICE INTERACTION

During the Labrador Sea Extreme Waves Experiment, a careful accounting of the ice edge was made, a hindcast was done in four overlapping runs between 9 and 19 March 1987, and the ice edge was updated at the beginning of each run. When the ice edge is included in the hindcast, the wave heights and the directions of the spectral peak may differ appreciably from those in the ice-free situation.

INTRODUCTION

Activities on the Grand Banks and off the coast of Labrador during the winter and spring months are significantly constrained by the presence of ice. The distribution and ice extent can be highly variable from year to year and even from day to day. At its extreme, the ice edge covers regions north of the Labrador Sea and the entire Grand Banks, and extends as far south as the Nova Scotian coast. The median extent to which the ice reaches is 48°N. On the northern side of the Grand Banks, ice comes to within 40 km of Hibernia about every other year. In addition to interannual variability, short-term and local changes caused by winds and currents can move the ice edge as much as 100 km in a single day. Ice behavior on these short time scales is not clearly understood. The ice varies up to about 1 m in thickness, and is a mosaic of complexity in composition.

On a time scale of days, the ice edge and the ice distribution within the marginal ice zone change in response to wave, current, and wind forces. In comparison with the ice-free situation, the nonlinear transfer of energy from wave-wave interactions among surface gravity waves is altered by the presence of a distribution of ice floes and the associated scattering of waves by ice. Wind input into the energy spectrum of the waves, the planetary boundary layer,¹ and wind stress, as well as dissipative mechanisms such as wave breaking, are also altered.

A multiyear study (the Labrador Ice Margin Experiment²) of the Labrador/Grand Banks ice margin dynamics began in 1987. In its first phase, the study coincided with the Labrador Sea Extreme Waves Experiment (LEWEX), resulting in a basic data set that included ocean currents, ice velocity, aerial photographs, wave-induced motion, ice-surface properties, and synthetic aperture radar imagery for estimating the energy and momentum coupling between waves and ice in the marginal ice zone.

Present wave models are limited by how well they represent the dominating physical processes: the input of energy caused by wind forcing, the nonlinear transfer between spectral components as a result of wave-wave interactions, the dissipation of energy in wave breaking and whitecap formation, and the propagation of energy at the wave group velocity. The manner in which these processes

balance and combine with one another is discussed by Kitaigorodskii,³ Komen et al.,⁴ Phillips,⁵ and others. An exact computation of the complete Boltzmann integral for the nonlinear transfer, as derived by Hasselmann,⁶ is not possible for any but the simplest two-dimensional wave situations. Second-generation models express the effects of nonlinear transfer on the evolution of the spectrum in terms of a small number of degrees of freedom. The models depend on the spectral growth with fetch as inferred in the Joint North Sea Wave Project study of Hasselmann et al.,⁷ Donelan et al.,⁸ Dobson et al.,⁹ and others. For the simple wave fields for which they are calibrated, these models generally perform well, but they do not have enough degrees of freedom to accurately describe complicated wind situations, as considered in the Sea Wave Modeling Project (SWAMP) study.¹⁰

The complete set of interaction configurations, allowed to nonlinearly transfer, is replaced by a small subset of these interaction configurations in the third-generation WAM wave models.¹¹⁻¹³ The subset is assumed to be independent of the spectral energy functional form and constitutes the discrete interaction approximation. It is also assumed to be a basis set, representative of nonlinear transfers involving other parts of the interaction configuration space.

Later we will describe the procedures for preparing both the wind field and the ice state during LEWEX. The forcing winds are those constructed for the North Atlantic by Cardone (this volume). Ice information is from the Canadian Atmospheric Environmental Service Ice Forecasting Centre. We computed the resultant wave field as height contours over the hindcast area and as two-dimensional wave spectra at the CFAV *Quest* and HNLMS *Tydemar*.

WIND FIELDS AND THE ICE EDGE

The wind fields use a fine-mesh grid from 38.75°N to 52.5°N and from 42.5°W to 75.0°W, with increments of 0.625° in latitude and 1.25° in longitude, embedded within a coarse-mesh grid extending from 25°N to 67.5°N and from 20°W to the coast of North America (80°W). Rather than nest grids in the WAM model, we

performed the hindcast on the fine-mesh grid for the entire area extending from 25°N to 67.5°N and from 20°W to the coast of North America. The wind field for this area was created by taking the fine-mesh Cardone winds over the fine-mesh grid. Coarse-mesh winds were interpolated linearly to give a fine-mesh wind field for the complete area extending from 25°N to 67.5°N and from 20°W to the coast of North America. Thus, we hindcasted the entire area using these fine-mesh winds.

Using the WAM model, we first did the hindcast from 9 March at 1200 UT to 19 March at 1200 UT, with no consideration for the ice edge, to give a baseline for comparison with ice-edge effects. Observations of $\geq 10\%$ ice cover are shown in Figure 1. A second hindcast was done in four overlapping runs, each beginning and ending at 1200 UT: 9 to 13 March, 12 to 16 March, 15 to 18 March, and 17 to 19 March. The first 24-hour interval of each run was regarded as model warm-up time and discarded. At the beginning of each run, the ice edge was updated and treated the same as the land boundary.

MODEL RESULTS

Time series of significant wave height (H_s) and mean frequency (\bar{f}) at the *Quest* and the *Tydean* are presented in Figure 2. Figure 3 shows significant wave heights in each frequency bin at the *Tydean* for each of the LEWEX wave systems. From the point of view of wave-ice modeling, LEWEX consists of three phases.

During the first days of the experiment until about 13 March, the winds are northwesterly from the Davis Strait and are associated with the formation of the ice tongue stretching to the southeast from Newfoundland. Ice in the Davis Strait shortens the effective fetch across the Labrador Sea, resulting in a reduced H_s and increased \bar{f} relative to when the ice is ignored. On 12–13 March, the reduction in H_s is about 25% and concerns locally generated 200- to 400-m waves, as shown in Figure 3.

From 13 March until about 16 March, the intermediate phase, the dominating winds vary from northeasterlies to easterlies to southerlies, and are toward the ice

as seen from the *Quest* and *Tydean*. The ice has no effect on the hindcast wave height.

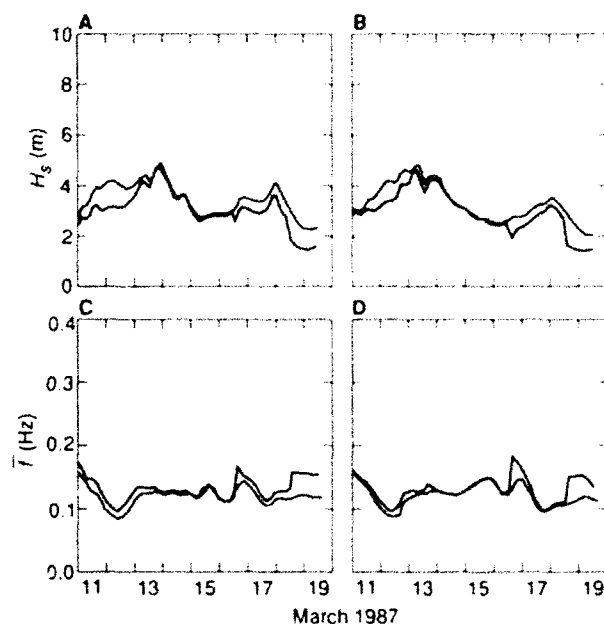


Figure 2. Time series at the *Quest* and the *Tydean*. **A** Significant wave height (H_s) at the *Quest*. **B** Significant wave height at the *Tydean*. **C** Mean frequency (\bar{f}) at the *Quest*. **D** Mean frequency at the *Tydean*. A black curve means the ice edge is modeled, a colored curve means it is not.

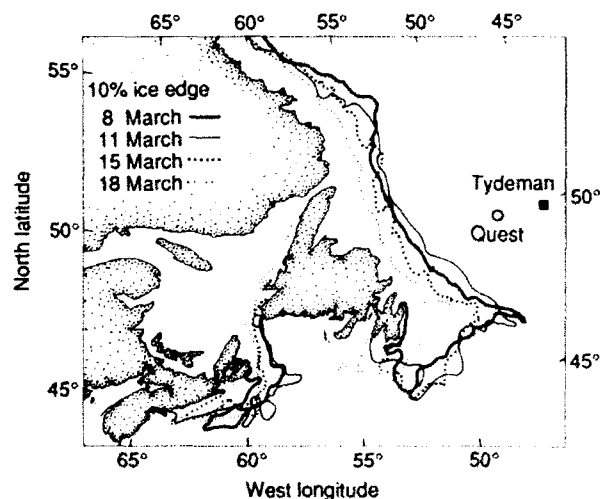


Figure 1. Time evolution of the ice edge bounding $\geq 10\%$ ice cover in the vicinity of LEWEX, between 8 and 18 March 1987.

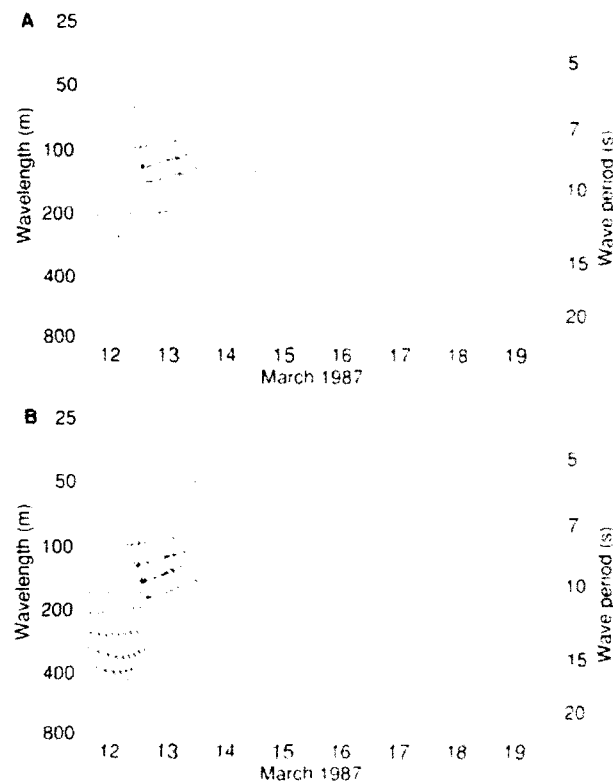


Figure 3. Time series at the *Tydean* for significant wave height H_s and the mean direction in each frequency bin. **A** The ice edge is modeled. **B** The ice edge is not modeled.

During the final phase of LEWEX from 16 March onward, the dominating winds are from the southwest, over the ice tongue stretching southeast from Newfoundland and now receding toward the Gulf of St. Lawrence. An intense cyclone is centered at about 40°N and 55°W (cf., Gerling, Fig. 7, this volume), with swell and winds propagating through and over the ice tongue, particularly on 17 March. Thereafter, the winds and seas subside. Locally generated waves have reduced energy for 150- to 300-m waves from the southwest on 17-18 March owing to reduced fetch, as shown in Figure 3A, compared with the ice-free situation in Figure 3B.

The moored Wavescan buoy is described by Krogstad (this volume). During the third phase of the experiment, from about 1200 UT on 16 March and later, the buoy tends to favor results obtained ignoring the ice edge rather than those obtained when a careful accounting is made of the ice distribution. This is perhaps accidental, because during the second phase, when the ice has little influence on model estimations, the buoy is not consistently close to the models. Alternatively, modeling of the ice edge at 20% coverage rather than 10%, as we have done, may improve the comparison of buoy to model.

Updating the ice edge on 12, 15, and 17 March at 1200 UT gives discontinuities in the time series on 13, 16, and 18 March at 1200 UT because of the sudden change in model prediction. This is evident in the plots of H_s and \bar{f} in Figures 2A and B. The discontinuity at 1200 UT on 16 March occurs because the 24-hour warm-up period is not long enough for the spectra to blend in with the previous overlapping run. Thus, as shown in Figures 3A and B, the mean waves travel in the same direction but are shifted to higher frequencies. This discontinuity is inevitable with the short overlapping runs of the study. Had the ice edge been continuously modeled, the problem would have been avoided. Similar discontinuities occurred on 13 and 18 March at 1200 UT.

The effect of the ice is felt in frequencies corresponding to locally generated waves. Figures 4A and B compare the two-dimensional spectral estimates at the *Tyde-man* on 13 March during a three-hour interval when the ice edge is modeled and when it is ignored. The spectral peak is at 150°E (from degrees true) in either situation. In the latter, swell from the previous wind direction is enhanced owing to an overestimated fetch. Therefore, although both peaks are at 120°W and northeasterly winds dominate by 0600 UT, the spectral peak first makes the transition from 150°E to 120°W when the ice edge is modeled. For a short period, the difference in direction of the spectral peak is 90°.

Computed H_s contours for the entire hindcast region in Figures 5A and B give information for regions other than the positions occupied by the *Quest* and *Tyde-man*. Ice reduces the effective fetch for northwesterlies relative to the situation when ice is ignored, as in Figures 2A and B.

CONCLUSION

Except for positions close to the ice distribution, duration-limited surface gravity waves have been shown

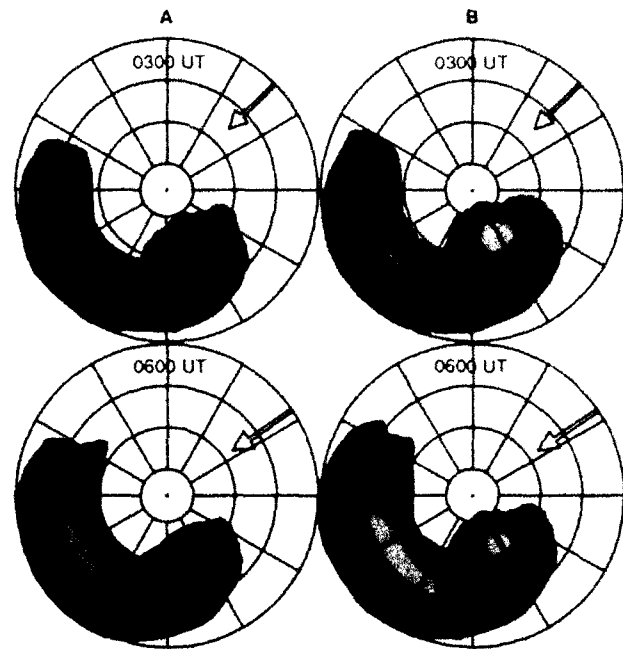


Figure 4. Comparisons of two-dimensional spectra at the *Tyde-man* on 13 March. **A.** The ice edge is modeled. **B.** The ice edge is not modeled. The yellow color indicates high spectral energy density.

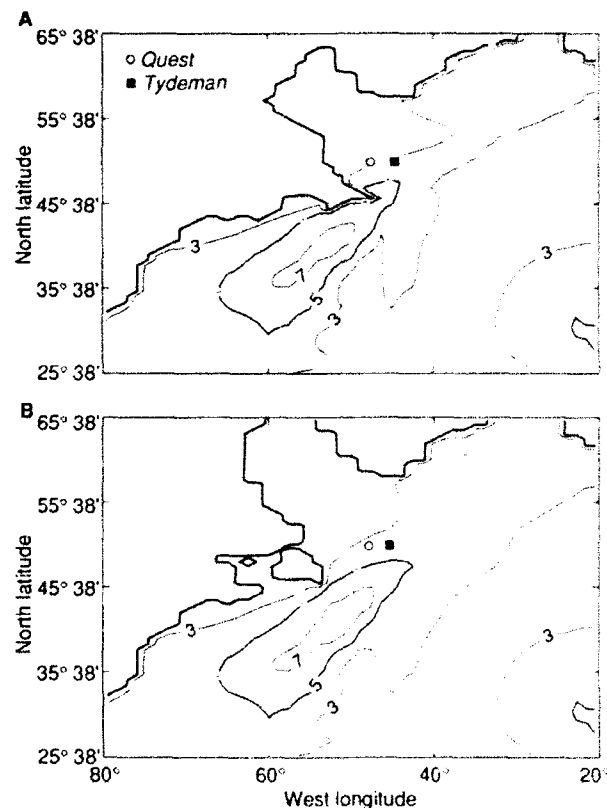


Figure 5. Contours of H_s (in meters) on 13 March at 0000 UT. **A.** The ice edge is modeled. **B.** The ice edge is not modeled. The ice in **A** and the land boundary in **B** are indicated by the heavy line.

to have essentially the same growth as in ice-free waters.^{14,15} Possibly our most restrictive assumptions are that (1) no accounting is made of low-frequency spectral energy that could be transmitted through bands of ice, such as the ice tongue stretching to the southeast from Newfoundland; (2) the ice floes can scatter wave energy but cannot drift; and (3) whereas the ice distribution is a mosaic of complexity, we modeled it simply as a solid boundary.

At the *Quest* and *Tydean*, the ice (1) reduced the effective fetch in the early days of LEWEX, (2) provided sheltering later in the experiment, and (3) was felt in frequencies corresponding to locally generated waves.

This work could be extended to an analysis of Geosat altimeter data to compare its H_s contours with those computed here. The data set for LEWEX remains significant for the investigation of data assimilation and model physics.

REFERENCES

- ¹ Overland, J., Reynolds, R. M., and Pease, C. H., "A Model of the Atmospheric Boundary Layer Over the Marginal Ice Zone," *J. Geophys. Res.* **88**, 2836-2840 (1983).
- ² McNutt, L., Argus, S., Carsey, F., Holt, B., Crawford, J., et al., "LIMEX '87: The Labrador Ice Margin Experiment, March 1987—A Pilot Experiment in Anticipation of RADARSAT and ERS-1 Data," *Eos Trans. Am. Geophys. Union* **69**, 634-635, 643 (1988).
- ³ Kitaigorodskii, S. A., "On the Theory of the Equilibrium Range in the Spectrum of Wind-Generated Gravity Waves," *J. Phys. Oceanogr.* **13**, 816-827 (1983).
- ⁴ Komen, G. J., Hasselmann, S., and Hasselmann, K., "On the Existence of a Fully Developed Wind-Sea Spectrum," *J. Phys. Oceanogr.* **14**, 1271-1285 (1984).
- ⁵ Phillips, O. M., "Spectral and Statistical Properties of the Equilibrium Range in Wind-Generated Gravity Waves," *J. Fluid Mech.* **156**, 505-531 (1985).
- ⁶ Hasselmann, K., "On the Nonlinear Energy Transfer in a Gravity Wave Spectrum. Part I: General Theory," *J. Fluid Mech.* **12**, 481-500 (1961).
- ⁷ Hasselmann, K., Barnett, T. P., Bouws, E., Carlson, H., Cartwright, D. E., et al., "Measurements of Wind-Wave Growth and Swell Decay during the Joint North Sea Wave Project (JONSWAP)," *Deutscher Hydrogr. Z.* **12** (1973).
- ⁸ Donelan, M. A., Hamilton, J., and Huai, W. H., "Directional Spectra of Wind-Generated Waves," *Philos. Trans. R. Soc. London A* **315**, 509-562 (1985).
- ⁹ Dobson, J., Perrie, W., and Toulany, B., "On the Deep-Water Fetch Laws for Wind-Generated Surface Gravity Waves," *Atmos. Ocean* **27**, 210-236 (1989).
- ¹⁰ Allender, J. H., Barnett, T. P., Bertotti, L., Brunsona, J., Cardone, V. J., et al., "Sea Wave Modelling Project (SWAMP): An Intercomparison Study of Wind-Wave Prediction Models, Part I: Principle Results and Conclusions," *Proc. IUCRM Symp. on Wave Dynamics and Radio Profiling of the Ocean Surface*, Plenum Press, Miami (1985).
- ¹¹ Hasselmann, S., and Hasselmann, K., "Computation and Parameterizations of the Nonlinear Transfer in a Gravity Wave Spectrum. Part I: A New Method for Efficient Computations of the Exact Nonlinear Transfer Integral," *J. Phys. Oceanogr.* **15**, 1369-1377 (1985).
- ¹² Hasselmann, S., Hasselmann, K., Allender, J. H., and Barnett, T. P., "Computation and Parameterizations of the Nonlinear Transfer in a Gravity Wave Spectrum. Part II: Parameterizations of the Nonlinear Energy Transfer for Application in Wave Models," *J. Phys. Oceanogr.* **15**, 1378-1391 (1985).
- ¹³ Hasselmann, S., Hasselmann, K., Komen, G. J., Janssen, P., Ewing, J. A., et al., "The WAM Model, a Third Generation Ocean Wave Prediction Model," *J. Phys. Oceanogr.* **18**, 1775-1810 (1988).
- ¹⁴ Masson, D., "Spectral Evolution of Wind Generated Surface Gravity Waves in a Dispersed Ice Field," *J. Fluid Mech.* **202**, 43-81 (1989).
- ¹⁵ Masson, D., and Perrie, W., "Introduction of an Ice Factor in a Third Generation Wave Model," in *Proc. 22nd Annual Congress of the Canadian Meteorological and Oceanographic Society*, p. 57 (1988).

ACKNOWLEDGMENT: We gratefully acknowledge helpful comments from the LEWEX collaborators in the analysis of the data. The format for Figure 3 was suggested by Klaus Hasselmann and provided by Thomas Gerling. The wave modeling program at the Bedford Institute of Oceanography is funded by the Federal (Canada) Panel on Energy Research and Development.

THE APPLICATION OF NASA'S THIRD-GENERATION WAVE MODEL TO LEWEX

The NASA version of the third-generation wave model contains modifications affecting both the horizontal advection scheme and the dissipation term. Results are presented both for idealized fetch-limited wave growth and for the more realistic conditions of the Labrador Sea Extreme Waves Experiment. The NASA model contains stronger dissipation at higher frequencies and weaker dissipation at lower frequencies, thereby inhibiting wave growth from direct wind input while allowing strong growth of spectral peaks from nonlinear wave-wave interactions.

INTRODUCTION

During the past several years, remarkable progress has been made in numerical wave modeling through the development of the so-called "third-generation" wave model (WAM).¹ The centerpiece of this model is the explicit calculation of the nonlinear wave-wave interactions by a discrete parameterization of the exact integral. Consequently, the nonlinear calculations are based on the model's actual spectra rather than on the idealized spectra (e.g., the Joint North Sea Wave Project), as is done in second-generation models.

One flaw in the WAM model lies in its dissipation function that parameterizes wave breaking. Numerical coefficients in WAM were chosen so that an equilibrium exists among growth, decay, and nonlinear wave-wave interactions for a particular spectrum. It is desirable to move away from this empirical approach to one based on a concrete physical model that may be modified as our understanding of wave physics grows.

At the NASA/Goddard Space Flight Center, we developed a wave model that parameterizes wave dissipation as two distinct processes. Wave breaking is given by a joint probability function and induces turbulence within the ocean that leads to further dissipation via eddy viscosity.

Any change to the current WAM model is meaningless unless it produces realistic results. Thus, after describing our changes to the WAM model, we apply it to the data set for the Labrador Sea Extreme Waves Experiment (LEWEX). The experiment was useful because it provided us with real oceanic wave heights and spectra and with the ability to compare models with one another.

THE MODEL

Our model is an extension of the WAM model. Except for the details given in this section, we adopted the WAM representation for wave growth, nonlinear wave-wave interactions, and the implicit numerical scheme for integrating the physics. Two changes were incorporated: a higher-order advection scheme and an entirely new dissipation function.

Presently, the WAM model employs a first-order advection scheme that is very dissipative but has the advantage of never producing negative wave energy. Because we felt that this scheme was too crude, we adopted a different scheme that minimizes dissipation and phase errors.² In our scheme, four grid points, instead of the usual three in second-order differencing, are used, as well as a local parameter that minimizes the error. Simple tests of this advection scheme show that it is superior to the first-order scheme in minimizing phase errors and amplitude dissipation. If negative wave energy is generated, these values are set to zero. Although a scheme that always produces positive energy and that minimizes phase and dissipative errors is desirable, the errors introduced by reducing the negative energy to zero are minor. Sample experiments showed that about 0.03% of advection calculations resulted in a negative energy of $-0.1 \text{ m}^2/\text{s}$ or less. All the negative quantities were on the order of $0.1 \text{ m}^2/\text{s}$.

Our model's dissipation parameterization consists of two parts. First, we envision the wave actually breaking, which induces turbulence within the ocean. The turbulence can then scatter waves (via current-wave interactions), which leads to further dissipation.³ We parameterize the phenomena later through the use of eddy viscosity.

Our dissipation source function for wave breaking has its origin in the modeling of joint probability density functions for wave amplitude and frequency. We begin our derivation by adopting a nondimensional density function for a finite bandwidth, as developed by Yuan.⁴ The density function can be written as

$$P(H, \Sigma) = \frac{8H^2\Sigma^3}{\pi (\theta^2 - 1) (1 + \theta)} \times \exp \left\{ -H^2 \left[1 + \frac{(\Sigma^2 - 1)^2}{\theta^2 - 1} \right] \right\}, \quad (1)$$

where

$$H = \frac{h}{(2m_0)^{1/2}},$$

$$\Sigma = \frac{\omega}{\alpha^{-1}\omega_0},$$

$$\theta = \left(\frac{m_0 m_4}{m_2^2} \right)^{1/2},$$

$$\omega_0 = \left(\frac{m_2}{m_0} \right)^{1/2},$$

$$\alpha = \left(\frac{\omega_p}{\omega_0} \right)^2 \frac{7}{\{2 + [25 + 21(\theta^2 - 1)]^{1/2}\}}.$$

Here, m_n is the n th moment of the spectrum, ω is the angular frequency, ω_0 is the mean frequency, ω_p is the frequency of the spectral peak, and h is the wave elevation. The dimensionless parameters H , Σ , and θ represent the maximum amplitude of the breaking wave, the frequency of the wave, and the ratio of wave extremes to zero crossings, respectively.

We adopt the breaking criterion of Papadimitrakakis et al.,⁵ in which the nondimensional maximum amplitude is

$$H_0 = (4\sqrt{2} \pi \alpha_1 \delta)^{-1} (\Sigma_p / \Sigma)^2, \quad 0 < \Sigma \leq A_1 \Sigma_p,$$

$$H_0 = (4\sqrt{2} \pi \alpha_1 \delta)^{-1} (\Sigma_p / \Sigma)^2 \times \left[1 - \alpha_2 \frac{u_*}{c} \left(\frac{\Sigma}{\Sigma_p} \right)^2 \right], \quad \Sigma > A_1 \Sigma_p, \quad (2)$$

where δ is the wave slope; Σ_p is the nondimensional wave peak frequency; u_* is the frictional velocity; c is the phase speed; and α_1, α_2 , and A_1 are physical constants determined from experiments. Once this breaking criterion is adopted, the energy loss is found immediately by integration; its nondimensional form is

$$PL(f) = \frac{4\Sigma^3}{\pi^{1/2} [\theta^2 - 1 + (\Sigma^2 - 1)^2]^{5/2} (1 + \theta)} \times \left\{ (\theta^2 - 1) \Gamma\left(\frac{5}{2}, H_0^2\right) - [\theta^2 - 1 + (\Sigma^2 - 1)^2] H_0^2 \Gamma\left(\frac{3}{2}, H_0^2\right) \right\}, \quad (3)$$

and its dimensional form for a given frequency is

$$S_{\text{diss}}^{\text{break}} = -f PL(f) E(f, \theta), \quad (4)$$

where Γ is an incomplete gamma function, and $E(f, \theta)$ is the two-dimensional wave energy (f is the frequency and θ is the direction). Our parameterization accounts for energy lost due to breaking at all frequencies.

Preliminary calculations showed that essentially all of the dissipation given by Equation 4 occurs near the spec-

tral peak, although experience suggests that dissipation also occurs at higher frequencies. We associate this dissipation with turbulent fluctuations in the water generated during wave breaking. This phenomenon is described by the well-known equation⁶

$$S_{\text{diss}}^{\text{turb}} = -2\nu k^2 E(f, \theta), \quad (5)$$

where ν is the eddy viscosity coefficient, and k is the wave number. Because higher frequencies are treated poorly in the model and dissipation at higher frequencies is used essentially to keep the model stable, only a numerical estimate of the eddy coefficient needs to be determined. Because we envision that the eddy viscosity arises from a mixing of momentum, ν should be given by a characteristic velocity scale multiplied by a characteristic length scale. An obvious length scale is k_p^{-1} , the inverse wave number of the spectral peak. The velocity magnitude is given by the total kinetic energy generated by the breaking wave:

$$U^2 = g \int_0^\infty PL(f) E(f, \theta) df, \quad (6)$$

where g is the acceleration due to gravity. Consequently, $\nu = U/k_p$.

This parameterization is incorporated into the model as follows: The model's spectrum is used to compute the various moments that give θ and ω_0 . We then approximate the peak of the spectrum by the mean frequency of the spectrum to ensure that the peak frequency evolves smoothly. Finally, we compute α .

With these parameters, we are ready to compute the dissipation function. For each frequency, we first compute the nondimensional frequency Σ , and then the wave slope $\delta = 0.157\omega^4 E(f)$, where $E(f)$ is the one-dimensional wave energy. This proportionality constant was chosen so that the wind input, dissipation, and wave-wave interaction source terms would balance for a Pierson-Moskowitz⁷ spectrum. Next, H_0 is computed from Equation 2, in which we have chosen the approximate values $A_1 = 2$, $\alpha_1 = 1$, and $\alpha_2 = 1/2$. Finally, the incomplete gamma function is computed by using the standard algorithm.⁸ All of these quantities are substituted into Equation 4. For $H_0 > 3$, an asymptotic expansion is used to evaluate the incomplete gamma function.

The integral in Equation 6 is computed as we compute the wave breaking. Consequently, once the wave-breaking portion of the code is completed, we have everything needed for Equation 6 so that turbulent dissipation can be found via Equation 5.

To test the dissipation scheme, the wave growth, nonlinear wave-wave interactions, and dissipation were computed for a Pierson-Moskowitz spectrum with a cosine-squared spreading function and a 20-m/s wind. The only unknown parameter occurs in the expression for wave slope. Following the WAM group,¹ we assumed that the wave slope was proportional to $f^4 E(f)$. The proportionality constant was chosen so that all source terms would balance when integrated over direction and frequency.

The current WAM model adds an f^{-4} tail at sufficiently high frequencies to keep the model stable. We found that this tail introduced too much dissipation at the higher frequencies, so we adopted an f^{-5} tail, which is closer to the Pierson-Moskowitz spectrum.

Figure 1 shows the balanced source terms as a function of frequency. The frequencies and source terms have been nondimensionalized by u_*^2/g and g^3/u_*^5 , respectively. A comparison of our dissipation function with the WAM parameterization shows that our scheme dissipates energy more uniformly over the various frequencies. Our computed value for the eddy viscosity was approximately $55 \text{ cm}^2/\text{s}$.

A more realistic test is to blow the wind off the shore at 20 m/s and allow the spectrum to reach equilibrium. The spectrum for fetch-limited wave growth is shown in Figure 2 as a function of nondimensional fetch $x^* = gx/u_*^2$ from the coast. The one-dimensional spectrum is nondimensionalized by g^3/u_*^5 . The evolution of the spectrum with distance is very similar to that of WAM. A detailed comparison shows that our spectrum has consistently higher peak values in comparison with the results given in Figure 5 of Ref. 1. At infinite fetch, the WAM model gives a nondimensional energy E^* and a nondimensional frequency f^* of 1.15×10^3 and 5.51×10^{-3} , respectively, compared with 1.56×10^3 and 5.00×10^{-3} in our model. These differences are attributable essentially to the new dissipation parameterization.

USE IN LEWEX

Although simple tests are useful in understanding a wave model, another test is its application to an observed data set. A set of observations against which a model may be compared is provided by LEWEX. Further, because many modelers use the so-called LEWEX "common winds," other modelers have a benchmark against which to compare their models.

The model was executed over the region where the coarse mesh winds were provided, namely 30°N to 60°N and 30°W to 80°W . The ice/sea boundary was not included, and the horizontal resolution was 1.25° latitude by 2.5° longitude. The model contains twenty-six frequency bands placed logarithmically from 0.042 to 0.487 Hz, and twenty-four azimuthal bands with $\Delta\theta = 15^\circ$. Although the time step was allowed to vary with the wind speed, a typical time step was 450 s.

The model was run on a Cyber 205 vector processing machine. For 548 ocean grid points, the average central processing unit time step was about 1 s. The nonlinear wave-wave calculations took 52% of the central processing unit time, the dissipation took 13%, reading out the data took 12%, and calculating the f^{-5} tail of the spectrum took 11%. Other processes took smaller percentages of time.

Figures 3A and 3B show the significant wave heights for the period from 12 March to 20 March 1987 at the grid points nearest the CFAV *Quest* and HNLMS *Tydemman*. Also, we have added wind barbs for the local winds given by the LEWEX common wind analysis.

The first thing to note is a slight undulation in the wave heights, resulting from the constant readjustment

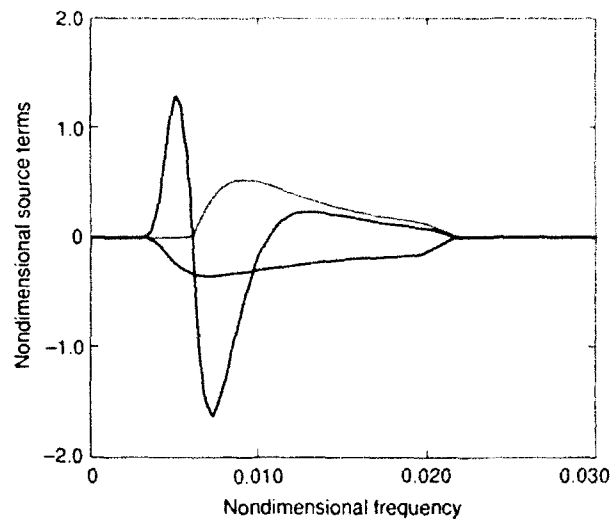


Figure 1. The balance of wind input (red curve), nonlinear energy transfer from wave-wave interactions (blue curve), and wave energy dissipation (black curve) that would occur in our model if the spectrum followed the shape suggested by Pierson and Moskowitz⁷ for a 20-m/s wind.

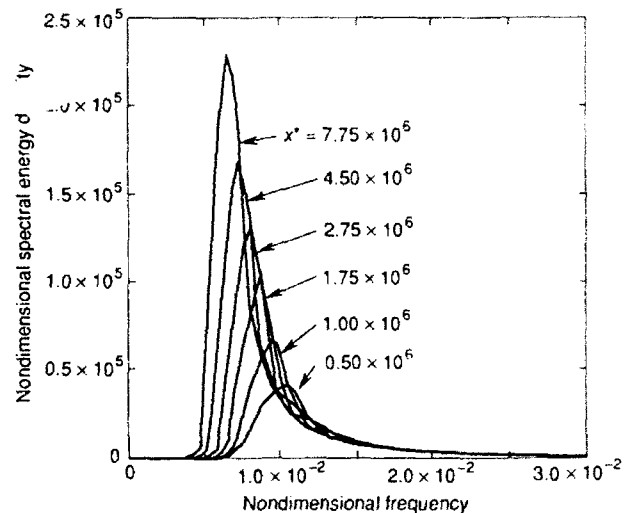


Figure 2. The evolution of a one-dimensional frequency spectrum for fetch-limited wave growth ($x^* =$ nondimensional fetch).

of the system as the magnitude and direction of the wind varied. Such ringing was possible in our system because our advective scheme is relatively nondissipative, unlike most models, which use a first-order advection scheme.

At the *Tydemman*, we found two major peaks in the wave height: the first around 14–15 March and the second around 18 March. These results are in general agreement with other models, although our wave heights are slightly lower. Further, the peak of the first event appeared twelve hours later than that of several other models.

The wave hindcast made at the location of the *Quest* contained a larger degree of variability than that made at the *Tydemman*. Upon comparing our results with oth-

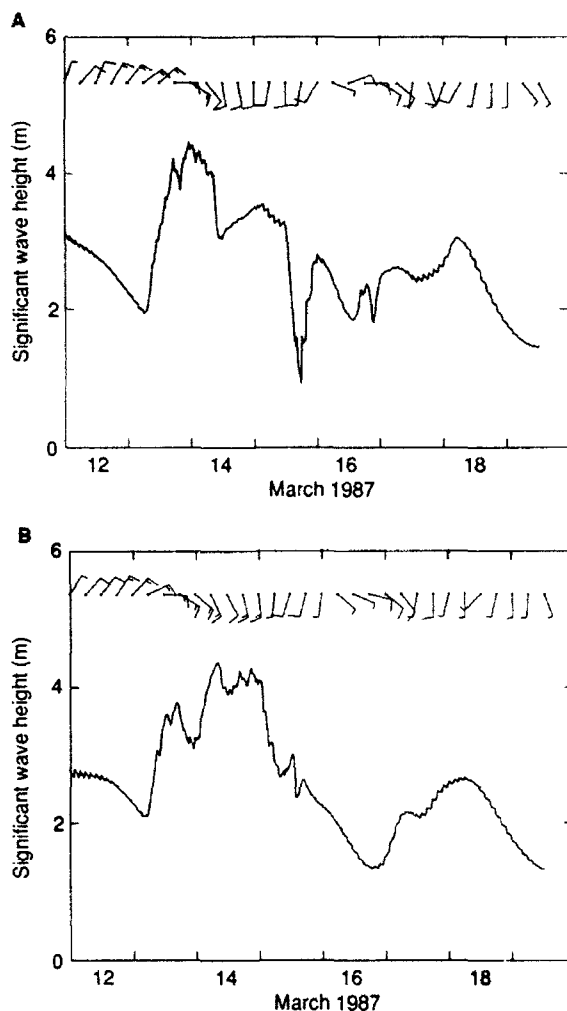


Figure 3. Hindcast of significant wave height between 12 March and 20 March. **A.** *Quest*. **B.** *Tydemar*. Wind barbs for the local winds are also plotted. Each full barb indicates 10 kt, and a half barb indicates 5 kt.

er models, the peaks near 0000 UT on the successive days of 14 through 18 March could also be discerned. The major difference between our model and other models was the rapid growth and decay of wave energy, especially around 1800 UT on 15 March. Again, our wave heights were not as large as those in other models.

Comparing the evolution of the spectra in our model with other models is also useful. In Figures 4A and 4B, we compare the two-dimensional spectra $E(f, \theta)$ for our model with the WAM model at the *Quest* in six-hour intervals from 0000 UT on 13 March to 0600 UT on 14 March. This particular example was chosen because different models behaved quite differently in this rapidly evolving situation.

Our spectra were similar to those of WAM. Both models showed a decaying swell located in the fourth quadrant and a growing wave energy in the second and third quadrants. The major difference was WAM's earlier and stronger growth of the new wave energy. Further, our wind-driven spectral peak was slightly clockwise

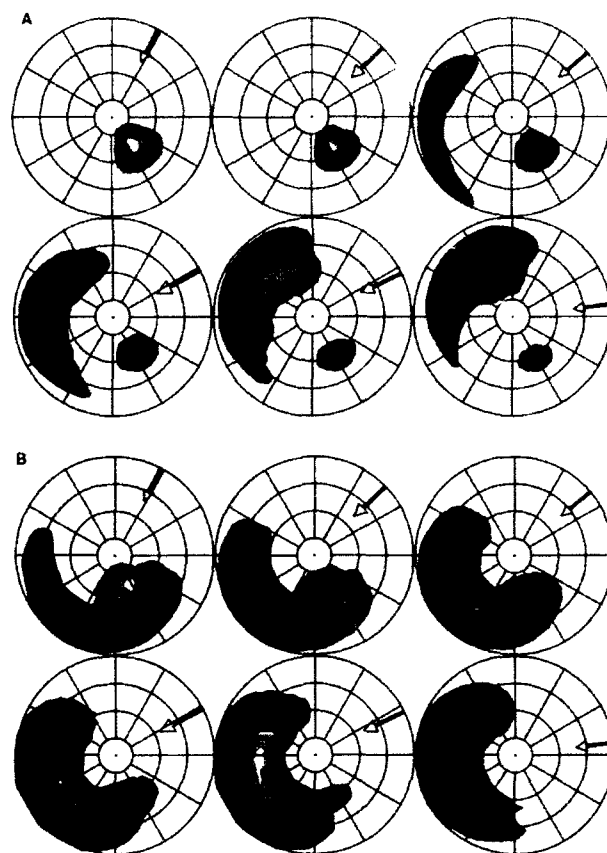


Figure 4. Two-dimensional wave spectra $\log E(f, \theta)$ versus $\log f$ at six-hour intervals for a rapidly evolving wave field at the *Quest* between 13 March at 0000 UT and 14 March at 0600 UT. **A.** NASA third-generation model. **B.** WAM third-generation model. The inner circle is at 400 m, and the outer circle is at 50 m. Sequences are from left to right by row.

from WAM's. These results suggest that our stronger dissipation at higher frequencies and weaker dissipation at lower frequencies inhibit wave growth due to direct wind input while allowing strong growth of spectral peaks due to nonlinear wave-wave interactions.

SUMMARY AND CONCLUSION

In this article, we have described a third-generation wave model that is similar to WAM but differs in both the horizontal advection scheme and dissipation. We have presented results for fetch-limited wave growth and for the conditions experienced during LEWEX. The results given by our model are similar to those given by WAM; the greatest difference is the rate at which wind-generated wave growth occurred.

Although our model is certainly not perfect, we can improve the current WAM formulation because our dissipation scheme is based on physical considerations.

REFERENCES

- 1 WAMDIG (Wave Model Development and Implementation Group), "The WAM Model—A Third-Generation Ocean Wave Prediction Model," *J. Phys. Oceanogr.*, **18**, 1775-1810 (1988).

- ² Takaacs, L. L., "A Two-Step Scheme for the Advection Equation with Minimized Dissipation and Dispersion Errors," *Mon. Weather Rev.* **113**, 1050-1065 (1985).
- ³ Phillips, O. M., "The Scattering of Gravity Waves by Turbulence," *J. Fluid Mech.* **5**, 177-192 (1959).
- ⁴ Yuan, Y. L., *On the Statistical Properties of Sea Waves*, Ph.D. dissertation, North Carolina State University, Raleigh, N.C. (1983).
- ⁵ Papadimitrakos, Y. A., Huang, N. E., Bliven, L. E., and Long, S. R., "An Estimate of Wave Breaking Probability for Deep Water Waves," in *Sea Surface Sound: Natural Mechanisms of Surface Generated Noise in the Ocean*, Kerman, B. R., ed., Kluwer Academic Publishers, Dordrecht, The Netherlands, pp. 71-83 (1989).

- ⁶ Lamb, H., *Hydrodynamics*, Dover Publications, New York, p. 624 (1945).
- ⁷ Pierson, W. J., Jr., and Moskowitz, I. L., "A Proposed Spectral Form for Fully Developed Windseas Based on the Similarity Theory of S. A. Kitaigorodskii," *J. Geophys. Res.* **69**, 5181-5190 (1964).
- ⁸ Press, W. H., Flannery, B. P., Teukolsky, S. A., and Vetterling, W. T., *Numerical Recipes*, Cambridge University Press, New York, pp. 160-163 (1986).

ACKNOWLEDGMENTS: Norden Huang derived the wave-breaking parameterization, Wayne Higgins made several helpful suggestions concerning the manuscript, and Monique Hall provided assistance in assembling the manuscript. Spectral plots shown in Figure 4 were provided by Tom Gerling of JHU/APL.

A COMPARATIVE ANATOMY OF THE LEWEX WAVE SYSTEMS

Directional spectral estimates from eight numerical wind-wave models and a directional wave buoy are compared by dissecting the directional spectrum into five or six independently evolving wave systems. Dissection more clearly reveals the connection between each wave system and its source wind field and may offer a valuable tool for interpretation of directional wave spectra and for global wave data assimilation schemes.

INTRODUCTION

The Labrador Sea Extreme Waves Experiment (LEWEX) was planned to provide a comparison among measured and modeled directional ocean gravity wave spectra in a geographic region where large, rapidly evolving wave systems were expected. The LEWEX goals are described in Bales et al.¹ and Beal (this volume). The variety of data sets obtained can be sensed from other articles in this volume. This article first provides a general description of the directional wave field at the location of HNLMS *Tydeman* (50°N, 45°W), one of the two experimental sites of LEWEX. The wave field then is examined in terms of its component wave systems, using either measured or model-derived directional spectra. Finally, the meteorological sources of these wave systems evident in the LEWEX hindcast wind field, or LEWEX "common winds" (see the article by Cardone in this volume), are briefly described. The data sources discussed in detail are the moored Wavescan buoy (Krogstad, this volume), the second-generation UKMO wave model (Rider and Stratton, this volume), and the third-generation WAM (Zambresky, this volume). The first-generation wave models GSOWM (Wittman and Clancy, this volume), ODGP (Cardone, this volume), and the second-generation wave models VAG (Guillaume, this volume) and HYPAC² are also discussed, as well as the model operational at the National Oceanic and Atmospheric Administration (NOAA) (Esteve and Chao, this volume). For a definition of this generational nomenclature and a description of various model implementations, see the SWAMP report.³

The Norwegian Wavescan buoy had the appealing property among LEWEX measurements of providing uninterrupted, statistically independent directional spectral estimates every 1.5 h for approximately 4 days. This continuous sampling allowed researchers to detect timing problems in the model spectra caused by the inaccurate specification of atmospheric pressure system movements. These timing errors can make spectral comparisons at a specific time so different that they appear unrelated. When the entire time series of spectra (or their associated reduced parameters) are viewed, however, these timing differences can easily be recognized and perhaps explained. This is an important aspect of the LEWEX comparisons because the wind field is not perfectly known.

Part of this article presents statistical summaries of the LEWEX spectral sequences in varying degrees of detail. The most highly averaged measures, such as total energy or significant wave height (SWH), tend to mask differences among the various data sources when, in fact, there are often great discrepancies among the directional spectra. At the most detailed level—that of examining individual two-dimensional spectra—it is sometimes difficult to find corresponding features in different data sources. Between these two levels of data reduction is one that preserves the most important differences among the data sources but averages out the less important ones. This reduction is a dissection of the time sequence of two-dimensional spectra into component wave systems, each of which is attributable to a distinct meteorological event and characterized by a relatively local concentration of spectral variance whose reduced parameters vary continuously in time.

SIGNIFICANT WAVE HEIGHTS AT THE TYDEMAN

Figure 1 shows time series of SWH's from five models that made predictions at 50°N, 45°W for the entire LEWEX time period and also for the Wavescan buoy moored there. The definition of SWH here is $4 \times$ (wave height variance)^{1/2}. Each model was driven by the LEWEX common winds. The total variation is from about 2 to 6 m over the duration of the experiment. Differences among models are generally less than 1-m SWH, which is a considerable improvement over the difference of more than 2 m that occurred when models were run with their own wind fields (see Fig. 7 in Beal, this volume). The GSOWM and UKMO models in particular are in considerably better agreement with the others than when run with their own winds. The French model VAG reproduces the SWH variation of the Wavescan buoy particularly well, not only approximating it in a pointwise sense, but also capturing the shape, especially between 14 and 16 March.

The agreement represented in these curves, however, is misleading for much of the experimental period. Consider, for example, the various estimates on 16 March at 0000 UT. As can be seen in the total SWH curves,

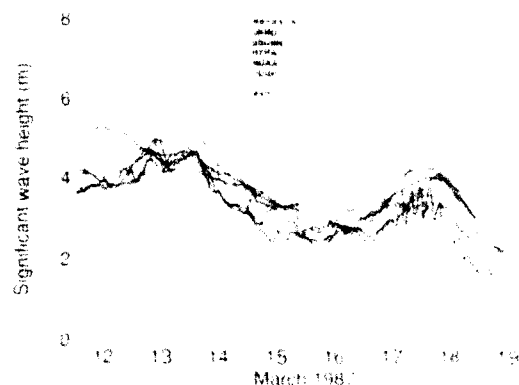


Figure 1. Significant wave heights at 50°N, 45°W for models run with the LEWEX common winds.

there is very good agreement (± 0.2 m SWH) among all data sources except GSOWM, which is higher because of a southeasterly system (arriving from the southeast) that was represented strongly only in that model's hindcast, although it was also present to a lesser degree in the Wavescan spectra. (See Wittmann and Clancy, this volume.)

Figure 2 shows spectra for WAM, VAG, and Wavescan. The radial scale is log frequency, with a range of 0.05 to 0.2 Hz and calibration circles corresponding to wavelengths of 400, 200, 100, and 50 m calculated using the dispersion relation for deep-water gravity waves ($\omega^2 = gk$). These calibration circles correspond to wave periods of about 16, 11.5, 8, and 5.5 s. The quantity contoured is $S(f, \theta)$, which satisfies

$$\text{wave height variance} = \int_{\theta} \int_{f, \theta} S(f, \theta) f df d\theta,$$

with $S(f, \theta)$ in units of $\text{m}^2 \cdot \text{s}^{-2}$. The spectral plots display equally spaced contours of $\log S(f, \theta)$ as a function of $\log f$. The spectra indicate the direction toward which waves propagate. With this logarithmic format, it is possible to display spectral energy in both wind sea and swell in absolute units, even when their peak spectral energy densities differ by an order of magnitude. In this format, however, the visual perception of spectral volume does not correspond to its total energy as it would in a linear format, with linearly spaced levels.

As Figure 2 shows, the spectral estimates differ significantly on 16 March at 0000 UT: the buoy places all the wave energy in a southerly system, while both the WAM and VAG models divide the energy about equally into a northerly and a southerly system. A similar misleading agreement in SWH occurs at other times, such as on 18 March at 0000 UT when WAM, VAG, and Wavescan agree to within ± 0.2 m SWH. The corresponding spectra are also shown in Figure 2. The northerly wave system, which is so strong in Wavescan at this time, has nearly disappeared in WAM and VAG, and there is also significant south-southeast energy in Wavescan that is lacking in the models.

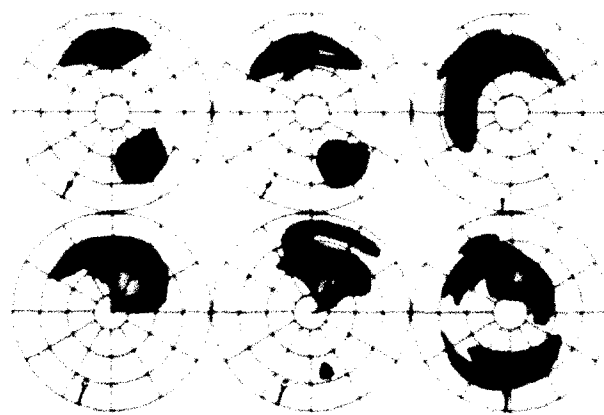


Figure 2. Top row: WAM, VAG, and Wavescan spectra at 50°N, 45°W on 16 March at 0000 UT. Bottom row: WAM, VAG, and Wavescan at 50°N, 45°W on 18 March at 0000 UT. Wind vector (arrow) magnitude is 10 m/s per ring.

THE LEWEX WAVE SYSTEMS

The preceding examples show that directional aspects of the spectrum need to be considered to compare data sources properly. The two-dimensional spectrum has this information, but, from a statistical point of view, it is often better to partition the two-dimensional spectrum into component wave systems and calculate parameters for each component. This partitioning compresses the information and permits comparisons among wave systems in terms of reduced parameters.

An algorithm has been devised that performs this partitioning.^{4,5} Each wave system is characterized by a spectral location estimate (that is, frequency and direction) and its associated wave-height variance estimate. The modal, or maximal, location estimate is used in this article. The variance estimate is a recursively calculated quantity that fractionates the total wave-height variance among all modes present in the spectrum.

Figure 3 shows the sequence of WAM hindcast spectra at the *Tydemar* over the LEWEX time period; WAM is illustrated here because its spectra are relatively simple, but they still show the evolution of all the important wave systems. The results of the spectral partitioning algorithm are plotted in Figure 4A, which shows the evolution of six wave systems, separated by color and numbered 0 through 5. These six wave systems largely determined the variability of the WAM hindcast waves at the *Tydemar*. Careful comparison of Figure 3 with Figure 4A will show the spectral signature of the individual wave systems. The evolution of each wave system is represented by a series of arrows whose direction indicates the direction of wave propagation as estimated from the corresponding spectral mode. For the WAM sequence, there is high temporal correlation within an individual wave system. The right-hand ordinate is the period of the spectral mode; the corresponding left-hand scale is transformed to wavelength through the dispersion relation for deep-water gravity waves. All modes were calculated from the previously described frequency spectra having units $\text{m}^2 \cdot \text{s}^{-2}$. The length of the arrow is proportional to the SWH of the individual system.

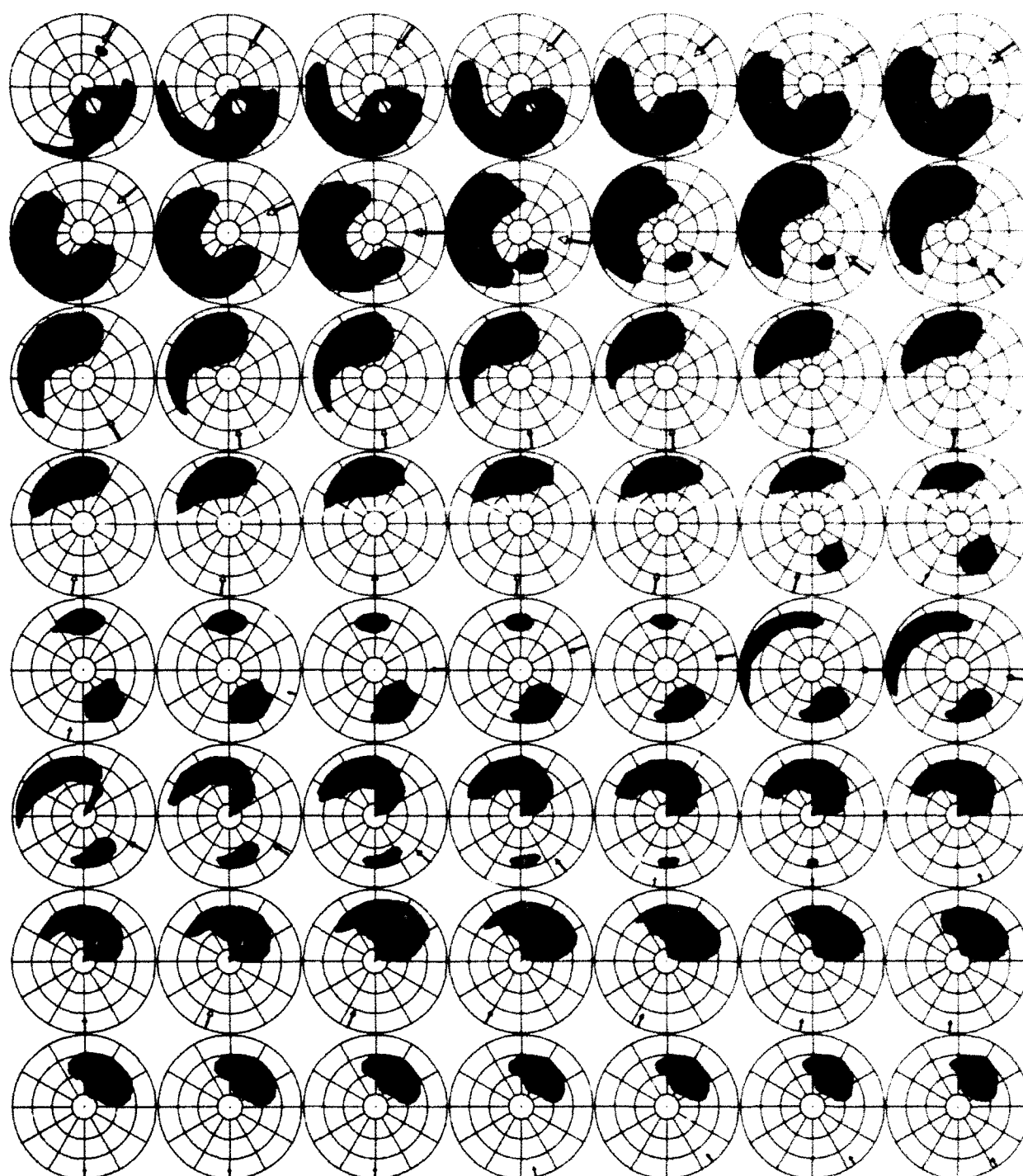


Figure 3. Three-hourly sequence of spectra from WAM with LEWEX common winds at 50°N, 45°W. Same scale as Fig. 2. Sequence begins on 12 March at 1500 UT (upper left) and ends on 19 March at 1200 UT (lower right).

The spectral partitioning algorithm is intended to describe wave field variability as Snodgrass et al.⁶ did, that is, as a superposition of remotely generated wave trains. In that article, the evolution of features present in sequences of frequency spectra was related to source regions of remotely generated waves. Spectra of a time series from a bottom-mounted pressure sensor were arranged in a two-dimensional format of energy as a function of frequency and time. In that format, remotely gen-

erated wave trains produced a ridge signature. The slope of the ridge was related to the distance to the source region, and the zero-frequency intercept was related to the time of generation. In contrast, the algorithm described here operates automatically and also produces an estimate of the variance attributable to each wave component. Since it operates on the full directional spectra, directional information emerges from a single time series at a single location.

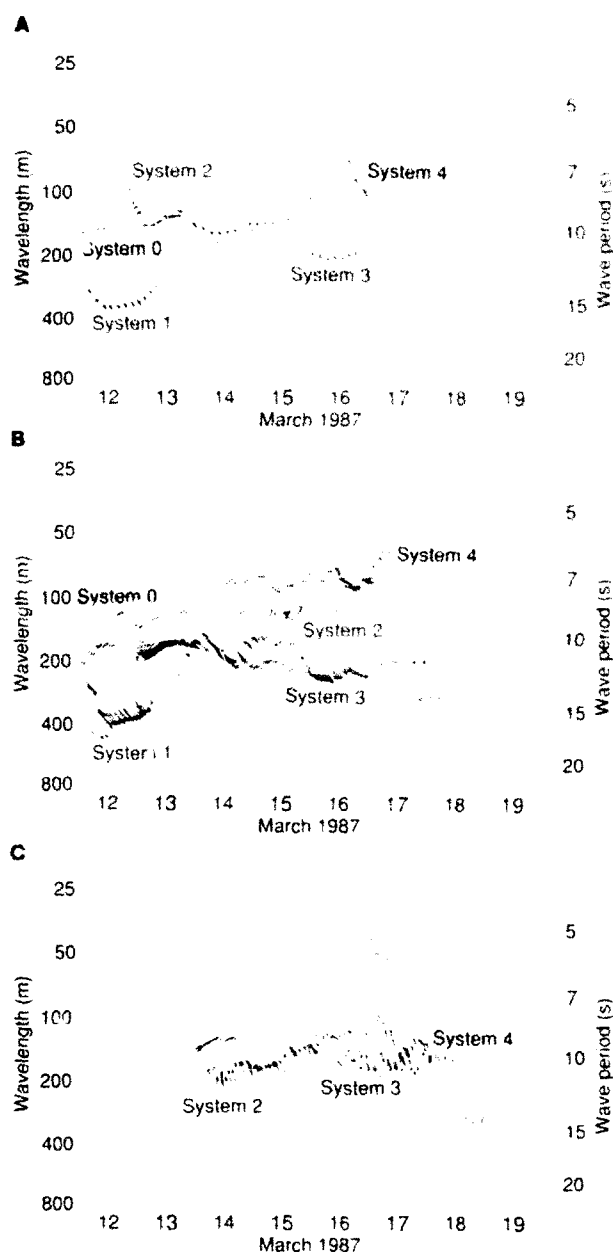


Figure 4. Evolution of LEWEX wave systems at 50°N, 45°W as modeled with (A) WAM and (B) UKMO, and as observed with (C) Wavescan. Arrow length is proportional to SWH.

Figure 4B shows the vector diagram for the second-generation UKMO model. Whereas WAM produced smoothly varying patterns in Figure 4A with relatively simple structure, the patterns in Figure 4B are more complicated, with many more spectral modes present. Moreover, these features are sometimes intermittent and sometimes have short persistence. This additional structure, which is not present in WAM, might be termed "secondary spectral structure." It can be seen from Figure 4B that the same six wave systems discussed in conjunction with WAM are also present in the UKMO model, so it is reasonable to compare data sources in terms of what might be termed "primary spectral structure," consisting

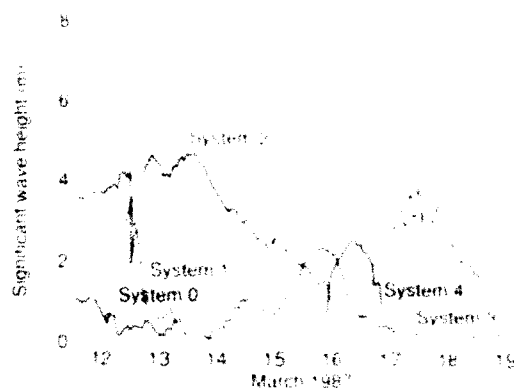


Figure 5. Partitioned SWH curves for the UKMO model run with the LEWEX hindcast winds at 50°N, 45°W.

of the more highly averaged parameters that characterize wave systems. In particular, the SWH curves of each of the partitioned wave systems preserve the major directional properties but average out this secondary structure. These curves are shown in Figure 5 for the UKMO model, along with the total SWH curve. (Other examples of partitioned SWH curves can be seen later in this article in Figures 8A-E, where the UKMO curves agree well with other models, even though the spectra have complicated shapes that contain many modes not found in spectra from other data sources.)

The vector diagram for the Wavescan buoy is shown in Figure 4C. Here, only four wave systems are observed because the buoy was not operational until 0430 UT on 14 March. The Wavescan provides time series of heave and also north- and east-surface slope, and from these, a directional maximum entropy spectral estimate is computed (see Ref. 7 and also the Krogstad article in this volume). In this case, not all spectral modes are plotted. Whereas WAM produces smoothly varying spectra with at most three modes in any LEWEX spectrum, the Wavescan maximum entropy estimate can have many modes. This is perhaps to be expected because the maximum entropy spectral estimates have independent frequency bands of width 0.01 Hz, causing a random element in the directional orientation of each band. If the estimates from each band are not quite in alignment, a spurious peak may arise. Most of these modes are insignificant and result in a small variance estimate. They have been eliminated in this comparison through a "pruning" procedure, so named because the data structure extracted from each spectrum has the shape of a tree. Each spectral mode represents a branch at the top of this tree. Pruning will produce more highly averaged statistics to characterize the remaining spectral modes. In particular, the variance estimate of a pruned branch is used to augment the variance estimate of the closest remaining branch.

Smoothing of either the heave and slope spectral estimates or the two-dimensional maximum entropy estimate will also reduce noise. In fact, the heave and slope estimates with standard processing have 32 degrees of freedom.⁸ The directional Fourier coefficients calculated

for each frequency band derived from the one-dimensional spectral estimates are also smoothed in time with the filter having weights $1/4$, $1/2$, and $1/4$. More smoothing would probably obscure spectral structures of interest.

Since highly nonlinear equations are used to compute maximum entropy estimates from the heave and slope time series, the standard spectral confidence intervals are appropriate only for the original time series but are of little use for interpretation of the directional spectral estimate or the quantities plotted in Figure 4C. An informal estimate of the variability in these quantities can be obtained, however, by assuming that the descriptive parameters vary smoothly in time within a wave system. Splines can be used to compute this smooth variation, and a variability estimate for the parameters can be obtained by computing residuals from it. This process will yield a variability estimate that will be an upper bound on the real sampling variability because it will contain some real wave-field variability. These estimates have not been computed for the Wavescan wave systems shown in Figure 4C, but it is apparent from the low scatter in the vector plots that sampling variability is not large for these parameters.

The secondary spectral structure is present in other second-generation models also, such as v_{x0} and u_{y0} , but is lacking in the second-generation model operational at NOAA, Figure 2, which shows the v_{x0} and w_{x0} hindcasts at 0000 UT on 16 March and 0000 UT on 18 March, is an example of v_{x0} spectra containing the additional structure. The southerly system on 16 March described by v_{x0} contains three modes, whereas that from w_{x0} is unimodal. On 18 March, the distribution of energy in w_{x0} is unimodal, compared with nearly separate wind sea and swell distributions in v_{x0} .

Figure 6 gives another example of the variability present in the various data sources. Sequences of spectra on 15 March from 0000 UT to 1200 UT are plotted for three models and the Wavescan buoy. Over the time interval represented, the models shown agree well in w_{x0} but are all significantly lower than Wavescan. The w_{x0} model shows a continuous unimodal evolution, whereas both u_{y0} and u_{x0} exhibit multimodal distributions with many differences between sequential spectra. One interesting feature in the u_{x0} sequence is the wave system with the approximately 9-s period propagating toward the north-northeast. The spectral signature is intermit-

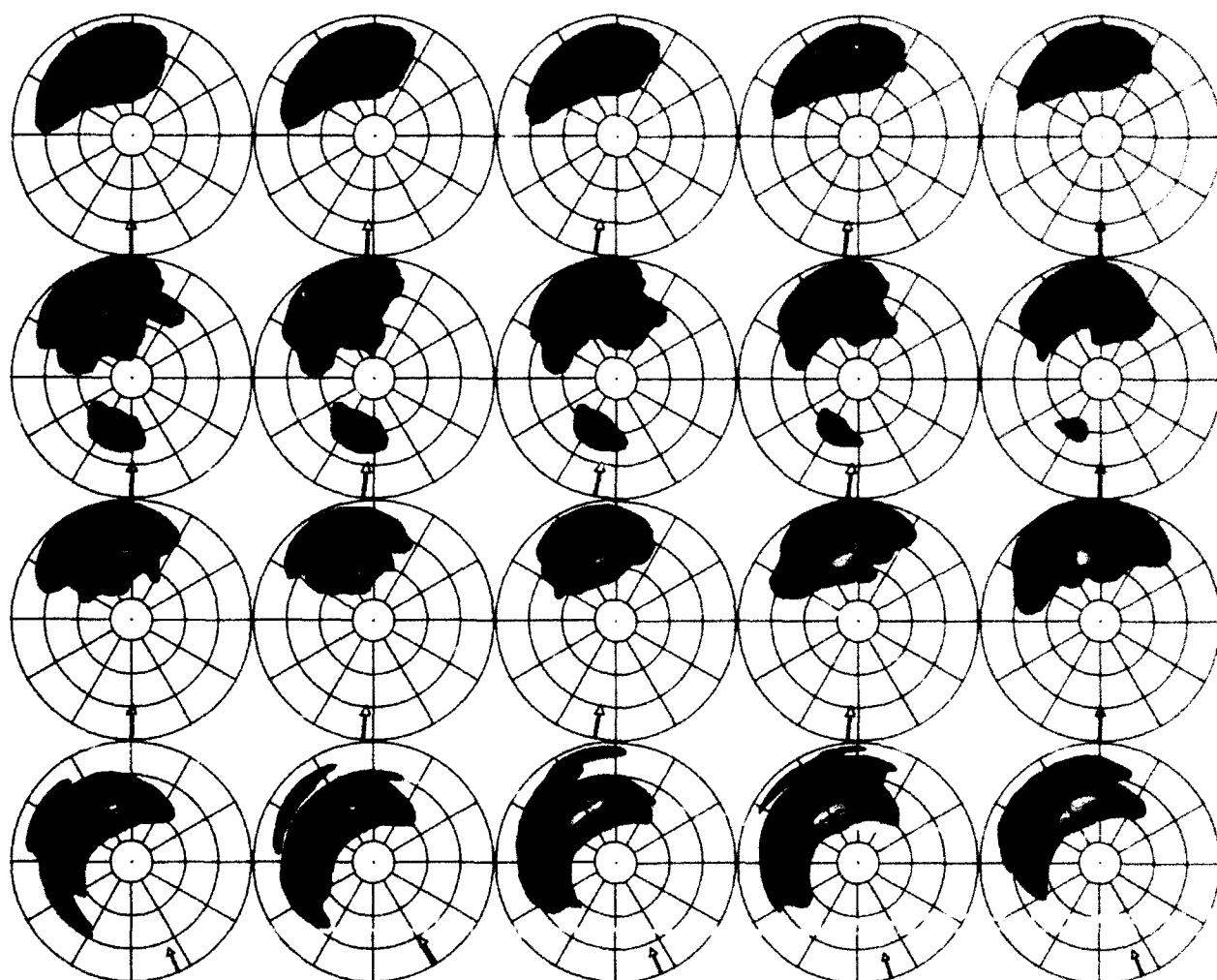


Figure 6. Spectral sequences beginning at 0000 UT on 15 March and continuing every 3 h through 1200 UT (left to right). Data sources are organized by rows, beginning with WAM, and followed by UKMO, HYPA, and Wavescan at 50°N, 45°W. Same scale as Fig. 2.

tent: it is present at 0000 UT, 0600 UT, and 1200 UT, but not at 0300 UT and 0900 UT. Curiously, there is a minimum in the UKMO spectrum at 0900 UT at the same location where the WAM spectrum has its maximum. Similar intermittent behavior is present during other portions of the UKMO spectral series, such as the swell system 4 of Figure 4B.

The Wavescan has a more complicated spectrum, reflecting the actual variability of the wave field. It is essentially a unimodal distribution, however. It exhibits a longer period (11 s) than WAM (10 s), but is in closer agreement with one of the modes present in HYPA (particularly at 0300 UT) and, to a lesser extent, UKMO.

The maximum spectral density of both Wavescan and HYPA agree well, and both exceed that of WAM and UKMO. Wavescan appears to have a broader angular distribution than any of the models and also contains less energy in the higher frequencies than any of the models shown. This high-frequency activity may be a result of local fluctuations in wind speed not modeled in the LEWEX common winds; the Wavescan-measured winds were in fact more highly variable than those of the modeled winds. The broader angular distribution may be caused by the swell propagating from a region close to Africa not included in the LEWEX common winds. The swell is barely detected in the Wavescan buoy but is quite prominent in the GSOWM spectra (Wittmann and Clancy, this volume, Fig. 5B).

The secondary spectral structure in VAG, UKMO, and HYPA probably arises from a separate treatment of sea and swell. The spectrum is parameterized over the region considered to be wind sea. For example, in HYPA³ the six Jonswap parameters are used to model the wind sea portion of the spectrum. The distinction between wind sea and swell varies according to changes in wind speed and direction. Energy in the wind sea will be transformed into swell as wind speed decreases, while swell may be reabsorbed into wind sea as wind speed increases. The swell spectral regime is processed separately, and in some models each of the discrete bins used to approximate a continuous wave spectrum propagates independently.³ The VAG, HYPA, and UKMO models tend to produce spectra with many modes in the swell regime. These modes sometimes do not have long persistence and are sometimes intermittent. The secondary spectral structure is impossible to verify, at least with the data collected in LEWEX. Much of the structure is probably not real, but it can indicate a lower limit to the resolution of features that may reliably be inferred from the complete two-dimensional spectrum. Even if not believable in small details, however, such spectra may accurately reproduce the more highly averaged, larger-scale spectral features.

COMPARISONS AMONG DATA SOURCES USING PARTITIONED SIGNIFICANT WAVE HEIGHTS

Each of the six wave systems shown in Figures 4A-C are seen with variations in the other models. Not all models show the high-frequency activity of the north-

easterly part of system 4, and not all models show system 0. As discussed previously, the GSOWM model shows an additional strong southeasterly wave system commencing late on 14 March and continuing through the end of the experiment (on 19 March). Essentially, these six systems characterize the wave field variability of the LEWEX hindcasts. They are generated as the result of the forcing by three low-pressure systems, which are visible in seven selected wind fields from the LEWEX common winds shown in Figures 7A-F.

Superimposed on these wind fields are Geosat wind speed estimates occurring within 1 h of hindcast time. The Geosat winds (described in Dobson and Chaykovsky, this volume) can be used to estimate the accuracy of the hindcast winds. Using the six wave systems apparent in Figures 4A-C, the discussion that follows identifies the source regions in selected wind fields and also the differences among data sources, expanding on the possible cause of these differences. A more detailed meteorological discussion can be found in Cardone (this volume). The differences will be discussed in terms of partitioned significant wave height curves mentioned previously, since these curves average out secondary spectral structure while retaining the more important directional aspects of the spectrum. The discussion includes the first-generation OROP and GSOWM models; the second-generation VAG, UKMO, HYPA, and NOAA models; the third-generation WAM; and finally the Wavescan buoy. Overlays of the partitioned SWH curves for these eight data sources are shown in Figures 8A-E for the wave systems 1 through 5 of Figures 4A-C.

System 0 represents low-energy swell (less than 1-m SWH) present in most of the hindcasts prior to about 0000 UT on 13 March. It may be traceable to the southwest flow evident at about 40°N, 50°W in Figure 7A. Since system 0 occurs near the beginning of the hindcast, variations in the time required for models to start up may result in the differences seen here.

System 1 (Fig. 8A) represents the swell from the Labrador Sea that was present at the beginning of the experiment but had disappeared by the time the first buoy measurements were made on 14 March at 0430 UT. The swell was caused by the low-pressure system centered at the southern tip of Greenland in the LEWEX hindcast wind field on 11 March at 1200 UT (Fig. 7A). In Figure 8A, the NOAA model differs the most from the others, exhibiting a maximum SWH of 5 m compared with 4 m for WAM, UKMO, and OROP, and about 3.2 m for VAG. The NOAA model also retains this energy about 18 h longer than the other models. The VAG estimate is lower than the others, and it persists longer. The UKMO model displays a rapid falloff of swell energy that is also seen in system 3 of Figure 8C.

The waves of system 2 (Fig. 8B) are nearly aligned with the local wind direction, which changes from northeasterly at about 1200 UT on 12 March to southerly at 1200 UT on 14 March. At first, the northeasterly waves are generated in the northwest quadrant of a low pressure system (see Fig. 7B), but gradually, the Tydemans' sampling location at 45°W changes with respect to the moving low to lie within its northeast quadrant (see Fig.

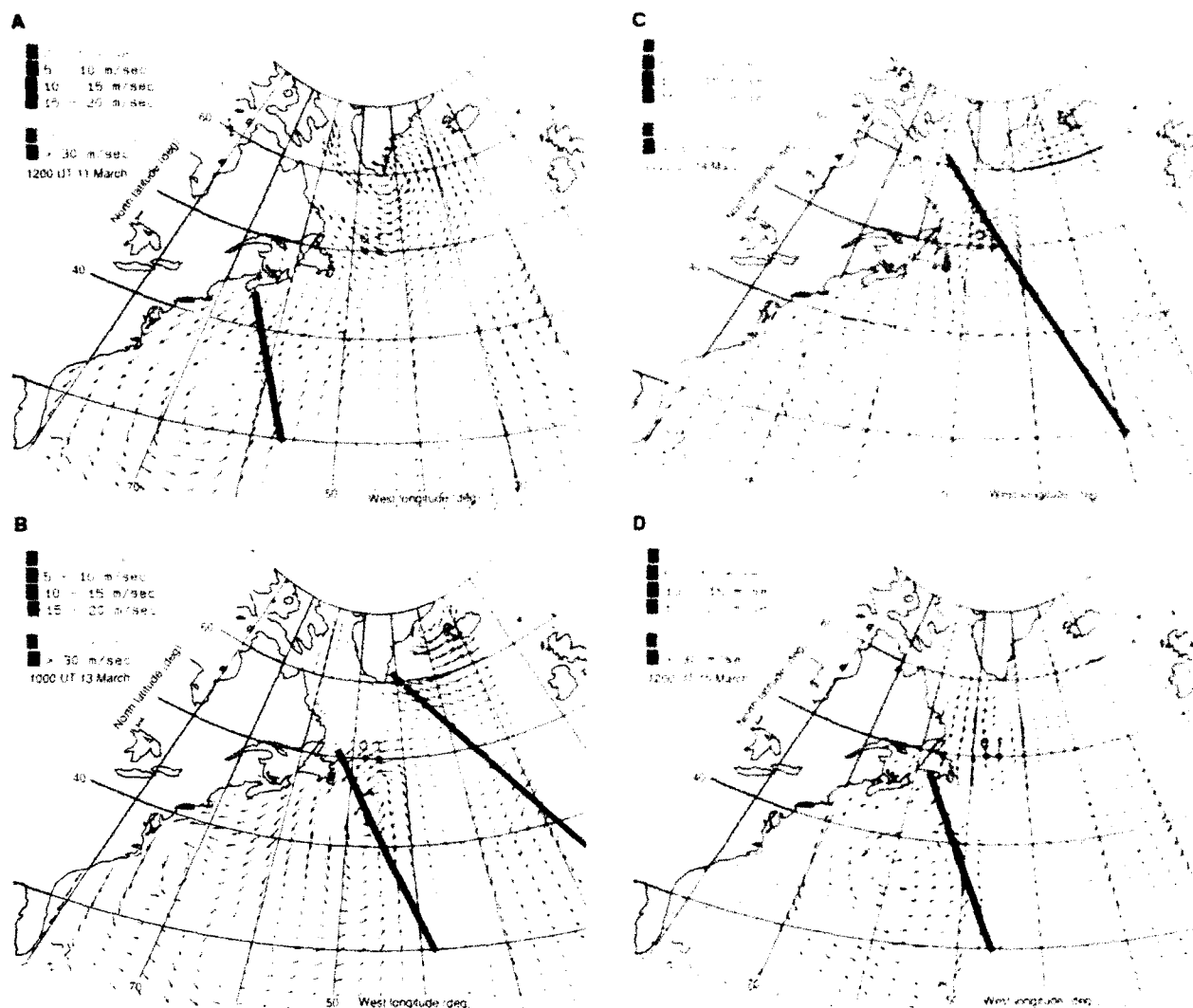


Figure 7. continued on next page.

7C), and southerly waves are experienced at the *Tyde-man*. In Figure 8B, all the models show a similar rate of increase, as indicated by the slope of the curves, but NOAA lags the other models by more than 18 h. The Wavescan buoy cannot provide total verification here since it did not begin measurements until 0430 UT on 14 March. After this time, NOAA, VAG, and ODGP all agree with Wavescan fairly well (± 0.5 m) until just prior to 0000 UT on 16 March. Perhaps the most interesting aspect of this wave system occurs around its most energetic phase from about 1200 UT on 13 March through 1200 UT on 14 March, during which time the LEWEX common winds show a wind shift of about 120° (see Fig. 7B-C). The WAM, UKMO, and HYPA models agree very well on this system but differ considerably from the other models at 0000 UT on 14 March. The ODGP and VAG values are both larger than the others; VAG exceeds WAM, UKMO, and HYPA by nearly 1-m SWH at that point.

The structure in the SWH curves for WAM, UKMO, and HYPA mirrors the variations in local wind speed in the region. A wind sea dominates until just after 0000 UT

on 14 March, when the south-southwest wind sea joins newly arrived swell energy propagating in nearly the same direction. The fact that swell arrives at this time is demonstrated in a number of ways. The Wavescan data in Figure 4C clearly show this swell energy, where system 2 comprises two distinct wave trains. Also, the peak wave direction for WAM at 0000 UT on 14 March experiences a jump which causes it to lead, rather than lag, the local wind direction. In Figure 8B, UKMO and WAM behave nearly identically, and the HYPA data are almost the same except for increases around 1200 UT on 15 March and 1200 UT on 16 March.

There is less agreement in other parameters characterizing this wave system. In Figure 9, the peak frequency is plotted for the various models and Wavescan. The WAM and HYPA data again agree well, with HYPA presenting a noisier locus, as usual. The VAG and ODGP data also again agree well, until just after 14 March, when the decreasing wind speed causes VAG to radiate low-frequency swell. Using this peak-frequency measure, UKMO, surprisingly, does not agree well with either WAM

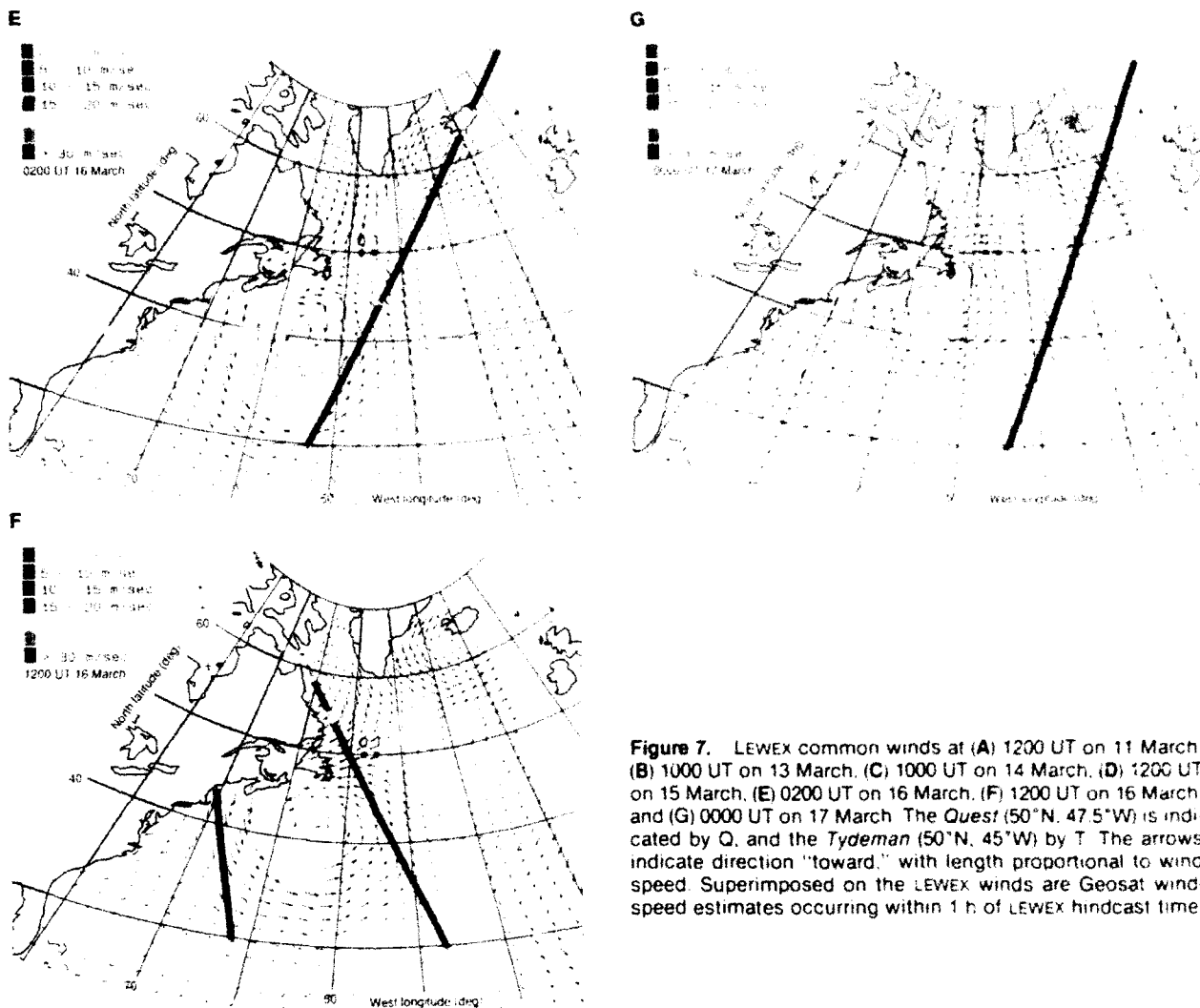


Figure 7. LEWEX common winds at (A) 1200 UT on 11 March, (B) 1000 UT on 13 March, (C) 1000 UT on 14 March, (D) 1200 UT on 15 March, (E) 0200 UT on 16 March, (F) 1200 UT on 16 March, and (G) 0000 UT on 17 March. The *Quest* (50°N, 47.5°W) is indicated by Q, and the *Tydem* (50°N, 45°W) by T. The arrows indicate direction "toward," with length proportional to wind speed. Superimposed on the LEWEX winds are Geosat wind-speed estimates occurring within 1 h of LEWEX hindcast time.

or HYPA, even though it matched nearly identically in SWH. Its frequency is essentially constant at 1/10 Hz during the period 0000 UT on 13 March to 0900 UT on 14 March. Over this same period, the other models begin at 1/8.5 Hz and finish at 1/11 Hz in the case of WAM and HYPA, and 1/13 Hz in the case of ODGP. The WAM and HYPA curves also clearly show the arrival of lower-frequency swell at 0300 UT on 14 March. The pure wind sea part, present before 14 March, exhibits a constant frequency of about 1/9 Hz in those two models.

In this situation, it is difficult to know which models are describing the conditions accurately. Young and Hasselman⁹ performed simulations of WAM and EXACT-NL (a model in which the nonlinear resonant interactions are explicitly computed and not parameterized, as in WAM) on a uniform wind field that suddenly shifted by multiples of 30°. In the model that uses parameters (WAM), the frequency of the spectral peak remained almost constant during the realignment process, whereas the EXACT-NL model showed a gradual shift of the spectral peak to lower frequencies. The shift apparent in the

LEWEX winds is 15° per 3 h during the 24-h period following 1200 UT on 13 March, whereas during the 15-h period following 1800 UT on 12 March, the wind direction is also shifting, but at only one-half its former rate. Over this latter period, WAM and ODGP track each other well, suggesting that the constant frequency behavior of WAM in turning winds might be an artifact of the nonlinear interaction parameterization.

An alternative explanation places the onus on wind field errors, as suggested in Figure 4C. Wavescan detects northeasterly waves of frequency 1/9 Hz from 0430 UT on 14 March through 0000 UT on 15 March, after the signature of these waves has disappeared from both WAM and other model spectra. A trace of these northeasterlies is also seen in the first two points of the Wavescan curve in Figure 9. It is possible that WAM is actually the most correct here and, if the easterly winds had been prolonged, that WAM might agree even better with Wavescan. To get agreement through 0000 UT on 15 March, however, the energy in the southerly waves would also have to increase. It seems unlikely that this

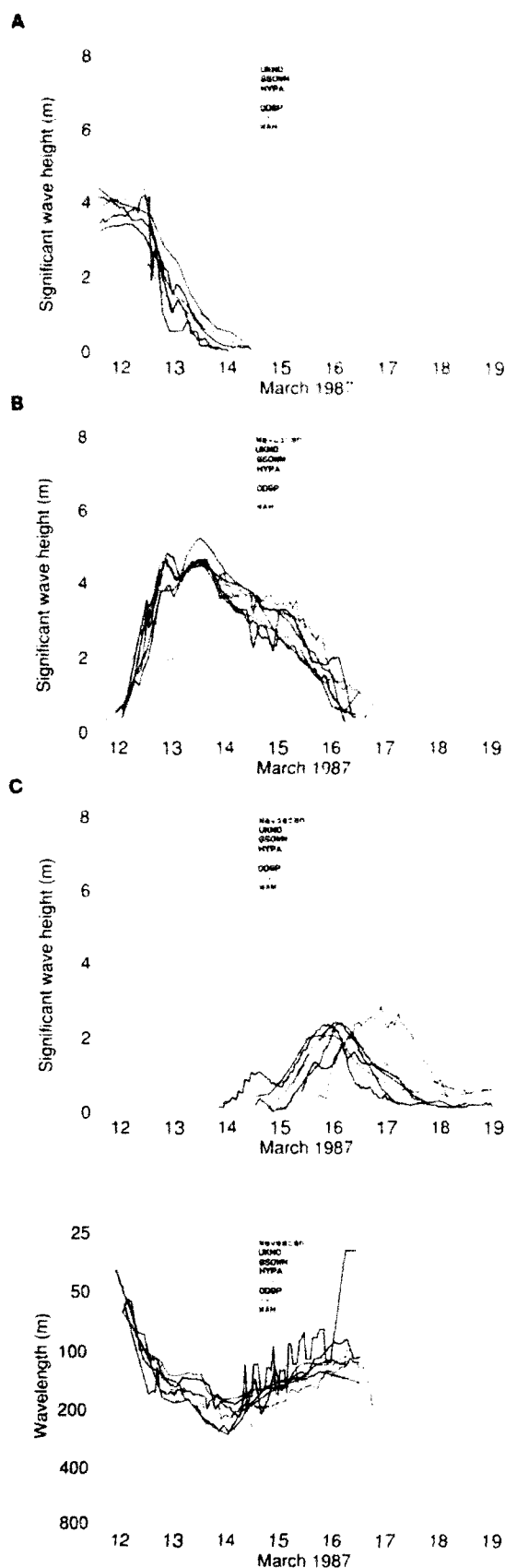


Figure 9. Wave system 2 peak frequency for ODP, WAM, VAG, UKMO, and HYPA models, and also Wavescan buoy at 50°N, 45°W.

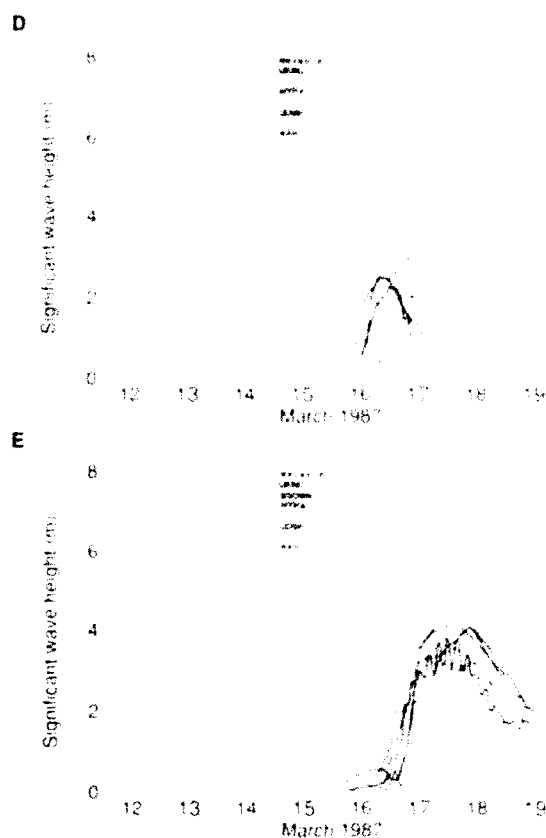


Figure 8A-E. Partitioned significant wave heights for ODP, WAM, VAG, UKMO, HYPA, GSOWM, NOAA, and Wavescan at 50°N, 45°W. Wave systems 1 through 5 are displayed in Figs. A through E, respectively.

aspect of the wind field is in error, since the VAG spectra agree well with the buoy over this period. This situation at 0000 UT on 14 March represents one of the major discrepancies among models occurring in 11-WLX.

The northerlies from system 3 result when the low that caused system 2 dissipates and becomes approximately centered midway between the *Tydemian* and the *Quest* at 47.5°W (see Fig. 7D). The northerlies on the western side of the low build, creating a northerly wave system at the *Quest* and a north-northwesterly wave system at the *Tydemian*. However, the local wind at the *Tydemian* remains southerly throughout this period. It is obvious from Figure 8C that the models agree better with each other than with the Wavescan buoy, which shows a similar wave system but one that lags by about 12 to 24 h and is of longer duration than the models. This discrep-

ancy is probably caused by errors in the location of the generating winds north of the measurement sites, since there are very few measurements in this region. A re-hindcast of the LEWEX wind field based on the spectral signature of this wave system was only partially successful in removing this lag (Cardone, this volume, Fig. 8).

Figure 8C shows subtle differences in model behavior also. The VAG and WAM models show nearly the same timing and rate of increase of wave energy, although WAM shows a more rapid decay. The UKMO model shows nearly the same rate of increase, but the increase occurs about 3 h prior to either WAM or VAG, with a north-northeast component present near 0000 UT on 15 March not seen in the other models. The rate of increase for ODGP is similar to the previously mentioned models but lags them by 6 to 9 h. The ODGP and UKMO models also exhibit a more rapid decay than WAM or VAG. The outlier among the models is NOAA, exhibiting both a slower rise and slower decay. The maximum development for NOAA is 1.75 m, lower than the approximately 2.25 m shared by the other models, and the 2.5 m measured by Wavescan. Energy in the second- and third-generation models (except UKMO) persists longer than in ODGP, showing a residual 0.5-m SWH well into 19 March.

Meanwhile, another cyclonic feature that first affected the wind fields on 13 March, visible in Figures 7B-G, builds to the southwest of the ship locations. It intensifies until about 0000 UT on 16 March, still well to the southwest of the ship locations. From this time on, it is the dominant feature in the region, and systems 4 and 5 are both traceable to it.

System 4 (Fig. 8D) represents a northeasterly wind sea that commences in the model hindcasts at about 1200 UT on 16 March (see Fig. 7F) and rapidly evolves with the movement of the low to a southeasterly sea by about 0300 UT on 17 March (see Fig. 7G). The LEWEX winds show a 90° shift over the 12-h period beginning at 0300 UT on 16 March. During this same period, the Wavescan shows an even larger shift of about 150°. The wind speeds and directions approximately agree over this period, but the Wavescan shows virtually no easterly waves prior to 0000 UT on 17 March, whereas all the models (except NOAA and GSOWM) show development of a nearly 3-m SWH. The Wavescan system 4 does show a 2-m southwesterly development at about 1200 UT on 17 March, which lags the models by about 6 to 12 h, and persists until 18 March. The low weakens and stalls well to the south of the *Tydemar*, and for the rest of the experiment only the residual southwesterly swell of system 5 remains.

System 5 (Fig. 8E) represents southwesterly swell that arrives at the *Tydemar* at about 2200 UT on 17 March according to the Wavescan but much earlier in all the models. From Figure 8E, the modeled swell appears to lead the measured swell by about 18 h. The ODGP model shows a maximum development that exceeds the other models and the buoy by nearly 1-m SWH; NOAA and GSOWM (not shown) both agree with ODGP. The UKMO model shows a chaotic behavior near its maximum value. An examination of Geosat wind speed data (see Dobson and Chaykovsky, this volume, for a description of

the available Geosat data) shows that wind speeds of the low-pressure system causing this swell may have been overestimated in the period prior to about 0600 UT on 16 March and underestimated subsequently. In Figure 7E in particular, the LEWEX winds exceed the Geosat winds by about 5 m/s along the Geosat pass. In Figure 7F, however, Geosat-measured winds exceeded 25 m/s when the corresponding LEWEX-modeled winds were only 10 to 15 m/s. If the winds actually peaked later than modeled, then swell would appear to arrive early in the models. Cardone (this volume, Fig. 8) shows a more recent hindcast that produces a later swell arrival time in the ODGP model, but still not in agreement with the Wavescan data.

AVERAGED PARAMETERS

Figure 10 shows the evolution of the average frequency f_m and direction θ_m computed for each WAM spectrum. Like SWH, these are commonly reported quantities computed as averages weighted by the spectral density:

$$f_m = \frac{\int_{f_{min}}^{f_{max}} S(f, \theta) f^2 df d\theta}{\int_{f_{min}}^{f_{max}} S(f, \theta) df d\theta},$$

$$\theta_m = \arg \int_{f_{min}}^{f_{max}} S(f, \theta) e^{i\theta} f df d\theta.$$

These quantities are simpler to compute than the partitioned quantities of Figures 6 and 8 but are more difficult to interpret for a multimodal spectrum. Spectra computed during 16 March are trimodal at times, so the average direction is meaningless. The situation occurring just prior to 0000 UT on 13 March is also difficult to interpret, since it represents a combination of a swell system with an orthogonal wind sea.

An averaged direction can also be computed for each individual wave system. In this case, f_m , θ_m are computed in the same way as previously described, except that f and θ range over the portion of the spectrum estimated to be most attributable to the wave system under consideration. Figure 11 shows the evolution of these parameters for UKMO, with coloring consistent with that

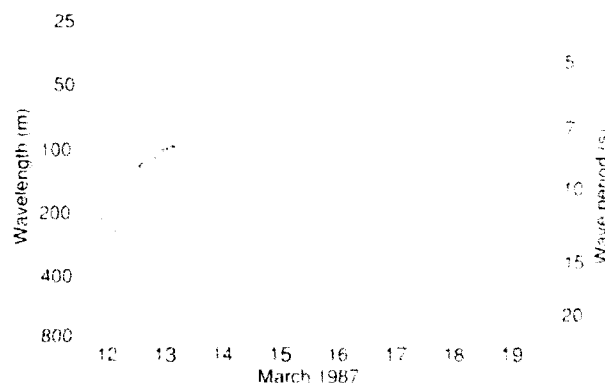


Figure 10. Time evolution of the average frequency and direction for WAM at 50°N, 45°W

in Figure 4B. The evolution of these parameters (f_{av} , θ_{av}) is more continuous than those plotted in Figure 4B, and, for many intervals, they provide a meaningful basis for comparisons. Also apparent in Figure 11 is the chaotic nature of the south-southwest swell present in UKMO starting on 17 March. This dichotomous behavior, the cause of which is unknown, is also seen in the total SWH of Figure 2. Finally, a deficiency of the partitioning method is apparent in Figure 11 between 1200 UT and 2300 UT on 12 March. During this time, wave system 1 begins to take on the characteristics of wave system 2 simply because they overlap, and wave system 2 does not manifest a separate peak. In this region, the separate wave systems are not well defined, and the reduced parameters should be interpreted with caution.

CONCLUSIONS

This article has focused on detailed comparisons of eight numerical models with the Wavescan buoy at 50°N, 45°W during the LEWEX experiment. Although first-, second-, and third-generation models are considered, the differences do not follow "generational" lines. With the data sets analyzed in this article, many model-buoy differences probably could be reconciled with a different, presumably "more correct" wind field. For example, the north-northwest swell (system 3) in all the models preceded that of Wavescan by about 18 h. Wind field errors may also be responsible for the lack of easterly waves in Wavescan relative to most of the models just before 0000 UT on 17 March and for the early arrival of low-frequency southwest swell in all the models relative to Wavescan early on 17 March. In these situations, where the models were in agreement among themselves but differed substantially from the buoy, the wind field might be the source of the error, but to date, efforts to generate a corrected wind field have been only partially successful.

Notwithstanding uncertainties in the wind field, however, there are clearly a number of model discrepancies. The differences among models in partitioned SWH for system 2 between 1200 UT on 13 March and 1200 UT on 14 March probably result from differing directional relaxations in the models, possibly confounded with oth-

er effects such as wind sea to swell transition. The peak frequencies also vary widely during this period. A slightly different wind field for this locally generated feature might show WAM to be most consistent with the Wavescan, but a simulation using EXACT 81 may be necessary to rule out the possibility that WAM's behavior is not an artifact of the parameterization of the nonlinear interactions. Clear model differences also occur with the southwest swell (system 5) toward the end of the LEWEX time frame, where OMAF is higher by nearly 1-m SWH than the other models and exhibits an evolution of peak frequency quite different from WAM.

From a methodological point of view, the partitioning of the two-dimensional wave spectra permits natural comparisons between data sources in terms of each of the component wave systems. These comparisons are more revealing than those using averaged quantities such as total SWH since there are situations in LEWEX when the significant wave heights agree, but the directional spectra are very different. Also, each of the five LEWEX wave systems is tied to a distinct meteorological event. Partitioning reveals differences between these buoy and model wave systems that can be associated with the development of sparsely observed meteorological events. Since each generating region is spatially and temporally distinct, measures that average the entire directional spectrum mix this information. Such average measures are not useful for inferring corrections to the surface wind field to reconcile buoy and model estimates. Moreover, the data sources agree well on some systems but not on others.

Spectral partitioning does not mix the spectral information from the distinct events, so it could be useful in data assimilation schemes where the objective is to determine wind-field corrections from errors in modeled-versus-measured spectra. The partitioning method, since it does not mix spectral signatures of distinct meteorological events, will make better use of measured spectra than schemes that compare only the direction averaged over the entire spectrum. It may also represent, informally at least, a type of "sufficient statistic" that contains all the essential spectral information, but in a highly compressed form.

Finally, the maximum entropy method produces believable directional spectra for the Wavescan buoy. Every major feature in the buoy spectra had an analog in model-predicted spectra. Where differences existed, they were generally credible. Moreover, persistence of features in a series of spectra gives an informal idea of the significance of that feature and its variability, at least partially compensating for the lack of a variability estimate on any one spectrum.

REFERENCES

- ¹Bales, S. L., Beal, R. C., and Freeman, N. G., *The Lubricator for Extreme Waves Experiment (LEWEX) Science Plan*, March 9-27 (9 Mar 1987).
- ²Ganther, H., Rosenthal, W., Weare, J. J., Worthington, B. A., Hasselmann, K., et al., "A Hybrid Parametrical Wave Prediction Model," *J. Geophys. Res.*, **84** (1979).
- ³The SWAMP Group, Sea Wave Modelling Project (SWAMP), "An Intercomparison Study of Wind Wave Prediction Models, Part I: Principal Results and Conclusions," in *Ocean Wave Modelling*, Plenum Press, New York (1985).

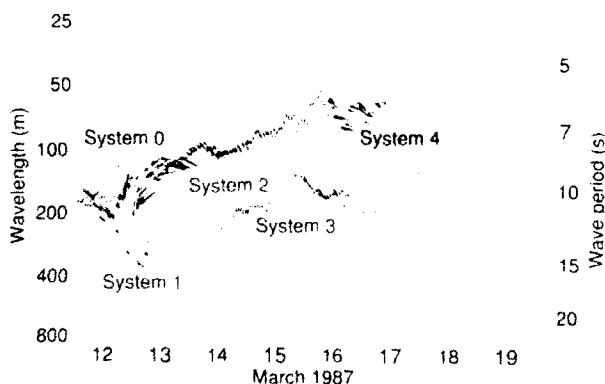


Figure 11. Partitioned average directions for the UKMO model at 50°N, 45°W.

- ⁴Gierling, T. W., "Common Processing and Display of EEWEX Directional Ocean Wave Spectra: Estimates from 12 March through 19 March 1987," IHO/APL/SIR890-011 (1989).
- ⁵Gierling, T. W., and R. C. Beal, "Dissection of Multimodal Directional Ocean Wave Spectra from EEWEX," in *Proc. ICOTSS*, Vancouver, Canada, 2311-2314 (1989).
- ⁶Snodgrass, F. E., Groves, G. W., Hasselmann, K. E., Miller, G. R., Munk, W. H. et al., "Propagation of Ocean Swell Across the Pacific," *Philos. Trans. Soc. London*, **4**, 259-431 (1966).
- ⁷Evers, A., and Kriststad, H. J., "Maximum Likelihood Estimation of the Direction Distribution of Ocean Wave Spectra," *J. Phys. Oceanogr.*, **16**, 2057-2059 (1986).
- ⁸Kriststad, H. J., *Wave Data collected by Wave and Particle Interferometer (Directional Wave Propagation) EEWEX*, Geophys. Inst. Univ. Oslo, Rep. 78-02 (October 1987) (Trondheim, Norway) (1987).
- ⁹Young, I. R., Hasselmann, S., and Hasselmann, K., "Computation of the Response of a Wave Spectrum to a Sudden Change in Wind Direction," *J. Phys. Oceanogr.*, **17**, 1317-1338 (1987).

FUTURE DIRECTIONS

*IN WHICH THE IMPLICATIONS OF LEWEX ARE
DEBATED, AND THE FUTURE ROLE OF WAVE
MODELING AND SATELLITE REMOTE SENSING IN
GLOBAL CLIMATE RESEARCH IS OUTLINED*

RESEARCH NEEDS FOR BETTER WAVE FORECASTING: LEWEX PANEL DISCUSSION

A panel discussion may not be the best forum to produce reasoned arguments and logical proofs, but it does promote spontaneous exchanges. Within the unguarded remarks and the generally loosely woven fabric of conversation among colleagues and friends is an outline of our perceived needs for research to promote better wave forecasting. The problems and research needs presented in this edited panel discussion have existed for many years, but adequate observations from satellites, thoughtful data assimilation schemes, and a better understanding of the underlying physics promise a new day for research in numerical wave forecasting.

M. Donelan

Opening Remarks

DONELAN: The two things that have struck me most about what we have learned in these past few days are that (1) one has to be very careful about understanding winds, and (2) it is apparent that all models do not have sufficiently good agreement that we can be complacent about our understanding of the modeling physics. I would like to ask each member of the panel to comment on how we should focus our attention in the near future to improve wave modeling.

LEZATY: The most important thing to me is the differences I have observed in the various experimental estimates of the wind fields. I am still wondering how we could more accurately take into account the real nature and variability of the wind. I would therefore like to put this question back to the modelers: How do you plan to better describe this wind variability in your models and demonstrate whether it can, in turn, improve the results?

BANNER: There are questions about the models. We need to consider the effect of waves on the drag coefficient and then feed that effect into the input source function. Proposed dissipation source functions need to be thoroughly tested, for example, with the extensive set of measurements proposed for SWADE [Surface Wave Dynamics Experiment; Donelan, 1987] in the winter of 1990-91. One could compare the model predictions with various asymptotic limits predicted for a fetch-limited situation.

HASSELMANN: In this symposium we have seen spectral intercomparisons among nine different models. We really do not have a basis for deciding which model is correct or where the model errors lie. I think the problem lies in the wind field. I think knowledge of the wind is necessary to tie down modeling inconsistencies. In SWADE, for example, that should be top priority. The LEWEX analysis, on its present level with these nine models, reminds me very much of the analysis we did with the SWAMP [Sea Wave Modeling Project] Group study [1985], where we had no measured winds at all. We just used several idealized wind field cases to find out how they were working differently. I think one can still do a very nice job in LEWEX on this aspect of the problem, but to assess the model performances in absolute terms may not be possible. My suggestion would be to go beyond the SWAMP level of analysis, look at the problem as a "joint" wave-model plus wind-field analysis problem, and try to do a data assimilation, or inverse modeling, to try to get the

Panelists

Mark Donelan	Canada Centre for Inland Waters
Chair	
Robert Lezaty	Institut Français de Recherche pour l'Exploration de la Mer
Michael Banner	University of New South Wales
Klaus Hasselmann	Max Planck Institut für Meteorologie
Peter Janssen	Royal Netherlands Meteorological Institute
Owen Phillips	The Johns Hopkins University
Fred Dobson	Bedford Institute of Oceanography

Participants

Willard Pierson	City College of New York
Sebastian Archer	Mitsui Limited
Roman Glazman	Jet Propulsion Laboratory
Kristina Katsaros	University of Washington
Gaspar Valenzuela	Naval Research Laboratory
Leo Holthuijsen	Delft University of Technology
Hisashi Mitsuyasu	Kyushu University
Dean Duffy	NASA Goddard Space Flight Center
Susan Bales	Office of the Chief of Naval Operations
Peter Kjeldsen	Mannetk A.S., Norway
James Brown	Admiralty Research Institute, Scotland
William Buckles	David W. Taylor Ship Research and Development Center
William Perrie	Bedford Institute of Oceanography
Robert Beal	IBM APL

best wind field to fit a given wave model, and then to examine the relation between wind field uncertainties and model uncertainties. That would be a new approach, at least from the point of view of modeling.

LEWEX has a very nice SAR [synthetic aperture radar] data set and a nice set of model results with buoy measurements. The LEWEX data set is unique for looking at the SAR wave spectrum and how to invert it. I am more optimistic that we can make progress there than in the identification of the model errors. If we want to understand the problems with the models and to improve the physics, we have to develop third-generation models further, because when we find a problem, for example, we can decide if it is the source

function and then fix it. If we have problems with a first- or second-generation model, we are always tinkering with the model results and not with the physics in the model.

JANSSEN: I agree with Mike [Banner] that it is really high time to look at the sea-state dependence of the wind stress. At ECMWF [European Centre for Medium-Range Weather Forecasts], we are attempting to couple the third-generation wam [Wave Model] with the ECMWF atmospheric model. We already have some encouraging initial results. They show that a young wind sea increases stress by 20% to 30%. When compared with the present wam, the increased stress will produce faster growth in the initial stages that might be fairly important. So there is a need to couple the planetary boundary layer model with wam. Second, there is a need for improved knowledge of wave energy dissipation from wave breaking. At the moment, we are using dissipation as a source term, which probably works very well for a wind sea. But we are not certain, when we have complicated wind sea/swell cases, whether this formulation works.

I have two comments on the LEWIS intercomparisons. LEWIS presents a unique opportunity: we are comparing two-dimensional spectra, both measured and modeled. However, it is not clear that the differences are statistically significant. I have not seen any error bars. People are identifying peaks and directions, but probably the number of degrees of freedom in those peaks is so small that I really doubt the differences are significant. Second, I have the impression, looking at the measured spectra, that we should compare only mean parameters, such as mean wave height, mean direction, and mean angular spread.

PHILLIPS: I think this has been a fascinating meeting, and some most remarkable results have been presented. There is a lot about the results that both confuses, as Klaus [Hasselmann] said, and also stimulates. We have a set of models that sometimes produces results that are consistent among themselves, but are very different from what a buoy seems to produce. Sometimes there is no agreement even among models. How then do we decide?

It is clear that we need to improve the connection between the modeling and the observation. Is the wind field the problem? That seems to be the thing that we blame, in the way that fluid mechanicians, if their theory and experiments do not agree, always blame turbulence. We can always blame the wind field because it is not right to start with. Have we used all the physics in the models that we need? I suspect there are a few little bits and pieces even in the third-generation models that are left out. Should one keep track of all the very-low-energy density levels in the ocean that may serve as a starting point for future instabilities? Presumably, that part of the physics is involved, but is it a part that we are going to keep track of? There are a lot of things we can do with the LEWIS data. There is a lot we can still learn from them.

DOBSON: My first comment is one that Bill Pierson will appreciate. I have now been to four conferences of this nature over the last five years, and at every one, the wind speed and the wind field were blamed for inconsistencies in model results. So nothing has changed. Having said that, from an experimentalist's point of view, what measurements might we consider over the next few years in order to fill some of the gaps that I see here?

The first one is a set of careful sea-state versus wind-stress intercomparisons, with microwave sensors present. Klaus will agree with me that that is absolutely crucial to the success of his highly optimistic plans for coupling wave models with atmospheric-oceanic numerical models in the hope of

understanding the air-sea fluxes. At the moment, he is saying his wave model does not really understand the drag coefficient, but he is also saying that he will be using his wave model to calculate the drag coefficient over the entire globe in order to learn something about the air-sea fluxes. So I see an inconsistency there, and such measurements might get around that problem.

I see a need for some young wave measurements of the input source function and some detailed quantitative optical microwave hydrodynamic field determinations of wave dissipation as well. In particular, for the LEWIS intercomparison, the models should not only have used the same wind field, they should also have used the same wind scaling. I do not think all of them did.

The second thing that really struck me forcefully about this intercomparison was that the buoy measurements, and maybe the sak measurements too, were woefully inadequate for the job at hand. They did not define the wave field sufficiently for anything to be said about how good the models were, in my estimation. Whoever designs the next wind-wave experiment has to think hard about an adequate measurement strategy. I have to say the same thing about the wind measurements.

DOBSON: From the preceding comments, it seems to me that a few things emerge as representing a quite clear consensus. I vote with the six panel members who insist that source functions need to be improved. Everyone agrees that the wind measurements need to be more carefully dealt with. These seem to be the two issues that are the crux of the matter. There is, of course, a need for much better measurements of waves, as well as of the wind. Klaus has pointed out that the sak may be a good candidate to measure the waves. Other microwave sensors may be also.

The point has been made, principally by Klaus, that third-generation wave models are needed to test the physics. In other words, the model has to be structurally correct before one can hope to use it as a tool to determine where the physics may be in short supply.

Peter [Janssen] raised the issue of statistical tests, which in my view is one of the things that emerges most clearly from intercomparisons of this sort. We do not really have the necessary structure to say what is correct and what is not, or how well one estimate compares with another, although Tom Gerling [this volume] has made some strides in the right direction. We need a consistent set of statistical criteria that everyone agrees on.

Wind Measurements

PIERSON: I have been interested in measurements of the wind for a very long time, even before Skylab and Seasat, when problems of validating the winds recovered by a scatterometer by means of conventional data first came up. It is impossible to get a decent 10- or 20-minute average from a conventional ship anemometer. Most observers are so poorly trained that they often cannot even obtain true wind from relative wind. Most modern ships have microprocessors that could keep a running account of the wind speed and direction, just as if the ships were data buoys. Large improvements could be made, just by automating the present ship observations. The poorest parameter in a conventional ship report is the wind data, but it may be the easiest to correct.

My second point is the propagation of swell. From what I have seen of the various second- and third-generation models, I think many of them do not propagate swell correctly. Wave propagation is equally important in areas of wave generation, so that many of the discrepancies found

by Gerling [for example, the tendency for all models to predict the arrival of swell earlier than it was actually measured] may be partially explained by this error. If swell arrives too soon, then it also left the area where it was generated too soon. The waves in the areas of wave generation diminish too soon when the wind dies down. For validating forecasts of sea plus swell with frequency spectra off the west coast of any continent, I think that within one winter, from the data, it will be clear that WAM is not doing it right. You might look at techniques used in the first-generation sowm [Spectral Ocean Wave Model; Pierson, 1982]. Great circle propagation on a sphere is not difficult. The envelope of each spectral component should be translated at its group velocity each time step, with no change in form. [For this problem, Lagrangian methods are superior to Eulerian methods.]

ARCHER: Regarding this problem of accurate wind measurements from ships, Peter K. Taylor of IOS [Institute for Oceanographic Science, Wormley, U.K.] has been working on it. The only way he has been able to get good wind measurements is with instruments mounted over the bow. They are now so equipping wmo [World Meteorological Organization] ships.

The Inversion Problem

PHILLIPS: I would like to suggest that an effort be made to use all the measurements during LEWEX that were gathered from the buoys, the aircraft overflights, and so forth. Each certainly has its own limitations, but surely they could be put together in some way to get an optimum estimate of the wave field. Each of those measurement devices has its own transfer function, and the spectra we see are the end result of those separate transformations. For example, there is a lot more information contained in the SCR [surface contour radar] spectrum, which could serve as a constraint on what you might call the "true" spectrum. Of course, the SCR has its own limitations, but all these sensors are supposed to be measuring roughly the same thing, even though each is reporting something different. It should be possible to produce an optimum estimate of the wave field, using all the information you have available. Such a goal is worth pursuing.

HASSELMANN: If I understand Owen's [Phillips] comment correctly, it is the same question that I was asking about the inverse modeling problem: Can you get from the observed wave data and the observed wind data to an optimal estimate both of the wind and wave field simultaneously? I think you can solve that problem only if you have a wave model for a dynamic interpolation in space and time between the rather few-and-far-between measurements. At the same time, you need the wind input to whatever extent it is available. Then you try to find the best fit to all of the available data that is consistent with the dynamics of the wave model. I think if one tries to go through that exercise with the LEWEX data, one would learn a lot about the models and also about the ability to reconstruct wind and wave data simultaneously. This is the problem we will be facing very much in the future, when we begin to acquire global wind and wave data sets from satellites again. The LEWEX data set is a good opportunity to pick up that challenge, and to gain some experience in one's "backyard," with a smaller data set, over a reasonably well-defined area.

DOBSON: Just a brief addition to that, Klaus. I think that there is another part that needs attention. Of course we have to look at the inversion problem. But we must continue to cal-

ibrate the models we have in terms of the data from experiments that we think are good. For instance, the JONSWAP [Joint North Sea Wave Project] data set could be reanalyzed using some of the ideas that came out of Mark Donelan's Lake Ontario experiment, which, as Hans Graber of Woods Hole pointed out to me, allows one to reconstruct the wave direction at a given fetch, knowing the wind direction. Even though you did not have good directional spectra, you could still go back through those data and calibrate against the projection of the wind in the direction of the wave, instead of the wind itself. We need to have a consistent calibration for the model in terms of wind speed before we will progress on other fronts.

Wind Variability

GLAZMAN: A comment about wind variability. In both wave theory and measurements, it is common to use the *mean* wind velocity. However, the corresponding wave number [k] spectra for air motion are dominated by an inertial range that has the form $k^{-1/3}$ or even k^{-1} . The magnitude of this exponent is, in a certain sense, rather small, equivalent to a cascade pattern in the geometry of the wind field or in its temporal history. As a result, the averages are difficult to define; strictly speaking, a "representative" averaging period for the wind does not exist. An alternative approach to the specification of such multiscale fields is being developed, based on fractal and multiple fractal formalisms [Schertzer and Lovejoy, 1989]. This approach appears promising also because it gives an adequate characterization of the highly intermittent [gusty] field of air motion.

Open ocean waves are usually highly developed, whereas in LEWEX, one is often dealing with a rather poorly developed sea. The inverse wave age [ratio of wind velocity to wave phase velocity] is typically greater than one or two, or even three. As a result, there exists a significant portion of the wave spectrum where the energy flows to larger scales. This inverse energy cascade is, I think, important for wave modeling. Since the energy eventually must be dissipated somewhere, the inverse cascade necessitates alternative dissipation mechanisms effective at large scales. For example, one may consider large-scale internal waves or currents as a possible sink of wave energy.

PHILLIPS: Energy transfer to larger scales is already intrinsically in the third-generation model, in the wave-wave interaction calculations.

KATSAROS: I wonder what the wind variability might do to the wave field. The models perform so differently from the measurements. Could it be that these fluctuations in the wind generate something that interacts crosswise? Might there be some kind of extra dissipation or changes in the model assumptions that could come from these subscales that are not described in the wind field? Might there not be errors from the various grids that were used?

JANSSEN: Gustiness has an enormous effect on the growth of the waves, especially the longer waves, which are affected by a factor of 2 or 3. I have been looking only at the large-scale effect, but it is enormous.

PHILLIPS: Perhaps one should reexamine some of the older measurements on wave growth. After all, random functions that depend upon each other in an other-than-linear way are not going to be related according to their means. Perhaps instead of trying to express our models in terms of an average wind speed, we should use the cube root of the average cubed wind speed, or something like that, depending upon the physics that is involved. If we look more care-

fully at the physics, to find out what function of the wind speed is producing it, we might get a lot less scatter in some of our experimental plots.

JANSSEN: I think we can do that already. The usual wind growth curve is fairly nonlinear. So Gerbrand [Komen] and I have looked at the fluctuation in the spectrum with the proper probability distribution function. From that we can calculate the effect of nonlinearity.

Surface Currents

VALENZUELA: I think we do need better measurement of the wind field, but geostrophic currents may also be important. Local currents can focus and defocus waves. You may have to do a modeling of waves with and without currents. Converging wave rays do not necessarily identify the source location.

HASSELMANN: This is an issue also for SWADE. My view is that currents are not very important in the ocean for most of the waves we are looking at, since we do not have a monochromatic wave field in the ocean but a continuous spectrum. I think a typical eddy current field will quasi-focus only small parts of the spectrum at a given time. The eddies just mix up the wave field, and, as we have a Gaussian wave field anyhow, they will not be noticed in a reasonably broadband measurement of the spectrum. Across a large shear zone like the Gulf Stream, they might be, but I would think that even there the eddies would not be very important. We are planning to do some experiments with WAM, both with and without large eddies, to see what effect they have on the wave field. In JONSWAP, tidal currents of 1 m/s really had a negligible influence on the observed waves. But I agree it is certainly a question to look at.

HOLTHUIJSEN [added in proof]: Recently, in the fall of 1989, Hendrik Tolman and I transported waves across a ring and across a straight section model of the Gulf Stream, courtesy of Scott Glenn of Harvard, with a third-generation wave model that included all relevant wave-current interactions. The computed wave modulations were significant, sometimes creating a significant wave height enhanced from 8 to 10 m in the countercurrent part of a ring. The modulations, in general, were restricted to an area of about two ring diameters.

Friction Velocity

MITSUYASU: In this meeting, I was surprised to find rapid progress in measuring techniques, in analysis techniques, and also in numerical modeling. But I would like to stress the importance of fundamental studies. In my opinion, we have presently exhausted the stock of good results of fundamental studies. So we need again to accumulate good data. I would like to show one example.

These [see Fig. 1] are laboratory data on the growth rate of waves under wind action [Mitsuyasu and Honda, 1982, Fig. 15]. At first sight, the result appears to show a reliable relation between dimensionless growth rate of water waves and dimensionless friction velocity of wind. However, because the coordinates are logarithmic, there is actually large scatter in the data. The scatter is larger for waves containing a surfactant, that is, for waves with a smooth surface. These data were obtained from a very carefully controlled experiment. The friction velocity u_* is also measured very carefully. Therefore, there still remain problems in understanding even such a fundamental process.

PIERSON: The major difference between WAM and other models is that, in WAM, dimensionless variables have been pa-

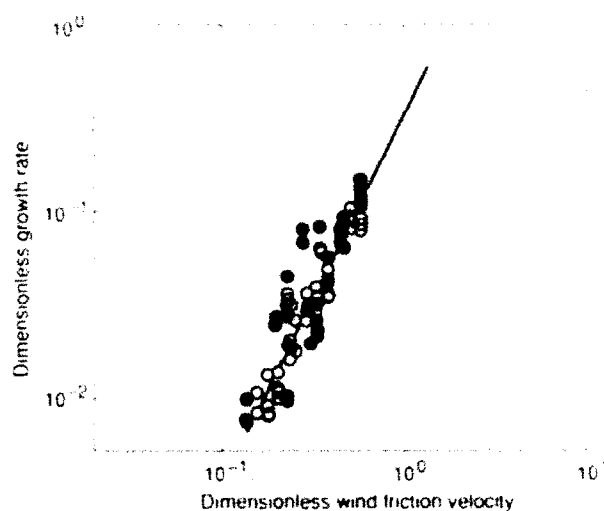


Figure 1. Dimensionless growth rate of waves as a function of wind friction velocity, both with surfactant (solid circles) and without surfactant (open circles) (Reprinted, with permission, from Mitsuyasu, H., and Honda, T., "Wind-Induced Growth of Water Waves," *J. Fluid Mech.* 123, p. 440, 1982 by Cambridge University Press.)

rameterized in terms of u_* instead of the mean wind at a 10-m height. This has a very important implication, having to do with the fully developed sea. The first important parameter from any model is the significant wave height for a fully developed sea. In the recent paper describing WAM [Wave Model Development and Implementation Group (WAMDIG), 1988], one can pick off the asymptotic value for large fetch and put that into the dimensionless energy. With a modest amount of algebra, one can get the significant wave height as a function of the 10-m wind. It turns out to be equal to a constant times the square of the 10-m wind, plus a second constant times the cube (Pierson, 1990). We have been working for many, many years with the concept that the significant wave height is proportional to the square of the 10-m wind. One could try to see which assumption looks better compared to the Ewing and Laing [1987] significant wave heights for a fully developed sea, expressed in terms of the 10-m wind. The WAM assumptions make quite a difference; for example, they drastically change the behavior of the first-generation GROWM [Global Spectral Ocean Wave Model]. The waves grow much more quickly at high winds. Up around 15 or 20 m/s, they are much higher than the square law would predict for the WAM drag coefficient. There is a spread of about 5 m in height for three or four of the most popular representations of the drag coefficient in the simple version, where drag coefficient is proportional to some constant plus a second constant times the 10-m wind. The crossover point is about 12 or 13 m/s. Below that, fully developed seas are lower, and above that they are higher. It might be worthwhile to check this discrepancy in as many ways as possible.

HASSELMANN: Both of the previous speakers have made very good points. First of all, what Professor Mitsuyasu was saying is very true. We are now discussing, for example for WAM, switching to a different input source function that has this u_*^2 dependence, based entirely on lab data. We really do not have in my view good convincing field data that would force us to switch, except for some secondary effects regarding the momentum transfer. But what really forces us to switch are these lab data, so I would very strong-

ly support the need to do more basic studies for the modeling. We cannot depend entirely on the field data; we are very much dependent on sorting out the different processes in the lab.

From the point of view of the amplitude, or peak frequency, you can live with the present source function of WAM or with the u_*^2 source function. It does not really make much difference, because the dissipation term can be tuned to get the same results. The main difference between the two source functions is in the momentum transfer, which depends more on the high frequencies. Again, I think we would not have been forced so strongly to consider changing our source function if we did not have these very good lab data.

To come to Bill Pierson's point, it is obviously very important whether we have a u_* or a U_{10} [wind speed at 10-m height] dependence in our source function if the drag coefficient is a function of wind speed. We looked at that question because we are aware, of course, that we would get much higher wave heights at the higher wind speeds than we had before. We talked to a lot of people. The general feeling was that it was okay to go to u_* , and we do indeed get the higher wave heights, but the data supported it. Because most people agreed, I myself was very comfortable just to relax and believe it. But if anybody wants to look at the data more closely and say that we should go back to U_{10} , we would immediately do it, because we really do not care, from the point of view of modeling. We simply put into the model whatever the latest theories on wave growth tell us. In summary, Bill, we did look at the data before we made that change. We were aware that it was an important change at high wind speeds.

PHILLIPS: Underscoring the importance of u_* versus U_{10} , although Professor Mitsuyasu did not mention it, the results he showed were plotted versus u_* , but the *mean* winds at a given value of u_* varied by a factor of 2, as I recall, between the absence or presence of a surfactant. Only when you use the u_* does the scatter collapse. The mean winds corresponding to a given u_* were very different in the two cases.

DOBSON: On Klaus's remarks, there are two important points. One of them is in the usage of the model going from U_{10} to u_* , which I understand Bill was talking about. The other is in the calibration of the model. Both are important; both matter in the final result. You say in the recent WAM paper [WAMDIG, 1988] that we should refer our results to u_* . People who calibrate your model use U_{10} . They have to use some drag coefficient to produce a result in u_* so that they can provide something for you to calibrate your model with.

PHILLIPS [with humor]: Sounds a bit circular to me.

JANSSEN: Regarding the u_* scaling, if you assume the Charnock relation for the roughness, you analyze the boundary layer, then you just end up with u_* scaling. There is no way around it.

DOBSON: That produces a number quite similar to all of the long-fetch U_{10} versus u_* relations if you use the Charnock relation. It does not reproduce the wave age dependence that people like Mark [Donelan] see.

JANSSEN: Oh, no. That is why we are looking at it now.

LEWEX Error Bars

DUFFY: I would like to turn back to an earlier point regarding verification of models and how we do that. Peter Jans-

sen made a comment about error bars, and I am curious if the panelists have some suggestions of how they might be established. In the atmospheric sciences we have fairly decent data over the continents. We can do things like errors, correlation coefficients, and so on. But the data that are around for wave model verification purposes do not seem to be accurate enough to do that. Are the panelists suggesting we might do some data impact studies, perhaps in the Southern Hemisphere, examining different types of data, trying to get an idea of how those data are handled in the models so that we can verify them?

HASSELMANN: I was not myself terribly concerned with this problem of error bars in LEWEX. I think all we have to do is put an error bar on the plot. We know how big it is for most of these spectra anyway. I did not understand Fred Dobson's comment earlier that the data were woefully inadequate to test the models, unless he was referring to a compass error of 30° or so, which occasionally appeared in one of the buoys. But apart from that, we have a fairly good idea of how good these maximum entropy techniques are for reproducing two-dimensional spectra. I had the impression, from the structure of the spectra that we saw, that they could be well reproduced by the maximum entropy techniques. In other more conventional spectra, it is just a question of the number of degrees of freedom. So I did not think it was important. Maybe I am confused there. It would be good practice obviously to put in the error bar so people know how many degrees of freedom you have. But in nearly all the LEWEX data, it really was not a big problem.

DOBSON: The only things I felt badly about were that there was only a single measurement at each ship and that there were big differences between the modeled and observed wave field at each ship. And I thought that these single measurements were inadequate to define the measured wave field. There were some excellent wave measurements from the NASA aircraft instruments. I only wish that there had been more.

DONELAN: This raises a more general question. Do we need some statistical structure different from the rather loose one we have now in order to compare models? And should a group like this try to develop that?

Ship As Wave Sensor

BALES: Perhaps the ship is the best wave sensor of all. Knowing the wave field, you can repeat over and over in a towing tank the ship responses, to say 10%, through about sea state 6. In Trondheim, Peter Kjeldsen is recreating the motions of the ship that were measured at sea, given his best estimate of the wave field. Owen Phillips suggested earlier that none of us would agree on which model is most correct. We might consider developing a standard set of ship response transfer functions that could be applied to all types of wave data.

DONELAN: Wouldn't the same thing be true of buoys? How does a ship differ from a buoy in that regard?

BALES: I do not think we have a good handle on the 6-degree-of-freedom motions in a buoy. Buoy manufacturers might disagree. There is a wealth of theory going back thirty years for predicting ship responses. It seems to work very well now, both in unidirectional and bidirectional seas.

HASSELMANN: I think many of you probably know that this idea was followed up by Tucker in his shipborne wave recorder. There is one problem: you can determine the ship

response given the wave field, but going back to the wave field from the ship motions is more complicated for a ship than it is for a buoy. That was the main reason that people switched to buoys and gave up the shipborne ocean wave recorder. I think Bill Pierson himself worked quite a bit with those data and was not too happy with them. My recollection was that the data were not as useful as one hoped they might be.

DONELAN [with humor]: Forgive me, Klaus, but I have the suspicion that getting from the ship motion to the wave field is probably no more difficult than getting from the SAR image to the wave field.

HASSELMANN: It is a question of the platform velocity. I know the velocity of a SAR. There is no captain out there fooling around.

PIERSON: The Tucker shipborne wave recorder works best when the ship is hove to, or progressing at perhaps a knot into head seas. There were problems in calibration with the Tucker recorder. The most fascinating thing ever done was to put the accelerometer on what we in the U.S. call a Ferris wheel and measure the acceleration. It worked surprisingly well at very low frequencies. The equilibrium spectral form, proposed by Pierson and Moskowitz, and which led to the *sowm*, was developed using these data. Also, you can control the vector velocity of the ship, change its heading every 10° in a steady sea, and get a long record. Then there is the horrible problem of matrix inversion to pull out the spectral components. You could not dream of trying it five years ago, but today you could do it.

Model Seeding Mechanisms

HOLTHUIJSEN: I have been puzzled that in *wam* there is no Phillips mechanism. I was not overly concerned until recently. In *wam*, it is not really a problem, because an initial spectrum starts off the model. But that initial spectrum has moved out of the model after a few days. If then the wind turns, there is nothing in the new wind direction to start the waves from. So you may have a much slower growth because the initial spectrum has moved out of the model, and there is no Phillips mechanism. I do not quite understand, if the computational effort is marginal, why we do not put that mechanism back into *wam*?

HASSELMANN: Maybe we could put that mechanism in as a trigger to get things going. I guess that is the point you are making. It is apparently a very small term if you just consider the measurements of pressure fluctuations in the atmospheric boundary layer and make a reasonable assumption on how they are distributed in the wave number domain. You require the spectral density of that wave number distribution on the dispersion curve. That triggers the growth, and you come up with a factor that is about 10^{-3} smaller than anything that you need in a model to get things going. So I really do not think it is a very important term. The mechanism is still extremely interesting, though, as a physical process. The reason it is small is because it goes as $(\rho_{\text{air}}/\rho_{\text{water}})^2$, rather than simply $(\rho_{\text{air}}/\rho_{\text{water}})$.

But I think Leo Holthuijsen's point was that one would like to have *something* to trigger the waves. He is quite right. The waves start off at very high frequencies. The way they start does not really matter very much, because the time it takes to grow through to equilibrium is short. So the model is not sensitive to how you seed the energy at high frequencies. But you do have to have the energy in there in the beginning. Because *wam* has a prognostic cutoff frequency of 0.4 Hz, we very often do not have any energy

there if we simply turn the wind. We have to wait until the energy diffuses through the nonlinear transfer, crossing into that part of the spectrum. That process is probably too slow, and we have been discussing whether maybe we should be putting in some seeding energy at high frequencies to get the thing going down there.

PHILLIPS: It is fairly unusual for the sea to be so calm that there is not half a centimeter of fairly low frequency oscillation sloshing around. That would serve as a seed at the low frequencies as well.

HASSELMANN: Well, I think there is some energy there, but it is probably just too weak, because the rms slope is small compared to what you need to get things going in the high frequency part. In other words, when the wind starts blowing from another direction, you start building up a short wind sea with rather high slope, and the nonlinear transfer can pick up pretty quickly from that and bring it in.

PHILLIPS: Yes, the nonlinear transfer will certainly do it, sooner or later. But I wonder whether in nature the wind input into those longer components is not building the energy up more rapidly.

HASSELMANN: Well, the wind input is in the wave model as well.

PHILLIPS: You have the Miles mechanism, which is building it up too?

HASSELMANN: Well, it is a hypothesis we have not tested, but we have the feeling that this high-frequency, low-background energy that is sloshing around in the ocean all the time, after the model has been spun up, may not be high enough to get the wave spectrum built up quickly enough when the wind turns suddenly. You may be right; if we actually look at the Miles mechanism more closely, it may be adequate, but I don't really think so. I should mention—we did not discuss it in this meeting—that we have been finding with one-year statistics of a quasi-operational forecast study that *wam* tends to be too slow in building up rapid events in the ocean. We have a number of different hypotheses as to what the cause of this could be. That is one of the hypotheses that we are considering. But we do not really know at this point what the answer will be.

DOBSON: I have listened to David Burridge from *ECMWF* talking about this same problem with storms, that is, that they are too slow to spin up in the *ECMWF* model. He had thought that it probably had to do with some feedback between the wave field and the wind field.

HOLTHUIJSEN [added in proof]: Van Vledder of Delft University recently [summer, 1989] did some tests with the personal computer version of *wam* with the Phillips mechanism added. He found only marginal effects on the wave growth in turning wind cases. Apparently, the nonlinear interactions provide enough "seeding."

Operational Significance

KJELDSEN: I have seen the *SAVO* portion of *ELWEN* grow from the first idea in 1984, under the leadership of Susan Bales and Warren Nethercote, as part of the *SAVO* Research Study Groups [RSG-1 and RSG-2]. Their main interest in *ELWEN* was as an experiment to both improve safety at sea and aid the efficient operation of vessels in high sea states. What you have seen at this symposium is only a small fragment of the work that actually has been done in the area of modeling, predicting, and applying directional wave spectra, that is, one sea trial consisting of five days of data acquisi-

tion in relatively low sea states. A statistical approach to use all sensors simultaneously—airborne, shipborne, and *in situ* wave sensors—has been proposed, wherein each sensor is assigned a weight, which is computed after an assessment of errors based on statistical comparisons with a common key sensor. A more complete account of the RSG-1 is available as a NATO publication [RSG-1 report, 1991].

If wave forecasts are to become practical operationally, I see no way to avoid developing a nonlinear algorithm for wave-current interactions. As a portion of LEWEX, directional spectra were measured in a strong current shear between the Labrador Current and the Gulf Stream. A freak wave was also measured in this area, close to a busy ship route [Kjeldsen, 1989]. The effect of meandering on the directional spectra is pronounced [Saeveraas et al., 1988]. The rms crest-front steepness of the individual waves in the time series is well correlated with the moments derived from the wave spectra.

Wave forecasts and hindcasts have already been run, giving rms crest-front steepness as a new wave parameter. From here, the next step to prepare a forecast for plunging breaking waves is easy and already under preparation, based on data assimilation in real time from satellites, with current and wave data combined.

There is a need for improvement of *in situ* measurements. Within a recent Norwegian experiment in the North Sea, some wave buoys capsized in 11-m significant wave heights. In LEWEX some of the same buoys survived, but the measurement scatter among them, even in low sea states, is too high.

The directional pattern of gravity waves obtained recently in high sea states is different from the results obtained in low sea states during LEWEX. RSG-1 and RSG-2 have therefore put much more effort in sea trials that took place before and after LEWEX [see the articles by Nethercote and Kjeldsen in this issue]. During the transit of the *Tydeman* from Europe to Newfoundland just prior to LEWEX, DeLuis [1988] performed a hindcast with two wave models using UKMO [U.K. Meteorological Office] wind fields as input to both models. There was a discrepancy of 40% between these two models in their prediction of significant wave height during a severe gale in the North Atlantic. With access to several independently prepared national wave forecasts, there exists an opportunity to prepare a weighted forecast to be used for large-scale coordinated operations at sea, such as search and rescue. At present, a one-hundred-year design wave is prepared for the offshore industry, using a hindcast database from only one wave model. The use of a weighted hindcast would be a considerable improvement.

The few days of measurements taken during LEWEX do not provide an adequate basis for an assessment of wave models. Longer-term wave statistics based on full-scale measurements are needed to perform a complete scientific validation of wave models. SWADE can be an important milestone in this area. I agree with Susan Bales that we should develop a standard set of ship response transfer functions from the LEWEX data. Also, I would like to emphasize that we are interested in safety at sea, due to the many accidents we have had in Norway. Therefore, we are interested in the reliability of the wave forecast. In such an evaluation, a long-term study would reduce the discrepancies among the various models that were evaluated in LEWEX.

BROWN: As Peter Kjeldsen has said, we clearly need better data in large sea states. The topics of this symposium include measuring, modeling, predicting, and applying. Most of the emphasis so far has been on the measuring, modeling, and

predicting, and very little on the application. I would like to request, on behalf of the ship designers, that more consideration be given to the very narrow band of wavelengths required for ship design, normally in the range of 50 to 150 m.

Extreme Waves

DONELAN: Since two ship people have raised points of this sort, I would like to mention something that struck me this morning. Earlier in the week, we talked about various aspects of the physics that seem to be in short supply. During Mr. Buckley's presentation, I was struck by another thing that seems to me a little surprising. I wonder what the theoreticians in particular think about it, that is, the appearance of these walls of water that are called "episodic waves" or "rogue waves." They appear—at least in the records that I have seen reported, and the ship people can correct me if I am wrong—to occur in only one size, the economy size, the really large size. Everything that we know about waves suggests that all of these things should be scaled, and so you should be able to see similar effects—although you would not notice them with the same degree of panic—on a very much smaller scale in a similar sea. Does that strike you as surprising? Does anyone want to comment on that?

BUCKLEY: We have something of a paradox here. First of all, I believe that as far as the mechanics of nonlinear, energy conserving waves is concerned, what Dr. Donelan suggests regarding the scaling of episodic waves is correct. But as far as observation at sea is concerned, I am not sure that such waves will be observed in smaller-scale seas. The reason for this is that I suspect the two types of episodic wave packets [i.e., "three sisters" and rogue waves] are nonlinear evolutions of the steep, long-crested wave [see Fig. 2]. Both the ship masters and Coast Guard officers whom I have interviewed indicated that this "parent" wave—most common of the episodic types—would be encountered only if a storm with central winds of at least 25 to 30 m/s was in the vicinity [ship masters' comments] or if waves at least 6 m high in a storm were being encountered [Coast Guard officers' comments]. If my conjecture is correct, these wave types will not be seen until the parent waves have been generated.

Given a seaway that is almost invariably short-crested, how do we end up with a single, huge, long-crested wave?



Figure 2. Example of an unusually large long-crested wave. (Reprinted with permission of the American Bureau of Shipping, *Surveyor*, May 1968, p. 23.)

The wave crest is perfectly straight. How does it grow from a group of short-crested waves to a huge, long-crested wave just breaking on the top? There must be a mechanism for that wave to acquire energy; otherwise, it would not grow laterally. There is apparently also a mechanism, and it is obvious in the photo [Fig. 2], for dissipating energy. Otherwise, a large, short-crested wave would result. Visual observations of these waves also suggest that they may be nondispersive, at least within an observer's field of view. The long-crested uniform height of the wave implies that it evolved over a fairly long time, not briefly as in the case of a typical short-crested wave. The governing equations must account for simultaneous acquisition and dissipation of energy, which is different from the usual modeling of conservative gravity waves.

Also, in some of the radar wave images from satellites, the waves are moderately long-crested, but every now and then some are inclined to the general wave direction at fairly sizable angles, perhaps 15° or 20° . Why?

HASSELMANN: If you watch from a plane flying over the ocean, you also see waves going at a different direction from what you expect. These can normally be explained away, by a theoretician at least, as being just random Gaussian fields that you would expect occasionally. But this freak wave that you described—have these waves really been recorded quantitatively so that you can get theoreticians upset, or are they just discussed in narratives?

BUCKLEY: There are several different types of storm-driven waves. So-called episodic waves are those that visually stand apart from the others in the sea. They are very clear, so that observers have absolutely no trouble telling you about them. You suggest they are part of a "random sea," but believe me, these waves stand apart. The type shown in the photo is the most common, as far as I know. Coast Guard officers characterized them as occurring every seventh or ninth large wave in a severe storm.

The other type are the so-called three sisters waves, a group of three waves that intervene in the seaway. Two Coast Guard officers told me you can see these waves coming at an angle of about 30° from the dominant wave direction, with a distinct intersection between this group of three and the other large waves in the sea. Waves of a similar character have been observed to evolve from steep, long-crested, regular waves as the result of nonlinear instabilities [see Fig. 19 in Su et al., 1982]. The intersection was described as "walking toward you." These waves coming in at an angle are also of an appreciably longer period than the others. Ship radars have tracked these wave groups approaching the observers.

PHILLIPS: There is a lot to learn about waves. It is not impossible that there are a few things of this kind still to be learned. After all, it was only twenty years ago that we first realized that a train of finite-amplitude waves was unstable. The Benjamin-Feir instability was discovered fairly recently. And there has been a lot of numerical work on the instability of periodic waves. I would not be a bit surprised if there is not some sort of "instability phenomenon," or maybe you can imagine something on a storm-size scale analogous to the wavemaker developed by Ken Melville [MIT] that changes its frequency. There may be some combination of winds that produces high-frequency waves, and then low-frequency waves that converge at one point to give you a couple of great big waves. The fact that it is long-crested suggests that it comes from a distance. It is not a random local superposition or anything like that. If it is a real phenomenon, it

is probably the result of something fairly distant that somehow accumulated in this particular area.

Implicitly, I believe in all of these things. I think they are very challenging to try to understand. We clearly do not understand them now.

HASSELMANN: Owen's description sounds highly speculative. Of course, we do not know what it is, so we just speculate. Let me speculate more conservatively. Maybe these freak waves do not presently come out of our models. But it is quite possible that if you take the small-scale gustiness of the wind into account—instead of having just the normal homogeneous Gaussian fields with a certain, maybe not very large, probability of something drastic happening on a smaller scale—you can get a modulation of that Gaussian field. You suddenly get a large local rms expectation value. Then maybe you could do something in the way of producing freak waves just by chance superposition. But that is just pure speculation.

In the present models, what Bill Pierson was referring to, and I think it is quite true, is that we have not really calibrated or tested the models with respect to the dissipation of swell over long distances. The reason we have not done that is that we do not have good data at this point. And, of course, Bill was also complaining about our dispersion of swell, which Liana Zambresky [this volume] showed in WAM, and we also saw in the NASA model of Dean Duffy [this volume], which does excessively spread the wave energies. On the other hand, I refrained from saying anything about your previous technique. Bill, because you were doing the "water sprinkler" technique, which we know is also not good. So what you really need is a model which has a linear dispersion as the waves propagate, and none of the present numerical schemes do that. On the other hand, looking at the errors that we have, we do not think this dispersion problem is a major one at this point. Otherwise, we would all be much more upset. It is very easy to quantify and understand. If you want to improve it, you just go to a higher-order scheme, if you think it is worth the effort. So I do not think it is a big problem to do that. But just to go back to what we used to use, the sort of pure Lagrangian propagation, with a little bit of jumping around from one grid point to another, does not have the right characteristics for a spreading, finite-bandwidth wave packet.

PIERSON [added in proof]: The water sprinkler technique for GSOWM did not originate with me. The method used in the SOWM can be easily applied to spherical coordinates. Waves do not diffuse, they disperse.

HOLTHUIJSEN: Van Vledder [1983] looked at the statistics of wave groups, and he *did* find that roughly every sixth or seventh is the highest wave. So there is observational evidence that every sixth or seventh wave is the highest.

PIERSON [added in proof]: Extreme waves are difficult to understand, but they have been modeled. Cummins [1962], Smith and Cummins [1964], and Davis and Zarnick [1964] created extremely high transient wave forms for the study of ship motions. Unfortunately, the analysis tools and theoretical concepts at that time were inadequate. These transient waves are very nonlinear, and these techniques do not appear to have been pursued by naval architects. Presently, two laboratories in Canada and one in the United States have produced extremely high breaking waves for various purposes, but most of their results are not yet available in the literature.

Closing Remarks

PERRIE: Do you think I can hope that all these LEWEX observations will be understood, so that if I change the wave model or introduce a new dissipation function, I can go back to this data set and check it with the buoy data and all the observations and be able to understand whether I have made an improvement or not?

What about the Geosat winds? I am very naive about how those are derived. Will they improve the wind field? What is the next step beyond this present comparison?

BEAL [added in proof]: The next step will be to produce a permanent record of the LEWEX intercomparisons, including accurate documentation of the measured and modeled spectra. But I really doubt that the LEWEX observations will ever allow one to choose unambiguously which model is superior. As Peter Kjeldsen has commented, a much longer database is required. Geosat passes during LEWEX are sparse, but should at least illustrate the spatial structure of the wind field errors.

DONELAN: That opens an opportunity for me to raise a question regarding the role of future remote sensing systems. How can the planned SIR-C SAR flight be coupled with the European ERS-1 scatterometer to improve our understanding of winds and waves over global scales?

JANSSEN: One could use the SIR-C SAR spectra in a wave assimilation scheme, supplemented by the winds derived from ERS-1, and show that they improve the wind analysis over the ocean. This improved wind analysis should, in turn, improve the wave field analysis.

DONELAN: This seems to be a good point to call it a day. I believe Bob Beal has some closing remarks. Does anyone on the panel have anything else?

PHILLIPS: I would like to thank Bob and the people who were responsible for the local arrangements. They have done a splendid job for all of us during these last three days.

BEAL: To the panelists and to the audience, I want to express my appreciation for your many insights and candid criticism. Your comments will be part of the record, and will certainly influence the way we handle the data and the way that we look at this problem in the years ahead. An important step, of course, will be to produce a written record of the LEWEX results that can be reviewed by the wave community. At the very least, LEWEX has stimulated many new ideas on how to conduct future open ocean experiments, such as SWADE, the ERS-1 validation and application efforts, and the SIR-C/ERS-1 wave intercomparison work. Perhaps the most valuable contribution of LEWEX will have been to serve as a unifying force to bring together those who predict and measure ocean waves with those who must live and operate in them.

On a personal level, I must say that much of the excitement of LEWEX has been its international aspect and the close relationships with colleagues that have developed and will surely endure well beyond this single experiment.

BIBLIOGRAPHY

- Cummins, W. E., "The Impulse Response Function and Ship Motions," *Schiffs- und Schiffbau*, 47, 101-109 (1962).
- Davis, M. C., and Zaruck, E. E., "Testing Ship Models in Transient Waves," in *5th Symp. on Naval Hydrodynamics, Ship Motions and Drag Reduction*, ACR-112, Office of Naval Research, Washington, D.C., pp. 509-540 (1964).
- Deluis, J. L., *LEWEX '87 Handcasting Experiment*, Preliminary Report, Programa de Clima Marino y Banco de Datos Oceanograficos, Madrid, Spain (1988).
- Donelan, M. A., *Surface Wave Dynamics Experiment (SWADE): Overview and Preliminary Plans*, National Water Research Institute, Canada Centre for Inland Waters, Burlington, Ontario (Jan 1987).
- Ewing, J. A., and Liang, A. K., "Directional Spectra of Seas Near Full Development," *J. Phys. Oceanogr.* 17, 1696-1706 (1987).
- Kjeldsen, S. P., "Current-Wave Interactions Observed in the Labrador Sea Extreme Waves Experiment," in *Proc. NATO Advanced Research Workshop on Water Wave Kinematics*, Molde, Norway (May 1989). [Available from Marintek A/S, Trondheim, Norway].
- Mitsuyasu, H., and Honda, T., "Wind-Induced Growth of Water Waves," *J. Fluid Mech.* 123, 425-442 (1982).
- Pierson, W. J., *The Spectral Ocean Wave Model (SOWM): a Northern Hemisphere Computer Model for Specifying and Forecasting Ocean Wave Spectra*, DTNSRDC-82-011, David W. Taylor Ship Research and Development Center, Carderock, Md. (1982).
- Pierson, W. J., "Dependence of Radar Backscatter on Environmental Parameters," in *Surface Waves and Fluxes: Current Theory and Remote Sensing*, Plant, W., and Geernaert, G., eds., Kluwer Academic Publishers, Dordrecht, The Netherlands, pp. 173-220 (1990).
- RSG-1 Final NATO Report on Full Scale Wave Measurements*, NATO Special Group of Experts on Naval Hydrodynamics, Defense Research Section, NATO Headquarters, 1110, Brussels (in press, 1991).
- Saeveraas, N., Kjeldsen, S. P., and Naerøy, A., *Report from the Court of Inquiry Made After Loss of M/S Sun Coast at Stad in Norway, 2nd December 1984*, Department of Justice (1988). [Available from Marintek A/S, Trondheim, Norway].
- Scherzer, D., and Lovejoy, S., "Generalized Scale Invariance and Multifractal Processes in the Atmosphere," *Pure Appl. Geophys.* 130, 57-81 (1989).
- Smith, W. E., and Cummins, W. E., "Force Pulse Testing of Ship Models," in *5th Symp. on Naval Hydrodynamics, Ship Motions and Drag Reduction*, ACR-112, Office of Naval Research, Washington, D.C., pp. 439-457 (1964).
- Su, M.-Y., Bergin, M., Marler, P., and Myrick, R., "Experiments on Nonlinear Instabilities and Evolution of Steep Gravity-Wave Trains," *J. Fluid Mech.* 124, 45-72 (1982).
- SWAMP Group, *Sea Wave Modeling Project (SWAMP): An Intercomparison Study of Wind-Wave Prediction Models, Part I: Principal Results and Conclusions, Ocean Wave Modeling*, Plenum Press, New York (1985).
- van Vledder, G. Ph., *Occurrence of Wave Groups in Seas and Swells*, R. 1983/6 'H, Delft University of Technology, Department of Civil Engineering (1983).
- WAMDIG (Wave Model Development and Implementation Group), "The WAM Model—A Third Generation Ocean Wave Prediction Model," *J. Phys. Oceanogr.* 18, 1775-1810 (1988).

EPILOGUE: WAVES, DREAMS, AND VISIONS

By Klaus Hasselmann

As a guest at this conference who has not been directly involved in LEWEX [Labrador Sea Extreme Waves Experiment], I can genuinely and convincingly extend my congratulations to all of its participants for carrying through this ambitious project so successfully. It has long been a goal of wave research to compare detailed *in situ* directional wave buoy measurements with various, potentially very powerful, remote sensing methods of measuring the two-dimensional wave spectrum, to make such measurements simultaneously at a sufficiently large number of stations to reconstruct the space-time history of the two-dimensional spectrum, and to combine all measurements in a comprehensive wave model intercomparison study. I think LEWEX is the first experiment that has really succeeded in bringing these three important aspects together. There is clearly still a long way to go to completely analyze all the many data sets and model simulations that have been presented at this meeting, but what we have already seen has been very impressive. The successful completion of the field exercise, and the collection and presentation of the extensive suite of *in situ* measurements, remote sensing data, and model hindcasts in a common format together represent major accomplishments. This well-organized analysis has provided a unique and impressive overview of the entire experiment and has set a clearly defined frame within which all participants will be able to interact effectively in their further in-depth investigations.

It is still too early to predict whether it will be possible to successfully disentangle the significant differences we have seen among the various model hindcasts, and whether one will succeed in attributing these differences uniquely to particular shortcomings in particular models. As often in the past, a major challenge will be to reconstruct the wind field with sufficient accuracy. Nevertheless, there is no doubt that this experiment has provided the best data set to date for testing two-dimensional wave models in real, complex wind situations, and one can safely predict that the experiment will generate many interesting new ideas and open up new avenues of research. Let me therefore extend my sincere congratulations to the entire LEWEX group.

I thought this might be a good excuse to indulge in some personal fantasies and visions, particularly about the future role of wave modeling in the evolving geosciences of the nineties. I have attempted this sometimes in the workshops of the WAM [Wave Model] Group. My inspired visions of the future were usually received with some bemusement, but only muted enthusiasm. However, I thought perhaps, in the pervasive atmosphere of

satiated contentment following this excellent banquet, that I could invite you to join me in a little speculative dreaming about where we may be going in future wave research.

Let me first summarize briefly what I think we have achieved in ocean wave modeling in the last forty years and explain then why I believe that wave modeling will play a completely different and far more central role in the geophysical sciences in the future.

There have been major landmarks in our understanding of wave dynamics and in the development of wave models since the pioneering paper of Sverdrup and Munk in 1947 [see the boxed insert for other landmark publications]. I need not dwell on the various stages of this development. But the development in our understanding of wave dynamics and our ability—or, more precisely, our belief in our ability—to model ocean waves have not always coincided.

Each landmark in wave research led to a significant increase in our understanding of wave dynamics. However, our confidence in our models suffered a severe setback in the early seventies. At this time we realized, through detailed field measurements, that the first-generation wave models developed in the sixties on the basis of the linear Phillips-Miles wave growth theories and Phillips's concept of a universal saturation spectrum were fundamentally incorrect. The growth of wind waves was found to be much more strongly controlled by the nonlinear transfer than we had hitherto believed.

The second-generation models that were introduced in the second half of the seventies to represent this revised spectral energy balance, then, essentially brought us right back, regarding the description of the wave field, to the original concepts of Sverdrup and Munk. The wind sea was again reduced to two characteristic parameters, the significant wave height and significant period, which could be represented as a function of a single parameter, the wave age. The dynamics were, of course, more sophisticated than in Sverdrup and Munk, in the sense that the evolution of these scale parameters was now determined by a transport equation. Also, the scale parameters were now used to define the full, two-dimensional windsea spectrum, and the swell was described independently by an additional arbitrary spectrum without any shape restrictions, as in a first-generation model.

In a talk I gave at a symposium to honor Walter Munk's sixty-fifth birthday in 1982 entitled "The Science and Art of Wave Prediction: An Ode to HO 601," I plotted the Sverdrup and Munk windsea data from their original report together with the JONSWAP [Joint North Sea Wave Project] data. The Hydrographic Office [HO 601] data were based almost entirely on visual observa-

Adapted from the LEWEX banquet address.

SOME LANDMARK PUBLICATIONS IN
WIND-WAVE MODELING

- Wave Heights and Period
- 1947 Sverdrup, H. U., and Munk, W. H., "Wind, Sea, and Swell. Theory of Relations for Forecasting," Hydrographic Office Publication No. 601, U.S. Naval Oceanographic Office, Washington, D.C.
- 1952 Bretschneider, C. L., "Revised Wave Forecasting Relations," in *Proc. 2nd Conf. Coastal Engineering*, Council of Wave Research, Engineering Foundation, Berkeley, Calif., pp. 1-5.
- Spectrum
- 1955 Pierson, W. J., Neumann, G., and James, R. W., *Practical Methods for Observing and Forecasting Ocean Waves by Means of Wave Spectra and Statistics*, U.S. Navy Hydrographic Office Publication No. 603, Washington, D.C.
- Dynamics
- 1957 Miles, J. W., "On the Generation of Surface Waves by Shear Flows," *J. Fluid Mech.* **3**, 185-204.
- 1957 Phillips, O. M., "On the Generation of Waves by Turbulent Wind," *J. Fluid Mech.* **2**, 417-445.
- 1958 Phillips, O. M., "The Equilibrium Range in the Spectrum of Wind-Generated Ocean Waves," *J. Fluid Mech.* **4**, 426-434.
- 1961 Hasselmann, K., "On the Non-Linear Energy Transfer in a Wave Spectrum," in *Ocean Wave Spectra*, Prentice-Hall, Englewood Cliffs, N.J., pp. 191-197.
- Transport Equation
- 1957 Gelc', R., Cazale, H., and Vassal, J., "Prevision de la houle, la méthode des densités spectroangulaires," *Extr. Bull. Inf. Com. Cent. Oceanogr. Etude Cotes* **9**, 416-431.
- First-Generation Models
- 1964 Pierson, W. J., and Moskowitz, L., "A Proposed Spectral Form for Fully Developed Wind Seas Based on the Similarity Theory of S. A. Kitaigorodskii," *J. Geophys. Res.* **69**, 5181-5190.
- 1967 Barnett, T. P., and Wilkerson, J. C., "On the Generation of Ocean Wind Waves as Inferred from Airborne Radar Measurements of Fetch-Limited Spectra," *J. Mar. Res.* **25**, 292-321.
- 1969 Ewing, J. A., "Some Measurements of the Directional Wave Spectrum," *J. Mar. Res.* **27**, 163-171.
- Joint North Sea Wave Project (JONSWAP)
- 1973 The JONSWAP Group, *Measurement of Wind Wave Growth and Swell Decay during the Joint North Sea Wave Project (JONSWAP)*, *Dtsch. Hydrogr. Z.* **12**, Suppl. A.
- Second-Generation Models
- 1976 Hasselmann, K., Ross, D. B., Muller, P., and Sell, W., "A Parametric Wave Prediction Model," *J. Phys. Oceanogr.* **6**, 200-228.
- Seasat
- 1982 Seasat Special Issue 1: Geophysical Evaluation, *J. Geophys. Res.* **87**, No. C5.
- 1983 Seasat Special Issue 2: Scientific Results, *J. Geophys. Res.* **88**, No. C3.
- Sea Wave Modeling Project (SWAMP)
- 1985 The SWAMP Group, *Sea Wave Modeling Project (SWAMP): An Intercomparison Study of Wind-Wave Prediction Models, Part 1: Principal Results and Conclusions*, *Ocean Wave Modeling*, Plenum Press.
- Third-Generation Models
- 1988 The WAMDI (Wave Model Development and Implementation) Group, "The WAM Model—A Third Generation Ocean Wave Prediction Model," *J. Geophys. Oceanogr.* **18**, 1775-1810.
- Labrador Sea Extreme Waves Experiment (LEWEX)
- 1991 Beal, R. C., ed., *Directional Ocean Wave Spectra*

tions from highly heterogeneous sources—including waves on the lake in Hyde Park and the observations of a ship's officer crossing the English Channel during D-Day—while the JONSWAP data were obtained under highly selective fetch-limited, uniform wind conditions using modern spectral wave instruments. Yet the agreement was astounding!

We have clearly still not entirely removed the art from wave prediction. However, today we have passed another significant landmark, the introduction of third-generation wave models following SWAMP [the Sea Wave

Modeling Project, 1979-81], and I believe we have now finally shifted the art to where it belongs—to the discussion of the source functions, rather than the manipulation of the spectrum itself.

In SWAMP, four first-generation and five second-generation models were intercompared. SWAMP clearly demonstrated that second-generation models, although representing a significant improvement over first-generation models, still suffered from basic shortcomings. The simplified parametrical description of the windsea spectrum was simply inadequate to treat the complex windsea

spectrum generated in more complicated real wind field situations. This motivated the WAM Group to develop a third-generation wave model in which the wave transport equation was integrated from first principles only, using prescribed source functions, without any additional assumptions regarding the shape of the resultant spectrum. After several years of joint efforts, an extensively tested and verified third-generation wave model is now available. We are thus finally in a position to seriously investigate competing hypotheses regarding the form of the input and dissipation source functions, and to compute the response of the wave field to extreme or unusual wind conditions, as documented in detailed field experiments such as JEWEL or the planned SWADE [Surface Wave Dynamics Experiment] project.

This development is particularly timely if I turn now to the tasks facing wave modelers in the future. For the scientist, the primary motivation for ocean wave research has undoubtedly always been its intellectual attraction as a field of fluid dynamics, which is both inherently complex and, at the same time, amenable to a certain level of rigorous mathematical-physical analysis. The support for research in this field, however, has traditionally been rooted in more mundane engineering and economic concerns: the great practical importance of wave forecasts or hindcasts for ship routing, offshore activities, coastal engineering, design criteria, risk assessment, accident investigations, and numerous other applications. Although these areas will continue to remain major drivers for wave research, particularly as the economical pressure to extend offshore activities into environmentally more hostile regions of the ocean increases, we may expect wave research and wave modeling in the future to assume a completely new role as an essential component of the expanding world climate research and global change programs (cf. Fig. 1). This will bring a new focus into wave research, with a much stronger emphasis on the symbiosis between basic wave research and wave modeling.

Ocean waves represent the interface between the ocean and the atmosphere, the two most important subsystems governing the dynamics of climate and global change. A realistic description of the physical processes occurring at the ocean-atmosphere interface is essential for a reliable determination of the air-sea fluxes of momentum, sensible and latent heat, CO_2 and other trace gases, and aerosols, which together determine the coupling between these two systems. We know that the wave field is intimately involved in these exchange processes, although this knowledge has yet to find its expression in most air-sea bulk formulae. In the future, wave models, therefore, will be needed to compute not only the wave spectrum itself, but also the processes at the air-sea interface that govern, in addition to the growth and the decay of the wave spectrum, the fluxes across the interface.

Third-generation wave models are an essential prerequisite for this task. We will need to look closely, for example, not only at the form of the high-frequency equilibrium spectrum, but also at the source functions determining this equilibrium, since these determine the momentum extracted from the atmosphere, the fraction

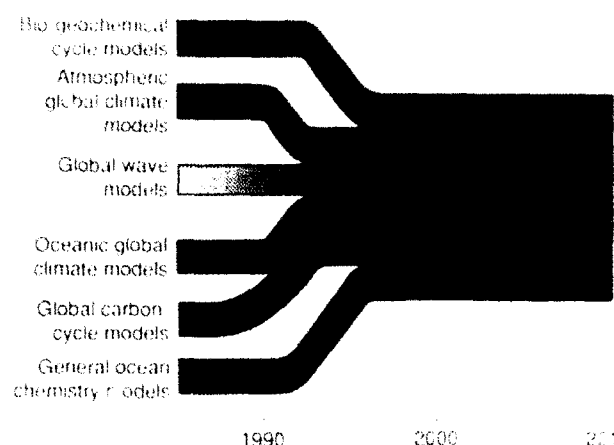


Figure 1. Future role of wave models as an essential coupling component for ocean-atmosphere-carbon-cycle models developed in the context of the World Climate and Global Change programs.

of the momentum flux transferred to currents, and the energy dissipation available for mixing. We are only just beginning to investigate these problems seriously.

Nobody has as yet attempted to couple an ocean model to an atmosphere model via an explicit model of the air-sea interface, that is, via a wave model. The coupling is still realized today using simple standard bulk formulae. Numerical climate simulation with coupled ocean-atmosphere models is a field that is still in its infancy, but one that can be expected to expand rapidly. Reasonably realistic global circulation models of both the ocean and the atmosphere now exist. The problem of model drift—the fact that the coupled system, when freed from the boundary conditions that constrain the individual subsystems in the uncoupled mode, slowly drifts into another, often unrealistic, equilibrium climate state—that has long plagued coupled model experiments, has now been largely resolved for response simulations by coupling the two systems through the flux anomalies rather than the net fluxes. Finally, the enhanced computer resources needed for coupled model experiments have now become available and will continue to be upgraded. In the next years, simulations of the coupled ocean-atmosphere system with high-resolution general-circulation models can be expected to yield a significantly better understanding—and, hopefully, useful predictions—of natural climate variability, such as the El Niño/Southern Oscillation phenomenon and decadal and century-scale climate variations. Still more importantly, they will provide an essential tool for the urgent task of assessing the time-dependent climate change induced by man's activities.

The problem of man's impact on climate will require coupled models, including not only the physical ocean-atmosphere system, but also the carbon cycle. Models of the carbon cycle based on realistic three-dimensional descriptions of the ocean and atmosphere circulation have now been developed, and it is, in principle, technically straightforward to combine such models

with coupled ocean-atmosphere models to predict the impact of CO₂ emissions on climate, taking into account all relevant feedbacks between variations in the ocean-atmosphere circulation and changes in the ocean-carbon constituents and the atmospheric CO₂ concentration.

As more experience with such coupled ocean-atmosphere and ocean-atmosphere-carbon-cycle models is gained, the details of the coupling at the air-sea interface will naturally begin to receive more attention. The need to introduce an explicit model of the interface, namely, a wave model, into coupled models may, in fact, arise sooner than some may anticipate. First experiments with coupled models have already clearly revealed the discrepancy between the relatively simple bulk formulae used to parameterize the fluxes across the air-sea interface in present atmospheric circulation models and the more sophisticated treatment of the dynamical processes at the air-sea interface commonly invoked in the interpretation of detailed field and laboratory experiments. Whereas the atmospheric circulation does not appear to be overly sensitive to the precise formulation of the air-sea transfer rates, the ocean circulation, carbon cycle, and surface wave field all respond strongly to small perturbations in these fluxes. A significant improvement of the present bulk flux parameterizations needed to drive these systems reliably can be achieved only by using a wave model with explicit, realistic representations of the dynamical source functions.

Technically, it is quite feasible to run an ocean wave model together with an atmospheric circulation model. This is indeed currently being pursued in several weather forecast centers. We can, therefore, expect future atmospheric circulation models to include wave models as a standard extension of their ocean boundary-layer packages, just as snow, soil moisture, and land vegetation must be included in a consistent treatment of the terrestrial boundary layer.

Looking farther down the road (cf. Fig. 1), coupled models will undoubtedly be extended within the context of the International Geosphere-Biosphere Programme and the activities of the World Climate and Global Change programs to include more sophisticated models of the hydrological and global biogeochemical cycles. But these models will still continue to be built on coupled ocean-atmosphere models as their core component, and the proper representation of the exchange processes at

the air-sea interface will continue to remain a high priority concern. Thus, the need to develop coupled ocean-atmosphere models, complete with a dynamical ocean wave interface model, applies not only for climate studies, but holds generally for the evolving Global Change programs.

Finally, ocean wave research and wave models also have an important role to play in the global observing system planned for the World Climate and Global Change programs. An essential component of this observing system is the measurement of ocean surface properties from space. However, the retrieval of geophysical parameters from many ocean satellite sensors—in particular, from all-weather microwave systems—depends critically on knowledge of the sea state and the associated dynamical processes at the sea surface that directly or indirectly affect the signals measured by these sensors. Reliable ocean wave models will therefore be needed in the future to routinely process ocean satellite data. For ERS-1 and ERS-2 [European Remote Sensing Satellites], an extensive program for the simultaneous analysis and assimilation of altimeter, scatterometer, and SAR [synthetic aperture radar] wave model data in near real time, using both atmospheric general circulation and global ocean wave models, is already being developed. In the long term, a comprehensive data analysis and processing system, combining data quality procedures, sensor algorithms, and data assimilation in a single processing suite, will need to be developed for all available ocean surface data.

From the global viewpoint, if mankind is to meet the challenge of understanding and managing the resources of the finite planet on which we all live, we will need to install and maintain a permanent global Earth observation system, consisting of space, land, and ocean segments, in conjunction with an operational data assimilation system based on sophisticated models to process the enormous data volumes continuously generated by such a system. Wave models will represent an important component in this model suite.

Thus, we may expect in the nineties an evolution of ocean wave studies from a discipline that has tended to live rather in the wings of traditional oceanographic and atmospheric scientific research, supported mainly by offshore, oceanic, and coastal engineering applications, to a pivotal discipline in the mainstream of Earth system science.

NOTES ON CONTRIBUTORS

Robert J. Bachman is an ocean engineer at the David Taylor Research Center, Bethesda, Md.

Susan L. Bales is the science advisor to the Chief of U.S. Naval Operations. She was previously involved in seakeeping and oceanographic research at the David Taylor Research Center, where she coordinated the NATO component of LEWEX.

Michael L. Banner is a professor in the Applied Mathematics Department in the School of Mathematics at the University of New South Wales, Sydney, Australia. His major research interests are in wind waves and air-sea interaction.

Robert C. Beal is a principal staff physicist at The Johns Hopkins University Applied Physics Laboratory, Laurel, Md., where he leads SAR ocean wave research efforts. He served as the LEWEX science coordinator.

A. S. (Pal) Bhogal is with the Canada Centre for Remote Sensing on contract from Intera Kenting, Ottawa, Canada. He is working on SAR oceanic remote sensing.

Claus Brüning is a research scientist at the Max-Planck-Institut für Meteorologie, Hamburg, Federal Republic of Germany. He has worked in the field of remote sensing, in particular on ocean wave imaging with synthetic aperture radars.

Vincent J. Cardone is the president of Oceanweather, Inc., a private wave forecasting company in Cos Cob, Conn.

Yung Y. Chao is an oceanographer at the National Meteorological Center, National Oceanic and Atmospheric Administration, Washington, D.C.

Stephen P. Chaykovsky is a student at The University of Maryland, College Park. He was a junior at Hammond High School when he collaborated on LEWEX.

R. Michael Clancy is head of the Ocean Models Division, Fleet Numerical Oceanography Center, Monterey, Calif.

Johan H. de Jong is head of the hydromechanics section of the Naval Engineering Department of the Royal Netherlands Navy, The Hague, The Netherlands.

Ella B. Dobson is a principal staff mathematician at The Johns Hopkins University Applied Physics Laboratory, Laurel, Md. She has conducted research on remote sensing of the atmosphere and oceans for most of her career.

Fred Dobson is a research scientist at the Canada Department of Fisheries and Oceans, Bedford Institute of Oceanography, Dartmouth, Nova Scotia. His specialty is ocean-atmosphere interactions on all scales from global to microscale.

Mark Donelan is a research scientist with Environment Canada at the Canada Centre for Inland Waters, Burlington, Ontario.

Dean G. Duffy is a research scientist in the Oceans/Atmospheres Branch of the NASA/Goddard Space Flight Center, Greenbelt, Md.

Dinorah C. Esteva is an oceanographer at the National Meteorological Center, National Oceanic and Atmospheric Administration, Washington, D.C.

Robert S. Ezraty is a project leader at Institut Français de Recherche pour l'Exploitation de la Mer, Brest, France. He has been involved with *in situ* measurements of wind and waves, and eagerly anticipates remote measurements from the European Remote Sensing Satellite Program.

Edward W. Foley is a hydrodynamic engineer at the David Taylor Research Center, Bethesda, Md.

Nelson G. Freeman is the senior advisor for strategic planning in the science sector of the Department of Fisheries and Oceans, Ottawa, Canada. He coordinated the Canadian participation in LEWEX.

Thomas W. Gerling is a mathematical scientist at The Johns Hopkins University Applied Physics Laboratory, Laurel, Md.

Anne Guillaume is a research engineer at the Météo France, Paris, where she has been in charge of the wave modeling activities since 1984.

Klaus Hasselmann is the director of the Max-Planck-Institut für Meteorologie, Hamburg, Federal Republic of Germany. His interests include climate dynamics and modeling, ocean wave research, and remote sensing of the sea surface.

Susanne Hasselmann is a research mathematician at the Max-Planck-Institut für Meteorologie, Hamburg, Federal Republic of Germany. She has developed the third-generation wave model WAM and is interested in wave dynamics and data assimilation.

Frederick C. Jackson is a research scientist at the Laboratory for Hydrospheric Processes, NASA/Goddard Space Flight Center, Greenbelt, Md.

Peter A. E. M. Janssen is a senior scientist in the Department of Oceanography, Royal Netherlands Meteorological Institute, De Bilt, The Netherlands.

J. Robert Keeley is chief of the Ocean Information and Systems Division at the Marine Environmental Data Service, Ottawa, Canada.

S. Peter Kjeldsen is a senior research engineer at Marintek A/S, Trondheim, Norway. In the later stages of LEWEX, he was chairman of the NATO Research Study Group on Full-Scale Wave Measurements.

Harald E. Krogstad is a research manager at SINTEF Industrial Mathematics. He is also a professor of industrial mathematics at the Norwegian Institute of Technology, University of Trondheim, Norway.

Warren C. E. Nethercote is the head of the Hydronautics Section at the Defence Research Establishment Atlantic, Dartmouth, Nova Scotia, and was chairman of NATO SGE(Hydro), RSG2.

William Perrie is a research scientist at the Bedford Institute of Oceanography, Dartmouth, Nova Scotia.

Owen M. Phillips is Decker Professor of science and engineering at The Johns Hopkins University, Baltimore, Md.

Willard J. Pierson, Jr. is professor of oceanography at the City University of New York Institute of Marine and Atmospheric Sciences, City College of New York.

R. Keith Raney is the chief radar scientist for the Canada Centre for Remote Sensing, Ottawa, Canada.

Kathy M. Rider was a research scientist in the Forecasting Products Branch, Meteorological Office, Bracknell, Berkshire, United Kingdom. She is now at the European Centre for Medium-Range Weather Forecasts, Reading, Berkshire, United Kingdom.

Wolfgang Rosenthal is head of the wave research group at Institut für Physik, GKSS Forschungszentrum, Geesthacht, Federal Republic of Germany. He is involved in the development of the HYPA wave model and the development of ship radar as a tool to measure surface waves.

Annegret Speidel is a graduate mathematics student at the Max-Planck-Institut für Meteorologie, Hamburg, Federal Republic of Germany. The work described in her paper is related to her diplom thesis.

Rachel A. Stratton is a research scientist in the Climate Research Division, Meteorological Office, Bracknell, Berkshire, United Kingdom. During LEWEX, she was in the Forecasting Products Branch.

David G. Tilley is a senior engineer at The Johns Hopkins University Applied Physics Laboratory, Laurel, Md. He has been performing analysis of SAR wave imagery since 1980.

Bechara Toulany is a research scientist at the Canada Department of Fisheries and Oceans, Bedford Institute of Oceanography, Dartmouth, Nova Scotia. He is an applied mathematician and numerical wave modeler.

Paris W. Vachon is a research scientist working on SAR problems at the Canada Centre for Remote Sensing, Ottawa, Canada.

Pieter Vermeij is a hydromechanic engineer in the Naval Engineering Department of the Royal Netherlands Navy, The Hague, The Netherlands.

Edward J. Walsh is a research scientist with the Laboratory for Hydrospheric Processes, NASA/Goddard Space Flight Center, Greenbelt, Md. He is currently on assignment at the NOAA Wave Propagation Laboratory, Boulder, Colo.

Paul A. Wittmann is a member of the Ocean Models Division, Fleet Numerical Oceanography Center, Monterey, Calif.

Liana F. Zambresky is an oceanographer at the U.S. Naval Postgraduate School, Monterey, Calif. During LEWEX, she was a visiting scientist at the European Centre for Medium-Range Weather Forecasts, Reading, Berkshire, United Kingdom.

Friedwart Ziemer is a scientist in the wave research group at GKSS Forschungszentrum, Geesthacht, Federal Republic of Germany.

LEWEX PARTICIPATING ORGANIZATIONS

Admiralty Research Establishment
Dunfermline, Fife, Scotland

Bassin d'Essais des Carnes
Paris, France

Bedford Institute of Oceanography
Dartmouth, Nova Scotia

Canada Centre for Remote Sensing
Ottawa, Ontario

Canal de Experiencias Hidrodinamicas
Madrid, Spain

Datawell
Haarlem, Netherlands

David Taylor Research Center
Bethesda, Maryland

Defence Research Establishment Atlantic
Dartmouth, Nova Scotia

Delft University of Technology
Delft, Netherlands

Department of Fisheries & Oceans
Ottawa, Ontario

European Centre for Medium-
Range Weather Forecasts
Reading, United Kingdom

Fleet Numerical Oceanography Center
Monterey, California

GKSS Institut für Physik
Geesthacht, Federal Republic of Germany

Institute for Marine Dynamics
St. John's, Newfoundland

The Johns Hopkins University
Applied Physics Laboratory
Laurel, Maryland

Klausdorfer
Keil, Federal Republic of Germany

MacLaren Plansearch, Ltd.
Halifax, Nova Scotia

Marine Environmental Data Service
Ottawa, Ontario

MARINTEK
Trondheim, Norway

Meteo-France
Paris, France

NASA/Goddard Space
Flight Center
Greenbelt, Maryland

Netherlands Ministry of Defense
The Hague, Netherlands

NOAA Ocean Products Center
Washington, D.C.

NORDCO, Ltd.
St. John's, Newfoundland

Norwegian Institute of Technology
Trondheim, Norway

OCEANOR
Trondheim, Norway

Oceanweather, Inc.
Cos Cob, Connecticut

Office of the Chief of Naval Operations
Alexandria, Virginia

Programa de Clima Maritimo
Madrid, Spain

U.K. Meteorological Office
Bracknell, United Kingdom

INDEX

Advection scheme, high order, in NASA wave model, 178
 aircraft remote sensors, temporal sampling during LEWEX, 8
 assimilation
 and inverse modeling, 196-198
 of wind fields, 31
 atmospheric instability in CASP, negligible effect of, 25
 Austri, Norwegian ship, damage to, 13
 averaged wave parameters, limitations of, 191
 azimuth wave number cutoff, in SAR imagery, 100

Bedford Institute of Oceanography, *see* BIO
 Benjamin-Feir instability, time scale of, 46
 bimodal seas, frequency of occurrence, 17
 BIO wave model, as WAM model modified for ice, 173
 bi-spectrum, as a measure of nonlinearity, 13
 Brunt-Väisälä frequency, 36
 buoy spectra
 resolution and reliability of, 67
 sampling variability of, 68
 buoys (*see also* specific type)
 maximum entropy estimate from, 67
 maximum likelihood estimates from, 66
 mean wave direction and angular spread from, 67
 spectral resolution, definition of, 68
 transfer functions of, 66

Canadian Atlantic Storms Program (CASP), 25
 cat's paws, 23
Challenger accident, impact on LEWEX of, 5
 coherence time, in SAR imagery, 99
 common wind fields
 compared to Geosat wind estimates, 188-189
 methods for deriving during LEWEX, 136
 Convair 580 aircraft
 as final catalyst for LEWEX, 5
 instruments on, 2
 role in LEWEX of, 104, 110

Directional ambiguity, removal of in SAR imagery, 102
 directional anisotropy, behavior beyond spectral peak, 44
 directional ocean wave spectra
 aircraft SAR, removing ambiguity in, 125-127
 and bending moments, 13
 and drag, 3
 and vessel fatigue, 13
 and vessel transfer functions, 2
 as an engineering tool, 13
 comparisons between Wavac buoy and ODGP model, 75

definition of, 40
 dependence on wave age of, 41
 dominant wave vectors from, 8
 effect of current shear on, 13
 effect of Doppler shifting on, 40
 effect of normalizing on interpretation of, 153
 Endeco vs five other sources at *Quest*, 78-79
 evolution during LEWEX, 8
 expanded in Fourier series, 66
 from 25 sources with common winds, 9
 from BIO hindcast, 173
 from BIO model, with and without ice, 175
 from marine radar on *Tydemar*, 82
 GSOWM vs WAM vs ship measurements, 149
 LEWEX, disparities in, 2
 modeling of, 16
 NASA vs WAM in turning winds, 181
 natural variability of, 11
 NOAA hindcast vs buoys, 165
 power law dependence of, 40
 reasons for diversity of, 30
 relation to frequency spectrum of, 40
 ROWS vs SCR, 92-95
 SAR vs Wavescan buoy, 125
 SCR vs ROWS overlays, 87-88
 simulation in model basins, 4
 spatial and temporal evolution of, 8
 specification of, 3
 UKMO vs WAM for turning wind field, 156
 WAM in three-hour intervals, 184
 WAM vs UKMO vs HYPA vs Wavescan, 186
 WAM vs VAG vs Wavescan, 183
 WAM vs Wavescan buoy, 171
 directional spread parameter, 13
 directional spreading function, definition and behavior at high wave numbers of, 41
 dispersion shell, and its role in marine radar wave analysis, 81
 dissection of wave vectors, in VAG model, 160-161
 dissipation
 in NASA wave model, 178-179
 in the VAG model, 158
 drag, as a dominant cause of wind stress, 24
 drag coefficient
 definition of, 23
 formulations from CASP, 26
 variation with wind speed of, 25
 vs wave age, 28
 dwell constant, in SAR imagery, 99

Earth Observation System, role in global change research of, 208
 eddies, along the Norwegian coast, 14
 empirical orthogonal functions, to describe wind field, 37
 Endeco Wavetrack buoy
 and possible bias from short wind

waves, 79
 deployment of, 76-77
 description of, 76
 episodic waves, *see* extreme waves
 equilibrium spectrum
 for deep water waves, 39
 form of, 39
 in hurricane, 39
 role of wave-wave interactions in, 3
 ERS-1
 effect of high range-to-velocity ratio in, 110
 role in global change research of, 208
 evolution of wave vectors, in VAG model, 160-161
 exposure time, in SAR imagery, 99
 extreme waves, 202-203

Fetch-limited growth
 effect of wave age on, 27
 in NASA wave model, 180
 flow separation, as an inadequate wave growth mechanism, 23, 24
 focus paradox, in SAR imagery, 101
 four-wave interactions, influence on spectral shape of, 46
 freak waves, 203
 frequency spectrum, relation to wave number spectrum of, 42
 friction velocity
 and relation to wind velocity, 23
 as a parameter to reduce scatter in wave growth, 199-200
 full-scale sea trials, difficulty of conducting, 17

Gander, as aircraft base for LEWEX, 5
 Geosat
 annually averaged wave height from, 5
 biases between LEWEX model winds and, 129, 132
 coverage during LEWEX of, 130
 evidence of wind field spatial structure from, 129-131
 role in LEWEX of, 128
 wind estimates, compared to LEWEX common wind fields, 188-189
 wind speed and wave height accuracies of, 129
 global change research, role of wave modeling in, 207-208
 global climate dynamics, dependence on air-sea coupling of, 2
 Global Spectral Ocean Wave Model, *see* GSOWM
 growth laws, as a function of wave age, 28
 GSOWM
 description of, 147
 vs WAM growth rates, 199

Hasselmann equation, for nonlinear energy transfer, adequacy of, 46
 Hasselmann nonlinear wave-wave interactions, 39
 height-to-velocity ratio, in CV-580 SAR,

effects of, 108
homogeneous wave field, definition of, 48

Ice

distribution and temporal evolution of during LEWEX, 173
effect of during LEWEX, 176
inhomogeneous wave field, and influence on energy transfer rate, 49
integration time, in SAR imagery, 99
inversion techniques, applied to LEWEX wind fields, 145
scattering of waves in, 173

Joint North Sea Wave Project (JONSWAP)

and agreement with earlier visual observations, 205-206
as a basis for the VAG model, 158
parametric models from, 25

Labrador Ice Margin Experiment, *see* LIMEX

Labrador Sea Extreme Waves Experiment, *see* LEWEX

Lake Ontario experiment, and benefits of wave age parameter, 25

LEWEX (*see also* individual instrument or model)

coordination with LIMEX, 5
error bars in, 200
highest waves recorded during, 5
interest groups in, 3, 4
lessons from, 11
model-predicted wave heights, 7
motivation for, 2
seakeeping trials, 15
sites with respect to US Navy wave model, 6
unique aspects of, 205
wind and wave conditions, 7

LIMEX, relation to LEWEX of, 5, 173
Longuet-Higgins method of buoy analysis, 72, 77

look-sum processing, in SAR imagery, 101

Marine boundary layer

characterization of, 22
from ships of opportunity, 30
non-uniform procedures to derive, 30
roughness of, 22

marine radar, as technique for eliminating spectral ambiguities, 80

marine radar spectra, comparison with Wavescan buoy spectra, 82

maximum entropy method, for buoy spectral estimates, 68-69

maximum likelihood method, advantages in multimodal seas, 73

mean square slope, in ROWS operation, 91

Miles mechanism, as a seeding mechanism in WAM, 201

model, *see* specific type

model basin results, 16

model errors, excess spatial diffusion from, 11

multimodal directional seas, generated in model basin, 16

multimodal seas

and strong currents, hazardous regions of, 15
definition of, 13

effect on ship operability of, 17, 18
effect on vessel resonances of, 16
influence on ship routing of, 64
ship heading to prevent capsizing in, 64

NASA third-generation model, description of, 178

NATO research study group (RSG)

charter of, 4

full-scale sea trials of, 5

goals of, 55, 61-62

significance of LEWEX to, 201-202

use of *Tydemar* and *Quest*, 4

NOAA ocean wave model, description of, 163

nonlinear energy transfer, time scales of, 46

nonlinear interactions

as a seeding mechanism in WAM, 201

as a wave generating mechanism, 23, 39

intractability of, 23

Ocean wave spectra, *see* directional ocean wave spectra

P-3 aircraft

availability of, 5

NASA, instruments on, 2

partitioning

of significant wave height for various models, 185-191

of wave systems, advantage for assimilation, 192

Phillips equilibrium spectrum, 39

Phillips mechanism, as seeding for WAM model, 201

Promess/Toscane I experiment, 34

Quality factor, relation to significant steepness of, 51

Quest

buoy deployment strategy during LEWEX, 77

Canadian research vessel, instruments on, 2, 56

performance in multimodal seas during LEWEX of, 55

Radar ocean wave spectrometer (ROWS) comparison with SCR, 95-96

data collected from during LEWEX,

summary of, 93

description of, 91

flight patterns and modes of operation in LEWEX of, 92-94

history of, 4

location of wave sources from, 97

slope distribution anisotropy from, 96

wave number spectra, computed noise

floor of, 95

wind speed estimates from, 93-96

Radarsat, relation to Labrador Ice Margin Experiment (LIMEX), 5

rogue waves, 202-203

ROWS, *see* radar ocean wave spectrometer

Safety at sea, as a goal of LEWEX, 202

safety of ships in high seas, 64

SAR, *see* synthetic aperture radar

satellite sensors, ocean, role in global

change research of, 208

satellite wave estimates, value of, 2

satellite wind estimates, value of, 2

scale distortion, in SAR imagery, 100

scatterometer

ERS 1, effect of spatial averaging of, 37

ERS 1, value of, 34

spaceborne, value of, 9, 32

SCR, *see* surface contour radar

sea loading, and ship performance during LEWEX, 57

Sea Wave Modeling Project (SWAMP)

as motivation to introduce third

generation wave models, 206

as test of nonlinear interactions, 25

relation to BIO wave model, 173

similarity to LEWEX of, 196

seakeeping trials

Quest, 55

Tydemar, 61

sensitivity coefficient, in ROWS modulation model, 91

shallow water intercomparison of models (SWIM), as test of nonlinear interactions, 25-28

shear-flow instability, as a wave generating mechanism, 23

ship motion

and ocean wave spectrum, 4

and ultimate stability, 64

nonlinear, 17

simulations of multimodal seas to determine, 64

ship operability, and response in multimodal seas, 13

ship reports, accuracy of, with and without anemometers, 31

Shuttle Imaging Radar experiment, as

predecessor to LEWEX, 4

significant wave height

BIO wave model, with and without ice, 174-175

disparity among estimates, 7, 183

GSOWM wave model, 148

inadequacy of, 13

NASA wave model, 181

NOAA wave model vs Wavescan buoy, 164

UKMO wave model driven with two wind fields, 154

UKMO wave model vs Wavec buoy for two wind fields, 155-156

VAG wave model, 159

WAM with LEWEX vs ECMWF wind fields, 170

Wavec buoy, 73

Wavetrack buoy vs Wavec buoy, 77

spectral comparisons, *see* directional ocean wave spectra

spectral energy density, definition of, 183

spectral moments, relation to crest front slope, 25

spectral stability, and its relation to spectral width, 50

spectral structure, primary and secondary in LEWEX, 187

spectral-sum processing, in SAR imagery, 100

spectral width, and relation to wave

steepness, 46

stability parameter, 35

Sun Coast, freighter disaster, 14

surface contour radar (SCR)

brief history of, 4

comparison with ROWS, 87-88

- data collection strategy during LEWEX from, 87
description of, 86
location of wave sources from, 89
SWAMP, *see* Sea Wave Modeling Project
swell
 early arrival of, 11
 sources of during LEWEX, 90, 97
SWIM, *see* Shallow Water Intercomparison of Models
synoptic scale wind, poor sampling of, 30
synthetic aperture radar (SAR)
 adequacy of quasi-linear approximation in, 124
 and evidence of null close to the range axis, 114
 argument for low R/V ratio and low off-nadir angle in, 115
 azimuthal cutoff factor in, 120
 azimuthal wave number response, effect of high R/V ratio on, 110
 azimuthal wave number response in, 110-111
 closed nonlinear spectral transform of, 119
 closed relation for surface wave to image spectrum from, 117
 coherent phase effects in MTF of, 113
 compared to SCR and ROWS spectra, 114
 corrections for finite aircraft velocity in, 100, 113
 distortion and azimuthal asymmetry in, 122, 123
 dynamic MTF correction in, 112
 effect of coherent and incoherent scene motion on, 98-100
 form of total MTF of, 119
 frozen surface (real aperture) contribution to MTF of, 118
 high and low altitude vs Wavescan buoy spectra, 106
 instrument transfer function, subtleties of, 4
 inverse MTF, two-dimensional form of, 115
 Monte Carlo simulations in, 117-122
 motion effects of, 119
 nonlinearities, methods of coping with, 117
 processing of aircraft, 105
 processing, radiometric aspects of, 99
 Seasat, 4
 spaceborne, for ice monitoring, 5
 spaceborne, to monitor wave vector evolution, 8
 spatial fidelity of, 99
 stationary MTF correction in, 112
 theoretical resolution limit of, 98
 value to ocean wave forecasting of, 117
 variation with platform velocity vector of, 108
 wave number response in LEWEX, 110
 wave number spectra, *see* directional ocean wave spectra
- T**aylor's hypothesis, 36
third-generation wave models
 advantage of, 196
 role in global change research of, 207
time scales, of spectral broadening compared to wind-wave growth, 51
Toscane 2 campaign, description of, 37
Toscane T campaign, 35
- Tucker shipborne wave recorder, 200-201
Tydeman and Quest
 availability of, 5
 buoy deployment and recovery limits of, 6
 instruments on, 2, 62
 motions in sea trials of, 16
 routes of, 5
- UKMO** wave model
 description of, 152
 effect of zero initial energy on, 153
unimodal sea state
 definition of, 13
 description of, 13
 inadequacy of, 13, 17, 59, 60, 64
- V**AG wave model
 description of, 158
 from Wavec buoy, 74
vector wave plots
 GSOWM vs WAM vs Wavec buoy, 150
 information from, 8
 WAM vs UKMO vs Wavescan buoy, 185
velocity bunching
 as source of SAR nonlinearities, 106
 effect of, 98-100
vessel motion
 in multimodal seas, 58
 safety factors in, 4
vessel transfer function
 and ocean wave spectrum, 4
 as method of obtaining spectral estimates, 200
- W**ADIC (Wave Direction Calibration) project, 69
WAM wave model
 description and history of, 167
 global version at ECMWF, 4
 previous verification of, 167
wave age parameter
 as a description of wind sea, 205
 definition of, 22
 in fully developed sea, 22
 in HEXOS (Humidity Exchange Over the Sea), 26
 in Lake Ontario and CASP experiments, 25
 in North Sea experiment, 26
wave breaking, and flow separation, 23
wave breaking criteria
 in NASA wave model, 179
 in WAM model, 197
wave-coherent pressure, definition on, 23
wave-current interaction
 importance for modeling of, 18
 importance for wave forecasting of, 202
wave development, fetch-limited, 24
wave energy vs fetch, from CASP, 27
wave energy vs wave age, from CASP, 27
wave field, coupling to wind field of, 201
wave forecasting errors, initial value problems leading to, 54
wave generation mechanisms, 23
wave group, relation of group length to spectral width, 46-51
wave growth rate
 and modeling errors, 3
 definition of, 23
 direct pressure measurements of, 24
 radar measurements of, 24
 square law dependence of, 24
wave height (see also significant wave height), mean squared, definition of, 41
wave modeling
 coupling to atmospheric models, 197
 brief history of, 205-206
 effect of surface currents on, 199
 future central role in geophysical sciences, 205
 future challenges for, 207
 major landmarks in, 206
 recommendations for improving, 196
wave modeling comparisons, need for statistical tests in, 197
wave models
 deficiencies in physics of, 197
 geographic grid areas of LEWEX, 152
 historical evolution of, 3
 need for young wave measurements in, 197
 need to better define wind fields for, 28
 participation in LEWEX, 3
 relative performance of, 3
 seeding mechanisms in, 201
wave phase velocity, effect on SAR imaging of, 98
wave predictions
 importance in ship safety of, 2
 value in ship guidance of, 2
wave refraction, and wave energy concentration, 13
wave vector plots, *see* vector wave plots
Wavec buoy
 description of, 72
 directional wave number estimates during LEWEX, 75
Wavescan buoy
 compared to VAG model for two wind fields, 161
 performance in WADIC, 70
Wavecraft buoy wave vector estimates, vs Wavescan buoy, 78
wind estimates, from VAG model, 159-160
wind field
 accuracy estimates during LEWEX, 143-144
 comparison of LEWEX, ECMWF, and ship reports, 167-170
 coupling to wave field of, 201
 effect of errors in, 8
 estimating spatial mean of, 34
 evolution during LEWEX, 138-142
 first-guess, 31
 fluctuations in, 34, 35, 37
 GSOWM estimates during LEWEX of, 148
 in LEWEX, accuracy of, 9
 kinematic analysis, specification and derivation of, 137
 LEWEX common, spatial variability of, 32
 LEWEX, controversies, 2
 LEWEX, variability of, 7
 smoothing, 31
 space-time continuity of, 34
 spatial average, choice of, 37
 spectrum, spectral gap in, 35
 spectrum, turbulent peak in, 35
 variability, effect on wave modeling of, 37

Index

- wind field fluctuations
 - along- and cross-wind, 35
 - effect of short averaging times in, 37
 - scales of variability in, 35
 - spectrum of, 35
 - time scale of, 37
- wind measurements, inadequacy of, 197-198
- wind stress
 - and wave age, 22, 196-197
 - effect of very young seas on, 24
- wind variability
 - and effect of gustiness on wave growth, 198-199
 - and fractals, 198
 - effects of land on, 31
 - effects of temporal sampling on, 31
- wind-wave coupling, weakness of, 22
- wind-wave modeling
 - initial value specification in, 30
 - tuning of, 30
- Z**akharov equation, as a starting point for random wave fields, 47